Modélisation numérique d'actionneurs plasma pour le contrôle d'écoulement

Konstantinos Kourtzanidis

Université de Toulouse

THÈSE

En vue de l'obtention du

DOCTORAT DE L'UNIVERSITÉ DE TOULOUSE

Délivré par : *l'Institut Supérieur de l'Aéronautique et de l'Espace (ISAE)*

Présentée et soutenue le *24/11/2014* **par :**

KONSTANTINOS KOURTZANIDIS

Modélisation numérique d'actionneurs plasma pour le contrôle d'écoulement

---

JURY

JEAN - PIERRE BOEUF	Directeur de thèse
FRANÇOIS ROGIER	Co-directeur de thèse
VINCENT GIOVANGIGLI	Rapporteur
KYROS YAKINTHOS	Rapporteur
JEAN LAROUR	Examinateur
OLIVIER PASCAL	Examinateur

École doctorale et spécialité :
AA : Dynamique des fluides et ingénierie des plasmas
Unité de Recherche :
ISAE-ONERA MOIS
Directeur(s) de Thèse :
Jean-Pierre Boeuf et *François Rogier*
Rapporteurs :
Vincent Giovangigli et *Kyros Yakinthos*

Abstract

As aerodynamic flow control still remains one of the top subjects of research in the aerospace scientific world, new ways to perform such a control are being constantly studied. Microwave plasma discharges have been proposed as a mean of a non-intrusive flow control method based on the creation of hot spots of air (via the creation of plasma discharges) which can eventually interact with the external flow and modify its attributes in a beneficial way to the aerodynamic coefficients of the body of interest. Moreover, other types of plasma actuators, based on the momentum addition in the flow instead of heat, have been proven capable of positively modifying the flow aerodynamic features. Nevertheless, the development and optimization of such actuators, require further understanding of the basic multi-scale physics involved. Experiments can provide such information, but they turn to be costly and incapable of capturing the complex interactions in small space and time scales. In this thesis, we are interested in the numerical modeling of plasma flow control actuators, in order to understand deeper their nature and applicability. Firstly, we present the theory behind aerodynamic flow control and plasma physics along with a literature review of the plasma actuators' physics, applicability and effects. Then, numerical simulations performed using adapted techniques for each different actuator, reveal interesting features of their physics and complex nature, on the way to a deeper understanding and possible optimization of their performance in aerodynamic flow control applications. Three types of plasma actuators are considered: Microwave Plasma Discharges (MPD), the Dielectric Barrier Discharge (DBD) and the Plasma Synthetic Jet (PSJ). Concerning microwave discharges, the objectives are more fundamental than the other types of actuators. Numerical simulations can provide the basic information on the physics and complex interaction between the EM waves the plasma and the gas, in order to understand the plasma creation, evolution and energy balance. Flow control applications of such discharges, as an energy deposition method, have been already quite well documented in the literature. In order to reduce the computational cost, a novel implicit coupling of the Maxwell equations with the momentum transfer equation for electrons has been developed which with the addition of a simplified model of plasma-fluid equations have enabled three-dimensional simulations in time domain. The microwave breakdown and evolution of the plasma due to the electromagnetic waves has been studied numerically, in order to quantify the energy absorbed by the plasma and transferred to neutral molecules as gas heating. Coupling of the EM-plasma model with an Euler

based solver accounting for real gas effects, have revealed interesting features of the complex interaction between the plasma itself and the pressure shock waves formed due to the intense gas heating during the plasma breakdown and evolution. Concerning the two other groups of actuators, the goals of this thesis is more applied as we are interested mostly on modeling their operation and consequent momentum production. For the PSJ actuator, the numerical solver consists of three coupled numerical models: One describing the plasma formation between both electrodes in an axisymmetrical configuration, one describing the electrical supply by an external generator, and a last one that focuses on the air's heating in the cylindrical cavity where the plasma is formed, and the actual operation of the actuator. It uses the energy distribution computed by the first sub-model as source term and calculates the jet's flow mass rate, momentum and energy, exiting the cavity at high speeds. An external CFD solver is used to integrate the calculated momentum source term into a global model of a flat plate flow, taking into account turbulent effects. Lastly, the DBD actuator model, developed in DTIM/ONERA, Toulouse, consists of solving the momentum equations for a set of simplified species and the Poisson's equation. The calculated body force produced by the DBD actuator is being compared with experimental results and the induced wall-jet flow due to this force is modeled in a CFD solver. A similar model developed in LAPLACE/UPS has been used to perform parametric studies on the influence of turbulence - studying different turbulent models in a RANS approach - as well as more applied simulations for flow control purposes, including laminar-turbulent transition over a flat plate and lift coefficient modification on an airfoil due to a leading edge DBD actuator. These studies offer new perspectives in the understanding and the optimization of plasma actuators for flow control purposes.

Résumé

Cette thèse porte sur une nouvelle approche pour le contrôle d'écoulement aérodynamique. Cette nouvelle approche est basée sur l'utilisation d'actionneurs plasma. La modélisation numérique peut être une outil puissante entre les mains des scientifiques et des ingénieurs pour comprendre, optimiser et ainsi ouvrir la voie à la commercialisation et l'application de cette technologie. Le couplage entre l'électromagnétisme, le plasma et l'écoulement, nécessite des modèles et des techniques numériques avancées. Le travail présenté dans cette thèse, a pour principaux objectifs : le développement et la validation de méthodes numériques pour simuler efficacement le fonctionnement de certains des plus importants types d'actionneurs plasma. Nous nous sommes intéressés à trois types d'actionneurs plasma : les décharges micro-ondes, la décharge à barrière diélectrique (DBD) et le jet synthétique plasma (JSP).

En ce qui concerne les décharges microondes, les objectifs sont plus fondamentaux que pour les autres types d'actionneurs. Il s'est agit de mieux comprendre la création du plasma, son évolution et de calculer l'efficacité énergétique de dispositifs microondes par la simulation numérique. Un schéma couplé implicite (ADI) - FDTD avec un modèle de plasma fluide simplifié est présenté. Cette formulation conserve la simplicité et la robustesse des systèmes de FDTD, tout en dépassant la barrière du critère de stabilité CFL. Elle conduit à un temps de calcul réduit et la possibilité de réaliser des simulations tridimensionnelles de la formation du plasma et de l'évolution d'un plasma dans un champ micro-ondes. Afin d'étudier l'énergie absorbée par le plasma et le transfert vers le gaz sous forme de chaleur ainsi que le changement consécutif de la densité du gaz, un solveur Euler a été couplé avec le modèle EM-plasma en tenant compte des effets de gaz réel. Diverses validations et applications sont ensuite étudiés. Des simulations tridimensionnelles de formation du plasma sont réalisée qui montrent la formation de structures dans une décharge micro-ondes librement localisée. Les effets de chauffage de gaz sur le développement d'un "streamer" et la durée d'un volume pré-ionisé avec des champs sous-critiques sont également calculés.

En ce qui concerne les deux autres groupes d'actionneurs, les objectifs de cette thèse se concentrent sur la modélisation de leur fonctionnement et sur la production d'écoulement qui en résulte. Le Jet Synthétique

Plasma a été numériquement étudié par trois modèles couplés. Les résultats obtenus sont prometteurs pour l'optimisation du JSP et une meilleure compréhension des mécanismes qui limitent ses performances. L'actionneur DBD a été modélisée en utilisant deux solveurs différents basés sur des modèles physiques similaires - celui développé à l'ONERA et l'autre à LAPLACE. Des études paramétriques ont montré que les modèles donnent une estimation assez précise de la force produite par le DBD par rapport à des mesures expérimentales. Des applications aérodynamiques de contrôle d'écoulement ont démontré les effets possibles de ces actionneurs pour la transition laminaire - turbulente et l'amélioration de la portance. Ces travaux ouvrent une perspective nouvelle dans la conception et l'optimisation de ces actionneurs.

Acknowledgments

Right from the beginning of my enrollment as a PhD candidate, I knew that it would be a long journey of intense work, continuous learning and personal development through the different phases that almost every PhD candidate goes through. During these three years of my PhD, I had the chance, or maybe better, I was lucky enough to have interacted and be surrounded by people that I consider as milestones for the completion of my dissertation and my PhD.

Firstly, I would like to express my extreme gratitude to my two supervisors : The director of my thesis, Prof. J.P. Boeuf and the co-director Dr. F. Rogier. Without their guidance, deep knowledge of the research subjects and overall supervision of this thesis, this dissertation would not be possible.

Prof. Boeuf, was the person who introduced me to the fascinating world of plasma physics and his unique pedagogical skills motivated me to learn more and discover this vast research domain. Despite his expertise in the field, he was always willing to discuss and return to basics, in order for me to clarify notions that were unclear. I do owe him, literately, my PhD on this field, as without him I would most probably never get involved in the research of plasma actuators and their applications.

For Dr. Rogier, it is really hard to find the words that can express my gratitude to him. He was my everyday supervisor, dealing daily with me and my questions - progress. As an expert of mathematical modeling and numerical simulation, his knowledge was a well of gold for me, and in addition with his superb pedagogical skills, provided the perfect environment to work in. I will always admire him, for his tranquility, methodology and eager spirit for innovating research even in domains that are outside his specialty. We have spent countless hours discussing new methods and ideas in order to progress in the field, constructed parallel projects with other research groups and interacted in a daily basis. His behavior towards me, was always leaving me the impression that he consider me as a researcher and not a student - a fact that I appreciated a lot and motivated me even more during my research. Besides the professional aspects, his personality and constant help in the various personal problems or issues I encountered during these three years was

overwhelming. I honestly can not imagine a better supervisor for a PhD candidate.

I am sincerely grateful to the two reviewers (and members of the jury) of my thesis, Dr. Giovangigli and Prof. Yakinthos for the time spent and their extremely useful comments on my research as well as to the other members of the jury : Dr. Larour and Prof. Pascal.

I need to express also my gratitude to all the other members of the research units that I have interacted with. The team of DTIM, Toulouse, who were all happy to help me in any aspect of my research and with whom we spent a lot of time discussing over various subjects of everyday life, fixing an excellent professional environment. I have to thank especially G. Dufour, with whom I have interacted greatly and spent many hours discussing scientific issues. All the interns and PhD students that have spent time in ONERA during these years, especially Tomasz, Cristophe, Alexandra. Researchers from other departments of ONERA, Toulouse especially X. Ferrieres and F. Isaak from DEMR, D. Caruana and F. Chedevergne from DMAE, for the discussions and research work we performed together. The people of the GREPHE research unit at LAPLACE, UPS for their help and interest in my research. G. Sary and T. Richard who worked as interns at DTIM under the supervision of Dr. Rogier, for the work we've done and time we've spent together.

Of course, I need to thank all of my close friends who made my stay in France more than pleasant, gave me the personal support and provided the necessary equilibrium between work and personal life. Flora, Kostaras, Julia, Iovi, Simon, Dora, Evangelia, Kushal, Joe, Velgos, Lefteris, Ronan, Aly, Satoshi, all the Greek team, all the ISAE master's team, all my friends in Greece (you know who you are and you are a lot) and everyone else who helped me out or just had a beer with me. I'd never made it without you - I love you all!

I feel also the need to thank from the bottom of my heart, the country of France for accepting me and giving me the opportunity to perform research in a high level, providing me a fellowship through ISAE, during the past three years.

Thank you God for a life that a few can have. Right now, we got to keep the Faith.

Last but not least, I am obliged to thank my family. This thesis is dedicated to my parents, Antonis and Maria, for their support, unlimited love and living almost a lifetime for their children, me and my brother Stratos. I can never repay but I hope you are proud of your son.

To my mother, Maria, and my father, Antonis, for living almost a lifetime for their children.

Στη μητέρα μου, Μαρία και στο πατέρα μου Αντώνη. Μας αφιερώσατε τη ζωή σας, σας αφιερώνω κατι ελάχιστο για να σας πω με πολύ αγάπη ένα μεγάλο ευχαριστώ.

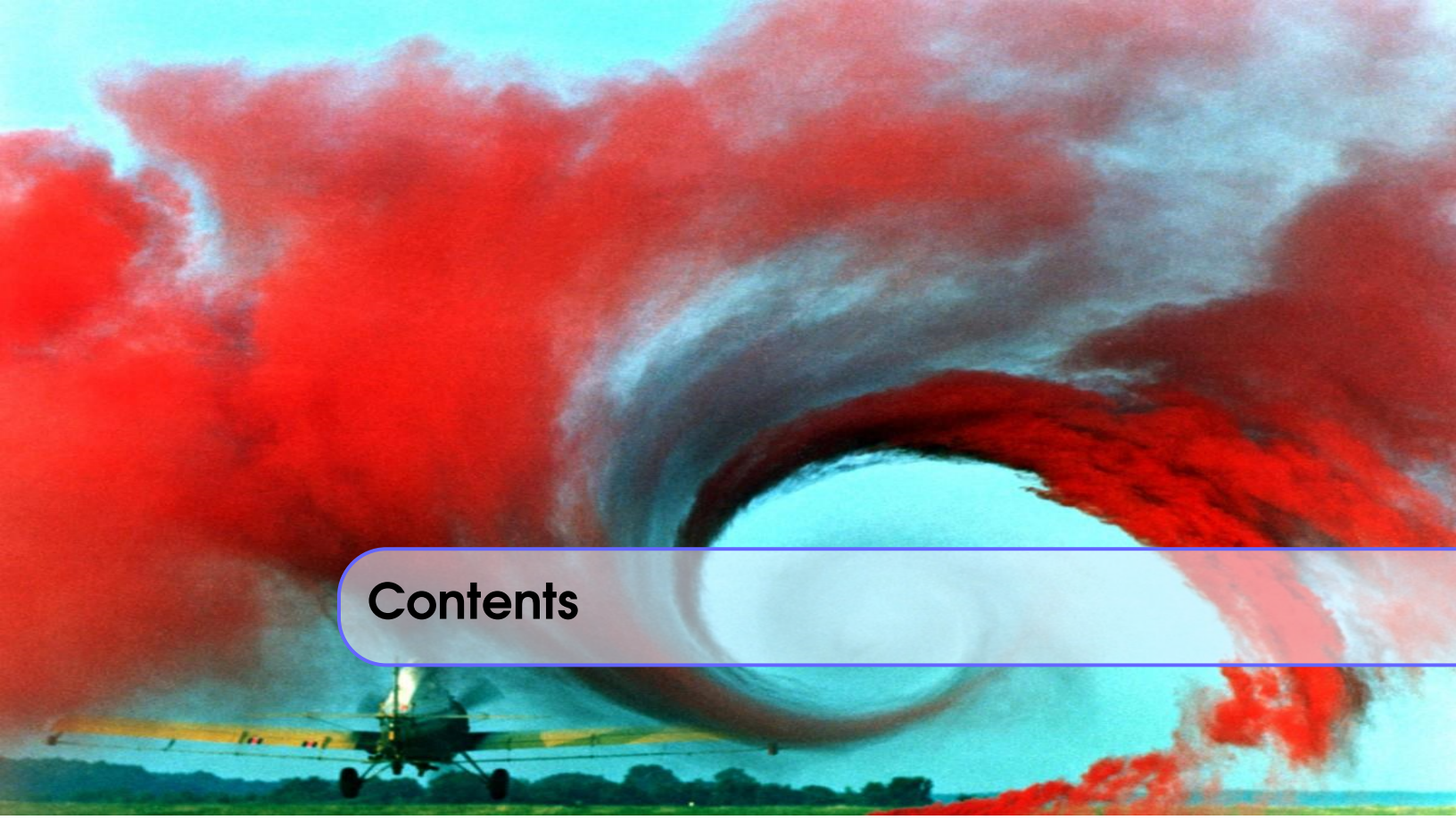

Contents

Photo by NASA-LaRC

Introduction - Théorie - État de l'art

Généralités

Dans l'histoire de la technologie de l'aviation et de l'aérospatiale, la nécessité et le défi de l'amélioration des avions qui volent plus coût-efficaces, plus sûrs et qui sont capables de s'adapter à n'importe quel scénario de vol ou des conditions environnementales a toujours été l'objectif prioritaire des activités de recherche. Pendant toutes ces années depuis le premier vol des frères Wright en 1903, d'énormes progrès ont été réalisés dans toutes les branches de l'ingénierie aérospatiale. Le domaine de l'aérodynamique comme la physique principale derrière un corps volant, était et est toujours un élément clé du processus d'optimisation pour améliorer la performance d'un avion.
Le domaine de l'aérospatiale intègre une telle variété de physiques différentes, que des solutions d'ingénierie intuitives doivent toujours collaborer avec la recherche théorique pluridisciplinaire. Cette recherche fondamentale sur l'interaction complexe entre les physiques différentes, peut et a déjà fourni des idées novatrices, dont de nombreux ont été incorporés dans les avions commerciaux et militaires. Cette thèse porte sur une nouvelle approche pour le contrôle d'écoulement aérodynamique. Cette nouvelle approche est basée sur l'utilisation d'actionneurs de plasma.

La recherche fondamentale sur la formation, le développement et l'interaction du plasma avec l'air et ses conséquences aérodynamiques, doit fournir toutes les informations par le biais de nombreuses expériences et de travaux théoriques - numériques. La modélisation numérique en particulier, peut être une arme puissante dans les mains des scientifiques et des ingénieurs pour comprendre, optimiser et ouvrir la voie à la commercialisation et l'application de cette technologie pour le bénéfice de l'humanité. Le couplage très exigeant entre l'électricité ou de l'électromagnétisme, le plasma et l'air, nécessite des modèles et des techniques numériques avancées pour faire face efficacement à ces problèmes.

Le travail présenté dans cette thèse a pour principaux objectifs : le développement et la validation de méthodes numériques pour simuler efficacement le fonctionnement de certains des plus importants types d'actionneurs plasma. Nous nous sommes intéressés à trois types d'actionneurs plasma

: les décharges micro-ondes, la décharge à barrière diélectrique (DBD) et le jet synthétique plasma (JSP). En ce qui concerne les décharges micro-ondes, les objectifs sont plus fondamentaux que pour les autres types d'actionneurs. Il s'est agit de mieux comprendre la création du plasma, son évolution et de calculer l'efficacité énergétique de dispositifs microondes par la simulation numérique. En ce qui concerne les deux autres groupes d'actionneurs, les objectifs de cette thèse sont plus appliqués et nous sommes intéressés principalement sur la modélisation de leur fonctionnement et sur la production de l'écoulement qui en résulte. Dans tous les cas, les modèles et les techniques numériques ont été développées ou utilisées en vue d'obtenir des résultats qui peuvent être validés par des expériences et fournir soit plus d'informations de leur physique et de leur fonctionnement ou une base pour leur développement et amélioration.

Ce travail de thèse, a été un des résultats de la collaboration entre l'unité de recherche de modélisation mathématique et simulation numérique (M2SN) au département de traitement de l'information et modélisation (DTIM), à l'ONERA, Toulouse, France et le laboratoire de LAPLACE, GREPHE de l'université Paul Sabatier, Toulouse. L'auteur a reçu une bourse de 3 ans de l'état français distribué par l'ISAE.

L'activité de recherche a fait partie de divers projets de recherche de niveau régional, national et international. En outre, les résultats obtenus ont été présentés dans de nombreuses conférences et journées scientifiques, et publié (ou en révision) dans des revues internationales. Une liste des publications et des présentations principales est présenté ci-dessous.

Publications liés à la thèse

- G. Sary, G. Dufour, F. Rogier, and K. Kourtzanidis, "Modeling and Parametric Study of a Plasma Synthetic Jet for Flow Control", AIAA Journal, 52.8 (2014): 1591-1603.
- K. Kourtzanidis, F. Rogier, J.P. Boeuf, "Implicit Finite Differenence Time Domain Modeling of Microwave Plasmas towards fully 3D Simulations", submitted and under review, Computer Physics Communications, 2014.
- K. Kourtzanidis, F. Rogier, J.P. Boeuf , "Three-dimensional Simulations of Plasmas Patterns Formation during Microwave Breakdown in Air", submitted and under review, Journal of Applied Physics, 2014.
- K. Kourtzanidis, F. Rogier, J.P. Boeuf , "Modeling of air's heating effects during the propagation of microwave streamers", in preparation for the Journal of Applied Physics.
- Kourtzanidis, K., Rogier, F., Dufour, G., Boeuf, J.P., Unfer, T. Numerical Modelling of Plasma Actuators, ERCOFTAC Bulletin 94, Special Theme: Plasma Aerodynamics, March 2013.
- Kok, J.C., Catalano, Kourtzanidis, K., Rogier, F., Unfer, T. Coupling CFD with Advanced Plasma Models, ERCOFTAC Bulletin 94, Special Theme: Plasma Aerodynamics, March 2013.
- Kourtzanidis, K., Numerical Simulation of Plasma Actuators for Flow Control, AIAA Meeting Paper, 2013-0134, January 2013
- F. Rogier, G. Dufour, K. Kourtzanidis, Numerical Simulation of sinusoidal DBD actuators and comparison with experiments, AIAA, Atlanta GA, 16-20 June 2014.

Présentations liés à la thèse

- Kourtzanidis, K., Numerical Simulation of Plasma Actuators for Flow Control, AIAA Meeting Paper, 2013-0134, January 2013. Invited as 1st prize winner of the 8th AIAA-Pegasus Student Conference.
- Kourtzanidis, K., Rogier, F., Boeuf, J.P., Numerical modelling of plasma for flow control in aerospace applications, Plasma Science (ICOPS), 2012 Abstracts IEEE International Conference on Plasma Science.
- Kourtzanidis, K., Rogier, F., Dufour, G., Boeuf, J.P., Unfer, T., Numerical simulation of plasma

actuators for flow control, ERCOFTAC-PLASMAERO 2012, Toulouse, France.
— Kourtzanidis, K., Rogier, F., Dufour, G., Sary, G., Numerical Modeling of the Plasma Synthetic Jet, EUCASS ATW, 2013, Aussois, France. Poster presentation.
— Kourtzanidis, K., Rogier, F., Boeuf, J.P., Numerical Modeling of Microwave Discharge Actuators, EUCASS ATW, 2013, Aussois, France. Poster presentation.
— Kourtzanidis, K., Rogier, F., Boeuf, J.P., Numerical Modeling of Microwave Discharges for Flow Control, Journées ONDES du Sud-Ouest, April 2014,Toulouse, France. Poster presentation.
— Kourtzanidis, K., Rogier, F., Boeuf, J.P., Numerical Modeling of Microwave Plasma Discharges for Aerodynamic Flow Control, ISEHD, 2014, Okinawa, Japan.
— Kourtzanidis, K., Sary, G., Rogier, F., Dufour, G., Numerical modelling of plasma actuators for flow control - The Plasma Synthetic Jet, ISEHD 2012, Gdansk, Poland.

Le contrôle d'écoulement aérodynamique

Pour comprendre l' importance de l'aérodynamique comme moyen d'amélioration de la performance des avions, nous avons besoin de poser une question simple: quel est le but de l'aérodynamique dans l'aérospatiale?

Une réponse générale pourrait être: La conception des avions qui peuvent produire une grande portance et d'avoir un faible traînée. Une représentation des forces agissant sur un profil aérodynamique (similaire à un objet volant) est représenté dans la figure 1. Définissons les coefficients de la portance et la traînée sans dimension comme:

$$\begin{aligned} C_l &= \frac{F_l}{\frac{1}{2}\rho V^2 A} \\ C_d &= \frac{F_d}{\frac{1}{2}\rho V^2 A} \end{aligned} \tag{1}$$

où $F_l$est la force de portance (la composante de force perpendiculaire à la direction de l'écoulement), $F_d$est la force de traînée (la composante de force dans le sens de la vitesse d'écoulement), Vest la la vitesse de l'air par rapport à l'avion et Ala zone de référence, il est facile de comprendre que les ingénieurs aérodynamiques cherchent à maximiser le coefficient de portance tout en minimisant la traînée, afin de parvenir à un comportement de vol efficace avec une consommation d'énergie réduite.

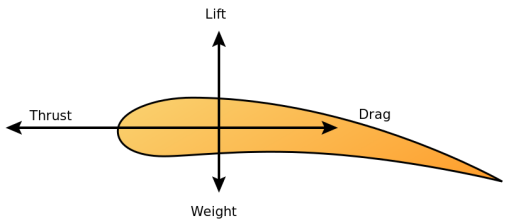

Figure 1: Forces agissant sur une aile en mouvement dans l'air.

Ces deux forces fondamentales peuvent être obtenues à partir des équations de gouvernance classiques de la mécanique des fluides - les équations de Navier - Stokes. [1].

La force totale exercée sur le fluide est une combinaison de forces de pression, de forces de viscosité, de forces du corps et ceux liés aux contraintes. Pour chaque régime différent d'écoulement, ces termes contribuent différemment à la génération de l'équilibre énergétique et de la force totale. Les deux forces aérodynamiques principales dépendent de divers paramètres. La portance ne peut exister que si le fluide est en contact avec la surface, de sorte qu'un écoulement séparé ne générera pas de portance. La vitesse du fluide est également un effet positif à la génération de portance ainsi que le tourbillon autour de la surface. La force de traînée dépend fortement de paramètres tels que les discontinuités, le frottement, la distribution de la pression et de manière significative, de la nature de l'écoulement en particulier à l'intérieur de la couche limite. L'interaction complexe entre les différents processus de génération ou de réduction de la traînée et la portance sont résumées dans la figure 2. L'objectif global d'un ingénieur peut être réduit à la maximisation du rapport portance - traînée.

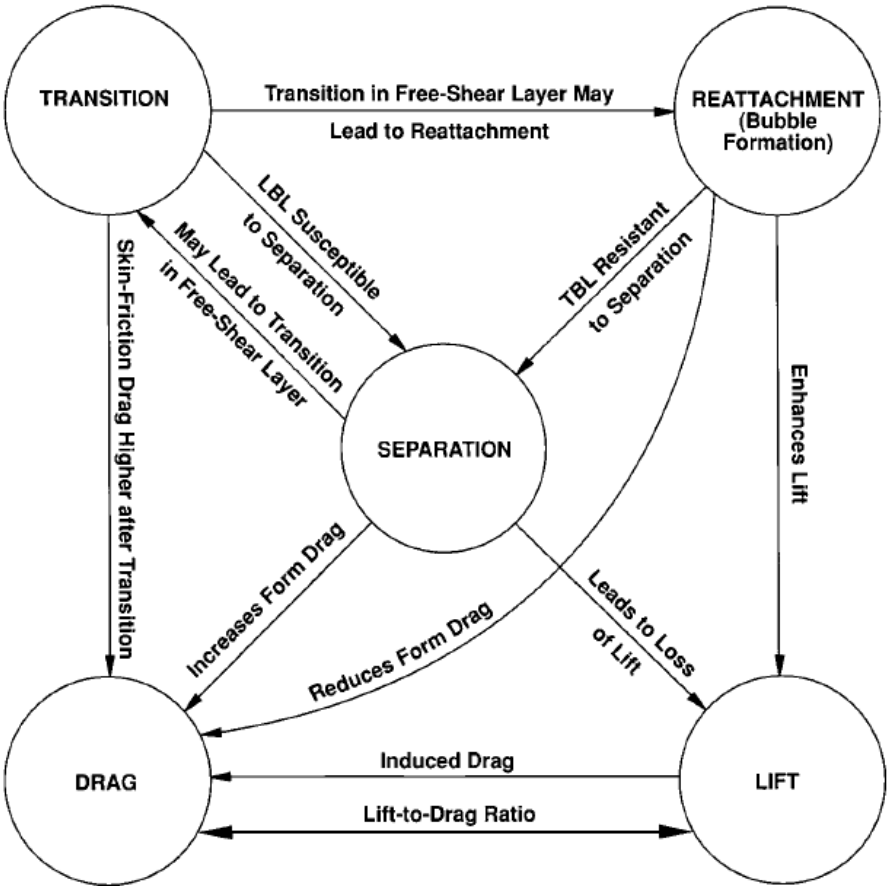

Figure 2: Influence de la nature et le comportement d'écoulement sur la portance et la traînée [2].

Pour les écoulements à grande vitesse, les effets de compressibilité et la formation d'ondes de choc

peuvent introduire une traînée d'onde, ce qui peut conduire à une augmentation spectaculaire de la traînée totale d'un objet volant. Le contrôle de tous ces effets aérodynamiques est essentiel pour les avions du futur. La réduction de la traînée et l'augmentation de la portance est évidemment important, mais une methode plus détaillée et sophistiquée doit être développé pour la nouvelle génération d'avions, comme une procédure adaptable pendant le vol. Ainsi, nous devons reposer notre question:

Quel est l'objectif de l'aérodynamique?

Contrôle d'écoulement

Reposons la question, nous pouvons peut-être maintenant, affiner notre réponse: La conception des avions doit fournir la capacité de contrôler l'écoulement autour du corps d'un aéronef ou à l'intérieur de ses moteurs, de telle manière que, dans tout moment d'un vol, l'avion peut répondre aussi rapide et précis que possible aux commandes (prédéfinis ou non) du pilote (ou n'importe quel opérateur), en minimisant l'énergie nécessaire pour le faire. Ce contrôle doit être adaptable à des conditions différentes et dans la volonté de l'opérateur.

Une description très détaillée de la théorie de contrôle d'écoulement et de méthodes pertinentes peuvent être trouvées dans [3, 2]. Parmi les différentes classifications des méthodes de contrôle d'écoulement, dans cette thèse, nous nous concentrons sur deux grandes catégories, les méthodes passives et actives. Cette classification nous permettra de mieux comprendre les avantages d'actionneurs à base de plasma comme moyen de contrôle d'écoulement aérodynamique
.

Le contrôle d'écoulement passif se réfère aux méthodes qui n'injectent pas directement d'énergie dans l'écoulement. Ces méthodes comprennent principalement des dispositifs tels que les générateurs de tourbillons, les riblets et les techniques d'aspiration, tandis que les volets et les ailerons peuvent également être considérés comme tels (surtout dénommé "surfaces de contrôle").

Les méthodes de contrôle d'écoulement passifs ont été déjà mis en œuvre sur les avions, car ils offrent un moyen non coûteux et facile d'améliorer les coefficients aérodynamiques. Ils présentent bien, des inconvénients majeurs. Leur utilisation est limitée: Leur influence dans l'écoulement est constante et intrusive car ils ne peuvent pas s'adapter à chaque configuration de vol. Pour dépasser cet inconvénient, les méthodes de contrôle doivent être actives (ou réactives) - avoir la capacité d'adapter leur performance pour chaque régime de vol.

Les méthodes actives sont toujours basés sur des actionneurs et ils introduisent d'énergie externe dans l'écoulement. Ces méthodes peuvent être utilisées dans un manière prédéterminé, soit de manière réactive où un système de contrôle en boucle fermée est nécessaire. Ici nous allons nous concentrer sur les méthodes de contrôle actives et réactives.

Le contrôle d'écoulement active implique la triade des phénomènes d'écoulement, actionneurs et commandes tel que présenté dans la figure 3.

Il convient à ce stade, de séparer ces méthodes en deux sous-catégories: la soufflage et les jets de parois [4], les jets - générateurs de vortex, les jets synthétiques et les actionneurs piézoélectriques [5, 6], peuvent être considérés comme des méthodes d'addition de quantité de mouvement. Le chauffage de surface, les bosses thermiques avec les éléments chauffants, peuvent être considéré comme des méthodes de dépôt d'énergie. Dans les méthodes d'addition de quantité de mouvement, l'addition de l'énergie cinétique dans l'écoulement est le mécanisme qui la manipule et est la cause de la variation de ses caractéristiques. Les méthodes de dépôt

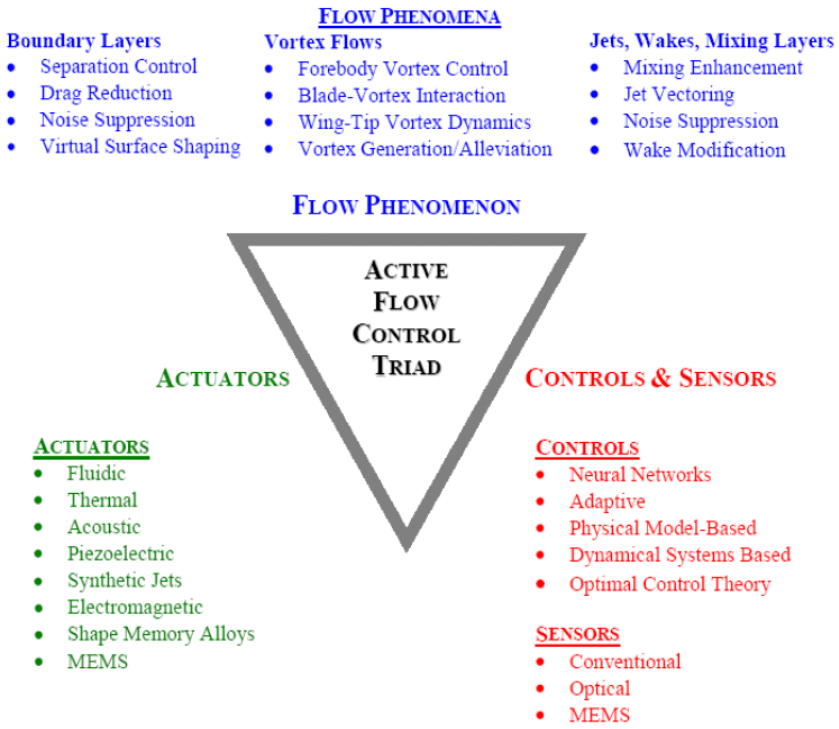

Figure 3: La triade de commande d'écoulement (D. E. Parekh, Georgia Tech Research Institute).

d'énergie en terme de perturbations thermiques localisées dans un écoulement présentent des similitudes avec des bosses physiques et diverses études ils ont été faites, en particulier dans les écoulements supersoniques et hypersoniques, où elles peuvent être particulièrement efficaces [7]. En outre, des études théoriques et expérimentales ont démontré que le chauffage ou le refroidissement d'une surface a un impact direct sur la transition laminaire à turbulent [8].

Bien que ce type d'actionneurs sont prometteurs et efficaces pour le contrôle d'écoulement, ils introduisent de nouveau un grand nombre de inconvénients. Beaucoup d'entre eux sont mécaniques, donc ils ont besoin d'entretien et leur coût de fabrication et d'intégration est élevé. Beaucoup d'entre eux sont intrusifs. Et peut-être le plus important: leur temps de réponse est grand. Les modifications du champ d'écoulement, en particulier dans des vitesses élevées ou lorsque la maniabilité est important, se produisent très rapidement et ainsi, un actionneur doit répondre aussi rapidement pour être capable de fournir un mécanisme de contrôle d'écoulement rigide.

Actionneurs de type plasma

Dernièrement un nouveau groupe d'actionneurs a été proposé par plusieurs chercheurs en fonction de décharges de plasma [9]. Ils peuvent fournir des possibilités de contrôle d'écoulement presque en temps réel, alors que beaucoup d'entre eux sont simples et faciles à fabriquer et facile à intégrer sur une surface. Ce type d'actionneurs comprennent, entre autres, les Dielectric Barrier Discharges (décharges à barrière diélectrique

ou DBD), le jet synthétique plasma (JSP) et les décharges micro-ondes, trois catégories d'actionneurs que nous nous concentrons dans cette thèse. Comme ce type d'actionneurs dépend de la formation de plasma et la modification conséquente de la structure de l'écoulement, il est essentiel de revoir quelques notions de base sur la physique des plasmas.

Physique des plasmas

Donc, que définit ce type novateur d'actionneurs et pourquoi sont-ils intéressants pour les applications de contrôle d'écoulement? Pour répondre à cette question, plasma lui-même doit être défini.

Le plasma est souvent appelé le quatrième état de la matière. En général, nous pouvons le définir comme un gaz ionisé dans lequel les effets collectifs dominent les collisions. Dans cette thèse, on focalise sur les plasmas quasi-neutre. Cela signifie que le plasma est macroscopiquement neutre et pour un plasma d'exister, la taille du plasma doit être grande par rapport à la distance (la longueur de Debye voir ci-dessous) nécessaire à une particule pour acquérir suffisamment d'énergie afin de perturber la distribution de la vitesse d'électrons initiales. La longueur de Debye s'écrit :

$$\lambda_D = \sqrt{\frac{\varepsilon_o T}{ne^2}} \tag{2}$$

La longueur de Debye peut être considéré comme l'échelle sur laquelle les porteurs de charge mobiles filtrent les champs électriques dans un plasma. Quand un objet est inséré dans un plasma, des perturbations de champ électrique ne peuvent être reproduits que dans la distance de la longueur de Debye.

La quasi-neutralité demande que:

$$n_e \simeq n_i = n \tag{3}$$

où $n_e$est la densité d'électrons (le nombre de particules par mètre cube), $n_i$est la densité de nombre d'ions et n est la densité du plasma et un plasma froid a un degré d'ionisation δ inférieur à 10^{-2}où δprend la forme

$$\delta = \frac{n_e}{n_e + N} \tag{4}$$

Pour créer le plasma sans la nécessité d'un chauffage excessif de gaz, un champ électrique peut être appliqué (par une tension DC, une tension alternative à haute fréquence ou des ondes EM). Les électrons libres, toujours présents à une petite fraction due aux rayons cosmiques, sont alors accélérés par le champ électrique et entrent en collision avec les molécules. Si l'énergie acquise par le champ électrique est suffisamment élevée, les collisions peuvent ioniser les molécules, créant une avalanche d'électrons. Par ce procédé, les différents types de plasmas peuvent être créés - ceux qui maintiennent un équilibre thermique et d'autres qui ne le font pas. Cette catégorie offre beaucoup d'avantages: les plasmas peuvent être formés sans la nécessité de l'énergie excédentaire, et de régimes différents peuvent être contrôlés.

Il est bien évident que les collisions entre les particules est la caractéristique la plus importante de ces plasmas. Leur fréquence et énergie est essentiel pour créer, maintenir et contrôler le plasma. La masse des électrons est beaucoup plus petit que les ions, et leur mobilité, μ_e, définie comme :

$$\mu_e = \frac{e}{m\nu_c} \tag{5}$$

est des centaines de fois plus élevés que les ions. Dans l'équation 5 ν_c est la fréquence des collisions qui est proportionnelle à la densité des particules neutres et à la vitesse des particules chargées. Ainsi, dans un plasma faiblement ionisé, ce sont les électrons et leurs collisions avec les neutres qui soutiendront le plasma et vont interagir de manière intensive avec des champs appliqués tandis que les ions (lorsque les champs ne sont pas trop forts) auront un effet indirect sur la motion de l'électron par la diffusion ambipolaire(voir ci-dessous).

Les électrons vont gagner de l'énergie entre deux collisions due au champ électrique, E, liée à leur vitesse de dérive, v_d, qui s'écrit :

$$v_d = \mu_e E \tag{6}$$

et perdre de l'énergie à chaque collision, liée à leur vitesse thermique. Les collisions entre les électrons et les particules neutres, peuvent prendre différentes formes. Nous parlons de collisions élastiques, re-combinaison, excitation vibratoire, électronique, dissociation et ionisation. Tous ces processus, font le plasma un milieu réactif. Les collisions élastiques provoquent le transfert d'énergie cinétique entre les particules entrent en collision en fonction de leur rapport de masse.

Le champ électrique étant la somme du champ électrique appliqué et du champ produit en raison des charges dans le plasma sera modifié par ces collisions, conduisant à la modification conséquente de la densité des particules chargées et neutres. Le nombre de collisions, N_c qu'un électron se rencontre au cours d'une certaine période de temps, dépend de la densité, N, la vitesse de la molécule, et la vitesse de l'électron. En supposant que la vitesse des molécules, v_M, est ainsi plus petite que la vitesse d'électrons, $v_e$ce nombre est donné par $n_c = QNdx$, où Q est la section efficace de collision. Le libre parcours moyen, $\lambda_e = dx/p_c = 1/(NQ)$, est la distance entre deux collisions et la fréquence de collision peut être définie comme:

$$\nu_c = \frac{v_e}{\lambda_e} = NQv_e \tag{7}$$

Cette fréquence de collision correspond à la somme de chaque type des collisions.

Un autre échelle important est la fréquence d'électrons du plasma, ce qui, en supposant que les ions restent immobiles et en négligeant les collisions, s'écrit :

$$\omega_p = (\frac{ne^2}{\varepsilon_o m})^{1/2} \tag{8}$$

C'est la réponse du mouvement des électrons à une perturbation locale de la distribution de charge et de densité.

Le transport des particules chargées peut être décrit de deux façons: soit en un niveau mésoscopique, où les équations de la fonction de distribution de chaque particule doit être écrit, ou à un niveau macroscopique, lorsque le comportement du plasma peut être décrite en termes des équations de dynamiques de fluide, en supposant que le plasma peut être défini par les valeurs moyennes de la densité, la vitesse et l'énergie des particules. Ici, nous allons concentrer notre intérêt sur la deuxième, la description macroscopique d'un plasma.

Les quantités macroscopiques correspondent aux moments de vitesse de la fonction de distribution i.e. les intégrales de certain puissance de la vitesse multipliée par la fonction de distribution sur l'espace des vitesses. En multipliant l'équation de Boltzmann par une variable y, qui dépend de la vitesse instantanée

d'une particule et après intégration sur l'espace des vitesses, on obtient l'équation de transport généralisée sous la forme:

$$\frac{\partial n\bar{y}}{\partial t} + \nabla_r.(n\overline{yv}) - n\overline{\alpha.\nabla_v y} = \int_v y[\frac{\partial f}{\partial t}]_{coll} dv^3 \tag{9}$$

où $\alpha = qE$ en supposant que les champs magnétiques sont faibles. En remplaçant $y$par 1, $v$et v, nous obtenons les 0, 1ère et 2ème moments de vitesse de l'équation de Boltzmann qui correspondent à les équations de la continuité, le transfert de quantité de mouvement et l'énergie respectivement. Comme les moments de vitesse de l'équation de Boltzmann forme de séries infinis où chaque équation dépend de un ordre supérieur, d'approximations de fermeture doivent être prises afin que nous puissions obtenir un système fermé de trois équations qui décrivent le comportement macroscopique du plasma.

Comme nous supposons des plasmas quasi-neutres, nous pouvons écrire les équations de transport que pour les électrons - les ions obéissent à des lois similaires. Par conséquent, le moment 0 de l'équation de Boltzmann intégré dans l'espace de vitesse, donne l'équation de continuité:

$$\frac{\partial n_e}{\partial t} + div\Gamma = S \tag{10}$$

où Γ est la densité de flux des électrons et $S = \sum_i N_i$ sont les sources de la création ou de la destruction des particules. Le terme source $S = Nn_eK_i$, dépend de la densité des électrons et des molécules de gaz, et le coefficient de taux K_i pour chaque collision ou réaction chimique i.

L'équation de transfert de quantité de mouvement est dérivé du premier moment de l'équation de Boltzmann intégré dans l'espace de la vitesse, dans l'hypothèse de tenseur de pression isotrope et diagonale :

$$m_e n_e(\frac{\partial v_e}{\partial t} + (v_e \cdot \nabla)v_e) = -n_e eE - \nabla P_e - n_e m_e v_e \nu_c \tag{11}$$

où $P_e = n_e K_B T_e$ est le tenseur de pression des électrons. Si nous laissons tomber le terme d'inertie en raison de la petite masse d'électrons, nous voyons que l'évolution temporelle de la quantité de mouvement des particules chargées (électrons par exemple ici) est due à trois forces: une liée au gradient de pression, celui lié à des forces électriques et un lié à des forces de frottement due aux collisions. Si on suppose en outre que les collisions ont lieu sur un temps et des échelles de longueur beaucoup plus court vis-à-vis des variations du champ macroscopique, on obtient l'équation de dérive-diffusion dans sa formulation stationnaire:

$$n_e v_e = -\frac{n_e eE}{m_e \nu c} - \nabla(n_e \frac{k_B T}{m_e \nu_c}) \tag{12}$$

donnant la densité de flux de particules $\Gamma = n_e \bar{v_e} = -n_e \mu_e E \nabla(D_e n_e)$ incorporant de dérive , de diffusion et de convection composants. Le coefficient de diffusion D pour les particules de Maxwell est donnée par la relation d'Einstein:

$$D_e = \frac{\mu_e k_B T}{e} \tag{13}$$

qui est inversement proportionnelle à la densité du gaz en tant que la mobilité $\mu_e$est inversement proportionnelle à la fréquence de collision qui est proportionnelle à la densité du gaz. Comme la mobilité des

ions est d'environ 100 fois plus faible que celle des électrons, et leur température plus élevée que celle des ions (dans un plasma de non-équilibre), le coefficient de diffusion des électrons est plus grande que celle des ions. Cela implique que les deux espèces dans un plasma, diffuseraient avec des taux différents, les électrons seraient transporter plus rapidement que les ions et le plasma ne pouvaient pas rester quasi-neutre. Ce qui se passe en réalité est que la divergence du transport d'espèces, entraîne une modification de la densité de charge, la charge d'espace, ce qui conduit en retour à la création d'un champ électrique qui va ralentir les électrons. Ensuite, les deux espèces se diffusent avec un coefficient ambipolaire commun, D_α. En supposant quasi-neutralité et l'absence de courant net ($\gamma_e = \gamma_i$), on trouve le coefficient ambipolaire de l'équation pour les électrons et les ions, comme:

$$D_\alpha = \frac{\mu_e D_e + \mu_i D_i}{\mu_e + \mu_i} \tag{14}$$

Enfin, l'équation de l'énergie pour les électrons s'écrit :

$$\frac{\partial n_e \overline{\mathscr{E}}}{\partial t} + \frac{5}{3}\nabla.(n_e \overline{v_e}\overline{\mathscr{E}}) - \frac{2}{3}\nabla.(K\nabla\overline{\mathscr{E}}) - e n_e E.\overline{v_e} = -n_e \nu_{\mathscr{E}}\overline{\mathscr{E}} \tag{15}$$

où K est la conductivité thermique, $e n_e E.\overline{v_e}$ est le terme de chauffage par effet Joule et $\nu_{\mathscr{E}}$ sont les pertes d'énergie (par unité de volume et unité de temps) en raison de collisions qui peuvent être écrits comme:

$$\nu_{\mathscr{E}}\overline{\mathscr{E}} = \frac{2m_e}{m_M}\nu_c\overline{\mathscr{E}} + \sum \nu_i \mathscr{E}_i \tag{16}$$

où l'indice i représente chaque processus de collision différents

.

La formation de décharges de plasma sous un champ DC ou lentement oscillant suit la description macroscopique fournie dans le paragraphe précédent. Dans de telles zones, le plasma est un milieu conducteur, dont la valeur dépend de sa densité en tant que (en négligeant la contribution ionique):

$$\sigma_e = e n_e \mu_e = \frac{e^2 n_e}{m_e \nu_c} \tag{17}$$

La densité de courant électrique dans un plasma est alors donnée par:

$$J = \sigma_e E = -e n_e \overline{v_e} \tag{18}$$

et le travail effectué en moyen par unité de temps par le champ sur un électron:

$$< -eEv_e >= \frac{e^2 E^2}{m\nu_c^2} \tag{19}$$

Pour initier un plasma, un champ électrique suffisamment élevé doit être appliqué. Cette valeur suffisante du champ électrique est appelé champ de claquage. La formation d'un plasma, est suivie d'une période transitoire de pertes et de la génération de particules chargées par de mécanismes différents. Pour que le plasma soit durable, la production doit compenser les pertes, ce qui signifie que le champ électrique doit fournir suffisamment d'énergie aux électrons de sorte qu'il puisse ioniser des particules neutres plus souvent

que les procédures des pertes.

Pour les décharges micro-ondes et par rapport aux champs DC, un électron oscille à une fréquence dont l'amplitude et la phase dépendent de la fréquence ω du champ EM et la fréquence efficace de collision ν_c.

Une onde électromagnétique général peut être décrit par les équations de Maxwell (en supposant une propagation dans l'espace libre):

$$\begin{aligned} \nabla \cdot E &= \frac{\rho}{\varepsilon_0} \\ \nabla \cdot B &= 0 \\ \nabla \times E &= -\frac{\partial B}{\partial t} \\ \frac{1}{\mu_0} \nabla \times B &= \varepsilon_o \frac{\partial E}{\partial t} + j \end{aligned} \tag{20}$$

où Eet H sont les vecteurs de champ électrique et magnétique, ρla densité de charge et j est la densité de courant. En supposant que la longueur de Debye est plus petite que la dimension de la longueur d'interaction de micro-ondes et en négligeant la contribution de la vitesse d'ions sur la densité de courant en raison de la mobilité ionique faible, on peut décomposer l'évolution de plasma et les interactions micro-ondes à différentes échelles de temps, alors que la densité de courant s'ecrit $j = j_e = \sigma e = -en_e v_e$. Ensuite, les équations de Maxwell d'intérêt deviennent:

$$\begin{aligned} \nabla \times E &= -\frac{\partial B}{\partial t} \\ \frac{1}{\mu_0} \nabla \times B &= \varepsilon_o \frac{\partial E}{\partial t} + j \\ \nabla \cdot j &= 0 \end{aligned} \tag{21}$$

La vitesse moyenne d'électron est donnée par l'équation de la quantité de mouvement locale dans sa forme générale (en supposant à nouveau que les distances parcourues par les électrons au cours d'une période de micro-ondes par rapport à la longueur de gradient - ainsi que la force magnétique par rapport à la force électrique - sont négligeables):

$$m_e \frac{\partial v_e}{\partial t} = -eE - m_e v_e \nu c \tag{22}$$

Comme le champ électrique est harmonique, la vitesse des électrons est ainsi harmonique et sa dérivée dans le temps peut être remplacé dans le domaine fréquentiel par $i\omega$. En substituant l'équation 22 dans la première équation du système 21 et en passant au domaine de fréquence, nous obtenons:

$$\frac{1}{\mu_0} \nabla \times B = (1 - \frac{{\omega_p}^2}{\omega^2 + i\omega {\nu_c}^2}) \varepsilon_0 (i\omega E) \tag{23}$$

où maintenant le courant de plasma est présentée par une permittivité diélectrique complexe:

$$\varepsilon_p = 1 - \frac{{\omega_p}^2}{\omega^2 + {\nu_c}^2} (1 + i\frac{\nu_c}{\omega}) \tag{24}$$

En permettant une solution d'onde électromagnétique plane sous la forme $E = E_0 \exp(-i\omega t + ikx)$, où k est le vecteur d'onde et en résolvant l'équation d'onde (obtenue en prenant la rotationnel de la première équation 21 et en utilisant l'équation 23), nous obtenons l 'équation d'onde:

$$\begin{aligned} \nabla^2 E + \frac{\omega^2}{c^2}\varepsilon_p E = 0 \\ \kappa^2 = \frac{\omega^2}{c^2}\varepsilon_p \end{aligned} \tag{25}$$

Lorsque la permittivité diélectrique devient négatif (sa partie réelle), k est purement imaginaire et les ondes électromagnétiques ne peut pas pénétrer dans le plasma, mais ils se reflètent. La réflexion commence à une densité de plasma à la limite critique $\omega_p = \omega$ pour un plasma sans collisions.

L'énergie électromagnétique dissipée dans le plasma par les ondes électromagnétiques, $< j \cdot E >= \sigma < E^2 >$ peut être atteint que par l'effet des collisions dans un champ oscillant : si les collisions ne se produisent pas la moyenne de travail sur le champ d'un électron est égal à zéro. Sous l'influence de collision, le travail effectué en moyen par unité de temps par le champ sur un électron est:

$$< -eEv >= \frac{e^2 E_0^2}{2m(\omega^2 + \nu_c^2)}\nu_c \tag{26}$$

Dans un claquage microondes, l'ionisation primaire en raison du mouvement électronique est le seul phénomène de production qui contrôle le claquage. Comme sous les champs DC, en fonction du champ appliqué et la «pression du gaz (ici la distance inter-électrodes n'a pas de sens), les différents régimes de décharge à micro-ondes peut être obtenue. Dans la figure 4 une classification des décharges micro-ondes dans l'air par rapport à la pression et l'amplitude du champ électrique est tracée.

Actionneurs Plasma

Maintenant que nous avons une idée de la physique de plasmas est ainsi que la façon dont nous pouvons et nous voulons parvenir à un contrôle de l'écoulement aérodynamique, la question suivante peut être posée. Comment pouvons-nous utiliser le plasma au moyen d'un dispositif de contrôle d'écoulement?

Actionneurs à Décharges Micro-ondes (MDA)

Les actionneurs à micro-ondes se trouvent dans la catégorie des dépôts d'énergie des méthodes de contrôle d'écoulement. L'effet de ce groupe d'actionneurs de plasma dans un écoulement est provoqué par le chauffage intense du fluide. Comme nous avons vu, les décharges micro-ondes sous-critiques peuvent être formés dans des conditions atmosphériques sans avoir besoin de sources d'énergie excessives. Le couplage entre le plasma et le gaz par le chauffage par effet Joule peut fournir la source d'énergie qui peut être utilisé pour le contrôle de l'écoulement aérodynamique.

Dans les applications supersoniques pour le contrôle d'écoulement, l'effet thermique de la disposition de plasma est le moyen le plus efficace pour modifier les propriétés d'écoulement. La disposition de plasma en face d'un corps massif ou d'un aéronef a été étudiée numériquement et expérimentalement et a montré une

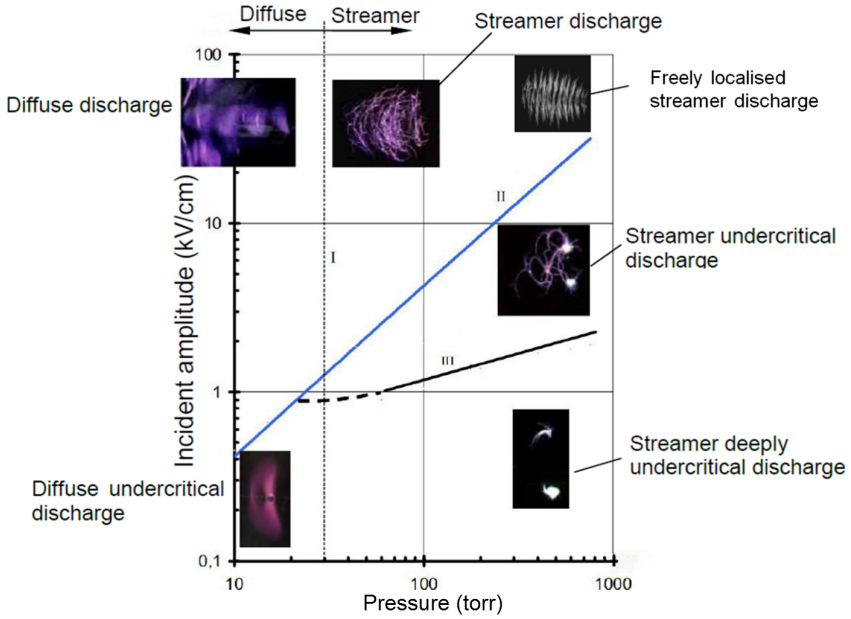

Figure 4: Classification des décharges micro-ondes dans l'air [10].

forte réduction du coefficient de traînée. Les applications de ces actionneurs dans les ecoulements super - hypersoniques ont été résumés par Knight [11]. La décharge peut être induit par un laser. En bref, l'interaction d'une décharge de plasma avec un écoulement supersonique-hypersonique avant un corps massif, conduit à une diminution de l'intensité de l'onde de choc oblique, et par conséquent à une diminution de coefficient de traînée.

Le dépôt de plasma est constitué généralement d'une colonne de plasma à haute densité ($n_e \approx 10^{16}\ cm^{-3}$ ou ultérieure) avec un rayon de 60-200 μm et une longueur de l'ordre de centimètres. La durée de la vie plasmatique est d'environ 5 ns (avec un laser femtoseconde). Cependant, l'effet du chauffage au gaz présente un effet important sur les performances aérodynamiques du corps. Dans [12], une réduction de la pression d'arrêt de 21 % a été mesurée à une fréquence de répétition supérieure à 60 kHz avec une énergie d'impulsion de 4,6 mJ et une durée d'impulsion de 10 ns.

En ce qui concerne les décharges purement micro-ondes, une grande partie du travail et de la recherche effectuée sur ces actionneurs a circulé autour de deux équipes. Le premier est l'équipe de l'institut de Radiotechnique RAS, Moscou, Russie en collaboration avec l'Institut de Hydromécanique, Académie nationale des sciences d'Ukraine et de l'Université nationale de l'aviation de l'Ukraine [13]. Cette équipe a concentré ses recherches sur des applications subsoniques. Après diverses optimisations et des études, ils ont proposé l'application d'une décharge micro-ondes initié par des vibrateurs électromagnétiques dans une aile [14]. Les expériences ont été effectuées dans le faisceau de rayonnement électromagnétique créé par un générateur de puissance moyenne ne dépassant pas $1,5kW$ avec une longueur d'onde de $12,3cm$. Ce concept ainsi que le profil aérodynamique expérimentale sont présentés dans la figure 5.

La puissance du magnetron etait de 6 à 8 kW. La durée de l'impulsion était de 100 μs et la fréquence

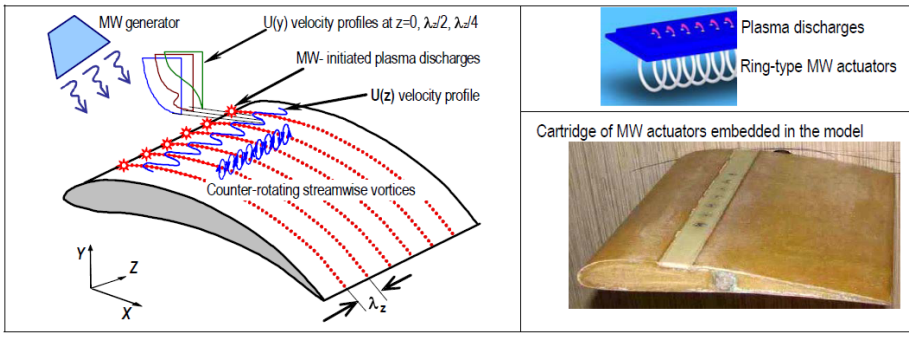

Figure 5: Contrôle avec vibrateurs E et cas expérimental [14].

d'impulsion de $f_{MW} = 500$ ou $1000Hz$. Pour ces conditions, le cycle de travail ("duty cycle") est égal (correspondant à la fréquence utilisée) à 20 ou 10. La puissance moyenne d'impulsion d'une source thermique a été estimée de 3 à 8 W. Les résultats sont présentés dans la figure 6.

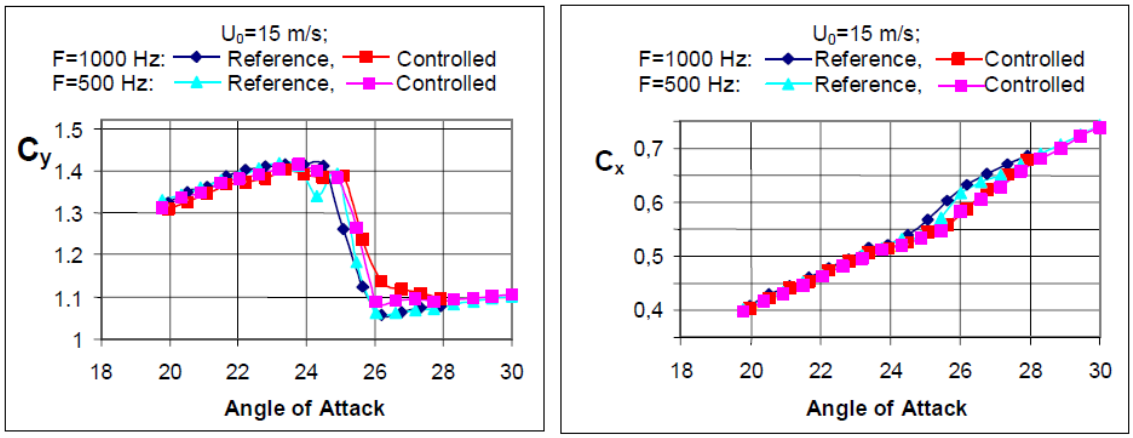

Figure 6: Coefficients de portance et traînée - comparaison entre les cas contrôlés et non contrôlés [15].

Les auteurs concluent que les décharges ont retardé la séparation de l'écoulement de 0,5 degrés. De cette façon, le contrôle de la couche limite en utilisant des décharges de plasma localisées traduit par une croissance de la coefficient de portance par 15 % et une diminution de trainée par 5 %.

Le deuxième groupe de recherche vient à nouveau de la Russie en collaboration avec le Département de génie mécanique à l'université Rutgers - L'Université d'Etat du New Jersey, USA. Les chercheurs de l'Institut de hautes températures de l'Académie des sciences de Russie (IVTAN) et de l'Université d'Etat de Saint-Pétersbourg., ont été des pionniers de la recherche de décharges micro-ondes pour le contrôle des écoulements supersoniques [16]. Dans [17], une excellent synthèse et analyse physique de l'interférence entre les écoulements supersoniques et des plasmas à micro-ondes est présenté.

Dans [18], les auteurs ont étudié expérimentalement un plasma micro-onde de 9 gigahertz, d'abord porté en amont d'un cylindre. Dans la figure 7, l'interaction de l'onde de choc avec la zone de décharge de plasma

à basse densité peut être observé et dans la figure 8 la pression de stagnation en fonction du temps est tracée, ce qui démontre la réduction significative de la pression, et donc la traînée.

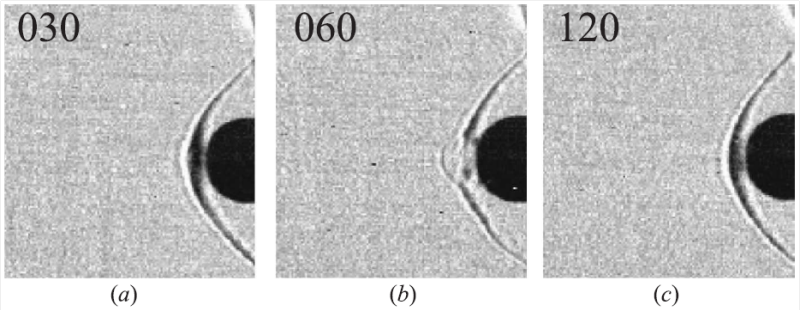

Figure 7: Interaction de plasma avec une onde de choc formée dans un écoulement de Mach 2.1 [18] (temps en μs).

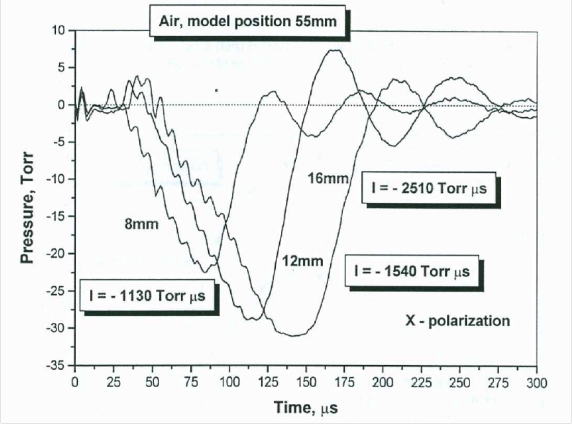

Figure 8: Pression de stagnation sur l'axe en fonction du temps[18].

Des simulations numériques liées à cette expérience ont été réalisées dans [19]. Les auteurs ont utilisé un code dynamique du gaz en trois dimensions et un modèle de thermochimie qui comprend 23 espèces et 238 réactions. Dans la figure 9, la pression de stagnation filtrée est tracée en fonction du temps et comparée avec les valeurs expérimentales, montrant un bon accord.

La plupart des expériences ont été menées dans les installations expérimentales à Saint-Pétersbourg, dans un ecoulement de M $= 2.1$. La puissance microondes était $195kW$ et la duree d'un impulsion $1.5\ \mu s$. L'energie EM a été concentré sur l'axe central de l'écoulement. Une décharge plasma micro-ondes sous la forme d'un plasmoïde d'environ 20 mm de longueur apparaît en face d'un corps. Sur la figure 10, l'interaction du plasmoïde à micro-ondes avec l'écoulement externe pour de pas de temps différents est présenté.

D'ailleurs, le dépôt d'énergie à plasma peut se produire par Localised Arc Filaments (LAFPA) [21] ou par des dispositifs DBD nano-secondes [22].

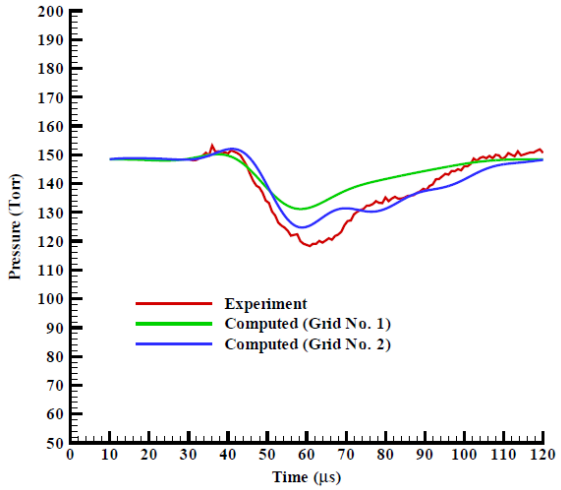

Figure 9: Pression de stagnation sur l'axe en fonction du temps[19].

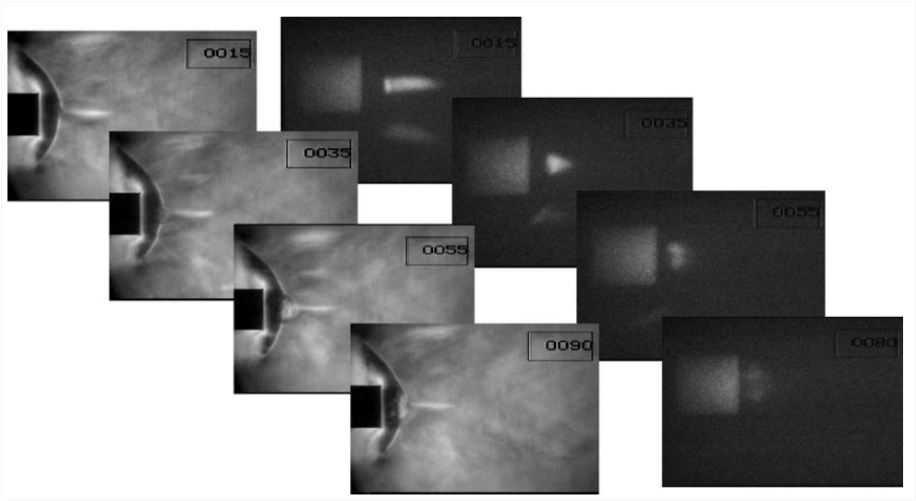

Figure 10: L'interaction du plasmoïde avec le corps de cylindre (M = 2,1, temps en ms) [20]. .

L'actionneur SDBD

Les actionneurs de décharges à barrière diélectrique surfaciques sont inclus dans la catégorie des méthodes d'addition de quantité de mouvement dans l'écoulement. L'effet de ce groupe est purement liée aux jets et jets de paroi. Dans les années 90, Roth et de son groupe a breveté un nouvel actionneur de DBD de surface en plaçant deux électrodes asymétrique de chaque côté d'un diélectrique [23]. Un électrode est exposé dans l'écoulement d'air et l'autre à la terre et, en outre encapsulé à l'intérieur un matériau diélectrique qui est placé sur la surface pour éviter la formation de plasma ci-dessous le diélectrique (cette configuration est principalement utilisé pour des applications aérospatiales en opposition à celui proposé par Roth dans [23]),

tel que présenté dans la figure 11.

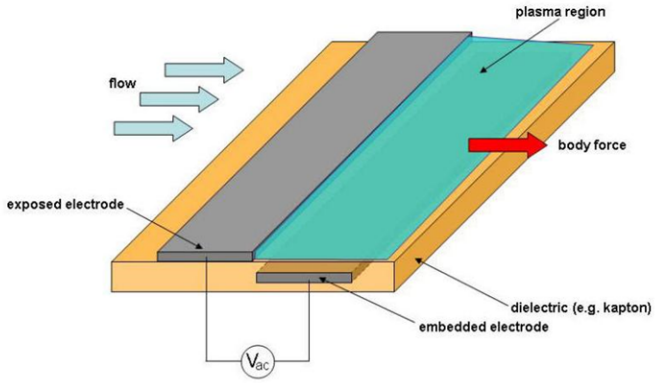

Figure 11: Représentation d'un SDBD sur une plaque plane (University of Maryland).

En excitant l'électrode exposée par une forme d'onde sinusoïdale (dans ce travail nous allons considérer excitations de forme d'onde sinusoïdale) et au-dessus de la tension d'allumage, un plasma apparaît sur la face supérieure du diélectrique à proximité de l'électrode exposée à l'air. La production de plasma induit un écoulement principalement en raison de l' transfert de quantité de mouvement entre les particules chargées et neutres, tandis que le chauffage du gaz est presque négligeable [24, 25].

La caractéristique unique des actionneurs SDBD est leur capacité à maintenir des décharges de plasma dans un volume relativement grand et d'éviter leur transition vers un arc thermique, en raison de l'auto-dénonciation de la décharge elle-même. L'accumulation d'électrons à la surface du diélectrique provoque une réduction de l'intensité du champ électrique local, qui conduit à l'extinction de la décharge [26].

La transformation de l'énergie électrique à cinétique par la force de Coulomb creer une force ou un «vent ionique». Cette force EHD produit par un actionneur de SDBD, est clairement liée à la variation de la morphologie de plasma au cours de son cycle alternatif. Dans [27], les auteurs ont mesuré une augmentation de la production de vitesse induite au cours de la demi-cycle négatif que dans le positif. Dans [28], les auteurs ont observé, une force x-dirigée positive dans les deux demi-cycles, avec 5 fois plus grande ampleur au cours du cycle négatif, et une force y dirigée négative dans les deux cycles. Bien que ces résultats semblent confirmer ceux de [29], les auteurs ont également observé une force de x-dirigé négatif lorsque la décharge est éteinte. Néanmoins, ils expliquent cette force négative en découplant son existence de la décharge de plasma, et en se référant aux effets visqueux et pertes turbulentes pour la décélération de la force totale. L'évolution du courant-tension dans le temps mesuré par [28] ainsi que l'évolution de la force dans le temps sont présentés dans les figures 12 et 13. Dans cette expérience, les auteurs ont utilisé un actionneur entraîné par une tension sinusoïdale de forte amplitude de 20kV et une fréquence de 1 kHz. Le diélectrique est en verre acrylique et était de 3 mm d'épaisseur.

Dans la plupart des résultats expérimentaux les vitesses maximales obtenues par un seul actionneur SDBD est dans l'ordre de $5-7m/s$. Une description détaillée des différentes demandes et configurations pour améliorer l'efficacité de ces actionneurs se trouve dans [30]. Diverses applications aérodynamiques peuvent être trouvés dans la littérature, démontrant les avantages de l'utilisation des actionneurs de SDBD pour le contrôle d'écoulement dans une variété de nombre de Reynolds [31, 32, 33].

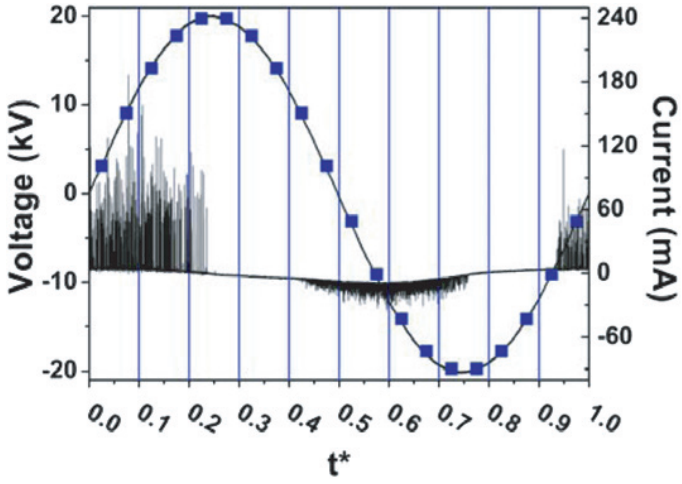

Figure 12: Courant et tension vs temps. $20kV, 1kHz$ [28].

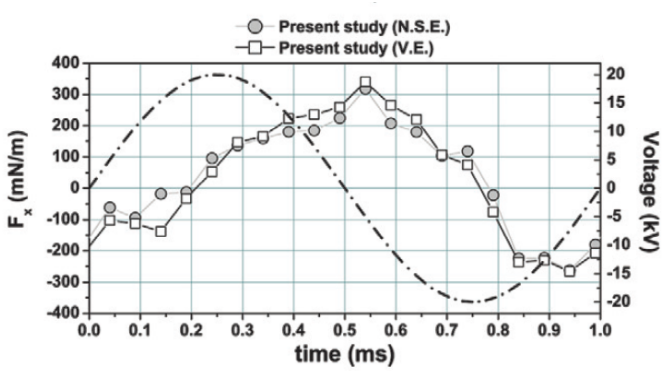

Figure 13: Force vs temps. $20kV, 1kHz$ [28].

L'actionneur Jet Synthetique Plasma (JSP)

Nous nous concentrons sur un nouveau concept qui a été récemment proposée par John Hopkins Applied Physics Lab [34] et améliorée par d'autres groupes [35, 36]: le jet synthétique plasma (JSP ou sparkjet à partir de maintenant).

Une vue schématique du fonctionnement de ce nouveau dispositif plasma de jet synthétique est représenté dans la figure 14. Le jet est créé par un dépôt d'énergie provenant d'une décharge d'arc pulsé qui chauffe l'air dans une petite cavité. La hausse de la température provoque l'expulsion de l'air de la cavité à travers le trou supérieur. Le jet à haute vitesse, est une masse nulle-net, comme une phase d'aspiration suit, le remplissage de la cavité. Les valeurs typiques de tensions utilisées est entre 3 kV et 5 kV, tandis que la fréquence de l'actionneur se trouve entre quelques Hertz et 2000. La buse de sortie de la JSP a typiquement un diamètre de l'ordre de 0,5 mm tandis que son volume capture $8mm^3$. Par rapport à des jets synthétiques plasmatiques traditionnels, ils offrent un rendement énergétique élevé, ce qui les rend intéressants pour des applications de

contrôle d'écoulement de véhicules à grande vitesse.

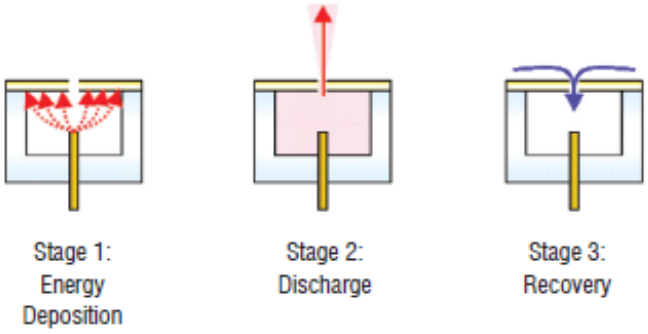

Figure 14: Schéma des étapes de fonctionnement du JSP [34].

L'efficacité de l'actionneur de JSP a été étudié dans [37, 38] tandis que la caractérisation et l'optimisation du dispositif dans [39, 40]. Dans [41], les auteurs ont caractérisé le jet expérimentalement et effectué des études paramétriques sur la fréquence de fonctionnement et la capacité. Ils ont mesuré les vitesses de jet jusqu'à $300 ms^{-1}$et les températures de réaction aussi élevé que $400K$. Les résultats d'une telle étude paramétrique de la puissance de la capacité de la pression de vitesse du jet et de la pression de stagnation sont présentés dans la figure 15.

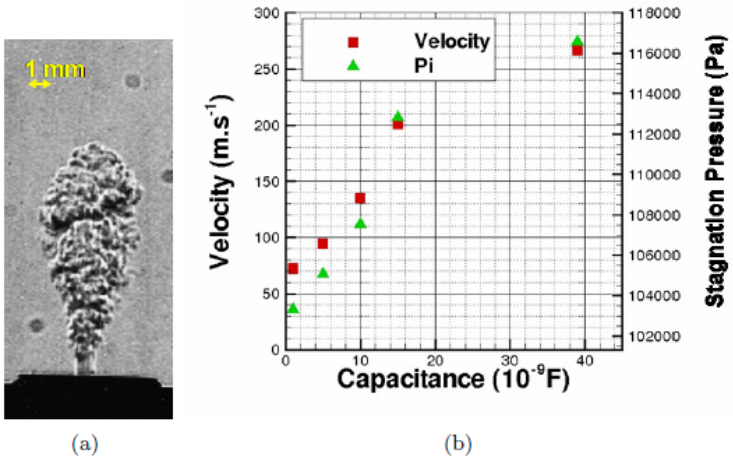

Figure 15: (a) Images Schlieren du jet circulaire 200 *mu* s après le début de l'échappement. (b) Vitesse (rouge carrés) et pression de stagnation (triangle vert) en fonction de la capacité. $f_{JSP} = 10Hz$ [41].

Une caractérisation aérodynamique d'un tel actionneur a été réalisée également dans [36]. Dans la figure 16, la vitesse du jet et le cycle de travail (le rapport entre la durée d'impulsion et la période d'une forme d'onde rectangulaire) avec des fréquences différentes sont représentées.

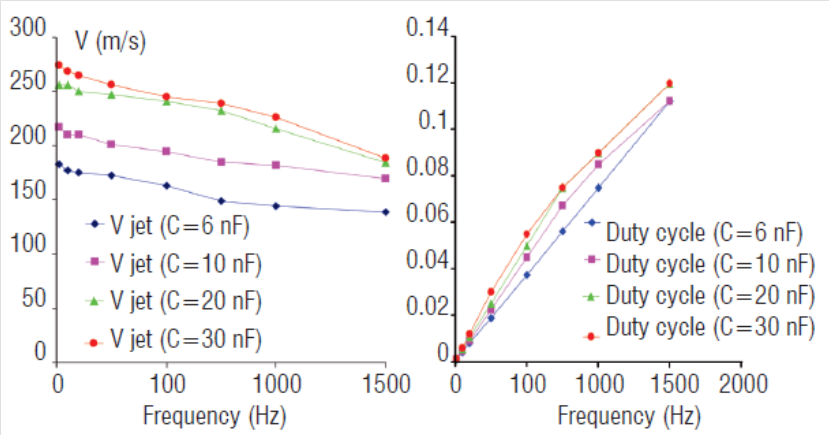

Figure 16: Etudes paramétriques sur la vitesse et le cycle du travail du jet en fonction de la fréquence pour le JSP de [36].

Modélisation numérique

Décrivant numériquement un problème tel que le contrôle d'écoulement aérodynamique basé sur des actionneurs de plasma, est un bon exemple d'un système complexe avec des physiques fortement. Pour avoir une meilleure idée du problème multi-échelle, nous allons donner quelques échelles typiques de longueur et de temps pour chaque type de plasma et d'actionneur. Pour les décharges micro-ondes, le libre parcours moyen à la pression atmosphérique est micrométrique ainsi que le front de plasma (qui s'écrit comme $\sqrt{D/\nu_i}$et dépend évidemment du champ réduit), tandis que la longueur d'onde est millimétrique. Le longueur caractéristique du système peut etre plusieurs longueurs d'onde. Les échelles de temps peuvent également être de plusieurs ordres de grandeur différente - la fréquence angulaire l'onde électromagnétique est de l'ordre de 10^{12}, celui de plasma en fonction de sa densité de l'ordre de $10^{10} - 10^{12}$tandis que la fréquence d'ionisation de l'ordre de $10^{8} - 10^{9}$. L'actionneur DBD a des longueurs caractéristiques du système de l'ordre de quelques centimètres, alors que la longueur de Debye est micrométrique. La fréquence d'ionisation est de l'ordre de $10^{11} - 10^{12}$, tandis que la fréquence du courant alternatif de l'ordre de $10^{3} - 10^{4}$. Les échelles de longueur de l'actionneur JSP sont principalement liés à la géométrie de la cavité et l'orifice (de l'ordre de millimètre) tandis que les structures turbulentes peut être très petite. Les échelles de temps sont également différents, comme par exemple le circuit électrique dont le temps caractéristique est de l'ordre de $10^{-5} - 10^{-6}$et la période de l'actionneur de l'ordre de $10^{-2} - 10^{-3}$. En outre, les échelles de temps et de longueur liées à la dynamique du gaz comme la diffusion thermique / conversion d'énergie et la formation et la propagation du choc sont importants pour le dépôt d'énergie à micro-ondes et bien sûr pour l'actionneur JSP.

C'est pourquoi nous parlons d'un problème multi-physique multi-échelles qui a finalement besoin d'hypothèses simplificatrices afin d'obtenir des modèles numériques couplés qui réussissent à décrire le comportement de ce système dans un coût acceptable (en ressources et en temps CPU).

Modèles de plasma

Comme décrit précédemment, la dynamique de transport de particules peuvent être représentés dans un niveau microscope ou macroscopique. Dans cette thèse, nous utilisons l'approximation fluide pour la modélisation de la dynamique du plasma. Nous avons affaire à des plasmas froids et en fonction de

l'actionneur d'intérêt et les différentes échelles de longueur associées à chaque type de plasma, différentes hypothèses doivent être faites. Pour les decharges micro-ondes, le plasma qui est fortement collisionnel conduit à un longueur de Debye très petit par rapport à la taille du plasma et donc à la quasi-neutralité. La température des électrons est d'ordres de grandeur plus élevée que celle du gaz qui reste dans les conditions ambiantes (au moins dans les premiers temps). L'approximation locale du champ efficace peut être utilisée pour déterminer les coefficients de transport de plasma au lieu d'une équation d'énergie pour les électrons, comme on suppose que le libre parcours moyen des électrons est plus petite que la longueur caractéristique des ondes électromagnétiques. Une équation simplifiée de diffusion que pour les électrons peut être utilisée car les ions produisent un courant négligeable et doit être couplée avec les équations de Maxwell par une équation de transfert de quantité de mouvement. Pour l'actionneur DBD, nous utilisons un modèle de dérive-diffusion couplée à l'équation de Poisson. La quasi-neutralité n'est pas valable ici, en particulier dans les régions où la force de corps est produit. Les électrons présentent de températures beaucoup plus élevées que la température des molécules de gaz qui reste ambiante aussi bien que pour les ions. Pour le jet synthétique plasma, le plasma d'arc est décrite par une hypothèse d'équilibre thermodynamique local (LTE) qui permet de ne faire aucune distinction entre les particules lourdes et des électrons et de prendre en compte une température unique pour représenter le comportement thermique de toutes les espèces comme un fluide unique. Le système ElectroMagnetoHydroDynamique (EMHD) d'équations est utilisé pour décrire le comportement du fluide associé à un circuit électrique équivalent de l'alimentation électrique. De lois des gaz réel sont intégrées dans les équations d'Euler du système EMHD pour faire face à des températures élevées atteintes dans un tel plasma et un schéma numérique adapté aux chocs est utilisé.

CFD et turbulence

Pour les écoulements subsoniques, (M $<$0.9), les équations de Navier-Stokes sont de type elliptique dans l'espace et parabolique dans le temps. La nature elliptique dans l'espace, souligne le fait qu'une perturbation dans un point du champ, peut causer influence en amont ou en aval du point (une zone de recirculation par exemple), et les méthodes numériques itératives sont appliquées. Les équations qui décrivent les ecoulements non visqueuses, compressibles et supersoniques (M $>$1) sont de type hyperbolique, ainsi l'insertion d'une perturbation dans le champ aura une incidence sur l'écoulement en aval en une zone limitée par les caractéristiques de l'équation différentielle. Ces perturbations peuvent être dans une forme d'ondes de choc.

La méthode numérique la plus courante pour résoudre les équations Navier-Stokes est la méthode de volumes finis. La nécessité de zones de calcul très raffinées (comme les régions de couche limite ou ondes de choc), des grilles non-cartésiennes pour modéliser des géométries complexes ou courbes (comme une aile d'avion) ainsi que les méthodes qui sont adaptables à différents régimes d'écoulement, a conduit à l'élaboration de la méthode de volumes finis pour la dynamique des fluides.

Il est important dans ce point de décrire la problématique principale des problèmes de CFD qui se trouve dans la nature chaotique et aléatoire de la turbulence. Les échelles de longueur et de temps impliqués dans les écoulements turbulents peuvent varier dans une grande extension. La résolution de tous ces échelles par une méthode numérique est plusieurs fois interdit car il devient extrêmement coûteux en termes de temps et de ressources de calcul.

Différentes approches ont été développées pour la modélisation des écoulements turbulents, en fonction de la résolution ou non de ses échelles typiques. Les simulations LES appliquent une technique d'un filtrage "low pass", basé sur les propriétés turbulentes afin de " tuer " les plus petites structures d'échelle de l'écoulement. Ensuite, les plus grandes structures sont totalement résolus tandis que les plus petits sont modélisés.

L'approche la plus courante pour la modélisation des écoulements turbulents sont les équations de Navier-Stokes moyennées (RANS ou URANS dans leur formulation instable). Ils décrivent une moyenne dans le temps ensemble d'équations avier-Stokes. Ces équations contiennent un tenseur des contraintes supplémentaires, la contraintes de Reynolds. La tâche principale de la modélisation de la turbulence est de développer de procédures de calcul précis suffisant pour que les ingénieurs puissent prévoir les tensions de Reynolds et les conditions de transport scalaires en precision. Ceci permettra alors le calcul des champs d'écoulement moyens sans avoir besoin de calculer le champs d'écoulement réels sur de longues périodes. Dans cette these, on est interessé par les modeles turbulentes de deux equations et notamment les trois modeles suivantes :

— Le modèle k-ε
— Le modèle k-ω
— Le modèle SST.

Références Bibliographiques

[1] James Luneau and Allan Bonnet. *Aérodynamique: théories de la dynamique des fluides*. Cépaduès-éd., 1989.

[2] Mohamed Gad-el Hak. "Modern developments in flow control". In: *Applied Mechanics Reviews* 49.7 (1996), pages 365–379.

[3] Mohamad Gad-el Hak. "Flow control". In: *Applied mechanics reviews* 42.10 (1989), pages 261–293.

[4] Brian N Nield. "An overview of the Boeing 777 high lift aerodynamic design". In: *Aeronautical Journal* 99.989 (1995), pages 361–371.

[5] Barton L Smith and Ari Glezer. "Vectoring and small-scale motions effected in free shear flows using synthetic jet actuators". In: *AIAA paper* 213 (1997), page 1997.

[6] Douglas R Smith et al. "Modification of lifting body aerodynamics using synthetic jet actuators". In: *AIAA paper* 209 (1998), page 1998.

[7] Jonathan Poggie. "Control of Shock-Wave/Boundary-Layer Interaction Using Volumetric Energy Deposition". In: *AIAA 2008 - 1090* (2008).

[8] Lester Lees. "The Stability of the Laminar Boundary Layer". In: (1947).

[9] D Caruana. "Plasmas for aerodynamic control". In: *Plasma Physics and Controlled Fusion* 52.12 (2010), page 124045.

[10] Kirill V Khodataev. "Microwave Discharges and Possible Applications in Aerospace Technologies". In: *Journal of Propulsion and Power* 24.5 (2008), pages 962–972.

[11] Doyle D Knight. "Survey of aerodynamic drag reduction at high speed by energy deposition". In: *Journal of Propulsion and Power* 24.6 (2008), pages 1153–1167.

[12] Jae-Hyung Kim et al. "Drag reduction with high-frequency repetitive side-on laser pulse energy depositions". In: *AIAA Paper* 5104 (2010).

[13] Nina Yurchenko et al. “Control of flow characteristics using localized plasma discharges”. In: *47th AIAA Aerospace Sciences Meeting and Exhibition*. 2009, pages 5–8.

[14] Vladimir L Bychkov et al. “A microwave discharge initiated by loop-shaped electromagnetic vibrator on a surface of radiotransparent plate in airflow”. In: *46th AIAA Aerospace Sciences Meeting*. 2008, pages 7–10.

[15] I Esakov et al. “Initiated surface microwave discharge as an efficient active boundary-layer control method”. In: *47th AIAA Aerospace Sciences Meeting and Exhibition*. 2009, pages 2009–0889.

[16] Yu F Kolesnichenko et al. “Microwave energy release regimes for drag reduction in supersonic flows”. In: *AIAA Paper* 353 (2002), page 2002.

[17] Yuri F Kolesnichenko et al. “Basics in beamed MW energy deposition for flow/flight control”. In: *AIAA Paper* 669 (2004), page 2004.

[18] MI Ryvkin and AA Gorynya. “Gas dynamic effect of microwave discharge on supersonic cone-shaped bodies”. In: (2004).

[19] Doyle Knight et al. “Interaction of microwave-generated plasma with a blunt body at Mach 2.1”. In: *AIAA Paper* 846 (2009), page 2009.

[20] Yuri F Kolesnichenko et al. “MW energy deposition for aerodynamic application”. In: *AIAA paper* 361 (2003), page 2003.

[21] Sergey Leonov et al. “The effect of plasma induced separation”. In: *AIAA paper* 3853 (2003), page 2003.

[22] Philip Peschke et al. “Interaction between nanosecond pulse DBD actuators and transonic flow”. In: *AIAA Paper* 3734 (2011), page 2011.

[23] J Reece Roth, Daniel M Sherman, and Stephen P Wilkinson. “Electrohydrodynamic flow control with a glow-discharge surface plasma”. In: *AIAA journal* 38.7 (2000), pages 1166–1172.

[24] Flint O Thomas et al. “Optimization of dielectric barrier discharge plasma actuators for active aerodynamic flow control”. In: *AIAA journal* 47.9 (2009), pages 2169–2178.

[25] Dmitriy M Orlov. *Modelling and simulation of single dielectric barrier discharge plasma actuators*. 2006.

[26] Zoran Falkenstein and John J Coogan. “Microdischarge behaviour in the silent discharge of nitrogen-oxygen and water-air mixtures”. In: *Journal of Physics D: Applied Physics* 30.5 (1997), page 817.

[27] Maxime Forte et al. “Optimization of a dielectric barrier discharge actuator by stationary and non-stationary measurements of the induced flow velocity: application to airflow control”. In: *Experiments in Fluids* 43.6 (2007), pages 917–928.

[28] N Benard, A Debien, and E Moreau. “Time-dependent volume force produced by a non-thermal plasma actuator from experimental velocity field”. In: *Journal of Physics D: Applied Physics* 46.24 (2013), page 245201.

[29] CL Enloe et al. “Plasma-induced force and self-induced drag in the dielectric barrier discharge aerodynamic plasma actuator”. In: *AIAA Paper* 1622 (2009), page 2009.

[30] Eric Moreau. “Airflow control by non-thermal plasma actuators”. In: *Journal of Physics D: Applied Physics* 40.3 (2007), page 605.

[31] Berkant Goeksel et al. “Steady and unsteady plasma wall jets for separation and circulation control”. In: *AIAA paper* 3686 (2006), page 2006.

[32] Mehul P Patel et al. “Plasma actuators for hingeless aerodynamic control of an unmanned air vehicle”. In: *Journal of Aircraft* 44.4 (2007), pages 1264–1274.

[33] ML Post. “Plasma actuators for separation control on stationary and unstationary airfoils”. In: *Doctor dissertation. Indiana: the University of Notre Dame* (2004).

[34] KR Grossman, BZ Cybyk, and DM VanWie. “Sparkjet actuators for flow control”. In: *AIAA Paper* 57 (2003), page 2003.

[35] Venkat Narayanaswamy et al. “Investigation of plasma-generated jets for supersonic flow control”. In: *46th AIAA Aerospace Sciences Meeting and Exhibit*. 2008, pages 2008–285.

[36] Daniel Caruana et al. “The “plasma synthetic jet” actuator. aero-thermodynamic characterization and first flow control applications”. In: *AIAA* 1307 (2009), page 2009.

[37] Mona Golbabaei-Asl et al. “SparkJet Efficiency”. In: *51st AIAA Aerospace Sciences Meeting including the New Horizons Forum and Aerospace Exposition*. 2013.

[38] SJ Haack et al. “Experimental Estimation of SparkJet Efficiency”. In: *42nd AIAA Plasmadynamics and Lasers Conference, Honolulu, AIAA Paper*. Volume 3997. 2011.

[39] KR Grossman et al. “Characterization of sparkjet actuators for flow control”. In: *AIAA Paper* 89 (2004), page 2004.

[40] BZ Cybyk, JT Wilkerson, and KR Grossman. “Performance characteristics of the sparkjet flow control actuator”. In: *AIAA Paper* 2131 (2004), page 2004.

[41] Pierrick Hardy et al. “Plasma synthetic jet for flow control”. In: *Proceedings of the 40th AIAA Fluid Dynamics Conference and Exhibit, AIAA Paper*. Volume 5103. 2010, page 2010.

Introduction

Generalities

Looking back in the history of aviation and aerospace technology, the need and challenge of improved aircrafts that fly more cost-efficient, safer and that are able to adapt in any flight scenario or environmental conditions was always the top goal of research activities. Moreover, in the last years, a lot of effort has been put on the reduction of the enviromental footprint of aircrafts as humanity seems to have understood that nature and human can only coexist in a mutual respective way. During all these years since the first flight from the Wright brothers in 1903, huge improvements have been made in every branch of aerospace engineering. Structural mechanics, propulsion systems, avionics and are just some of the sectors that still under non-stop research targeting more efficient aircrafts. The field of aerodynamics though, as the main physics behind a flying body, was and still is a key element of the optimization process for enhanced aircraft performance.
The aerospace field incorporates such a variety of different physics, that intuitive engineering solutions have always to walk hand-in-hand with multi-disciplinary theoretical research. This fundamental research on the complex interaction between different physics, can and has already provided innovative ideas, many of whose have been incorporated in commercial and military aircrafts. This thesis deals with a novel approach for aerodynamic flow control, as means of an integrated solution for high-lift, low-drag, adapting performance enhancement of modern aircrafts. This novel approach, is based on the usage of plasma actuators, in order to actively control the aerodynamic flow around an aircraft's body. In 2009, AIAA announced the plasma actuators as the 5th most promising technology for the future of aviation as it is indeed an innovating and rapidly emerging technology that can increase the flight envelope and decrease the environmental impact of aircrafts.

The usage of plasma actuators on commercial aircrafts (or even military ones), as almost every novel and innovating technology, has to be proven safe, efficient, adaptive in different environmental conditions and of course it has to be optimized. Therefore, it is quite clear that fundamental research on the formation,

Photo by NASA, ESA, and the Hubble Heritage Team (STScI/AURA)

development and interaction of plasma with the air and its aerodynamic consequences, has to provide all such information through extensive experiments and theoretical - numerical work. Numerical modeling in particular, can be a powerful weapon in the hands of scientists and engineers in order to understand, optimize and lead the way to the commercialization and application of this technology for the benefit of humanity. The highly demanding coupling between electricity or electromagnetism, plasma and air though, requires advanced numerical models and techniques to deal efficiently with such problems.

The work presented in this thesis, has as its main objectives exactly this: The development and validation of numerical methods in order to efficiently simulate the operation of some of the most important types of plasma based actuators as means of aerodynamic flow control. We are interested in three types of plasma actuators : Microwave discharges, the Dielectric Barrier Discharge and the Plasma Synthetic Jet. Concerning microwave discharges, the objectives are more fundamental than the other types of actuators. Numerical simulations can provide the basic informations on the physics and complex interaction between the EM waves the plasma and the gas, in order to understand the plasma creation, evolution and energy balance. Flow control applications of such discharges, as an energy deposition method, have been already quite well documented in the literature. Concerning the two other groups of actuators, the goals of this thesis is more applied as we are interested mostly on modeling their operation and consequent momentum production. In all cases, numerical models and techniques have been developed or utilized in order to obtain results that can be validated with experiments and provide either more information of their physics and operation or a basis for further development and improvement.

This thesis work, has been a results of the collaboration between the mathematical modeling and numerical simulation research unit (M2SN) at the department of information treatment and modeling (DTIM), at ONERA - The French Aerospace Lab, Toulouse and the laboratory of LAPLACE, GREPHE of the university of Paul Sabatier, Toulouse. The author has received a 3 year fellowship from the French state distributed by ISAE.

The research activity has been a part of various research projects in regional, national and international level. Moreover, the obtained results have been presented in numerous conferences and scientific days, and published (or under review) in international journals. A list of the publications and main presentations is presented below.

Publications linked to this thesis work

- G. Sary, G. Dufour, F. Rogier, and K. Kourtzanidis, "Modeling and Parametric Study of a Plasma Synthetic Jet for Flow Control", AIAA Journal, 52.8 (2014): 1591-1603.
- K. Kourtzanidis, F. Rogier, J.P. Boeuf, “Implicit Finite Differenence Time Domain Modeling of Microwave Plasmas towards fully 3D Simulations”, submitted and under review, Computer Physics Communications, 2014.
- K. Kourtzanidis, F. Rogier, J.P. Boeuf , “Three-dimensional Simulations of Plasmas Patterns Formation during Microwave Breakdown in Air”, submitted and under review, Journal of Applied Physics, 2014.
- K. Kourtzanidis, F. Rogier, J.P. Boeuf , “Modeling of air’s heating effects during the propagation of microwave streamers”, in preparation for the Journal of Applied Physics.
- Kourtzanidis, K., Rogier, F., Dufour, G., Boeuf, J.P., Unfer, T. Numerical Modelling of Plasma Actuators, ERCOFTAC Bulletin 94, Special Theme: Plasma Aerodynamics, March 2013.
- Kok, J.C., Catalano, Kourtzanidis, K., Rogier, F., Unfer, T. Coupling CFD with Advanced Plasma Models, ERCOFTAC Bulletin 94, Special Theme: Plasma Aerodynamics, March 2013.

— Kourtzanidis, K., Numerical Simulation of Plasma Actuators for Flow Control, AIAA Meeting Paper, 2013-0134, January 2013
— F. Rogier, G. Dufour, K. Kourtzanidis, Numerical Simulation of sinusoidal DBD actuators and comparison with experiments, AIAA, Atlanta GA, 16-20 June 2014.

Main presentations linked to this thesis work

— Kourtzanidis, K., Numerical Simulation of Plasma Actuators for Flow Control, AIAA Meeting Paper, 2013-0134, January 2013. Invited as 1st prize winner of the 8th AIAA-Pegasus Student Conference.
— Kourtzanidis, K., Rogier, F., Boeuf, J.P., Numerical modelling of plasma for flow control in aerospace applications, Plasma Science (ICOPS), 2012 Abstracts IEEE International Conference on Plasma Science.
— Kourtzanidis, K., Rogier, F., Dufour, G., Boeuf, J.P., Unfer, T., Numerical simulation of plasma actuators for flow control, ERCOFTAC-PLASMAERO 2012, Toulouse, France.
— Kourtzanidis, K., Rogier, F., Dufour, G., Sary, G., Numerical Modeling of the Plasma Synthetic Jet, EUCASS ATW, 2013, Aussois, France. Poster presentation.
— Kourtzanidis, K., Rogier, F., Boeuf, J.P., Numerical Modeling of Microwave Discharge Actuators, EUCASS ATW, 2013, Aussois, France. Poster presentation.
— Kourtzanidis, K., Rogier, F., Boeuf, J.P., Numerical Modeling of Microwave Discharges for Flow Control, Journées ONDES du Sud-Ouest, April 2014,Toulouse, France. Poster presentation.
— Kourtzanidis, K., Rogier, F., Boeuf, J.P., Numerical Modeling of Microwave Plasma Discharges for Aerodynamic Flow Control, ISEHD, 2014, Okinawa, Japan.
— Kourtzanidis, K., Sary, G., Rogier, F., Dufour, G., Numerical modelling of plasma actuators for flow control - The Plasma Synthetic Jet, ISEHD 2012, Gdansk, Poland.

Thesis Structure

The structure of this thesis is as follows : In chapter 1, theoretical aspects about aerodynamics, flow control, plasma, plasma actuators and numerical modeling are presented. In chapter 2, we present the numerical models and techniques used to simulate microwave discharges as well as numerical results and comparisons with experiments. In 3, we are studying numerically the DBD actuator, with the help of two different numerical codes based on the same physical model, and present numerical results of its operation characteristics and flow control applications. In 4, we address our interest into the PSJ actuator (or SparkJet), presenting again the numerical model used and results obtained, along with parametric studies on various parameters and a simplified aerodynamic study. In chapter 5, a general conclusion of this research is provided, followed by some perspectives for future work. All chapters include an introduction - presentation section as well as conclusion - perspectives linked to each chapter's work. All chapters are preceded by an extended summary in french, as required by the doctoral school of Aeronautics and Astronautics.

1. Theoretical Aspects and Literature Review

1.1 Aerodynamic Flow Control

Aerodynamic flow control integrates different approaches in order to achieve enhanced aerodynamical performance of an aircraft. As the roots of all the different approaches lay on the classic external aerodynamics, it is necessary to review some basic physics to move forward in the more detailed description of flow control methods.

1.1.1 Aerodynamics

To understand the importance of aerodynamics as means of improving an aircraft's performance , we need to ask a simple question: What is the goal of aerodynamics in aerospace?

A general answer could be: Designing aircrafts which can produce high lift and experience low drag. A representation of the forces acting on an airfoil section (similar to a flying object) is shown in figure 1.1. Defining the dimensionless lift and drag coefficients as:

$$\begin{aligned} C_l &= \frac{F_l}{\frac{1}{2}\rho V^2 A} \\ C_d &= \frac{F_d}{\frac{1}{2}\rho V^2 A} \end{aligned} \tag{1.1}$$

where F_l is the lift force (the force component perpendicular to the flow direction), F_d is the drag force (the force component in the direction of the flow velocity), V is the air's speed relative to the aircraft and A the reference area, it's easily understood that aerodynamic engineers seek to maximize the lift coefficient while minimizing the drag one, in order to achieve efficient flight behaviour with reduced power consumption. The force due to the weight of the object and the thrust force concern mostly structures and propulsion engineering.

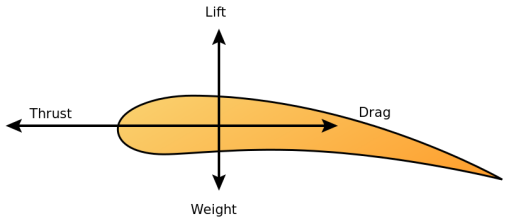

Figure 1.1: Forces acting on an airfoil moving in air.

These two fundamental forces can be derived from the classic governing equations of fluid mechanics, which are presented below as they are essential in understanding the different mechanisms of generation of these forces [1]. Note that in reality, there is a single, net, integrated force caused by the pressure variations along a body. This aerodynamic force acts through the average location of the pressure variation which is called the center of pressure.

Governing equations

The three main principles of physics applied into a Newtonian, isotropic, Fourier, ideal gas , can be written in their conservative differential form :

$$\frac{\partial \rho}{\partial t} + \nabla \cdot (\rho \vec{V}) = 0 \tag{1.2}$$

the conservation of mass,

$$\frac{\partial (\rho \vec{V})}{\partial t} + \nabla \cdot (\rho \vec{V} \otimes \vec{V} - \vec{\vec{\Sigma}}.\vec{V}) = \rho \vec{F} \tag{1.3}$$

the conservation of momentum,

$$\frac{\partial (\rho E)}{\partial t} + \nabla \cdot (\rho E \vec{V} - \vec{\vec{\Sigma}}.\vec{V} - \lambda_c \vec{\nabla} T) = \rho \vec{F}.\vec{V} + \rho \phi_\tau \tag{1.4}$$

the conservation of energy.

In the above equations, ρ is the gas density, $\vec{V}$ is the velocity vector, F is the body force vector, E is the total energy of the gas, λ_c is the gas thermal conductivity, T is the gas temperature and $\vec{\vec{\Sigma}}$ is the stress tensor defined as:

$$\vec{\vec{\Sigma}} = -(p + 2\mu/3 \nabla \cdot \vec{V})\vec{\vec{I}} + \mu(\vec{\nabla}\vec{V} + \vec{\nabla}\vec{V}^T) \tag{1.5}$$

where I is the unity tensor, μ is the gas dynamic viscosity and p is the pressure. Note that the the stress tensor can be seen as the sum of one related to the pressure and one related to the viscous forces, named here as S_v.

These equations consist the famous Navier-Stokes equations, derived independently by G.G. Stokes, in England, and M. Navier, in France, in the early 1800's. Along with two equations of state, which read for an ideal gas :

$$\begin{aligned} de &= C_v dT \\ p &= \rho RT \end{aligned} \tag{1.6}$$

where $e = E - \frac{V^2}{2}$ is the internal energy and R is the gas constant per unit mass, they describe the dependence between velocity, pressure, density and temperature of a moving continuum fluid including viscous effects. They provide an excellent model for most flows of air (and other fluids) including turbulent flows and high speed flows with shock waves. Further simplifications can be made assuming for example incompressible flow (the density is assumed to be either a constant or a given function of temperature) or inviscid flow (leading to the Euler equations).

A scaling and non-dimensionalization process for the N-S equation 1.3, lead to the non-dimensional form [1]:

$$\omega\rho\frac{\partial\vec{V}}{\partial t} + \rho\nabla\vec{V}.\vec{V} = -\frac{1}{\gamma M^2}\nabla p + \frac{1}{R_e}\nabla\cdot\vec{\vec{\Sigma}}_v + \frac{\rho}{F_r^2}\frac{\vec{F}}{F} \tag{1.7}$$

where γ is the adiabatic index (the isentropic expansion factor) and the Mach number M, the Reynolds number R_e, the reduced frequency ω and the Froude number F_r are defined as:

$$\begin{aligned} M &= \frac{V_\infty}{\alpha_\infty} \\ R_e &= \frac{\rho_\infty V_\infty L}{\mu_\infty} \\ \omega &= \frac{L}{V_\infty t_\infty} \\ F_r &= \frac{V_r}{\sqrt{FL}} \end{aligned} \tag{1.8}$$

The subscript ∞, implies the unperturbed by any obstacle quantities of free-stream and $\alpha_\infty = \sqrt{\gamma\frac{p_\infty}{\rho_\infty}}$ is the speed of sound.

Observing the N-S equations, we see that the total force exerted to the fluid is a combination of pressure forces, viscous forces, body forces and stress ones. For each different flow regime - free shear flows, boundary layer flows, turbulent or laminar flows, high or low speed flows - these terms contribute differently into the energy balance and force generation. Wall friction, vorticity production, favorable or adverse pressure gradient due to curvature of a surface, wall viscosity, turbulent stresses, shock waves will all be key factors in determining the flow behavior.

Let's take a look more closer to these terms, starting with the ones contributing to the aerodynamic drag and focusing on flows around an aircraft - simplified as an airfoil section. We are focusing on boundary layer flows, i.e. flows over a surface where a distinction of the flow to a boundary layer one (where the viscous effects are significant) and an external one can be made. The boundary layer flow obeys a simplified

closed-form solution of the N-S equations and the equations of the external, assumed inviscid flow, can also be significantly simplified. The total drag force is a sum of the forces exerted by the pressure distribution over the surface (pressure or form drag), the forces due to friction that depend mostly on the boundary layer nature, the viscosity and wall friction, the induced by the lift production forces related to the vortex generation as wing tip and trailing edge vortices, and any wave drag due to shock waves and the subsequently modification of the pressure field around the airfoil - wing.

The lift force is generated by the change of direction of a fluid by a solid object. It is a straight-forward consequence of Newton's third law of action-reaction, which implies that the turning of a fluid into one direction will generate a force into the opposite direction. Thus for an airfoil, the total contribution of the turning of the flow by the upper and lower surface will lead to the generation (or not) of the lift. It is obvious, that the geometry of the airfoil is essential for the lift production as well as the air's relative speed and its viscosity. To calculate the total lift force around an airfoil, different approaches can be applied. Using the bernoulli principle the total lift can be found by taking the integral of the pressure normal forces over the surface. Potential flow, based on the Kutta-Joukowski theorem that relates the lift generated by an object to the fluid's density, velocity and circulation (the line integral of the velocity field over the surface which is related to vorticity by the Stoke's theorem) and in addition with the Kutta condition (that states : "A body with a sharp trailing edge which is moving through a fluid will create about itself a circulation of sufficient strength to hold the rear stagnation point at the trailing edge."), can also be used to estimate the lift force.

We see that the two main aerodynamic forces depend on various parameters. Lift can only exist, if the fluid is in contact with the surface, so a separated flow will not generate any lift. The speed of the fluid is also effecting positively the lift generation as well as the vorticity around the surface. Drag force depend strongly on parameters as discontinuities, friction, pressure distribution and significantly the nature of the flow especially inside the boundary layer. This last parameter is extremely important both for lift and drag forces, so a few notions about boundary layer theory and turbulent flows have to be discussed here.

Figure 1.2, represents a flow over a solid surface. When a fluid flows over a solid surface, it becomes attached to the solid in the vicinity of the surface. That implies that its tangential (and normal) velocity is zero relative to the boundary. This is the so called no-slip condition. The layers of the fluid just above the surface are moving, generating a shear stress between the wall and the fluid. The boundary layer is defined as the region of the flow near the surface until a height where $V = 99\%V_\infty$. This height is called the boundary layer thickness and denoted with δ. For a flow over a flat plate, the boundary layer grows over the distance from the leading edge until it becomes fully developed. A crucial parameter for the nature of the boundary layer is the Reynolds number, R_e. At low R_e, the flow is laminar and depending on the distance traveled and other parameters that can cause disturbances (such as surface geometry or wall roughness) may remain laminar or transit to a turbulent one. A laminar boundary layer experiences a streamwise velocity that changes uniformly as one moves away from the wall, i.e. the streamlines are parallel. At high R_e, the flow is turbulent. A turbulent boundary layer experiences unsteady changes of the velocity components and the streamlines are no longer parallel. A chaotic distribution of swirling flows inside a boundary turbulent layer, make it more energized that a laminar one as intense mixing between the different fluid layers is taking place. In figure 1.3, the evolution of a boundary layer over a flat plate is represented. Note that a turbulent boundary layer consists of a laminar inviscid zone close to the surface, a buffer zone where mixing starts to take place, and a fully turbulent one.

The nature of the boundary layer, as mentioned, will have an direct impact to the drag force due to friction.

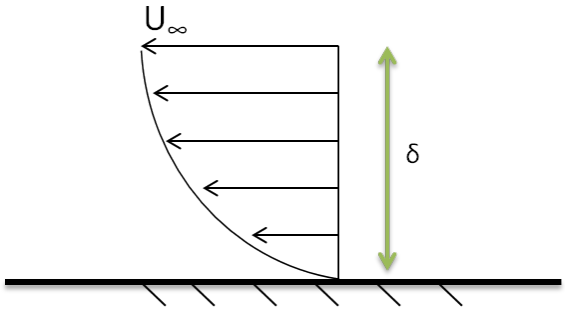

Figure 1.2: Streamlines of flow over a surface. Note that the velocity V corresponds to U in the figure.

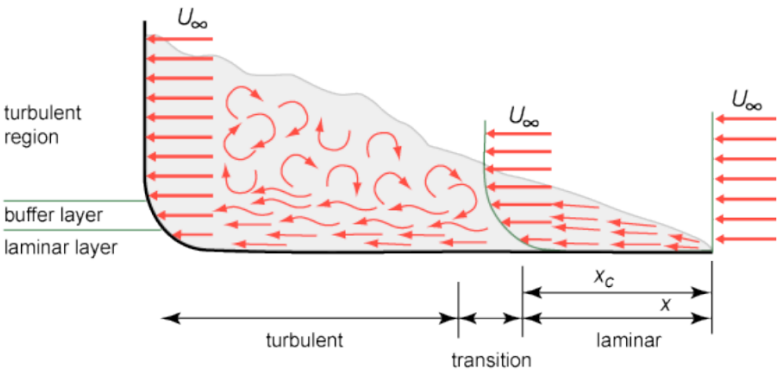

Figure 1.3: Boundary layer formation over a flat plate. Note that the velocity V corresponds to U in the figure.

Defining the skin drag due to friction as :

$$D_f = \tau_w A \tag{1.9}$$

where A is the wetted surface and τ_w the wall shear stress defined as:

$$\tau_w = \mu(\frac{\partial V}{\partial y})_{y=0} \tag{1.10}$$

we note that the dynamic viscosity and the gradient of the parallel to the surface component of the fluid velocity V, to the normal to the surface direction y are the determining parametres for the skin drag evaluation. Turbulent boundary layers present a more steep gradient of velocity at the wall, resulting to a larger shear stress compared to laminar layers.

The influence of the nature of the boundary layer is important also for the pressure-form drag. Due to the low energy fluid layers close to the surface, the boundary layer is sensitive to changes of pressure, that can cause the separation of the flow from the surface. A continuous or sudden adverse pressure gradient for example, can lead to a reduction of the relative to the surface speed of the boundary layer to values near zero or even a reverse of its flow. The reversed or near to zero flow fluid layers near the surface cause the boundary

layer to detach from the surface, resulting into vortical structures or eddies. Flow separation leads to an increased pressure drag due to the pressure field modification of the external potential flow. As a turbulent boundary layer is more energetic and thicker, it is can sustain larger and longer adverse pressure gradients making it more difficult to be separated and thus reducing the pressure drag. When a laminar boundary layer has separated, transition to turbulence of the free-shear layer may lead to a reattachment and a formation of a laminar bubble. The complex interplay between the different drag and lift generation or reduction processes are summarized in figure 1.4. The overall goal of an engineer can be reduced to the maximization of the lift to drag ratio.

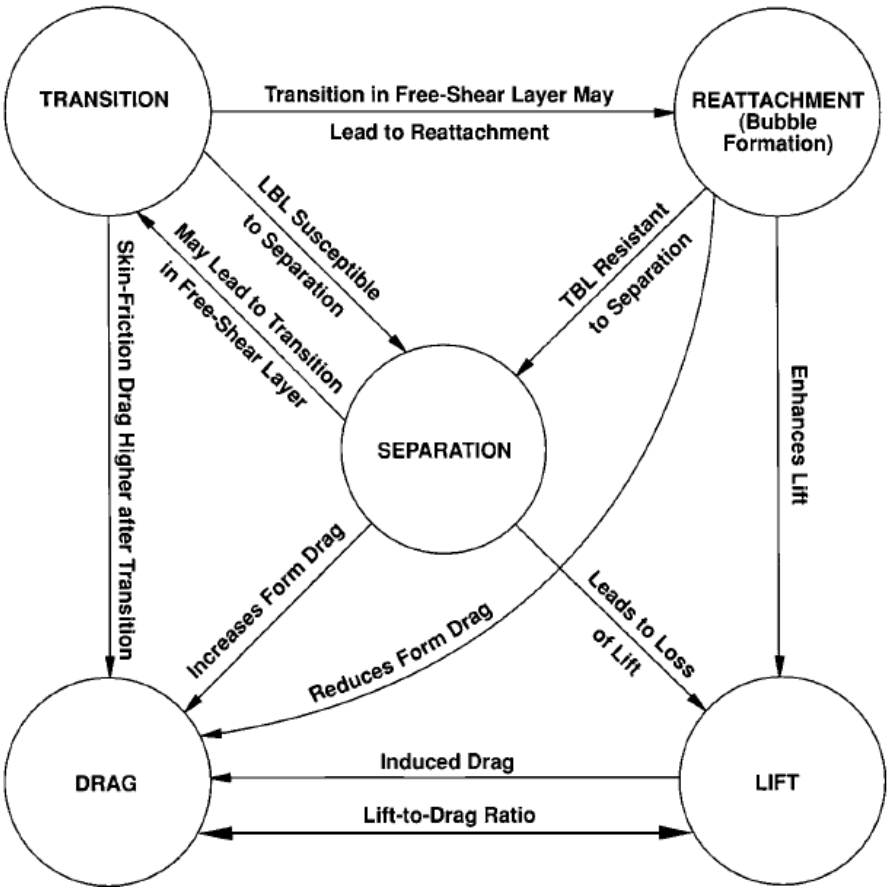

Figure 1.4: Influence of flow nature and behaviour on lift and drag [2].

For high-speed flows, compressibility effects and shock wave formation can introduce wave drag, which can lead to a dramatic increase of the total drag of a flying object. These severe discontinuities of pressure, density, temperature and velocity can have a huge impact to the overall pressure distribution as well as the boundary layer thickness.

A supersonic airstream passing through a normal shock wave experiences these changes:

— The airstream is slowed to subsonic.

— The airflow immediately behind the shock wave does not change direction.
— The static pressure and density of the airstream behind the wave is greatly increased.
— The energy of the airstream (indicated by total pressure—dynamic plus static) is greatly reduced.

Shock wave formation causes an increase in drag. One of the principal effects of a shock wave is the formation of a dense high pressure region immediately behind the wave. The instability of the high pressure region, and the fact that part of the velocity energy of the airstream is converted to heat as it flows through the wave is a contributing factor in the drag increase. The drag resulting from airflow separation is another one. If the shock wave is strong, the boundary layer may not have sufficient kinetic energy to withstand airflow separation. The drag incurred in the transonic region due to shock wave formation and airflow separation is known as wave drag. A considerable increase in thrust(power) is required to increase flight speed beyond this point into the supersonic range where, depending on the airfoil shape and the angle of attack, the boundary layer may reattach.

At this point, it worths giving some more details on a crucial physical notion described above: Turbulence. Turbulence is an unsteady,aperiodic motion in which all three velocity components fluctuate, mixing matter, momentum, and energy. Turbulent flows have the following characteristics:

— They are always chaotic and commonly described statistically.
— They always occur at high Reynolds numbers. They are caused by the complex interaction between the viscous terms and the inertia terms in the momentum equations.
— They are rotational; that is, they have non-zero vorticity.
— Turbulent flows are dissipative. Kinetic energy gets converted into heat due to viscous shear stresses. Turbulent flows die out quickly when no energy is supplied. Random motions that have insignificant viscous losses, such as random sound waves, are not turbulent.
— Their diffusivity leads to increased rates of momentum, mass and heat transfer with rapid mixing.

The energy of the turbulence structures or the energy spectrum has been studied a lot through the years. Turbulence quantities can include really small rotational structures or big ones, called eddies or big ones – each one containing a different amount of energy.

The turbulent length scales can be summarized as:

— Largest eddies. Integral length scale $= k^{3/2}/\varepsilon$.
— Length scales at which turbulence is isotropic. Taylor microscale $= (15\nu V^2/\varepsilon)^{1/2}$.
— Smallest eddies. Kolmogorov length scale $= (\nu^3/\varepsilon)^{1/4}$. These eddies have a velocity scale $= (\nu\varepsilon)^{1/4}$ and a time scale $= (\nu/\varepsilon)^{1/2}$.

where ε here is the energy dissipation rate in m^2/s^3, k is the turbulent kinetic energy in m^2/s^2 and ν is the kinematic viscosity in m^2/s.

Typically energy gets transferred from the large eddies to the smaller eddies. However, sometimes smaller eddies can interact with each other and transfer energy to the (i.e. form) larger eddies, a process known as back-scatter. Viscous dissipation in the smallest eddies converts kinetic energy into thermal energy. Vortex-stretching cascade process maintains the turbulence and dissipation is approximately equal to the rate of production of turbulent kinetic energy. We will see in the last section of this chapter that all these different scales, lead to an increased complexity regarding numerical simulations and appropriate for each flow conditions, turbulence models have been developed through the years.

It's worth mentioning, that there are several other aerodynamic effects that may do not influence directly the aerodynamic force components (even if most of them do so by induced drag), but are important for the overall performance of an aircraft. Von-Karman (or not) vortex shedding caused by flow separation, can lead to strong oscillations of the pressure field that can damage the structure of the aircraft. Wing tip

vortices are a major drawback in efficient and rapid take-off of commercial aircrafts. Turbulence, shock waves, and vortices are sources of noise. Modern jet engines or propeller technology are based on advanced aerodynamics of bladed turbomachines, where the same principles apply for efficient conversion of energy to thrust. All combined, these aerodynamic basic feautures are the core for highly-efficient aircrafts and the way of controlling them is more than essential. Reducing drag and increasing lift is obviously important, but a more detailed and sophisticated way has to be developed for the new generation of aircrafts, as an adaptable procedure during flight. Thus, we need to repose our question :

What is the goal of aerodynamics ?

1.1.2 Flow control

Re-posing the question, we can maybe now, refine our answer: Aircraft designs need to provide the ability of controlling the flow around an aircraft's body or inside its engines, in such a way that in any time of a flight, the aircraft can respond as quick and accurate as possible to the (pre-defined or not) orders of the pilot (or any operator), minimizing the energy needed in doing so. This control has to be adaptable under different conditions (the design of an aerodynamic body that has the best overall performance for a specific flight scenario can also be thought as a flow control method but it is not adaptable - it is a given factor) and under the will of the operator.

Flow control methods have been developing since the Wright brothers and the era of Prandlt and his great and pioneering work on boundary layer control. Ailerons, spoilers, elevators etc. are mechanical actuators which are used for aircraft control. Thus, flow control can be used to 'create' or 'destroy' lift and drag forces on the wings producing moments that will maneuver or stabilize the aircraft. Wing-tip devices, vortex generators, blowing and sucking are actuators (or structural modifications) that are used also for improving the lift-to-drag ratio. Hence, flow control can be used to control flow structures in smaller scales (such as turbulent parameters) or bigger ones (such as wing tip vortices) and interact with boundary layer dynamics or even shock wave ones, improving the overall aerodynamic coefficients of the aircraft.

A fully detailed description of flow control theory and relevant methods can be found in [3, 2]. Among different classifications of flow control methods, in this thesis we focus on two big categories, passive and active methods. This classification will permit us to understand better the benefits of plasma based actuators as means of aerodynamic flow control.

Passive Flow Control Methods

Passive flow control refers to control methods that do not directly inject energy into the flow. These methods include mainly devices such as vortex generators, riblets and suction techniques, while flaps, slats ailerons can also be considered as such (mostly referred to as control surfaces). They are mostly structural features of a surface that introduce either small scale disturbances to the flow or modify the overall aerodynamic profile of the surface, leading to a modification to the lift to drag ratio of the body.

Physical bumps, in the form of three-dimensional symmetric cylinders have been investigated in [4] to study the vortical structures and turbulence enhancement of a $U_\infty = 27.5m/s$ flow. As seen in figure 1.5 , they have measured a downwash towards the centerline right after the bump and two streamwise vortices of high turbulent levels forming downstream of the bump's position.

In [5], direct numerical simulation of a physical hemispherical bump of $d = 4mm$ in Mach numbers of $3.3, 5.2, 8.2$ flows over a flat plate have been performed, demonstrating the effectiveness of the bump on

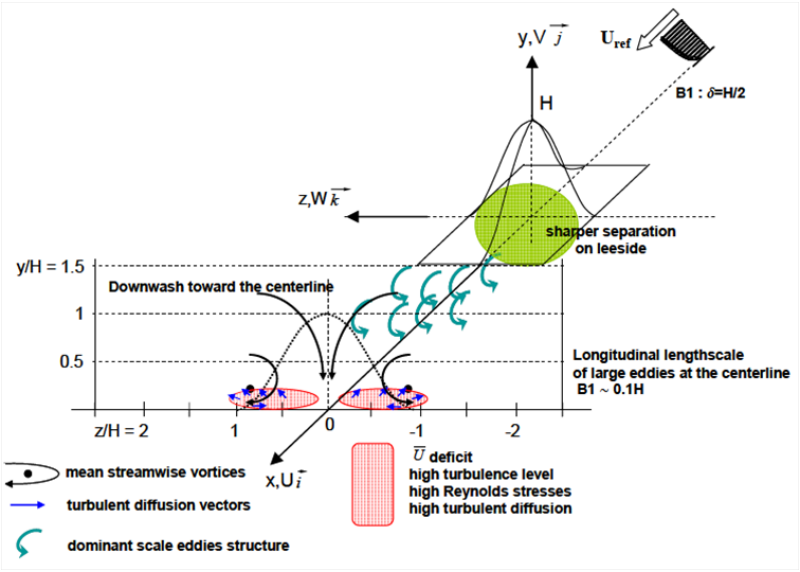

Figure 1.5: Structures formation due to a gaussian shape physical bump[4].

transition provoking for the lower Mach number flows, as seen in figure 1.6. The authors results are in good agreement with experimental results of [6].

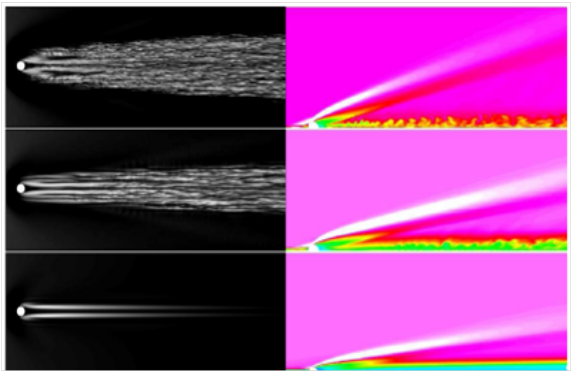

Figure 1.6: Transition provocation due to a hemisperical bump over a flat plate at M=3.3, 5.2, 8.2 (from up to down)[5].

Vortex generators (VGs) typically consist of small vanes attached to the surface of a wing. These vanes generate small scale tip vortices that take energy from the main flow and re-energize the boundary layer over the surface, or provoke transition to turbulence and thus making the BL more stable and more resistive to separation. A review of the research of low profile vortex generators (defined as those with a device height between 10% and 50% of the boundary-layer thickness) can be found in [7]. Micro-vortex generators have been proved to reduce boundary layer separation of a flap control surface at landing, by experimental investigations in [8]. Transonic and supersonic shock wave - boundary layer interaction and separation control

via vortex generators has been studied in [9, 10], and their efficienty in reducing the shock wave induced separation of the boundary layer has been also demonstrated. A general review of the effectiveness of such actuators as well geometrical configurations can be found in [7] is shown in figure 1.7.

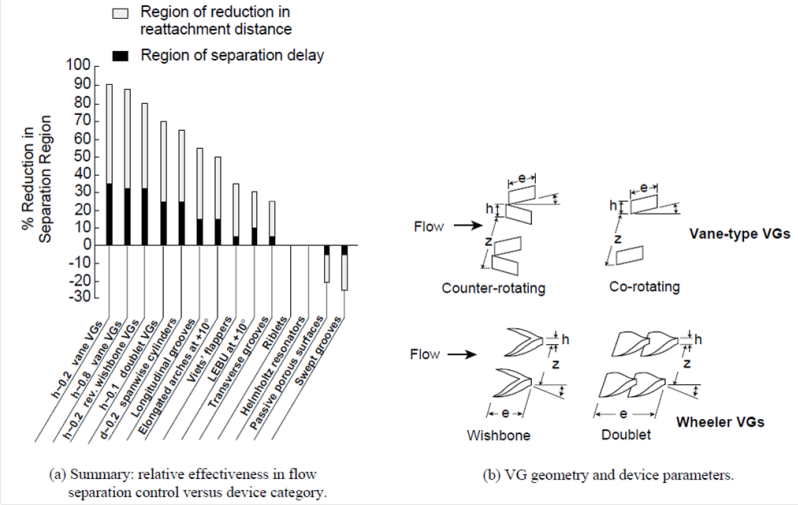

Figure 1.7: Effectiveness of different geometrical configurations of vortex generators [7].

Riblets are small surface protrusions mostly aligned in the streamwise direction of the flow, an efficient approach for drag reduction [11]. The vortical structures that they create interfere with the viscous sub-layer of the boundary layer and studies point that they modify the near wall cycle of streaks and quasi streamwise vortices [5,6] in a manner that reduces the overall velocity gradient near the wall. This effect, leads to a reduction of the skin-friction drag that can be as high as 10%, for optimized riblet length scales as demonstrated in [12]. Such devices have been widely researched in the past decades and even commercialized in the aerospace sector. A recent analysis of its effects in turbulent boundary layer parameters and consequent drag reduction can be found in [13].

Suction of near wall fluid can lead to transition delay as it inhibits the growth of the boundary layer and alters its velocity profile [14]. It can be achieved through porous media, small cavities or other methods in a steady or unsteady operation. The alteration of the velocity distribution over a surface via passive suction though, can lead to unwanted results under different conditions and the integration of such devices, both in structural and operational means, limit their performance and applicability.

Passive flow control methods have been already implemented onto aircrafts, as they offer a non-expensive and easy way to enhance the aerodynamic coefficients. They present although, major drawbacks. Their use is limited : Their influence into the flow is constant and intrusive as they can not adapt to each flow configuration - becoming optimal for just some phases of the flight envelope of a modern aircraft while they can become less efficient or even induce negative effects for other phases. To surpass this drawback, flow control methods need to be active (and moreover reactive as we will see in a while) - having the ability to adapt their performance for each flight regime and energetic - modulating their intensity into flow modification depending on the aircraft's needs.

Active Flow Control Methods

Active flow control methods, provide as described before, the solution to the necessary adaptability of flow control. They are always based on actuators and they introduce external energy in the flow. These methods can be operated in a predetermined (no sensors/feed-back control included), or a reactive way where a closed or open loop control system provides continuously flow information via sensors to adapt the actuators operation according to the needs of each flight phase. It is quite clear that predetermined methods present the same drawback of non-adaptability as the passive methods (although they can be introduce high energy into the flow, strongly modifying it), so we will focus on reactive active control methods.

Active flow control involves the triad of flow phenomena, actuators-sensors, and controls as presented in figure 1.8.

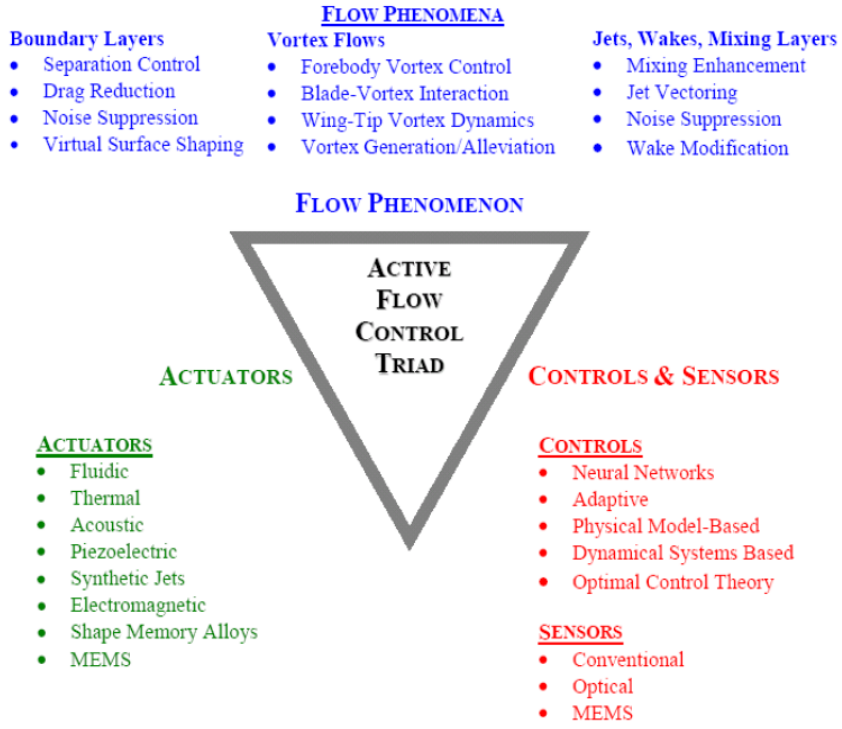

Figure 1.8: The feedback flow control triad. (Courtesy D. E. Parekh, Georgia Tech Research Institute)

It is convenient at this point, to separate such methods into two sub-categories : Blowing and wall jets, vortex generator jets, synthetic jets, piezoelectric actuators, can be considered as momentum addition active flow control methods, while surface heating, thermal bumps with heating elements, can be considered as energy(in terms of heat) deposition methods.

Momentum addition methods

In this sub-category, the addition of kinetic energy into the flow is the mechanism that will manipulate it and will lead to the change of its characteristics. These methods present zero or negligible induced heat into the flow.

Active pulsed suction and blowing are two classic methods of active flow control. Suction methods described in the previous section can also be applied in an (re)active way. Blowing through leading edge slats and trailing edge flaps have been already integrated in aircrafts enhancing their aerodynamic performance [15]. Their effect in separation delay and drag reduction via vortex generation or re-energizing the boundary layer's velocity profiles has been demonstrated by various studies [16, 17]. In [17] the authors have demonstrated that steady blowing is significantly inferior to periodic excitation in terms of performance benefits. In [18], pulsed blowing over an axisymmetric body has been investigated experimentally and computationally, showing that pulsed blowing can lead to separation control and drag reduction while suction delays transition but had presented limited overall performance. Oscillatory momentum addition can lead to small or large scale vortical structures that can efficiently interfere with turbulent parametres of the flow, or even large scale vortices such as wing tip ones. These vortex generator jets can be be actuated in an efficient net-zero mass synthetic jet operation [19]. A jet is being generated by the oscillatory motion of a surface within a small cavity embedded on a surface. As synthetic jets are operating with the working fluid of the flow and have a zero mass flux, their interaction with the cross-flow leads to the formation of vortex rings due to the shear layer between the jet's flow and the external one. In [20], studies on a cylinder model demonstrate the efficiency of such actuators on drag reduction and lift enhancement. In [21], wing tip trailing vortex control using synthetic jets have been compared to steady continuous jet actuators, demonstrating the beneficial effects of the first method on diffusing the vortex.

A varierty of flow control applications have been demonstrated using synthetic jet actuators as enhanced mixing, separation control and virtual shaping [22, 23]. In [19], the authors proposed a piezoelectric synthetic jet actuator, where the zero-net-mass jet is generated by a piezoelectric diaphragm in a periodic manner. Piezoelectric actuators utilise piezoelectric materials to produce flow disturbances that allow for flow control [24]. The efficiency in terms of energy expenditure and enhanced aerodynamic performance as means of separation control devices have been demonstrated in [25].

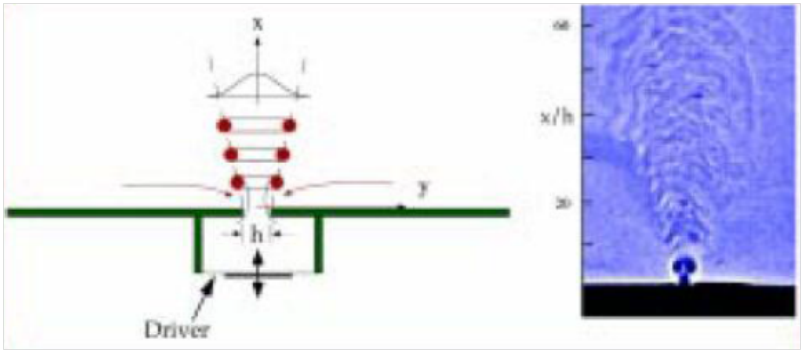

Figure 1.9: The piezoelectric synthetic jet actuator and its flow field in quiescent air [19].

A relative new concept of active flow control actuators is the use of the Lorentz force to create wall jets like actuators. Flush mounted Lorentz force actuators are used to induce a current density field j , and a magnetic field, B , in the vicinity of the wall to provide a three dimensional body force corresponding to the Lorentz force, $L = jxB$. In [26, 27] the authors have investigated such kind of actuators for turbulent boundary layer control in terms of separation. In [28], the authors have experimentally studied the effects of a streamwise Lorentz force actuators on a NACA-0017 hydrofoil's suction side. Separation prevention was

observed in near to critical angles of attack due to the high momentum addition in the boundary layer due to the Lorentz force. The actuators geometry is shown in figure 1.10, while the effects on the lift coefficient for the NACA-0017 hydrofoil over different angles of attack is shown in figure 1.11.

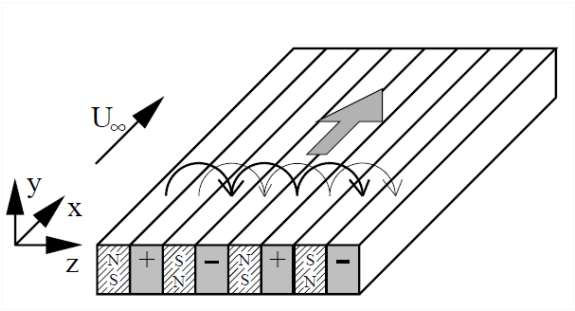

Figure 1.10: Lorentz force actuator configuration for a streamwise body force production [28].

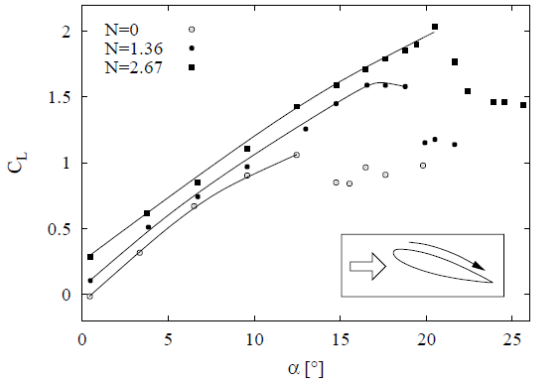

Figure 1.11: C_L versus angle of attack with different magnitudes of the Lorentz force ($Re = 2.9 \times 10^4$, electrode width$= 0.03\times$ chord length)[28].

Energy deposition methods

Theoretical and experimental investigations have demonstrated that heating or cooling of a surface has a direct impact on laminar to turbulent transition. In general for gases, cooling results to an increase of the critical Reynolds number - the Reynolds number for which laminar to turbulent transition occurs as it affects the viscosity and density in a beneficial way for boundary layer disturbances reduction (growth rate of Tollmien–Schlichting (T-S) waves and rate of amplified frequencies).

The author in [29] showed theoretically that the critical Reynolds number based on distance from the leading edge increases from 10^5 to 10^7 when the wall of a flat plate placed in an air stream is cooled to 70% of the absolute ambient temperature. Experimental investigations in [30] have demonstrated this effect: a cooling of the wall to $0.95 \times T_\infty$ results in doubling of the critical Reynolds number.

Energy deposition methods in terms of localized thermal disturbances in a flow present some similarities with physical bumps and lately they have been various studies concerning them, especially in supersonic and hypersonic flows, where the can be particularly effective. These thermal bumps were extensively studied numerically, in [31, 32], where cases over a flat plate for a supersonic flow of Mach 1.5 were studied. The pulsed heating under a frequency of 100 Hz and duty cycle of 0.5 has been compared to steady heating. Again, the formation of counter rotating stream wise vortices has been observed along with a series of compression and expansion waves. The shedding of the vortices as they move downstream are stronger under the pulsed mode and their intensity increases with increased energy levels. In figure 1.12 the streamwise vorticity and spanwise velocity contour is being shown.

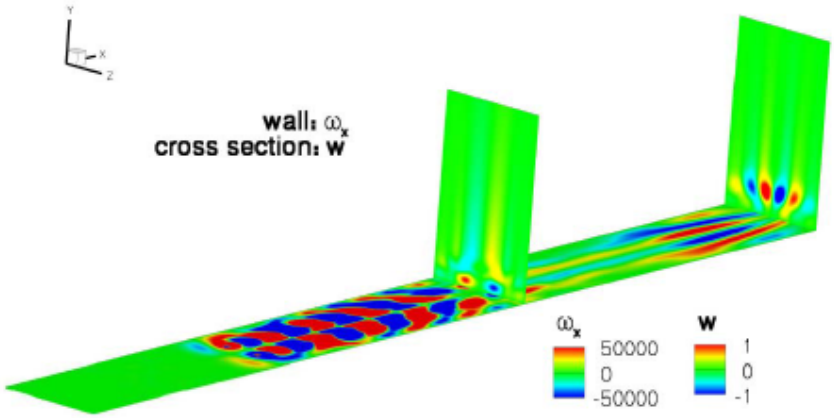

Figure 1.12: Streamwise vorticity and spanwise velocity contour for the pulsed heating case ($T = 10 \times T_0$) [31].

Via parametric studies, it was shown that the rectangular element was more effective than the circular counterpart and as stated, the smaller width of the rectangular element produced higher disturbance energy, while the full-span heating indicated delayed growth of the disturbances. The disturbance energy increased with the initial temperature variation, and the lower frequency produced less disturbance energy. In [33], a thermal surface element has been placed on a flat plate, inside a Mach 1.5 flow as seen in figure 1.13. The author, used a pulsed heating with a frequency of $100kHz$ and an increase of temperature corresponding to $0.76 \times T_{ad}$. He noticed vortices formation from the edge of the heating element, and an increased boundary layer thickness downstream of the element.

Poggie[34], has simulated the effect of a 100W power energy source over a flat plate (at a height of 8mm). The Mach number of the external flow was hypersonic at a Mach 14. This high external velocity is justified to the fact that the perturbation due to the energy addition is amplified by the viscous-inviscid interaction that's governed by the cube power of the incoming Mach number. Vorticity and flow distortion has been observed, that propagate downstream the heated region.

Although such kind of actuators are promising and efficient for flow control, they again introduce a lot of inconveniences. Many of them are mechanical. Consequently they need maintenance and their fabrication and integration cost is high. Many of them are intrusive, they induce drag or require surface modifications

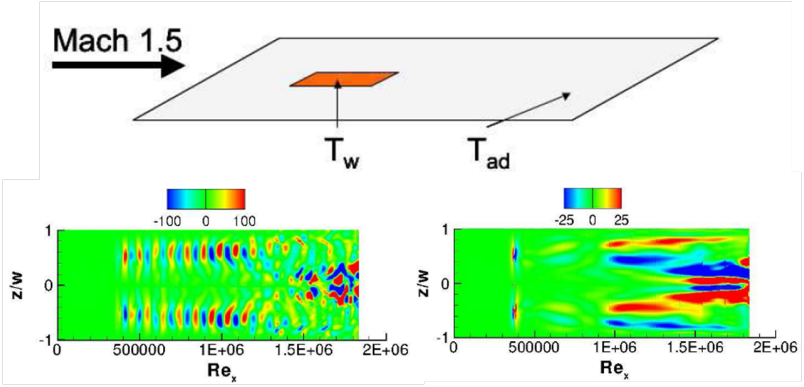

Figure 1.13: Streamwise instantaneous and time mean vorticity contours on the wall ($Re = 1.4 \times 10^6$) [33].

that will alter the aerodynamic profile of an aircraft/wing. And maybe most importantly: their response time is big. Modifications of the flow field, especially in high speeds or when maneuverability is important, are occurring extremely fast and so, an actuator need to respond as quick as possible to be able to provide a rigid flow control mechanism.

Innovations in active flow control methods and plasma actuators

Lately a new group of actuators has been proposed by various scientists based on plasma discharges[35]. They can provide flow control possibilities through momentum addition or heat deposition in almost real time, while many of them are simple and simple to fabricate and easy to integrate on a surface. Such kind of actuators include, amongst others, the DBDs, the Plasma Synthetic Jet and Microwave discharges, three categories of actuators that we are focusing on in this thesis. As these type of actuators, depend on plasma formation and the consequent modification of the air flow structure, it is essential to review some basic notions of plasma physics .

1.2 Plasma Physics

1.2.1 Basic notions

So, what defines this innovative type of actuators and why are they interesting for flow control applications? To answer this question, plasma itself has to be defined.

Plasma is often called the fourth state of matter. In general we can define it as an ionized gas in which collective effects dominate over collisions. Plasmas resulting from ionization of neutral gases generally contain equal numbers of positive and negative charge carriers.The fraction of the atoms that are ionized is called the degree of ionization. In this situation, the oppositely charged fluids are strongly coupled, and tend to electrically neutralize one another on macroscopic length-scales. Such plasmas are termed quasi-neutral ("quasi" because the small deviations from exact neutrality have important dynamical consequences for certain types of plasma modes). Strongly non-neutral plasmas, which may even contain charges of only one sign, occur primarily in laboratory experiments: their equilibrium depends on the existence of intense

magnetic fields, about which the charged fluid rotates.

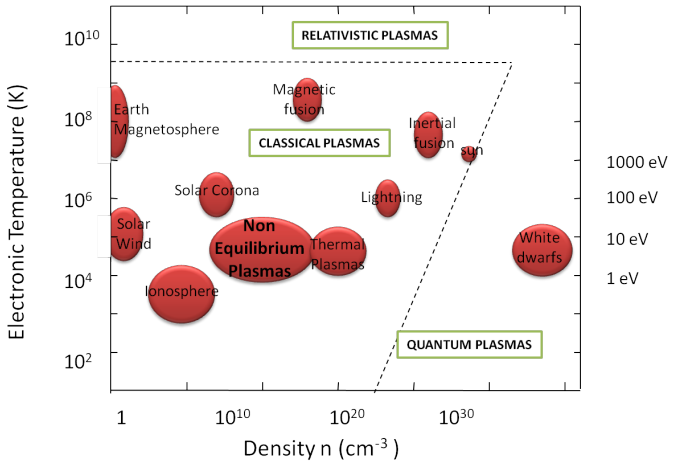

Figure 1.14: Different types of plasma versus temperature and density.

We distinguish here, two main categories of plasmas : Hot and cold ones. This kind of plasmas are mainly observed as arc discharges under high pressure. Hot plasmas are fully ionized and magnetically confined plasmas that reach high temperatures in order as the ones used to achieve nuclear fusion. Cold plasmas, are weakly ionized plasmas in either equilibrium (thermal plasmas) or non-thermal equilibrium. Plasmas used for aerospace flow control purposes are cold plasmas, therefore we focus on them.

We have spoken of quasi-neutral plasmas. This means that the plasma is macroscopically neutral and for a plasma to exist, the size of the plasma has to be big in respect to the distance (the Debye length see below) needed for a particle to gain enough energy (due to the plasma charges and related to the electron's thermal velocity see below) to perturb the initial electron's velocity distribution : Enough charged particles have to exist so that the electric interaction perturbs strongly the thermal motion of the electrons. The smaller scales in which the plasma neutrality is not valid and charged regions can appear, are linked to the Debye length. The Debye length reads:

$$\lambda_D = \sqrt{\frac{\varepsilon_o T}{ne^2}} \tag{1.11}$$

The Debye length can be considered as the scale over which mobile charge carriers screen out electric fields in a plasma. When an object is inserted into a plasma, electric field perturbations can only be reproduced in the distance of the Debye length.

Quasi-neutrality demands that

$$n_e \simeq n_i = n \tag{1.12}$$

where n_e is the electron density (i.e., the number of particles per cubic meter) of electrons, n_i is the number density of ions and n is the plasma density and a cold plasma is one when its degree of ionization δ is

smaller than 10^{-2} where δ takes the form

$$\delta = \frac{n_e}{n_e + N} \tag{1.13}$$

Briefly we can summarize the main characteristics of a non-equilibrium, quasi-neutral, cold plasma that distinguish it from the 3 other forms of matter:

— It contains charged particles(electrons,ions) as well as neutral ones in fundamental or excited states that make the plasma electrically conductive so that it responds strongly to electromagnetic fields.

— The particles' densities and temperatures are different and defines the plasma's behavior as well as the velocity distribution of the particles inside it (the collisions mostly lead to a Maxwellian distribution of the velocity). Thermodynamically the plasma is considered to be in non-equilibrium.

— The collisions among the charged particles and the neutral ones, can excite the last ones , leading to a modification of the initial gas' properties.This phenomenon explains also the production of light (photons). The excited particles can be de-excitated and thus emit photons.

In a plasma, the statistical fluctuations of the number of particles contained in an arbitrary phase space interval can be neglected and a velocity distribution function $f_s(r,v,t)$ can be used to define the density of the particle s, in the phase space (r,v). Defining an volumic element as (d^3rd^3v), the number of s type particles contained in that volumic element at an instant t, is given by:

$$Nb_s = f_s(r,v,t)d^3rd^3v \tag{1.14}$$

Supposing a cold plasma where the collisions between the particles are instantaneous and local, the evolution of the transport of the charged particles is described by the Boltzmann's equation, which in that case reads:

$$\frac{\partial f_s}{\partial t} + v.\nabla_r f_s = -q(E + v \times B).\nabla_v f_s + C[f_s] \tag{1.15}$$

where the first term of the second hand of the equation corresponds to forces and the second term to the collisions contribution. From the velocity distribution function, the mean values for the density, velocity and energy of the particles (averaged on the velocity of the particles) can be deduced with the help of the density probability of the presence of the particles in the space of phases which reads :

$$P_{s_{r,v,t}} = \frac{f_s(r,v,t)d^3v}{n_s(r,t)} \tag{1.16}$$

where the density of particles s reads :

$$n_s(r,t) = \int_v f_s(r,v,t)d^3v \tag{1.17}$$

Then any variable ξ can be expressed with its average value as :

$$\bar{\xi}(r,t) = \frac{1}{n(r,t)} \int_v \xi(v) f_s(r,v,t)d^3v \tag{1.18}$$

Then we can define the average velocity as :

$$\vec{u} = \bar{v}(r,t) = \frac{1}{n(r,t)} \int_v v f_s(r,v,t) d^3v \tag{1.19}$$

and the thermal velocity of a particle as :

$$\vec{V} = \vec{v} - \vec{u} \tag{1.20}$$

The thermal velocity is related to collisions while the mean velocity to electric or other forces applied to the charged particles. The mean value of the thermal velocity vector is zero due to the random collisions, but not of the module of its vector and thus it contributes to the mean kinetic energy of a particle, which reads:

$$\bar{\mathscr{E}} = \frac{1}{2} m \bar{V^2} + \frac{1}{2} m u^2 \tag{1.21}$$

The mean kinetic energy is therefore, the results of the thermal motion and a movement caused by external forces (flow, electric forces, etc..). Note here that in a non-equilibrium plasma the distribution of the velocities of the charged particles does not obey a Maxwellian distribution, as happens for plasmas in thermal equilibrium. Nevertheless, the mean energy of the thermal motion of the particles is being defined as such, characterized by their temperature, T, as:

$$\frac{1}{2} m \bar{V^2} = \frac{3}{2} k_B T \tag{1.22}$$

where k_B is the boltzmann's constant.

Under normal atmospheric conditions, the thermal energy of the molecules is low. The low energy collisions between different molecules can not provide sufficient energy for electronic change of orbit and thus modification of the molecule's atomic structure. If the temperature of the gas is increased, such procedure can be possible as the molecules gain thermal energy and make more energetic collisions. Under such conditions, electrons can be detached and the gas can be ionized. In argon for example, a raise of temperature to approximately 6000 K is necessary for sufficient ionization and plasma formation.

To create plasma without the need of excessive gas heating, an electric field can be applied to the gas (via DC, AC voltage or high-frequency EM waves). The free electrons, always present at a small fraction due to cosmic rays, will then be accelerated by the electric field and collide with the molecules. If the energy gained by the electric field is high enough, the collisions can ionize the molecules creating an avalanche of electrons as the newly "born" ones will continue the ionization process under the electric field's effect. By this process, different types of plasmas can be created - ones that maintain a thermal equilibrium and others that do not. This category offers a lot of advantages : plasmas can be formed without the need of excess energy, and different regimes can be controlled. The interaction of the plasma charges and the electric field provides also unique features that make this type of plasmas, extremely interesting and they have been the base of research for aerospace applications.

It is quite obvious that the inter-particle collisions is the most important feature of such plasmas. Their frequency and energy is essential for creating, maintaining and controlling the plasma. As the electrons mass

is a lot smaller than the ions one, their mobility, μ_e, defined as:

$$\mu_e = \frac{e}{m\nu_c} \tag{1.23}$$

is hundred of times higher than the ions one. In equation 1.23, ν_c is the frequency of collisions which is proportional to the density of the neutral particles and to the velocity of the charged particles. Thus, in a weakly ionized plasma, it's the electrons and their collisions with neutrals that will sustain the plasma and interact intensively with applied fields while the ions (when the fields are not too strong) will have an indirect effect to the electron's motion through ambipolar diffusion (see below).

Electrons will gain energy between two collisions due to the electric field, E, related to their drift velocity, v_d, which reads:

$$v_d = \mu_e E \tag{1.24}$$

and lose energy at each collision, related to their thermal velocity. The collisions among the electrons and neutral particles, can take different forms. We talk about elastic collisions, recombination, rotational vibrational and electronic excitation, dissociation and ionization. All these processes, make the plasma a reactive medium. Elastic collisions cause kinetic energy transfer between the collided particles depending on their mass ratio. As the electrons mass is very small, its mostly the ions that participate in such collisional procedures.

The electric field being the sum of the electric field applied and the field produced due to the charges in plasma will be modified by these collisions and the consequent modification of the charged and neutral particles densities. The number of collisions, n_c that an electron will experience during a certain period of time, depends on the molecule's density, N and velocity, and the electron's velocity. In figure 1.15, a representation of an electron being in collisional path with a seed molecular density is presented. Supposing that the velocity of the molecules, v_M, are way smaller than the electrons one, v_e this number is given by $n_c = QNdx$, where Q is the effective collisional cross section. The mean free path, $\lambda_e = dx/n_c = 1/(NQ)$, is the distance between two collisions and the frequency of collision can be defined as:

$$\nu_c = \frac{v_e}{\lambda_e} = NQv_e \tag{1.25}$$

This collisional frequency is the sum of each different type of collisions.

Another important time scale factor in plasma physics is the plasma electron frequency, which by assuming that the ions stay motionless and neglecting collisions read :

$$\omega_p = (\frac{ne^2}{\varepsilon_o m})^{1/2} \tag{1.26}$$

, which corresponds to the plasma's electrostatic oscillation frequency (with $t_p = 1/\omega_p$ being the plasma period). It's the response of the motion of the electrons to a local perturbation of the charge distribution and density. Under collisional plasma conditions these oscillations are being damped. The spatial equivalent of t_p is the debye length which gives the distance traveled by a typical plasma particle during a plasma period.

Table 1.1, summarizes some orders of magnitude for the space and time scales defined.

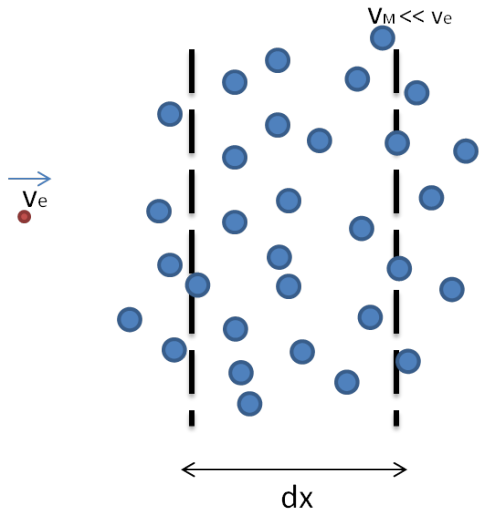

Figure 1.15: Electron in collisional path with a seed molecular density.

Pressure (Pa)	λ_d **(μm)**	λ_e	ν_c **(s^{-1})**	ω_p **(rad/s)**
10^2	75	1mm	10^9	5×10^{10}
10^5	75	1μm	10^{12}	5×10^{10}

Table 1.1: Plasma length and time scales for $N = 10^{19}\ cm^{-3}$, $Q = 10^{-15}cm^{-2}$, $T_e = 1eV$, $n_e = 10^{12}cm^{-3}$, $v_e = 10^8 cm/s$

1.2.2 Macroscopic approach

The transport of the charged particles can be described in two ways: Either in a mesoscopic level, where equations for the distribution function of each particle has to be written or in a macroscopic level, where the behavior of the plasma can be described in terms of the ordinary equations of fluid-gas dynamics, assuming that the plasma can be defined by the mean values of density, velocity and energy of the particles. Here, we will focus our interest on the second, macroscopic description of a plasma.

The macroscopic quantities correspond to velocity moments of the distribution function i.e. integrals of some power of velocity times the distribution function over velocity-space. Multiplying Boltzmann's equation (eq. 1.15) by a variable y that depends on the instantaneous velocity of a particle and after integration over the velocity space, we obtain the generalized transport equation in the form :

$$\frac{\partial n\bar{y}}{\partial t} + \nabla_r.(n\overline{yv}) - n\overline{\alpha.\nabla_v y} = \int_v y[\frac{\partial f}{\partial t}]_{coll} dv^3 \tag{1.27}$$

where $\alpha = qE$ supposing that there is weak or no magnetic fields. By replacing y by 1, v and vv we obtain the 0th, 1st and 2nd velocity moments of the Boltzmann's equation that correspond to the continuity, momentum transfer and energy equations respectively. As the velocity moments of the Boltzmann's equation

form infinite series where each equation depends on the higher order one (via the gradient of the higher's order moment), closure approximations have to be made so that we can obtain a closed system of three equations that describe the plasma's macroscopic behavior.

As we are assuming quasi-neutral plasmas, we can write the transport equations only for the electrons - the ions obey similar laws. Therefore, the 0th moment of Boltzmann's equation integrated over velocity space, gives the equation of continuity as :

$$\frac{\partial n_e}{\partial t} + div\Gamma = S \tag{1.28}$$

where Γ is the flux density of the electrons and $S = \sum_i N_i$ is the bulk sources of creation or annihilation of particles. The source term $S = Nn_e k_i$, depends on the densities of electrons and gas molecules, and the rate coefficient k_i for each collision or chemical reaction i.

The momentum transfer equation is derived from the first moment of Boltzmann's equation integrated in velocity space, under the assumption of isotropic and diagonal tensor of pressure :

$$m_e n_e(\frac{\partial v_e}{\partial t} + (v_e \cdot \nabla)v_e) = -n_e eE - \nabla P_e - n_e m_e v_e \nu_c \tag{1.29}$$

where $P_e = n_e k_B T_e$ is the electrons pressure tensor. If we drop the inertia term due to the small electron mass, we see that the temporal evolution of the charged particles (electrons for example here) momentum is due to three forces : One related to the gradient of pressure, one related to the electric (neglecting the magnetic) forces and one related to frictional forces due to collisions. If we assume furthermore that collisions take place on a much shorter time and length scales vis-a-vis to the macroscopic field variations, we obtain the drift-diffusion equation in its stationary formulation:

$$n_e v_e = -\frac{n_e eE}{m_e \nu c} - \nabla(n_e \frac{k_B T}{m_e \nu_c}) \tag{1.30}$$

giving the particles' flux density $\Gamma = n_e \bar{v_e} = -n_e \mu_e E - \nabla(D_e n_e)$ incorporating drift, diffusion and convective components. The diffusion coefficient D for Maxwellian particles is given by the Einstein's relation :

$$D_e = \frac{\mu_e k_B T}{e} \tag{1.31}$$

which is inversely proportional to the gas density as the mobility term μ_e depends inversely to the collisional frequency that is proportional to the gas density. As the mobility of the ions is approximately 100 times smaller than the one of electrons, and their temperature higher than the ionic one (in a non-equilibrium plasma), the electron's diffusion coefficient is larger than the ionic one (for $T_{ions} = 300$ K, the diffusion coefficient of electrons is approx. 5000 times larger than the ionic one). This implies that the two species in a plasma, would diffuse with different rates, the electrons would transport faster than the ions and the plasma could not stay quasi-neutral. What happens in reality is that the divergence of the species transport, results in a change of the charge density, the space charge, which leads in return to the creation of an electric field that will slow down the electrons. Then, both species diffuse with a common ambipolar coefficient, D_α.

Assuming quasi-neutrality and zero net current ($\Gamma_e = \Gamma_i$), we find the ambipolar coefficient from equation 1.29 for electrons and ions, as:

$$D_\alpha = \frac{\mu_e D_e + \mu_i D_i}{\mu_e + \mu_i} \tag{1.32}$$

Finally the energy equation reads for electrons:

$$\frac{\partial n_e \overline{\mathscr{E}}}{\partial t} + \frac{5}{3}\nabla.(n_e \overline{v_e}\overline{\mathscr{E}}) - \frac{2}{3}\nabla.(K\nabla\overline{\mathscr{E}}) - e n_e E.\overline{v_e} = -n_e \nu_{\mathscr{E}}\overline{\mathscr{E}} \tag{1.33}$$

where K is the thermal conductivity, $e n_e E.\overline{v_e}$ is the Joule heating term (power density absorbed by the electrons) and $\nu_{\mathscr{E}}$ is the energy losses (per unit volume and time) due to collisions that can be written as:

$$\nu_{\mathscr{E}}\overline{\mathscr{E}} = \frac{2m_e}{m_M}\nu_c\overline{\mathscr{E}} + \sum \nu_i \mathscr{E}_i \tag{1.34}$$

where the subscript i denotes each different collisional process.

The presence of walls in a plasma modifies strongly its transport and behavior. The electrons (due to their large mobility) fly out of the plasma and move to the wall due to the electronic pressure gradient and charge the wall negatively relative to the bulk plasma. The density of the electrons there is low and the plasma is no longer quasineutral locally. This region is known as the Debye sheath and it can be several Debye lengths thick. It is a transition zone between a plasma and a solid surface. The negatively charged wall creates an local electric field that produces an electric force, repulsive to the electrons, pushing them back to the plasma. As the sheath potential grows, more and more electrons are being repulsed back to the plasma until an equilibrium stationary state forms. The electrons density can be described by an one dimensional Boltzmann's law in the form:

$$n_e(x) = n_\infty \exp\left[\frac{e(V(x) - V_\infty)}{k_B T_e}\right] \tag{1.35}$$

where V in this equation denotes potential, x is the distance from the wall and the subscript ∞ denotes a distance where the plasma is locally unperturbed from the wall's presence.

Taking a look in equation 1.29, we see that the total momentum balance is characterized by the gain of momentum proportionally to the electric field E and the collisional losses proportionally to the gas density N. So it is convenient to define the ratio E/N as the reduced electric field, which is the main parameter for the charged particles transport or similarly, defining a constant gas temperature of $300K$, we can use the ratio E/p. E/N has units of $V.m^2$ or $V.cm^2$ while the more convenient Townsend (Td) unit is often used in literature. Note that 1 Td=10^{-17} $V.cm^2$. E/p has units of $V/m/torr$ where 1 $Torr$ = 133.322 Pa.

1.2.3 Quasi-neutral plasmas under DC fields

The formation of plasma discharges under DC or slowly oscillating fields follows the macroscopic description provided in the previous subsection. Under such fields, the plasma is a conducting medium, whose value depends on its density as (neglecting the ionic contribution):

$$\sigma_e = e n_e \mu_e = \frac{e^2 n_e}{m_e \nu_c} \tag{1.36}$$

The electric current density in a plasma is then given as :

$$J = \sigma_e E = -en_e\overline{v_e} \tag{1.37}$$

and the field performs a mean work per unit time to an electron:

$$< -eEv_e >= \frac{e^2E^2}{mv_c^2} \tag{1.38}$$

How plasma is created though under such conditions and what are the main parameters to initiate its breakdown?

To initiate a plasma, a sufficient high electric field has to be applied. This sufficient value of the electric field is called breakdown field. The formation of a plasma, is followed by a transient period of losses and generation of charged particles via the different mechanisms. In order for the plasma to be sustained, the generation has to compensate the losses, which means that the electric field has to provide enough energy to the electrons so that can ionize neutral particles more often than the losses procedures.

The formation of these discharges are based on the Townsend discharge mechanism , that can be explained if we think of 2 plane electrodes in a glass tube. A representation of the process that we are describing below is presented in figure 1.16.

If a high voltage (DC or AC) is applied between them , the electrons that are formed in the gap due to photo-ionization or the free ones, are being accelerated due to the current towards the anode, resulting to an avalanche of electrons, produced by the collision of the drifting initial electrons with the neutral molecules. The positive ions created by the ionization process are moving towards the cathode but a lot slower. Hence, the density of the ions becomes larger than the electrons in the region near the anode. Due to ion bombardment, the cathode emits secondary electrons, increasing the electrons density also. Due to electron multiplication now, the ions density continues to increase until it creates a space charge that can no longer be neglected in Poisson's equation:

$$\frac{dE}{dx} = \frac{e}{\varepsilon_0}(n_p - n_e) \tag{1.39}$$

where n_p denotes the positive ions density. The electric field consequently is being modified in the inter-electrode region, being weaker near the anode and stronger near the cathode. If the applied field is always above the breakdown critical value, this procedure continues until the electric field near the anode becomes zero or even reverses its sign. Then the electrons can no longer pass to the anode, decelerate and their density increases in order to to compensate the ions density and react to the electric field's inversion. After a while, a macroscopically neutral region forms which is the plasma. The plasma can move towards the cathode forming a stationary state of a quasi-neutral plasma region and a high electric field one, the plasma sheath.

Discharges are often categorized by their Current-Voltage characteristics, the current density and breakdown voltage as presented in figure 1.17. These main characteristics depend on the geometry of the electrodes and the vessel, the gas used, the electrode material.

The avalanche-electron multiplication-secondary emission mechanism leads to a discharge current which differs when the applied voltage increases (for constant pressure) and which determines the discharge regime. This mechanism assures the self-sustainability of the discharge (autonomous region). In the non-autonomous region of figure 1.17, an external process is necessary to sustain the discharge and allow the current pass through the gas.

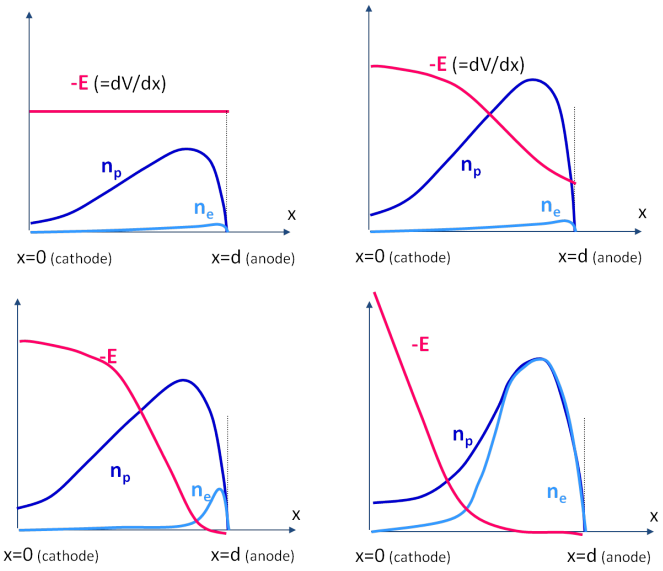

Figure 1.16: Townsend discharge formation due to electron avalanche and secondary emmision.

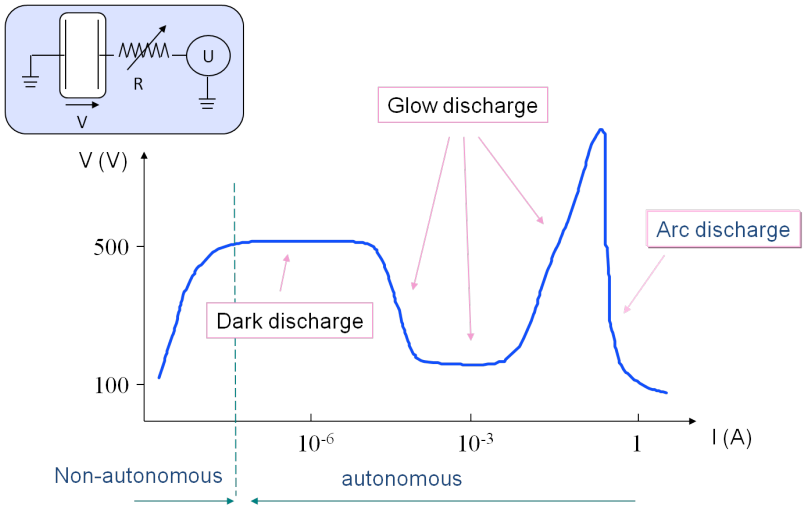

Figure 1.17: Current-voltage characteristics of different discharges (p=100 Pa, electrodes of cms).

For low applied voltages the process characterized by very low current densities: in common gas filled tubes, typical magnitude of currents flowing during this process range from about 10^{-18} A to about 10^{-5} A, while applied voltages are almost constant. We talk more about an ionized gas rather than a plasma, as the charged particles densities are low. This is the dark or Townsend discharge. For higher potential differences between the electrodes, a glow discharge develops. The uniform electrically neutral (everywhere except in the regions close to the electrodes) plasma is weakly ionized ($\delta = 10^{-8} - 10^{-6}$), and in a thermal

non-equilibrium : The electron's temperature can reach values in the order of 1 eV in the plasma, absorbing energy directly by the electric field, while the neutral gas particles as well as the ions have temperatures close to the ambient one (300K). The voltage is lower than the dark discharge because of the more efficient electronic multiplication in this non-uniform electric field (due to the space charge). Even further increase of the potential difference between the electrodes leads to the transition to the arc discharge. This transition occurs when the ion current becomes sufficiently high, that thermionic emission occurs by the cathode as it's being heated by ion bombardment. As the electron emission at the cathode increases, the plasma can be sustained in lower voltages.

The necessary voltage for breakdown, (the starting of the ionization process due to electron avalanche and thus the creation of the plasma), differs for different gases and pressures and geometries. At pressure of 1 Torr and an inter-electrode gap of 1cm, the breakdown voltage is several hundred volts. For plane parallel electrodes, the ionization coefficient (which drives the electron multiplication mechanism) as well as the secondary emission coefficient depend on the ratio $E/p = V/(p.d)$, where d is the inter-electrode distance. Therefore, the breakdown voltage is a function of the product $p.d$ and the curve $V = f(p.d)$ is called the Paschen curve. An example of the form of the Paschen curve is plotted in figure 1.18.

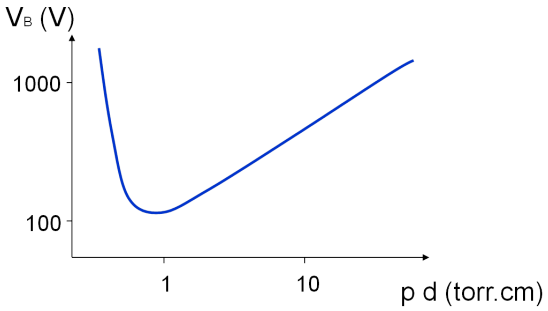

Figure 1.18: Typical form of the Paschen curve.

When the product $p.d$ is low, the necessary voltage for breakdown is high because the electrons experience few collisions between the electrodes. As this product increases, the breakdown voltage decreases until a minimum value : After this value, the electric field is decreased (because the product $p.d$ has increased) at such levels that the multiplication is not sufficient for breakdown. To overcome this problem, the only way to cause breakdown is to increase the applied voltage.

At high pressure (atmospheric one for example), the diffusion of the charged particles is slower and thus, the creation of an uniform plasma between two electrodes is not possible: micro plasmas of a filamentary nature form locally wherever the electron multiplication takes place. In the case of sufficient high applied voltage, high pressure breakdown and streamer formation can occur too: If an electron avalanche reaches high levels in order to produce a space charge that is comparable to the background field, the ions do not have the time to return to the cathode. As now, in some regions the electric field will be enhanced, new avalanches can form and a self propagating streamer structure is produced. The propagation can be towards or opposite to the direction of the electric field, forming positive or negative streamers. This is almost always the case for inter-electrode plasma formation under atmospheric pressure. The streamers formation leads to an uncontrolled increase of the current and can lead to arc transition. They are of a transient and filamentary nature. Streamer discharges are often encountered in plasma discharges under high frequency oscillating fields and high pressures such as microwave discharges.

1.2.4 Microwave plasma discharges

To begin with, we study the effects of general oscillating fields on the motion of charged particles (electrons here), and we recognize that any periodical field can be decomposed into harmonic components, the amplitude of electron oscillations in discharge processes is usually small in comparison with the wavelength and the magnetic force is orders of magnitude smaller than the electric one. Hence, we assume a sinusoidal monochromatic stationary wave in the form:

$$E = E_0 sin\omega t \tag{1.40}$$

where E_0 is the amplitude of the field. The equation of momentum transfer in a simplified form reads:

$$m_e \frac{\partial v_e}{\partial t} = -eE_0 sin\omega t - m_e v_e \nu c \tag{1.41}$$

and after several collisions we can solve this equation to find the mean velocity v_e and displacement, r_e, of an electron:

$$\begin{aligned} v_e &= \frac{eE_0}{m\sqrt{\omega^2+\nu_c^2}} cos(\omega t+\phi),\ \ \phi = arctan(\nu_c/\omega) \\ r_e &= \frac{eE_0}{m\sqrt{\omega^2+\nu_c^2}} sin(\omega t+\phi) \end{aligned} \tag{1.42}$$

Compared to DC fields, an electron oscillates at a frequency which amplitude and phase that depend on the EM field's frequency ω and the effective collision frequency ν_c. The higher the effective collision frequency, the lower the amplitudes of displacement and velocity of the electron and the higher the displacement phase shift (relative to the field). For relatively low frequencies or very frequent collisions, the electrons behave as they were in a constant field varying slowly with the field with the instantaneous drift velocity.

An general electromagnetic wave can be described by the Maxwell's equations (assuming propagation in free space):

$$\begin{aligned} \nabla \cdot E &= \frac{\rho}{\varepsilon_0} \\ \nabla \cdot B &= 0 \\ \nabla \times E &= -\frac{\partial B}{\partial t} \\ \frac{1}{\mu_0}\nabla \times B &= \varepsilon_o \frac{\partial E}{\partial t} + j \end{aligned} \tag{1.43}$$

where E and H is the electric and magnetic field vectors, ρ the charge density and j is the current density. Assuming that the Debye length is smaller than the microwave interaction length scale (which is related to the skin depth - the depth that the EM waves penetrate the plasma) and neglecting the contribution of ion velocity on the current density due to the low ion mobility, we can decompose the plasma evolution and the

microwave interactions in different time scales, while the current density reads $j = j_e = \sigma E = -en_e v_e$. Then the Maxwell equations of interest become :

$$\begin{aligned} \nabla\times E &= -\frac{\partial B}{\partial t} \\ \frac{1}{\mu_0}\nabla\times B &= \varepsilon_o \frac{\partial E}{\partial t} + j \\ \nabla\cdot j &= 0 \end{aligned} \tag{1.44}$$

The electron mean velocity is given by the local momentum equation in its general form as (assuming again that the distances traveled by the electrons during a microwave period with respect to any gradient length is negligible as well as the magnetic force with respect to the electric one) :

$$m_e \frac{\partial v_e}{\partial t} = -eE - m_e v_e \nu c \tag{1.45}$$

As the electric field is harmonic, the electron velocity is harmonic as well and its time derivative can be replaced in the frequency domain by $i\omega$. Substituting equation 1.45 in the first equation of the set 1.44 and passing to the frequency domain, we obtain :

$$\frac{1}{\mu_0}\nabla\times B = (1 - \frac{{\omega_p}^2}{\omega^2 + i\omega {\nu_c}^2})\varepsilon_0 (i\omega E) \tag{1.46}$$

where now the plasma current is presented by a complex dielectric permittivity:

$$\varepsilon_p = 1 - \frac{{\omega_p}^2}{\omega^2 + {\nu_c}^2}(1 + i\frac{\nu_c}{\omega}) \tag{1.47}$$

Allowing for a plane electromagnetic wave solution in the form $E = E_0 \exp(-i\omega t + ikx)$, where k is the wavevector and solving the wave equation (obtained by taking the curl of the first equation of 1.44 and substituting 1.46 in it) , we obtain the wave equation :

$$\begin{aligned} \nabla^2 E + \frac{\omega^2}{c^2}\varepsilon_p E &= 0 \\ \kappa^2 &= \frac{\omega^2}{c^2}\varepsilon_p \end{aligned} \tag{1.48}$$

When the dielectric permittivity becomes negative (its real part), k becomes purely imaginary and the electromagnetic waves cannot penetrate the plasma but they are being reflected. The reflection starts at a critical plasma density at the limit $\omega_p = \omega$ for a collisionless plasma. When the imaginary permittivity part is much greater than the absolute value of the real part, electromagnetic waves are being damped strongly over a distance of the wavelength's order. The penetration depth is called the skin depth - AC current flows only on the skin layer of the plasma-conductor. In intermediate ratios of the imaginary and real part of the complex plasma permittivity, electromagnetic waves propagate in the plasma, being attenuated and refracted. The energy flux decays exponentially and the absorption coefficient is proportional to the conductivity of the plasma and the plasma's density.

The electromagnetic energy dissipated in the plasma by the electromagnetic waves as joule heat, $< j \cdot E >= \sigma < E^2 >$ can be achieved only by the effect of collisions in an oscillating field such as a microwave one : if collisions do not occur the average work of the field on an electron is zero. Under the collisional influence, the field performs a mean work per unit time to an electron:

$$< -eEv >= \frac{e^2 E_0^2}{2m(\omega^2 + \nu_c^2)} \nu_c \tag{1.49}$$

In a high-frequency gas discharge breakdown, the primary ionization due to the electron motion is the only production phenomenon which controls the breakdown. As under DC fields though, depending on the applied field and the gas' pressure (here the interelectrode distance has no meaning), different regimes of microwave discharges can be obtained. In figure 1.19 a classification of microwave discharges in air versus pressure and electric field amplitude is plotted.

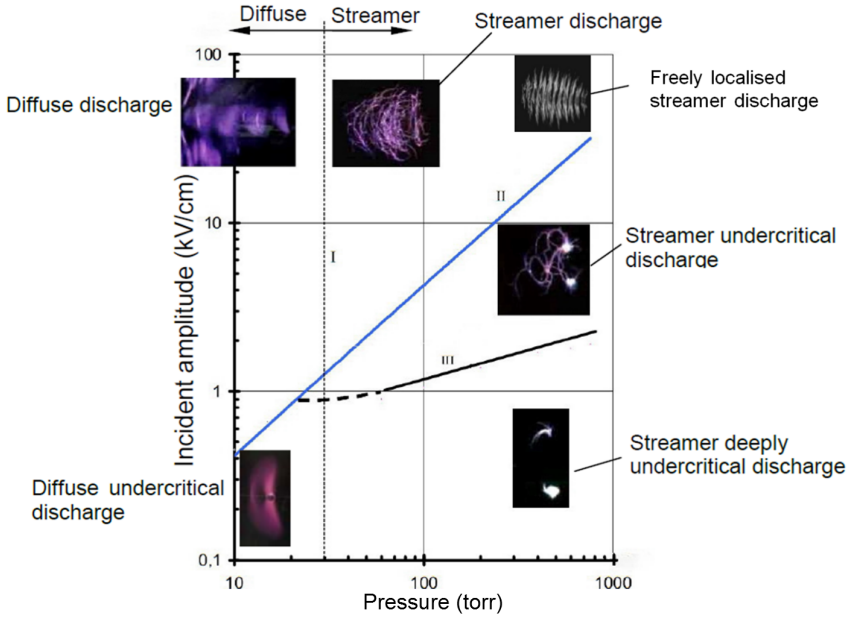

Figure 1.19: Classification of microwave discharges in air [36].

We can distinguish two big categories of MW discharges: The overcritical ones and the sub-critical ones, divided by the line II in figure 1.19.

The overcritical discharges are discharges that are created when the electric field is overcritical, that's to say that ionization dominates over the loss mechanisms. Depending on the pressure or the reduced electric field (E/N, where N is the density of the gas), they can have a diffusion nature (in low pressures, zone I in figure 1.19) or a streamer nature(zone II). Diffusion discharges are reflecting really well EM waves and are weakly ionized. The streamer nature absorbs EM power more efficiently. The streamer formation is a non-linear process of a combination and interplay between ionization and diffusion and can be found also in subcritical regimes. More on the formation of plasma in air due to MW radiation can be found in [37].

Subcritical regimes are more interesting in terms of power efficiency. In such conditions, even if the electric field is lower than the critical for breakdown field, a streamer microwave discharge can propagate and create a volumetric discharge in air. This only requires a local excess of the electric field over the critical electric field value [36]. A metalic initiator or vibrator can provide this excess but ways to initiate the discharge can also include laser radiation, focusing of MW radiation with mirrors etc. The propagation is a coupled process of the initial electric density, ionization, diffusion and change of the initial MW field due to the induced plasma current. This induced current creates an increased conductivity in the initial streamer which has higher values on its tips. It is there, where the electric field is locally increased and when this field reaches over-critical values, ionization and diffusion conclude to the streamer's propagation in the direction of the electric field polarization. The heating of the streamer's body leads to a decreased density of the gas in that region and so the reduced field value increases sustaining the plasma discharge and prolonging the streamer's life. The streamer's length is still under research as resonant effects play an essential role after a certain length and branching of the streamers lead to a filamentary nature of such discharges as shown in figure 1.20.

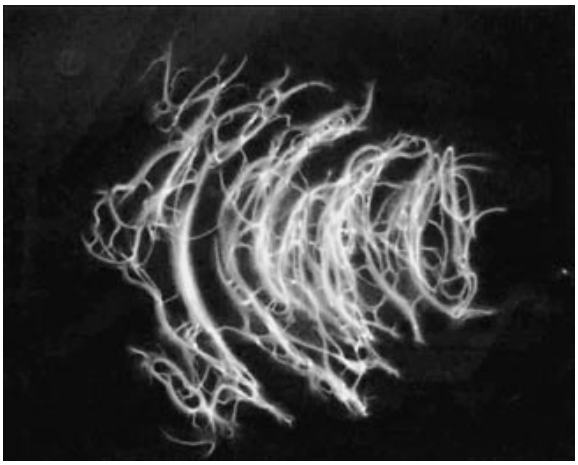

Figure 1.20: A freely localized volumetric microwave discharge in air [36].

Other forms of the sub-critical discharges include attached and surface discharges, though in this thesis we focus on volumetric discharges as mentioned above.

1.3 Plasma Actuators

Now that we have an idea of what plasma is as well as how we can and why we want to achieve aerodynamic flow control, the next question can be posed. How can we use plasma as means of a flow control actuator device?

Generally speaking, we will proceed as we did for the non-plasma flow control methods and divide the families of plasma actuators in two groups: The first includes actuators whose main effect in an external flow is the addition of momentum. Such actuators are the surface Dielectric Barrier Discharge actuators and the Plasma Synthetic Jet ones. The second group includes actuators that interfere with the external flow by

means of energy addition and fast gas heating. The nanosecond DBD's, laser induced plasmas, as well as the microwave discharge actuators fall in this category. Let's start exploring these actuators by the second family, focusing on Microwave Discharge Actuators.

1.3.1 Microwave Discharge Actuators (MDA) and laser discharges

Microwave Discharge Actuators fall in the category of energy deposition flow control methods. The effect of this group of plasma actuators in a flow is provoked by the intense heating of the fluid. As we have seen, sub-critical microwave discharges can be formed under atmospheric conditions without the need of excessive power sources. The coupling of the plasma formation which can propagate in still air as well as even supersonic flow conditions (due to the high electronic velocity as seen above), with the gas' properties by the joule heating of the latter can provide the energy source that will be used for aerodynamic flow control.

The increased drag due to the strong shock waves in front of an aircraft limits its performance and therefore, is crucial for the supersonic flights. Trying to modify the shock waves has led the research community to the physical or mechanical spike. This spike interferes with the incoming flow, forming an additional conical oblique shock further from the nose of the bulk body. By this, the initial bow or normal shock weakens, resulting in reduced drag. As drawbacks are almost inevitable though, the mechanical spike is a mean of an additional drag due to its physical properties(friction,etc), and has poor performance in off-design flights [38].

In supersonic applications for flow control, the thermal effect of the plasma disposition is the most efficient way to modify the flow properties and reduce the drag of an aircraft in opposition to the plasma actuators used in subsonic flows were the ionic wind effect is the main contributor of drag reduction. The plasma disposition in front of a bulk body or an aircraft has been investigated numerically and experimentally and has shown a big reduction of the drag coefficient. Various papers investigate similar energy disposition effects for supersonic flow control [38, 39]. Furthermore in [40] the possibility of creating steering moments by off-axis plasma heat addition in front of a cone is investigated.

The cold plasma can be created by a laser of some millijoules and of a duration less that some picoseconds. The laser that propagates in the air has the form of a filament of light. In its wake the plasma is created by multi-photonic ionisation. In such discharges, the free electrons in air are being multiplied by the energy absorption from the laser beam. As energy is being added in the electrons , they gain more momentum and thermal energy and create more electrons by collisions with neutral molecules. Thus, plasma breakdown occurs that leads to a high temperature of the air in the breakdown region. Laser breakdown in air can been summarized in figure 1.21. The plasma keeps absorbing energy from the laser beam and it develops in space, typically taking an ellipsoidal shape due to the laser beam focusing. In the plasma region, the gas density decreases importantly and as the plasma propagates it compresses the surrounding air resulting to a blast wave that travels with high speed. The blast wave propagation and creation is linked with the huge pressure and temperature gradients between the plasma and the external region. As the plasma develops towards the direction of the laser beam, a shear layer is being created between itself and the surrounding gas. This shear layer and the flow of the external air into the plasma region due to the density difference cause the formation of a vortex ring that eventually propagates in the surrounding gas.

The electron's temperature can go up to roughly 45,000 K at 50 ns for a laser pulse focusing with laser energy of 150 mJ per pulse. Approximate 80% of the spark emission completes in 500 nanoseconds after the laser pulse and this emission rapidly decays with time [42].

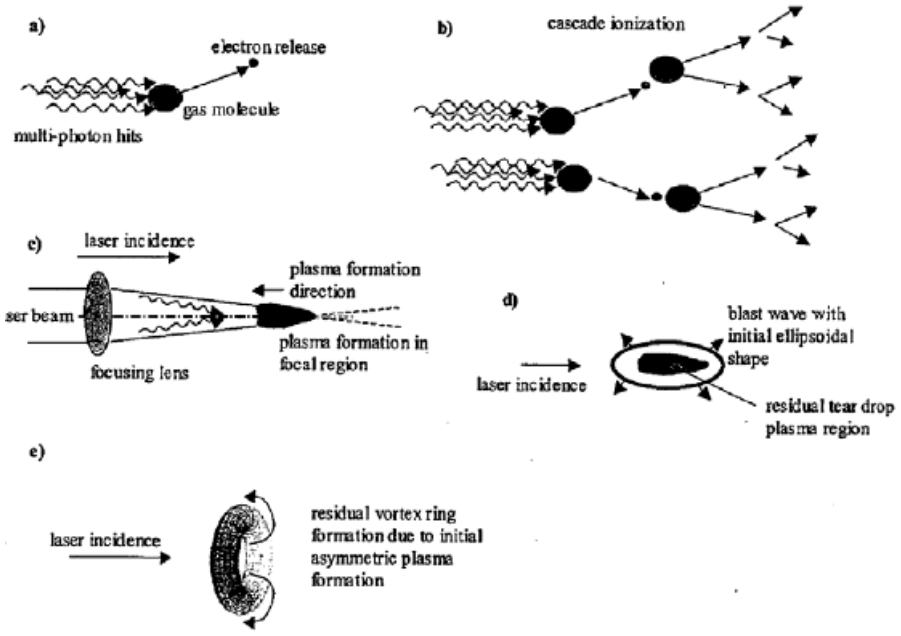

Figure 1.21: Laser induced breakdown in air[41].

The applications of such actuators mostly for hypersonic flows has been summarized by Knight [43]. Briefly, the interaction of a laser induced plasma discharge with a supersonic-hypersonic flow before a bulk body, leads to a decrease of the oblique shock wave's intensity and consequently to a decreased drag coefficient.

The plasma deposition typically consists of a high density plasma column ($n_e \approx 10^{16} cm^{-3}$ or higher) with a radius of 60-200μm and a length in the order of centimeters. The duration of the plasma life is about 5 ns (with a femtosecond laser). Still, the effect of the gas heating has a big effect on the aerodynamic performance of the body. In [44] the authors used a simplified plasma fluid model to investigate the thermal effect on a incoming flow at Mach 3. Decoupling the plasma generation from its effects of the fluid, the investigation was held on the introduction of a plasma of determined energy on the fluid.

The energy deposition initially affects the shock wave's profile, as a spike is added to it. In this initial state the heated gas region is stronger behind the bow shock where the density and pressure of the fluid are much higher and so the energy transmitted to the fluid too and then the temperature becomes higher ahead of the shock. The gas heating inside the plasma channel leads to a decrease of the density in this channel and consequently to a increase of the velocity of the fluid. This column of high velocity fluid leads to a modification of the velocity shock which is pushed inside and forms two regions of reversed fluid flow. Consequently the new shock that forms travels ahead of the plane nose and the drag due to it is reduced. Figure 1.22 visualizes the Mach number for different time steps where the previously described procedure can be seen.

A comparison graph of the bow shock modification is plotted in figure 1.23. Even 180ms after the plasma disposition the bow shock is still moved away from the noise of the aircraft leading to reduced drag.

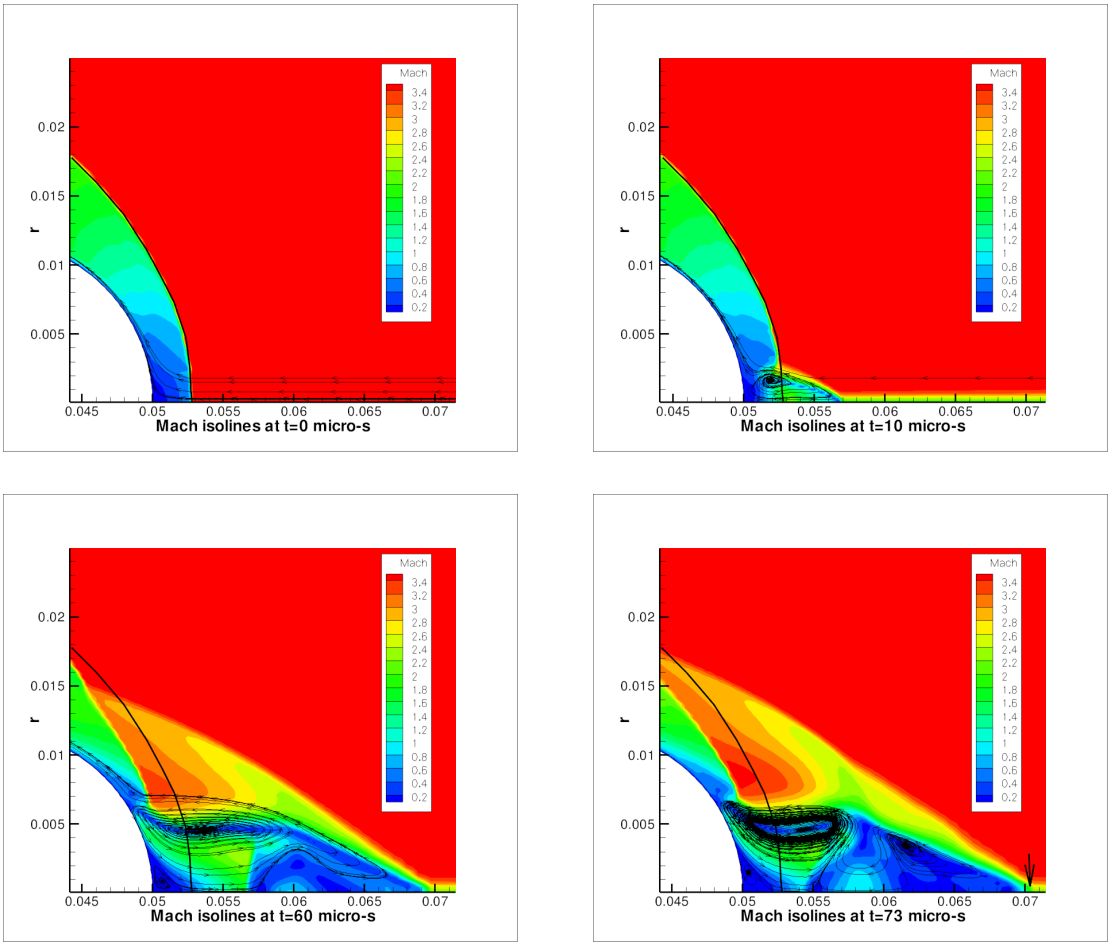

Figure 1.22: Mach number at different time steps [44].

The numerical simulations show a drag reduction up to about 18 percent, 73 ms after the plasma was introduced as figure 1.24 shows.

Experimentally, similar results have been obtained in [45]. In [46], a stagnation pressure reduction of 21% has been measured at a higher repetition rate of 60 kHz with pulse energy of 4.6 mJ and pulse duration of 10 ns. Applications of such discharges close to a surface (of an airfoil/flat plate) have also been investigated lately [47, 48]. Boundary layer transition control is one of these applications. The formation of the induced shock wave due to the highly thermal plasma generation, and the interaction of this shock wave with the surface introduces disturbances in the flow depending on the repetition rate of the laser beam and causes the boundary layer to separate. Control of turbulent structures or on-will drag induction is then possible. In figure 1.25, the induced shock wave due to the plasma formation is clearly observed.

The efficiency and effectiveness of energy deposition before a cylinder has been investigated numerically by Knight et al [50, 51, 52]. In figure 1.26, the numerical configuration as well as Mach contours and numerical Schlieren images are shown for a ration of $L/D = 1$ and $\Delta T/T_\infty = 1$. The dimensionless number τ

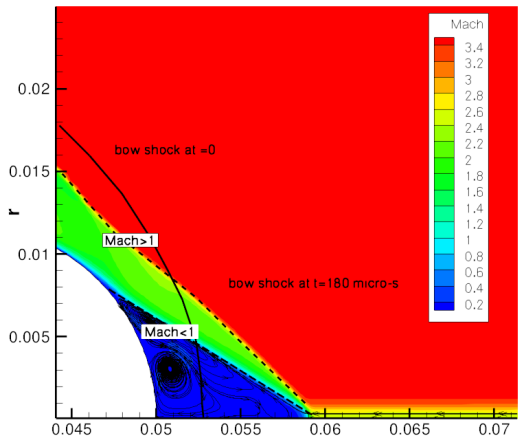

Figure 1.23: Bow shock modification for $t = 0$ and $t = 180ms$ - Mach number contours [44].

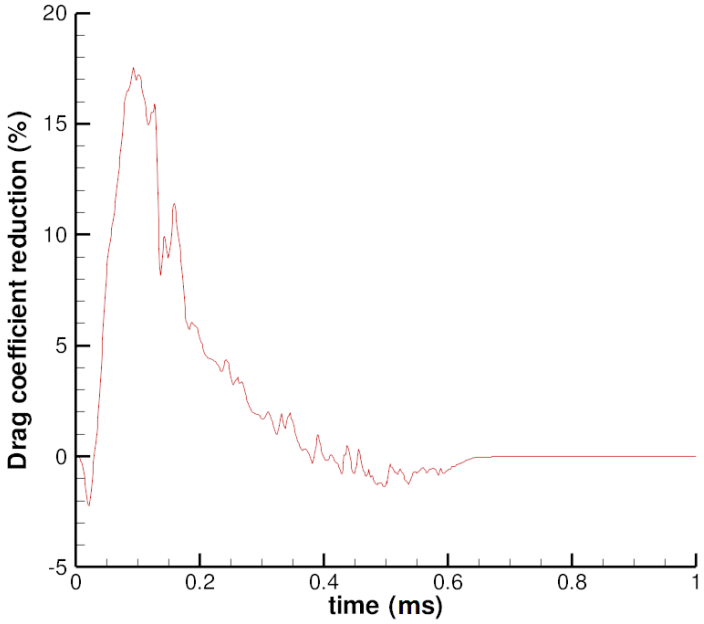

Figure 1.24: Drag coefficient vs Time [44].

is equal to $\tau = U_\infty t/D$. The interaction of the heated filament-column with the shock wave and subsequent vortex formation is evident.

The authors have performed parametric studies on the filament-column length and temperature, to conclude that efficiency and effectiveness increase with longer filaments while higher temperatures lead to decreased efficiency but increased effectiveness. They have defined the efficiency as the ratio of saved energy

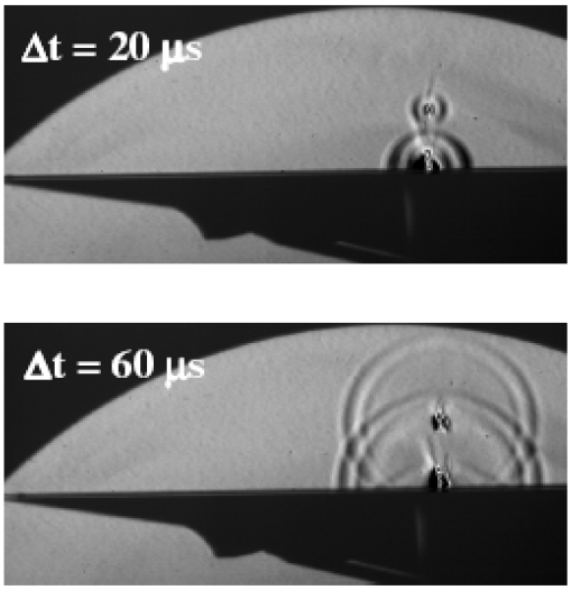

Figure 1.25: Laser discharge over a flat plate in hypersonic flow [49].

(in terms of pressure reduction) to energy spent (for heating) and the effectiveness as the ratio of the average drag reduction by heated filament to the undisturbed drag. Furthermore they have demonstrated, when the filament is inserted upstream of the shock wave, the efficiency is higher but the drag reduction is similar presenting only a time shift. Drag reduction is due to the formation of the recirculation region while the average minimum drag lasts longer for higher temperature filaments. In figures 1.27 and 1.28, the parametric study on the drag coefficient versus time and the efficiency and effectiveness are presented.

Laser discharges provide the ability to create energy sources in a distance, controlling the position and the focus size-volume and enabling energy delivery in the speed of light. These features make them extremely interesting for flow control applications especially in super-hyper sonic conditions. Yet, such discharges need high power inputs sources to cause air breakdown. An alternative is given by microwave sources. As we have seen, microwave discharges can take different forms depending on pressure and applied field. Under regimes of interest for high energetic coupling between the EM energy and the plasma, the MW discharges take the form of high density filaments.

Concerning purely microwave discharged, a lot of the work and research performed on such actuators have been circulating around two teams. The first is the team from Moscow Radiotechnical Institute RAS, Moscow, Russia in collaboration with Institute of Hydromechanics, National Academy of Sciences of Ukraine and the National Aviation University of Ukraine[53]. This team has focused its research on subsonic flow control applications. After various optimizations and studies, they have proposed the application of a microwave discharge initiated by looped-shaped electromagnetic vibrators flushed into an airfoil [54]. Experiments were carried out in the beam of electromagnetic radiation created by a generator of average power no greater than $1.5kW$ with the wavelength $12.3cm$. This concept as well as the experimental airfoil and vibrators are presented in figure 1.29. The actuation of the discharges can be observed in 1.30 for different times, velocities and MW power.

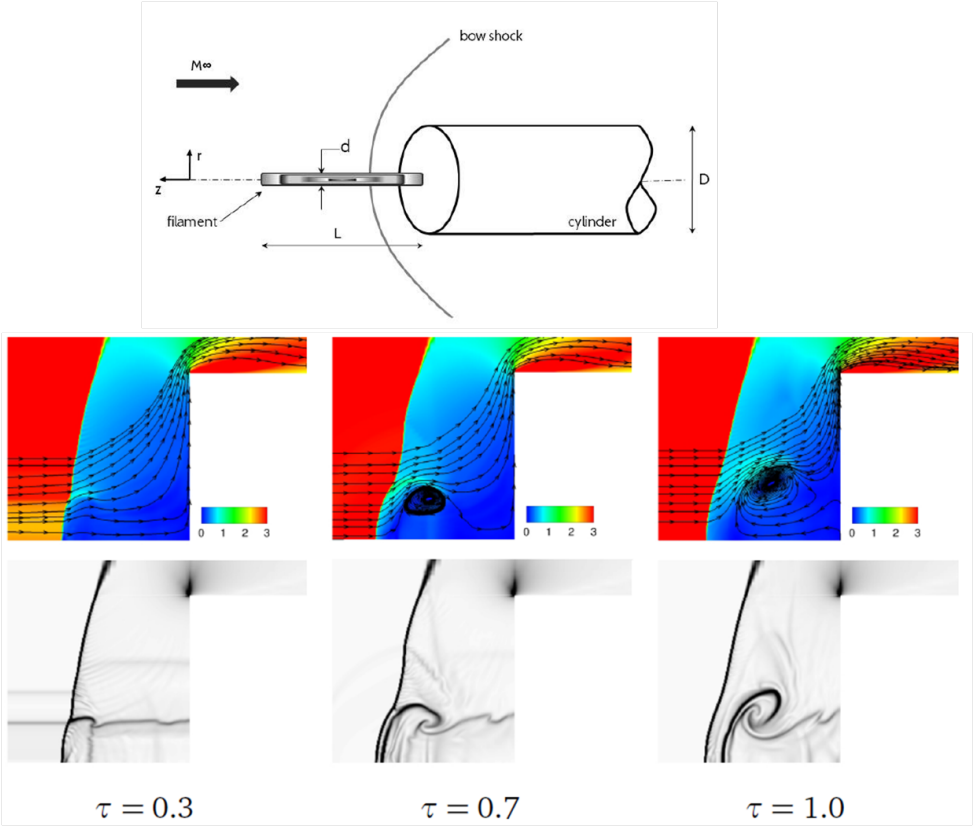

Figure 1.26: Numerical domain (top), Mach contours (middle) and numerical Schlieren images (bottom) at different time steps by Knight et al.

In their experiments , the MW system was set to operate in a pulse regime to get sufficient values of radiation energy for stable discharges along the whole spanwise array of 11 actuators which covered a half (an axial part) of the model span. It enabled the usage of a relatively low-power magnetron with MW radiation power of 6 to 8 kW. The pulse duration was $100\mu s$ and pulse frequency $f_{MW} = 500$ or $1000Hz$. For these conditions, the duty cycle was equal (corresponding to the frequency used) to 20 or 10. Energy estimations with account of a dissipated portion of the radiated energy gave the following: the averaged pulse power of a single thermal source within the plasma array in experiments was 3 to 8 W. The results of these simulations are presented in figure 1.31.

The authors conclude that the discharges delay flow separation by 0.5 degrees of an angle-of-attack. This way of the boundary-layer control using localized plasma discharges resulted in lift coefficients growth by 15% together with the 5% decreasing drag. Within the range of tested parameters, greater flow-control effects are obtained for greater averaged MW radiation power.

Numerical simulations of energy deposition over a cylindrical surface have been also conducted based on recommendations of the MRTI institute. The thermal sources of of 0.5×0.8 mm size with $T = 1000$ C were placed at $1mm$ above the surface; z-spacing was taken as $\lambda_z = 5$ and $10mm$, the array was located at a

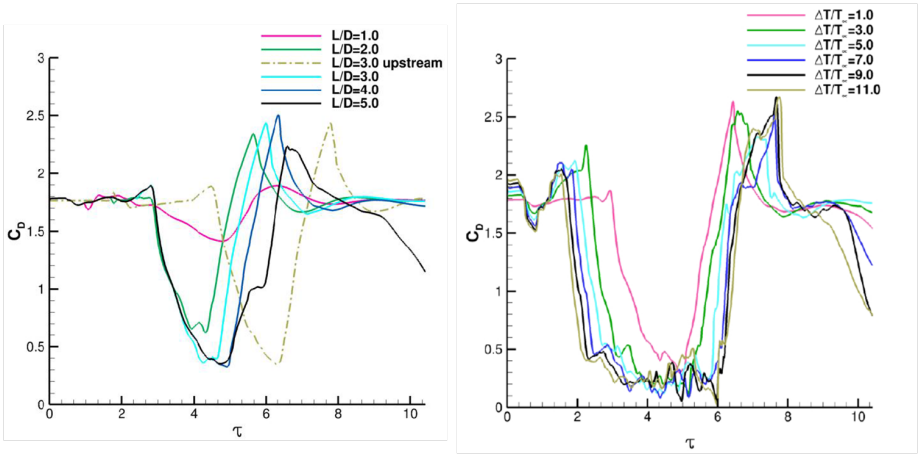

Figure 1.27: Parametric studies on drag coefficient by Knight et al.

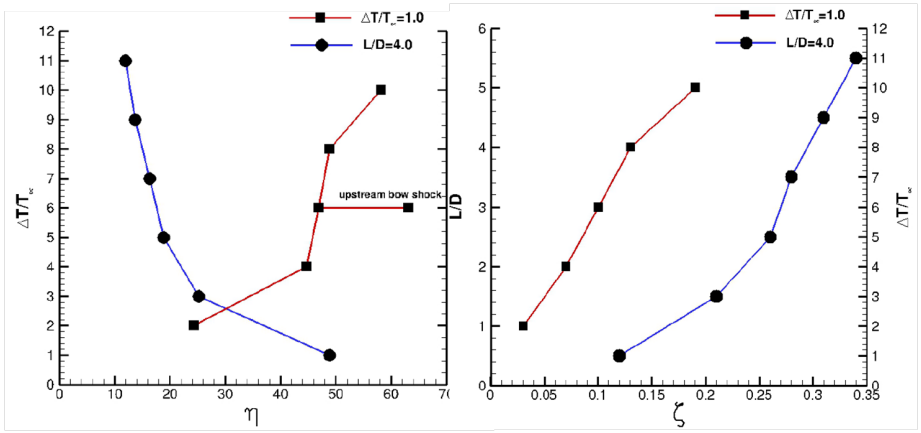

Figure 1.28: Parametric studies on efficiency and effectiveness by Knight et al.

downstream section of $x = 4cm$. These simulations proved the creation of vortical disturbances in the flow that can be used for manipulation of the turbulent or not flow structures as can be seen in figure 1.32.

To confirm such results qualitatively, we have performed simple two dimensional calculations of a 10 m/s flow over a flat plate. These simulations were performed with the commercial CFD solver FLUENT® while the mesh was created in ICEM® . The mesh was highly refined near the heating zone as well as inside the boundary layer in order to achieve y+ values lower than 1. A compressible unsteady solver was used. The air was assumed to be ideal. The $k-\varepsilon$ realizable turbulent model was used in order to properly describe the flow. A gaussian energy profile has been added as a source term in the NS equation of energy, corresponding to an elevation of 1000 C in 100 μ s (corresponding to the indications of [55]) as seen in figure 1.33. The "plasma" zone was placed 1mm above the flat plate or 10% of its B.L. thickness at $x = 0.5 * c$ ($c = 1m$, $U_0 = 10m/s$). The frequency of the energy deposition was f=1000 Hz or a duty cycle of 10%. Two periods of 1ms each, have been simulated.

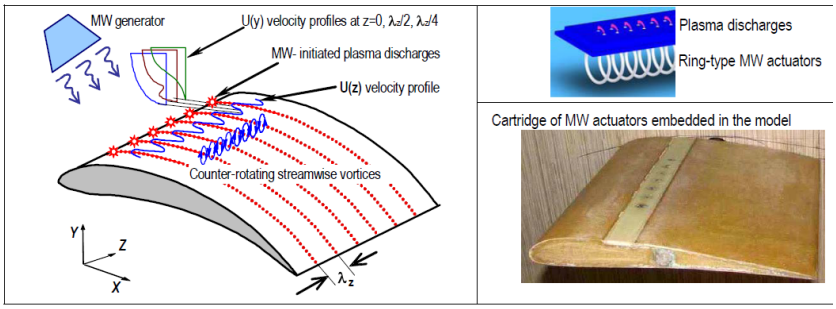

Figure 1.29: Flow control concept with loop-shaped vibrators and experimental case [54].

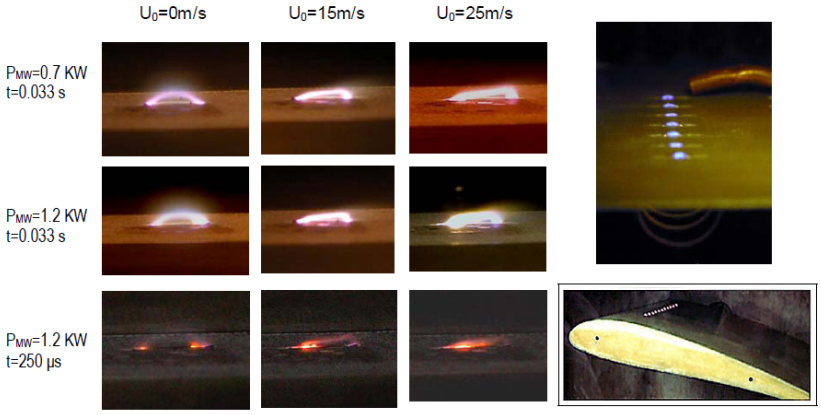

Figure 1.30: Microwave discharges over an airfoil for different flow and power inputs [55].

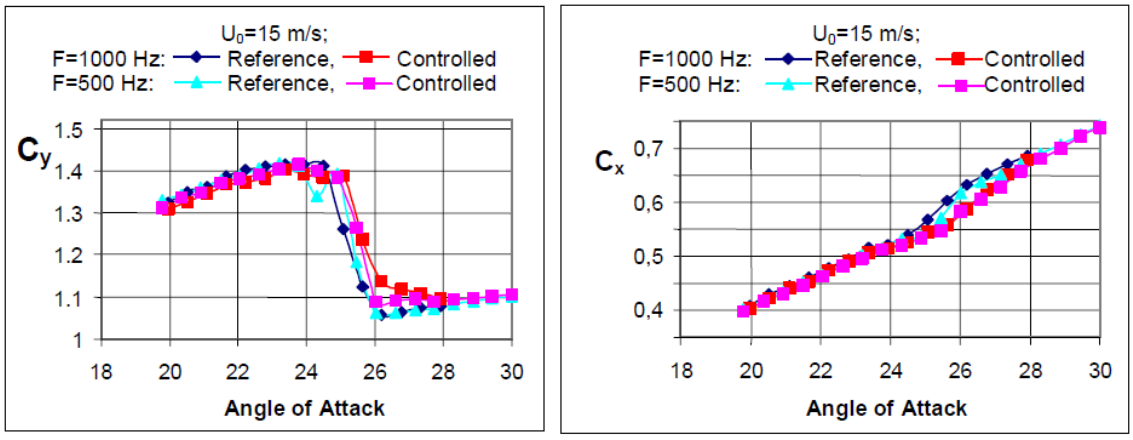

Figure 1.31: Lift and drag coefficients comparison between the controlled and uncontrolled cases [55].

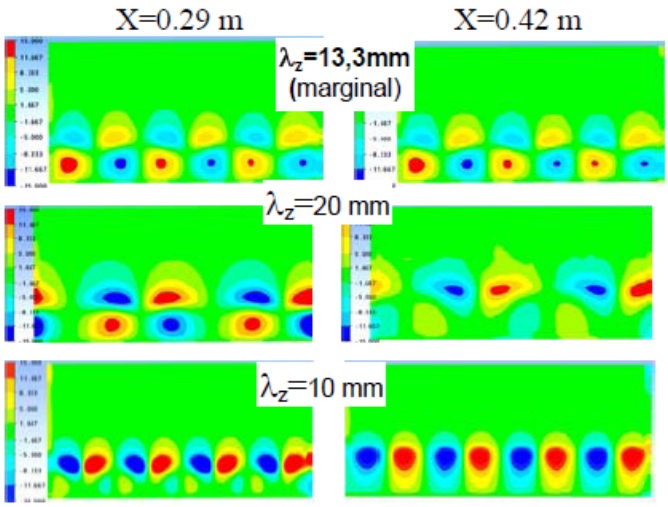

Figure 1.32: Longitudinal vorticity downstream of the plasma actuators ($U_0 = 35m/s$) [55].

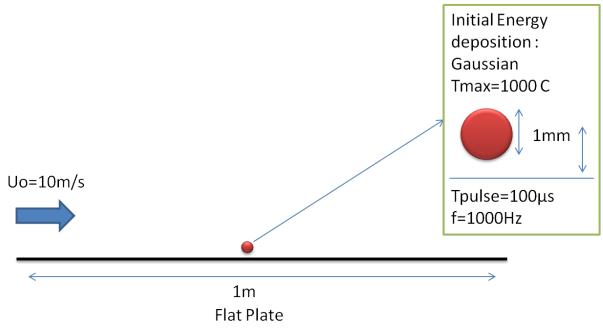

Figure 1.33: The configuration for the 2D flat plate simulations.

The unsteady simulations reveal that the deposited energy is accumulated under such frequency of operation. In figure 1.34, static temperature contours at times of 1 and 2 μs are presented. After the first period the maximum temperature is 760 C while after the second period it reaches values of 1060 C.

Regions of increased velocity angle and thus vorticity form around the energy deposition region as shown in figure 1.35. These regions are stronger below the hot plasma zone due to the wall-viscous interaction. The region is enforced quantitatively as well as expanded, as repetitive pulses add energy in the flow. No influence was observed in the flow as soon as the repetitive energy deposition stops. The flow returns to its initial state in approximately 10 ms.

The heating of the boundary layer results to an increase of the turbulent intensity locally possible due to viscous heating (figure 1.36). The external flow is being accelerated on the y-direction just before the heated region and being sucked towards the flat plate just after it (figure 1.37).

The vortical structures created by the heat sources, are naturally three-dimensional. Thus, 3D simulations can provide more accurate information of these structures. In order to reproduce similar results as in [55], a

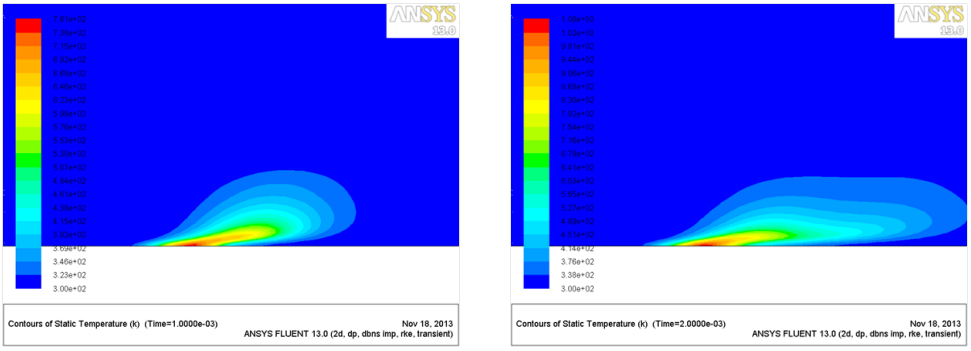

Figure 1.34: Temperature contours at $t = 1 and 2 \mu s$.

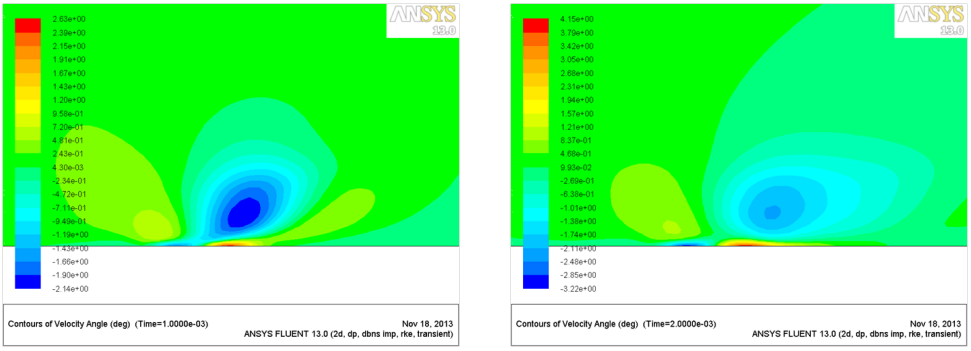

Figure 1.35: Velocity angle contours at $t = 1 and 2 \mu s$.

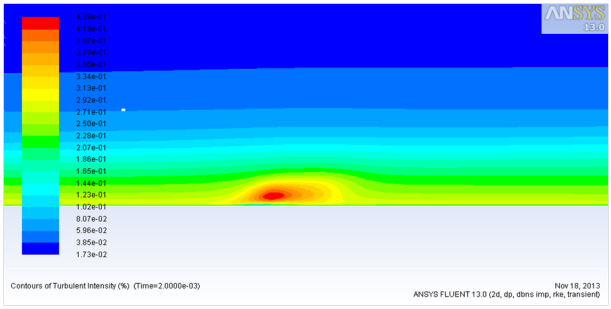

Figure 1.36: Turbulent intensity contours at $t = 2 \mu s$.

computational 3D mesh has been created to describe a flat plate flow similar to the two dimensional case presented above. In figure 1.38, the simulation domain and the corresponding mesh is shown.

The mesh is highly refined near the heat source which is placed in the center of a 0.2x0.1x0.1 meters domain. The heat source is a cylinder of 0.5 mm diameter and 0.8 mm height, and the temperature elevation in 100 μs is 1000 C, corresponding to suggestions of [55]. The free-stream velocity is 10 m/s. The frequency of actuation is again 1 kHz. ONERA's in-house built CFD solver, CEDRE, has been used for this set of

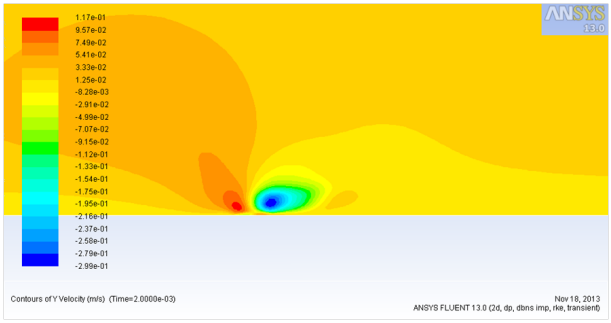

Figure 1.37: Y-velocity contours at $t = 2\mu s$.

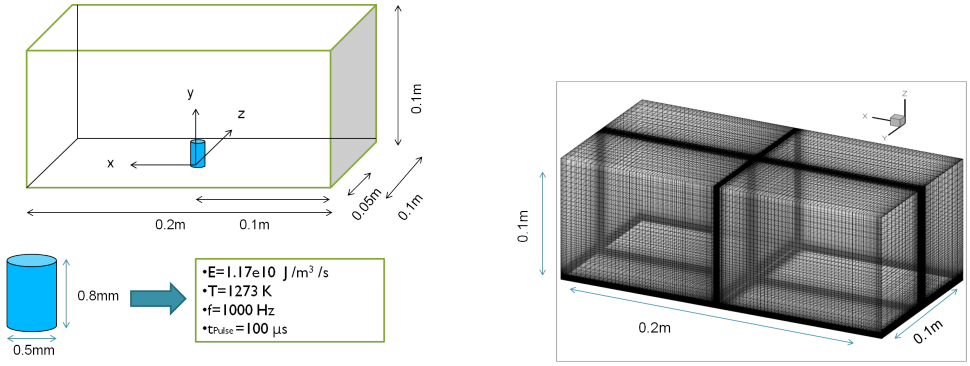

Figure 1.38: Computational domain, dimensions and mesh for the 3D simulation.

simulations. The numerical results obtained, confirm the experimental and computational observations of the authors in [55]. As shown in figure 1.39, the heated region introduces vorticity in the flow that spans in the transverse direction of the flow and being convected downstream. At a time of $t = 1.1ms$, the first pulse has already been convected by the external flow, leaving behind a region of increased vorticity while the newly born vortical structures (linked to the second pulse) are concentrated in a region just before the heated region and spanning symmetrically to the z-direction. The induced vorticity, just as observed in the two dimensional simulations, accumulates at each repetitive pulse of actuation as the two increased vorticity regions merge, signifying that the pulsed mode can lead to a long vortical zone that can have significant effects in the initial boundary flow even at distances quite far from the actuation region. The maximum values in the figures are limited to the colorbar values for visualization purposes.

After $4ms$ or 4 pulses, the energy continues to accumulate and the disturbances are moved further downstream in the flow. Each heated region, as it moves inside the flow, produces a double set of counter-rotating vortices, symmetrically to the xy plane. This can be seen in figure 1.40, where the temperature iso-surfaces are being presented along with vorticity magnitude contours on the centered xy plane and x-vorticity contours on the zy planes. It is important to note that each set of double-vortices on the zy plane, is being produced in the region just below the heated zone, and so, the height of actuation can have an essential role for different boundary layer thicknesses or flow characteristics.

The pulsed actuation of energy deposition inside a boundary layer subsonic flow as seen can be a method

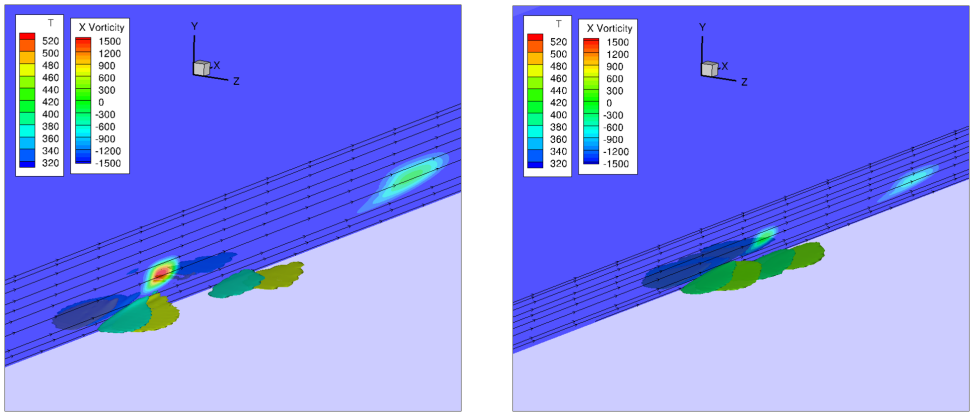

Figure 1.39: Temperature contours in the centered to the heated region xy plane and x-vorticity iso-surfaces at time $t = 1.1ms$ and $2ms$.

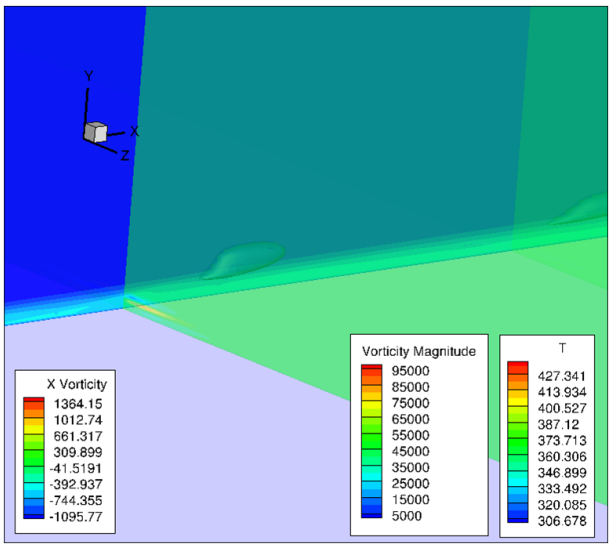

Figure 1.40: Temperature iso-surfaces, x-vorticity contours (zy planes) and vorticity magnitude contours (xy plane) at $t = 4ms$

of producing vorticity and thus disturbances inside the flow that can modify its turbulent parameters. These effects, are much alike to physical or thermal bumps as reviewed in the introduction chapter. Although, the heating of a boundary layer can directly modify its viscosity, leading to a modification of the skin friction drag. To study this effect and decouple the unsteady actuation from the aerodynamic influence of a heating region inside a boundary layer flow, steady simulations have been performed using the k-kl transitional model provided in FLUENT® . The initial turbulent intensity was assumed to be 3.8% while we chose a freestream flow of 5.4 m/s. This choice has been made in order to validate the results with the ERCOFTAC test case T3A. Excellent agreement has been observed for the case with no energy addition concerning the transition point.

We have performed parametric studies with different levels of energy input that correspond to a temperature raise of approximately 300, 1000 and 1900 C. In figure 1.41, the skin friction coefficient is plotted for these cases as well as for the non actuated case.

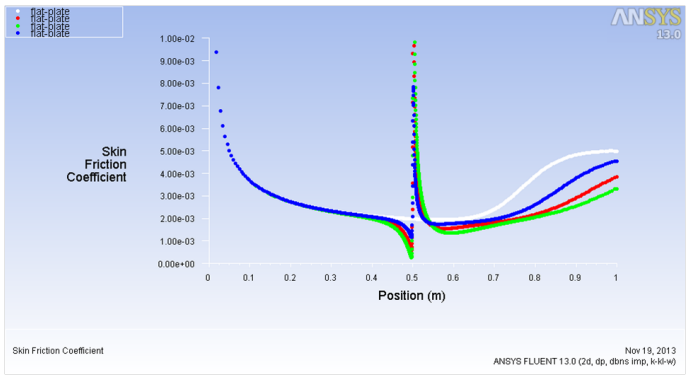

Figure 1.41: Skin friction coefficient for the steady state case and for different levels of energy addition. White : No actuation, Blue : $T_{max} = 500C$, Red : $T_{max} = 1200C$, Green : $T_{max} = 2100C$.

The steady energy addition seems to have a weak influence on the laminar to turbulent transition point. Though, as demonstrated by the experiments of [56], the heating of the boundary layer results to a significant decrease of the skin friction coefficient in the turbulent region of the flow. This reduction is a function of the skin temperature to the ambient one and increases with increasing energy addition. So it can be concluded, that heat addition inside the boundary layer can have different effects depending on the frequency of actuation : For unsteady actuation or high frequencies, the disturbances and the consequent vorticity produced can be a means of destabilizing the boundary layer and thus provoking transition while for steady heating or low frequencies the heating results to a lower skin friction inside the turbulent region of the flow and thus drag reduction. These simplified preliminary numerical results seem to agree with the investigations of the previously mentioned authors qualitatively.

The second research group that have dealt greatly with microwave discharges comes again from Russia in collaboration with the Department of Mechanical Engineering at Rutgers - The State University of New Jersey, USA. The researchers of the Institute of High Temperatures of the Russian Academy of Sciences (IVTAN) and St.-Petersburg State University., have been pioneers of the research of microwave plasma discharges for supersonic flow control [57]. In [58], an excellent overview and in depth physical analysis of the interference between supersonic flows and microwave plasmas is presented.

In [59], the authors have investigated experimentally a 9-gigahertz microwave plasma, initially focused upstream of the hemisphere cylinder. In figure 1.42, the interaction of the bow shock with the plasma discharge low density zone can be observed while in figure 1.43 the centerline surface pressure versus time is plotted, demonstrating as before the significant reduction of surface pressure and thus drag.

Numerical simulations related to this experiment have been performed in [60]. The authors used a fully three- dimensional, time-accurate gas dynamic code with a thermochemistry model that includes 23 species and 238 reactions. In figure 1.44, the filtered stagnation pressure is plotted versus time and compared with the experimental values, showing good agreement especially for the more refined (doubled) grid 2. The authors conclude that significant real gas effects are observed throughout the interaction as they have calculated high

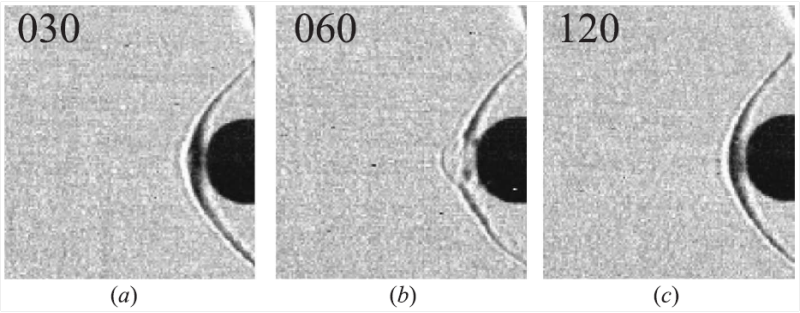

Figure 1.42: Interaction of MW plasma discharge with a bow shock formed in a Mach 2.1 hemisphere cylinder flow[59] (time in μs).

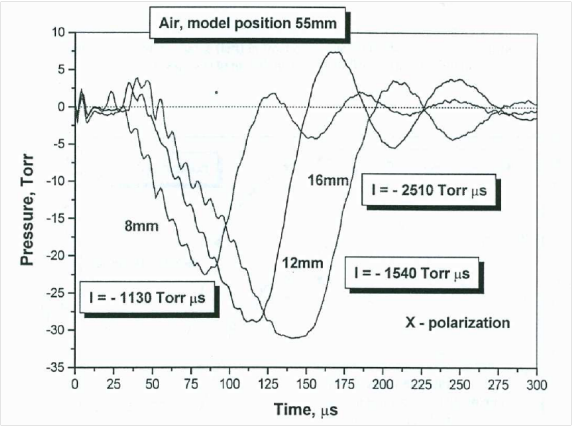

Figure 1.43: Centerline stagnation pressure vs time[59].

levels of atomic oxygen during the interaction of the plasma with the blunt body.

Most of the experiments were conducted at the experimental facilities in St. Petersburg, under an airflow of $M = 2.1$. Impulse MW power was $195kW$ with pulse duration $1.5\mu s$, and was focused along the central axis of the flow, causing breakdown in it. As a result a microwave plasma discharge in the form of a plasmoid of about 20 mm length appears in a flow in front of a body as seen in figure 1.45.

In figure 1.46, the interaction of the microwave plasmoid with the external flow for different time-steps is shown and in figure 1.47 the stagnation pressure in the centerline versus the time is plotted, showing the strong reduction due to the plasmoid interaction with the shock wave that forms before the cylinder.

The evolution of the stagnation pressure has been summarized in [57] as follows:

— arrival of shock and/or rarefaction wave;
— phase of relatively constant pressure (vortex formation in front of body surface);
— interaction with vortex (pressure and temperature drop-down);
— post -vortex relaxation (pressure and temperature rise at stagnation point).

, concluding that the most effective is the phase of vortex interaction with the front surface of a model.

As the energy absorbed by the plasma and transfered to the gas as heating, as well its volumetric existence

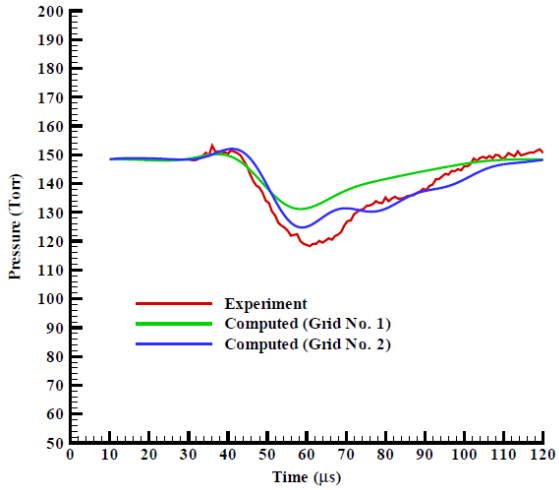

Figure 1.44: Centerline stagnation pressure vs time[60].

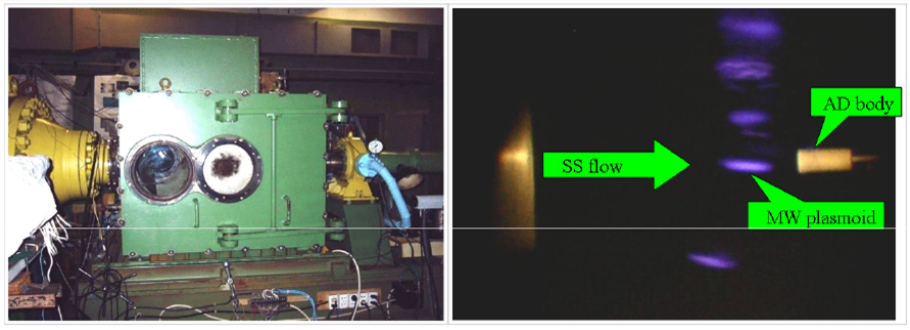

Figure 1.45: Experimental facility and plasmoid formation in front of a 20 mm blunt cylinder [61]. .

are essential for evaluating the efficiency of such actuators in the work of this group, a lot of attention has been put in order to obtain reliable data for the plasma structure and its energetic parameters. They have measured an energy deposition in a single plasmoid to be about $30mJ$ due to a $10GHz$ microwave field while the volume it occupied approximately $0.4cm^3$. The temperature rise should then correspond to about $100K$. As this results contradict the experimental results and the interaction with the shock wave, they have concluded that an internal filament structure must exist where the temperature rises to more than $2000K$. Due to the big difference in dimensions of the plasmoid bulk and its internal filament, they used a combination of experimental curves fitting and direct kinetic modeling let obtain verified information about the local discharge parameters [62]. Then indeed, they were able to characterize the plasma bulk and the internal filament-s. At $70Torr$ of air pressure and under the previously mentioned conditions, they have calculated a rate of heating for the bulk plasmoid in the order of $100K/\mu s$ corresponding to an absorbed energy of $35mJ$ while the internal filament is heated in a rate of $3kK/\mu s$ corresponding to an absorbed energy of $1mJ$. In this analysis they have assumed that 10% of the absorbed energy goes directly to gas heating. They concluded that the filament's big energy density is responsible for all the gas dynamic effects and thus the drag reduction.

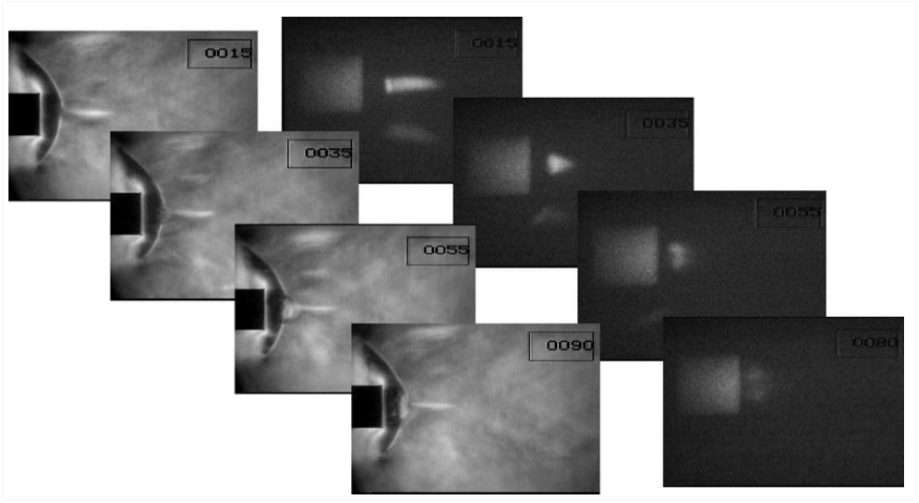

Figure 1.46: Interaction of the MW plasmoid with the cylinder body (M=2.1, time in ms) [61]. .

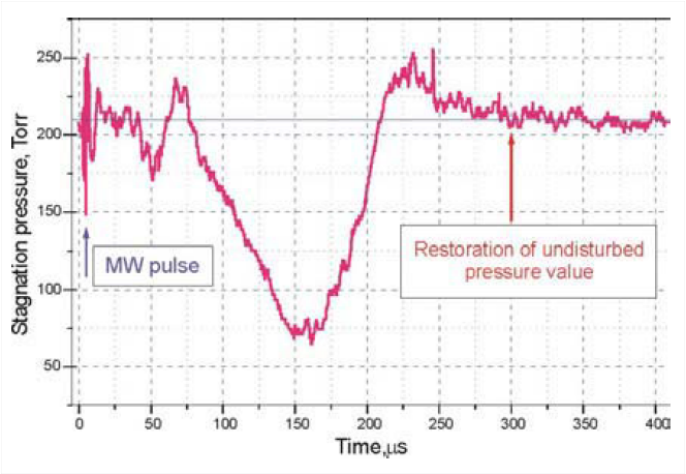

Figure 1.47: Centerline stagnation pressure versus time[61]. .

Finally, interesting results have been obtained in [63], where the authors used a pulsed magnetron as a microwave source, and a rectangular waveguide ending to a horn antenna to inject the MW energy into the test section. The EM frequency was $12.5GHz$ while the pulsed microwave power was $W < 300kW$ at a frequency of $100Hz$. The energy then was focused with a mirror into a dielectric cylindrical nozel serving as the air flow test section. The nozzle was designed for a Mach number of $M = 2$ under different static pressure conditions. Experiments in quiescent air as well as in a Mach 2 flow demonstrated that the discharge under pressures lower than 100 torr was of a plasmoid diffusive form, while in higher pressures a highly nonuniform filamentary nature exists. In both cases, and under the external supersonic flow, the plasma is not being blown

off by the flow and the power needed for creating the discharge depended only slightly on the flow's speed. Translational and vibrational gas temperatures have been measured as a function of air pressure (near the threshold for breakdown microwave power) and microwave power. Their measurements, show that the gas temperature increases with increasing gas pressure consistent with the Paschen curve. Under high power electromagnetic fields, the gas temperature saturates and decreases as a results of microwave screening and skin effects.

1.3.2 Other energy deposition plasma flow control actuators

Except MDAs, energy deposition with plasma can occur via Localized Arc Filaments or DBD nano-second devices.

The group of LAFPA (Localized Arc Filaments Plasma Actuators) actuators have been firstly studied by the team of Leonov et al[64]. Their work was mostly focused on supersonic flows where the already known and well studied typical plasma actuators as DBDs offer little to no positive aerodynamic effects. Their motivation was indeed the thermal effects of arc discharge actuators and they have proved their ability to create local shock waves that can interact and modify the already supersonic flow. These localized arc discharges play the role of thermal sources in the external flow that excite instabilities and are able to modify the flow structure. These actuators provide the advantage of simple construction and applicability in aerospace applications. Typically, they simply consist of two electrodes connected with a high voltage DC power supply which can produce output pulses (up to 10 kV), at a variable repetition rate (from 0 to 200 kHz) and duty cycle (from 0% to 100%), with a short rise/fall time ($0.1\mu s$)[65]. In this last reference, the authors managed to excite the flapping mode of a cylindrical jet by using azimuthally placed LAFPA actuators on the nozzle's surface. An important remark of their work is that most of the plasma effect in the flow is being produced by the intense heat addition in the first micro seconds of the actuation. It is then, when the strong compression shock wave is formed and the DC actuation in further times provide no more instabilities. This remark is essential as the rise time of the discharge and its frequency of operation is what will control the energy deposition and consequently the heat addition and shock wave formation in the flow.

The power consumption of each actuator was measured to values of 20W at 20% duty cycle. The temperature rapidly increases over the first $10-20\mu s$ of arc operation, from below $1000C$ to up to about 2000 C while at longer discharge pulse durations, $20-100\mu s$, the plasma temperature levels off at approximately $2000C$.

Shang et al. [66] have studied the interaction of a DC LAFPA over a flat plate with an external flow of Mach 5.15. The main effect of the discharge has been found to be the Joule heating that dominates over the electrode conductive heating. The pressure variation due to the plasma discharge is clearly visible in figure 1.48.

Nano-second Dielectric Barrier Discharge actuators are relatively a new concept of DBD actuators. Their main difference compared to conventional DBD is the nano-second rise time of the voltage in each circle that leads to the development of high current streamers and the negligible production of ionic wind. The high current streamers though are highly energetic in terms of thermal power. The temperature increase can reach values of several thousands Kelvins and pressure waves are generated locally over the actuator's region. The energy per unit length of such actuators is in the order of 1 mJ/cm. The pressure wave is propagating in sonic speeds and they induced pressure variation can reach very high levels. The effect in the flow of such actuators is similar to the one described in the previous section : Shock wave formation and propagation, vorticity induction in the flow, manipulation of flow structures in different frequencies. A discharge of such form can

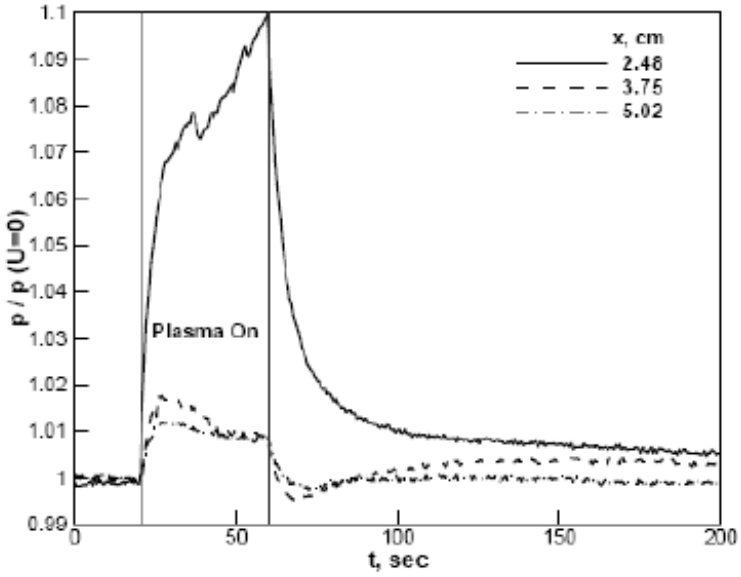

Figure 1.48: Surface pressure variation fue to a DC LAFPA over a flat plate [66].

be seen in figure 1.49.

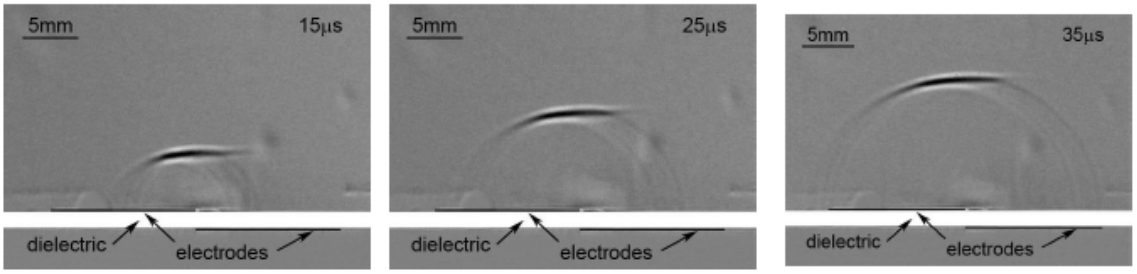

Figure 1.49: Shock wave formation due to nano-second DBD actuation[67].

This type of actuators are quite promising for flow control applications. Their efficiency in different flow regimes have been hugely studied in the previous years and methods to provide a flow control loop is still under research[68].

1.3.3 The Surface Dielectric Barrier Discharge (SDBDs) actuator

DBD actuators are included in the category of momentum addition flow control methods. This group's effect in a flow is purely related to such of pulsed or not, jets and wall jets.

To avoid the corona-to-ark transition which leads to instabilities of the discharge , the use of a dielectric barrier in the discharge gap, which stops the current and prevents the spark formation has been used. This is a

DBD actuator, conceived and developed firstly by Engle et al [69], while various authors have studied it in the late 80s [70]. The presence of the dielectric barrier limits the current so an ac or pulsed excitation of the DBD's is required, usually by a sine HV waveform in order to avoid the destruction of the dielectric layer due to charge accumulation. This excitation leads to impulse discharges which can be very small with very high pressure. The discharges are in general filaments of high pressure and it is difficult (but desirable) to generate a uniform plasma under these conditions. DBDs have a large number of industrial applications because they can operate in air at atmospheric pressure, and do not need sophisticated pulsed power supplies.

The gas-filled gap is small (typically a few millimeters) . A voltage of $1-100kV$ with frequencies of $50Hz-1MHz$ is necessary to sustain these discharges. The charge carriers streaming from the plasma to the dielectric remain on the surface of the dielectric and compensate the external electric field. Therefore, the lifetime of the filaments is very short ($1-10ns$). The current density in the filaments is $100-1000Acm^{-2}$, the electron density is $10^{12}-10^{14}cm^{-3}$, and typical electron energies are in the range $1-10eV$.

In the middle '90s, Roth and its group has patented a new Surface DBD actuator by placing two electrodes asymmetrically on each side of a dielectric [71]. The discharge is generated in the same way as described above but one of the electrodes is exposed to the air flow and the other grounded and moreover encapsulated inside the dielectric material that is placed on the surface (flat plate, airfoil etc.) to prevent plasma formation below the dielectric (this configuration is mainly used for aerospace applications in opposition to the one proposed by Roth in [71]), as presented in figure 1.50.

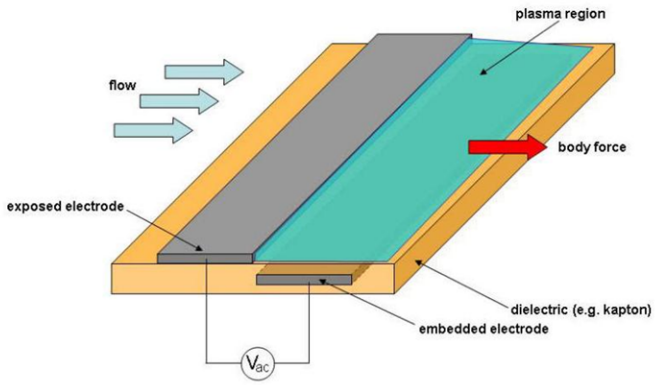

Figure 1.50: Representation of a SDBD over a flat plate (courtesy of University of Maryland).

By exciting the exposed electrode by a sine waveform (in this work we will consider sine waveform excitations) and above the ignition voltage, a plasma sheet appears on the upper side of the dielectric near the air-exposed electrode. In practical experiments with DBDs for flow control, the voltage wave form is sinusoidal, with frequencies between $1 and 10kHz$. When the applied voltage is time dependent sinusoidal, the voltage at which the discharge forms depends on the amplitude of the voltage and its time derivatives i.e., the frequencies. At low enough frequencies and because of the slow rise of the voltage, the discharge will operate close to a Townsend or subnormal regime. At higher frequencies the discharge will operate in a glow or filamentary glow regime at a frequency-dependent voltage.The plasma is composed of a set of micro-discharges during the positive half-period and the negative one. The exposed electrode plays the role of an anode in the positive phase and of a cathode in the negative phase.

The production of plasma with surface actuators induces a flow mainly due to the momentum transfer between charged and neutral particles, while the heating of the gas is almost negligible [72, 73]. In a corona discharge the plasma is generated in a small volume around the small electrode and the electric wind is a result of that momentum-transfer transfer in the non-neutral collection region outside the plasma where the ions drift toward the large electron. The situation is similar in a DBD but the region where the force that induces the flow is nonzero (ion sheath) is much smaller and the force is larger.

As mentioned, the unique feature of the DBD actuators is their ability to sustain plasma discharges in a relatively big volume, avoiding their transition to a thermal arc, due to the self-termination of the discharge itself. The accumulation of electrons at the dielectric surface causes a reduction of the local electric field strength, leading to the extinction of the discharge [74].

Various experimental results, reveal the nature of the plasma discharges during a whole ac cycle [72, 75, 76]. In [73], Orlov used a photo multiplier tube to capture the evolution of the ionized air light emission from a SDBD actuator. It observed, that the ionization process occurs only in part of each half-cycle of the AC excitation source, and it has the form of separated spikes indicating micro-discharges formation. Moreover, as observed also in [75], the form of the discharges during the 2 half-cycles differs significantly. They explain this phenomenon as follows : During the negative half-cycle, electrons are emitted from the exposed electrode and deposited onto the dielectric surface reducing the potential between the exposed electrode and the dielectric, and thus the electric field. When the potential reverses, the ionization stops as the electric field becomes less than the critical for breakdown one. In this cycle, the exposed electron is a continuous source of electrons, making the discharge more uniform, in a glow regime as the fast accumulation of electrons by the dielectric surface shields the electric field and prevents the formation of streamers. This has been also demonstrated numerically in [77, 78, 79]. In the positive cycle, electrons are emitted by the dielectric surface to the exposed electrode until the potential reverses once again. In this case though, the emission of the electrons is not continuous, forming micro-discharges that could initiate more due to photoionisation [80], leading to the peaks observed also in [81]. The different nature of the plasma discharge in each half-cycle is observed clearly by the experiments of Moreau et al [82] and are presented in figure 1.51.

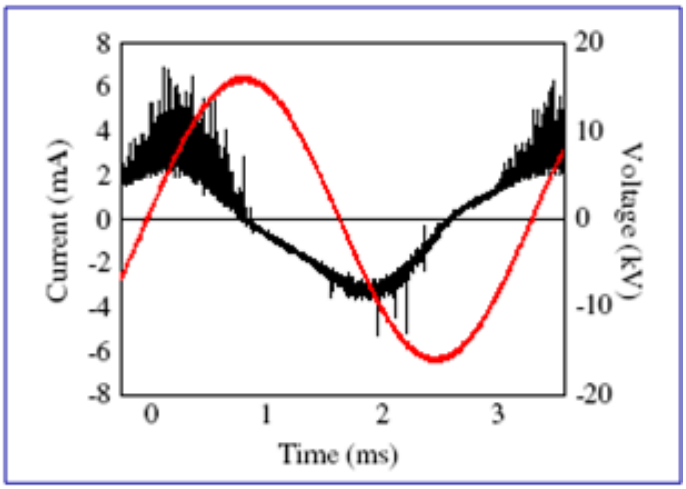

Figure 1.51: Current and Voltage vs time in a SDBD [82].

The transformation of electric energy to kinetic one by means of momentum transfer from the charged particles to the neutral ones (via the Coulomb force), gives rise to the so-called "ionic wind". Neglecting the mean velocity of the neutral particles with respect to the charged particles ones, and the diffusion terms of the current density drift-diffusion formulation, the ElectroHydroDynamic force produced by this transfer, can be written as :
$F_{EHD} = \pm J_s/\mu_s = Ee(n_i - n_e - n_n)$
, which represents the force per unit of volume transmitted to the neutral particles by the ionic wind [83]. This formula can be derived based on 2 basic assumptions. Firstly, we assume that the ion number density in non-neutral regions is much larger than the electron number density. Secondly, the force exerted by the charged particles on the neutral gas are significant only in the non-neutral regions of the discharge where the ion current density is large. So we assume that the contribution of the neutral, uniform plasma and the quasi-neutral, nonuniform plasma regions are negligible. For a more detailed justification of these assumptions refer to [84].

This EHD force produced by a SDBD actuator, is clearly linked to the change of the plasma morphology during its AC cycle. In [85], the authors measured a higher production of induced velocity during the negative half cycle than the positive one. In [86], the authors used interferometry techniques to measure the displacement of a pendulum on which the SDBD actuator was mounted. They have observed, that positive force is produced in both half cycles, with the same magnitude, but skin friction losses cause most of the positive cycle's force to be canceled. Thus, they proposed a PUSH-push effect in a whole AC period, in contrast with [87, 88], where the force has been calculated using integral methods on PIV and Laser-Doppler measurements of the velocity field. The latter results, demonstrate that at the beginning of each positive half-cycle, a negative force is produced, opposite to the negative phase, proposing thus a push-pull scenario. In [89], the authors used the PIV technique to construct the time-resolved description of the flow field , determining the body force via a differential method of resolving the Navier-Stokes equations. They have observed, a positive x-directed force in both the half cycles, with a 5 times larger magnitude during the negative cycle, and a negative y-directed force in both the cycles. Although these results, seem to confirm the ones of [86], the authors have also observed a negative x-directed force when the discharge is quenched. Nevertheless, they explain this negative force by decoupling its existence from the plasma discharge, and referring to viscous effects and turbulent losses for the deceleration of the total force until the streamer regime positive half cycle starts again. The current-voltage versus time plot measured by [89] as well as the evolution of the force in time are presented in figures 1.52 and 1.53. In this experiment, they have used an actuator driven by a sine high voltage of magnitude $20kV$ and a frequency of 1 kHz. The dielectric was made of acrylic glass and was $3mm$ thick. Note that for the force estimation the differential method was applied to the vorticity equations (VEs) in addition to the Navier-Stokes ones (NSEs) for comparison.

In [90], the authors have measured the induced body force by two experimental techniques : A high precision force balance as means of direct measurement of the thrust produced and a control volume analysis based on PIV measurements. They have used a $3mm$ thick dielectric material (Kapton) and excited the actuator with a sine signal of 7 and 14 kHz frequency and varying voltage. The schematic overview and dimensions of the actuator are presented in figure 1.54 Their results on the integrated force over space and time are presented in figure 1.55. Note that different lengths L of the actuator have been studied and the tendency of the force seems to propose that shorter actuator's lengths produce higher forces for high voltages. As expected the total force increases with the increasing voltage supplied, as its highly related to the electric field produced by the potential differences.

Several measurements of the velocity profiles produced due to the EHD force can be found in literature as

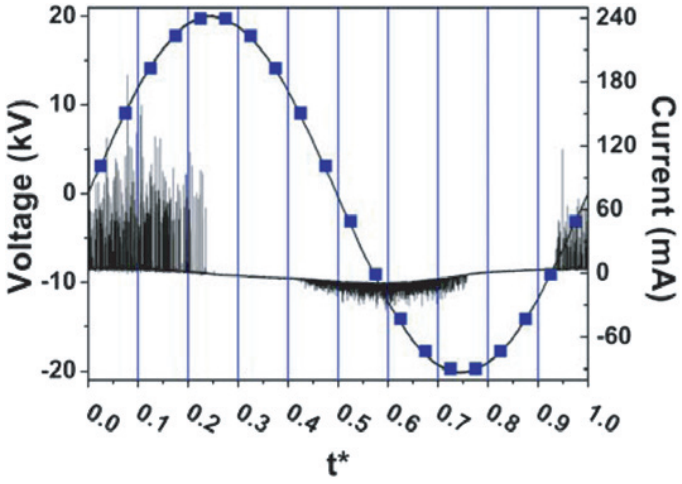

Figure 1.52: Current and Voltage vs time for the $20kV, 1kHz$ actuator of [89].

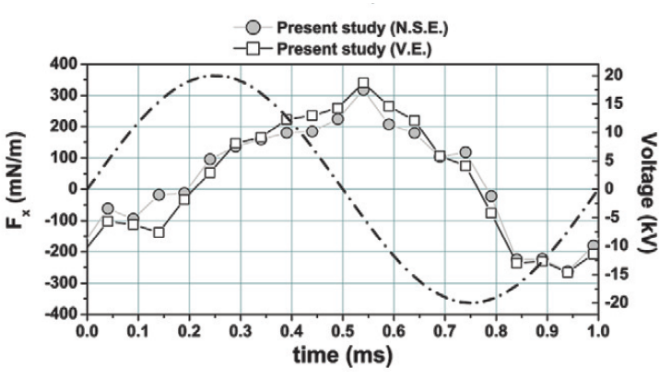

Figure 1.53: Force evolution in time for the $20kV, 1kHz$ actuator of [89].

well as applications for aerodynamic flow control, noise reduction, combustion optimization. Its maximum values, depend on various parameters such as the voltage and frequency applied, geometrical configuration of the electrodes, dielectric properties and air conditions. In [75], a sawtooth waveform has been used instead of a sine one, corresponding to higher values of the produced force (and consequently velocities), linked to the PUSH-push or push-pull phenomenon described above.

Most authors [91, 81], have observed velocity profiles that present maximum values at a height of less of or equals to a millimeter above the surface of the plate-dielectric and at a length that corresponds to the extension of the plasma, near the embedded-grounded electrode. The frequency-voltage dependence of the maximum velocity was analyzed in [92, 93]. The net-force and corresponding velocity increases with increased voltage (linearly). The frequency dependence is different. In [94], the authors state that the optimum frequency of the plasma actuator depends on the dielectric properties of the material, or more specifically on the bulk capacitance of the actuator as the capacitance is proportional to εh, where h is the thickness of the

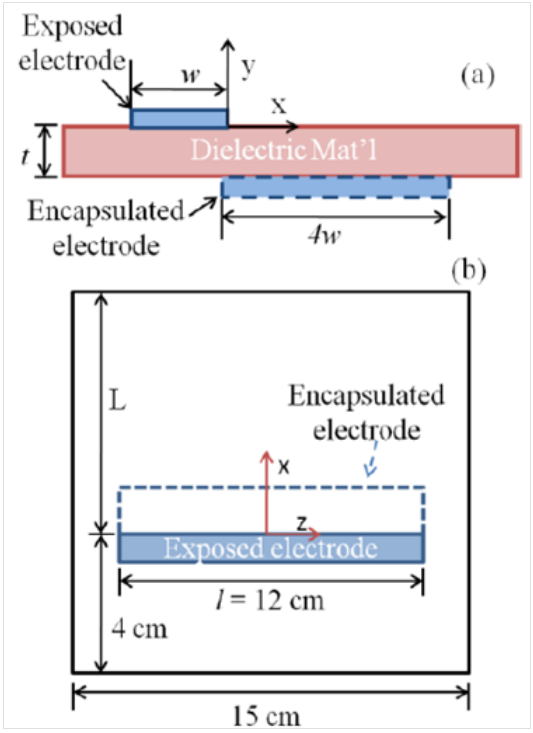

Figure 1.54: Schematic view of the actuator studied in [90].

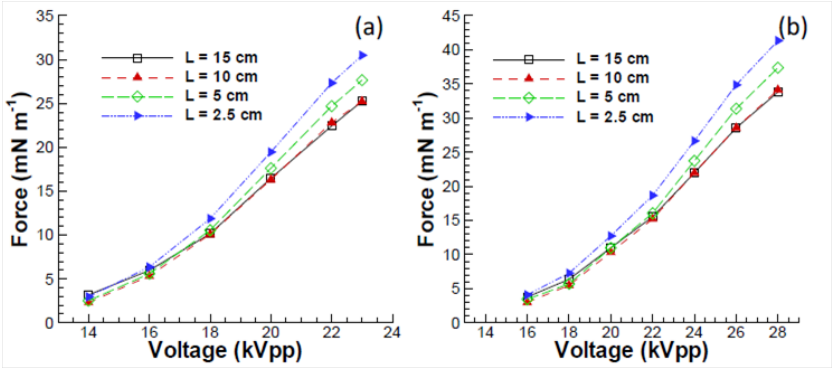

Figure 1.55: Force versus voltage for various actuator plate lengths [90]. a) 7 kHz b) 14 kHz.

dielectric. This has been numerically confirmed in [73], by calculating the body force produced for different ac frequencies and dielectric properties. Their results are plotted in figure 1.56.

In [95], the authors have performed a parametric study on a SDBD in order to enhance its performance. They fixed the frequency of the applied ac source to a value of 1 kHz They summarize their findings as follows :

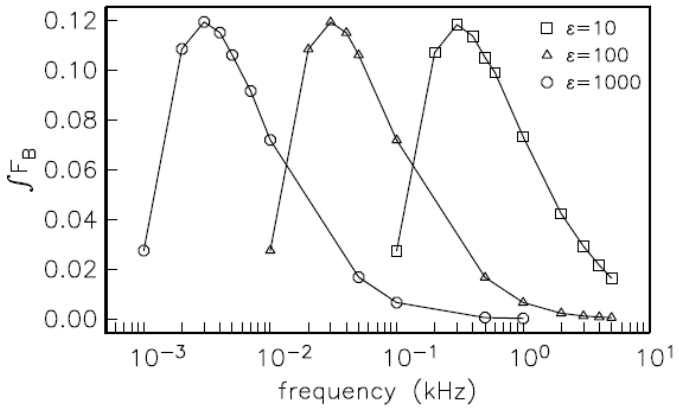

Figure 1.56: Body force ($F_B = F_{EHD}$) produced by a SDBD vs ac frequency and dielectric constant [73].

— Thicker dielectric materials tend to be more favorable for enhanced induced flow, as they do not favor the dielectric's breakdown. The efficiency of the actuator (mechanical power delivered/electrical power consumed) also follows the same trend.
— The electrical consumption of the actuator increases (as expected) with the applied voltage and waveforms of steep slopes increase the consumption due to the higher current peaks presented 1.57.
— Steep slopes of the ac waveform signal (square or positive sawtooth for example), reduces the induced flow for same electrical power consumption (figure 1.58) as they result into a more intense positive half-cycle discharge in contrast with the negative one, leading to smaller body force and thus induced flow .
— The induced flow reaches higher velocities with increased electrical power consumption/voltage following a asymptotic dependance as plotted in figure 1.58.

In [96] experiments were made on a single DBD actuator on a flat plate, obtaining the velocity profiles plotted in figure 1.59 with V=11kV and f=11.7kHz and for different sections on the flat plate.

In [90], the authors measured, using both PIV and pitot techniques, the velocity profiles of a 21kV (peak-to-peak) and 14kHz SDBD actuator. They are plotted in figure 1.60 at a distance of 15 mm downstream of the exposed electrode.

In [97, 98], the authors have measured the induced velocity due to a SDBD for different pressures and levels of humidity, showing that a maximum velocity can be achieved at approximatelly 0.6 atmospheres while the levels of humidity showed little effect.

In most of the experimental results the maximum velocities obtained by a single SDBD actuator reach values of around $5-7m/s$. Its worth to mention that the induced wall-jet flow can be enhanced by using multiple actuators or novel materials and configurations. We are focusing here in single SDBD configurations. A detailed description of different applications and configurations for improving the efficiency of such actuators can be found in [82].

Various aerodynamic applications can be found in literature, demonstrating the benefits of the use of the SDBD actuators for flow control in a variety of Reynolds number flows [99, 100, 101]. The authors in [102], have used leading edge SDBD actuators in steady and unsteady mode to study its effects on stall and lift coefficients versus different angles of attack on a NACA 0015 airfoil at a $Re = 2.15 \times 10^5$ flow. They have

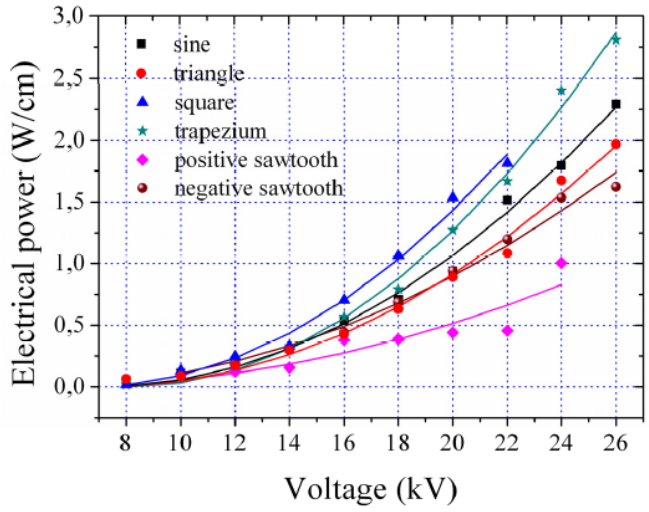

Figure 1.57: Electrical power consumption vs voltage applied for different waveforms- $f = 14kHz$ [95].

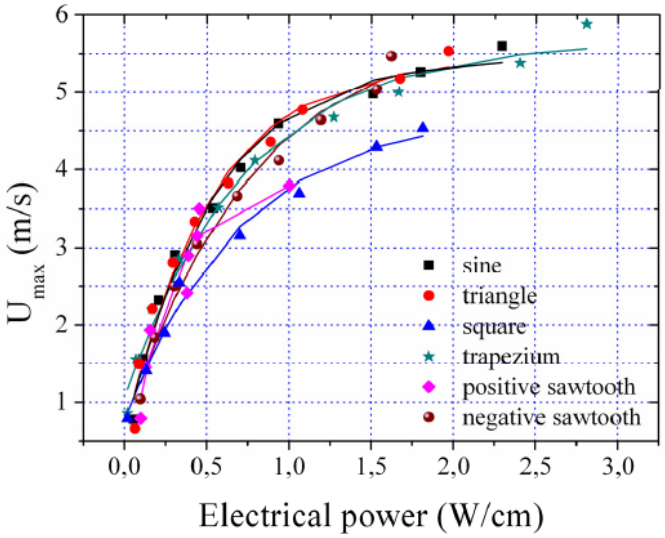

Figure 1.58: Maximum velocities vs electrical power consumption for different waveforms - $f = 1kHz$ [95].

demonstrated as seen in figure 1.61, that unsteady actuation allows for higher critical stall angles while steady actuation has smaller but still important effects on stall.

1.3.4 The Plasma Synthetic Jet (PSJ) actuator

Synthetic jets as we have seen provide means of flow control via the momentum addition mechanism and vortex generation. Compared to traditional blowing or suction devices, they present advantages such as the

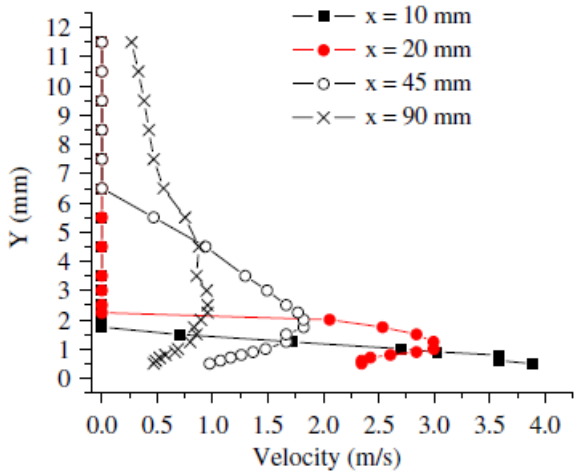

Figure 1.59: Velocity profiles over a flat plate SDBD actuator in still air [96] - $V = 11kV f = 11.7kHz$.

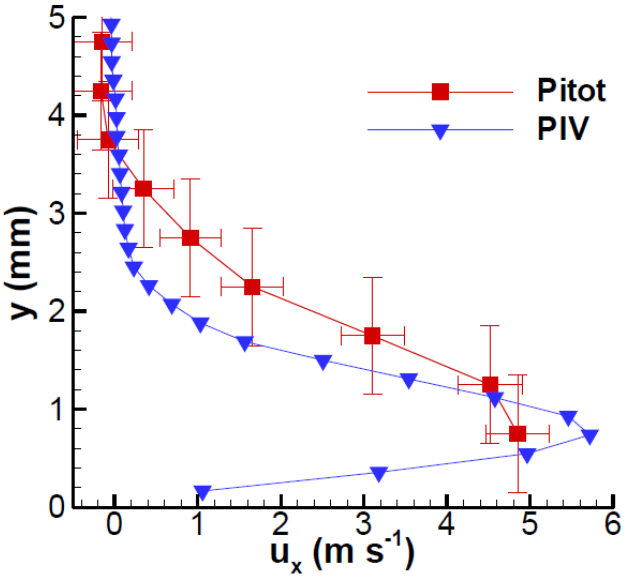

Figure 1.60: Velocity profiles over a flat plate SDBD actuator in still air [90] - $V = 21kV ppf = 14kHz$.

lack of complex piping systems, no external air supply requirements, reduced weight and size. Although, their responses times and complexity are often large (piston driven actuators) and their energy output small (piezoelectric actuators). Thus new devices need to be developed that can retain the advantages of such methods and in the same time offer easy frequency modulation, small response times, facilitation of integration and high power input. Plasma synthetic jets meet such requirements in a great extend.

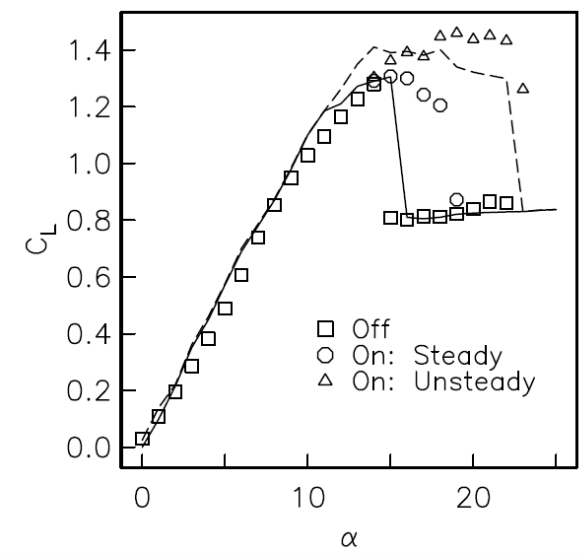

Figure 1.61: Lift coefficient versus angle of attack with leading-edge actuator off and on at optimum unsteady frequency and steady actuation. Lines correspond to numerical simulations performed in [103].

Plasma synthetic jets can be produced in a three-dimensional way by an annular electrode configuration over a surface. The generation of a zero-net-mass flow, vertically oriented in quiescent flows, has similar effects to mechanical synthetic jets as described in previous sections [104]. In [105], the authors used numerical simulation coupled with a phenomenological model that represented the body force from the plasma actuator. The have found that the unsteady actuation is similar to conventional jets and steady actuation in terms of the time-averaged flowfield, while the volume and momentum flux is larger. A schematic representation of such actuators is presented in figure 1.62.

The jet's velocities of such actuators can reach some meters per second, making them unable to strongly modify a flowfield of increased velocity. Here, we are focusing on a new concept that has been recently proposed by John's Hopkins Applied Physics Lab [106] and improved by others groups [107, 108] : the sparkjet plasma synthetic jet actuator (referred to PSJ or sparkjet from now on).

A schematic view of the operation of this novel plasma synthetic jet device is shown in figure 1.63. The jet is created by an energy deposition coming from a pulsed arc discharge heating the air in a small cavity. A temperature rise causes the expulsion of the air from the cavity through the upper hole. The high speed jet formed, is a zero-net mass one, as a suction phase follows, refilling the cavity. Typical values of voltages used to trigger the discharge range between 3 kV and 5 kV, while the frequency of the actuator lies between a few and 2000 Hertz. The exit nozzle of the PSJ has typically a diameter of around 0.5 mm while its volume captures 8 mm^3. Compared to traditional plasma synthetic jets, they offer a high energy output, making them interesting for flow control applications of high-speed vehicles.

The creation of the arc discharge requires a high power supply. In [109], this has been achieved via capacitive power supply - a low voltage power supply associated to a high voltage transformer and a transistor.

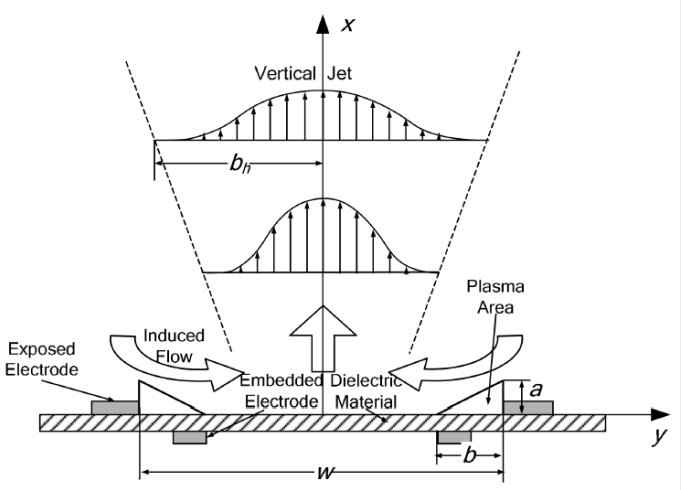

Figure 1.62: Schematic view of the PSJ actuator and its induced flowfield as studied in [105].

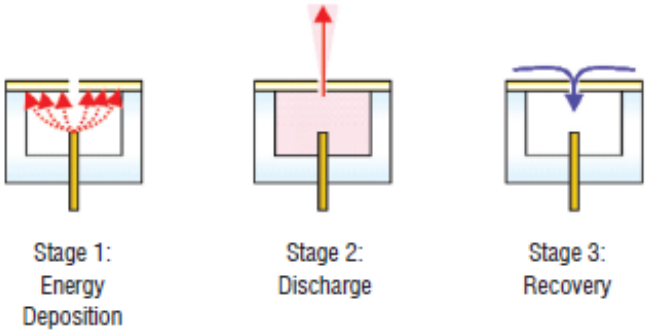

Figure 1.63: Schematic view of the operation stages of the PSJ - sparkjet actuator [106].

The efficiency of the PSJ actuator has been studied in [110, 111] while characterisation and optimization of the device in [112, 113]. In [114], the authors have experimentally characterized the jet and performed parametric studies on the operation frequency and capacitance power supply. They have measured jet's velocities up to $300ms^{-1}$ and jet's temperatures as high as $400K$. Results of such a parametric study of the capacitance power to the velocity and stagnation pressure of the jet are shown in figure 1.64.

An aerodynamic characterization of such an actuator has been performed also in [108]. In figure 1.65, the jet's velocities and duty cycles (the ratio between the pulse duration and the period of a rectangular waveform) with different frequencies are plotted.

The same authors have performed flow control applications. An array of 20 PSJ actuators has been embedded in a NACA-0015 model as seen in figure 1.66 . Amongst different flow control applications, the have experimentally studied the mid-cord separation control by the PSJ array. The flow's Reynolds number was 1.2 millions corresponding to a free-stream velocity of $40m/s$, and the angle of attack was fixed to $\alpha = 11.5^{\circ}$. In figure 1.67, the velocity profiles in a distance corresponding to separated flow are plotted for

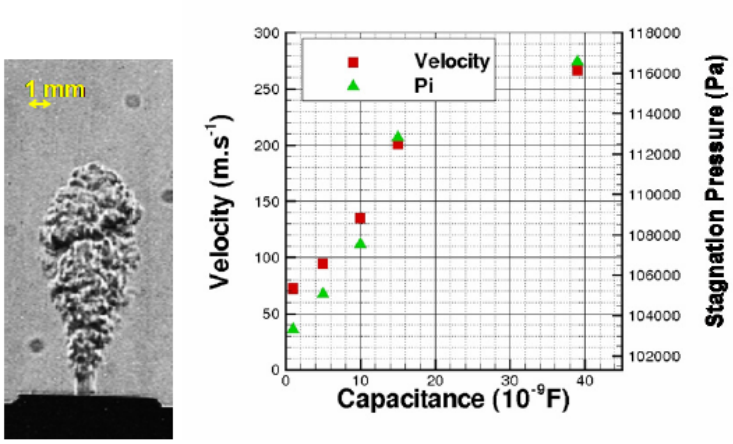

Figure 1.64: (a) Schlieren image of the circular jet $200\mu s$ after the beginning of the exhaust. (b) Velocity (red squares) and stagnation pressure (green triangle) function of the capacitance. $fPSJ = 10Hz$. [114].

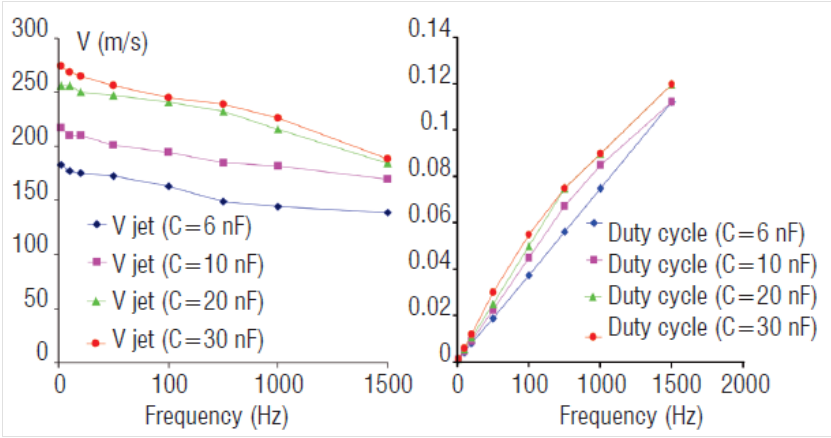

Figure 1.65: Parametric studies on jet's velocity and duty cycle vs frequency for the PSJ of [108].

different frequencies of actuation. It is clear that the PSJ actuation leads to reattachment of the flow.

In [115], a three electrode configuration has been investigated experimentally. Its geometrical configuration and dimensions are shown in figure 1.68 while the actuation in quiescent air is presented with shadowgraph images at different times in 1.69. The have measured velocities of the plasma synthetic jet (jet front) as high as $315m/s$ with a capacitor of $1.6\mu F$, and a spherically symmetric precursor shock with constant velocity of $345m/s$ is found above the jet front for different capacitor. The three-electrode configuration allows for larger volumes of the cavity and thus larger values of expelled mass.

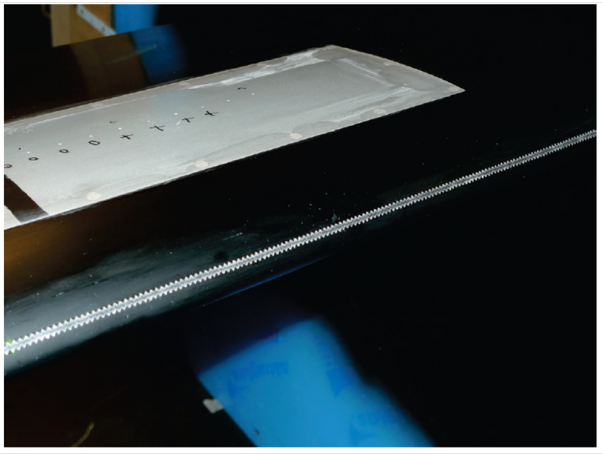

Figure 1.66: The positioning of the PSJ array in a NACA-0015 model [108].

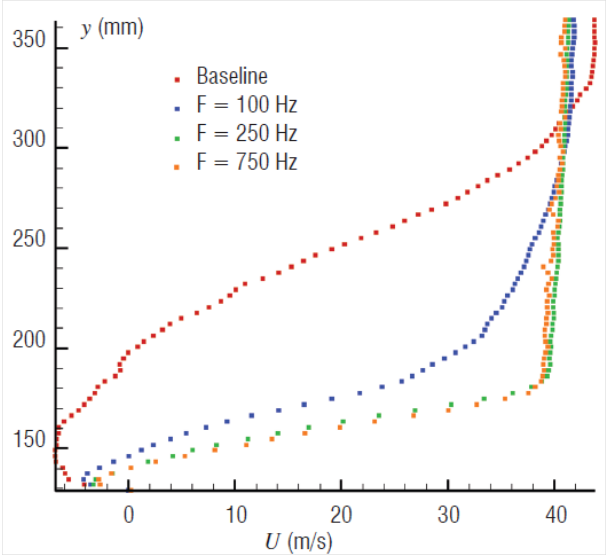

Figure 1.67: Velocity profiles at a separated (in the uncontrolled case) position over the airfoil. [108].

1.3.5 Other momentum addition plasma flow control actuators

The category of momentum addition plasma flow control methods, includes other types of actuators, with the most commonly used to be the corona discharges.

The corona discharge is a weakly luminous discharge which usually appears at atmospheric pressure near sharp point of thin wires where the electric field is sufficiently large. Corona may be considered as a Townsend discharge (depending on the field and potential distribution). Typically, this type of actuators consist of 2 electrodes, one of them grounded, embedded on the surface of an isolating material [116].

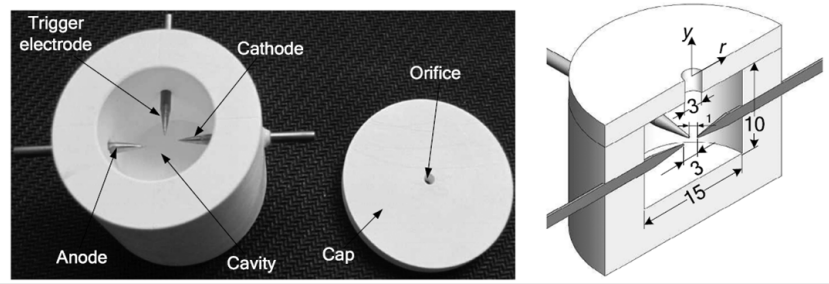

Figure 1.68: Geometrical configuration and dimensions (in mm) of the PSJ proposed in [115].

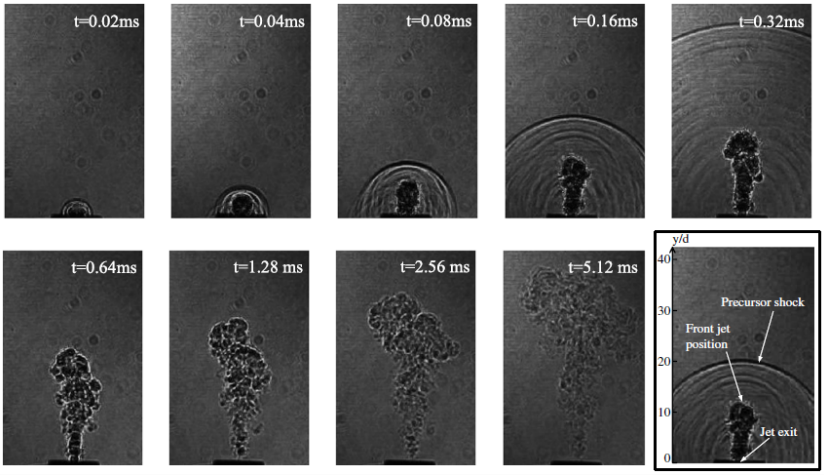

Figure 1.69: Flow visualisation with shadowgraph images of the three-electrode PSJ at different times [115].

The volumetric corona discharge that is created due to the application of the DC voltage between the electrodes, can be categorized in five regimes with increasing voltage [117, 118]:

— The spot regime. Small current intensity , negligible electric wind.
— The streamer regime. Higher current intensity and wind. A thin sheet of blue ionized air between the electrodes is observed and the current is composed by a continuous component due to ion drift and an alternative one due to streamer propagation.
— Glow regime. No thin sheet, but a set of adjacent luminescent spots around the electrodes. Stable.The alternative component of the current here is negligible.
— Filamentary regime.The entire current is concentrated in a few filaments. Sparks may appear. Great difficulty of controlling the discharge.

The desirable regime is easily determined as the glow regime. The filaments regime is unstable, and it produces a non uniform plasma that is difficult to control . Thus, in the corona discharges we choose one of the electrodes to be very small so that the field is concentrated in the vicinity of the small electrode and it is weak elsewhere. This geometrical effect limits the volume of plasma and thus the current and the transition to an arc - a channeled, hot discharge of small volume.

Corona DC discharges have been widely investigated in the past years for flow control purposes [119, 120, 121]. In [122] for example, the authors use a DC corona actuator of a $300\mu m$ radius cooper wire ($270mm$ length) at about $+20kV$ and an aluminum plate electrode ($25 \times 270mm$) at about $-10kV$, to study its effect on an inclined flat plate low Reynolds flow in terms of boundary layer separation control. Indeed as can be seen in figure 1.70, the flow is either reattached to the flat plate or its recirculation area is highly reduced for high angles of attack. The induced flow due to the ionic wind though, is small and so their applicability is quite restricted to low Reynolds number flows.

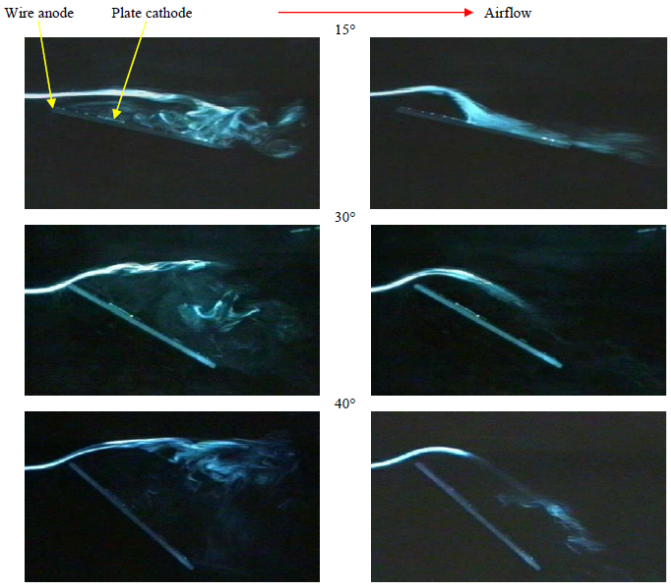

Figure 1.70: Uncontrolled flow (left) and controlled flow with DC corona actuator (right) for different angles of attack[122].

Summary :

Both these families of actuators have their positive points as well as their drawbacks. Still, they overcome a lot of the inconveniences of today's actuators, accelerating the research on them in terms of optimization, by a deeper understanding of their physics and potential. This kind of understanding, lies mainly on numerical models due to the fact that non-intrusive experimental techniques struggle to capture time and space scales related to plasma quantities, failing to describe properly its formation and effects on the gas properties - not to mention that such experiments most of the times require extensive resources. As it becomes obvious from the very title of this thesis, the interest of this research is focused on such numerical models that can accurate and in the same time efficiently describe the physics of such applications.

1.4 Numerical Modeling

Numerical simulations have become extremely useful in the last decades as computational resources have been extensively upgraded and the cost of complex experiments often limits the advance in research. In the hands of scientists and engineers, numerical tools can provide predictions of a physical system's behavior that can accelerate the concept design and in the same time give insights of the physics in time and space scales that an experiment would be incapable to capture. In the aerospace sector, CFD (Computational Fluid Dynamics) tools are nowadays a standard way to proceed especially in the initial stages of an aircraft design. The coupling of such tools with numerical models capable of describing accurately the interaction of the aerodynamic behavior of air with other states of matter as plasma, remains still a huge challenge, as the complexity of the coupled physics increases dramatically.

Modeling is fundamentally the core of engineering. A model is an appropriate simplification of reality. Partial differential equations can describe as we have seen a variety of physical phenomena, including fluid dynamics, electrodynamics and plasma physics. A problem in differential equations can rarely be solved analytically, and so often is discretized, resulting in a discrete problem which can be solved in a finite sequence of algebraic operations, efficiently implementable on a computer. When a numerical model (or simplification of reality) is formed, numerical techniques can be used to solve computationally these equations and obtain information on the quantity of interest. These numerical methods, require a simulation grid (mesh) of the flow, which is a number of control volumes (or lines or elements) that discretize the solution domain in time and space. They also require, the determination of all the physical characteristics of the flow and appropriate conditions on the simulation's domain boundaries (wall, outlets, etc). Such methods, include amongst others finite differences, finite volumes and finite elements methods, spectral methods, domain decomposition ones etc. Each of this method, can be formulated in different manner and thus hundreds of various numerical techniques exist - each one more adapted for one particular physical problem and each one presenting advantages and disadvantages.

Numerical analysis provides methods of solving different types of equations in an approximative way. An analytical solution, would give the exact value of a variable while algorithms of numerical analysis only an approximate one. The difference between the approximate value, ϕ' calculated by an numerical algorithm and the exact value, ϕ, obtained by the analytical solution of an equation, defines the absolute error of the algorithm $\sigma = \phi' - \phi$. This error emerge during a computational solution, due to round-off errors or truncation-discretization errors (approximations to Taylor's expansion series for example) that can accumulate in time. Various numerical algorithms exist for solving linear and not linear equations or system of equations. Direct methods such as Gaussian elimination for a system of linear equations, compute the solution to a problem in a finite number of solution steps, while iterative methods, such as Newton's method, use successive approximations of an initial solution guess to converge to the exact solution (or an approximate one with a truncation error).

Numerical discretization schemes and algorithms need to have basic properties :

— Consistency of a discretization refers to a quantitative measure of the extent to which the exact solution satisfies the discrete problem. A numerical scheme is consistent if its discrete operator converges towards the continuous operator when the discrete step (in space and time) tends to zero.

— Stability of a discretization refers to a quantitative measure of the "well-posedness" of the discrete problem. This means that small disturbances from initial or round-off errors are not growing with time.

— Convergence refers to the convergence of the solution of the numerical scheme towards the real solution of the PDE when the discrete step (in space and time) tends to zero.

An important result of numerical analysis is that the error of a discretization may be bounded in terms of its consistency and stability.

In continuum mechanics, the equations that describe the kinetic and mechanical behavior of a general body are often called the conservation laws. These laws can be formed in weak or strong forms, corresponding to the integral and partial differential equations of mass, momentum and energy conservation. Restricting ourselves on the analysis of the conservation law that describes the transport of a quantity $u(x,t)$ over space and time in one dimension, we can write a general form of the convection-diffusion-reaction equation as :

$$\frac{\partial u}{\partial t} + \frac{\partial}{\partial x}(au - b\frac{\partial u}{\partial x}) - cu = S \tag{1.50}$$

, where the coefficients a, b and c will define the nature of the equation. If these coefficients depend on the solution u, then the equation is non-linear, while if they depend only on x and t it is linear. By posing $a = S = 0$ in steady state, we obtain an equation that depends only on x : This equation is elliptic and by defining appropriate boundary conditions on the boundaries of the domain (Neumman's or Dirichlet's for example), the integration coefficients can be obtained and the equation can be solved numerically in the computational domain. Let's take for example Laplace's equation, which is of elliptic type:

$$\nabla^2 u = 0 \tag{1.51}$$

where u is a quantity that is part of a flow, here the potential. Setting $a = c = S = 0$ in equation 1.50, we obtain the second family of partial differential equations : The parabolic type. To solve such type of equations we need in addition of the boundary conditions an initial condition for time $t = 0$. The most common example of such equations is the diffusion (or heat) equation which reads in one dimension:

$$\frac{\partial u}{\partial t} = b\frac{\partial u^2}{\partial x^2} \tag{1.52}$$

Finally the third family of equations is obtained by setting $b = c = S = 0$: These equations are hyperbolic. The solution of this family of equations also demands an initial condition as well as boundary conditions, which though can not be prescribed as their necessity depend on the coefficient a and its sign. The wave equation is of hyperbolic type:

$$\frac{\partial u^2}{\partial t^2} = a\frac{\partial u^2}{\partial x^2} \tag{1.53}$$

More details can be found in [123].

The name of each family of equations derives from the conical area that can be defined by the analytical geometry that these equations describe. In two dimensions the general equation for a cone is:

$$ax^2 + bxy + cy^2 + dx + ey + f = 0 \tag{1.54}$$

where if $b^2 - 4ac > 0$, the conical surface is a hyperbola, if $b^2 - 4ac < 0$ is a parabola and if $b^2 - 4ac = 0$ it is an ellipse.

A more generalized way to categorize the families of partial differential equations is by the eigenvalues method. Considering a general system of equations (that are similar to the conservation laws of interest) similar to 1.50 , with $S = 0$ for simplification as :

$$\begin{aligned} a_1\frac{\partial u}{\partial x} + b_1\frac{\partial u}{\partial y} + c_1\frac{\partial v}{\partial x} + d_1\frac{\partial v}{\partial y} = 0 \\ a_2\frac{\partial u}{\partial x} + b_2\frac{\partial u}{\partial y} + c_2\frac{\partial v}{\partial x} + d_2\frac{\partial v}{\partial y} = 0 \end{aligned} \tag{1.55}$$

with u(x,y), v(x,y) continuous functions in the space of x,y and their derivatives too. All the above coefficients are functions of x, y, u and v. Writing the above system in matrix form for the vector $W = [u, v]^{-1}$, we have:

$$\begin{bmatrix} a_1 & c_1 \\ a_2 & c_2 \end{bmatrix} \frac{\partial W}{\partial x} + \begin{bmatrix} b_1 & d_1 \\ b_2 & d_2 \end{bmatrix} \frac{\partial W}{\partial y} = 0 \tag{1.56}$$

After some mathematical manipulations, and defining the 2x2 matrices as [K] and [M] respectively, we obtain:

$$\frac{\partial W}{\partial x} + [K]^{-1}[M]\frac{\partial W}{\partial y} = 0 \tag{1.57}$$

The eigenvalues of the matrix $[N] = [K]^{-1}[M]$, will define the nature of the equation. If its eigenvalues are real, the equations are hyperbolic. If the eigenvalues are imaginary, the equations are elliptic and if they are zero, the equations are parabolic.

The nature of the equation of interest, is important as they determine the necessary approach of numerical solution. As we have seen, different boundary and initial conditions have to be determined for each family. The importance of of boundary and initial conditions, are essential for the computational analysis and solution of partial differential equations. A real and correct solution can be possible only if these conditions are well determined, so that the problem is well-posed. If the solution of a problem changes in a small amount, due to small changes of the problem's data, we have a well-conditioned problem.

The equations of conservation, together with the boundary (or/and initial) conditions form boundary or initial value problems of partial differential equations, that can be solved by different numerical methods and algorithms. In this thesis we will be focusing on methods : The Finite Difference Method (FDM) and the Finite Volume Method (FVM).

In the FDM, a computational grid has to be created, in such a way that the derivative of a function can be approximated by finite differences. A computational grid has to be defined, so that the discretized equations of interest can assign the variables on each grid point of the computational domain. A one-dimensional computational grid is shown in figure 1.71.

Then a value of a function at a local point can be can be related to a value of a neighbour point and written as a Taylor series expansion as:

$$f(x+\Delta x) = f(x) + \frac{\partial f}{\partial x}\Delta x + \frac{\partial f^2}{\partial x^2}\frac{(\Delta x)^2}{2} + ... + \frac{\partial f^n}{\partial x^n}\frac{(\Delta x)^n}{n!} + ... \tag{1.58}$$

where Δx is the distance between the two points and $f(x)$ is the assumed know value of the function.

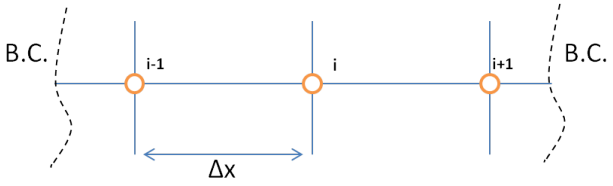

Figure 1.71: A one-dimensional computational grid.

The more neighbour points we use for approximating a derivative, the less the truncation error will be. Different accuracy finite differences expressions can easily be obtained for any derivative form and order. The choice of a forward, central or backward scheme has to do with mesh refinement and accuracy requirements as well as boundary conditions.

When we are dealing with the equations of conservation, time partial derivatives exist too (if we not consider the stationary solution of a given problem). Then a discretization in time has to be also considered. In explicit temporal schemes, the value of the function u at time $n+1$ depends only on spatial values of the function at the previous - known time n. The problem with such a scheme is that it is only conditionally stable. Briefly, this statement means that errors can grow over time, leading to an unrealistic or a diverged solution. The analysis of a scheme's stability can be performed via a decomposition of the errors into Fourier series, the so-called Von Neumann stability analysis [124]. Although this method normally has a restricted applicability on a small range of linear, constant coefficient finite differences schemes on regular grids, it is a useful method to understand concepts of stability for such schemes.

The Courant–Friedrichs–Lewy (CFL) condition for stability derived in [125], provides a different approach for the stability analysis of partial differential equations.

The need of restrictions on the time and space steps used for explicit methods, led scientists to the creation of implicit schemes. Implicit schemes can be easily obtained if a different temporal finite difference approach is adopted. For example a backward-Euler scheme leads to equations that involve both the current state of the system and the later one. This scheme has be proven to be unconditionally stable (A-Stable), but it requires the use of direct or iterative algorithms to solve the system of linear or not equations that form. Implicit schemes are for example the Crank-Nicolson[126] and the Alternative-Direction-Implicit (ADI)[127]. For parabolic type equations, the matrix form of the system that forms in the computational domain with the ADI (for example) scheme and a three-point stencil, leads to tridiagonal structure of the iterative matrix that can be efficiently solved by the Thomas algorithm. Equations of elliptic type, lead to a system of equations that also has to be solved via direct or iterative algorithms of linear algebra but they do not give tridiagonal iterative matrices. Common algorithms for such type of equations are often iterative and include the Jacobi, Gauss-Seidel and successive over relaxation (SOR) algorithms. Conjugate or biconjugate gradient methods as well as GMRES (generalized minimal residual) ones are also very popular for such linear systems. Equations of hyperbolic type, as for example the advection or wave equations, have to be solved taking into account the advection velocity and possible discontinuities (shock waves in compressible supersonic flows for example) in the field's solution. Several schemes, explicit and implicit, have been developed to deal with such equations, as for example the explicit Lax-Wendroff or Leap-Frog schemes and the Euler and MacCormack implicit scheme which falls in the category of predictor-corrector schemes [123].

The Finite Difference Method has to be adapted for each family of partial differential equations. A method

that is global and successfully transits for each family problem has been in the research for many years. The finite volumes method (FVM) provides such superior behavior. This method is essentially an integration of the equations of interest in a control volume CV (a finite volume). Values are calculated again at discrete places on a meshed geometry. Considering a central method where the values of interest are placed in the center of each volume-cell, the finite volume is surrounding each node (point) of the mesh as shown in figure 1.72, in one dimension. The central point here, corresponds to the subscript i and the CV's boundaries to the points $i+1/2$ and $i-1/2$. Commonly a different compass notation [128] is used as seen in the bottom figure of figure 1.72. The central point is denoted with the letter P, and the nodal points on the faces of the control volume with the letters e and w corresponding to east and west nodes. Then the central points of the neighbor cells-CVs are denoted with the capital letters E and W, again corresponding to east and west cells. In this method, volume integrals of a partial differential equation are converted to surface integrals using the divergence (Gauss) theorem. This conversion, does not concern source terms of course that are related to a quantity inside the control volume but to divergence terms (as diffusion) that are developed in its boundaries. These surface integral terms can then be evaluated as fluxes on each finite volume, assuring that the flux entering the volume equals the flux exiting it: The FVM method is thus conservative.

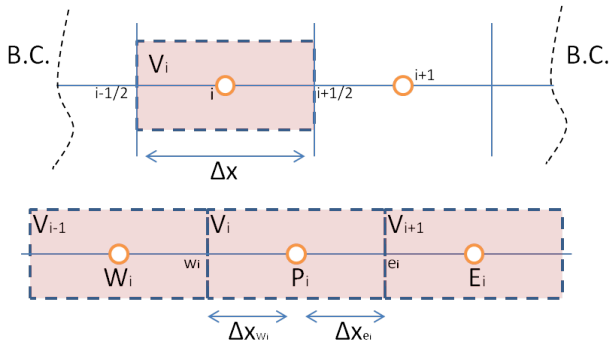

Figure 1.72: A central finite volume discretization of an one dimensional problem.

Once again, the discretization of the whole computational domain, leads to a system of linear equations of the form:

$$AU = c \tag{1.59}$$

, where the properties of the matrix A are important for the successful solution of the system with a numerical analysis algorithm. Two and three dimensional problems often result to non-diagonal dominated matrix (while in the one dimensional case the matrix is tridiagonal), and iterative algorithms have to be implemented as direct ones become inefficient. Numerical stability issues arise though with iterative solvers when the diagonal dominance of the matrix A is weak. For stability such algorithms require such dominance.

Deferred correction methods, can be beneficial on the diagonal dominance of a matrix, leading to improved convergence-stability [129]. In general, Finite Volume Methods in order to provide solutions that behave "good" and are stable and accurate, need to obey some basic characteristics. Noting the most important, as we have seen they need to be stable, obeying for iterative schemes the diagonal dominance of matrix A. In addition, it has been demonstrated that the coefficients of the matrix, need to have the same sign in order to achieve convergence. Secondly, they need to be conservative, so the flux that enters a control volume shall

equal the flux that exits, and the expression for the flux calculation need to be the same for all the volumes of the computational domain. Thirdly, the transportability and locality properties has to be fulfilled. That means, that information is transported within the characteristics and only adjacent cells affect the forecast at a given point.

Central schemes, do not take into account the direction of the transport and so the transportability is not satisfied. To overcome such problems of central schemes, a big variety of different higher or lower order schemes have been developed : The first-order upwind scheme [130], where the transported quantity flux sign is taken into account.

As a first-order scheme, its accuracy is not high and moreover it introduces numerical diffusion to the solution for multidimensional problems. The hybrid scheme [131], changes from the central to the first order upwind scheme depending on the Peclet number, Pe, (the ratio of the rate of advection of a physical quantity by the flow to the rate of diffusion of the same quantity driven by an appropriate gradient), thus providing second order accuracy for small Pe and stability for larger Pe. Its overall accuracy though is still of first order for multidimensional problems, exhibiting numerical diffusion unless the Peclet number is low. The exponential [132] and power [133] schemes are based on analytical expressions for a one-dimensional transport problems, and it provides improved accuracy compared to the hybrid scheme but again it suffers from numerical diffusion for multidimensional problems. Higher order schemes, as the second order upwind one [134], can provide more accurate solutions and when implemented as deferred correction methods and with the addition of flux-limiter methods [135] they give accurate, stable and non-oscillatory solutions. One of the most common higher order methods, is the third order upwind scheme (or QUICK). QUICK (Quadratic Upstream Interpolation for Convective Kinetics) [136], uses a second order interpolation method with three points for the calculation of a variable on the faces of the control volume, while the calculation of a variable at a computation cell is performed with a second order function that connects the computation cell and the upstream neighbor's cell. A summary of different differencing methods can be found in [137].

Both in the Finite Volumes and in the Finite Differences methods, boundary conditions have to be applied in order to truncate the computational domain and define the solution obtained. Dirichlet, Neumann or other boundary conditions can be implemented easily, assuming a boundary ghost cell outside of the computational domain and appropriate expressions for the discretized equations at the boundary cells.

For the time discretization, similar schemes as the ones described for the Finite Differences method, can be obtained, in an explicit or implicit way. Depending on the time of evaluation for the temporal integrals, Forward Euler, Backward Euler and Crank Nicolson schemes are commonly used in finite volumes methods. In a compact matrix form, the system of equation that is produced can be written as:

$$AU^{n+1} = c - BU^n \tag{1.60}$$

Again, depending on the form of the matrix A and thus the temporal discretization scheme used, stability criteria have to be fulfilled. Implicit schemes are unconditionally stable while explicit ones require time and space steps constraints for stability.

The form of the matrix A, will dictate the use of the numerical algorithm for solving the system of equations like in the case of the FDM. Tridiagonal matrices can be efficiently solved by the Thomas algorithm while linear solvers can be used in a direct or iterative way for inverting more complicated forms of the A matrix.

1.4.1 A Multi-scales Multi-Physics Problem

Describing numerically a problem such as the aerodynamic flow control based on plasma actuators, is a good example of a complex system with highly coupled physics that need to be accurately and simultaneously time-efficiently resolved. For microwave discharges for example, the plasma creation and evolution-interaction due to and with the microwave electromagnetic field has to be coupled with the exchange of physical information between the plasma itself and the macroscopic behavior of the gas. Briefly, the strong coupling between these 3 "physical regimes" can be described as follows: The EM waves transfer energy to the electrons which ionize the gas, producing an avalanche of electrons in the form of a plasma. The plasma itself interacts constantly with the EM waves, absorbing or reflecting energy and thus modifying the initial EM field. As the plasma is strongly coupled to the gas pressure and density, it modifies the initial gas' state which in return affects the plasma evolution. One can distinguish several time and space scales in this system, that can be largely different. The EM waves include time and space scales connected to the waves frequency and their wave-length. The plasma itself is being governed by the electron frequency and the Debye length. Finally the aerodynamics of the gas, require discretization in time and space linked to the external velocity of the flow and its characteristic length, not mentioning that for accurate CFD simulations of turbulent flows these scales reduce to those that can resolve the turbulent length-time scales, that most of the times are even more restraining.

To have a better idea of the multi-scale problem, we will give some typical length and time scales for each plasma type and actuator. For microwave discharges, the mean free path under atmospheric pressure is micrometric as well as the plasma front characteristic length (which scales as $\sqrt{D/\nu_i}$ and obviously depends on the reduced field), while the wavelength milimetric. The system's characteristic length can be several wavelengths too. Time scales also can be orders of magnitude different - the EM waves angular frequency is in the order of 10^{12} rad/s, the plasma one depending on its density in the order of $10^{10} - 10^{12}$ rad/s while the ionization frequency in the order of $10^{8} - 10^{9}$ rad/s. The DBD actuator has system characteristic lengths in the order of some centimeters, while the Debye length is micrometric. The ionization frequency is in the order of $10^{11} - 10^{12}$ Hz, while the AC frequency in the order of $10^{3} - 10^{4}$ Hz. The PSJ actuator's length scales are mostly related to the geometry of the cavity and the orifice (in the milimeter range) while turbulent structures related to eddy formation can be quite smaller. The time scales are also various, as for example the electric circuit characteristic time is in the order of in the order of $10^{-5} - 10^{-6}$ s and the actuator's period in the order of $10^{-2} - 10^{-3}$ s. Besides, time and length scales related to gas dynamics as thermal diffusion/energy conversion and shock wave formation and propagation are important for microwave energy deposition and of course the PSJ actuator.

This is why we are talking about a multi-scales multi-physics problem that eventually needs a lot of simplifying assumptions in order to obtain coupled numerical models that succeed in describing this system's behavior in acceptable cost (in CPU resources and time).

Plasma Models

As described before, the particles transport dynamics can be represented in a microscopic or a macroscopic level. In both approaches, collisional effects are described by cross sections, transport and rate coefficients taken from measurements or quantum-mechanical collision calculations. In the first approach, the most common method to proceed for the numerical solution of the plasma dynamics is the particle (Monte-Carlo) method.Particle models are more usual at low gas density. These models describe the trajectories of individual plasma particles interacting with surrounding materials and other particles. Instead of describing the whole physical particle population as individual particles, a random sampling of these particles can be obtained, called macro-particles. The total population of each species can be approximated by averaging over a large

number of macro-particles, giving macroscopic quantities and distribution functions. The trajectory of a macro-particle is calculated by integration of Newton's equations.
When the Maxwell's equations are solved to obtain the electromagnetic fields, statistically relevant space charge densities and currents have to be calculated so a large number of particles must be followed simultaneously. This method is called Particle-In-Cell method (PIC) [138, 139]. In such a technique, Monte-Carlo collision methods are used to determine the effects of collisions (elastic and Coulomb collisions most often), via random sampling from probability distributions. The probability of collision per unit time is given by the collision frequency that depends on the target's particles density, its cross section and the relative speed of the macro particle to the target one. The most common way to integrate numerically equations like the Newton's ones, is by a leap-frog method that gives a central-difference approximation in time of the particle mover solver. The sampling of particles is performed via statistical numerical techniques on probabilities distribution functions, in order to obtain the random positions and velocity vectors of particles groups (in the case of PIC). A null collision method [140] is often used for the collisional effects, where the maximum collision probability for each charged species is used. The self-consistent electromagnetic fields as well as particles densities are computed on a fixed mesh by a field solver. As particles can be situated anywhere on the continuous domain, weighting functions are used to assign macro-quantities at the grid's points. The fields need also to be weighted-interpolated, so that the forces acting on the randomly positioned particles can be calculated in the particle-mover.

For high gas density and collisional plasmas the most common modeling approach is the macroscopic one and the consequent plasma-fluid models. In general the statistical fluctuations of the number of particles in a plasma can be neglected as this number is often too high. As seen before, the plasma can then be described as a continuum by a distribution function, whose evolution is described by the Boltzmann equation 1.15. This kinetic description of plasmas is complicated and computationally expensive to obtain, and thus based on different approximations, various models can be formed to solve the Boltzmann equation, as the two-term approximation based on a nonlocal or homogeneous approach. The charges and currents produced by the distribution functions self-consistently determine the electromagnetic fields via Maxwell's or Poisson's equations.

The electrodynamic fields in non-static electromagnetic fields are described as seen by the Maxwell's equations. The Poisson equation can be solved for the electrostatic applied field and the ambipolar field. The coupling between the fields and the plasma equations are based on a self-consistent description of the fields. Finite differences or Finite Volumes methods can be used to solve the discretized equations in conservative or not form for the plasma equations as well as the Maxwell's ones. The Maxwell's equations can be formulated as an hyperbolic system of partial differential equations (PDEs) and thus enabling their efficient numerical solution. More on other methods and numerical schemes used for plasma models will be presented in the following chapters. Note that hybrid fluid/kinetic models have been also developed. Such models provide increased accuracy compared to a fluid model with lower computational cost compared to a kinetic model.

In this thesis, we are using the fluid approximation for modeling the plasma dynamics. We are dealing with cold plasmas and depending on the actuator of interest and the different length scales associated to the each kind of plasma, different hypothesis need to be made. In figure 1.73, the different models are being summarized along with the main corresponding approximations. Each of these models along with the corresponding approximations will be presented in detail, in the following chapters.

For microwave discharges (MWD), the highly collisional plasma leads to very small Debye lengths with respect to the plasma size and thus quasi-neutrality. The electron temperature is orders of magnitude higher than the gas one that stays in ambient conditions (at least in early times). The local effective field

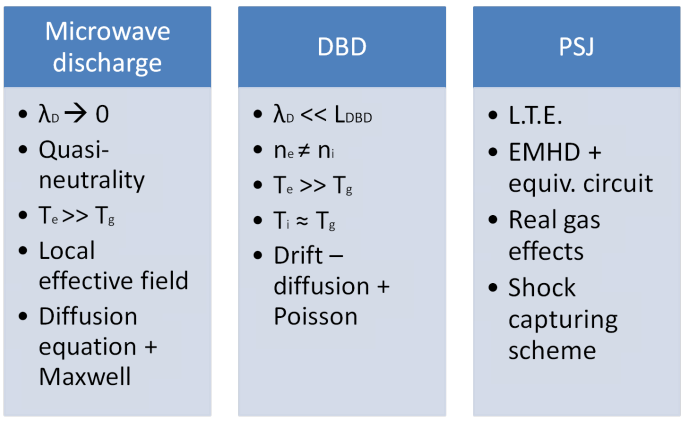

Figure 1.73: Plasma hypothesis and models used for each type of actuator.

approximation can be used to determine the plasma transport coefficients instead of an energy equation for the electrons, as we assume that the electrons mean free path is smaller than the characteristic length of the EM waves . A simplified diffusion equation for the electrons only can be used as the ions produce negligible current and needs to be coupled with the Maxwell equations via a momentum transfer equation. For the DBD actuator, we use a drift-diffusion model coupled with Poisson's equation. The quasi-neutrality is not valid here, especially in the regions where the body force is produced. Electrons present temperatures much higher than the gas molecules temperature which remains equals to the ambient one as is the case for the ions too. For the plasma synthetic jet, the arc plasma is described by a Local Thermodynamic Equilibrium (LTE) assumption that allows to make no distinction between the heavy particles and electrons behavior and take into account a unique temperature to represent the thermal behavior of all species as a global single fluid. The ElectroMagnetoHydroDynamical (EMHD) system of equations is used to describe the fluid's behavior coupled with an equivalent electric circuit of the power supply. Real gas laws are incorporated in the Euler equations of the EMHD system to deal with the high temperatures reached in such a plasma and a shock capturing numerical scheme is used.

Computational Fluid Dynamics (CFD) and turbulence modeling

The partial differential equations of fluid dynamics are the Navier-Stokes equations 1.3 described in section 1.1.1. For subsonic flows, ($M < 0.9$) these equations are of elliptic type in space and parabolic in time. The elliptic nature in space, points out the fact that a disturbance in a point of the field, can cause influence upstream or downstream of the point (a recirculation area for example), and iterative numerical methods are applied. Depending on the flow regime, different models can be obtained. For example for high Reynolds flows, the inviscid approximation can be valid (except inside boundary layers and highly turbulent regions) and the N-S equations become the Euler equations where the viscous terms are neglected (ideal fluid approximation). Compressibility effects are only crucial for Mach numbers above approximately 0.3 or when intense heating occurs, so the incompressible N-S equations can be used for the rest of the cases. Equations that describe supersonic compressible inviscid flows ($M > 1$) are of hyperbolic type, so the insertion of a disturbance in the field will affect the downstream flow in a region limited by the characteristics of the differential equation. Such disturbances can be in a form of shock waves.

The most common numerical method for solving the Navier-Stokes equations is the Finite Volume method. The need of highly refined computational zones (as the boundary layer or shock wave regions), non-cartesian grids for modeling complex or curved geometries (such as an airfoil) as well as methods that are adaptable at different flow regimes (i.e. different type family of the conservation equations) has led in the development of the Finite Volume method especially for fluid dynamics problems.

It is important in this point to describe maybe the main problematic of CFD problems that lies in the chaotic and stochastic nature of turbulence. As seen before, the length and time scales involved in turbulent flows can vary in a great extend. The resolution of all these scales through a numerical method is many times prohibited as it becomes extremely expensive in terms of computational time and resources.

To understand better this fact, we start by considering the Direct Numerical Simulation approach, where the Navier Stokes equations are solver without any turbulence model and so all the scales are resolved. This means that the space step of the discretized grid has to be in the order of the Kologorov scale $\eta = (\nu^3/\varepsilon)^{1/4}$, where L is the integral length scale of the main flow and $\varepsilon \approx U^3/L$, with U being the root mean square of the flow's velocity .

Noting as h the space step, and defining the turbulent Reynolds number as $Re_t = UL/\nu$ we need for a three dimensional DNS simulation :

$$\begin{aligned} h &\approx \eta \\ N^3 &= Re^{9/4} \end{aligned} \tag{1.61}$$

where N is the number of grid points required. An explicit scheme for the temporal integration has to be used as the memory usage is huge that means that the Courant stability criteria has to be satisfied : $C = U\Delta t/h < 1$ that gives :

$$n \sim Re^{3/4} \tag{1.62}$$

where n is the number of time steps needed. We can easily understand that even for low Reynolds numbers the computational cost of a DNS simulation is enormous.

Different approaches have been developed for modeling turbulent flows, depending on the resolution or not of such scales. Large eddy simulations (LES) apply a low pass filtering technique based on flow and turbulent properties to "kill" the smallest scale structures of the flow. Then larger structures are totally resolved while smaller ones are modeled.

The most common approach for modeling turbulent flows is the Reynolds-averaged Navier–Stokes equations (RANS equations or URANS in their unsteady formulation). They describe a time-averaged N-S set of equations.

In the RANS approach, a turbulent flow is being decomposed into mean and fluctuating parts of the velocity and pressure fields: $U(t) = U + u'(t)$, where here U describes the RMS value of the velocity and u' the unsteady fluctuating part (similar for the other components and pressure). The instantaneous governing equations (N-S) can then be time averaged or otherwise manipulated to remove the resolution of small scales resulting in a modified set of equations that are computationally less expensive to solve. However the modified equations contain additional unknown variables and turbulence models are needed to determine these variables

in terms of known quantities. By this time-averaging procedure and after some statistical manipulations [141], we obtain the so called Reynolds equations for a turbulent flow that read for the continuity and momentum conservation law in Einstein's notation:

$$\begin{aligned} &\frac{\partial \overline{U_i}}{\partial x_i} = 0 \\ &\rho[\frac{\partial \overline{U_i}}{\partial t} + \overline{U_j}\frac{\partial \overline{U_i}}{\partial x_j}] = \rho\overline{F} - \frac{\partial \overline{p}}{\partial x_j} + \frac{\partial}{\partial x_j}(\mu\frac{\partial \overline{U_i}}{\partial x_j} - \rho\overline{u_i' u_j'}) \end{aligned} \tag{1.63}$$

where we have assumed incompressible flow.

These equations contain an additional stress tensor , the Reynolds Stresses that writes for its components:

$$\tau_{ij}' = \rho\overline{u_i' u_j'} \tag{1.64}$$

In turbulent flow, the Reynolds stresses are usually large compared to the viscous stresses. The normal stresses τ_{ii}' and τ_{jj}' are always non-zero because they contain squared velocity fluctuations. The shear stresses (corresponding to the mixed components of equation 1.64) would be zero if the fluctuations were statistically independent. However, they are correlated (because of continuity amongst other reasons) and the shear stresses are therefore usually also non-zero.The time averaged equations now contain six additional unknowns in the momentum equations. The main task of turbulence modeling as we said is to develop computational procedures of sufficient accuracy and generality for engineers to be able to accurately predict the Reynolds stresses and the scalar transport terms. This will then allow for the computation of the time averaged flow and scalar fields without having to calculate the actual flow fields over long time periods.

In order to define the Reynolds stresses in terms of known (averaged) quantities, several methods have been introduced over the years :

— Linear eddy viscosity models based on the Boussinesq hypothesis, which provides a simple relationship between Reynolds stresses and velocity gradients through the eddy viscosity (similar to molecular viscosity). It assumes isotropic turbulent viscosity.
— Reynolds stress transport models, where equations derived directly manipulating the NS equations. Such models are very complicated and expensive to solve.
— Non-linear Eddy viscosity models.

Details about the most important eddy-viscosity models models can be found in [142]. We are emphasizing in the three following two-equation turbulent models, that have been used in this thesis :

— The k-ε model
— The k-ω model
— The SST transitional mode.

The k-ε model is one of the most common turbulence models. It is a two equation model, that means, it includes two extra transport equations to represent the turbulent properties of the flow: The turbulent kinetic energy k, and the turbulent dissipation rate ω. This allows a two equation model to account for history effects like convection and diffusion of turbulent energy. The k-ε model is a simple and computationally afordable model that has given accurate results for a variaty of flows and has been validated with different flow configurations. Although it requires near wall treatment, it is diffusive and needs calibration of its coefficients for different flows or regimes.

A major breakthrough in turbulence models for CFD applications is due to Menter [143]; he blended two existing models, the k-ε and the k-ω in order to overcome the shortcomings of both. The original k-ω model developed by Wilcox[144] presents strong advantages:

— It is the reference model in the viscous sublayer of the boundary layer; it is very simple, stable and does not involve any damping function because it is possible to impose non slip boundary conditions at the non slip surfaces (the walls).
— It predicts correctly the skin friction and the velocity profile approaching the wall.
— It behaves better than the k-ε model in the logarithmic region of the boundary layer especially in adverse pressure gradient conditions and in compressible flows.

These two models have been incorporated in Menter's baseline model using a blending function that allows switching between the k-ω model in the sub and log layer and the k-ε model in the outer region of the boundary layer and in free shear flows. The successive step was to modify the baseline model to take into account the convection of the principal turbulent shear stresses. The reason for this choice lays in the fact that the RSM model performs better than the eddy viscosity models because, as previously said, it solves a transport equation for the turbulent shear stresses. The SST (Shear Stress Transport) model does not calculate a convection equation for the shear stresses because it is actually convecting k and ω but accounts for their transport effect by means of the so-called Bradshaw's assumption: this hypothesis states that the turbulent shear stress in the log and outer regions of the boundary layer is proportional to the turbulent kinetic energy. Bradshaw's assumption cease to hold in free shear layers, where the original formulation of the turbulent viscosity is restored.

Finally, the SST – transitional model [145], is based on the coupling of the SST k-w transport equations with two other transport equations one for the intemittency and one for the transition onset criteria, in terms of momentum-thickness Reynolds number. The intermittency factor is a measure of the probability that a given point is located inside a turbulent region. Upstream of transition the intermittency is zero. Once the transition occurs, the intermittency is ramped up to one until the fully turbulent boundary layer regime is achieved.

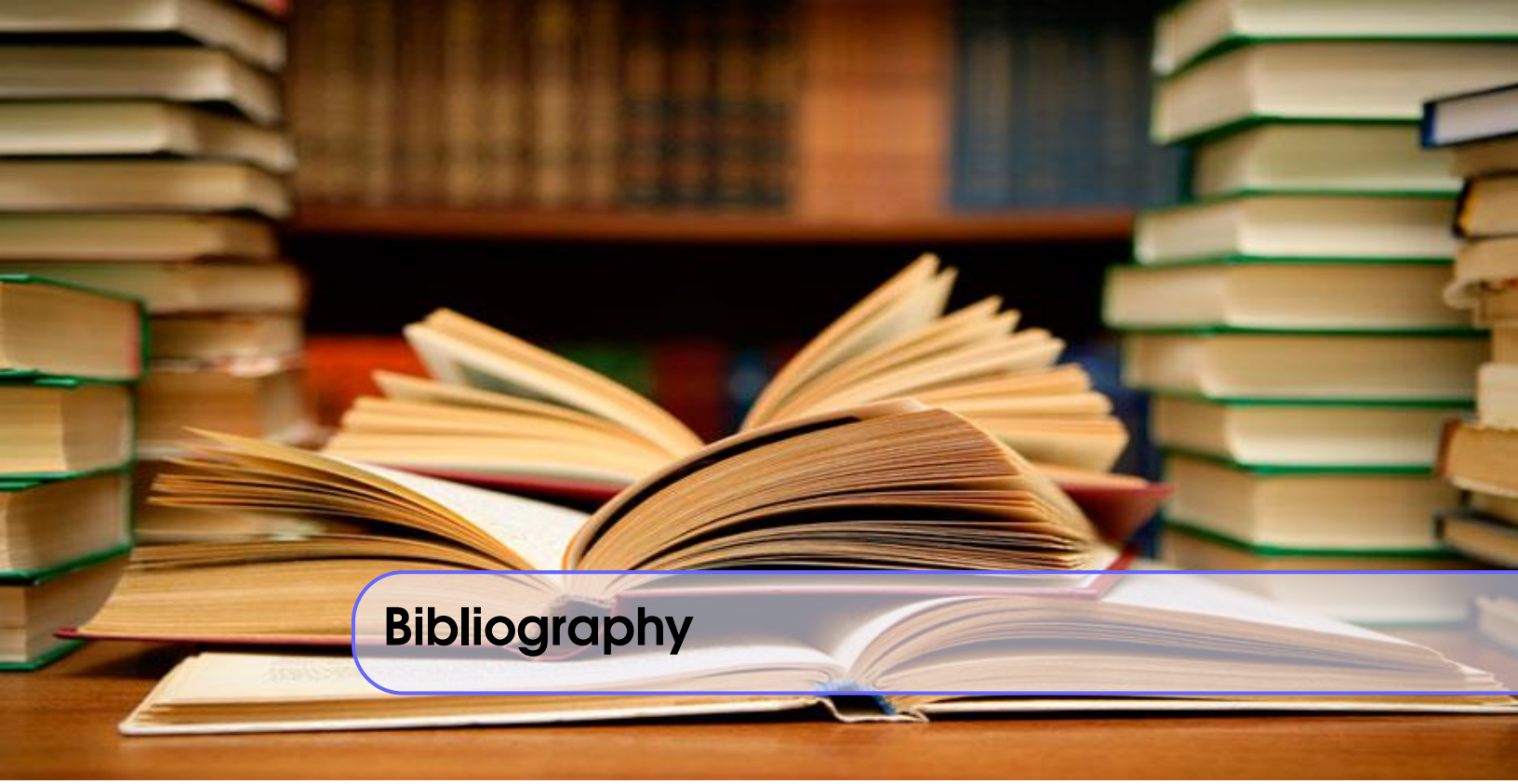

Bibliography

[1] James Luneau and Allan Bonnet. *Aérodynamique: théories de la dynamique des fluides*. Cépaduès-éd., 1989.

[2] Mohamed Gad-el Hak. "Modern developments in flow control". In: *Applied Mechanics Reviews* 49.7 (1996), pages 365–379.

[3] Mohamad Gad-el Hak. "Flow control". In: *Applied mechanics reviews* 42.10 (1989), pages 261–293.

[4] Gwibo Byun, Roger L Simpson, and CH Long. "Study of vortical separation from three-dimensional symmetric bumps". In: *AIAA journal* 42.4 (2004), pages 754–765.

[5] Prahladh S Iyer, Suman Muppidi, and Krishnan Mahesh. "Transition of hypersonic flow past flat plate with roughness elements". In: *AIAA paper* 5015 (2010), page 2010.

[6] Paul M Danehy et al. "NO PLIF study of hypersonic transition over a discrete hemispherical roughness element". In: *AIAA* 394 (2009), pages 5–8.

[7] John C Lin. "Review of research on low-profile vortex generators to control boundary-layer separation". In: *Progress in Aerospace Sciences* 38.4 (2002), pages 389–420.

[8] John C Lin et al. "Separation control on high-lift airfoils via micro-vortex generators". In: *Journal of aircraft* 31.6 (1994), pages 1317–1323.

[9] DC McCormick. "Shock/boundary-layer interaction control with vortex generators and passive cavity". In: *AIAA journal* 31.1 (1993), pages 91–96.

[10] Reynald Bur, Didier Coponet, and Yves Carpels. "Separation control by vortex generator devices in a transonic channel flow". In: *Shock Waves* 19.6 (2009), pages 521–530.

[11] DM Bushnell. "Aircraft drag reduction—a review". In: *Proceedings of the Institution of Mechanical Engineers, Part G: Journal of Aerospace Engineering* 217.1 (2003), pages 1–18.

[12] MJ Walsh and AM Lindemann. *Optimization and application of riblets for turbulent drag reduction*. American Institute of Aeronautics and Astronautics, 1984.

[13] Ricardo García-Mayoral and Javier Jiménez. "Drag reduction by riblets". In: *Philosophical Transactions of the Royal Society A: Mathematical, Physical and Engineering Sciences* 369.1940 (2011), pages 1412–1427.

[14] Gregory A Reynolds and WS Saric. "Experiments on the stability of the flat-plate boundary layer with suction". In: *AIAA journal* 24.2 (1986), pages 202–207.

[15] Brian N Nield. "An overview of the Boeing 777 high lift aerodynamic design". In: *Aeronautical Journal* 99.989 (1995), pages 361–371.

[16] A Seifert et al. "Oscillatory blowing: a tool to delay boundary-layer separation". In: *AIAA journal* 31.11 (1993), pages 2052–2060.

[17] Avi Seifert and LG Pack. "Separation Control at Flight Reynolds Numbers: Lessons Learned and Future Directions". In: *AIAA paper* 2542 (2000), page 2000.

[18] Jacob Wilson et al. "Suction and pulsed-blowing flow control applied to an axisymmetric body". In: *AIAA journal* 51.10 (2013), pages 2432–2446.

[19] Barton L Smith and Ari Glezer. "The formation and evolution of synthetic jets". In: *Physics of Fluids (1994-present)* 10.9 (1998), pages 2281–2297.

[20] Michael Amitay, Barton L Smith, and Ari Glezer. "Aerodynamic flow control using synthetic jet technology". In: *AIAA paper* 208 (1998), page 1998.

[21] P Margaris and I Gursul. "Wing tip vortex control using synthetic jets". In: *Aeronautical Journal* 110.1112 (2006), pages 673–681.

[22] Barton L Smith and Ari Glezer. "Vectoring and small-scale motions effected in free shear flows using synthetic jet actuators". In: *AIAA paper* 213 (1997), page 1997.

[23] Douglas R Smith et al. "Modification of lifting body aerodynamics using synthetic jet actuators". In: *AIAA paper* 209 (1998), page 1998.

[24] Louis N Cattafesta, Sanjay Garg, and Deepak Shukla. "Development of piezoelectric actuators for active flow control". In: *AIAA journal* 39.8 (2001), pages 1562–1568.

[25] A Seifert et al. "Use of piezoelectric actuators for airfoil separation control". In: *AIAA journal* 36.8 (1998), pages 1535–1537.

[26] T Weier and G Gerbeth. "Control of separated flows by time periodic Lorentz forces". In: *European Journal of Mechanics-B/Fluids* 23.6 (2004), pages 835–849.

[27] Timothy W Berger et al. "Turbulent boundary layer control utilizing the Lorentz force". In: *Physics of Fluids (1994-present)* 12.3 (2000), pages 631–649.

[28] T Weier et al. "Boundary layer control by means of wall parallel Lorentz forces". In: *Magnetohydrodynamics* 37.1/2 (2001), pages 177–186.

[29] Lester Lees. "The Stability of the Laminar Boundary Layer". In: (1947).

[30] YS Kachanov, VV Koslov, and V Ya Levchenko. "Experimental Study of the Influence of Cooling on the Stability of Laminar Boundary Layers". In: *Izvestia Sibirskogo Otdielenia Ak. Nauk SSSR, Seria Technicheskikh Nauk, Novosibirsk* 8-2 (1974), pages 75–79.

[31] Hong Yan and Datta Gaitonde. "Effect of thermally induced perturbation in supersonic boundary layers". In: *Physics of Fluids (1994-present)* 22.6 (2010), page 064101.

[32] Hong Yan, Datta Gaitonde, and Joseph Shang. "The effect of a thermal bump in supersonic flow". In: *AIAA Paper* 1096 (2008), page 2008.

[33] Hong Yan. “Thermal Perturbations in Supersonic Transition”. In: *Low Reynolds Number Aerodynamics and Transition* ISBN: 978-953-51-0492-6 ().

[34] Jonathan Poggie. “Control of Shock-Wave/Boundary-Layer Interaction Using Volumetric Energy Deposition”. In: *AIAA 2008 - 1090* (2008).

[35] D Caruana. “Plasmas for aerodynamic control”. In: *Plasma Physics and Controlled Fusion* 52.12 (2010), page 124045.

[36] Kirill V Khodataev. “Microwave Discharges and Possible Applications in Aerospace Technologies”. In: *Journal of Propulsion and Power* 24.5 (2008), pages 962–972.

[37] LP Grachev et al. “Development stages of an electrodeless microwave discharge”. In: *Journal of Technical Physics* 41 (1996), pages 652–659.

[38] Daniel Bivolaru and SP Kuo. “Observation of supersonic shock wave mitigation by a plasma aerospike”. In: *Physics of Plasmas (1994-present)* 9.2 (2002), pages 721–723.

[39] Richard B Miles. “Flow control by energy addition into high-speed air”. In: *Proceedings of the AIAA Fluids Conference*. 2000.

[40] I G Girgis et al. “Steering moments creation in supersonic flow by off-axis plasma heat addition”. In: *Journal of spacecraft and rockets* 43.3 (2006), pages 607–613.

[41] Russell G Adelgren et al. “Control of Edney IV interaction by pulsed laser energy deposition”. In: *AIAA journal* 43.2 (2005), pages 256–269.

[42] Y-L Chen, JWL Lewis, and C Parigger. “Spatial and temporal profiles of pulsed laser-induced air plasma emissions”. In: *Journal of Quantitative Spectroscopy and Radiative Transfer* 67.2 (2000), pages 91–103.

[43] Doyle D Knight. “Survey of aerodynamic drag reduction at high speed by energy deposition”. In: *Journal of Propulsion and Power* 24.6 (2008), pages 1153–1167.

[44] Guillaume Dufour, Bruno Fornet, and François Rogier. “Numerical modelling of supersonic flow actuated by laser-induced plasma”. In: *International Journal of Aerodynamics* 3.1 (2013), pages 122–134.

[45] Jae-Hyung Kim et al. “Wave drag reduction with acting spike induced by laser-pulse energy depositions”. In: *AIAA journal* 49.9 (2011), pages 2076–2078.

[46] Jae-Hyung Kim et al. “Drag reduction with high-frequency repetitive side-on laser pulse energy depositions”. In: *AIAA Paper* 5104 (2010).

[47] Dirk Heitmann, CJ Kahler, and Rolf Radespiel. “Investigation of laser-generated flow perturbations in hypersonic flow over a flat plate”. In: *AIAA paper* 3737 (2008).

[48] CJ Kähler, M Dreyer, and Bienroder Weg. “Dynamic 3D stereoscopic PIV and Schlieren investigation of turbulent flow structures generated by laser induced plasma”. In: *12th International Symposium on Applications of Laser Techniques to Fluid Mechanics, Lisbon, Portugal*. 2004.

[49] Dirk Heitmann, C Kähler, and Rolf Radespiel. “Installation of a System for Laser-Generated Perturbations in Hypersonic Flow”. In: *14th International Symposium on Application of Laser Techniques to Fluid Mechanics*. 2008.

[50] AA Zheltovodov, EA Pimonov, and DD Knight. “Energy deposition influence on supersonic flow over axisymmetric bodies”. In: *AIAA paper* 1230.2007 (2007), page 31.

[51] Doyle Knight, Olga Azarova, and Yuri Kolesnichenko. “On details of flow control via characteristics and location of microwave filament during its interaction with supersonic blunt body”. In: *AIAA Paper No* 847 (2009), page 2009.

[52] OA Azarova, VG Grudnitsky, and Y Kolesnichenko. “Some gas dynamic aspects of flow control by MW energy deposition”. In: *Sixth Workshop on Magneto-Plasma-Aerodynamics for Aerospace Applications*. 2005, pages 152–163.

[53] Nina Yurchenko et al. “Control of flow characteristics using localized plasma discharges”. In: *47th AIAA Aerospace Sciences Meeting and Exhibition*. 2009, pages 5–8.

[54] Vladimir L Bychkov et al. “A microwave discharge initiated by loop-shaped electromagnetic vibrator on a surface of radiotransparent plate in airflow”. In: *46th AIAA Aerospace Sciences Meeting*. 2008, pages 7–10.

[55] I Esakov et al. “Initiated surface microwave discharge as an efficient active boundary-layer control method”. In: *47th AIAA Aerospace Sciences Meeting and Exhibition*. 2009, pages 2009–0889.

[56] Brian R Kramer, C Brooke, and JP Smith. “Drag reduction experiments using boundary layer heating”. In: *37th AIAA Aerospace Sciences Meeting and Conference, Reno, NV*. 1999.

[57] Yu F Kolesnichenko et al. “Microwave energy release regimes for drag reduction in supersonic flows”. In: *AIAA Paper* 353 (2002), page 2002.

[58] Yuri F Kolesnichenko et al. “Basics in beamed MW energy deposition for flow/flight control”. In: *AIAA Paper* 669 (2004), page 2004.

[59] MI Ryvkin and AA Gorynya. “Gas dynamic effect of microwave discharge on supersonic cone-shaped bodies”. In: (2004).

[60] Doyle Knight et al. “Interaction of microwave-generated plasma with a blunt body at Mach 2.1”. In: *AIAA Paper* 846 (2009), page 2009.

[61] Yuri F Kolesnichenko et al. “MW energy deposition for aerodynamic application”. In: *AIAA paper* 361 (2003), page 2003.

[62] Yu Kolesnichenko, V Brovkin, et al. “Local Parameters of Microwave Discharge Determination in Plasma-Aerodynamic Experiment via Optic Information Processing”. In: *II Workshop “Thermochemical processes in plasma aerodynamics" St-Petersburg*. 2001, pages 61–66.

[63] VM Shibkov et al. “Freely localized microwave discharge in a supersonic gas flow”. In: *Plasma physics reports* 31.9 (2005), pages 795–801.

[64] Sergey Leonov et al. “The effect of plasma induced separation”. In: *AIAA paper* 3853 (2003), page 2003.

[65] Yurii G Utkin et al. “Development and use of localized arc filament plasma actuators for high-speed flow control”. In: *Journal of Physics D: Applied Physics* 40.3 (2007), page 685.

[66] JS Shang. “Surface direct current discharge for hypersonic flow control”. In: *Journal of Spacecraft and Rockets* 45.6 (2008), pages 1213–1222.

[67] Philip Peschke et al. “Interaction between nanosecond pulse DBD actuators and transonic flow”. In: *AIAA Paper* 3734 (2011), page 2011.

[68] Christopher Rethmel et al. “Flow separation control over an airfoil with nanosecond pulse driven DBD plasma actuators”. In: *AIAA paper* 487 (2011), page 2011.

[69] A Von Engle, R Seeliger, and M Steenback. “On the glow discharge at high pressure”. In: *Zeit. fur Physik* 85.144 (1933), pages 144–160.

[70] T Yokoyama et al. “The mechanism of the stabilisation of glow plasma at atmospheric pressure”. In: *Journal of Physics D: Applied Physics* 23.8 (1990), page 1125.

[71] J Reece Roth, Daniel M Sherman, and Stephen P Wilkinson. “Electrohydrodynamic flow control with a glow-discharge surface plasma”. In: *AIAA journal* 38.7 (2000), pages 1166–1172.

[72] Flint O Thomas et al. “Optimization of dielectric barrier discharge plasma actuators for active aerodynamic flow control”. In: *AIAA journal* 47.9 (2009), pages 2169–2178.

[73] Dmitriy M Orlov. *Modelling and simulation of single dielectric barrier discharge plasma actuators*. 2006.

[74] Zoran Falkenstein and John J Coogan. “Microdischarge behaviour in the silent discharge of nitrogen-oxygen and water-air mixtures”. In: *Journal of Physics D: Applied Physics* 30.5 (1997), page 817.

[75] CL Enloe et al. “Mechanisms and responses of a single dielectric barrier plasma actuator: plasma morphology”. In: *AIAA journal* 42.3 (2004), pages 589–594.

[76] Valentin I Gibalov and Gerhard J Pietsch. “The development of dielectric barrier discharges in gas gaps and on surfaces”. In: *Journal of Physics D: Applied Physics* 33.20 (2000), page 2618.

[77] Hiroyuki Nishida and Takashi Abe. “Numerical analysis of plasma evolution on dielectric barrier discharge plasma actuator”. In: *Journal of applied physics* 110.1 (2011), page 013302.

[78] Y Lagmich et al. “Electrohydrodynamic force and scaling laws in surface dielectric barrier discharges”. In: *Applied physics letters* 90.5 (2007), page 051502.

[79] JP Boeuf, Y Lagmich, and LC Pitchford. “Contribution of positive and negative ions to the electrohydrodynamic force in a dielectric barrier discharge plasma actuator operating in air”. In: *Journal of Applied Physics* 106.2 (2009), page 023115.

[80] K Allegraud, O Guaitella, and A Rousseau. “Spatio-temporal breakdown in surface DBDs: evidence of collective effect”. In: *Journal of Physics D: Applied Physics* 40.24 (2007), page 7698.

[81] Jerome Pons, Eric Moreau, and Gérard Touchard. “Asymmetric surface dielectric barrier discharge in air at atmospheric pressure: electrical properties and induced airflow characteristics”. In: *Journal of physics D: applied physics* 38.19 (2005), page 3635.

[82] Eric Moreau. “Airflow control by non-thermal plasma actuators”. In: *Journal of Physics D: Applied Physics* 40.3 (2007), page 605.

[83] JP Boeuf and LC Pitchford. “Electrohydrodynamic force and aerodynamic flow acceleration in surface dielectric barrier discharge”. In: *Journal of Applied Physics* 97.10 (2005), page 103307.

[84] JP Boeuf et al. “Electrohydrodynamic force in dielectric barrier discharge plasma actuators”. In: *Journal of Physics D: Applied Physics* 40.3 (2007), page 652.

[85] Maxime Forte et al. “Optimization of a dielectric barrier discharge actuator by stationary and non-stationary measurements of the induced flow velocity: application to airflow control”. In: *Experiments in Fluids* 43.6 (2007), pages 917–928.

[86] CL Enloe et al. “Plasma-induced force and self-induced drag in the dielectric barrier discharge aerodynamic plasma actuator”. In: *AIAA Paper* 1622 (2009), page 2009.

[87] A Debien et al. “Unsteady aspect of the electrohydrodynamic force produced by surface dielectric barrier discharge actuators”. In: *Applied Physics Letters* 100.1 (2012), page 013901.

[88] Mathias Neumann et al. “Determination of the phase-resolved body force produced by a dielectric barrier discharge plasma actuator”. In: *Journal of Physics D: Applied Physics* 46.4 (2013), page 042001.

[89] N Benard, A Debien, and E Moreau. “Time-dependent volume force produced by a non-thermal plasma actuator from experimental velocity field”. In: *Journal of Physics D: Applied Physics* 46.24 (2013), page 245201.

[90] Ryan Durscher and Subrata Roy. “Force measurement techniques and preliminary results using aerogels and ferroelectrics for dielectric barrier discharge actuators”. In: *41st AIAA Fluid Dynamics Conference and Exhibit, AIAA Paper*. Volume 3735. 2011, page 2011.

[91] J Reece Roth, Daniel M Sherman, and Stephen P Wilkinson. *Boundary layer flow control with a one atmosphere uniform glow discharge surface plasma*. American Institute of Aeronautics and Astronautics, 1998.

[92] JW Baughn et al. “Momentum transfer for an aerodynamic plasma actuator with an imposed boundary layer”. In: *AIAA paper* 168 (2006), page 2006.

[93] CO Porter et al. “Temporal force measurements on an aerodynamic plasma actuator”. In: *AIAA paper* 104 (2006), page 2006.

[94] Thomas C Corke, Martiqua L Post, and Dmitriy M Orlov. “Single dielectric barrier discharge plasma enhanced aerodynamics: physics, modeling and applications”. In: *Experiments in Fluids* 46.1 (2009), pages 1–26.

[95] J Jolibois and E Moreau. “Enhancement of the electromechanical performances of a single dielectric barrier discharge actuator”. In: *Dielectrics and Electrical Insulation, IEEE Transactions on* 16.3 (2009), pages 758–767.

[96] Eric Moreau, Roberto Sosa, and Guillermo Artana. “Electric wind produced by surface plasma actuators: a new dielectric barrier discharge based on a three-electrode geometry”. In: *Journal of Physics D: Applied Physics* 41.11 (2008), page 115204.

[97] N Benard, N Balcon, and E Moreau. “Electric wind produced by a surface dielectric barrier discharge operating in air at different pressures: aeronautical control insights”. In: *Journal of Physics D: Applied Physics* 41.4 (2008), page 042002.

[98] Nicolas Benard, Nicolas Balcon, and Eric Moreau. “Electric Wind Produced by a Single Dielectric Barrier Discharge Actuator Operating in Atmospheric Flight Conditions: Pressure Outcome”. In: *AIAA paper* 3792 (2008), page 2008.

[99] Berkant Goeksel et al. “Steady and unsteady plasma wall jets for separation and circulation control”. In: *AIAA paper* 3686 (2006), page 2006.

[100] Mehul P Patel et al. “Plasma actuators for hingeless aerodynamic control of an unmanned air vehicle”. In: *Journal of Aircraft* 44.4 (2007), pages 1264–1274.

[101] ML Post. “Plasma actuators for separation control on stationary and unstationary airfoils”. In: *Doctor dissertation. Indiana: the University of Notre Dame* (2004).

[102] Chuan He, Thomas C Corke, and Mehul P Patel. “Plasma flaps and slats: an application of weakly ionized plasma actuators”. In: *Journal of Aircraft* 46.3 (2009), pages 864–873.

[103] Vladimir Voikov, Thomas Corke, and Osamah Haddad. “Numerical simulation of flow control over airfoils using plasma actuators”. In: *APS Division of Fluid Dynamics Meeting Abstracts*. Volume 1. 2004.

[104] Arvind Santhanakrishnan and Jamey D Jacob. “Flow control with plasma synthetic jet actuators”. In: *Journal of Physics D: Applied Physics* 40.3 (2007), page 637.

[105] AB Liu et al. “Flow characteristics of synthetic jet induced by plasma actuator”. In: *AIAA journal* 49.3 (2011), pages 544–553.

[106] KR Grossman, BZ Cybyk, and DM VanWie. “Sparkjet actuators for flow control”. In: *AIAA Paper* 57 (2003), page 2003.

[107] Venkat Narayanaswamy et al. “Investigation of plasma-generated jets for supersonic flow control”. In: *46th AIAA Aerospace Sciences Meeting and Exhibit*. 2008, pages 2008–285.

[108] Daniel Caruana et al. “The “plasma synthetic jet” actuator. aero-thermodynamic characterization and first flow control applications”. In: *AIAA* 1307 (2009), page 2009.

[109] A Belinger et al. “Influence of the energy dissipation rate in the discharge of a plasma synthetic jet actuator”. In: *Journal of Physics D: Applied Physics* 44.36 (2011), page 365201.

[110] Mona Golbabaei-Asl et al. “SparkJet Efficiency”. In: *51st AIAA Aerospace Sciences Meeting including the New Horizons Forum and Aerospace Exposition*. 2013.

[111] SJ Haack et al. “Experimental Estimation of SparkJet Efficiency”. In: *42nd AIAA Plasmadynamics and Lasers Conference, Honolulu, AIAA Paper*. Volume 3997. 2011.

[112] KR Grossman et al. “Characterization of sparkjet actuators for flow control”. In: *AIAA Paper* 89 (2004), page 2004.

[113] BZ Cybyk, JT Wilkerson, and KR Grossman. “Performance characteristics of the sparkjet flow control actuator”. In: *AIAA Paper* 2131 (2004), page 2004.

[114] Pierrick Hardy et al. “Plasma synthetic jet for flow control”. In: *Proceedings of the 40th AIAA Fluid Dynamics Conference and Exhibit, AIAA Paper*. Volume 5103. 2010, page 2010.

[115] Lin Wang et al. “Three-Electrode Plasma Synthetic Jet Actuator for High-Speed Flow Control”. In: *AIAA Journal* 52.4 (2013), pages 879–882.

[116] Luc Léger. “Contrôle actif d’un écoulement d’air par un plasma froid surfacique”. PhD thesis. Poitiers, 2003.

[117] Alexandre Labergue. “Etude de décharges électriques dans l’air pour le développement d’actionneurs plasmas–Application au contrôle de décollements d’écoulements”. PhD thesis. Université de Poitiers, 2005.

[118] A Labergue, E Moreau, and G Touchard. “A parametric study of surface corona discharge along an insulating flat plate in atmospheric pressure”. In: *Electrical Insulation and Dielectric Phenomena, 2005. CEIDP’05. 2005 Annual Report Conference on*. IEEE. 2005, pages 490–494.

[119] Pierre Magnier et al. “A DC corona discharge on a flat plate to induce air movement”. In: *Journal of electrostatics* 65.10 (2007), pages 655–659.

[120] Eric Moreau, Luc Léger, and Gérard Touchard. “Effect of a DC surface-corona discharge on a flat plate boundary layer for air flow velocity up to 25m/s”. In: *Journal of electrostatics* 64.3 (2006), pages 215–225.

[121] Luc Leger, Eric Moreau, and Gérard G Touchard. “Effect of a DC corona electrical discharge on the airflow along a flat plate”. In: *Industry Applications, IEEE Transactions on* 38.6 (2002), pages 1478–1485.

[122] Luc Léger et al. “Influence of a DC corona discharge on the airflow along an inclined flat plate”. In: *Journal of Electrostatics* 51 (2001), pages 300–306.

[123] Gwynne A Evans, Jonathan M Blackledge, and Peter D Yardley. *Numerical methods for partial differential equations*. Springer, 2000.

[124] Jules G Charney, Ragnar Fjörtoft, and J von Neumann. “Numerical integration of the barotropic vorticity equation”. In: *Tellus* 2.4 (1950), pages 237–254.

[125] Richard Courant, Kurt Friedrichs, and Hans Lewy. “On the partial difference equations of mathematical physics”. In: *IBM journal of Research and Development* 11.2 (1967), pages 215–234.

[126] John Crank and Phyllis Nicolson. “A practical method for numerical evaluation of solutions of partial differential equations of the heat-conduction type”. In: *Mathematical Proceedings of the Cambridge Philosophical Society*. Volume 43. 01. Cambridge Univ Press. 1947, pages 50–67.

[127] Jim Douglas and James E Gunn. “A general formulation of alternating direction methods”. In: *Numerische Mathematik* 6.1 (1964), pages 428–453.

[128] Joel H Ferziger and Milovan Perić. *Computational methods for fluid dynamics*. Volume 3. Springer Berlin, 2002.

[129] PK Khosla and SG Rubin. “A diagonally dominant second-order accurate implicit scheme”. In: *Computers & Fluids* 2.2 (1974), pages 207–209.

[130] Richard Courant, Eugene Isaacson, and Mina Rees. “On the solution of nonlinear hyperbolic differential equations by finite differences”. In: *Communications on Pure and Applied Mathematics* 5.3 (1952), pages 243–255.

[131] DB Spalding. “A novel finite difference formulation for differential expressions involving both first and second derivatives”. In: *International Journal for Numerical Methods in Engineering* 4.4 (1972), pages 551–559.

[132] DN de G Allen and RV Southwell. “Relaxation methods applied to determine the motion, in two dimensions, of a viscous fluid past a fixed cylinder”. In: *The Quarterly Journal of Mechanics and Applied Mathematics* 8.2 (1955), pages 129–145.

[133] GD Raithby and GE Schneider. “Elliptic system: finite difference method II”. In: *Handbook of Numerical Heat Transfer* (1988), pages 241–289.

[134] Panos Tamamidis and Dennis N Assanis. “Evaluation of various high-order-accuracy schemes with and without flux limiters”. In: *International Journal for Numerical Methods in Fluids* 16.10 (1993), pages 931–948.

[135] BP Leonard and Simin Mokhtari. “Beyond first-order upwinding: The ultra-sharp alternative for non-oscillatory steady-state simulation of convection”. In: *International Journal for Numerical Methods in Engineering* 30.4 (1990), pages 729–766.

[136] Brian P Leonard. “A stable and accurate convective modelling procedure based on quadratic upstream interpolation”. In: *Computer methods in applied mechanics and engineering* 19.1 (1979), pages 59–98.

[137] Suhas Patankar. *Numerical heat transfer and fluid flow*. CRC Press, 1980.

[138] Graeme Austin Bird. “Molecular gas dynamics and the direct simulation of gas flows”. In: (1994).

[139] Charles K Birdsall and A Bruce Langdon. *Plasma physics via computer simulation*. CRC Press, 2004.

[140] John P Verboncoeur. “Particle simulation of plasmas: review and advances”. In: *Plasma Physics and Controlled Fusion* 47.5A (2005), A231.

[141] Patrick Chassaing. *Turbulence en mécanique des fluides*. 2000.

[142] David C Wilcox et al. *Turbulence modeling for CFD*. Volume 2. DCW industries La Canada, CA, 1998.

[143] Florian R Menter. “Zonal two equation k-turbulence models for aerodynamic flows”. In: *AIAA paper* 2906 (1993), page 1993.

[144] David Alem Wilcox. “Simulation of transition with a two-equation turbulence model”. In: *AIAA journal* 32.2 (1994), pages 247–255.

[145] FR Menter et al. “A correlation-based transition model using local variables—Part I: model formulation”. In: *Journal of turbomachinery* 128.3 (2006), pages 413–422.

Modélisation de décharges micro-ondes

Présentation

La formation de plasma due à un champ électromagnétique intense dans la gamme des micro-ondes peut jouer un rôle important dans une grande variété d'applications, y compris les antennes et les guides d'ondes. Comme nous avons vu, dans le domaine de l'aérospatiale, de méthodes de dépôt d'énergie ont été suggérés comme prometteurs pour les applications de contrôle d'ecoulement et l'amélioration des coefficients aérodynamiques. L'absorption très efficace de l'énergie de micro-ondes par le plasma sous certaines conditions place ces décharges sur le centre de l'intérêt de la recherche. L'interaction entre le champ de micro-ondes, le plasma et le gaz est essentielle pour comprendre l'échange d'énergie entre eux, ainsi que le volume que le plasma sera finalement occuper. **L'objectif de ce chapitre est donc, dans un niveau plus fondamental que la recherche de l'application de ce type de décharges de plasma pour les applications de contrôle d'écoulement. Nous sommes intéressés par la création d'un modèle numérique simplifié, précis et de coût de calcul réduit, afin d'étudier ces interactions complexes, non linéaires et fournir des indications plus physiques de la nature des décharges micro-ondes. Les simulations numériques de tels systèmes, demandent de vastes ressources techniques ou elles sont complexes. Ceci est la raison pour laquelle, dans la littérature, il y a juste quelques efforts numériques de décrire l'évolution des décharges micro-ondes dans le temps. Par conséquent, le développement de modèles physiques simplifiés et dans le même temps conservent la physique principal impliqué et la construction de modèles numériques qui peuvent efficacement résoudre le système d'équations, est en soi une tâche très exigeante - une tâche bien, qui est essentiel pour atteindre progrès dans le concept de décharges micro-ondes et par conséquent leur potentiel d'application dans les techniques de contrôle d'écoulement.**

Dans ce chapitre, un schéma couplé implicite (ADI) - FDTD avec un modèle de plasma fluide simplifié (un modèle de plasma similaire à celui proposé initialement dans [1]), est présenté. Cette formulation conserve la simplicité et la robustesse des systèmes de FDTD, tout en dépassant la barrière du critère de stabilité CFL, conduisant à un temps de calcul réduit et la possibilité pour des simulations tridimensionnelles de la formation du plasma et l'évolution due à des champs micro-ondes. Afin d'étudier l'énergie absorbée par le plasma et le

transfert de gaz sous forme de chaleur et le changement consécutif de la densité du gaz, un solveur Euler a été couplé avec le modèle EM-plasma en tenant compte des effets de gaz réel. Divers validations et applications sont ensuite étudiés, y compris de simulations tridimensionnelles de formation de motif dans une décharge micro-ondes librement localisée, les effets de chauffage au gaz sur le développement d'un "streamer" et la durabilité d'un volume pré-ionisé avec des champs sous-critiques.

Modèles physiques et numériques

Modèle physique

Le modèle physique est constitué par les équations de Maxwell couplés avec un modèle de plasma fluide par la densité de courant d'électrons. Les équations de Maxwell s'écrivent:

$$\nabla\times E+\mu\frac{\partial H}{\partial t}=0$$

$$\nabla\times H-\varepsilon\frac{\partial E}{\partial t}+J=0 \tag{A.1}$$

$$\nabla\cdot(\varepsilon E)-\rho=0 \tag{A.2}$$

$$\nabla\cdot(\mu H)=0 \tag{A.3}$$

où E et H sont les champs électriques et magnétiques, ε et μ sont la permittivité et la perméabilité, ρ est la densité de charge et J la densité de courant totale qui peut être approchée comme:

$$J=\sigma E \tag{A.4}$$

où σ est la conductivité électrique.

Les principales hypothèses du modèle peuvent être résumées comme suit:

— Le plasma est quasi-neutre car la longueur de Debye est faible par rapport à la taille de plasma.
— La densité de courant ionique est beaucoup plus petite que la densité de courant d'électrons et est négligée.
— La force magnétique est négligé car il est petit par rapport à la force électrique.
— Les distances parcourues par les électrons en raison de collisions au cours d'une période micro-ondes sont petites par rapport à l'échelle de longueur de champ, les variations de pression et le mouvement cyclotronique.
— Approximation du champ local: Le gain d'énergie du champ électrique et l'élan de collision sont équilibrés avec les pertes d'énergie, de sorte que les fréquences d'ionisation ne dépendent que du champ électrique local E, ou plus précisément du champ électrique réduit E / N (ou E / p) car la fréquence de collision est proportionnel à la densité du gaz N (ou pression p).

Dans ces hypothèses, la densité de courant totale induite par un plasma micro-ondes s'écrit:

$$J=-en_e v_e \tag{A.5}$$

Dans l'équation A.5, e, n_e, v_e sont la charge de l'électron, la densité et la vitesse moyenne respectivement.

La vitesse d'électrons dans l'équation A.5 est obtenu à partir de l'équation de transfert de quantité de mouvement électronique locale, qui s'écrit :

$$\frac{\partial v_e}{\partial t} = -\frac{eE}{m_e} - \nu_c v_e \tag{A.6}$$

où m_e est la mass d'électrons et v_c la fréquence de collision électron-neutre donnée par [2]:

$$v_c = 5.3x10^9 p \tag{A.7}$$

où v_c est en s^{-1} et p est la pression à température ambiante en torr

.

Comme le plasma est quasi-neutre, les variations spatiales et temporelles de la densité de plasma sont obtenus à partir d'une équation de diffusion simple qui s'écrit en moyenne sur une période du champ de micro-ondes:

$$\frac{\partial n_e}{\partial t} - \Delta(D_{eff} n_e) = \nu_{eff} n_e - r{n_e}^2 \tag{A.8}$$

Le côté droit de l'équation représente la production et des pertes de particules chargées. ν_{eff} est la fréquence d'ionisation efficace, y compris l'ionisation et de l'attachement, et r est le coefficient de recombinaison électron-ion. ν_{eff} dépend de la fonction de distribution des électrons locale et une approximation habituelle à haute pression est à supposer que la fonction de distribution des électrons en moyenne sur une période a la même forme que sous un champ uniforme, mais calculée pour un champ effectif E_{eff} définie par:

$$E_{eff} = \frac{E_{rms}}{\sqrt{1 + \frac{\omega^2}{\nu_c^2}}} \tag{A.9}$$

Nous rappelons ici que le travail fait par un champ électrique alternatif sur un électron en moyen est :

$$< -eEv >_{AC} = \frac{e^2 E_0^2}{2m(\omega^2 + \nu_c^2)} \nu_c \tag{A.10}$$

tandis que pour un champ continu:

$$< -eEv >_{DC} = \frac{e^2 E_0^2}{m\nu_c} \tag{A.11}$$

Par ces équations, et en remplacant le champ E_0 par le champ RMS définie comme $E^2 = E_0^2/2$, nous obtenons l'équation A.9 . Par conséquent, ν_{eff} est une fonction du champ local efficace et la fonction $\nu_{eff}(E_{eff})$ est déduit à partir d'une forme d'analyse de données expérimentales [3].

D_{eff} et r dépend de la température des électrons T_e, ce qui est également une fonction du champ effectif local, mais peut être considéré comme à peu près constante et égale à 2 eV dans les limites considérées. Le coefficient de recombinaison est supposée constante et égale à zéro, sauf si mentionné autrement. La diffusion

du plasma est ambipolaire dans le plasma. Au bord du plasma, où la densité du plasma est très basse, la diffusion est plus ambipolaire et les électrons diffusent librement. La transition de la diffusion ambipolaire à la diffusion electronique est représenté par la forme du coefficient de diffusion effectif D_{eff} [1]:

$$D_{eff} = \frac{D_\alpha + \alpha D_e}{1+\alpha} \tag{A.12}$$

où D_α, D_e sont les coefficients de diffusion ambipolaire et électronique respectivement (défini ci-dessous) et $\alpha = \nu_i \tau_M$ (où ν_i est la fréquence d'ionisation) et τ_M est le temps de relaxation de Maxwell donnée par:

$$\tau_M = \frac{\varepsilon_0}{en(\mu_e + \mu_i)} \tag{A.13}$$

Cette expression permet une bonne évaluation de la vitesse du front de plasma[1]. Les coefficients de diffusion s'ecrivent $D_e = \mu_e \kappa_B T_e / e$ et $D_\alpha = \mu_i \kappa_B T_e / e$ respectivement , où κ_B est la constante de Botlzmann. La mobilité des électrons μ_e est liée à la fréquence des collisions électron-neutre par $\mu_e = e/(m_e \nu_c)$ et on suppose que $\mu_i = 0.5 \times 10^{-2} \mu_e$.

Modèle numérique

Les schémas implicites FDTD pour résoudre les équations de Maxwell ont été récemment mis au point par des chercheurs, afin de réduire les ressources nécessaires. Une étude de ces méthodes peut être trouvé dans [4]. Dans cette thèse, nous présentons un schéma implicite ADI-FDTD couplé afin de réduire le temps CPU. De conditions aux limites de type CPML ont été utilisés et le code a été parallélisé en utilisant la bibliothèque MPI.

Le schéma de Yee FDTD classique est utilisé pour la discrétisation spatiale des équations du système [5].

Les équations ADI-FDTD discrétisée avec un schéma de saute-mouton en temps s'écrivent en trois dimensions:

$$\begin{aligned} E^{n+1/2}_{x_{i,j-1,k}} - Q_1 E^{n+1/2}_{x_{i,j,k}} + E^{n+1/2}_{x_{i,j+1,k}} =& Q_2 E^{n-1/2}_{x_{i,j,k}} + Q_3 (H^n_{z_{i,j,k}} - H^n_{z_{i,j-1,k}}) - Q_4 (H^n_{y_{i,j,k}} - H^n_{y_{i,j,k-1}}) \\ & - (E^{n-1/2}_{x_{i,j+1,k}} - E^{n-1/2}_{x_{i,j-1,k}}) - \frac{Q_1}{\varepsilon_0} (\psi^n_{exy_{i,j,k}} - \psi^n_{exz_{i,j,k}}) + Q_5 \end{aligned} \tag{A.14}$$

, où les coefficients Q s'écrivent:

$$\begin{aligned} &Q_1 = (2\Delta y \sqrt{k_x k_y})/(c\Delta t))^2 + 2, \;\; Q_2 = (2\Delta y \sqrt{k_x k_y}/(c\Delta t))^2, \\ &Q_3 = 4\mu_0 \Delta y k_x/(\Delta t), \;\; Q_4 = 4\mu_0 \Delta y^2 k_x k_y/(k_z \Delta z \Delta t), \;\; Q_5 = 0 \end{aligned}$$

Avec l'ajout de la densité de courant d'électrons la mise à jour du champ électrique nécessite des coefficients transformés comme suit:

$$\begin{aligned} Q_1 &= (2\Delta y \sqrt{k_x k_y})/(c\Delta t))^2 + 2 + \mu_o \frac{\Delta y^2}{\Delta t} e n^p_{i,j,k} \alpha \\ Q_5 &= \mu_o \frac{\Delta y^2}{\Delta t} e n^p_{i,j,k} v^{n-1/2}_{x_{i,j,k}} (1+\beta) \end{aligned}$$

où les coefficients α et β s'écrivent:

$$\alpha = e\Delta t/(m_e(1+\frac{1}{2}\Delta t\nu_c))$$
$$\beta = (1-\frac{1}{2}\Delta t\nu_c)/(1+\frac{1}{2}\Delta t\nu_c)$$

Les autres équations discrétisées peuvent être facilement obtenues par permutation circulaire en x, y, z

.

L'équation de transfert d'énergie cinétique est discrétisé en utilisant un schéma CN implicite dans le temps comme suit:

$$v_{x_{i,j,k}}^{n+0.5} = \beta v_{x_{i,j,k}}^{n-0.5} - \alpha(\frac{E_{x_{i,j,k}}^{n+0.5} + E_{x_{i,j,k}}^{n-0.5}}{2}) \tag{A.15}$$

et pareil pour le y, z composants.
Enfin l'équation de plasma est discrétisée en utilisant un schéma de Euler explicite:

$$\begin{aligned}\frac{n_{i,j,k}^{p+1} - n_{i,j,k}^{p}}{\Delta t} =& \nu_{eff_{i,j,k}}^{p} n_{i,j,k}^{p} - r n_{i,j,k}^{p} + D_{eff_{i,j,k}}^{p} \\ & [\frac{n_{i,j+1,k}^{p} + n_{i,j-1,k}^{p} - 2n_{i,j,k}^{p}}{\Delta y^2} \\ & + \frac{n_{i+1,j,k}^{p} + n_{i-1,j,k}^{p} - 2n_{i,j,k}^{p}}{\Delta x^2} \\ & + \frac{n_{i,j,k+1}^{p} + n_{i,j,k-1}^{p} - 2n_{i,j,k}^{p}}{\Delta z^2}\end{aligned} \tag{A.16}$$

Dans les équations ci-dessus le pas de temps p utilisé pour la densité du plasma est différente dul pas de temps n et correspond à un $t_\Delta plasma = T$, où T est la période des vagues EM.

.

La stabilité du schéma saute-mouton ADI-FDTD en trois dimensions avec ses propriétés de dispersion ont été étudiés dans [6] par la méthode de Von-Neumman. L'auteur a conclu que la méthode est inconditionnellement stable et non dissipatif. Dans cette thèse, nous considérons la méthode de l'énergie comme un moyen d'étudier la stabilité du schéma et de l'étendre au cas de couplage avec l'équation de transfert de quantité de mouvement. En tenant compte des conditions aux limites PEC nous avons prouvé que l'estimation d'énergie pour le système ADI couplé reste limitée et donc le schéma numérique est inconditionnellement stable.

Dans les cas où la dynamique du plasma sont couplées avec celles des fluides, un solveur CFD approprié devait être développé. Comme le principal effet d'une décharge de plasma localisée librement dans l'air, est le chauffage de ce dernier, ce solveur doit être capable de capter les ondes de choc produites par le dépôt d'énergie intense. Dans cette thèse, le solveur Riemann approximatif de Roe [7] est utilisé car il intègre des avantages importants tels que: Il est strictement conservatrice. Il a un très faible coefficient de diffusion numérique et de la viscosité. Il capture des chocs avec précision et en haute résolution. Il est tout à fait stable. En outre, le solveur prend en compte les effets des gaz réels.

Résultats

Nous considérons une configuration simple pour étudier la performance du système proposé par rapport à son formulation explicite , en termes de temps CPU et précision - erreur.

Le domaine de la simulation de cas test est un $0,5\lambda x\lambda$ carré bidimensionnel terminé avec de CPML aux limites pour les ondes électromagnétiques, tel que représenté dans la figure A.1.

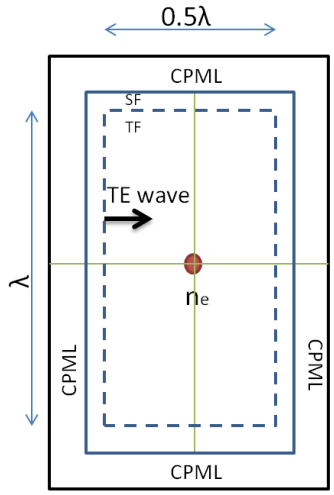

Figure A.1: Le domaine de la simulation.

Nous fixons une grille cartésienne uniforme de $\Delta x = \Delta y = \lambda/200$. Un mode TE, y-polarisée (onde plane) d'amplitude $Eo = 5MV/m$ se propage de la gauche à droit. La fréquence de l'onde électromagnétique est $f = 110$ GHz. Nous considérons que les ondes se propagent dans l'air à de pression atmosphérique. Une densité de plasma initial d'un profil gaussien avec un maximum de $10^{22}m^{-3}$ et un écart type de $6.10^{-5}m$ est placé à une distance de $0,5\lambda$, tandis que la recombinaison est négligée.

Le nombre CFL pour le FDTD - 3D, est défini :

$$CFL = c\Delta t\sqrt{\frac{1}{\Delta x^2}+\frac{1}{\Delta y^2}+\frac{1}{\Delta z^2}} \tag{A.17}$$

Nous simulons plus de 100 périodes, en changeant le nombre CFL de 1 à 32. Cette étude paramétrique de la réduction du temps de CPU en fonction du nombre CFL est présenté dans le tableau A.1. Le temps CPU a été normalisée à celui obtenu avec le schéma explicite pour $CFL = 1$.

		CFL					
		1	2	4	8	16	32
temps CPU	$\lambda/200$	2.5	2	0.625	0.3	0.12	0.05

Table A.1: Temps CPU normalisé vs CFL

Pour des CFL supérieur à 4, le temps CPU est considérablement réduite: pour $CFL = 32$ le temps CPU était $0,05$ fois l'explicite, correspondant à une réduction de plus de 90%.

Il convient de noter ici que la réduction de temps de calcul est liée au pas de temps qui dépend non seulement du nombre CFL mais aussi de la taille de maille. Ainsi, nous définissons un nombre CFL normalisée à la taille de la maille et de la période EM (T_{EM}):

$$CFL_N = (\frac{T_{EM}}{\Delta t})^{-1} \tag{A.18}$$

correspondant à l'inverse du nombre d'incréments de temps par période EM. On peut en déduire qu'au-delà de la limite de la $CFL = 4$ pour la discrétisation spatiale décrite ci-dessus, nous obtenons une accélération du temps CPU d'environ $2,2 * CFL_N^{-1}$ %.

Ensuite, nous étudions l'erreur de schéma numérique. Nous avons choisi une densité de plasma initial assez élevé, de sorte que les ondes électromagnétiques sont fortement affectés par le plasma. Nous considérons deux estimations de l'erreur :

$$\begin{aligned} Error_2 &= \sqrt{\frac{\sum_{i,j,k} |E^{Explicit}_{RMS_{i,j,k}} - E^{Implicit}_{RMS_{i,j,k}}|^2}{\sum_{i,j,k} |E^{Explicit}_{RMS_{i,j,k}}|^2}} \\ Error_\infty &= \frac{max(|E^{Explicit}_{RMS_{i,j,k}} - E^{Implicit}_{RMS_{i,j,k}}|)}{max(|E^{Explicit}_{RMS_{i,j,k}}|)} \end{aligned} \tag{A.19}$$

où $E^{Explicit}_{RMS_{i,j,k}}$ est le champ obtenu avec le solveur explicite à $t = t_{final} = 100T$, $\Delta x = \Delta yRMSlocales = \lambda/200$ et $CFL = 1$.

Dans les tableau A.2 et A.3, les erreurs ci-dessus définis sont présenté pour différentes valeurs du nombre CFL ainsi que pour un maillage plus raffiné de $\Delta x = \Delta y = \lambda/400$.

		CFL_N			
		0.00390625	0.015625	0.03125	0.0625
$Error_2$ (%)	$\lambda/200$	0.02	0.52	1.3	2.9
	$\lambda/400$	0.026	0.59	1.41	3.17

Table A.2: $Error_2$ vs CFL normalisé

		CFL_N			
		0.00390625	0.015625	0.03125	0.0625
$Error_\infty$ (%)	$\lambda/200$	0.8	2.25	5.66	10.28
	$\lambda/400$	0.24	1	2.45	5.74

Table A.3: $Error_\infty$ vs CFL normalisé

Le temps CPU normalisé et l'erreur par rapport au nombre CFL normalisé sont tracées dans la figure A.2, pour comparaison. Le choix optimal pour le nombre CFL pour réduire au maximum le temps CPU avec une erreur minimale correspondante est une valeur de $CFL_N \approx 0.028$ correspondant pour le cas-test de $\lambda/200$ à une CFL ≈ 7.

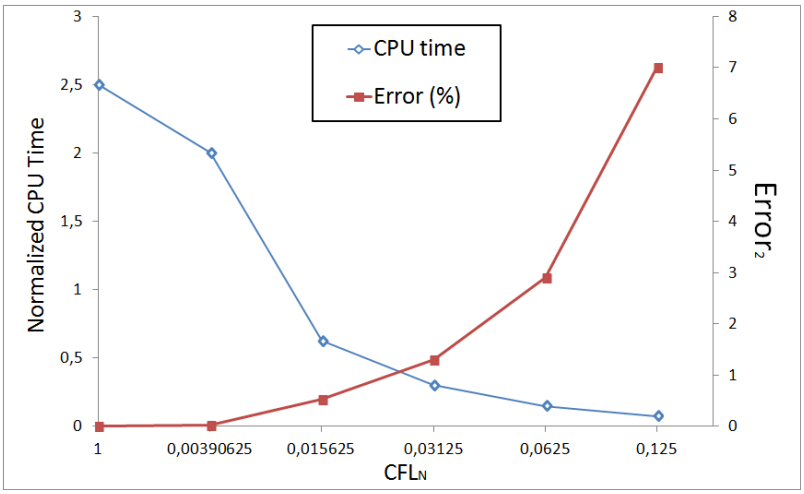

Figure A.2: Temps CPU normalisé et erreur vs CFL_N.

Simulations tridimensionnelles de la formation de structures au cours de claquage micro-ondes librement localisé dans l'air en haute pression.

Nous nous concentrons sur les expériences de [8] . Ces expériences démontrent clairement la nature tridimensionnelle d'un décharge microondes librement localisé dans l'air en haute pression et frequence sous un champ polarisé linéairement. Une polarisation circulaire, produit un plasma presque axisymétrique et plus uniforme. D'images des deux cas sont présentés dans la figure A.3.

Le domaine de calcul pour les simulations tridimensionnelles est une boite de $2.2\lambda \times 1,5\lambda \times 2\lambda$. Le plasma initial est placé à une distance de $1,6\lambda$ dans le x - direction et centré sur l'axe dans les Y et Z - directions. A 110 GHz, une onde TE avec une intensité de champ électrique de 6 MV / m est injecté de gauche à droit et d'autres conditions initiales sont similaires au cas bidimensionnel A.1. Le maillage a été fixé à $\lambda/200$, et le nombre CFL à 10. Une simulation de plus de 60 ns de temps de simulation dans un cluster parallèle de 64 processeurs a duré environ 1 semaine.

L'évolution du plasma en fonction du temps peut être observé dans les figures A.4 et A.5, dans les deux plans XY et XZ. Comme les expériences de [8, 9] ont démontré, le plasma forme un motif différent sur chaque plan.

C'est clair que le motif de plasma est non périodique (ou plus précisément sa structure périodique ne correspond pas à la formation de chaque filament), mais il présente des maximas et des différentes régions de concentration de plasma au cours de sa propagation vers la source de micro-ondes. Qui démontre clairement la nature tridimensionnelle de ces décharges. Dans le cas à deux dimensions, le motif de plasma présente des maximas quasi périodiques, ce qui entraîne à une distance constante de filament d'environ $\lambda/4$. Dans la figure A.6, la densité de l'électron est tracée sur l'axe x centrale au temps $t = 70ns$, et la différence entre la distance des filaments en fonction de la position peut être observée. Ce comportement est en accord complet avec les images fournies dans [8], même si les auteurs parlent d'une distance constante de $\lambda/4$.

Dans la figure A.7, contours iso-surface de la densité des électrons à une valeur de $1 \times 10^{21}\ m^{-3}$ sont présentés.

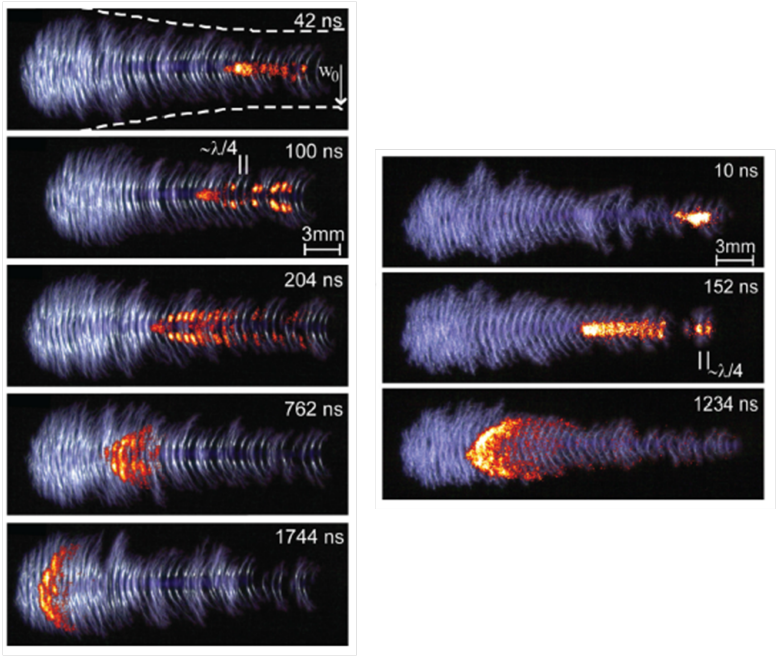

Figure A.3: Decharge microondes avec une polarisation linéaire (gauche) et circulaire (droite) [8].

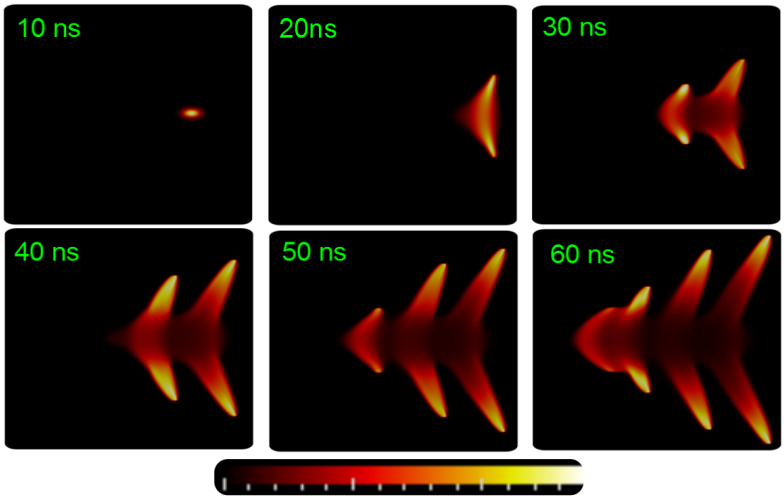

Figure A.4: Densité électronique vs temps, plan XY. Valeurs max. 6.45×10^{19},5.22×10^{21}, 1×10^{22}, 9×10^{21}, 8.9×10^{21}, 8.45×10^{21} m^{-3} respectivement.

En comparant les résultats avec le cas à deux dimensions, nous notons que la vitesse de propagation du front de plasma est plus petit pour le cas tridimensionnel, atteignant des vitesses qui varient entre 30-38 km /

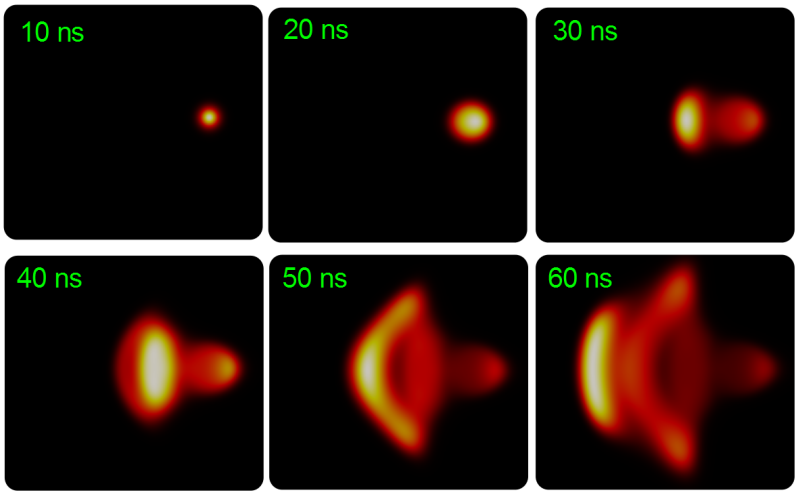

Figure A.5: Densité électronique vs temps, plan XZ. Valeurs max. 6.45×10^{19},5.22×10^{21}, 5.03×10^{21}, 2.39×10^{21}, 3×10^{21} , 2.98×10^{21} m^{-3} respectivement.

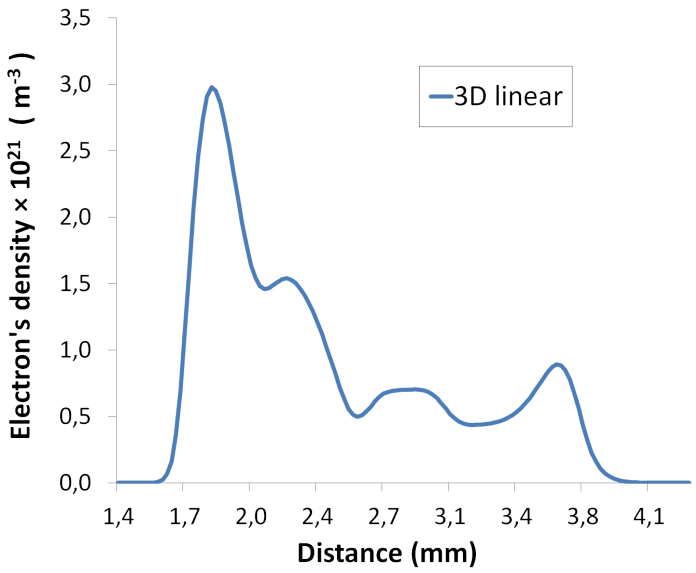

Figure A.6: Densité électronique sur l'axe x centrale, $t = 70ns$.

s, tandis que dans le cas à deux dimensions le front de plasma a une vitesse de propagation presque constante et d'environ 41 km / s. Dans la figure A.8, la distance parcourue dans le x - axe est tracé au fil du temps, ce qui démontre la déclaration ci-dessus.

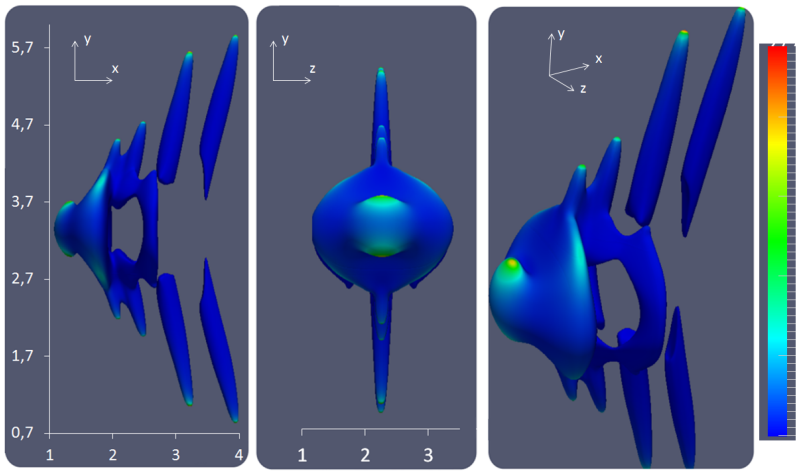

Figure A.7: Iso-surfaces (1×10^{21} m^{-3}) contours de la densité électronique colorés par la fréquence d'ionisation, $t = 70ns$, XY (gauche), YZ (milieu) et 3D (droite). Valeurs max. 9.7×10^{9} s^{-1}.

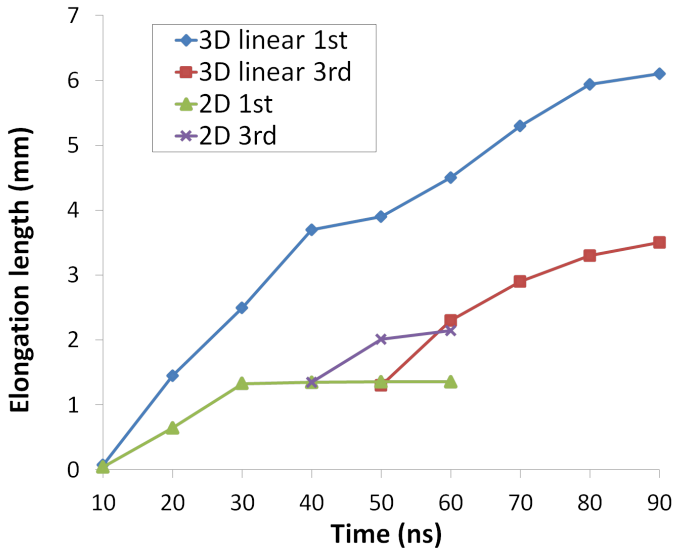

Figure A.8: Distance parcourue dans le x - axe vs temps - polarisation linéaire.

Polarisation circulaire

Le domaine de calcul pour ce paragraphe, est une boite de $2\lambda \times 1,5\lambda 2\lambda$. Les conditions initiales sont identiques au paragraphe précédent, à l'exception de la condition de l'onde incidente. Nous considérons ici une polarisation circulaire. Dans la figure A.9, la densité électronique est tracée en fonction du temps sur le plan XY (centrée sur le z - direction). Sous une telle polarisation, le plasma n'a pas de sens préférable d'allongement et donc, les structures filamenteuses de plasma forment comme des disques circulaires, avec

des profils presque identiques aux plans XY et XZ.

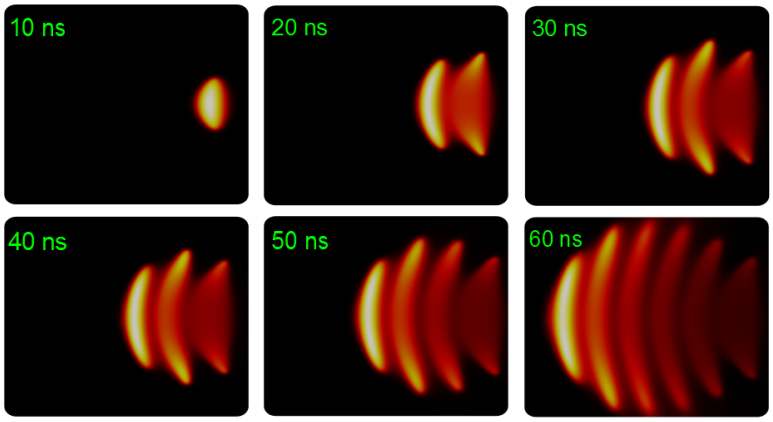

Figure A.9: Densité électronique vs temps, plan XY. Valeurs max. 2.79×10^{21},3.6×10^{21}, 3.34×10^{21}, 3.2×10^{21}, 3×10^{21}, 2.83×10^{21} m^{-3} respectivement.

Figure A.10, montre les contours de densité d'électrons sur une iso-surface de 3×10^{20} m^{-3} colorée par la fréquence d'ionisation efficace à $t = 60$ ns pour les plans XY et YZ. La décharge de plasma prend une forme d'un motif en forme de champignon. Les structures discoïdes ont des sections transversales circulaires d'un diamètre maximum d'environ 0,75 λ.

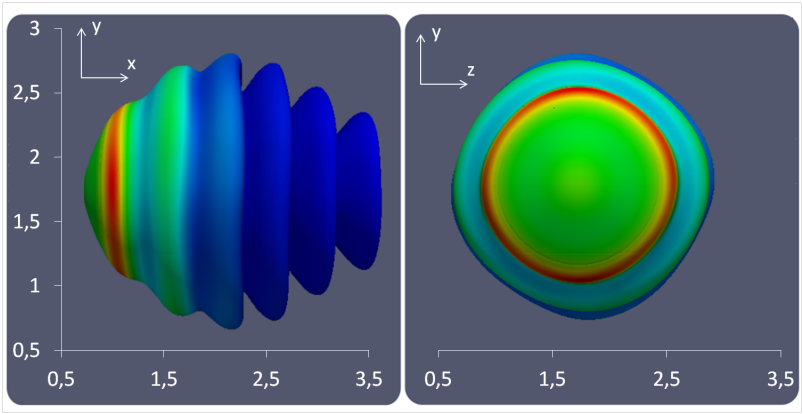

Figure A.10: Iso-surfaces (3×10^{20} m^{-3}) contours de la densité électronique colorés par la fréquence d'ionisation, Valeurs max. 1.7×10^{9} s^{-1}.

La vitesse de propagation du front de plasma est constante et atteint des valeurs de 54 km / s. Dans la figure A.11, la distance parcourue par le front de plasma dans le x - direction est tracée en fonction du temps. A titre de comparaison sur le même graphe, les résultats obtenus dans le cas polarisée linéaire sont également représentées.

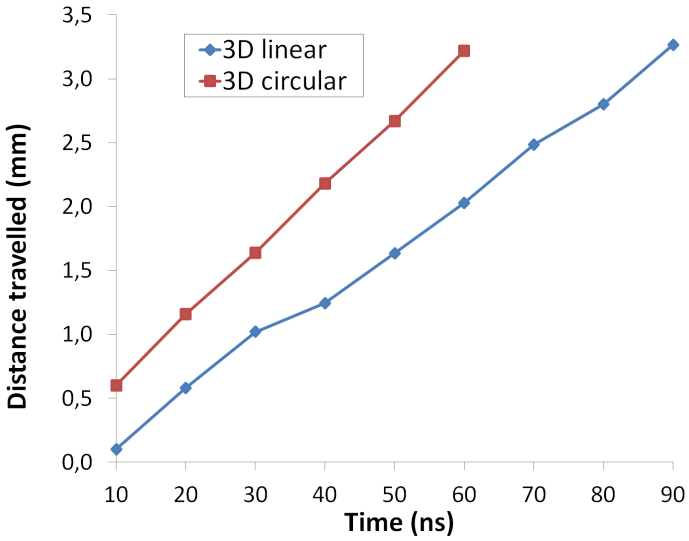

Figure A.11: Distance parcourue dans le x - axe vs temps.

Effets de chauffage au développement d'un plasma-streamer

Dans une décharge micro-ondes librement localisée, les effets de résonance sont supposés jouer un rôle important sur le développement et l'allongement du streamer. Les auteurs de [10], mentionne que la croissance de plasma-streamer est limitée par la longueur de résonance, typiquement $\lambda/2$ pour une antenne dipôle. L'explication d'un tel comportement est pas clair, car les effets de résonance normalement conduisent à des valeurs plus élevées de champ accrue au niveau des pôles du plasma, et des vitesses d'ionisation et d'allongement ainsi plus forts. Ceci est démontré numériquement dans [11].

En réalité, le plasma-streamer absorbe de grandes quantités d'énergie électromagnétique, conduisant à un chauffage du gaz rapide. Dans la plupart des approches expérimentales, théoriques et numériques, les effets de chauffage au gaz ne sont pas prises en compte. Ces effets non-linéaires peuvent fournir des informations importantes sur ces paramètres et donc, des simulations numériques couplées sont nécessaires
.

Dans cette section, nous présentons des simulations numériques en deux dimensions de répartition et de l'évolution d'une seule plasma streamer librement localisée en prenant en compte les effets de chauffage du gaz. Dans les schémas A.12 et A.13, la structure de la procédure numérique est présente.

Nous envisageons un domaine prolongé dans le direction y et mêmes conditions initiales comme dans figure A.1 sauf que ici on considere une onde stationnaire d'intensité maximale de 5 MV/m ($E_0 = 2,5MV/m$ pour chaque onde plane). Le plasma initial est placé au centre du domaine. Le coefficient de recombinaison est supposée constante et égale à 3×10^{-14} compatibles avec les données fournies dans [12]. L'allongement du streamer dans la direction du champ électrique est continue dans le temps. Dans la figure A.14, la densité du plasma à des temps différentes peut être observée.

La longueur du streamer, atteint la longueur de résonance de $\lambda/2$, à environ 100 ns et continue de croître (figure A.15). À 210 ns, la longueur a atteint environ la longueur d'onde λ des ondes électromagnétiques (2,7

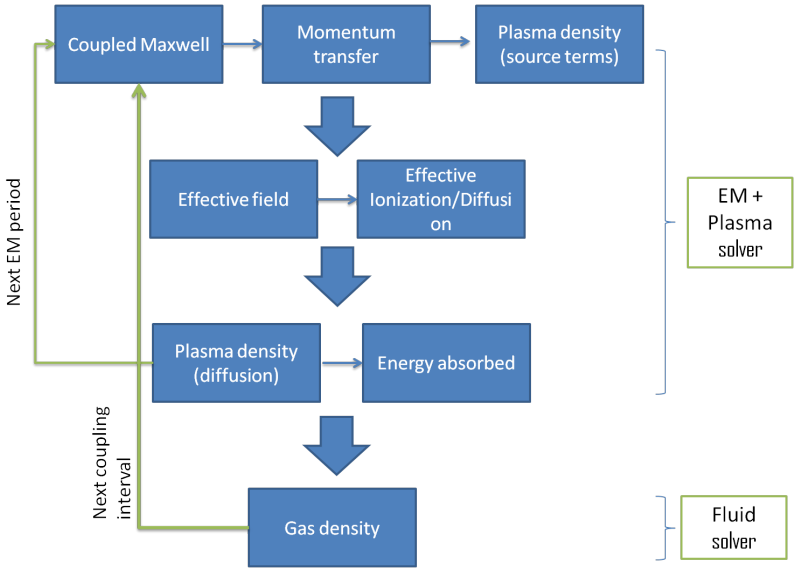

Figure A.12: Couplage entre les solveurs.

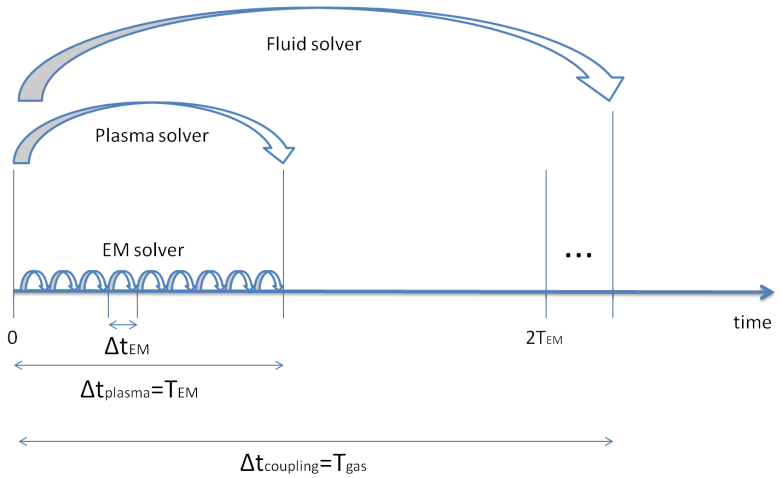

Figure A.13: Processus en temps.

mm dans ce cas). Sous une telle configuration d'onde plane idéalement symétrique, le plasma a aucune raison d'arrêter l'élongation.

Nous conservons les conditions de simulation décrites dans le paragraphe précédent, et on couple le solveur EM-plasma avec le solveur Euler à chaque 1 ns: l'énergie absorbée par le plasma , est introduit comme un terme source dans les équations Euler, simulant le chauffage de l'air et la formation de choc qui en résulte. Puis le champ de densité est injecté dans le solveur plasma - EM pour recalculer les coefficients de transport de plasma avec la densité de gaz modifiée.

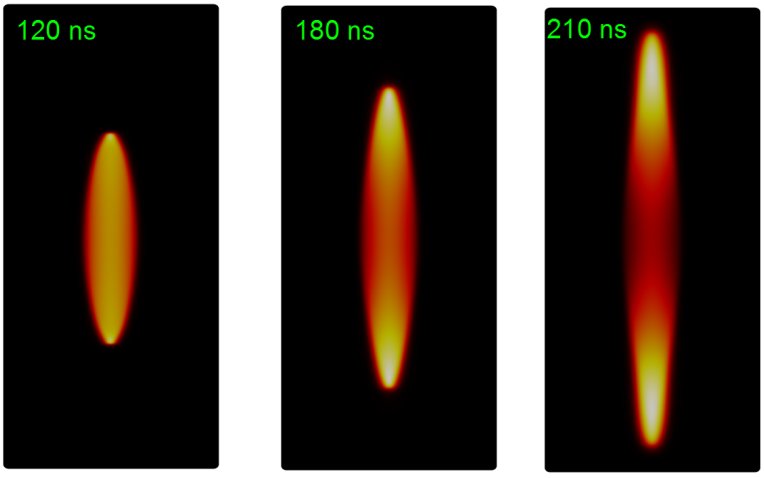

Figure A.14: Densité électronique vs temps. Valeurs max. 2.1×10^{21},1.9×10^{21}, 2.2×10^{21} m^{-3} respectivement.

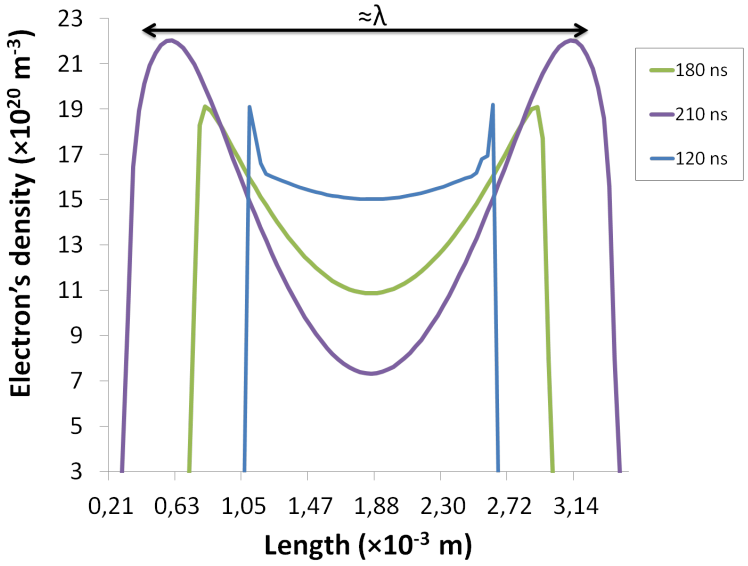

Figure A.15: Densité électronique vs distance.

Nos simulations montrent que à un moment plus de 100 ns, les effets de chauffage au gaz ne peuvent pas être négligés car ils conduisent à une modification substantielle du comportement du plasma. Dans la figure A.16, les contours de la densité du plasma sont tracées pour différents instants.

Pour des temps inférieurs à 100 ns, le chauffage du gaz est peu intense et la température maximale du

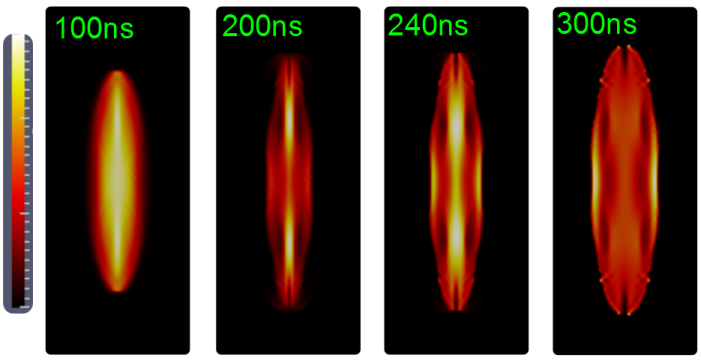

Figure A.16: Densité électronique vs temps. Valeurs max. 2.7×10^{21},8×10^{21}, 5.8×10^{21} et 5.7×10^{21} m^{-3} respectivement.

gaz atteint des valeurs de 400 à 500 K. Dans les temps plus long, une onde de choc de pression est formé, dont l'intensité augmente à mesure que plus d'énergie est absorbée par le gaz (voir figure A.17). A noter que la densité du gaz dans toutes les figures, est représentée comme une fraction de la densité ambiante initiale, $\rho_{amb} = 1,184\ kg/m^3$ à $T = 300K$ L'onde de choc limite la croissance de plasma et la diffusion dans une

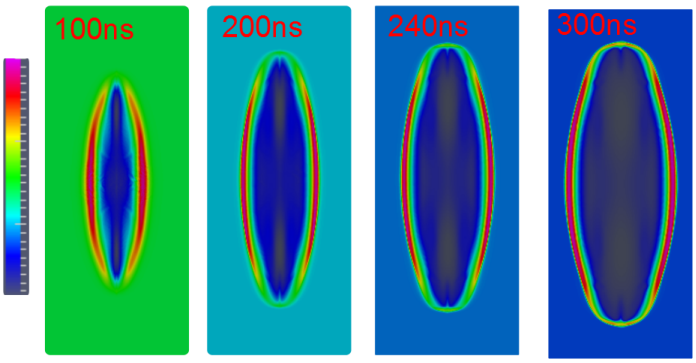

Figure A.17: Densité du gaz vs temps, plan XY. Valeurs max. 1.138,2.48, 3.25 and 3.94 $\times\rho_{amb}$ respectively. Valeurs min. 0.88, 0.319, 0.223 et 0.162 $\times\rho_{amb}$ respectivement. $\rho_{amb} = 1.184\ kg/m^3$.

région mince à l'intérieur du noyau du streamer. Quand l'onde de choc qui entoure le plasma devient assez fort pour faire diminuer l'ionisation efficace dans les valeurs négatives, l'élongation du streamer s'arrête. Ceci est clairement démontré par la figure A.18. Même à un temps de 300 ns, la longueur du streamer ne dépasse pas la moitié de la longueur d'onde des ondes EM, et il reste à peu près constante pendant 100 ns.

Décharge maintenu due aux effets du chauffage par pré-ionisation

La création de zones de plasma chaud par micro-ondes dans l'air, nécessite comme nous avons vu un champ électrique qui est sur- critique. Dans [13], un laser femtoseconde a été utilisé pour pré-ioniser l'air dans une zone mince. Un champ de micro-ondes sous-critique a été couplé à la zone de pré-ionisation, ce qui

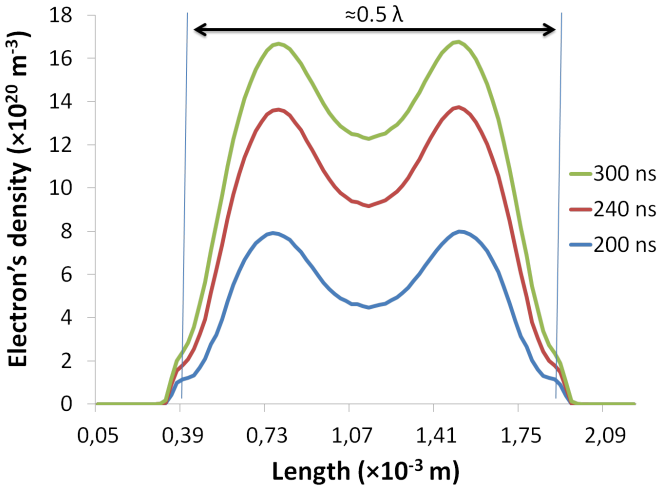

Figure A.18: Densité électronique vs distance.

démontre que le plasma de départ peut être non seulement maintenue, mais également propagée comme une décharge-streamer. Ces résultats expérimentaux, sont d'un intérêt extrême, comme le plasma semble suivre la population d'électrons initiale due au laser, même si sa direction n'est aligné à la polarisation du champ électrique [14]. Cela pourrait être un moyen efficace de créer des décharges de plasma lointaines, localisée et facilement contrôlables. Le même groupe d'auteurs, ont utilisé un modèle numérique simplifié de démontrer qu'une région pré-ionisé peut être maintenue en raison de sources MW sous-critiques, même si le champ incident est 50 % du champ critique .

L'objectif de cette section est, pas la reproduction exacte des résultats expérimentaux, mais plutôt l'obtention de certains résultats qualitatifs qui permettront de démontrer dans un premier temps, la capacité des champs micro-ondes sous-critiques à provoquer le claquage de plasma dans l'air, lorsqu'il est couplé avec une région de forte densité électronique. Ce résultat peut être la base pour de futures études paramétriques sur les limites exactes de cette application. Nous considérons une densité d'électrons de $10^{22}\ m^{-3}$ (distribution gaussienne centrée dans le domaine de calcul) qui coïncide avec la valeur utilisée dans [13]. Le pas de maillage est λ / 800 et le nombre CFL 32. Afin d'avoir des résultats comparables avec les cas étudiés précédemment nous avons utilisé de nouveau une fréquence des ondes EM de110 GHz. Le champ incident est réglé à 1,1 MV / m, ce qui correspond à un champ de l'onde stationnaire de 1,55 MV / m en RMS. Nous acceptons le champ critique expérimentalement calculé dans [13], de 3 MV / m pour déterminer cette valeur à 52 % du champ de claquage E_b. Si nous négligeons les effets de chauffage au gaz, la population d'électrons initial se attache rapidement et le plasma est disparu. En réalité, le plasma chauffe l'air, et le plasma est non seulement soutenue mais se transforme en un streamer, allongeant dans la direction du champ électrique tout comme nous l'avons vu dans les simulations avec de champs surcritiques. Dans la figure A.20, la densité de plasma est présenté pour les différents instants de temps.

Au début des temps, les électrons initiales sont diffusées et attachés comme le chauffage du gaz a pas atteint des valeurs critiques pour l'ionisation de surmonter l'attachement. Cela commence à avoir lieu à des moments de plus de 450 ns. Puis la densité du plasma commence à augmenter jusqu'à des valeurs proches

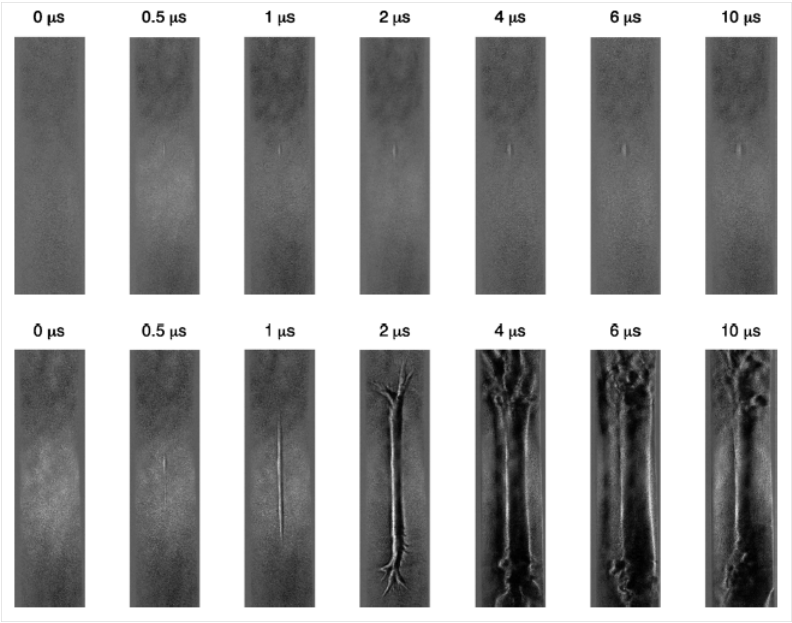

Figure A.19: . Images Schlieren dans l'air [13]. En haut : Pas de couplage avec EM. En bas : Couplage et formation d'un streamer.

de "cut-off". Le champ est alors renforcée au bout de plasma, tout comme le streamer microondes dans les sections précédentes. La température du gaz augmente rapidement à partir de 450 K à plus de 3000 K à $t = 600ns$ (figure A.21). La formation du streamer et la forte interaction avec l'onde de choc qui limite son expansion et l'augmentation de l'ionisation (et donc l'absorption de l'énergie) au niveau des extrémités du plasma, conduit à une augmentation extrême de la température du gaz qui dépasse 4000 K à 700 ns.

Des études paramétriques ont été réalisées avec différentes puissances incidents, afin d'enquêter sur la limite d'un champ sous-critique qui peut être utilisé pour créer et maintenir un plasma dans une région pré-ionisé. Nos études ont montré qu'un champ inférieur à 1 MV / m, ne peut pas maintenir une décharge de plasma dans nos conditions de simulation.

Conclusion

Un modèle numérique a été développé pour décrire la formation et l'évolution de décharges micro-ondes en fonction d'un modèle de plasma fluide simplifié et couplé avec les équations de Maxwell qui décrivent le comportement de propagation des ondes électromagnétiques. Ce couplage a été réalisé par le terme courant d'électrons et une équation de mouvement simplifiée. Afin d'étudier les décharges micro-ondes dans un niveau plus précis, le code numérique a été développé en trois dimensions. Un couplage implicite pour des équations basé sur le schéma ADI pour les équations de Maxwell, a été développé, permettant une réduction du temps de calcul. Des expériences numériques sur la précision et la réduction du temps de calcul ont été effectuées, ce qui démontre l'efficacité de la méthode proposée notamment pour les maillages très raffinés. Ensuite, nous avons étudié la formation de structures dans les décharges librement localisées, en trois dimensions, et les comparé avec des résultats expérimentaux. Ces simulations démontrent clairement,

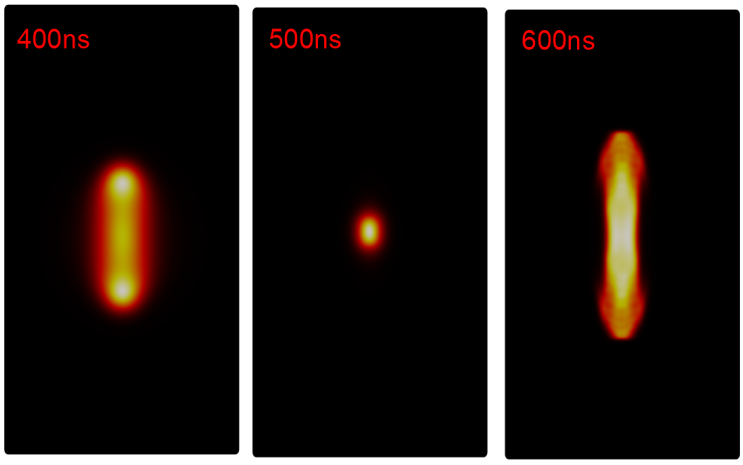

Figure A.20: Densité électronique vs temps pour $E = 52\%E_b$. Valeurs max 1.5×10^{18}, 7.6×10^{20} et 2.9×10^{21} m^{-3} respectivement.

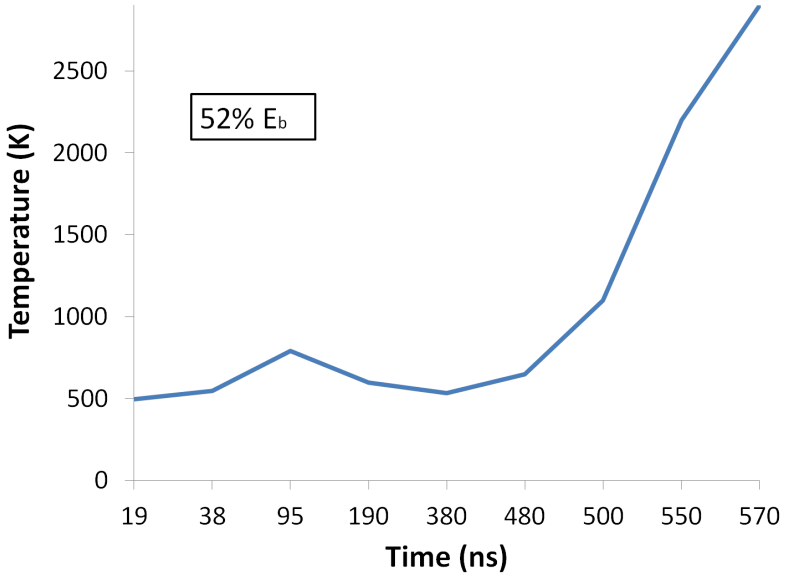

Figure A.21: Température du gaz pour $E = 52\%E_b$.

les effets tridimensionnels de ces décharges de plasma, qui ne peuvent pas être négligés si des calculs précis du volume occupé par le plasma et de l'absorption de chaleur (liée à la densité d'électrons) sont nécessaires - comme cela est le cas pour les applications de dépôt d'énergie pour le contrôle d'écoulement. En outre, les effets de chauffage du gaz ont été étudiés, par le couplage du solveur numérique avec un solveur Euler

compressible en tenant compte des effets des gaz réels. Les résultats de ces simulations, montrent très clairement que l'évolution des décharges micro-ondes comprend une interaction complexe entre les différents phénomènes physiques: le chauffage de gaz intense en raison de l'absorption d'énergie électromagnétique par effet Joule, conduit à un changement de la densité du gaz initial et donc un changement dans les coefficients de transport de plasma. En outre, en vertu d'une onde électromagnétique stationnaire, le développement d'un plasma-streamer arrête à longueurs à proximité de sa longueur de résonance. Ce phénomène, observé expérimentalement par différents auteurs, mais pas expliqué correctement, est due à la formation de l'onde de choc due à l'échauffement rapide du gaz , et la conséquente baisse de la fréquence d'ionisation dans la zone de l'onde de choc. En outre, nous avons étudié la possibilité d'utiliser les champs sous-critiques pour soutenir et développer une zone pré-ionisé (par laser par exemple). En effet, comme cela a été observé dans des expériences, une décharge plasma micro-ondes ne peut pas seulement être maintenue mais également allongée dans la direction du champ électrique formant un streamer. Cet effet est dû à l'absorption d'énergie initiale de la zone de plasma dense et le chauffage du gaz - conduisant à un champ effectif réduit dans le noyau de la zone de plasma initial qui est surcritique et donc l'ionisation devient dominante.

Références Bibliographiques

[1] Jean-Pierre Boeuf, Bhaskar Chaudhury, and Guo Qiang Zhu. “Theory and of self-organization and propagation of filamentary plasma arrays in microwave breakdown at atmospheric pressure”. In: *Physical review letters* 104.1 (2010), page 015002.

[2] Joseph T Mayhan and Ronald L Fante. “Microwave Breakdown Over a Semi-Infinite Interval”. In: *Journal of Applied Physics* 40.13 (1969), pages 5207–5211.

[3] Larry K Warne, Roy E Jorgenson, and Scott D Nicolaysen. “Ionization coefficient approach to breakdown in nonuniform geometries”. In: *Sandia Report SAND2003-4078* (2003).

[4] Jongwoo Lee and Bengt Fornberg. “Some unconditionally stable time stepping methods for the 3D Maxwell’s equations”. In: *Journal of Computational and Applied Mathematics* 166.2 (2004), pages 497–523.

[5] Kane S Yee et al. “Numerical solution of initial boundary value problems involving Maxwell’s equations in isotropic media”. In: *IEEE Trans. Antennas Propag* 14.3 (1966), pages 302–307.

[6] Theng Huat Gan and Eng Leong Tan. “Stability and dispersion analysis for three-dimensional (3-D) leapfrog ADI-FDTD method.” In: (2012).

[7] Philip L Roe. “Approximate Riemann solvers, parameter vectors, and difference schemes”. In: *Journal of computational physics* 43.2 (1981), pages 357–372.

[8] Alan M Cook et al. “Observation of plasma array dynamics in 110 GHz millimeter-wave air breakdown”. In: *Physics of Plasmas (1994-present)* 18.10 (2011), page 100704.

[9] Yoshiteru Hidaka et al. “Plasma structures observed in gas breakdown using a 1.5 MW, 110 GHz pulsed gyrotrona)”. In: *Physics of Plasmas (1994-present)* 16.5 (2009), page 055702.

[10] AL Vikharev et al. “Formation of the small-scale structure in a microwave discharge in high-pressure gas”. In: *Soviet Journal of Plasma Physics* 18.8 (1992), pages 554–560.

[11] Bhaskar Chaudhury et al. “Physics and modelling of microwave streamers at atmospheric pressure”. In: *Journal of Applied Physics* 110.11 (2011), page 113306.

[12] Mario Capitelli et al. *Plasma kinetics in atmospheric gases*. Springer, 2000.

[13] JB Michael et al. “Subcritical microwave coupling to femtosecond and picosecond laser ionization for localized, multipoint ignition of methane/air mixtures”. In: *Journal of Applied Physics* 108.9 (2010), page 093308.

[14] James B Michael, Matthew R Edwards, and Richard B Miles. “Time-resolved temperature measurements of laser-designated, microwave driven ignition”. In: *AIAA 2011 - 1020* (2011).

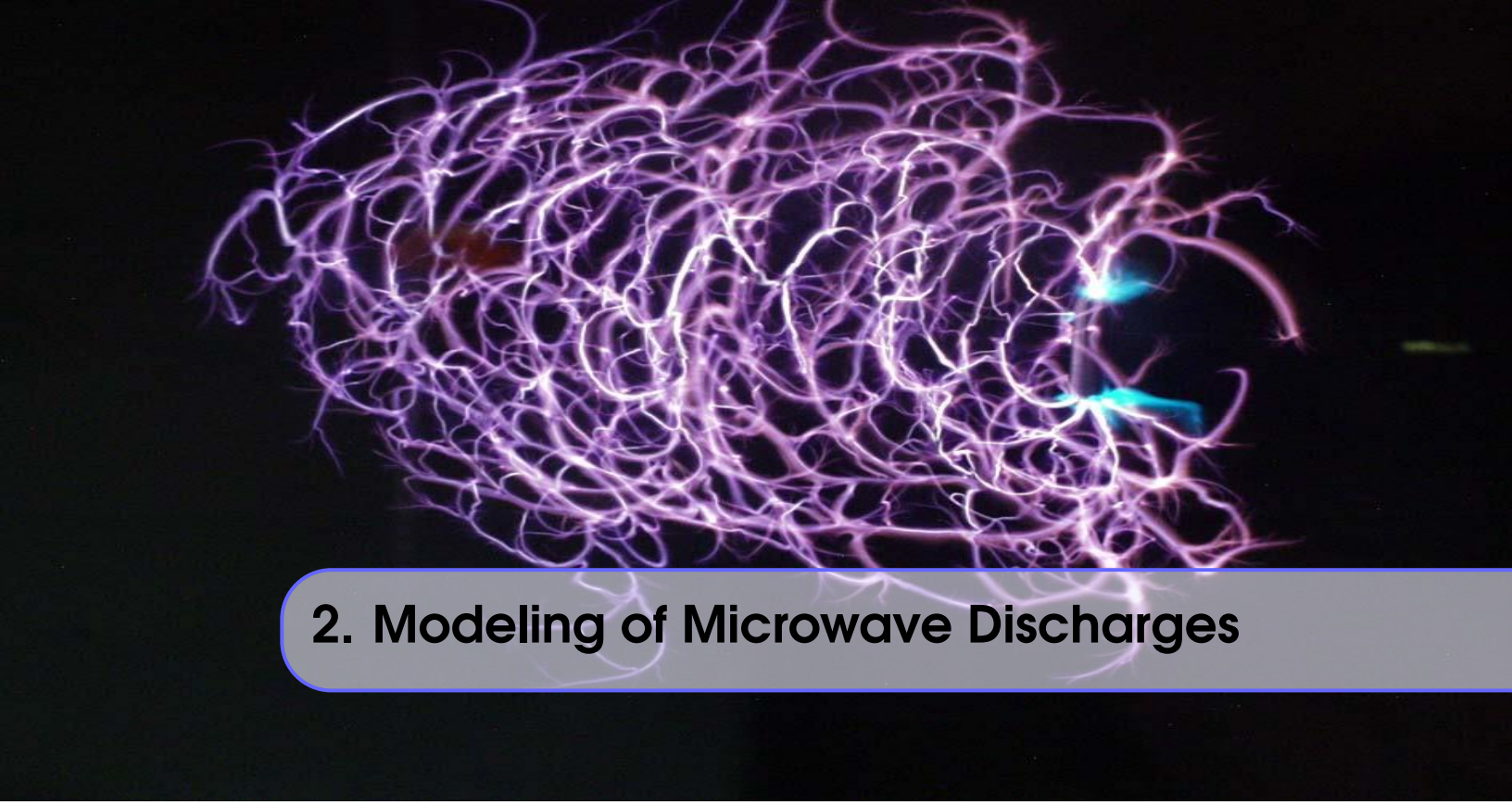

2. Modeling of Microwave Discharges

2.1 Presentation

Plasma formation due to an intense electromagnetic field in the microwave range can play an important role in a large variety of applications including antennas and waveguides. As we have seen, in the aerospace field, methods for energy addition in the flow have been suggested as promising for flow control applications and improved aerodynamic coefficients. Focusing on the latter, the highly efficient absorption of microwave energy by the plasma under some conditions place such discharges on the top of the research interest. Plasma breakdown can be caused by a local enhancement of the electric field due to a geometrical feature or by a focusing of the waves to a small volume. A detailed description of the different regimes of a microwave plasma according to pressure and electric field can be found in [1]. In [2], the authors provide an extensive study on experimental, theoritical and numerical approaches to understand how energy deposition can lead to aerodynamic drag at high speed. In [3], numerical simulations of energy deposition via a plasma column in front of a bulk body in a Mach 3 flow have been performed. The high temperature-low density zone created by the plasma interacts with the external flow leading to a less intense shock wave in front of the bulk body and thus a reduction to its drag coefficient. Experiments in [4, 5] and numerical results in [6] demonstrate the positive effects of microwave discharges on the aerodynamic coefficients of a bulk body inside a supersonic flow. In subsonic flow conditions, the authors in [7] have performed numerical and experimental studies of initiated microwave discharges over a cylinder and an airfoil, demonstrating that the energy addition inside a boundary layer flow, leads to the production of vorticity that can be used as means of boundary layer flow control. Indeed they have shown that the aerodynamic coefficients of an airfoil can be improved, in terms of stall angle and lift enhancement, due to an array of microwave discharges acting in a small height from the airfoil's surface.

Photo by MRTI, Russia

Although such experiments and numerical simulations are promising, the interaction between the microwave field, the plasma and the gas is crucial to understand the exchange of energy between them as well as the volume that the plasma will eventually occupy. **The objective of this chapter lies thus, in a more fundamental level of research than the actual application of such type of plasma discharges for flow control applications. We are interested in creating a simplified numerical model, accurate and of reduced computational cost, in order to study these complex, non-linear interactions and provide more physical insights of the nature of microwave discharges, serving as a basis for future analysis and understanding of the latter. Such simulations, are they key for the understanding of the underlying physics in microwave discharges, as experiments are costly and provide limited quantitative information. Moreover, numerical simulations of systems like this, demand either extensive resources or complicated techniques. This is the reason why, as we will see below, in the literature there are just a few numerical efforts of describing the evolution of microwave discharges in time. Therefore, the development of physical models that are simplified and in the same time retain the main physics involved and numerical models that can efficiently solve the system of equations, is by itself a highly demanding task - a task though, that's essential in order to achieve progress in the concept of microwave discharges and consequently their potential application in aerospace flow control techniques.**

As mentioned, a few numerical studies exist on this problematic. Recently, two dimensional simulations of microwave breakdown under atmospheric pressure based on explicit Finite Difference Time Domain (FDTD) methods have been reported in [8, 9] using a simplified physical model that was proved to reproduce quite well experimental data obtained by [10, 11, 12]. Nevertheless, the CPU cost of these simulations was too high, making three dimensional applications almost impossible. The huge computational cost arises from the following facts : under high pressure microwave breakdown the plasma density gradients can be so large that a very fine grid is necessary to accurately capture the characteristic length scales of the problem. As reported in [13], for a $110GHz$ microwave field the grid spacing has to be 10^3 times smaller than the wavelength. We remind here that a FDTD simulation with a grid spacing of $\lambda/30$ is sufficiently accurate. As the explicit FDTD method is being restrained by the CFL criterion, the time step of the simulation is linked to the space step. Having in mind that the plasma characteristic time is large enough so that the plasma can be updated each period of the EM waves, it is easily understood that the CFL criterion is a major drawback in such a coupled method and the CPU time could be significantly reduced by an implicit scheme, allowing for the passage to three dimensional simulations.

FDTD methods, dating back to 1980 [14], are the most popular numerical methods for solving electromagnetic problems in the time domain, making it suitable for simulating the time evolving interaction of microwaves with plasma. They present strong advantages compared to other time domain methods. They are simple to implement, versatile and robust, they allow for modeling of complex media and materials and they can be efficiently parallelized. Based on classical space and time integrating techniques, they can provide second order accuracy while being non-disipative [15]. Finite Volume Time Domain simulations is an alternative approach for solving the Maxwell equations, initially developed for fluid mechanics problems. They present a more complex structure for parallelization while they are dissipative, but in the other hand they deal efficiently with complex geometries and unstructured grids. A comparative study of FDTD and FVTD methods along with hybrid schemes can be found in [16]. The authors in [17], have used a FVTD technique coupled with a plasma-fluid model to study the shielding of a metallic aperture by the plasma generated by an incident high power electromagnetic wave. Higher order schemes such as Discontinuous Galerkin methods have also been proposed to accurately deal with electromagnetic propagation problems and non-linear coupling, although these methods present an increased complexity. In [18] an analysis of these methods for time domain electromagnetic problems is presented, while the authors in [19] used a

discontinuous Galerkin scheme for Particle In Cell (PIC) simulations to solve the Maxwell-Vlasov equations in time-domain. PIC simulations using a high-order discontinuous Galerkin Maxwell solver for plasma waves simulations have been perfomed in [20]. Concerning the EM waves and plasma coupling, different simplified or not numerical and theoritical approaches have been developed during the years. A self-consistent two dimensional plasma model to study a microwave plasma reactor can be found in [21] while high power microwave plasmas at atmospheric pressure have been numerically investigated in [22], using a FDTD approach coupled with a materialistic description of the plasma through its complex permittivity.

In this chapter, an original coupled Alternative Direction Implicit (ADI) - FDTD scheme with a simplified plasma-fluid model (a plasma model similar to the one originally proposed in [23]), is presented. This formulation retains the simplicity and robustness of the FDTD schemes, while surpassing the barrier of the CFL stability criterion, leading to a reduced computational time and the possibility for more realistic, three dimensional simulations of the plasma formation and evolution due to microwave fields. In order to study the energy absorbed by the plasma and transfer to the gas as heat and the consequent gas density change, an Euler solver has been coupled with the EM-Plasma model taking into account real gas effects. Various validation and application results are then studied, including three dimensional simulations of pattern formation in a freely localized microwave discharge, gas heating effects on microwave streamer development and sustainability of a pre-ionized volume with undercritical fields.
The organization of this chapter is as follows. In section 2.2, the physical and numerical models and techniques are presented. In section 2.3, firstly we present numerical experiments on the computational time and accuracy of the method. Then we present 2D numerical results of microwave breakdown and streamer formation under atmospheric pressure to validate the model, and we compare them with three-dimensional simulations. Our numerical code, provides for the first time the possibility to study the pattern formation and propagation of a microwave plasma under different incident polarization fields in three dimensions. Furthermore, the effect of gas heating is studied taking into account real gas effects. The elongation of a single plasma streamer is studied and its maximum length is linked to the shock wave formation due to the intense gas heating. Finally, we study also the possibility of using sub-critical fields to maintain a pre-ionised plasma discharge. In section 2.4 we conclude and give some perspectives.

2.2 Physical and numerical models

2.2.1 Physical model

The physical model consists of the Maxwell equations coupled with a simplified plasma fluid model via the electron current density. The Maxwell equations read for the Faraday's, Ampere's and Gauss' (for electrism and magnetism) laws respectively:

$$\nabla\times E+\mu\frac{\partial H}{\partial t}=0$$

$$\nabla\times H-\varepsilon\frac{\partial E}{\partial t}+J=0 \tag{2.1}$$

$$\nabla\cdot(\varepsilon E)-\rho=0 \tag{2.2}$$

$$\nabla\cdot(\mu H)=0 \tag{2.3}$$

where E and H are the electric and magnetic fields, ε and μ are the medium's permittivity and permeability, ρ is the charge density and J the total current density that can be approximated as :

$$J = \sigma E \tag{2.4}$$

where σ is the electrical conductivity.

The main assumptions of the model can be summarized as :

— The plasma is quasi-neutral since the Debye length is small with respect to the plasma size.
— The ion current density is much smaller than the electron current density and is neglected.
— The magnetic force is neglected as it is small in respect to the electric force.
— The distances traveled by the electrons due to collisions during a microwave period are small in respect to the length scale of field, pressure variations and cyclotron motion.
— Local field approximation : The energy gain from the electric field and collisional momentum are balanced with the energy losses, so that the ionization frequencies depend only on the local electric field E, or more precisely on the reduced electric field E/N (or E/p) since the collision frequency is proportional to the gas density N (or pressure p).

Under these assumptions, the total current density induced by a microwave plasma reads :

$$J = -en_e v_e \tag{2.5}$$

In equation 2.5, e, n_e, v_e are the electron charge, density and mean velocity respectively.

The instantaneous electron mean velocity in equation 2.5 is obtained from the simplified, local electron momentum transfer equation, which reads:

$$\frac{\partial v_e}{\partial t} = -\frac{eE}{m_e} - \nu_c v_e \tag{2.6}$$

where m_e is the electron mas and v_c the electron-neutral collision frequency given by [24] :

$$v_c = 5.3x10^9 p \tag{2.7}$$

where v_c is in s^{-1} and p is the pressure at ambient temperature in torr.

As the plasma is supposed to be quasi-neutral, the space and time variations of the plasma density are obtained from a simple diffusion equation that is averaged over a period of the microwave field:

$$\frac{\partial n_e}{\partial t} - \Delta(D_{eff} n_e) = \nu_{eff} n_e - r{n_e}^2 \tag{2.8}$$

The right hand side of the equation represents the charged particle production and losses. ν_{eff} is an effective electron impact ionization frequency including ionization and attachment, and r is the electron-ion recombination coefficient. ν_{eff} depends on the local electron distribution function and a usual approximation for microwave breakdown at high pressure is to assume that the electron distribution function averaged over a period has the same form as under a uniform field, but calculated for an effective field E_{eff} defined by:

$$E_{eff} = \frac{E_{rms}}{\sqrt{1 + \frac{\omega^2}{\nu_c^2}}} \tag{2.9}$$

We remind here that the mean work done by an AC electric field on an electron reads :

$$< -eEv >_{AC} = \frac{e^2 E_0^2}{2m(\omega^2 + \nu_c^2)} \nu_c \tag{2.10}$$

while for a DC field :

$$< -eEv >_{DC} = \frac{e^2 E_0^2}{m\nu_c} \tag{2.11}$$

Matching these equations, and replacing the field E_0 by the mean square field defined as $E^2 = E_0^2/2$, we obtain equation 2.9. Therefore, ν_{eff} is a function of the local effective field and the function $\nu_{eff}(E_{eff})$ is deduced from an analytical fit of experimental data. From the data in [25], it reads :

$$\begin{aligned}
\frac{\nu_{eff}}{p} &= v_d \alpha_{eff} = \mu_e E_{eff} \alpha_{eff} \\
\alpha_{eff} &= A_0 [e^{-B_0(p/E_{eff} - p/E_0) - 1}] \quad , \quad E_{eff}/p < 50 \\
\alpha_{eff} &= A_1 e^{-B_1(p/E_{eff})} \quad , \quad E_{eff}/p > 200 \\
\alpha_{eff} &= A_2 e^{-B_2(p/E_{eff})} \quad , \quad 50 < E_{eff}/p < 200
\end{aligned} \tag{2.12}$$

where v_d is the drift velocity, α is the effective ionization coefficient, $E_0/p = 31.25 V cm^{-1} T^{-1}$ is the critical field for which ionization balances attachment, $A_0 = 0.005\ cm^{-1}T^{-1}$, $E_0/p = 31.25\ V cm^{-1}T^{-1}$, $B_0 = 200\ V cm^{-1}T^{-1}$, $A_1 = 15\ cm^{-1}T^{-1}$, $B_1 = 365\ V cm^{-1}T^{-1}$, $A_2 = 8.805\ cm^{-1}T^{-1}$, $B_2 = 285.45\ V cm^{-1}T^{-1}$.

or from [24] in a more compact form:

$$\frac{\nu_{eff}}{p} = 4.9 \times 10^3 [(\frac{E_{eff}}{E_0})^{\beta} - 1] \tag{2.13}$$

where $\beta = 5.3$ and $E_0/p = 32 V cm^{-1} T^{-1}$. A general agreement for the values of the ionization frequency does not exist, and as referred to different papers in [24], various expressions are used. In this thesis, we use the expressions of [25] except if mentioned otherwise. A plot of $\nu_{eff}(E_{eff})$ is shown in figure 2.1.

The other transport coefficients of eq. 2.8, D_{eff} and r depends on the electron temperature T_e, which is also a function of the local effective field but can be considered as approximately constant and equal to 2 eV in the considered range of electric fields. The recombination coefficient is assumed to be constant and equal to zero, except if mentioned otherwise. The plasma diffusion is ambipolar in the bulk plasma. At the edge of the plasma where the plasma density becomes very low the diffusion is no longer ambipolar and the electrons diffuse freely. The transition from ambipolar to free diffusion is heuristically represented by the following form of the effective diffusion coefficient D_{eff} [23]:

$$D_{eff} = \frac{D_\alpha + \alpha D_e}{1 + \alpha} \tag{2.14}$$

where D_α, D_e are the ambipolar and electron diffusion coefficients respectively (defined below) and $\alpha = \nu_i \tau_M$ (where ν_i is the ionization frequency) and τ_M is the Maxwell relation time given by:

$$\tau_M = \frac{\varepsilon_0}{en(\mu_e + \mu_i)} \tag{2.15}$$

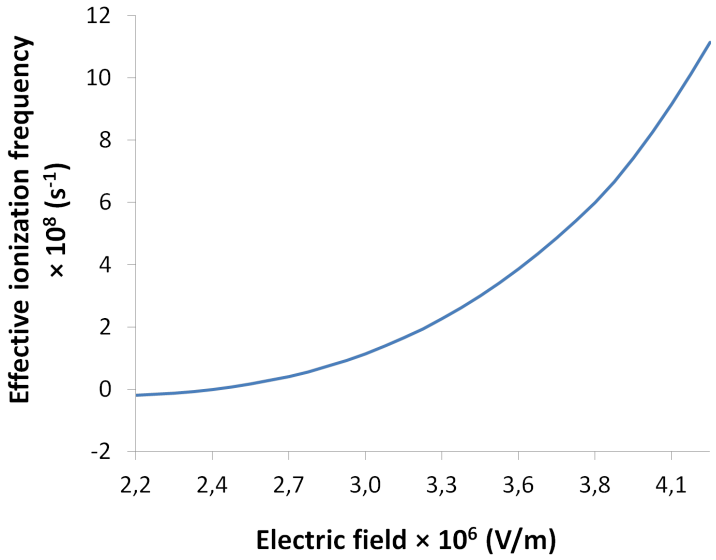

Figure 2.1: Effective ionization frequency versus effective electric field for constant pressure of 760 Torr.

This expression allows for correct evaluation of the plasma front speed as demonstrated in [23]. The free electron and ambipolar diffusion coefficients are given by $D_e = \mu_e \kappa_B T_e/e$ and $D_\alpha = \mu_i \kappa_B T_e/e$ respectively, where κ_B is the Botlzmann constant. The electron mobility μ_e is related to the electron-neutral collision frequency by $\mu_e = e/(m_e \nu_c)$ and we assume that $\mu_i = 0.5 \times 10^{-2} \mu_e$.

2.2.2 Numerical model and discretization

In this section, the numerical schemes and techniques used to simulate the interaction between the electromagnetic waves, the plasma and the gas will be described.

The Explicit FDTD Method for Solving the Maxwell Equations

The Finite-Difference Time-Domain method for solving numerically the Maxwell equations,introduced by Yee in 1966 [26]) still remains the most used computational solution approach in the field of electromagnetism. Briefly we can summarize the benefits of this method as:

1. Being a fully explicit computation, FDTD uses no linear algebra that limits the size of other methods of electromagnetic models(such as the frequency domain integral equation or the finite element model).
2. It is accurate and robust.
3. It treats impulsive and nonlinear behavior naturally, as a result of its time domain formation.
4. Its results can be easily post-treated and visualized.
5. Its memory capacities are increasing rapidly due to the general improvement of numerical techniques for mesh generation.

The FDTD method is based on the Yee algorithm that solves for both the electric and magnetic fields in time and space using the coupled Maxwell equations (as opposed to solving for the electric or magnetic field alone using a wave equation). These equations describe the Faraday's and Ampere's laws and in addition with the

two Gauss' Laws relations:

$$\nabla \cdot \vec{D} = \varepsilon \nabla \cdot E = 0 \tag{2.16}$$

$$\nabla \cdot \vec{B} = \mu \nabla \cdot H = 0 \tag{2.17}$$

describe the electromagnetic waves interaction and is the base of the Yee algorithm and space grid. These equations with or without electric or magnetic source terms will be the equations solved by the Yee algorithm for each component of a 3D, 2D or 1D domain while the 2 Gauss' laws that indicate zero free electric and magnetic charge will be treated implicitly in the Yee space lattice because they are consequence of the curl equations.

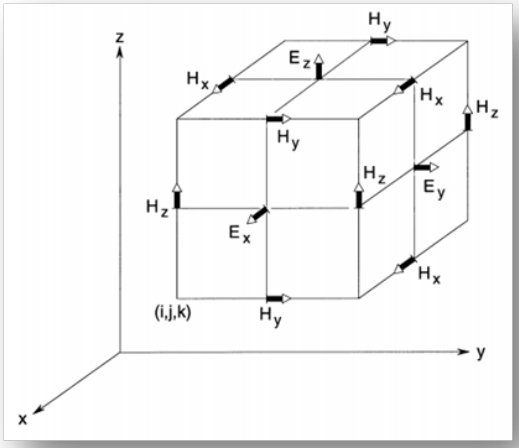

Figure 2.2: The 3D Yee space lattice

For simplicity the Maxwell equations read in two dimensions :

$$\varepsilon_0 \cdot \frac{\partial E_x}{\partial t} = \frac{\partial H_z}{\partial y} \tag{2.18}$$

$$\varepsilon_0 \cdot \frac{\partial E_y}{\partial t} = -\frac{\partial H_z}{\partial x} \tag{2.19}$$

$$\mu_0 \cdot \frac{\partial H_z}{\partial t} = \frac{\partial E_x}{\partial y} - \frac{\partial E_y}{\partial x} \tag{2.20}$$

The finite-difference expressions for the space derivatives used in the curl operators of the coupled Maxwell equations are central difference in nature and second order accurate. If we denote a space point in a two dimensional (for simplicity) uniform rectangular lattice as $(i, j) = (i\Delta x, j\Delta y)$, any function u of space and time evaluated at a discrete point in the grid and at a discrete point in time as $u(i\Delta x, j\Delta y) = u^n_{i,j}$ will have an expression for the first partial space derivative in the x (for example) direction at a fixed time, in the form:

$$\frac{\partial u}{\partial x}(i\Delta x, j\Delta y, n\Delta t) = \frac{u^n_{i+1/2,j} - u^n_{i-1/2,j}}{\Delta x} + O\left[(\Delta x)^2\right] \tag{2.21}$$

noting that a +1/2 or -1/2 increment in the i subscript denotes a space finite-difference over $1/2\Delta x$.

For the time treatment of the Maxwell equations, the Yee algorithm uses a leapfrog arrangement, which centers the E and H components in time as it does for space. The leap-frog time stepping is a fully explicit scheme and non-dissipative which means that numerical waves modes that propagate in the mesh do not face a nonphysical dissipation due to the time stepping algorithm. The E components are computed and stored in the memory using previously stored H data. Then the H components are being calculated using the E data that are available now in the memory. This cycle goes on and on until the time stepping is concluded. The time derivatives in the FDTD method are central difference again in nature and second order accurate. The first partial derivative of a function u at a fixed space point, takes the form:

$$\frac{\partial u}{\partial t}(i\Delta x, j\Delta y, n\Delta t) = \frac{u^{n+1/2}_{i,j} - u^{n-1/2}_{i,j}}{\Delta t} + O\left[(\Delta t)^2\right] \tag{2.22}$$

noting again that a +1/2 or -1/2 increment in the n subscript denotes a time finite-difference over $1/2\Delta t$.

Now that we have the finite difference expressions in space and time, the two dimensional Maxwell equations can be written in their discretized form as:

$$E_x|^{n+1}_{i,j} = E_x|^n_{i,j} + \frac{\Delta t}{\varepsilon_0 \Delta x} H_z|^{n+1/2}_{i+1,j} - \frac{\Delta t}{\varepsilon_o \Delta x} H_z|^{n+1/2}_{i,j} \tag{2.23}$$

$$E_y|^{n+1}_{i,j} = E_y|^n_{i,j} - \frac{\Delta t}{\varepsilon_0 \Delta z}(H_z|^{n+1/2}_{i,j} - H_z|^{n+1/2}_{i,j-1}) \tag{2.24}$$

$$H_z|^{n+1/2}_{i,j} = H_z|^{n-1/2}_{i,j} + \frac{\Delta t}{\Delta x \mu_0}(E_x|^n_{i+1,j} - E_x|^n_{i,j}) - \frac{\Delta t}{\Delta x \mu_0}(E_y|^n_{i,j+1} - E_y|^n_{i,y}) \tag{2.25}$$

for a TE wave, for vacuum as medium where $\varepsilon = \varepsilon_0$ and $\mu = \mu_0$ and lossless material $\sigma = 0$.

Boundary Conditions

As the computational domain has to be limited due to memory needs, the numerical scheme previously described needs boundary conditions that will describe the extension of the field to infinity. We need boundary conditions that will permit the numerical waves to exit the domain as if the simulation was performed in a computational domain of infinite extend and will prevent reflective numerical waves to enter the domain and modify the field. This type of boundary conditions are called Absorbing Boundary Conditions (ABC). During the years, various types of ABCs have been developed providing first or higher order accuracy. A first order absorbing boundary condition is given by the so-called Silver Muller (SM) radiation condition [27] which is

based on the Sommerfield's radiation condition [28]. The SM ABC reads for the tangent plane of a boundary Γ :

$$\begin{aligned} \vec{n} \times (n \times H) &= \sqrt{\frac{\varepsilon_0}{\mu_0}} n \times (E \times n) \\ \vec{n} \times (n \times E) &= \sqrt{\frac{\mu_0}{\varepsilon_0}} n \times (H \times n) \end{aligned} \tag{2.26}$$

where n is the outer unit normal to the boundary and $n \times (E \times n)$, $n \times (H \times n)$ are the tangential electric and magnetic fields on the boundary. Such boundary condition is exact for electromagnetic plane waves that propagate normally to the boundary, which are being absorbed. The Engquist-Majda one way wave equation [29], provides another first order ABC with similar problems as the SM ABC : They require a non-dispersive wave with normal incidence. This is not practical for typical problems, such as scattering problems, which can have arbitrary angles of incidence on the exterior boundary. Based on this latter, Mur [30] has developed a second order accurate ABC which annihilates a normally incident wave highly accurately. However, for obliquely incident waves, large reflections can occur. While other boundary operators have been introduced to annihilate waves at multiple angles, their complexity and consequent computational cost becomes higher. In [31], the author has proposed a novel absorbing boundary condition called the Perfectly Matched Layer (PML) ABC. This ABC uses a an absorbing material layer in order to absorb outgoing waves. In order to be effective, both in computational cost and reduced reflection, this condition zone needs to have only a few lattice cells in thickness, be effective in the near field of source or scatterer and reflectionless to all impinging waves (polarization, angle). In [32, 33], the authors used an anisotropic lossy medium as the PML's medium. With this formulation, the waves are rapidly attenuated due to the lossy medium, while the medium is perfectly matched for any kind (in terms of polarization, angle of incidence or frequency) of electromagnetic waves impinging the PML boundary. Matching an anisotropic medium through the product with an uniaxial tensor leads to an uniaxial perfectly matched layer condition (UPML)(see [34]). In this thesis we are interested in the Convolutional Perfectly Matched Layer ABC which can be derived by posing the PML in stretched coordinates.

The Convolutional Perfectly Matched Layer ABCs

Following the work of [35], we pose the PML formulation in the stretched coordinate space. We define the stretched coordinate metrics as proposed by Berenger [36] :

$$s_i = 1 + \frac{\sigma_i}{j\omega\varepsilon_0}, \quad \text{i=x,y or z} \tag{2.27}$$

where $j^2 = -1$ is the imaginary unit.

Considering the half space problem as illustrated in figure 2.3 and assuming a time-harmonic arbitrarily polarized plane wave in the form $\vec{H}^{inc} = \vec{H}_0 e^{-jk_{1x}x - jk_{1y}y}$, where $\vec{k} = \hat{x}k_{1x} + \hat{y}k_{1y} = \hat{x}k_1 cos\phi^{inc} + \hat{y}k_1 sin\phi^{inc}$ and $k_1 = \omega\sqrt{\varepsilon_1\mu_1}$. The waves excited by the PML medium are plane waves that satisfy the Maxwell's curl equations :

$$\omega\mu_2\vec{H} = \vec{k}_2 \times E, \quad \omega\varepsilon_2\vec{E} = -\vec{k}_2 \times H \tag{2.28}$$

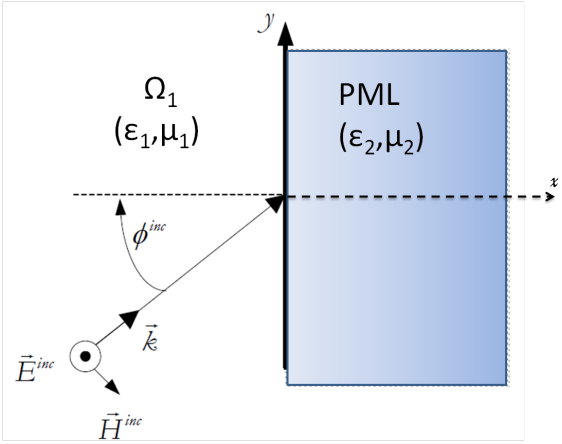

Figure 2.3: EM wave impinging a PML boundary.

Assuming now, a TE incident wave of the form :

$$\begin{aligned}
\vec{H}_1 &= \hat{z}H_0(1+\Gamma e^{2jk_{1x}x})e^{-jk_{1x}x-jk_{1y}y} \\
\vec{E}_1 &= [-\hat{x}\frac{k_{1y}}{\omega\varepsilon_1}(1+\Gamma e^{2jk_{1x}x})+\hat{y}\frac{k_{1x}}{\omega\varepsilon_1}(1-\Gamma e^{2jk_{1x}x})]H_0e^{-jk_{1x}x-jk_{1y}y}] \\
\vec{H}_2 &= \hat{z}H_0\tau e^{-jk_{2x}x-jk_{2y}y} \\
\vec{E}_2 &= [-\hat{x}\frac{k_{2y}}{\omega\varepsilon_2}+\hat{y}\frac{k_{2x}}{\omega\varepsilon_2 s_x}]H_0\tau e^{-jk_{1x}x-jk_{1y}y}]
\end{aligned} \tag{2.29}$$

At the interface field continuity implies that $k_{2y} = k_{1y}$ and so the dispersion relation reads $k_{2x} = s_x\sqrt{{k_2}^2 - {k_{1y}}^2}$. The tangential field continuity, allows us to solve for Γ and τ, which read:

$$\Gamma = \frac{k_{1x}/\varepsilon_1 - k_{2x}/(\varepsilon_2 s_x)}{k_{1x}/\varepsilon_1 + k_{2x}/(\varepsilon_2 s_x)}, \quad \tau = 1+\Gamma \tag{2.30}$$

We note that when $\varepsilon_2 = \varepsilon_1$ and $\mu_1 = \mu_2$, Γ becomes zero and $\tau = 1$. So a plane wave of arbitrary polarization and angle of incidence will be purely transmitted into the PML medium. Waves penetrating into the PML will have the spatial dependence along the normal axis:

$$e^{-jk_1 s_x x} = e^{-jk_{1x}s_x x}e^{-\sqrt{\varepsilon_{r1}\mu_{r1}}\eta_0\sigma_x cos\phi^{inc}x} \tag{2.31}$$

where $\eta_0 = \sqrt{\mu_0/\varepsilon_0}$ and σ_x has a spatially scaled profile (as proposed by Berenger to reduce the discretization error) in the form (for a polynomial scaling):

$$\sigma_x = \begin{cases} \frac{|x-x_0|^m}{d^m}\sigma_{xmax}, & x_0 \le x \le x_0+d \\ 0, & \text{otherwise} \end{cases} \tag{2.32}$$

So waves will attenuate along x-direction inside the PML region. Ending the computational domain with Perfect Electric Conductor (PEC) boundary conditions, reflected waves are again reflected in the PML

region. Extensive experimental studies [34] have demonstrated that for a 10 cell thick PML region, an optimal reflection error can be achieved with a $\sigma_{max} = (m+1)/(150\pi\sqrt{\varepsilon_r}\Delta x)$. Note that σ_x is zero at the interface at takes maximum values at the PEC wall.

By using the complex frequency shifted PML tensor, that reads :

$$s_i = \kappa_i + \frac{\sigma_i}{\alpha_i + j\omega\varepsilon_0}, \quad \text{i=x,y or z} \tag{2.33}$$

and by proper scaling of κ_i and α_i, evanescent and slowly varying waves can be efficiently attenuated too. κ_i is 1 inside the FDTD domain, while it takes values greater than one inside the PML region, following the scaling of σ_i. α_i has opposite scaling to these two terms, taking larger values at the interface of the two regions in order to reduce reflection of low frequency evanescent waves off the interface while it takes smaller values inside the PML region allowing for attenuation of low frequency propagating waves.

The discrete form of the CPML can be obtained by a transformation of the stretched forms equations to the time domain. For the sake of simplicity we consider only the x-projection of Ampere's law which reads :

$$j\omega\varepsilon_0 E_x = \frac{1}{s_y}\frac{\partial}{\partial y}H_z - \frac{1}{s_z}\frac{\partial}{\partial z}H_y \tag{2.34}$$

The frequency dependence of the stretched coordinate metrics results in a convolution, when transformed to the time domain. By using Laplace theory, it can be shown that the inverse laplacian transform of ${s_i}^{-1}$ has an impulse response that is analytically known due to its simple rational nature. A recursive convolution method [37] can be used to perform the convolution operation efficiently. Then, by introducing a set of auxiliary variables ψ_i, equation 2.34 reads in its discretized form in the time domain [34] and in three dimensions:

$$\begin{aligned} E_x|^{n+1/2}_{i,j,k} =& E_x|^{n-1/2}_{i,j,k} + \frac{\Delta t}{\varepsilon_0\Delta x}H_z|^{n}_{i+1,j,k} - \frac{\Delta t}{\varepsilon_o\Delta x}H_z|^{n}_{i,j,k} \\ & - \frac{\Delta t}{\varepsilon_0\Delta z}H_y|^{n}_{i,j,k+1} - \frac{\Delta t}{\varepsilon_o\Delta z}H_y|^{n}_{i,j,k} + \frac{\Delta t}{\varepsilon_o}(\psi_{exy}|^{n}_{i,j,k} - \psi_{exz}|^{n}_{i,j,k}) \end{aligned} \tag{2.35}$$

where the auxiliary variable are updated as :

$$\begin{aligned} \psi_{exy}|^{n+1}_{i,j,k} =& b_y\psi_{exy}|^{n}_{i,j,k} + c_y\frac{H_z|^{n+1}_{i+1,j,k} - H_z|^{n+1}_{i,j,k}}{\Delta y} \\ \psi_{exz}|^{n+1}_{i,j,k} =& b_z\psi_{exy}|^{n}_{i,j,k} + c_z\frac{H_y|^{n+1}_{i,j,k+1} - H_y|^{n+1}_{i,j,k}}{\Delta z} \end{aligned} \tag{2.36}$$

and b_i, c_i read :

$$\begin{aligned} b_i =& e^{-(\frac{\sigma_i}{\kappa_i}+\alpha_i)\frac{\Delta t}{\varepsilon_0}} \\ c_i =& \frac{\sigma_i}{(\sigma_i\kappa_i + {\kappa_i}^2\alpha_i)}(b_i - 1) \end{aligned} \tag{2.37}$$

The scheme is then second-order accurate and stable inside the Courant limit for all real values of σ_i, α_i and $\kappa > 1$.

Numerical dispersion and stability of the explicit FDTD method

The numerical non-physical dispersion introduced by the FDTD algorithms for the Maxwell's curl equations means that the phase velocity of a numerical wave can be different than the speed of light depending on various parameters. Assuming a three dimensional plane monochromatic traveling wave solution in the form of $U = U_0 e^{i(\omega n\Delta t - k_x\Delta x - k_y\Delta y - k_z\Delta z}$, where k denotes the numerical wavevectors in x, y and z directions, we can introduce such solution to equations 2.23 to obtain after some mathematical manipulations:

$$[\frac{1}{c\Delta t} sin(\frac{\omega\Delta t}{2})]^2 = [\frac{1}{\Delta x} sin(\frac{k_x\Delta x}{2})]^2 + [\frac{1}{\Delta y} sin(\frac{k_y\Delta y}{2})]^2 + [\frac{1}{\Delta z} sin(\frac{k_z\Delta z}{2})]^2 \tag{2.38}$$

This is the general dispersion relation of the explicit FDTD yee algorithm. We notice that when the space step size approaches zero equation 2.39, becomes the analytical (ideal) dispersion relation [34]:

$$(\frac{\omega}{c})^2 = k_x^2 + k_y^2 + k_z^2 \tag{2.39}$$

Furthermore, its is easy to notice that depending on the direction of propagation in the grid, the wavelength and the grid discretization the numerical dispersion varies, and proper choices of such parameters can lead to more accurate simulations.

It is convenient to write the dispersion relation more compactly as :

$$\frac{1}{c\Delta t} sin(\frac{\omega\Delta t}{2}) = \pm\kappa_n \tag{2.40}$$

where κ_n is the modulus of the numerical wave-vector that reads :

$$\vec{\kappa_n} = (\kappa_{nx}, \kappa_{ny}, \kappa_{nz}) \qquad\qquad \kappa_{n\alpha} = \frac{2}{\Delta\alpha} sin(\kappa_\alpha \frac{\Delta\alpha}{2}) \tag{2.41}$$

where α denotes x, y and z directions.

The explicit finite difference scheme used for the FDTD simulation has stability restrictions on the choices for the space and time increments. Observing the dispersion relation (equation 2.40) for the scheme we notice that the function that gives the numerical frequency ω is an inverse sine. The inverse sine function supports complex values with positive and negative imaginary parts and thus it is evident that the scheme is Von-Neumann unstable for such values. The numerical stability Courant condition (CFL) reads in three dimensions after a complex-frequency analysis [15]:

$$\Delta t \leq \frac{1}{c\sqrt{\frac{1}{(\Delta x)^2} + \frac{1}{(\Delta y)^2} + \frac{1}{(\Delta z)^2}}} \tag{2.42}$$

The CFL criterion for the Maxwell equations can be a huge drawback for simulations that include structures which need a highly refined numerical grid. In that case the time step of the simulation is limited for stability by the space-step and thus the computational cost of such simulations becomes prohibited, especially when dealing with 3D simulations.

Implicit Methods For Solving the Maxwell Equations

FDTD implicit schemes for solving the Maxwell equations have been recently developed by researchers, in order to reduce the computational resources needed by the classic explicit FDTD scheme. A review of such schemes can be found in [38].

Let us write the Maxwell equations, in three dimensions matrix form as :

$$\frac{\partial \vec{U}}{\partial t} = [C]\vec{U} \tag{2.43}$$

where $[C] = [A] + [B]$ and the matrices $[A]$ and $[B]$ read :

$$[A] = \begin{bmatrix} 0 & 0 & 0 & 0 & 0 & \frac{\partial}{\varepsilon_o \partial y} \\ 0 & 0 & 0 & \frac{\partial}{\varepsilon_o \partial z} & 0 & 0 \\ 0 & 0 & 0 & 0 & \frac{\partial}{\varepsilon_o \partial x} & 0 \\ 0 & -\frac{\partial}{\mu_o \partial z} & 0 & 0 & 0 & 0 \\ 0 & 0 & -\frac{\partial}{\mu_o \partial x} & 0 & 0 & 0 \\ -\frac{\partial}{\mu_o \partial y} & 0 & 0 & 0 & 0 & 0 \end{bmatrix}$$

$$[B] = \begin{bmatrix} 0 & 0 & 0 & 0 & -\frac{\partial}{\varepsilon_o \partial z} & 0 \\ 0 & 0 & 0 & 0 & 0 & -\frac{\partial}{\varepsilon_o \partial x} \\ 0 & 0 & 0 & -\frac{\partial}{\varepsilon_o \partial y} & 0 & 0 \\ 0 & 0 & \frac{\partial}{\mu_o \partial y} & 0 & 0 & 0 \\ \frac{\partial}{\mu_o \partial z} & 0 & 0 & 0 & 0 & 0 \\ 0 & \frac{\partial}{\mu_o \partial x} & 0 & 0 & 0 & 0 \end{bmatrix}$$

An unconditionally stable implicit scheme based on the Crank-Nicolson (C-N) time integration method has been proposed in [39] for 2D Maxwell equations and in [40] for 3D ones. Applying the C-N scheme at time $n+1/2$, we have:

$$\begin{aligned} &(Id - \frac{\Delta t}{2}[A] - \frac{\Delta t}{2}[B])\vec{U_{n+1}} = \\ &\quad (Id + \frac{\Delta t}{2}[A] + \frac{\Delta t}{2}[B])\vec{U_n} \end{aligned} \tag{2.44}$$

where I_d is the identity matrix. The use of the C-N FDTD, even though provides the benefit of unconditionally stability, requires iterative or splitting techniques for solving the inverse matrix problem, thus making it computationally expensive and complex.

In 1999, the authors in [41], have proposed a new FDTD algorithm based on an alternating-direction implicit method (ADI) and in [42] they have extended the method to three dimensions. They have proven its unconditional stability and its free from the Courant-Friedrich-Levy condition restraint nature. Applying the ADI scheme to equation 2.43, we have:

$$\begin{aligned} &(Id - \frac{\Delta t}{2}[A])(Id - \frac{\Delta t}{2}[B])\vec{U_{n+1}} = \\ &\quad (Id + \frac{\Delta t}{2}[A])(Id + \frac{\Delta t}{2}[B])\vec{U_n} \end{aligned} \tag{2.45}$$

with an obvious splitting error compared to C-N of $\frac{\Delta t^2}{4}[A][B](\vec{U_{n+1}} - \vec{U_n})$.

The ADI-FDTD scheme can be efficiently solved without the need of a sparse matrix inversion (opposed to the C-N scheme) by dividing the time step into two sub-steps and solving :

$$(Id - \frac{\Delta t}{2}[A])\vec{U_{n+1/2}} = (Id + \frac{\Delta t}{2}[B])\vec{U_n} \tag{2.46}$$

and

$$(Id - \frac{\Delta t}{2}[B])\vec{U_{n+1}} = (Id + \frac{\Delta t}{2}[A])\vec{U_{n+1/2}} \tag{2.47}$$

A simple mathematical manipulation of this ADI scheme can lead to an one-step Leap-Frog formulation in time as presented in [43], resulting in a reduction of the algorithm's computational time (see next sections).

The ADI-FDTD leapfrog scheme reads :

$$(I_d - [A])U^{n+1} = (I_d - [B])U^n \tag{2.48}$$

where the vectors U^{n+1} and U^n read:

$$\begin{aligned} U^{n+1} =& [E_x^{n+1/2}\, E_y^{n+1/2}\, E_z^{n+1/2}\, H_x^{n+1}\, H_y^{n+1}\, H_z^{n+1}]^T \\ U^n =& [E_x^{n-1/2}\, E_y^{n-1/2}\, E_z^{n-1/2}\, H_x^n\, H_y^n\, H_z^n]^T \end{aligned} \tag{2.49}$$

and the matrices $[A]$ and $[B]$ read:

$$[A] = \begin{bmatrix} \frac{\Delta t^2}{4\varepsilon_o \mu o}\partial_y^2 & 0 & 0 & 0 & 0 & 0 \\ 0 & \frac{\Delta t^2}{4\varepsilon_o \mu o}\partial_z^2 & 0 & 0 & 0 & 0 \\ 0 & 0 & \frac{\Delta t^2}{4\varepsilon_o \mu o}\partial_x^2 & 0 & 0 & 0 \\ 0 & \frac{\Delta t}{\mu_o}\partial_z & \frac{-\Delta t}{\mu_o}\partial_y & \frac{\Delta t^2}{4\varepsilon_o \mu o}\partial_y^2 & 0 & 0 \\ \frac{-\Delta t}{\mu_o}\partial_z & 0 & \frac{\Delta t}{\mu_o}\partial_x & 0 & \frac{\Delta t^2}{4\varepsilon_o \mu o}\partial_z^2 & 0 \\ \frac{\Delta t}{\mu_o}\partial_y & -\frac{\Delta t}{\mu_o}\partial_x & 0 & 0 & 0 & \frac{\Delta t^2}{4\varepsilon_o \mu o}\partial_x^2 \end{bmatrix}$$

$$[B] = \begin{bmatrix} \frac{\Delta t^2}{4\varepsilon_o \mu o}\partial_y^2 & 0 & 0 & 0 & \frac{\Delta t}{\mu_o}\partial_z & -\frac{\Delta t}{\mu_o}\partial_y \\ 0 & \frac{\Delta t^2}{4\varepsilon_o \mu o}\partial_z^2 & 0 & -\frac{\Delta t}{\mu_o}\partial_z & 0 & \frac{\Delta t}{\mu_o}\partial_x \\ 0 & 0 & \frac{\Delta t^2}{4\varepsilon_o \mu o}\partial_x^2 & \frac{\Delta t}{\mu_o}\partial_y & -\frac{\Delta t}{\mu_o}\partial_x & 0 \\ 0 & 0 & 0 & \frac{\Delta t^2}{4\varepsilon_o \mu o}\partial_y^2 & 0 & 0 \\ 0 & 0 & 0 & 0 & \frac{\Delta t^2}{4\varepsilon_o \mu o}\partial_z^2 & 0 \\ 0 & 0 & 0 & 0 & 0 & \frac{\Delta t^2}{4\varepsilon_o \mu o}\partial_x^2 \end{bmatrix}$$

where the operators ∂ and ∂^2, read for a central difference scheme for yee's grid (see following section):

$$\begin{aligned}\partial_a U &= \frac{U_{l+1} - U_l}{\Delta a} \\ \partial_a^2 U &= \frac{U_{l+1} - 2U_l + U_{l-1}}{\Delta a^2}\end{aligned} \tag{2.50}$$

and $a = x, y, z$, $l = a/\Delta a = i, j, k$ for each component.

For problems of microwave discharges that can be described by the previously described physical model, the usage of implicit methods has a straight-forward benefit : As the plasma evolution takes place in time scales longer than the electromagnetic wave period, an important gain in computational time can be achieved by overpassing the CFL stability criterion and advancing in the EM waves period with time-steps as large as possible. Therefore, the implicit resolution of the EM equations coupled with the plasma ones, is essential in order to study problems where the computational domain is large and the mesh refinement quite demanding due to the plasma density gradients. The leapfrog ADI formulation provides an efficient method of resolving the implicit system of equations via a Thomas algorithm, reducing the number of operations greatly when compared with a classic CN scheme.

The CPML ADI - FDTD discretization

We consider firstly, the classic formulation of the ADI - FDTD equations with CPML absorbing boundary conditions. The whole time step is dividing into two sub-steps and we are solving the FDTD equations implicitly for each direction in such successive sub-time step. This formulation reads for the first sub-time step, in the classic FDTD Yee scheme which is used for the spatial discretization of the system's equations [44].:

$$\begin{aligned}E_x^{n+1/2}{}_{i,j,k} =& E_x^n{}_{i,j,k} + \frac{\Delta t}{2\varepsilon_0}\Big(\frac{1}{\kappa_y \Delta y}\big(H_z^{n+1/2}{}_{i,j,k} - H_z^{n+1/2}{}_{i,j-1,k}\big) - \frac{1}{\kappa_z \Delta z}\big(H_y^n{}_{i,j,k} - H_y^n{}_{i,j,k-1}\big) \\ &+ \psi_{exy}^{n+1/2}{}_{i,j,k} - \psi_{exzi,j,k}^n\Big)\end{aligned} \tag{2.51}$$

$$\begin{aligned}H_z^{n+1/2}{}_{i,j,k} =& H_z^n{}_{i,j,k} + \frac{\Delta t}{2\mu_0}\Big(\frac{1}{\kappa_y \Delta y}\big(E_x^{n+1/2}{}_{i,j,k} - E_x^{n+1/2}{}_{i,j-1,k}\big) - \frac{1}{\kappa_x \Delta x}\big(E_y^n{}_{i+1,j,k} - E_y^n{}_{i,j,k}\big) \\ &+ \psi_{hzy}^{n+1/2}{}_{i,j,k} - \psi_{hzxi,j,k}^n\Big)\end{aligned} \tag{2.52}$$

and for the second time-step:

$$\begin{aligned}E_x^{n+1}{}_{i,j,k} =& E_x^{n+1/2}{}_{i,j,k} + \frac{\Delta t}{2\varepsilon_0}\Big(\frac{1}{\kappa_y \Delta y}\big(H_z^{n+1/2}{}_{i,j,k} - H_z^{n+1/2}{}_{i,j-1,k}\big) - \frac{1}{\kappa_z \Delta z}\big(H_y^{n+1}{}_{i,j,k} - H_y^{n+1}{}_{i,j,k-1}\big) \\ &+ \psi_{exy}^{n+1/2}{}_{i,j,k} - \psi_{exz}^{n+1}{}_{i,j,k}\Big)\end{aligned} \tag{2.53}$$

$$\begin{aligned}H_z^{n+1}{}_{i,j,k} =& H_z^{n+1/2}{}_{i,j,k} + \frac{\Delta t}{2\mu_0}\Big(\frac{1}{\kappa_y \Delta y}\big(E_x^{n+1/2}{}_{i,j,k} - E_x^{n+1/2}{}_{i,j-1,k}\big) - \frac{1}{\kappa_x \Delta x}\big(E_y^{n+1}{}_{i+1,j,k} - E_y^{n+1}{}_{i,j,k}\big) \\ &+ \psi_{hzy}^{n+1/2}{}_{i,j,k} - \psi_{hzx}^{n+1}{}_{i,j,k}\Big)\end{aligned} \tag{2.54}$$

and the rest electric and magnetic components can be derived by cyclic permutation and the CPML terms are updated with recursive relations as described in previous sections.

The solution for each sub step results to a tridiagonal matrix formulation for each component that can be efficiently solved by an appropriate algorithm such as the Thomas one.

The CPML ADI-FDTD Leapfrog discretization and coupling with the plasma model

The ADI scheme for solving the maxwell equations under the FDTD method is promising for problems that couple electromagnetism with other physics as the refinement of the mesh has no longer a strong impact to the time step restrictions on the algorithm's stability. The fact though, that we are obliged to use two sub-time steps for only one in the conventional FDTD method as well as problems on the correct implementation of current sources using the TFSF technique or even CPML formulations for absorbing boundary conditions, gave motivation to a leap-frog time formulation of the implicit ADI scheme. We will derive its discretized equations with CPML absorbing boundary conditions and then couple it with the discretized plasma fluid equations.
To be consistent with the leap-frog formulation in time, the electric field components have to be expressed in times $n+1/2$ while the magnetic component at times n. Substituting equation 2.52 to 2.51, we obtain:

$$\begin{aligned}
{E_x^{n+1/2}}_{i,j,k} =& {E_x^n}_{i,j,k} + \frac{\Delta t}{2\varepsilon_0 \kappa_y \Delta y}({H_z^n}_{i,j,k} - {H_z^n}_{i,j-1,k}) - \frac{\Delta t}{2\varepsilon_0 \kappa_z \Delta z}({H_y^n}_{i,j,k} - {H_y^n}_{i,j-1,k}) \\
&+ (\frac{\Delta t}{2\sqrt{\kappa_x \kappa_y \mu_0 \varepsilon_0}\Delta y})^2({E_x^{n+1/2}}_{i,j+1,k} - 2{E_x^{n+1/2}}_{i,j,k} + {E_x^{n+1/2}}_{i,j-1,k}) \\
&+ (\frac{\Delta t}{2\kappa_y\sqrt{\mu_0 \varepsilon_0}})^2 \frac{1}{\Delta x \Delta y}(-{E_y^n}_{i+1,j,k} + 2{E_y^n}_{i,j,k} - {E_y^n}_{i-1,j,k}) \\
&+ \frac{\Delta t}{2\varepsilon_0}({\psi_{exy}^{n+1/2}}_{i,j,k} - {\psi_{exzi,j,k}^n}) + (\frac{\Delta t}{2\sqrt{\Delta y \kappa_y \mu_0 \varepsilon_0}})^2({\psi_{hzy}^{n+1/2}}_{i,j,k} - {\psi_{hzxi,j,k}^n})
\end{aligned} \tag{2.55}$$

Replacing the time indexes $n+1$ and $n+1/2$ by n and $n-1/2$ respectively in equations 2.53 and 2.54 and substituting 2.54 into 2.53, we obtain :

$$\begin{aligned}
{E_x^n}_{i,j,k} =& {E_x^{n-1/2}}_{i,j,k} + \frac{\Delta t}{2\varepsilon_0 \kappa_y \Delta y}({H_z^n}_{i,j,k} - {H_z^n}_{i,j-1,k}) - \frac{\Delta t}{2\varepsilon_0 \kappa_z \Delta z}({H_y^n}_{i,j,k} - {H_y^n}_{i,j-1,k}) \\
&+ (\frac{\Delta t}{2\sqrt{\kappa_x \kappa_y \mu_0 \varepsilon_0}\Delta y})^2(-{E_x^{n-1/2}}_{i,j+1,k} + 2{E_x^{n-1/2}}_{i,j,k} - {E_x^{n-1/2}}_{i,j-1,k}) \\
&+ (\frac{\Delta t}{2\kappa_y\sqrt{\mu_0 \varepsilon_0}})^2 \frac{1}{\Delta x \Delta y}({E_y^n}_{i+1,j,k} - 2{E_y^n}_{i,j,k} + {E_y^n}_{i-1,j,k}) \\
&+ \frac{\Delta t}{2\varepsilon_0}(-{\psi_{exy}^{n-1/2}}_{i,j,k} + {\psi_{exzi,j,k}^n}) + (\frac{\Delta t}{2\sqrt{\Delta y \kappa_y \mu_0 \varepsilon_0}})^2(-{\psi_{hzy}^{n-1/2}}_{i,j,k} + {\psi_{hzxi,j,k}^n})
\end{aligned} \tag{2.56}$$

Adding 2.55 and 2.56 , we obtain the implicit update equation for the x-component of the electric field,

which reads:

$$\begin{aligned} E^{n+1/2}_{x_{i,j-1,k}} - Q_1 E^{n+1/2}_{x_{i,j,k}} + E^{n+1/2}_{x_{i,j+1,k}} =& Q_2 E^{n-1/2}_{x_{i,j,k}} + Q_3 (H^n_{z_{i,j,k}} - H^n_{z_{i,j-1,k}}) - Q_4 (H^n_{y_{i,j,k}} - H^n_{y_{i,j,k-1}}) \\ & - (E^{n-1/2}_{x_{i,j+1,k}} - E^{n-1/2}_{x_{i,j-1,k}}) - \frac{Q_1}{\varepsilon_0} (\psi^n_{exy_{i,j,k}} - \psi^n_{exz_{i,j,k}}) + Q_5 \end{aligned} \tag{2.57}$$

where the coefficients Q read:

$$\begin{aligned} &Q_1 = (2\Delta y \sqrt{k_x k_y})/(c\Delta t))^2 + 2, \;\; Q_2 = (2\Delta y \sqrt{k_x k_y}/(c\Delta t))^2, \\ &Q_3 = 4\mu_0 \Delta y k_x/(\Delta t), \;\; Q_4 = 4\mu_0 \Delta y^2 k_x k_y/(k_z \Delta z \Delta t), \;\; Q_5 = 0 \end{aligned}$$

The other discretized equations can be easily derived by cyclic permutation of the x, y, z components. Note that in the above expression the CPML terms have been simplified by a first order Taylor approximation as in [45]. The authors there provide a numerical proof of the numerical stability of this scheme's formulation as well as numerical experiments demonstrating the superior performance of this ABC . The recursive relations and iteration equations for the auxiliary terms ψ follow the conventional CPML FDTD relations as described in section 2.2.2.

Coupling with the plasma equations

To impose stability, the momentum transfer equation is discretized using an implicit C-N scheme in time as follows:

$$v^{n+1/2}_{x_{i,j,k}} = \beta v^{n-1/2}_{x_{i,j,k}} - \alpha \left(\frac{E^{n+1/2}_{x_{i,j,k}} + E^{n-1/2}_{x_{i,j,k}}}{2}\right) \tag{2.58}$$

and similar for the y, z components.

With the addition of the electron current density the electric field update equations coefficients in equation 2.57 are tranformed as follows :

$$\begin{aligned} &Q_1 = (2\Delta y \sqrt{k_x k_y})/(c\Delta t))^2 + 2 + \mu_o \frac{\Delta y^2}{\Delta t} e n^p_{i,j,k} \alpha \\ &Q_5 = \mu_o \frac{\Delta y^2}{\Delta t} e n^p_{i,j,k} v^{n-1/2}_{x_{i,j,k}} (1+\beta) \end{aligned}$$

where the coefficients α and β read:

$$\begin{aligned} &\alpha = e\Delta t/(m_e(1 + \frac{1}{2}\Delta t \nu_c)) \\ &\beta = (1 - \frac{1}{2}\Delta t \nu_c)/(1 + \frac{1}{2}\Delta t \nu_c) \end{aligned}$$

The plasma diffusion equation is being discretized using an explicit Euler scheme and it reads in its

non-conservative form :

$$\begin{aligned}\frac{n_{i,j,k}^{p+1}-n_{i,j,k}^{p}}{\Delta t} =& \nu_{eff_{i,j,k}}^{p} n_{i,j,k}^{p} - r n_{i,j,k}^{p} + D_{eff_{i,j,k}}^{p} \\ & [\frac{n_{i,j+1,k}^{p}+n_{i,j-1,k}^{p}-2n_{i,j,k}^{p}}{\Delta y^2} \\ & + \frac{n_{i+1,j,k}^{p}+n_{i-1,j,k}^{p}-2n_{i,j,k}^{p}}{\Delta x^2} \\ & + \frac{n_{i,j,k+1}^{p}+n_{i,j,k-1}^{p}-2n_{i,j,k}^{p}}{\Delta z^2}\end{aligned} \tag{2.59}$$

As the plasma's diffusion is taking place in time scales much longer than the waves evolution, the plasma's diffusion equation is solved on each EM's period. The source terms contribution (ionization, attachment in terms of the effective ionization frequency and recombination) are solved on each EM's time-step using a Runge-Kutta 2 scheme as shown in equation 2.60. This formulation allows a proper description of the local source terms, even when the effective ionization frequency reaches high values. We use this formulation for the cases where the gas heating effects are studied (leading to strong ionization) while we retain the formulation of equation 2.59 for the rest of our simulations.

$$\begin{aligned} n_{i,j,k}^{temp} &= n_{i,j,k}^{n} + \frac{\Delta t}{2}(\nu_{eff_{i,j,k}}^{n} n_{i,j,k}^{n} - r_{e_{i,j,k}}^{n}(n_{i,j,k}^{n})^2) \\ n_{i,j,k}^{n+1} &= n_{i,j,k}^{n} + \Delta t(\nu_{eff_{i,j,k}}^{n} n_{i,j,k}^{temp} - r_{e_{i,j,k}}^{n}(n_{i,j,k}^{temp})^2)\end{aligned} \tag{2.60}$$

The diffusion contribution is then solved over each EM period through a conservative centered finite-volume scheme in space, which reads for an one-dimensional grid (in sake of simplicity):

$$\begin{aligned} n_{i}^{p+1} =& [1 - \frac{\Delta t_p}{2\Delta x^2}(2D_{eff_i}^{p} + D_{eff_{i+1}}^{p} + D_{eff_{i-1}}^{p})] n_{i}^{p} \\ & + \frac{\Delta t_p}{2\Delta x^2}(D_{eff_i}^{p} + D_{eff_{i+1}}^{p}) n_{i+1,j,k}^{p} \\ & + \frac{\Delta t_p}{2\Delta x^2}(D_{eff_i}^{p} + D_{eff_{i-1}}^{p}) n_{i-1,j,k}^{p}\end{aligned} \tag{2.61}$$

These equations complete the set of the discretized equations of our model that permit us to model the interaction between the EM waves and the plasma.

Numerical dispersion, stability and time scales revisited

The evolution of the plasma is slow compared to the one of the EM waves and as described, we have used two different time steps for the Maxwell equations and the ones that describe the plasma evolution, as shown in figure 2.4. The Maxwell time step Δt_n is set as $\Delta t_n = \Delta t_p / n_T$ that implies that the plasma time step Δt_p is equal to the period T of the incident wave source and n_T is an even integer. The magnetic field is computed in times $(t, t+\Delta t_n, t+2\Delta t_n, ...)$ while the electric field and the electron velocity due to the leap frog scheme at times $(t, t+\Delta t_n/2, t+3\Delta t_n/2, ...)$. Finally the plasma density, diffusion coefficient and effective ionization rate are computed at times $(t, t+\Delta t_p, t+2\Delta t_p, ...)$ or $(t, t+\Delta t_n/2, t+3\Delta t_n/2, ...)$ depending on the choice of scheme, as mentioned in the previous section.

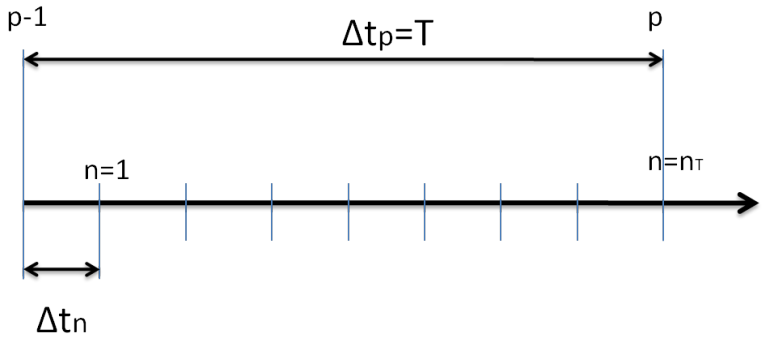

Figure 2.4: The temporal discretized grid

The Von-Neumann criterion for the plasma simulation comes from the diffusion equation. We take for $v_{eff} = 0$ and $D_{eff} = constant$:

$$\Delta t_p \leq \min(\Delta x^2, \Delta y^2)/(2D_{eff}) \tag{2.62}$$

and we apply this criterion for all our simulations.

The stability of the three dimensional ADI-FDTD leapfrog scheme along with its dispersion properties have been studied in [46] using the Von-Neumann method. They have proven that the all the eigenvalues of the scheme's amplification matrix have unity magnitude and concluded that the leapfrog ADI-FDTD method is unconditionally stable and non-dissipative. The ADI - FDTD leapfrog scheme has the exact same numerical dispersion expression as the typical ADI - FDTD scheme [46] that reads [47] :

$$\frac{2}{\Delta t}\tan(\frac{\omega\Delta t}{2}) = \pm\sqrt{\frac{{\kappa_n}^2 + \zeta^2}{\varepsilon\mu + \xi^2}} \tag{2.63}$$

where κ_n is the modulus of the numerical wave-vector as defined for the classic FDTD algorithm and $\zeta^2 = \Delta t^2({\kappa_{nx}}^2{\kappa_{ny}}^2 + {\kappa_{ny}}^2{\kappa_{nz}}^2 + {\kappa_{nx}}^2{\kappa_{nz}}^2)/(4\varepsilon\mu)$ and $\xi^2 = \Delta t^6{\kappa_{nx}}^2{\kappa_{ny}}^2{\kappa_{nz}}^2/(64\varepsilon^2\mu^2)$. The function that gives the numerical dispersion in this scheme, is an inverse tangent and since the term inside the square root in the right hand side of the dispersion equation is always positive, the inverse tangent function is always real. This provides a fast evidence of the unconditional stability of the scheme as imaginary frequencies can not exist for any real value of the wave numbers.

The authors in [48], have extended the scheme for allowing lossy media modeling, and proved its unconditionally stability via a Von-Neumann combined with a Jury criterion method. These approaches though, needs extensive computer-aided algebra, making it hard to generalize the stability properties for more complex conditions - different types of boundary ones or coupled schemes as the one presented her. In this thesis, we consider the energy method as a mean to study the stability of the ADI-leapfrog scheme and expand it to the case of the coupling with the momentum transfer equation. The authors in [49] were pioneers in establishing an energy estimate for proving the stability of a finite volume scheme for the Maxwell's equations and serves as the basis for the following analysis. An energy criterion stability study for the two steps FDTD-ADI scheme has been performed in [50].

Starting from equation 2.48 , we write the system in the form :

$$(M-D-A)U^{n+1} = (M-D-B)U^n \tag{2.64}$$

where the new matrices A and B as well as the mass matrix M (note that in equation 2.64 and all equations that follow the brackets notation for the matrices has been omitted), read:

$$[A] = \begin{bmatrix} 0 & 0 & 0 & 0 & 0 & 0 \\ 0 & 0 & 0 & 0 & 0 & 0 \\ 0 & 0 & 0 & 0 & 0 & 0 \\ 0 & \Delta t\partial_z & -\Delta t\partial_y & 0 & 0 & 0 \\ -\Delta t\partial_z & 0 & \Delta t\partial_x & 0 & 0 & 0 \\ \Delta t\partial_y & -\Delta t\partial_x & 0 & 0 & 0 & 0 \end{bmatrix}$$

$$[B] = \begin{bmatrix} 0 & 0 & 0 & 0 & \Delta t\partial_z & -\Delta t\partial_y \\ 0 & 0 & 0 & -\Delta t\partial_z & 0 & \Delta t\partial_x \\ 0 & 0 & 0 & \Delta t\partial_y & -\Delta t\partial_x & 0 \\ 0 & 0 & 0 & 0 & 0 & 0 \\ 0 & 0 & 0 & 0 & 0 & 0 \\ 0 & 0 & 0 & 0 & 0 & 0 \end{bmatrix}$$

$$[M] = \begin{bmatrix} \varepsilon & 0 & 0 & 0 & 0 & 0 \\ 0 & \varepsilon & 0 & 0 & 0 & 0 \\ 0 & 0 & \varepsilon & 0 & 0 & 0 \\ 0 & 0 & 0 & \mu & 0 & 0 \\ 0 & 0 & 0 & 0 & \mu & 0 \\ 0 & 0 & 0 & 0 & 0 & \mu \end{bmatrix}$$

and the diagonal matrix D, reads:

$$[D] = \begin{bmatrix} \frac{\Delta t^2}{4\mu}\partial_y^2 & 0 & 0 & 0 & 0 & 0 \\ 0 & \frac{\Delta t^2}{4\mu}\partial_z^2 & 0 & 0 & 0 & 0 \\ 0 & 0 & \frac{\Delta t^2}{4\mu}\partial_x^2 & 0 & 0 & 0 \\ 0 & 0 & 0 & \frac{\Delta t^2}{4\varepsilon}\partial_y^2 & 0 & 0 \\ 0 & 0 & 0 & 0 & \frac{\Delta t^2}{4\varepsilon}\partial_z^2 & 0 \\ 0 & 0 & 0 & 0 & 0 & \frac{\Delta t^2}{4\varepsilon}\partial_x^2 \end{bmatrix}$$

Note that, we consider propagation in a medium of $\varepsilon = \varepsilon_o\varepsilon_r, \mu = \mu_o\mu_r$ and recall that the operators ∂ and ∂^2, read for a central difference scheme for yee's grid:

$$\begin{aligned} \partial_a U &= \frac{U_{l+1} - U_l}{\Delta a} \\ \partial_a^2 U &= \frac{U_{l+1} - 2U_l + U_{l-1}}{\Delta a^2} \end{aligned} \tag{2.65}$$

and $a = x, y, z$, $l = a/\Delta a = i, j, k$ for each component.

Now equation 2.64 can be written as :

$$(M-D)(U^{n+1}-U^n) = AU^{n+1} - BU^n \tag{2.66}$$

Multiplying both sides by $1/2(U^{n+1}+U^n)$, we have:

$$\frac{1}{2}(\langle (M-D)U^{n+1}, U^{n+1}\rangle - \langle (M-D)U^n, U^n\rangle) = \frac{1}{2}(\langle AU^{n+1}, U^{n+1}\rangle - \langle BU^n, U^n\rangle + \langle AU^{n+1}, U^n\rangle - \langle BU^n, U^{n+1}\rangle) \tag{2.67}$$

Assuming, PEC (Perfect Electric Conductor i.e. zero parallel electric field and zero perpendicular magnetic field) type boundary conditions for the computational domain, the term $\langle AU^{n+1}, U^n\rangle$ on the second hand of this equation, can be written as:

$$\begin{aligned}
\langle AU^{n+1}, U^n\rangle &= \sum_{i,j,k} [(\Delta t \partial_z E^{n+1/2}_{y_{i,j,k}} - \Delta t \partial_y E^{n+1/2}_{z_{i,j,k}}) H^n_{x_{i,j,k}} + (-\Delta t \partial_z E^{n+1/2}_{x_{i,j,k}} + \Delta t \partial_x E^{n+1/2}_{z_{i,j,k}}) H^n_{y_{i,j,k}} \\
&+ (\Delta t \partial_y E^{n+1/2}_{x_{i,j,k}} - \Delta t \partial_x E^{n+1/2}_{y_{i,j,k}}) H^n_{z_{i,j,k}}] \\
&= \sum_{i,j,k} [\Delta t E^{n+1/2}_{x_{i,j,k}} (\partial_z H^n_{y_{i,j,k}} - \partial_y H^n_{z_{i,j,k}}) + \Delta t E^{n+1/2}_{y_{i,j,k}} (-\partial_z H^n_{x_{i,j,k}} + \partial_x H^n_{z_{i,j,k}}) \\
&+ \Delta t E^{n+1/2}_{z_{i,j,k}} (-\partial_x H^n_{y_{i,j,k}} + \partial_y H^n_{x_{i,j,k}})] \\
&= \langle BU^n, U^{n+1}\rangle
\end{aligned} \tag{2.68}$$

Note that the above justification can be obtained also by observing the matrices A and B, which are symmetric to each other (note also that the transpose of the derivatives equals the opposite of the derivative), ie $A^T = B$ and thus the inner product equality $\langle Bx, y\rangle = \langle Ay, x\rangle$ holds. Moreover the matrix M is diagonal, so $\langle Mx, y\rangle = \langle My, x\rangle$.
Consequently, equation 2.67 gives:

$$\begin{aligned}
&\frac{1}{2}\langle (M-D)U^{n+1}, U^{n+1}\rangle - \langle AU^{n+1}, U^{n+1}\rangle = \\
&\qquad \frac{1}{2}\langle (M-D)U^n, U^n\rangle - \langle AU^n, U^n\rangle
\end{aligned} \tag{2.69}$$

which means that the pseudo-energy $\mathscr{E}_{pseudo} = \frac{1}{2}(\langle MU, U\rangle - \langle DU, U\rangle - \langle AU, U\rangle)$, remains constant in each time step and equals to the initial energy, namely $\mathscr{E}_{pseudo}(0)$.

To prove the stability of the numerical scheme, the following inequality relation has to be satisfied :

$$\mathscr{E}_{pseudo} \geq \frac{1}{2}\alpha \langle MU, U\rangle = \alpha \mathscr{E}_{EM} \tag{2.70}$$

The first term of the pseudo-energy equation, reads:

$$\begin{aligned}\langle MU,U\rangle = \sum_{i,j,k}\Big(&\varepsilon|E_{x_{i,j,k}}|^2+\mu|H_{x_{i,j,k}}|^2+\varepsilon|E_{y_{i,j,k}}|^2\\ &+\mu|H_{y_{i,j,k}}|^2+\varepsilon|E_{z_{i,j,k}}|^2+\mu|H_{z_{i,j,k}}|^2\Big)\end{aligned} \tag{2.71}$$

The second term of the pseudo-energy equation, reads:

$$\begin{aligned}-\langle DU,U\rangle = \sum_{i,j,k}\Big(&\frac{\Delta t^2}{4\mu}|\partial_y E_{x_{i,j,k}}|^2+\frac{\Delta t^2}{4\mu}|\partial_z E_{y_{i,j,k}}|^2\\ &+\frac{\Delta t^2}{4\mu}|\partial_x E_{z_{i,j,k}}|^2+\frac{\Delta t^2}{4\varepsilon}|\partial_y H_{x_{i,j,k}}|^2\\ &+\frac{\Delta t^2}{4\varepsilon}|\partial_z H_{y_{i,j,k}}|^2+\frac{\Delta t^2}{4\varepsilon}|\partial_x H_{z_{i,j,k}}|^2\Big)\end{aligned} \tag{2.72}$$

This term contributes to the positivity of the pseudo-energy. The last term of the pseudo-energy equation, reads:

$$\begin{aligned}\langle AU,U\rangle =&\frac{1}{2}\langle AU,U\rangle+\frac{1}{2}\langle BU,U\rangle = \sum_{i,j,k}\frac{1}{2}\Big(\Delta t(\partial_z E_{y_{i,j,k}}-\partial_y E_{z_{i,j,k}})H_{x_{i,j,k}}+\Delta t(\partial_x E_{z_{i,j,k}}-\partial_z E_{x_{i,j,k}})H_{y_{i,j,k}}\\ &+\Delta t(\partial_y E_{x_{i,j,k}}-\partial_x E_{y_{i,j,k}})H_{z_{i,j,k}}\Big)+\sum_{i,j,k}\frac{1}{2}\Big(\Delta t(\partial_y H_{z_{i,j,k}}-\partial_z H_{y_{i,j,k}})E_{x_{i,j,k}}\\ &+\Delta t(\partial_z H_{x_{i,j,k}}-\partial_x H_{z_{i,j,k}})E_{y_{i,j,k}}+\Delta t(\partial_x H_{y_{i,j,k}}-\partial_y H_{x_{i,j,k}})E_{z_{i,j,k}}\Big)\end{aligned} \tag{2.73}$$

We need to prove that this last term, can be controlled by the other terms of the pseudo-energy so that it won't reduce the real energy of the system.

We note firstly that due to the PEC boundary conditions :

$$\sum_{i,j,k}\partial_y E_{z_{i,j,k}}H_{x_{i,j,k}}+\sum_{i,j,k}\partial_y H_{x_{i,j,k}}E_{z_{i,j,k}}=0 \tag{2.74}$$

and similar relations are valid with cyclic permutation of the x,y,z components. Therefore equation 2.73 becomes :

$$\begin{aligned}\langle AU,U\rangle = &\sum_{i,j,k}\frac{1}{2}\Delta t\Big(\partial_z E_{y_{i,j,k}}H_{x_{i,j,k}}+\partial_x E_{z_{i,j,k}}H_{y_{i,j,k}}+\partial_y E_{x_{i,j,k}}H_{z_{i,j,k}}\Big)\\ &+\sum_{i,j,k}\frac{1}{2}\Delta t\Big(-\partial_z H_{y_{i,j,k}}E_{x_{i,j,k}}\qquad\qquad -\partial_x H_{z_{i,j,k}}E_{y_{i,j,k}}-\partial_y H_{x_{i,j,k}}E_{z_{i,j,k}}\Big)\end{aligned} \tag{2.75}$$

Using the inequality:

$$ab\leq\frac{1}{2}(a^2\kappa^2+b^2/\kappa^2) \tag{2.76}$$

we get from equation 2.73 with $\kappa = \sqrt{\Delta t/\mu}$ for the first 3 terms of the second hand member and $\kappa = \sqrt{\Delta t/\varepsilon}$ for the last 3 terms :

$$\begin{aligned}\langle AU,U\rangle \leq & \frac{1}{4}\Big(\frac{\Delta t^2}{\mu}|\partial_z E_{y_{i,j,k}}|^2 + 2\mu|H_{x_{i,j,k}}|^2 + \frac{\Delta t^2}{\mu}|\partial_x E_{z_{i,j,k}}|^2 + 2\mu|H_{y_{i,j,k}}|^2 \\ & + \frac{\Delta t^2}{\mu}|\partial_y E_{x_{i,j,k}}|^2 + 2\mu|H_{z_{i,j,k}}|^2\Big) \\ & + \frac{1}{4}\Big(\frac{\Delta t^2}{\varepsilon}|\partial_z H_{y_{i,j,k}}|^2 + 2\varepsilon|E_{x_{i,j,k}}|^2 + \frac{\Delta t^2}{\varepsilon}|\partial_x H_{z_{i,j,k}}|^2 + 2\varepsilon|E_{y_{i,j,k}}|^2 \\ & + \frac{\Delta t^2}{\varepsilon}|\partial_y H_{x_{i,j,k}}|^2 + 2\varepsilon|E_{z_{i,j,k}}|^2\Big)\end{aligned} \tag{2.77}$$

Taking the limit of equality of the above equation as the case when the last term becomes more negative, the pseudo-energy reads:

$$\begin{aligned}\mathscr{E}_{pseudo} = & \frac{1}{2}(\varepsilon|E|^2 + \mu|H|^2) \\ & \geq \frac{1}{2}(\varepsilon|E|^2 + \mu|H|^2) = \alpha\mathscr{E}_{EM}\end{aligned} \tag{2.78}$$

where $\alpha = 1$. This inequality proves that the electromagnetic energy remains bounded during the time-stepping of the ADI-leapfrog scheme and thus the scheme is unconditionally stable.

Moving to the stability analysis of the coupled scheme (with the momentum transfer equation 2.58), the vectors U^{n+1} and U^n now include (here right after the electric field block matrices) the current density components , $J_x^{n+1/2}$, $J_y^{n+1/2}$, $J_z^{n+1/2}$ and $J_x^{n-1/2}$, $J_y^{n-1/2}$, $J_z^{n-1/2}$.

We write equation 2.66 in the form:

$$\begin{aligned}(M-D)(U^{n+1}-U^n) = & AU^{n+1} - BU^n + C_{11}U^{n+1} \\ & - C_{21}U^n + C_{12}U^{n+1} - C_{22}U^n\end{aligned} \tag{2.79}$$

with matrices:

$$[M] = \begin{bmatrix} \varepsilon & 0 & 0 & 0 & 0 & 0 & 0 & 0 & 0 \\ 0 & \varepsilon & 0 & 0 & 0 & 0 & 0 & 0 & 0 \\ 0 & 0 & \varepsilon & 0 & 0 & 0 & 0 & 0 & 0 \\ 0 & 0 & 0 & \frac{m_e}{e^2 n_e} & 0 & 0 & 0 & 0 & 0 \\ 0 & 0 & 0 & 0 & \frac{m_e}{e^2 n_e} & 0 & 0 & 0 & 0 \\ 0 & 0 & 0 & 0 & 0 & \frac{m_e}{e^2 n_e} & 0 & 0 & 0 \\ 0 & 0 & 0 & 0 & 0 & 0 & \mu & 0 & 0 \\ 0 & 0 & 0 & 0 & 0 & 0 & 0 & \mu & 0 \\ 0 & 0 & 0 & 0 & 0 & 0 & 0 & 0 & \mu \end{bmatrix}$$

$$[C_{11}] = \begin{bmatrix} 0 & 0 & 0 & -\gamma_2 & 0 & 0 & 0 & 0 & 0 \\ 0 & 0 & 0 & 0 & -\gamma_2 & 0 & 0 & 0 & 0 \\ 0 & 0 & 0 & 0 & 0 & -\gamma_2 & 0 & 0 & 0 \\ \gamma_2 & 0 & 0 & 0 & 0 & 0 & 0 & 0 & 0 \\ 0 & \gamma_2 & 0 & 0 & 0 & 0 & 0 & 0 & 0 \\ 0 & 0 & \gamma_2 & 0 & 0 & 0 & 0 & 0 & 0 \\ 0 & 0 & 0 & 0 & 0 & 0 & 0 & 0 & 0 \\ 0 & 0 & 0 & 0 & 0 & 0 & 0 & 0 & 0 \\ 0 & 0 & 0 & 0 & 0 & 0 & 0 & 0 & 0 \end{bmatrix}$$

$$[C_{12}] = \begin{bmatrix} 0 & 0 & 0 & 0 & 0 & 0 & 0 & 0 & 0 \\ 0 & 0 & 0 & 0 & 0 & 0 & 0 & 0 & 0 \\ 0 & 0 & 0 & 0 & 0 & 0 & 0 & 0 & 0 \\ 0 & 0 & 0 & -\gamma_1 & 0 & 0 & 0 & 0 & 0 \\ 0 & 0 & 0 & 0 & -\gamma_1 & 0 & 0 & 0 & 0 \\ 0 & 0 & 0 & 0 & 0 & -\gamma_1 & 0 & 0 & 0 \\ 0 & 0 & 0 & 0 & 0 & 0 & 0 & 0 & 0 \\ 0 & 0 & 0 & 0 & 0 & 0 & 0 & 0 & 0 \\ 0 & 0 & 0 & 0 & 0 & 0 & 0 & 0 & 0 \end{bmatrix}$$

and $C_{21} = -C_{11}, C_{22} = -C_{12}$.

The coefficients γ_1, γ_2 read :

$$\gamma_1 = \frac{\Delta t \nu_c m_e}{2 n_e e^2}$$
$$\gamma_2 = \frac{\Delta t}{2}$$

The following properties hold for the matrices C_{11}, C_{21} and C_{21}, C_{22}:

$$\begin{aligned} C_{11}^T &= -C_{11} \\ C_{12}^T &= C_{12} \\ \langle C_{ij}x, x\rangle &= 0 \quad \forall x \in \mathbb{R}^n \quad i = 1,2,\ j = 1 \\ \langle C_{ij}x, y\rangle &= -\langle C_{ij}y, x\rangle \quad \forall x, y \in \mathbb{R}^n \quad i = 1,2,\ j = 1 \\ \langle C_{ij}x, y\rangle &= \langle C_{ij}y, x\rangle \quad \forall x, y \in \mathbb{R}^n \quad i = 1,\ j = 1,2 \end{aligned} \tag{2.80}$$

The matrices A, B and D are the same as before, with zeros added for the current vectors blocks' contributions and are not presented here in the sake of space reduction.

We proceed with the same technique as before, multiplying both sides by $1/2(U^{n+1} + U^n)$, and we obtain

by taking into account the properties of the matrices $C_{i,j}$:

$$\begin{aligned}\frac{1}{2}\langle (M-D)U^{n+1},U^{n+1}\rangle - \langle AU^{n+1},U^{n+1}\rangle = \\ \frac{1}{2}\langle (M-D)U^{n},U^{n}\rangle - \langle AU^{n},U^{n}\rangle \\ +\frac{1}{2}(\langle C_{12}U^{n+1},U^{n+1}\rangle + \langle C_{12}U^{n},U^{n}\rangle)\end{aligned} \tag{2.81}$$

The term $P = \frac{1}{2}(\langle C_{12}U^{n+1},U^{n+1}\rangle + \langle C_{12}U^{n},U^{n}\rangle)$, is obvious negative as the matrix C_{12} is diagonal and negative definite. This leads to:

$$\mathscr{E}^{n+1}_{pseudo} = \mathscr{E}^{n}_{pseudo} - |P| \Leftrightarrow \mathscr{E}^{n+1}_{pseudo} \leq \mathscr{E}^{n}_{pseudo} \tag{2.82}$$

that means that the pseudo-energy estimate reduces at each time step and thus, due to equation 2.78, the real EM energy, $\mathscr{E}_{EM}$ also reduces during the time-stepping scheme. Thus the coupled scheme is unconditionally stable. Note here that the stability of the leapfrog ADI-FDTD with CPML have been studied and verified semi-analytically in [45]. The energy method described in the previous section can provide a complete stability analysis of the inclusion of such absorbing boundary conditions in the scheme and it's left for a future study.

Parallelization and other numerical aspects

The numerical code has been parallelized using the Message Passing Interface (MPI) library and a domain decomposition technique. The parallelization was essential for computational time reduction. The explicit equations (for the explicit FDTD scheme, the plasma density equation and the momentum transfer equation where no differential operators exist) have been coded with a parallel-by-point scheme, as to advance to a next time step, computations can be done at each grid point independently of the computations at the other grid points. For the Thomas algorithm used to resolve the implicit update ADI equations, a parallel-by-line scheme has been used based on the linearity of the implicit update equations for the ADI-leapfrog scheme. The tridiagonal system of equations can be written as:

$$\alpha_i x_{i-1} + b_i x_i + c_{i+1} x_{i+1} = d_i, \quad i = 1...n \tag{2.83}$$

where $\alpha_1 = 0$ and $c_n = 0$ or known solutions (as boundary conditions).

As the update equations are implicit in one dimension, the solutions on each interface of the decomposed domains can be calculated in function of the solutions of the other interfaces. This occurs due to the linearity of the above equation, where the unknown interface values can be transfered to the RHS and the solution at each neighboring point to the interface, $x_{neighbor}$, can be written as a linear combination of its solution posing $x_{interface} = 0$ and its solution posing $x_{interface} = 1, \quad d_{neighbor} = 0$ multiplied by $x_{interface}$. Then the system of equations reduce to the each implicit direction, to the number of domain interfaces. Communication between each domain is required for solving this reduced system by again a Thomas algorithm, but the computational cost is greatly reduced compared to a pipeline scheme. The Thomas algorithm for the system 2.83 reads in

the forward sweep :

$$\begin{aligned} &\text{do j=2, n} \\ &\quad q = \frac{\alpha_j}{b_{j-1}} \\ &\quad b_j = b_j - q c_{j-1} \\ &\quad d_j = d_j - q d_{j-1} \\ &\text{end do} \end{aligned} \tag{2.84}$$

and for the backward sweep:

$$\begin{aligned} &x_n = \frac{d_n}{b_n} \\ &\text{do j=n-1, 1} \\ &\quad x_j = \frac{d_j - c_j x_{j+1}}{b_j} \\ &\text{end do} \end{aligned} \tag{2.85}$$

The wave injection has been achieved via the Total Field Scattered Field (TFSF) approach, in which, the FDTD space lattice is zoned into two distinct regions separated by a nonphysical virtual surface that serves to connect the fields in each region and inject the incident waves. In region 1, the Yee algorithm operates on total-field components and it is the region where our simulation of interest will take place. The region 2, is the reflected-field region where only scattered field components is assumed that exist. With a single mathematical operation, access to total or scattered fields can be easily obtained during the simulation.

The numerical code has been written in FORTRAN 90.

2.2.3 Fluid dynamics solver

In the cases where the plasma dynamics are coupled with the fluid ones, an appropriate cfd solver had to be developed. As the main effect of a freely localized plasma discharge in air, is the heating of the latter, this solver has to be capable to capture the blast and shock waves produced by the intense energy deposition. Such discontinuities, occur in a variety of conservation laws problems, defining a family called the Riemann problems (for constant piecewise data and a single discontinuity). In computational fluid dynamics, and especially considering the Euler equations (a hyperbolic family of partial differential equations), the Riemann problem provides exact solutions as the discontinuities appear as characteristics of the solution. To numerically resolve the Euler equations under a Riemann problem, a Riemann solver is necessary. In this thesis, the Roe approximate Riemann solver [51] is used as it incorporates important advantages such as : It is strictly conservative. It has very low numerical diffusivity and viscosity. It captures shocks accurately and in high resolution. It is quite stable.

The analysis of Riemann problems, their extension to Euler equations and Riemann solvers is out of the scope of this thesis and an extensive study can be found in [52, 53]. Although, we will briefly describe the main features of the developed solver.

Let's write (in 1D for simplicity) the Euler system of equations in a more compact form :

$$\frac{\partial}{\partial t}(\mathbf{U}) + \frac{\partial}{\partial x}[\mathbf{F}(\mathbf{U})] = \mathbf{S},$$

with

$$\begin{aligned} \mathbf{U} &= (\rho, \rho u, \rho E)^t \\ \mathbf{F}(\mathbf{U}) &= \left[\rho u,\ \rho u^2 + p,\ u(\rho E + p)\right]^t \\ \mathbf{S} &= \left[0,\ p,\ 0,\ S_{JH} + S_{diff}\right]^t \end{aligned}$$

where U is the vector of conservative variables, F is the flux vector in x-direction and S is the source terms vector where we split it in thermal diffusion (S_{diff}) and joule heating terms (S_{JH}). A Riemann problem for the Euler equations, is defined as:

$$\rho, u, p = \begin{cases} \rho_l, u_l, p_l & \text{for x} < 0 \\ \rho_r, u_r, p_r & \text{for x} > 0 \end{cases} \tag{2.86}$$

for the density ρ, the velocity u and the pressure p, where the subscripts l and r denote the left and right values respectively around the point $x = 0$. Depending on the values of the left and right quantities, the general solution of the Riemann problem varies and can become quite complex due to the non-linearity of the Euler equations. This set of equations though have a self-similar semi-analytical solution that can be used in order to calculate the solutions of the Euler's equations inside a computational cell. We split the system of equations into two components : The conductive one is firstly solve (neglecting source terms) and the solution time advance is carried out explicitly using the finite volume scheme:

$$U_i^{n+1} = U_i^n - \frac{\Delta t}{\Delta x}(x_{i+1/2}F_E - x_{i-1/2}F_W) \tag{2.87}$$

The fluxes crossing the west (W) and east (E) interfaces of the cell i, are calculated with the flux vector equation and a dissipation function ϕ :

$$\begin{aligned} F_W &= \frac{1}{2}(F(U_{i-1}) + F(U_i) - \phi_{i-1/2}) \\ F_E &= \frac{1}{2}(F(U_{i+1}) + F(U_i) - \phi_{i+1/2}) \end{aligned} \tag{2.88}$$

The dissipation function ϕ depends on Roe mean states and equals to the matrix-vector product of the right eigenvalues matrix R, the eigenvalues vector Λ and the conservative variables vector written in the base formed by the eigenvectors W:

$$\phi = \Lambda R W \tag{2.89}$$

, where the right eigen vectors matrix read :

$$R = \begin{pmatrix} 1 & 1 & 1 \\ u + \alpha_s & u - \alpha_s & u \\ H + u\alpha_s & H - u\alpha_s & E - \rho\frac{p_\rho}{p_e} \end{pmatrix} \tag{2.90}$$

Note that the real gas numerical scheme for the convective component of Euler's equations, is similar to the one originally proposed by Roe but it incorporates real gas effects via the partial derivatives of pressure with respect to density and internal energy, denoted as p_ρ and p_e respectively. This scheme has been presented in [54] and used also in [55]. For the cases of microwave discharges, the gas can reach temperatures that are quite high for a perfect gas law to be valid. Therefore, this real gas approach is essential in order to capture the real physics under such conditions.A minmod slope limiter has been used in order to reduce instability problems often encountered with this numerical scheme [56]. The speed of sound, α_s under this approach, reads :

$$\alpha_s = \frac{p}{\rho^2}\frac{\partial p}{\partial e} + \frac{\partial p}{\partial \rho} \tag{2.91}$$

The projection of the conservative variables jump into the eigenvector space W, reads:

$$\begin{aligned} W_1 =& \frac{1}{2\alpha_s^2}(\Delta p + \rho\,\alpha_s \Delta u) \\ W_2 =& \frac{1}{2\alpha_s^2}(\Delta p - \rho\,\alpha_s \Delta u) \\ W_3 =& \Delta\rho - \frac{\Delta p}{\alpha_s^2} \end{aligned} \tag{2.92}$$

The numerical solver, neglecting source terms, has been validated with shock-tube test cases and compared with literature. After the calculation of the conductive component solution, we solve the diffusion component of the energy equation including the source terms using again an explicit finite volume scheme :

$$(\rho E)_i^{n+1} = (\rho E)_i^n - \frac{\Delta t}{(\Delta x)^2}[\xi_{i+1/2}(T_{i+1}^n - T_i^n) - \xi_{i-1/2}(T_i^n - T_{i-1}^n)] \tag{2.93}$$

where ξ is the thermal conductivity. The evolution of the temperature and the pressure with respect to the density and internal energy of the gas, is taken into account via a tabulated approach : From the coefficients in [57], the specific enthalpy is being tabulated for each couple of (T, p). Then the density and internal energy are calculated as :

$$\begin{aligned} \rho(T,p) &= \frac{p}{RT}M(T,p) \\ e(T,p) &= h(t,p) - \frac{p}{\rho} \end{aligned} \tag{2.94}$$

With a discretized approach and after proper interpolation the values of $p(\rho,e)$ and $T(\rho,e)$ are then calculated.

2.2.4 Summary

To summarize this section, let's see what we have seen so far :

— The physical model used to describe the interaction between the electromagnetic waves and the plasma evolution has been described. It is based on the Maxwell's equations and a simplified fluid-plasma model taking into account transition from ambipolar to electronic diffusion. The coupling is achieved via the electron's current density.

— The numerical schemes used have been presented. Maxwell's equations are solved with an ADI-FDTD scheme, the momentum equation uses a CN scheme while the plasma continuity equation is solved with an explicit Euler scheme. CPML absorbing boundary conditions have been used to truncate the computational domain for the electromagnetic waves.
— The stability of the coupled scheme has been studied proving its unconditionally stability via an energy method.
— A Roe solver taking into account real gas effects is used for simulating the gas heating effects due to the energy absorption from the plasma and consequent energy transfer to gas molecules.

In the following sections, simulations' results are presented concerning numerical experiments for the coupled scheme, and applications - comparisons with experimental results.

2.3 Results - Applications

2.3.1 Numerical experiments on CPU time and accuracy

We consider a simple configuration to study the computational performance of the proposed scheme in comparison with its explicit formulation, in terms of CPU time and precision - error.

The domain of this test-case simulation is a $0.5\lambda x\lambda$ two-dimensional square terminated with CPML boundary conditions for the EM waves, as depicted in figure 2.5.

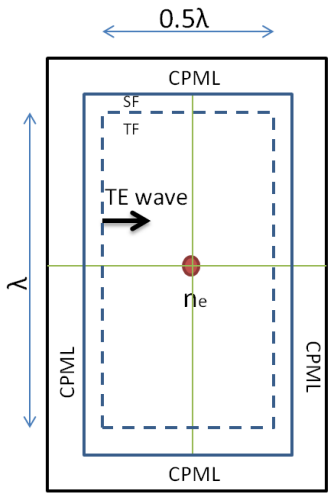

Figure 2.5: The test-case's computational domain and initial configuration.

We fix a uniform Cartesian grid of $\Delta x = \Delta y = \lambda/200$. A TE mode, y-polarized plane wave of an amplitude $Eo = 5MV/m$ is generated from the left total field - scattered field boundary (TFSF), and it propagates in the positive X direction. The frequency of the EM wave is $f = 110GHz$. We consider the wave to propagate in air at atmospheric pressure. An initial plasma density of a Gaussian profile with maximum of $10^{22}m^{-3}$ and a standard deviation of $6.10^{-5}m$ is placed at a distance of 0.5λ while the recombination coefficient is neglected. The structure of the numerical solver is presented in figure 2.6. In the same figure, the time marching for the EM solver and the plasma one is also presented. The Maxwell equations and the momentum transfer

equation are solved consecutively in each EM time step, corresponding to the CFL choice. At each plasma time step that corresponds to the period of the EM waves T_{EM}, the effective field is being calculated and the effective ionization and diffusion coefficients that depend on it. With these values the plasma density equation is solved to move forward to the next cycle/period of calculation. Note that in this section, the source terms contribution are incorporated in the plasma solver as the ionization frequency does not reach high values (with respect to the EM time step).

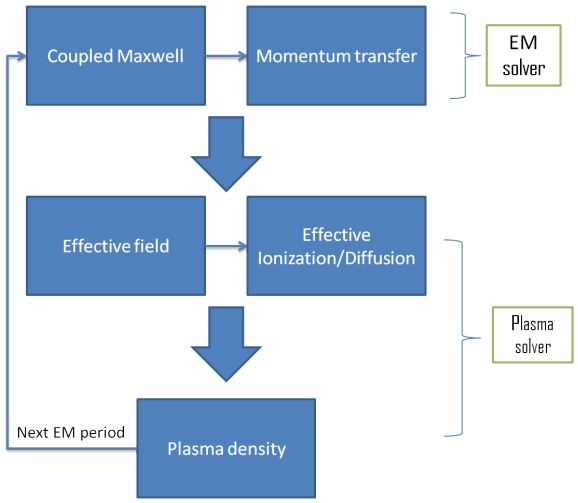

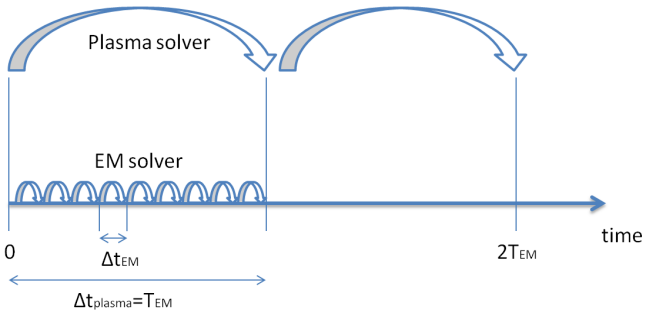

Figure 2.6: Structure of the numerical solver and time stepping representation of the scheme.

CPU time

The CFL number for the general 3D FDTD, is defined as :

$$CFL = c\Delta t \sqrt{\frac{1}{\Delta x^2} + \frac{1}{\Delta y^2} + \frac{1}{\Delta z^2}} \tag{2.95}$$

We run the solver over 100 periods, changing the CFL number from 1 to 32. This parametric study of the CPU time reduction over the CFL number is presented in table 2.1. The CPU time has been normalized to the one, obtained with the explicit scheme for $CFL = 1$.

		CFL					
		1	2	4	8	16	32
CPU time	$\lambda/200$	2.5	2	0.625	0.3	0.12	0.05

Table 2.1: Normalized CPU time vs CFL number

We note that for small values of the CFL number, the proposed scheme presents no gain in comparison with the explicit formulation. This is due the extra calculations necessary for solving the tridiagonal system of the implicit scheme. For CFL numbers greater than 4, the CPU time is reduced significantly : for $CFL = 32$ the CPU time was 0.05 times the explicit one, corresponding to a reduction of more than 90% .

We should note here that the CPU time reduction is related to the time step size which depends not only on the CFL number but also on the mesh size. Thus, we define a normalized CFL number to the mesh size and to the EM period (T_{EM}) as :

$$CFL_N = (\frac{T_{EM}}{\Delta t})^{-1} \tag{2.96}$$

corresponding to the inverse of the number of time steps per EM period. We can deduce that beyond the limit of $CFL = 4$ for the above described spatial discretization, we achieve a CPU time acceleration of approximately $2.2 * CFL_N^{-1}$ %.

Numerical error

Next, we study the error of numerical scheme. We have chosen an initial plasma density high enough, so that the EM waves are strongly affected by the plasma, that acts as a conductor when its frequency approaches or surpasses the EM wave frequency. We consider two estimates for the error. The normalized L_2-norm as an estimate of the root-mean-square error between the explicit and the implicit solutions r at $t = t_{final} = 100T$ - normalized by the explicit solution (noted as $Error_2$)and the L_∞-norm as the normalized instantaneous maximum error (noted as $Error_\infty$).

$$\begin{aligned} Error_2 &= \sqrt{\frac{\sum_{i,j,k} |E^{Explicit}_{RMS_{i,j,k}} - E^{Implicit}_{RMS_{i,j,k}}|^2}{\sum_{i,j,k} |E^{Explicit}_{RMS_{i,j,k}}|^2}} \\ Error_\infty &= \frac{max(|E^{Explicit}_{RMS_{i,j,k}} - E^{Implicit}_{RMS_{i,j,k}}|)}{max(|E^{Explicit}_{RMS_{i,j,k}}|)} \end{aligned} \tag{2.97}$$

where $E^{Explicit}_{RMS_{i,j,k}}$ is the local RMS field obtained with the explicit solver at $t = t_{final} = 100T$, $\Delta x = \Delta y = \lambda/200$ and $CFL = 1$.

In table 2.2 , the above defined error is presented for different values of the CFL number as well as for a more refined mesh of $\Delta x = \Delta y = \lambda/400$.

		CFL_N			
		0.00390625	0.015625	0.03125	0.0625
$Error_2$ (%)	$\lambda/200$	0.02	0.52	1.3	2.9
	$\lambda/400$	0.026	0.59	1.41	3.17

Table 2.2: $Error_2$ vs normalized CFL number

The error is as expected increasing, with the CFL_N number. Note that the error (the one due to the temporal discretization), remains of the same level for the more refined spatial discretization, confirming that the choice of the CFL number depends almost linear to the inverse of the mesh size step for retaining the same error's order of magnitude.

The maximum local error is presented in table 2.3. The increase of the CFL number leads to an increased maximum local error that is higher than the RMS one.

		CFL_N			
		0.00390625	0.015625	0.03125	0.0625
$Error_\infty$ (%)	$\lambda/200$	0.8	2.25	5.66	10.28
	$\lambda/400$	0.24	1	2.45	5.74

Table 2.3: $Error_\infty$ vs normalized CFL number

This localization of the maximum error can be observed in figures 2.7 and 2.8, where the RMS field is plotted over the vertical and horizontal lines of figure 2.5 for different values of the CFL number and the $\lambda/200$ spatial discretization. We observe that the increase of the CFL, lead to an underestimation of the RMS field at the tips of the plasma streamer (see figure 2.7). As the ionization and diffusion coefficients depend on the RMS field in a non-linear way, this difference - strongly related to the mixed derivative splitting error term of the ADI scheme - they can influence the plasma evolution. A more refined mesh reduces this error. Thus depending on the EM field's strength, careful choice of the CFL_N number has to been made in order to retain an acceptable precision.

The normalized CPU time and the error versus the normalized CFL number are plotted in figure 2.9, for comparison. The optimal choice for the CFL number for maximum CPU time reduction with minimum corresponding error is at a value of $CFL_N \approx 0.028$ corresponding for the test-case of $\lambda/200$ spatial discretization to a $CFL \approx 7$.

Parallelization remarks

As mentioned in the previous section, the numerical code has been parallelized using the Message Passing Interface (MPI) library and a domain decomposition technique. ADI-FDTD advances in parallelization have been reported in [58]. Good scalability has been obtained for our solver while compared to explicit FDTD solvers speed-up deviates from linearity, mainly due to the gauss-like decomposition technique used for the implicit solver. For the same number of processors, the optimal decomposition seems to be the one with a uniform division in all directions. The explanation of such a behavior can be explained by the parallel algorithm for solving the tridiagonal system of the ADI-leapfrog scheme. Each time that this system is solved, the values on the interfaces between the domains have to be exchanged. For a three dimensional cubic domain with same number of cells in each direction $Nx = Ny = Nz = N$, table 2.4 summarizes the number of

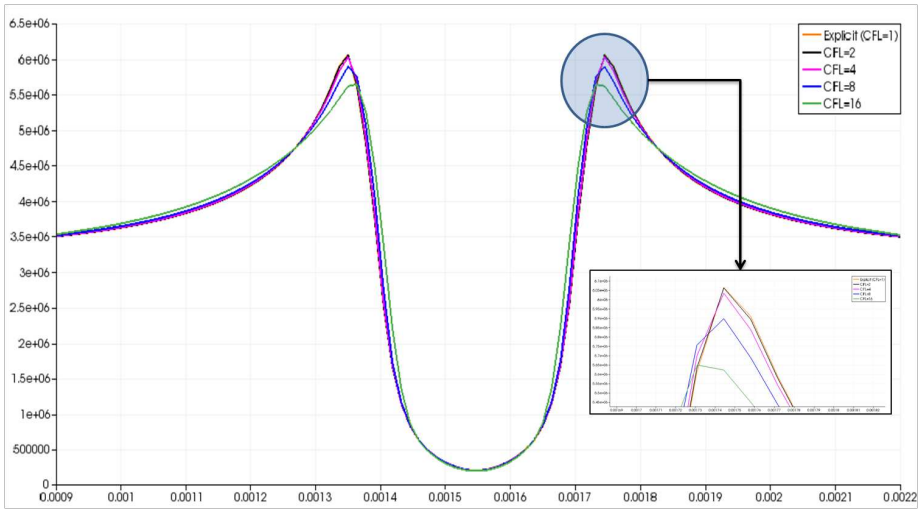

Figure 2.7: E_{RMS} field for the explicit scheme and the implicit one with different CFL numbers plotted over the vertical line of figure 2.5 .

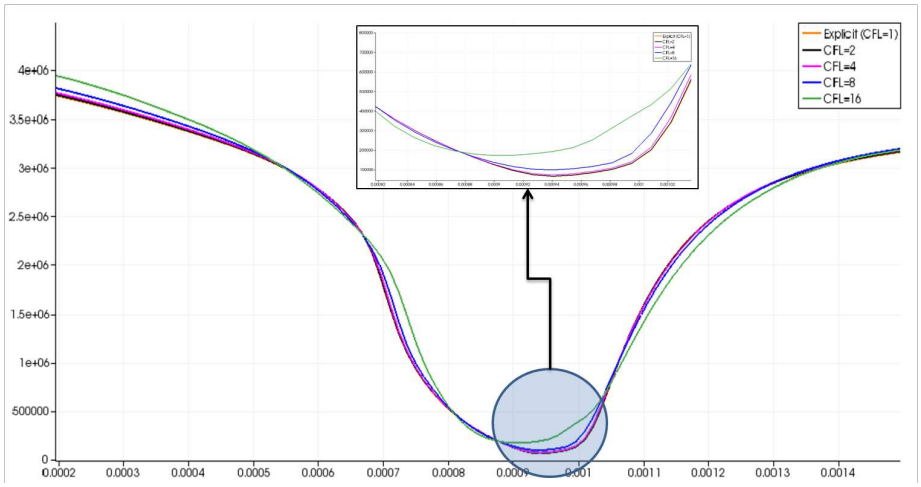

Figure 2.8: E_{RMS} field for the explicit scheme and the implicit one with different CFL numbers - plotted over the horizontal line of figure 2.5.

exchanges needed for different decompositions as well as the CPU time obtained for a 3D cubic domain of 2 million cells, uniformly discretized in all directions and $t_{final} = T$. Note that in serial mode, the CPU time for 1 period was $180s$.

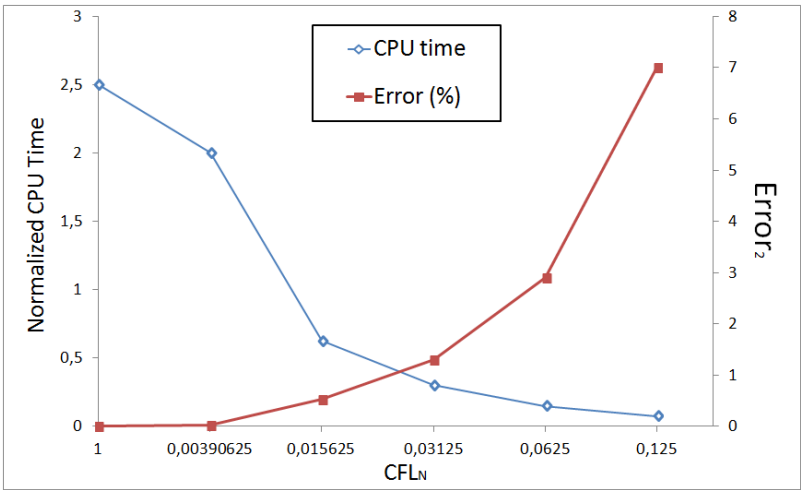

Figure 2.9: Normalized computational time and error versus CFL_N.

	Domain Decomposition				
	2x1x1	4x1x1	2x2x1	4x2x1	2x2x2
Nr. of exchanges	N^2	$3N^2$	$2N^2$	$4N^2$	$3N^2$
CPU time (s)	97	61	53	31	29

Table 2.4: Number of inter-proc exchanges needed for solving the tridiagonal system and CPU time vs different decompositions of a domain.

A more uniform decomposition in all directions, lead to less number exchanges and thus less CPU time.

Validation in two dimensional microwave breakdown in air

The breakdown of MW discharges in air is the first step in our simulations in order to validate our model and obtain more interesting results for such a configuration which will be a basis for the following applications. Considering the 2D case for our numerical model, a microwave discharge initiated by a stationary wave in air and under atmospheric pressure has been simulated. These simulations correspond to the experiments of [10, 11]. The authors in [11] have used a two mirror microwave resonator (figure 2.10) to concentrate the electromagnetic power in a small volume, where due to the, higher than the critical for breakdown, value of the electric field ($E_c \approx 2.5MV/m$ for air), a plasma discharge has been initiated and propagated in the direction of the electric field's polarization (figure 2.11). The so-called plasma streamer stops propagating at a certain length ot breaks into a complex filamentary form.

Numerical experiments in [8] using an explicit formulation of the plasma-EM model have demonstrated that the evolution of the plasma streamer is due to a combination of diffusion and strong ionization at the streamer tips due to the locally amplification of the electric field (similar to the amplification observed in a metallic conductor placed parallel to the polarization of the electric field), though the highly dense grid used, led to CPU times of more than a week in a parallel machine of 24 procs.

The initial values for this case are summarized below:

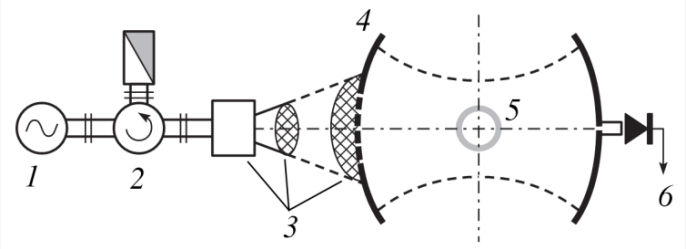

Figure 2.10: Experimental configurationt of an open two mirror cavity: (1) gyrotron, (2) circulator, (3) matching transmission line, (4) open cavity with spherical mirrors, (5) gas filled cell, and (6) connection to an oscillograph [11].

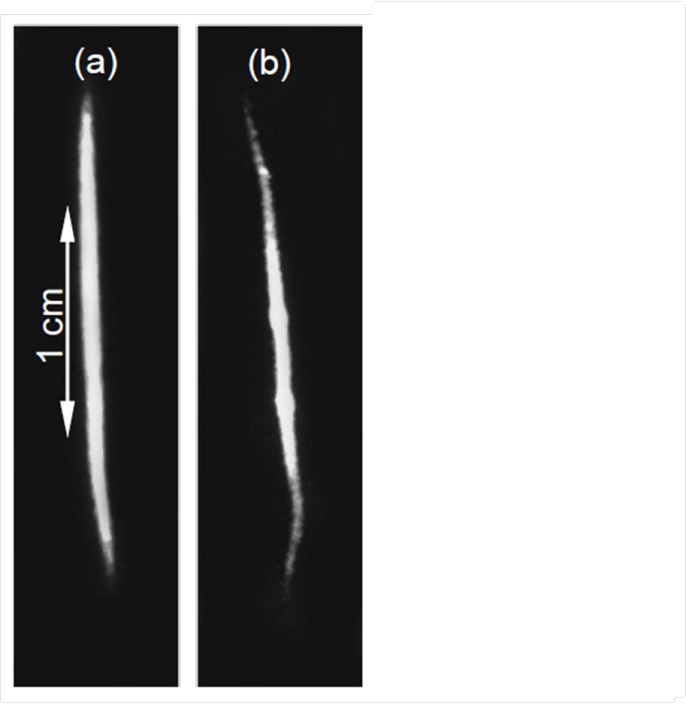

Figure 2.11: Microwave streamer in air at pressure of (a) 480 and (b) 760 Torrs [11].

— TE mode y-polarized plane waves with opposite x-directed wave-vectors of an amplitude $Eo = 2.5MV/m$ each, forming a stationary wave ($Erms = 3.5MV/m$). The frequency of the EM waves is $f = 110GHz$.
— Initial plasma density of a Gaussian profile with maximum of $10^{15}m^{-3}$ in the center of the simulation domain and standard deviation $6 \times 10^{-5}m$. Recombination coefficient neglected.
— Atmospheric pressure ($p = 760torr$)
— Grid spacing equals to $\lambda/1000$.
— Domain dimensions as shown in figure 2.12.

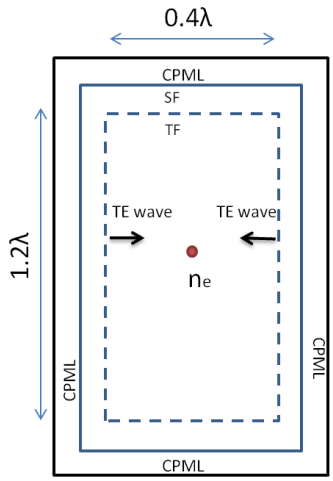

Figure 2.12: Simulation domain and dimensions.

We choose a $CFL_N = 0.03125$. The computational time in a parallel cluster of 24 procs was approximately 2 days for a simulation time of 100 ns. In figures 2.13 and 2.14, the plasma density is presented for different time steps.

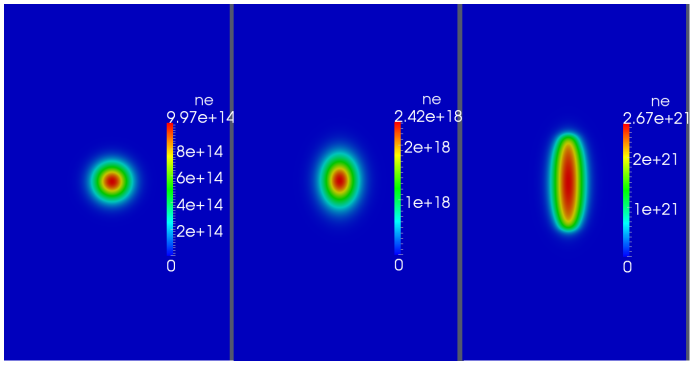

Figure 2.13: Plasma density (m-3) at t=0, 20 and 40ns.

The initial plasma starts to grow due to the overcritical field firstly uniformly until approximately 20 ns. The increase of the plasma density results to an increased plasma frequency, ω_p that soon approaches the critical for shielding one. The plasma starts to behave as a conductor and the electric field is being reflected – reinforcing its amplitude at the plasmoid poles. This reinforcement leads to a stronger ionization coefficient at that region, stretching the plasma towards the electric field polarization direction. When the plasma frequency becomes overcritical the reflection of the waves is stronger (especially in the streamer center where the density is high) and thus the electromagnetic energy is no longer absorbed by the plasma and its density is reduced ($t = 70 - 80ns$).

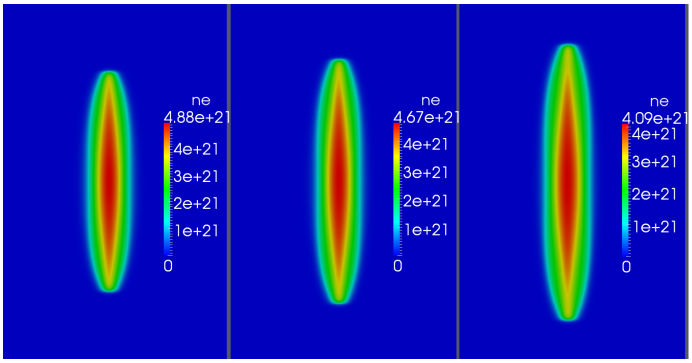

Figure 2.14: Plasma density (m-3) at t=60, 70 and 80ns.

The implicit simulations present remarkable similar results to the explicit calculations of [8]. Note that simulations with a fully explicit scheme have also been performed in order to validate our code and are in excellent agreement with the results obtained in [8]. In table 2.5, the maximum plasma density and the length of the plasma streamer at a time $t = 100ns$, are compared to the results obtained by the explicit scheme and the implicit scheme with a spatial discretization of $\Delta x = \Delta y = \lambda/400$. The error between the explicit and the implicit solver for the same discretization is less than 1%, as expected by the choice of the CFL_N. Moreover, the coarser grid with the same CFL_N choice, leads to an acceptable error, concerning the plasma's density and elongation speed, of approximately 2%.

These simulations validate the model under the described numerical choices. According to these results, for the three-dimensional simulations we fix a grid size of $\lambda/400$ and a CFL number of 16.

	Spatial Discretization		
	λ/1000 - Expl.[8]	λ /1000 - Impl.	λ /400 - Impl.
Length (λ)	0.68	0.685	0.695
Max. density (m^{-3})	5×10^{21}	5.01×10^{21}	5.1×10^{21}

Table 2.5: Streamer's length (in units of λ and maximum plasma density at $t = 100ns$ for two spatial discretizations

Three dimensional simulations of microwave breakdown in air

In this section, we present three-dimensional microwave-plasma simulations in time domain. The 2D case described and simulated in the previous section is here studied in its 3D form. Thus we consider the same initial conditions as before. The numerical domain in the Z-direction spans 0.35λ. The total number of cells for this simulation was 10.752.000. The computational time was more than one week in a parallel cluster of 64 processors.

In figure 2.15 the evolution of the plasma density is observed during time. Figures 2.16 and 2.17, we plot a comparative graph of the maximum plasma density and the streamer's length for the 2D and the 3D case versus time.

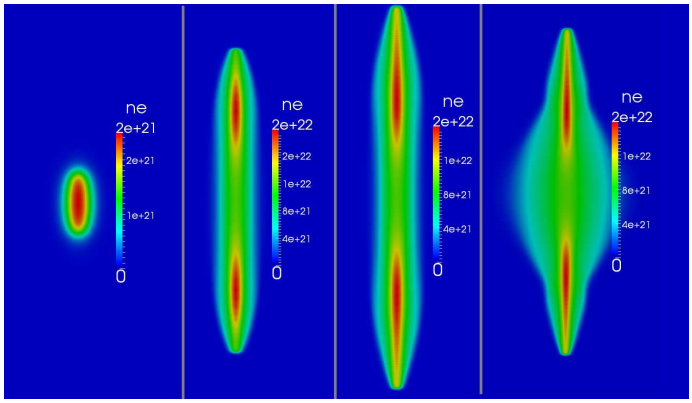

Figure 2.15: From left to right : Plasma density (m^{-3}) in the XY plane at t=40 ns, 60 ns, 80 ns and in the ZY plane at t=80 ns.

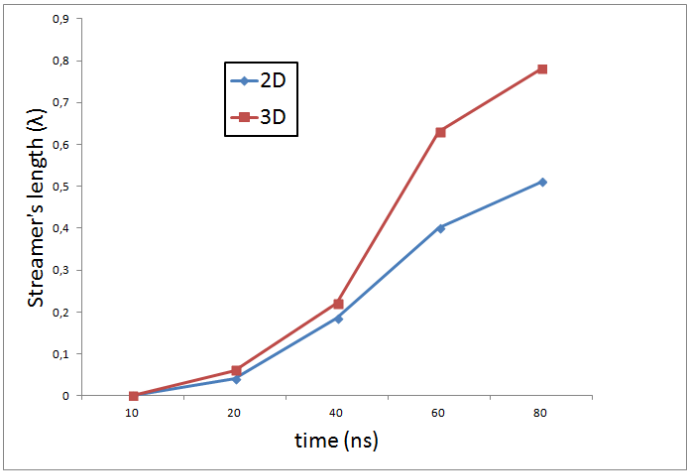

Figure 2.16: Streamer's length in units of λ vs time for the 2D and 3D case.

The plasma streamer behaves in a two-dimensional manner until approximately $t = 40ns$. After that point, three-dimensional effects come to play, as the z-component of the electric field reinforces the total RMS field producing stronger effective fields and thus ionization rates. This three-dimensional effect can be understood if we consider the plasma streamer as a metallic (or) conductor. The reflection of an EM wave by a pin-like conductor is stronger than the one by an infinite plate (the 2D case). In t=60ns, the plasma density is already an order of magnitude higher than the one calculated in the 2D case, leading to a faster elongation of the streamer. The reflection of the electric field is also stronger in this case, consistent with the fact that a metallic initiator of a length equals to 0.4λ, allows for maximum radiation due to resonant effects. Similarly, the dense plasma streamer, resonates at a similar length ($\approx 0.3\lambda$), increasing the electric field at its tips and consequently allowing for a local growth of its density. At a time of 80 ns, the streamer continues its growth

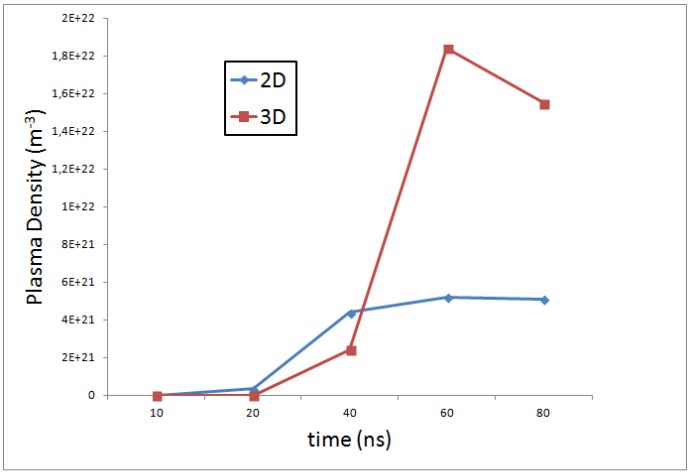

Figure 2.17: Plasma density (m^{-3}) vs time for the 2D and 3D case.

reaching density values higher than $10^{22}m^{-3}$. The electric field is uniform in the z-direction (compared to the x-direction) as we model a stationary plane wave, what explains the more "diffused" plasma in the z-axis.

Figure 2.18, depicts the volume occupied by the plasma streamer at t=80ns. Its length in the y-direction is equal to 0.4λ, while in the x-direction 0.06λ and in the z-direction 0.13λ. Notice that the ionization coefficient is, as observed also in the two dimensional simulations and expected by the elongation direction of the plasma, largely stronger at the tip of the streamer.

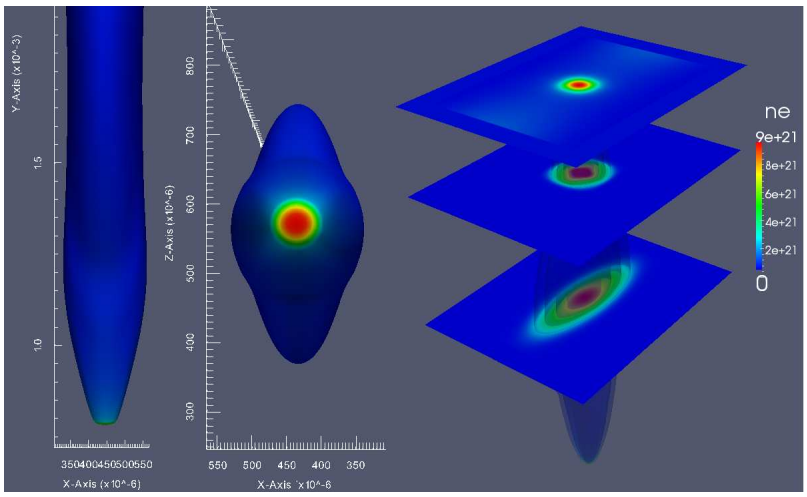

Figure 2.18: Plasma density contours colored by the ionization coefficient in the XY (left) and XZ (middle) plane. Plasma density (m-3) slices in the XZ plane (right). t=80 ns.

These preliminary results open the way to more complex and complete description of the microwave discharges development - a purely and strongly three dimensional phenomenon in real world. Furthermore, it is by such kind of simulations that the amount of energy absorbed by the plasma and eventually transferred to the gas as well as its volume, can be calculated – an essential quantity to be used in fluid dynamics codes to study the aerodynamic effect of the heat deposition. The energy transfer from the plasma to the neutral gas is due to collisions between charged particles and neutral species. Here we assume that a significant part of this energy is transferred instantaneous into the gas for heating [59], since a detailed model of air chemistry is outside the scope of this study. This assumption is consistent with finding of various authors, as a large part of the energy spent from the electrons in electronic excitation of N_2 is transferred quickly into gas heating [60] and the energy spent in elastic collisions or rotational excitation is instantaneously converted into gas heating [61]. The total power density absorbed by the electrons, in terms of joule heating is given by $P_{abs} = jE$, and we assume that the amount transfered to gas equals to $P_{trasf} = 60\%P_{abs}$. By the 3D simulation of the plasma streamer we calculate the energy transfered to gas in $t = 80$ ns, which reaches a value of 0.5 mJ. The volume occupied by the plasma streamer in this time, is approximately 0.06141 mm^3. Supposing that the rate of energy transfer is constant during the 80 ns (although most of it happens after the first 40 ns), we calculate the rate of the energy transfer to gas per unit volume equals to $q = 1 \times 10^8\ Wm^{-3}$. The gas temperature rise corresponding to such rate of heat will reach high values in a short time, modifying the gas density and thus the reduced effective field and the plasma's transport coefficients. The study of gas heating on plasma's evolution will be presented in in a following subsection.

2.3.2 Two and three dimensional simulations of pattern formation during high-pressure, freely-localized microwave breakdown in air.

In order to retrieve information for the energy absorbed and volume occupied by a microwave plasma discharge, we need first to qualify and quantify the breakdown, formation and evolution of plasma structures under microwave radiation. Freely localized microwave plasma discharges are rarely two-dimensional : The complex interaction between them and the electromagnetic waves can lead to a complicated plasma structure, depending on the electric field polarization and focus. This means that one-dimensional models as in [62], can only provide basic qualitatively informations that fail to describe the whole phenomena that take place. Recently, two dimensional simulations based on a more precise theoretical approach [23, 13] and using a simplified plasma model and coupled with a FDTD solver for the Maxwell's equations, showed the capability of such an approach to reproduce experimental results quite well. Though, these simulations are restricted by their two dimensional nature to linearly polarized waves and moreover, they ignore important three-dimensional features of wave reflection and diffraction that could be essential for the microwave discharges of interest.

We focus on the experiments of [63], and we present three-dimensional numerical simulations of a freely localized, high power, millimeter microwave plasma discharge in air and the consequent pattern formation and propagation towards the microwave source. A 1.5 MW, 110 GHz gyrotron oscillator has been used to produce a Gaussian microwave beam that is focused by a high-density polyethylene lens to a peak intensity of 5 MW/cm^2 corresponding to a peak electric field intensity of 6 MV/m. The polarization of the field could be changed from linear to circular. Open-shutter and fast gated photographs reveal the pattern formation and propagation of the plasma discharge towards the microwave source. The plasma breakdown occurs in air and under atmospheric pressure. The experimental configuration is shown in figure 2.19.

The 6 MV/m electric field in atmospheric pressure, provides a reduced field that satisfies largely the

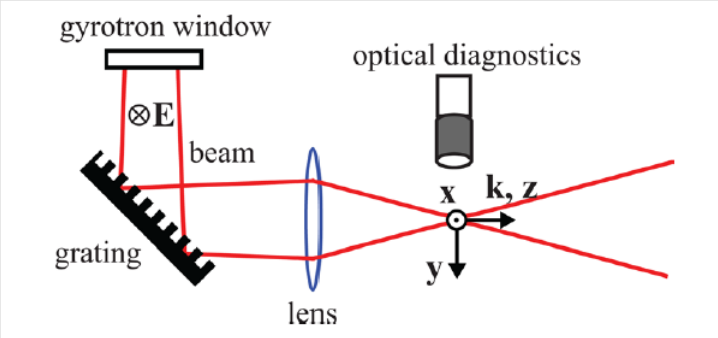

Figure 2.19: Experimental setup for freely localized microwave pattern formation in air [63].

breakdown criterion. Note that the critical effective field for breakdown in air and under atmospheric pressure is approximately 2.5 MV/m. The 6 MV/m field used in the experiments results to a RMS field of approximately 4.24 MV/m , thus way higher than the critical value for breakdown. The initial free electrons are being multiplied due to ionization and the plasma is elongating in the direction of the field's polarization, forming a plasma streamer, similar to the one experimentally investigated in [64]. The elongation continues until its density reaches high values for cut-off to occur. At that point, the plasma frequency ($\omega_p = (n_e e^2/\varepsilon_0 m_e)^{1/2}$), exceeds the microwave field's angular frequency ($\omega = 2\pi f$), and the electromagnetic waves are being reflected from the plasma front. The reflection and diffraction of the electromagnetic waves lead to standing waves formation downstream of the initial streamer filament, where another filament starts to develop. This mechanism continues and the plasma is propagating towards the microwave source in supersonic speeds. A schematic representation of this mechanism is shown in figure 2.20.

These experiments, clearly demonstrate the three-dimensional nature of this discharge under a linearly polarized field. Circular polarization, produces a more uniform almost axisymmetric plasma. Images of the two cases are shown in figure 2.21. As the ionization is a non-linear function of the reduced electric field, small changes on any crucial parameter (electric field intensity, focus, gas' initial pressure, etc) can lead to highly different behaviors. Experiments then, can barely reproduce the exact same pattern.

Linearly polarized case: Two dimensional validation and three dimensional results

We first consider a linearly polarized TE plane wave, to approximate the linearly polarized Gaussian beam produced in the experiments of [63]. The two dimensional and three dimensional cases are compared and various insights are discussed for the three dimensional case.

Model validation with two-dimensional simulations

In order to validate our numerical model, we perform two dimensional simulations of a 110 GHz, TE plane wave. In figure 2.22, the computational domain is shown along with the initial conditions considered. We are studying the electromagnetic wave propagation in the E plane. We assume an initial Gaussian distribution of electrons with a maximum density of $1 \times 10^{15} m^{-3}$ and a standard deviation of 50 μ m corresponding to free seed electrons in air, centered around the x - centerline at a distance of 0.8 times the total field computational domain in the x - direction.

The space step of our simulations is uniform for both directions and correspond to $\Delta x = \Delta y = \lambda/1000$. CFL number has been chosen to correspond to 36 or more time steps per waves' period, limiting the relative error to less than 1% [65]. The results are in excellent agreement with the numerical results obtained in [66],

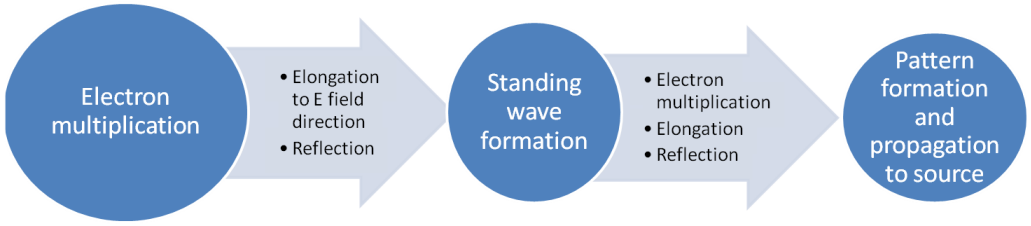

Figure 2.20: Schematic representation of freely localized microwave plasma pattern formation and propagation.

under the same initial conditions (with a peak electric field intensity of 4-6 MV/m). Propagation speeds in the order of 10-40 km/s have been calculated and maximum densities in the order of $1-6\times10^{21}\ m^{-3}$. Different mesh space steps have been used in order to define the necessary mesh size for the three dimensional simulations. This mesh convergence procedure has implied that a spatial discretization of $\lambda/200$, is sufficient for an propagation speed error estimate bounded to $< 3\%$. As we are interested on more qualitative than quantitative results, the resolution of all gradients and length scales is outside the scope of this study. We note though, that a mesh size in the order of micrometer or less is needed (according to the values of ionization frequency and diffusion coefficient in the cases studied) , in order to properly resolve all scales involved. In figure 2.23, the plasma density is shown at $t = 60ns$. More results from the 2D simulations will be presented in the following sections in comparative plots.

Three-dimensional numerical results

The computational domain for the three dimensional simulations is a $2\lambda\times2.2\lambda\times1.5\lambda$ box. The initial plasma is placed at a distance of 1.6λ in the x - direction and centered in the y and z - directions. A 110 GHz, TE plane wave with a peak electric field intensity of 6 MV/m is injected from the left TF-SF boundary and other initial conditions are similar to the two dimensional case 2.22. The mesh size was fixed to $\lambda/200$, and the CFL number to 10. Simulation over 60 ns of simulation time in a parallel cluster of 64 processors lasted approximately 1 week.

The evolution of the plasma versus time can be observed in figures 2.24 and 2.25, in both the XY and XZ

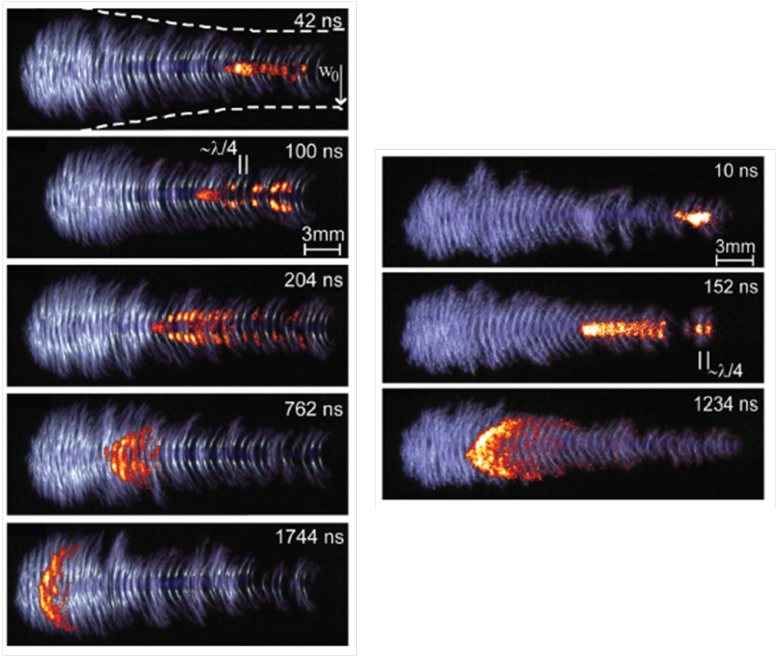

Figure 2.21: Open-shutter (background image, blue) and fast-gated (overlay, orange) photographs of breakdowns with linearly (left) and circularly (right) polarized beam [63].

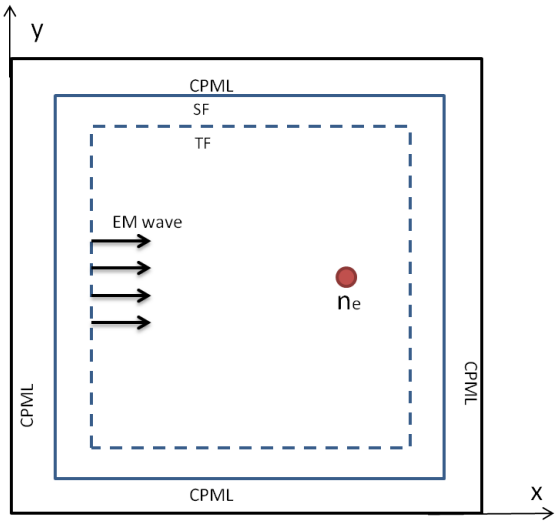

Figure 2.22: Computational domain for the 2D case. Three-dimensional simulations use the same configuration with a z - extension of the domain.

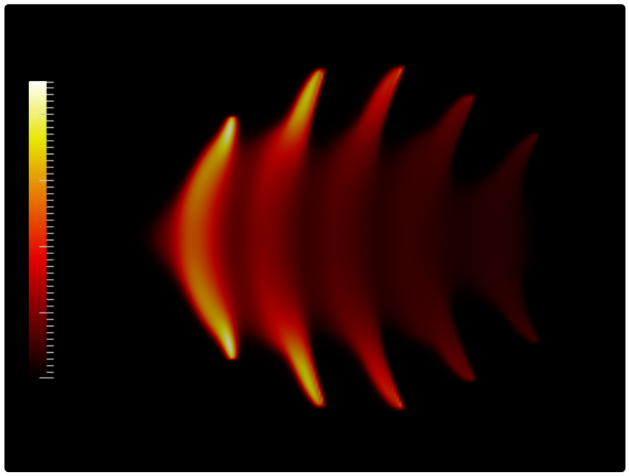

Figure 2.23: Plasma density at time $t = 60ns$. Maximum density is 4.52×10^{21}.

planes. As the experiments of [63, 12] demonstrated, the plasma forms a different pattern on each plane.

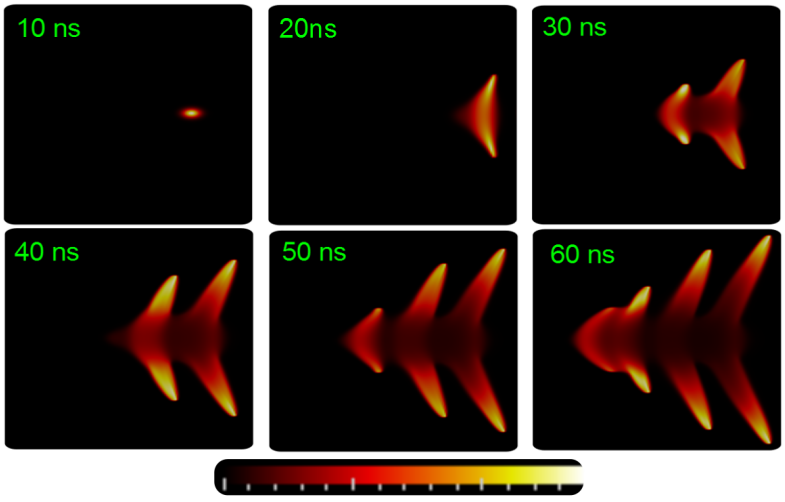

Figure 2.24: Electron density versus time, centered XY plane. Maximum densities are 6.45×10^{19},5.22×10^{21}, 1×10^{22}, 9×10^{21}, 8.9×10^{21}, 8.45×10^{21} m^{-3} respectively.

On the XY plane, which corresponds to the plane where the electric field polarization is directed, the initial plasma starts diffusing and elongating at the y - direction due to the field enhancement on his poles. After approximately 30 ns, a second filament is formed at a distance that corresponds approximately to $\lambda/4$ due to reflection by the initial plasma filament and maxima formation at such distance. The second filament is again elongating to the y - direction until its density becomes again overcritical and reflection begins. Then, the complex interaction between the waves and the two plasma filaments leads to reflection and diffraction

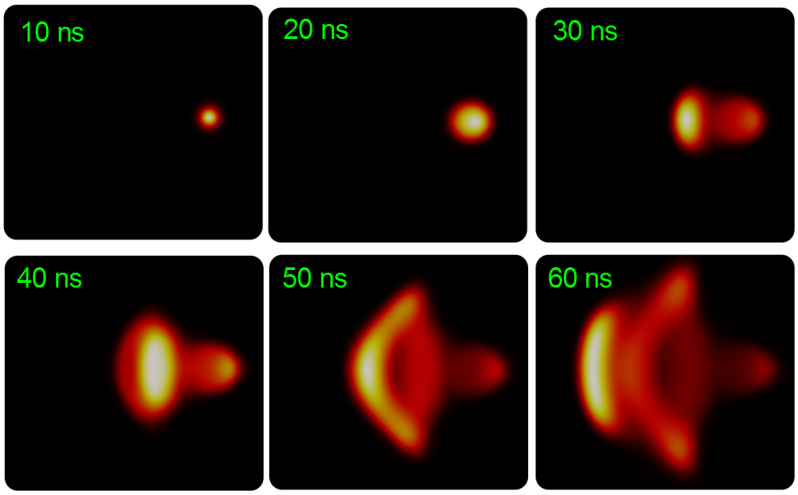

Figure 2.25: Electron density versus time, centered XZ plane. Maximum densities are 6.45×10^{19},5.22×10^{21}, 5.03×10^{21}, 2.39×10^{21}, 3×10^{21} , 2.98×10^{21} m^{-3} respectively.

that causes the formation of two extra field maxima, not in the centerline axis of waves propagation but displaced symmetrical to the z-direction along it. The more spherical now profile of the plasma, leads to a more efficient reflection and concentration of energy at the centerline again, where another filament forms, at a distance of approximately $\lambda/5$. This behavior indicates that, the plasma pattern is not periodic (or more precisely its periodic structure does not correspond to each filament formation), but it exhibits different maximas and thus electron concentration regions during its propagation towards the microwave source. That is clearly demonstrating the three dimensional nature of such discharges. In the two dimensional case, the plasma pattern presents almost periodic maximas, resulting to a constant filament distance of approximately $\lambda/4$. In figure 2.26, the electron's density is plotted on the centerline x - axis at time $t = 70ns$, and the difference between the filaments distance according to position can be observed. This behavior, is in complete agreement with the images provided in [63], even though the authors talk about a constant distance of $\lambda/4$.

In figure 2.27, iso-surface contours of the electrons' density at a value of 1×10^{21} m^{-3} are presented, showing the fish-bone structure of the plasma discharge with its extension to the transverse to the z - direction. The contours are colored by the effective ionization frequency and also the dimensions of the discharge are shown. The plasma discharge is highly elongated at the beginning (the two first filaments) reaching lengths of more than 2λ in 70 ns , while at the z - direction it extends to a width of approximately $\lambda/2$.

Comparing the results with the two dimensional case, we note that the propagation speed of the plasma patterns front is quite smaller for the three dimensional case, reaching speeds of that vary between 30-38 km/s while in the two dimensional case the plasma front propagation speed is almost constant and approximately 41 km/s. In figure 2.28, the distance traveled in the x - axis is plotted over time, demonstrating the above statement.

We also note that in the 3D case and due to the stronger field enhancement around the initial plasma poles, the elongation of each streamer is faster. This is clearly seen in figure 2.29, where the maximum length at the transverse to waves propagation dimension, of the first and third plasma filament is plotted versus time. Two dimensional simulations, result to shorter plasma filaments, that stop growing as soon as they are blocked to the electromagnetic waves by the subsequent filaments. This is not the case at least for the 1st filament in the

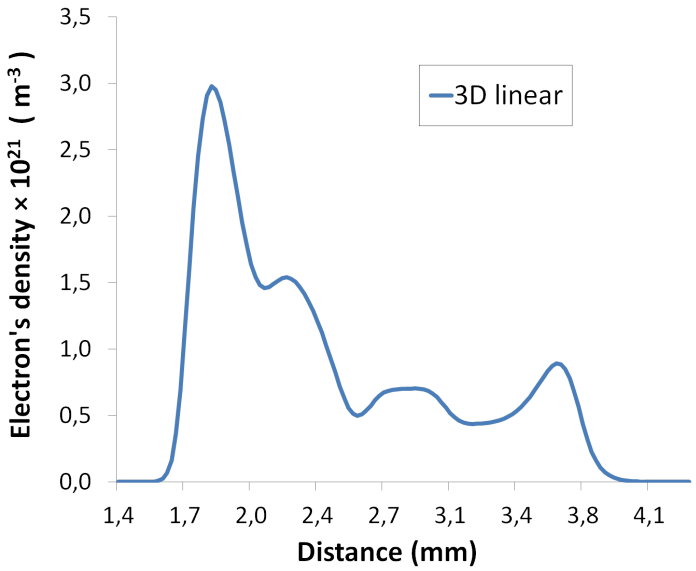

Figure 2.26: Electron density at the centerline x - axis, $t = 70ns$.

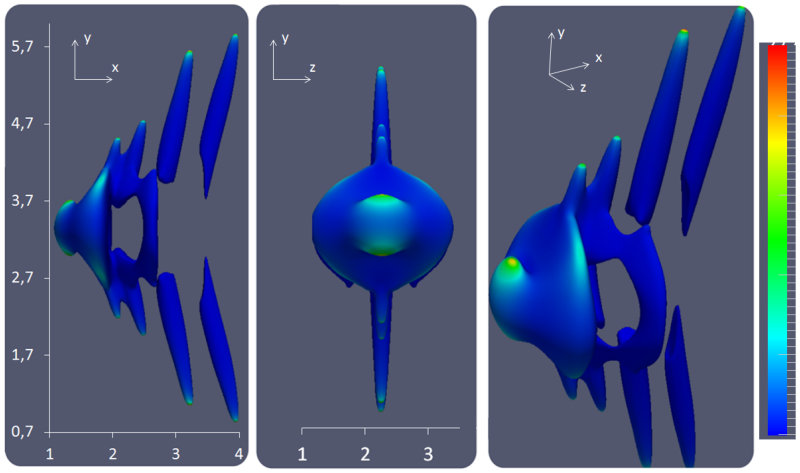

Figure 2.27: Electron density iso-surface ($1 \times 10^{21}\ m^{-3}$) contours colored by ionization frequency, $t = 70ns$, XY (left), YZ (middle) planes and 3D view (right). Maximum effective ionization frequency $9.7 \times 10^9\ s^{-1}$. Axis lengths in mm.

three dimensional case, which continues growing even 90 ns after the initial breakdown.

More on these effects, are discussed in subsection 2.3.2, where we are trying to explain this difference using a simplified approach.

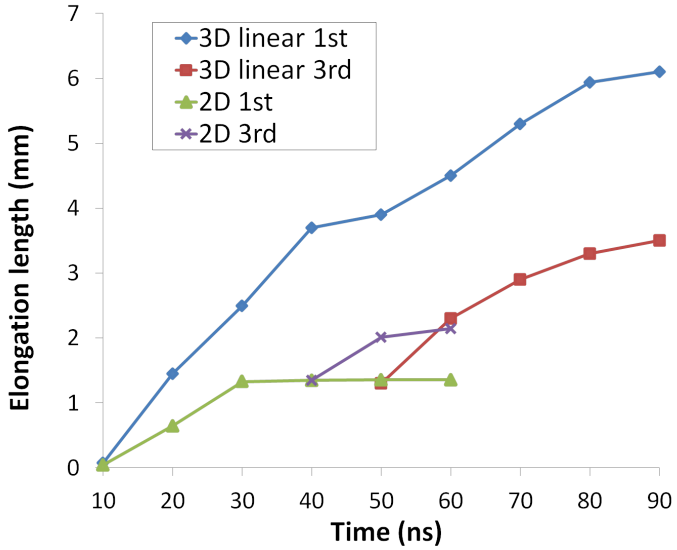

Figure 2.28: Distance of plasma patterns front traveled versus time for linear polarized three and two dimensional cases.

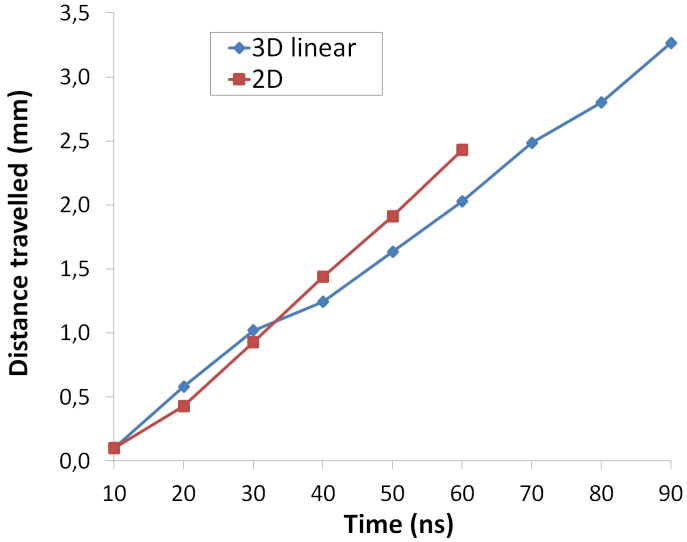

Figure 2.29: Elongation length of the first and third filament versus time for linear polarized three and two dimensional cases.

Circular Polarized case : Three dimensional results

Numerical Results

The computational domain for this subsection, is a $2\lambda \times 2\lambda \times 1.5\lambda$ box. Initial conditions are identical to subsection 2.3.2, except from the incident wave condition. Here we consider, a 110 GHz circularly polarized

plane EM wave with a peak electric field intensity of 6 MV/m , propagating in the x-direction similar to the two dimensional case as shown in 2.22. In figure 2.30, the electron density is plotted versus time on the XY plane (centered to the z - direction). Under such polarization, the plasma streamer has no preferable direction of elongation and so, the plasma filamentary structures form as circular discs, with almost identical profiles at the XY and XZ planes.

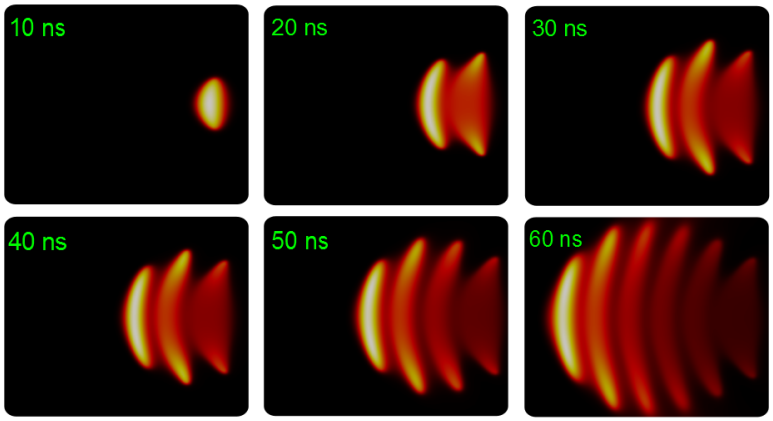

Figure 2.30: Electron density versus time, centered XY plane. Maximum densities are 2.79×10^{21},3.6×10^{21}, 3.34×10^{21}, 3.2×10^{21}, 3×10^{21}, 2.83×10^{21} m^{-3} respectively.

Figure 2.31, shows contours of electron density on an iso-surface of 3×10^{20} m^{-3} colored by the effective ionization frequency at $t = 60$ ns for the XY and YZ planes. The plasma discharge takes a form of a mushroom-like pattern of varying discoid cross-sections, as it propagates towards the microwave source. The discoid structures have almost circular cross sections of an approximate maximum diameter of 0.75λ.

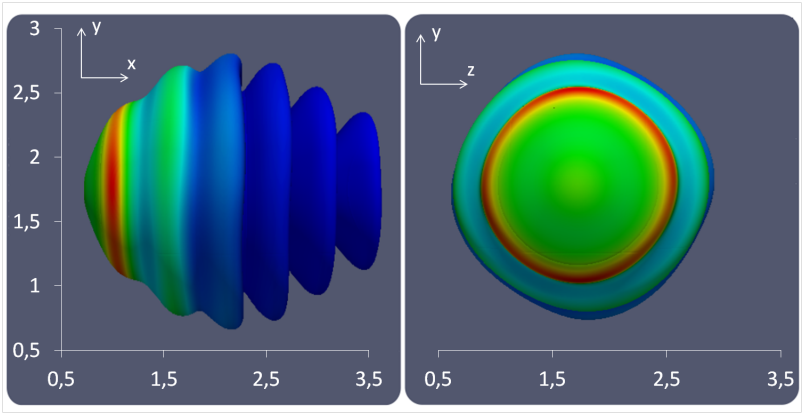

Figure 2.31: Electron density iso-surface (3×10^{20} m^{-3}) contours colored by ionization frequency, $t = 60ns$, XY (left) and YZ (right) planes. Maximum ionization frequency 1.7×10^{9} s^{-1}. Axis lengths in mm.

The distance between each plasma disc - filament is constant and corresponds to a length of approximately $\lambda/4$. In figure 2.32, the electron's density is plotted on the centerline x - axis at time $t = 60ns$ clearly

demonstrating the equal distanced filaments and the periodic propagation of the discharge in the opposite direction of the electromagnetic wavevector.

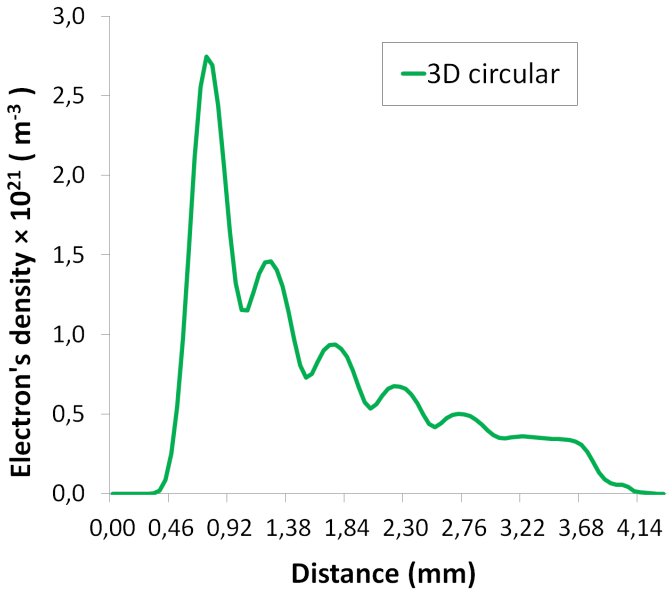

Figure 2.32: Electron density at the centerline x - axis, $t = 60ns$.

Comparative plots

The propagation speed of the plasma patterns front is constant and reaches values of 54 km/s. In figure 2.33, the distance traveled by the plasma front in the x - direction is plotted versus time. For comparison on the same graph, the results from the linear polarized case are also plotted.

As we did in the previous subsection, we are interested in the maximum elongation of each plasma filament at the transverse directions to the waves propagation. In figure 2.34, the 1st and 3rd filaments elongation length are plotted versus time, comparing the linear polarization to the circular one. The uniform elongation for the circular polarization results to shorter filamentary discs, that seem to retain their maximum length for a long time. In that case, it is the third filament and not the initial one that reaches higher lengths, while its breakdown at that position occurs faster in time compared to the linear polarization.

Discussion on patterns' propagation speed and experimental observations

In order to investigate the parameters controlling the propagation speed of the plasma patterns as well the elongation of the individual streamers, we study the reflection and diffraction of a linear polarized 110 GHz plane wave with peak field intensity of 6 MV/m, from a constant density plasma structure. This decoupled, simplified approach allows us to understand the reasons behind the difference observed under the two and three dimensional cases as well as the polarization effects.

The computational domain is a $0.6\lambda \times 0.6\lambda \times 0.6\lambda$ cube. We study three different forms of a plasma structure, centered around the x - centerline at a distance of 0.48λ : A two dimensional plasmoid, extending uniformly to the z-direction, a three dimensional prolate plasmoid corresponding to the linear polarized form

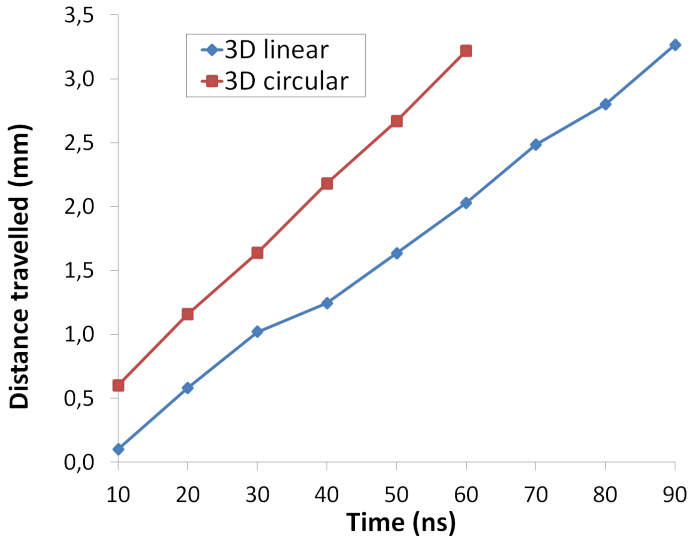

Figure 2.33: Distance of plasma patterns front traveled versus time for linear and circular polarized incident waves.

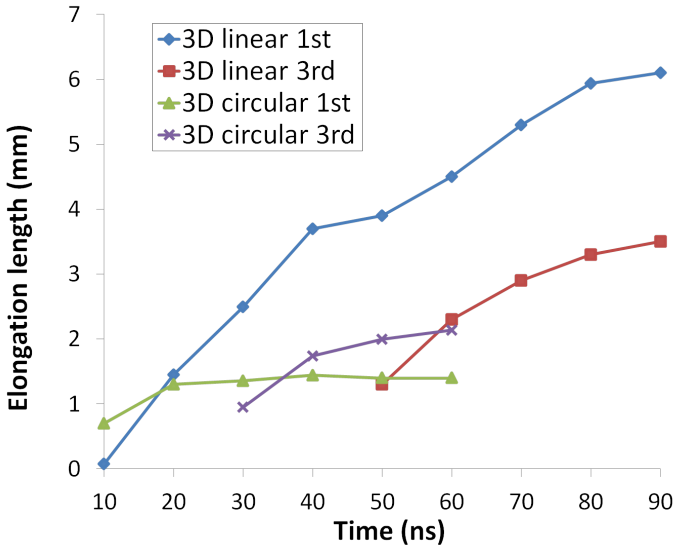

Figure 2.34: Elongation length of the first and third filament versus time for for linear and circular polarized incident waves.

of first plasma filament, and a three dimensional plasmoid in the form of a disc, corresponding to the plasma filament structure formed by a circular polarized wave. The constant plasma density in the plasmoids follow a

gaussian profile with a maximum density of 8×10^{21} m^{-3} and a standard deviation of 6×10^{-5}, 2.5×10^{-4}, 6×10^{-5} m in x, y and z directions respectively, for the 2D (with infinite extension in z-direction) and the prolate plasmoid, while for the disc plasmoid the deviation is 6×10^{-5}, 2.5×10^{-4}, 2.5×10^{-4} m in x, y and z directions respectively. The form of the plasmoids for the 3D cases, is presented in figure 2.35 as the 1×10^{21} plasma density iso-surface contour.

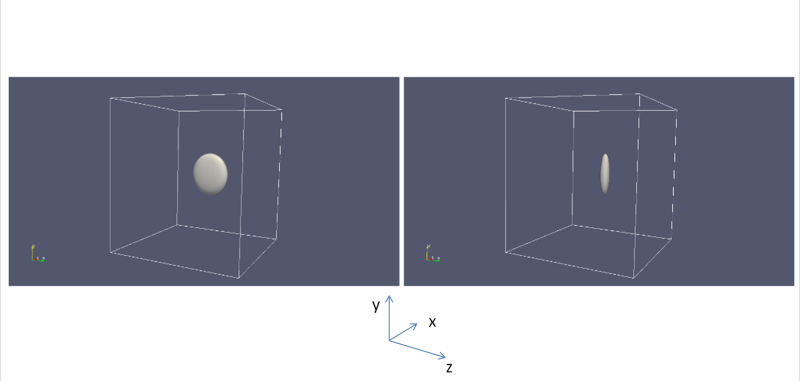

Figure 2.35: Plasmoid forms for the disc (left) and prolate (right) simplified approximations.

Note that the critical plasma density for cut-off for a 110 GHz wave is $n_{cr} = \omega^2 \varepsilon_0 m_e / e^2 = 1.5 \times 10^{20}$ m^{-3}, so the plasmoids are strongly reflecting the EM waves corresponding to density values close to the ones calculated in the previous subsections. In figure 2.36, the RMS electric field is plotted at the centerline x - axis, for the three cases. The reflection and corresponding maxima of the RMS electric field is higher for the 2D case, followed by the 3D disc and the 3D prolate plasmoid cases. As the ionization frequency depends on the RMS field under constant density, the resulting propagation of the plasma pattern towards the source (in the direction of propagation of the EM waves) occurs at higher speeds for the 2D case and lower speeds for the prolate plasmoid case, in agreement with our simulations results. To study the elongation of a simple plasma filament or structure, in figure 2.37 the RMS electric field for the 2D, 3D prolate and 3D disc cases are plotted on the y-line centered at the plasmoid's elongation axis. The enhancement of the field at the plasmoid's poles, is stronger for the 3D prolate plasmoid, resulting to longer individual filaments in the y - direction as observed in our simulations. The higher electron density calculated for the linear polarized three dimensional case, are also consistent with such effect.

Note that even a small increase of the RMS field can lead to a high increase of the ionization frequency (due to the exponential dependence see figure 2.1) and thus to an equivalent increase of the filament's elongation or the pattern's propagation speed.

Discussion on experimental observations :

The results of the three-dimensional simulations are in excellent agreement qualitatively with the experimental observations of [63]. The authors there, present some quantitative results regarding the patterns' propagation speed as well as the elongation of the filaments for both a linear and a circular polarized Gaussian beam. Compared to our work, they have measured higher speeds for the linear polarized wave that reach values of 100 km/s in the initial stage and fall down to 10 km/s later. They note that the Gaussian beam focus is responsible for this effect, as the intensity of the electric field reduces as the discharge moves out of the focal point. Although the numerical results are not far from the observed range of propagation speeds, we

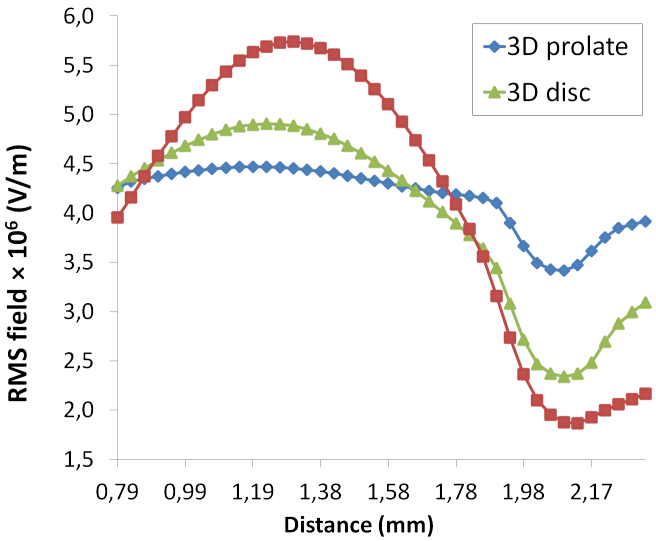

Figure 2.36: RMS electric field for the 2D, 3D prolate and 3D disc cases plotted on the centerline x axis.

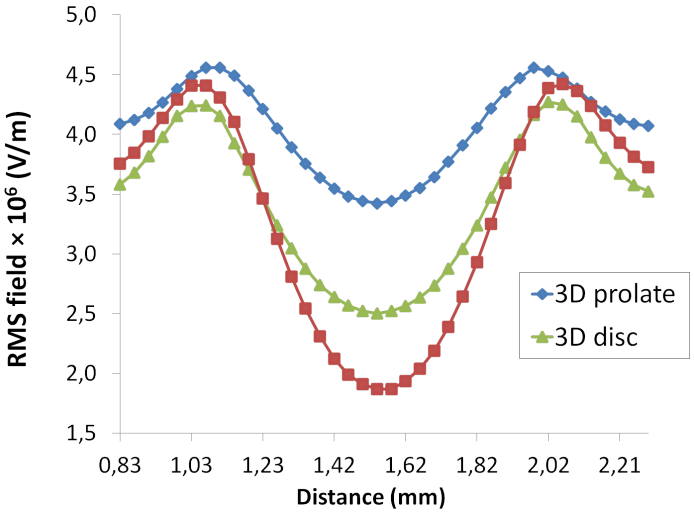

Figure 2.37: RMS electric field for the 2D, 3D prolate and 3D disc cases plotted on the y-line centered at the plasmoid's elongation axis.

must note that besides the numerical discretization errors that can certainly be a cause for this discrepancy, exact agreement to experiments is hard to obtain, due to the uncertainty on the exact intensity of the electric field at the experimental setup and the strongly non-linear dependence of the ionization coefficient on the electric field. Moreover, the elongation of a single filament in the experiments is restricted by the envelope of the gaussian beam. This results to shorter filaments at the early stages of the propagation and to longer ones

at later stages. Thus, exact comparison with our numerical results is again uncertain. Surprisingly though, the authors have measured lower propagation speeds for the circular polarization compared to the linear one. This contradicts both our simulations and the simplified study we have performed, raising doubts about the mentioned (6 MV/m) and achieved maximum field at the experiments.

2.3.3 Effects of gas heating on streamer's development

In a freely localized microwave discharge of such streamer form, resonant effects are thought to play an important role on its development and elongation speed. Indeed, it is known that a dipole antenna formed by two conductor elements placed back to back and driven by a sinusoidal current allows for optimum radiation due to resonant effects when its length is $\lambda/2$. The high density plasma streamer, can be considered as a conductor element, that produces different maximas and its poles according to its elongation length. The authors in [67], mention that the streamer's growth is bounded by this resonant length and its at such length that complex filament branching takes place, as observed in [1]. The explanation of such a behavior is not clear, as resonant effects would normally lead to higher values of enhanced field at the poles of the streamer plasma, and thus stronger ionization and elongation speeds. This is numerically demonstrated in [8].

In reality, the plasma streamer absorbs large amounts of electromagnetic energy, leading to a relative fast gas heating. The rate of absorption depends on various parameters but it is known that plasma streamers present a very good efficiency of such absorption. In most of experimental, theoretical and numerical approaches, the effects of gas heating is not taken into account in order to explain the plasma streamer's evolution and length's restriction. These non-linear effects can provide important insights on such parameters and therefore, coupled numerical simulations are necessary.

In this section, we present numerical simulations of breakdown and evolution of a freely localized, single microwave streamer in air taking into account gas heating effects. With this more simplified than the propagating discharge case, we can better investigate the interaction between the underlying physics.

The effects of gas heating on the evolution of a streamer microwave discharge is essential as the plasma's transport coefficients depend on the reduced field E/N, where N is the gas density. The heating of neutral gas molecules due to the Joule heating by the microwaves results in a change of the temperature and density distribution of the gas. As gas density decreases the following consequent relations hold, assuming an instantaneous response to the change of gas density :

— The frequency of collisions decreases.
— The effective field decreases.
— The effective ionization frequency decreases.
— The electron's mobility increases.
— The electron and ambipolar diffusion coefficients increase.

The time scales for the gas and plasma transport are essential in that point. The above relations hold instantaneously, but the plasma density will respond to these changes and vary accordingly, modifying in its turn the joule heating source term and thus the gas density. It is indeed the plasma evolution time scales that vary faster than the gas ones. As the plasma keeps absorbing energy from the EM field and transferring it as heat to the gas' molecules, the fast energy deposition can lead to shock wave formation or more accurately a blast wave that propagates outwards from the plasma zone. This blast wave, introduces a discontinuity in the flow, modifying brutally its properties. After the formation of the blast wave, it is traveling in high speeds (that can reach several times the speed of sound), so the time scale of this phenomenon can be comparable to the plasma ones.

The production of a blast wave is due to the intense heating of an air volume during a small period of time. As the temperature of air increases, its pressure increases too. The air is thus expanding to equalize the pressure difference with the surrounding air, sending a pressure wave into it. As the high pressure air expands, its density is increased and with it its pressure. The shock wave that forms due to the expansion of the hot gases propagates outwards at high velocities. This blast-shock wave is a discontinuity for the flow, presenting pressures at the shock front that can be some times larger than the already high pressure in the interior of the hot zone. As the blast wave travels away from the heated zone, its intensity decreases as well as the pressure distribution behind it. For long distances, a negative phase of the blast wave can form : The pressure just behind the shock front becomes lower than the surrounding atmosphere, forming a zone where the air is sucked it instead of pushed away from the energy source. The under-pressure is always lower than the overpressure. Both the positive and negative phases of the blast wave, reduce with increasing distance from the source until the pressure returns to the ambient one.

In the case of plasma formation by microwaves, intense heating can be achieved in a small time scale. In the previous section we showed that rates of volumetric energy transfer in the order of $q = 1 \times 10^8\ Wm^{-3}$ can be achieved. A simplified calculation shows with such rate, a small volume of air (for example the streamer's volume calculated in the previous section) can be heated to more than $1000K$ in less than a $0.1\mu s$. Such temperature rise results to a density drop in the plasma zone, that can affect greatly its evolution, in terms of ionization rate and propagation. Thus, the energy absorption by the plasma - as it depends directly on the electric field and the plasma density - as well as its volume can be accurately reproduced only if the gas heating effects are taken into account.

In order to investigate a microwave streamer creation and development under the effect of gas heating taking into account real gas effects, we retain the two - dimensional solver for this set of simulations and couple it with the real-gas Euler solver in predescribed time-steps. In figures 2.38 and 2.39, the structure of the numerical procedure is shown as well as the time marching scheme.

The Maxwell equations including the plasma current is first solved inside the EM waves period T_{EM}, with the time-step that corresponds to the CFL number of choice. In this section we use a mesh size of λ / 800 and a corresponding CFL number of 32 as the gas heating effects lead to strong gradients of the plasma density that are important to be resolved. At the same time-step, the plasma density is recalculated taking into account only the source terms contribution. The plasma diffusion equation is then resolved at each EM wave period. The energy absorbed as joule heating from the plasma is calculated at the end of each EM period and it's being accumulated and stored. We make the choice of coupling the gas dynamics with the EM-Plasma solver each $T_{gas} = 1ns$ that corresponds to 110 periods for an EM wave of 110 GHz. The absorbed energy is then introduced as a source term in the fluid solver and the consequent gas heating during this time interval is being calculated, providing at the end the density field which is injected in the plasma - EM solver in order to recalculate the plasma transport coefficients with the modified gas density. The whole circle starts then again until the next coupling interval. The CFL number for the fluid solver is set to 0.5 assuring stability.

The results presented here are structured as follows : Firstly, the evolution of a, decoupled from the gas effects, plasma streamer in times longer than 100 ns is presented, demonstrating that the streamer has no reason to stop elongating when the gas heating effects are not taken into account. Next, numerical results of the coupled solver are presented as well as some numerical experiments on the coupling time-step and the mesh size. A discussion on the validity of our results and the possible improvement is finally performed.

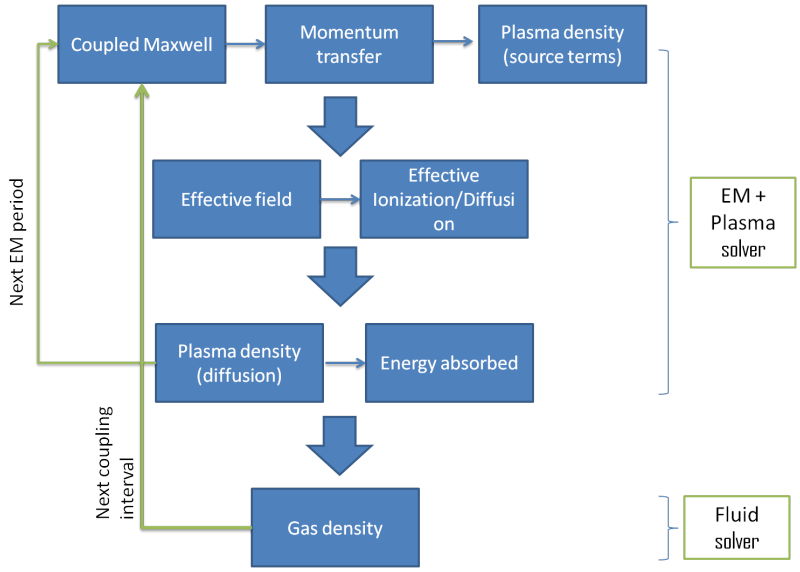

Figure 2.38: Coupling procedure and time scales for the EM - Plasma - Fluid solver.

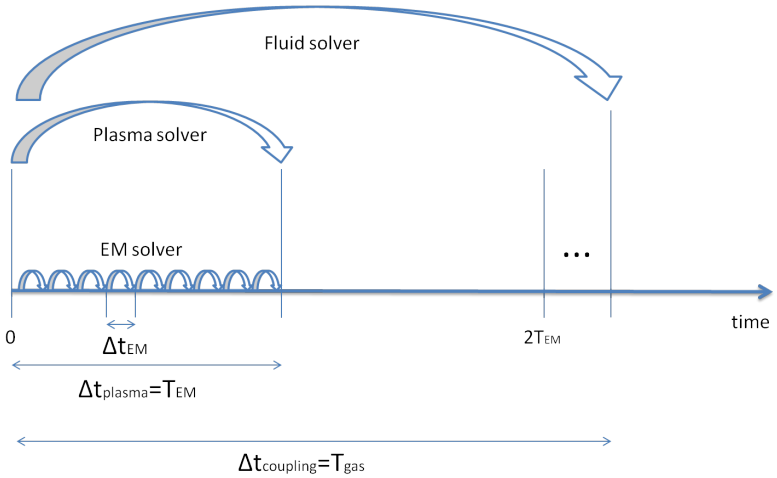

Figure 2.39: Time stepping representation for the EM - Plasma - Fluid solver.

Plasma streamer breakdown and elongation with no gas effects

We are considering a prolongating in the y-direction computational domain and same initial conditions as described in subsection 2.3.1. The recombination coefficient is assumed to be constant and equal to 3×10^{-14} consistent with data provided in [68]. The elongation of the plasma streamer in the direction of the electric field is continuous in time, as a result of the ionization-diffusion mechanism. In figure 2.40, the plasma density in different times can be observed.

The effective ionization at the tips of the plasma streamer is always positive, denoting that strong ionization

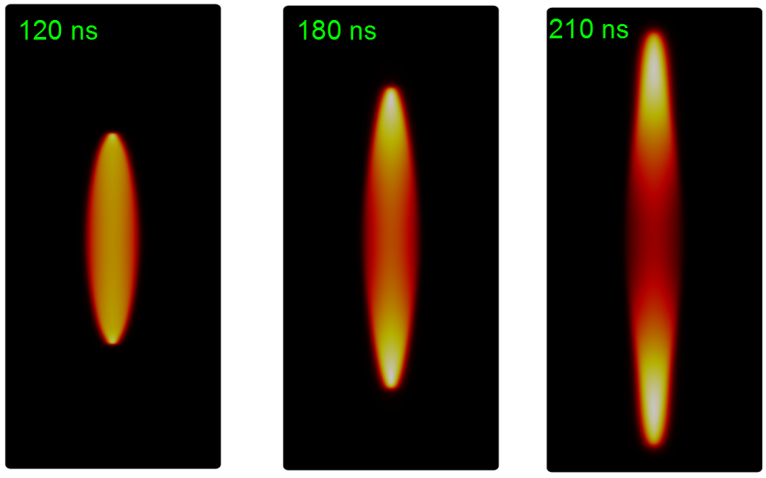

Figure 2.40: Plasma density versus time. Maximum densities are 2.1×10^{21},1.9×10^{21}, 2.2×10^{21} m^{-3} respectively.

takes place at that regions, leading to the elongation of the plasma in the y-direction. The length of the streamer, reached the resonant length of $\lambda/2$, in approximately 100 ns and continues growing for further times as plotted in figure 2.41. At 210 ns, the length of the streamer has reached approximately the wavelength λ of the EM waves (2.7 mm in this case).

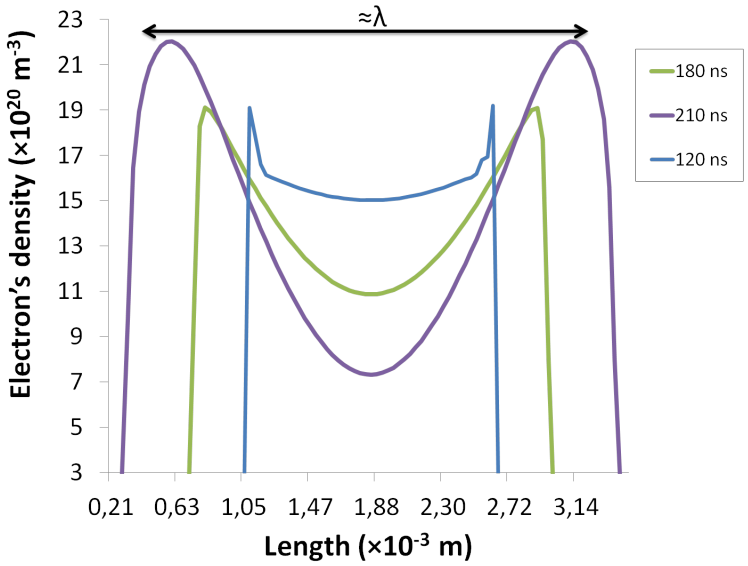

Figure 2.41: Electron's density versus distance plotted over the centerline y axis for different times.

Under such ideally symmetric plane wave configuration, the plasma has no reason to stop elongating. This is clearly seen also in the case of a less strong incident electric field. In figure 2.42, a 2 MV/m incident EM wave has been used and as it can be observed the elongation of the plasma streamer is still continuous. Of course, as the reduced effective field and the corresponding enhanced field at the tips of the streamer is less than the previous case, the elongation of the streamer is slower.

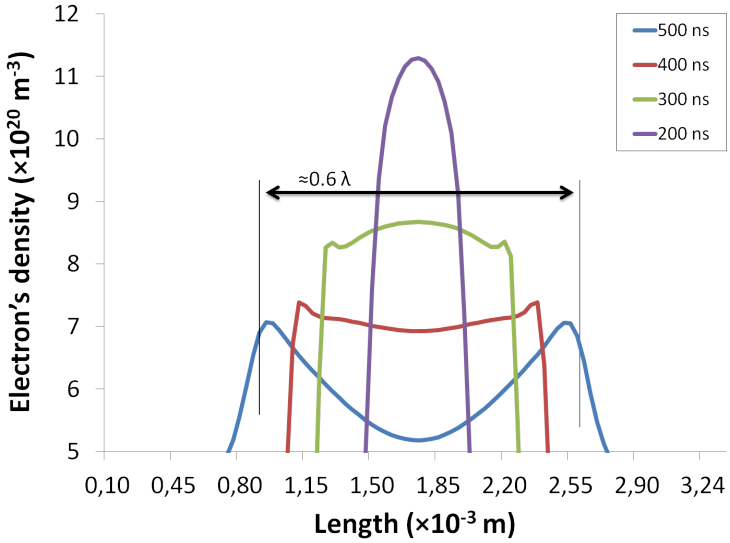

Figure 2.42: Electron's density versus distance plotted over the centerline y axis for different times.

Plasma streamer breakdown and elongation under the gas heating influence

The above simulations clearly demonstrate that the elongation of a plasma streamer and the experimentally observed confinement of it at lengths smaller than the EM wavelength, include more physics than just the coupling of the EM waves and the plasma. To study the effect of gas heating and thus density change, we perform simulations of microwave breakdown in air, coupled with the real-gas Euler fluid solver. We retain the simulation conditions described in the previous subsection ($E_0 = 2.5MV/m$ here), and couple the EM-plasma solver with the Euler one at each 1 ns: The energy absorbed as joule heating from the plasma, is introduced as a source term in the Eulers equations, simulating the heating of air and consequent shock formation. Then the density field is injected in the plasma - EM solver in order to recalculate the plasma transport coefficients with the modified gas density.

Our simulations demonstrate that at a time longer than 100 ns, the gas heating effects can not be neglected as they lead to a substantial modification of the plasma streamer's behavior. In figure 2.43, plasma density contours are plotted for different time instants.

As the initial plasma transfers energy to the gas, the density of the latter diminishes. This leads to a higher reduced field E/N (or E/p), and thus to stronger ionization in the plasma bulk. For times lower than 100 ns, the heating of the gas is not intense and the maximum temperature of the gas reaches values of 400-500 K. As more energy is being transfered to the gas in time, the temperatures exceed 1000 degrees K in approximately than 100 ns. A pressure blast wave is then formed, whose intensity increases as more energy is being absorbed

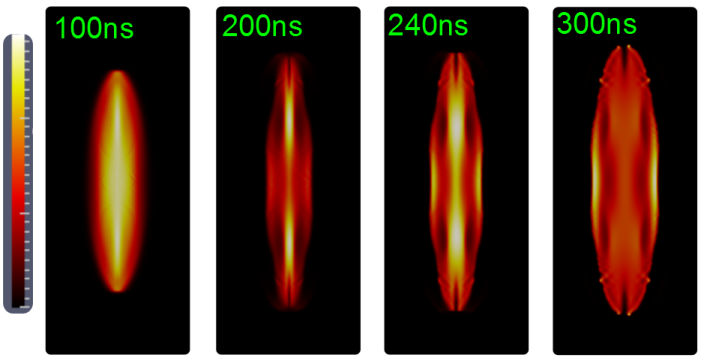

Figure 2.43: Plasma density versus time. Maximum densities are 2.7×10^{21},8×10^{21}, 5.8×10^{21} and 5.7×10^{21} m^{-3} respectively.

by the gas (see figure 2.44). Note that the gas density in all figures, is plotted as a fraction of the initial ambient density, $\rho_{amb} = 1.184\ kg/m^3$ for $T = 300$ K.

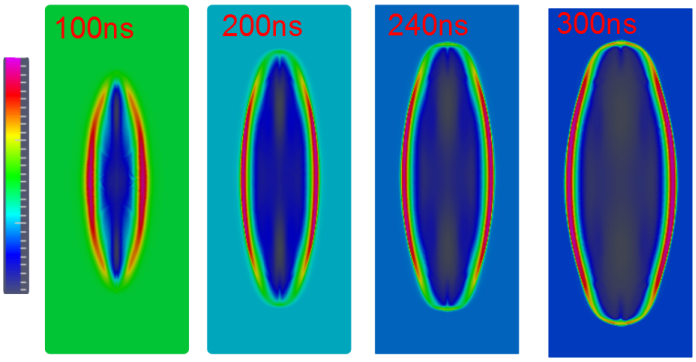

Figure 2.44: Gas density versus time. Maximum values are 1.138,2.48, 3.25 and 3.94 $\times\rho_{amb}$ respectively. Minimum values are 0.88, 0.319, 0.223 and 0.162 $\times\rho_{amb}$ respectively, where $\rho_{amb} = 1.184\ kg/m^3$.

The blast wave restricts the plasma growth and diffusion in a thin region inside the core of the plasma streamer. When the plasma streamer reaches its resonant length, the ionization is being reinforced at its tips, leading to the two symmetrical to the central x-axis areas of increased plasma density , while at the plasma bulk the density is being reduced due to the reflection of the EM waves from the conductor-like streamer, just like we have seen before. The difference here is that in these two areas near the streamer edges, the energy absorption is higher. There, the gas is heated locally, producing again blast waves that interfere with the initial one, changing the form of the strong ionization region (initially placed just ahead of the plasma tips), as seen in figure 2.45. The small zone of negative effective ionization frequency, that forms just on the tips of the streamer at less than 200 ns, forces the plasma to break into a horn like structure that keeps elongating until the blast wave that encircles the streamer becomes strong enough to drop the effective ionization into negative values in this whole ring zone (see figure 2.47. Note that the effective ionization frequency becomes

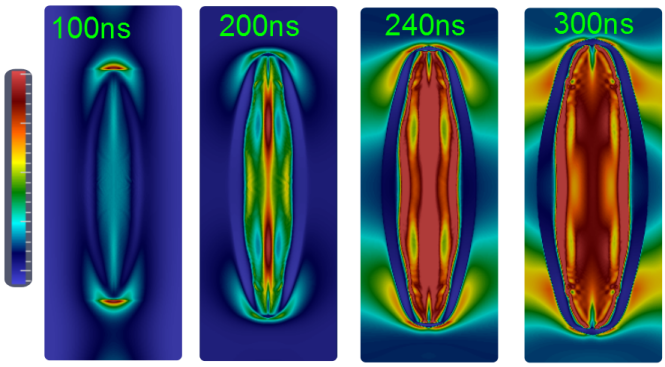

Figure 2.45: Effective ionization frequency versus time. Maximum values are 4×10^8, 2.3×10^8, 1×10^8 (scaled) and 1×10^8 s^{-1} (scaled) respectively. Minimum values are -2.6×10^7,-4.4×10^7, -5.1×10^7 and -5.6×10^7 s^{-1} respectively.

negative at a density of around $1.43\times\rho_{amb}$ (for the given incident field) as shown in figure 2.46.

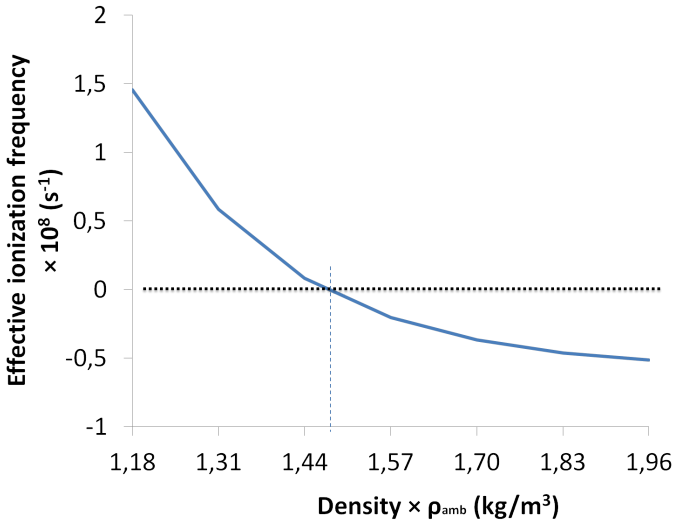

Figure 2.46: Effective ionization frequency versus gas density.

The streamer then, stops elongating in the y-direction, due to the high density shock wave ring that forms around it. This is clearly demonstrated by figure 2.48. Even at a time of 300 ns, the length of the streamer does not exceed half the EM waves wavelength, remaining almost constant during 100 ns.

The gas temperature increases greatly in time reaching values of more than 5000 K in 300 ns as shown in figure 1.34

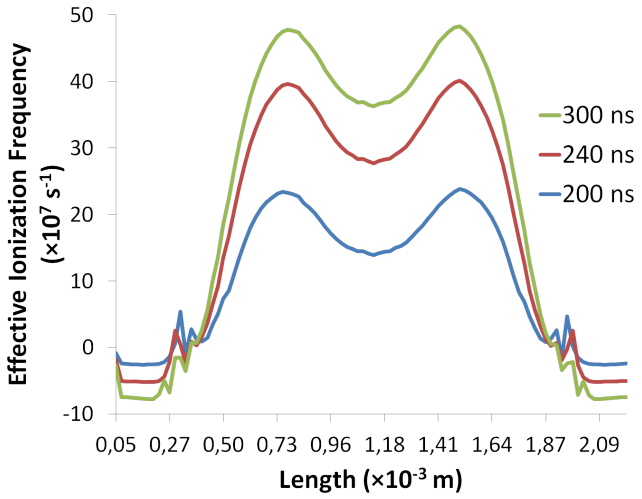

Figure 2.47: Effective ionization frequency versus distance plotted over the centerline y axis for different times.

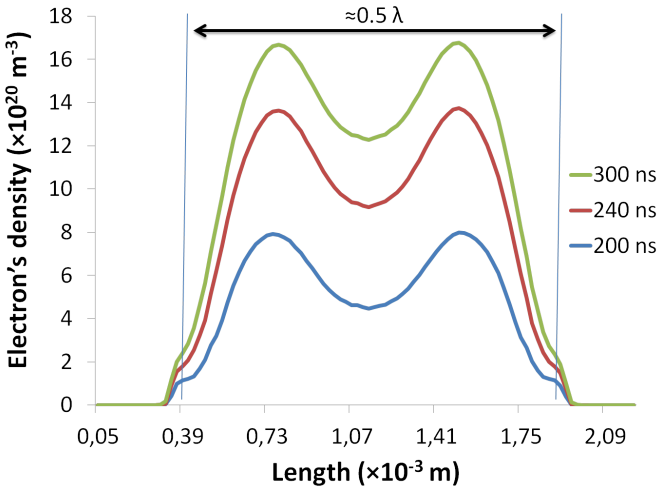

Figure 2.48: Electron's density versus distance plotted over the centerline y axis for different times.

Summary and discussion on validity and possible improvements :

These simulations clearly demonstrate the strong coupling between the plasma dynamics and the gas ones. Neglecting such interaction, leads to false results that can not explain the experimental observations. As shown, the intense gas heating leads to a strong modification of the density field that has a large non -linear impact to the effective ionization rate and thus to the evolution of the plasma streamer. Moreover, the blast wave produced by the fast gas heating, leads to a discontinuity zone of high density that blocks the plasma propagation.

The study presented above can explain the evolution and restriction of growth of a plasma streamer due to gas heating effects. Nevertheless, we need to note that the physical model reached its limits as the density drop caused by the gas heating leads to an increase of the electrons mean free path. Under atmospheric conditions the mean free path is approximately 1 μm and scales with the inverse of the gas density while the front's gradient - linked to the EM field characteristic length scale, $L = \sqrt{D/\nu_i}$, is in the order of some μm (around 5 μ m in the cases studied here). It is evident that the mean free path of the electrons can reach values larger than L for low gas densities. The local field approximation is then not valid and energy equation for the electrons may be necessary. Besides, the physical model used it is not well suited to deal with temperatures as high as calculated in times longer than 250-300 ns. Under such temperatures, attachment does not longer occur and complicated chemical reactions can take place. These improvements of the physical model along with more refined calculations (as the gradients and the length scales of the plasma filaments become tiny) can provide a more accurate description of such phenomenon for longer time scales.

2.3.4 Sustained discharge due to gas heating effects via pre-ionization

The creation of hot plasma zones by microwaves, freely in air, requires as we have seen an electric field that is overcritical. To achieve such fields under atmospheric conditions, high power microwave sources have to be used. The efficiency of such discharges is linked directly to the power spent and thus means of reducing this power have been investigated by various research teams. Metallic initiators and vibrators have been studied in [1], to create zones of overcritical fields where microwave breakdown can occur while the microwave power source emits under-critical field. Another interesting method to achieve breakdown with under-critical microwave fields is based on the pre-ionization of a small volume of air via short laser pulses. The small in volume but high in density initial electron population, can serve as a heating source for the gas when microwave energy is injected to the system. Even if the the EM field's intensity is sub-critical, the gas heating can lead to a subsequent increase of the reduced effective field to levels higher than the critical for breakdown one, sustaining-multiplying the initial electron population. In [69], a femtosecond laser has been used to pre-ionize the air inside a thin zone. The authors have used a microwave resonator configuration for 3 GHz pulsed microwave operation with shadowgraph illumination as shown in figure 2.51. A sub-critical microwave field has been coupled to the pre-ionized zone, demonstrating that the initial plasma can be not only sustained, but also propagated as a streamer discharge. These experimental results, are of extreme interest, as the plasma seems to follow the initial electron population due to the laser, even if its direction is on an angle to the electric field's polarization [70]. This could be an efficient means of creating distant, localized and easily controllable plasma discharges - an essential aspect especially for hypersonic shock wave reduction techniques, or plasma assisted combustion. The same group of authors, have used a simplified numerical model to demonstrate that a pre-ionized region can be sustained due to sub-critical MW sources, even if the incident field is 50% of the critical for breakdown one.

In this section, we are performing simulations under such conditions to investigate with our, more complete, model this claim as well as the experimental results. The objective of this section is , not the exact reproduction of the experimental results, but rather the obtention of some qualitative results that will demonstrate as a first step, the ability of under-critical microwave fields to cause plasma breakdown in air, when coupled with an high electron density region. This results can be the basis for future parametric studies on the exact limits of such application.

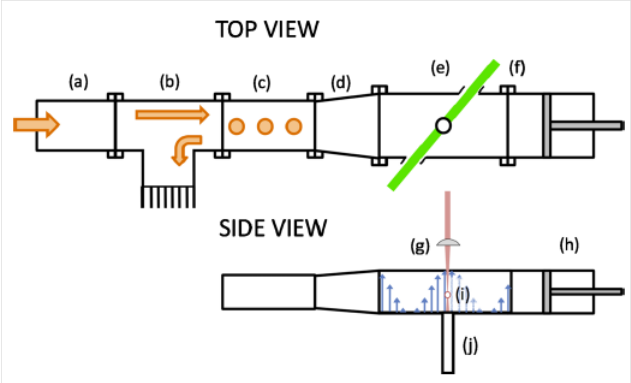

Figure 2.49: Experimental setup for laser - microwave coupling [69]. (i) shows the femtosecond/picosecond laser focal volume and the coupled stationary EM wave.

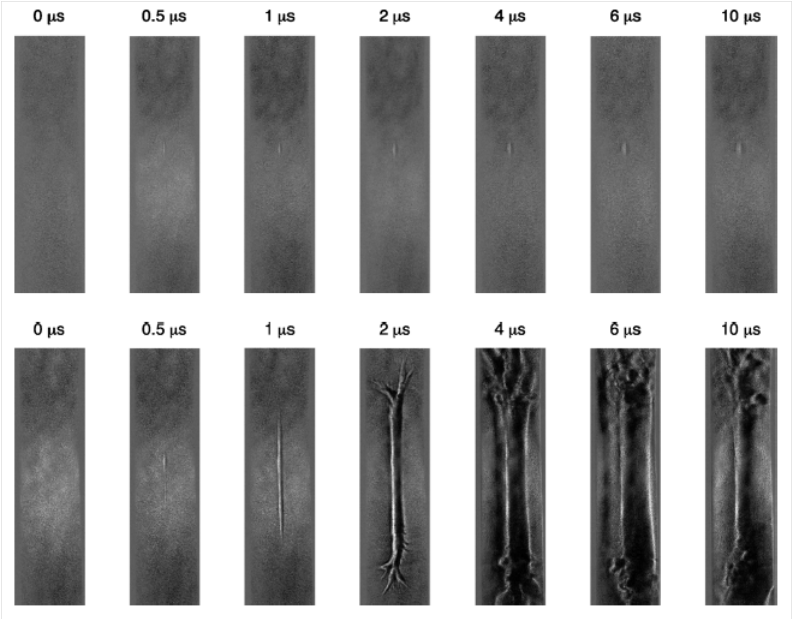

Figure 2.50: . Schlieren images with nanosecond illumination in quiescent air [69]. Top row : no microwave coupling. Bottom row : Microwave coupling and streamer formation.

Numerical results

We consider a seed electron density of $10^{22}\ m^{-3}$ (Gaussian distribution with a standard deviation of 50 μ m centered in the computational domain) which coincides with the value used in [69], and agrees with numerical estimations of ionization by a ultra short laser pulse [71]. The mesh size is set to λ /800 and the CFL number to 32. In order to have comparable results with the previously studied cases we set the EM waves frequency again at 110 GHz. The incident field is set to 1.1 MV/m, corresponding to a RMS field of

the stationary wave of 1,55 MV/m. We accept the experimentally calculated breakdown field given in [69], of 3 MV/m to determine this value as approximately 52 % of the breakdown field E_b (note here that normally the breakdown field under our conditions is approximately 2.4 MV/m). If we neglect the gas heating effects, the initial electron population quickly attaches and the plasma is vanished. In reality though, as the plasma heats up the air, the plasma is not only sustained but transforms to a streamer, elongating in the direction of the electric field just like we saw in the overcritical microwave breakdown simulations. In figures 2.51 and 2.52, the plasma density is shown for different time instants.

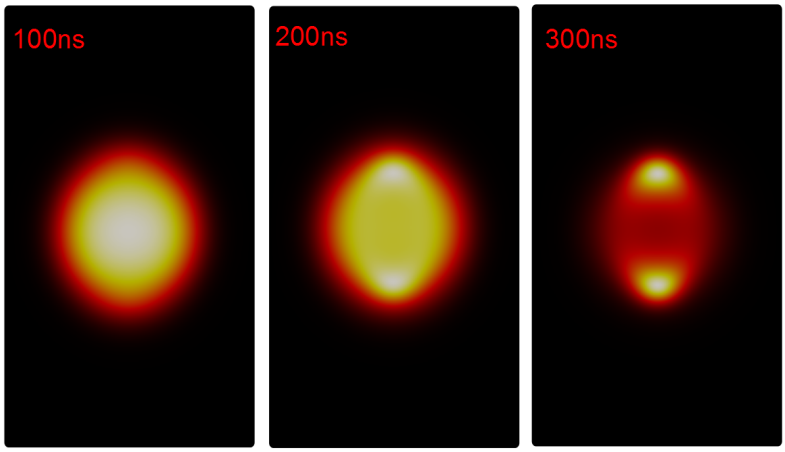

Figure 2.51: Plasma density versus time for $E = 52\%E_b$. Maximum densities are 7.15×10^{19},6.43×10^{18}, 2×10^{18} m^{-3} respectively.

At early times, the initial seed electrons are being diffused and attached as the gas heating has not reached critical values for ionization to overcome attachment. This starts to take place at times longer than 450 ns. Then the plasma density starts to increase until values close to cut-off. The field is then being reinforced at the plasma tips just like the microwave streamer studied in the previous sections. Strong ionization is taking place at the tips of the plasma, elongating it to the y-direction, the direction of the electric field. In figure 2.53, the effective ionization frequency is plotted in different time instants. For times lower than approximately 500 ns, the attachment dominates and the ν_{eff} remains negative. When the gas density drops in the core of the initial plasma has reached the critical value in order to produce a reduced effective field that causes ionization to overcome attachment, electrons start to multiply firstly in the zone of the plasma's core. The gas density field until the time of 500 ns is shown in figure 2.55. The density drop to values lower than $0.6 \times \rho_{amb}$ (approx.) denote a reduced electric field that becomes overcritical. At times longer than 500 ns, a strong blast wave is formed (stronger than the initial one), due to the higher energy absorption of the multiplying now plasma, blocking the elongation of the streamer for further times (see figure 2.56). The reinforced ionization at the plasma tips and the consequent streamer elongation is evident in figure 2.54. Note, as we will point below, the asymmetry of the ionization coefficient at times further than 700 ns, linked to numerical aspects of the simulation.

The energy absorbed by the plasma versus time is plotted in figure 2.57. We note that, the energy absorption increases almost linearly in early times, and it reaches a constant value at a time of less than 100 ns. Beyond this time instant, the absorption is constant denoting that the plasma has reached an equilibrium

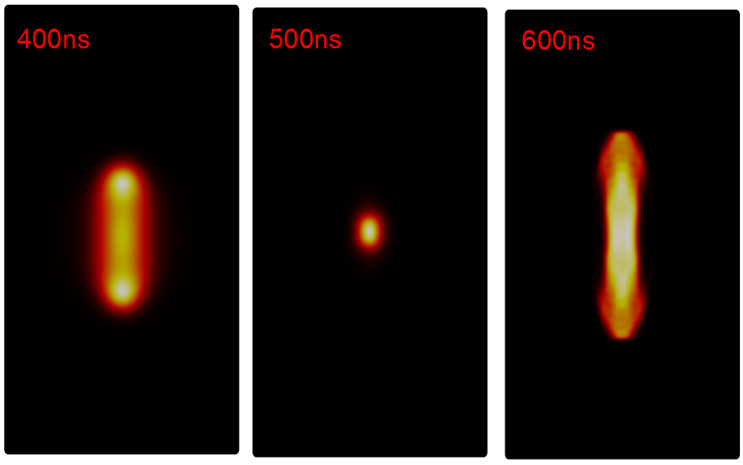

Figure 2.52: Plasma density versus time for $E = 52\%E_b$. Maximum densities are 1.5×10^{18}, 7.6×10^{20} and 2.9×10^{21} m^{-3} respectively.

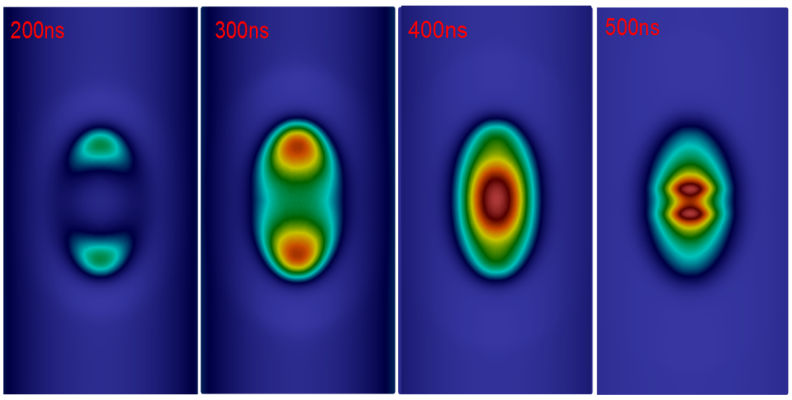

Figure 2.53: Effective ionization frequency versus time for $E = 52\%E_b$. Maximum values are 0,0, 3.2×10^7 and 1.2×10^8 s^{-1} respectively. Minimum values are -2.58$\times 10^7$,-2.59×10^7, -2.59×10^7 and -2.58×10^7 s^{-1} respectively.

state. At a time of less than 550 ns though, the absorption starts to increase again, due to the ionization taking hold, and the consequent increase of plasma density. The gas temperature quickly rises from 450 K to more than 3000 K at $t = 600ns$ (figure 2.58). The formation of the streamer and the intense interaction with the blast wave that is restricting its growth and reinforcing the ionization (and thus the plasma density and energy absorption) at the tips of the streamer (figure 2.59), leads to an extreme rise of the gas temperature that

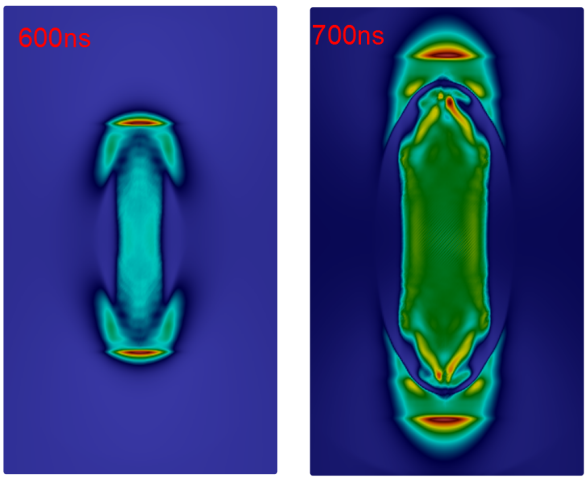

Figure 2.54: Effective ionization frequency versus time for $E = 52\%E_b$. Maximum values are 3.7×10^8,2.4×10^8 s^{-1} respectively. Minimum values are -3×10^7, -5×10^7 s^{-1} respectively.

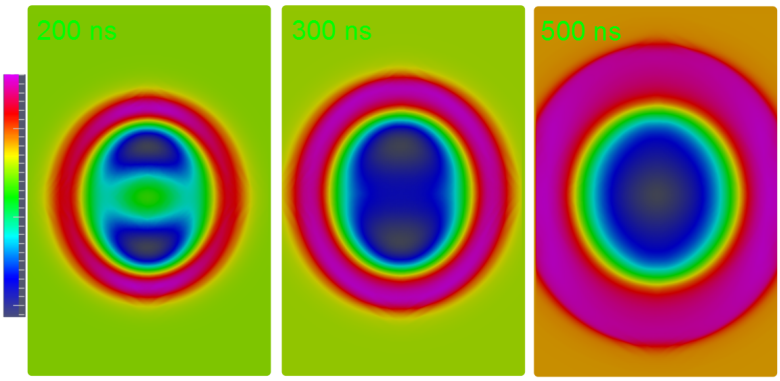

Figure 2.55: Gas density versus time for $E = 52\%E_b$. Maximum values are 1.163,1.19, 2.104 $\times\rho_{amb}$ respectively. Minimum values are 0.74,0.67, 0.478 $\times\rho_{amb}$ respectively, where $\rho_{amb} = 1.184\ kg/m^3$.

surpasses 4000 K at 700 ns. Non-linear effects, physical and mesh requirements make the results questionable for further times. The extreme gas heating leads to large values of the ionization frequency that reach the limits of the physical model used. The density gradients that occur, linked to the ionization frequency, are extremely small and thus the mesh requirements become also very high in order to properly resolve these space-scales. Moreover, the strong non-linear dependence of the different set of equations and the coupling between the different solvers, lead to reinforcement of numerical errors locally, resulting to the asymmetrical

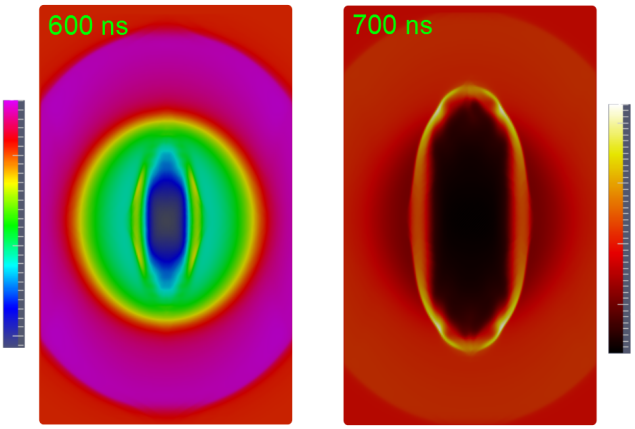

Figure 2.56: Gas density versus time for $E = 52\%E_b$. Maximum values are 1.183,2.25 $\times\rho_{amb}$ respectively. Minimum values are 0.213,0.1 $\times\rho_{amb}$ respectively, where $\rho_{amb} = 1.184\ kg/m^3$. (The change in the color-bar is for better visualization of the strong shock wave.)

behavior and the local high density points that is shown in figures 2.54 and 2.59.

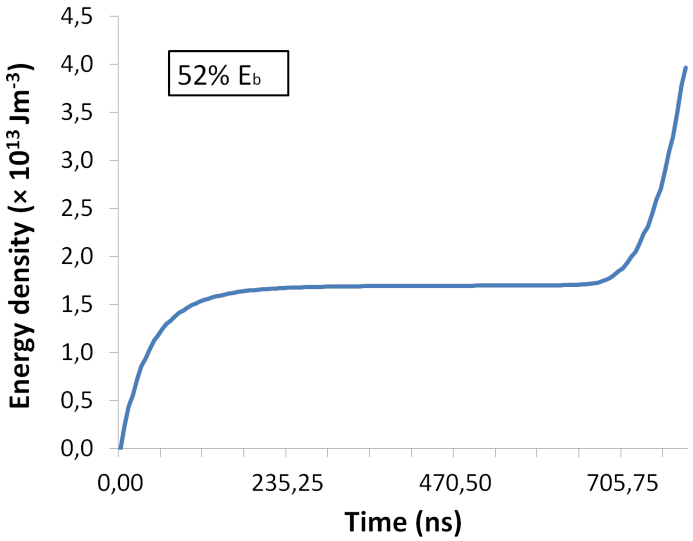

Figure 2.57: Absorbed energy density versus time for $E = 52\%E_b$.

Parametric studies have been conducted with different incident powers, in order to investigate the limit of a subcritical field that can be used to create and sustain a plasma in a pre-ionised region. Our studies showed, that a field lower than 1 MV/m, can not sustain a plasma discharge under our conditions of simulation. For the

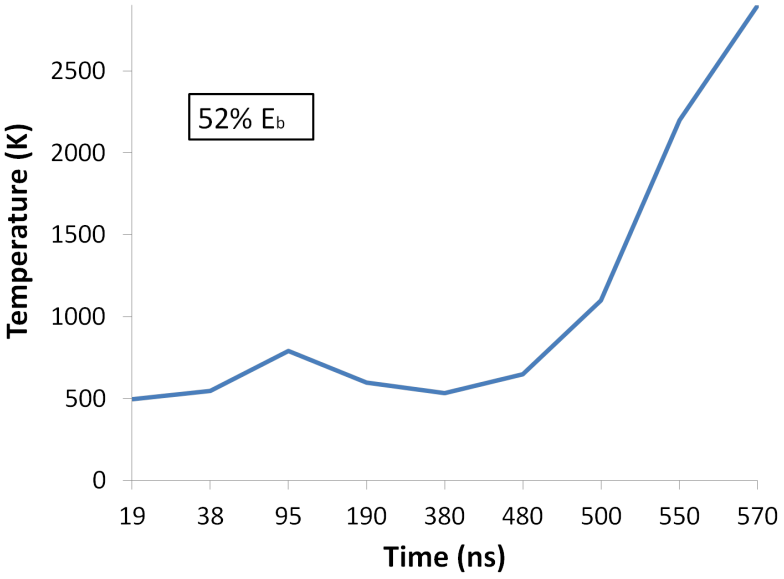

Figure 2.58: Gas temperature versus time for $E = 52\%E_b$.

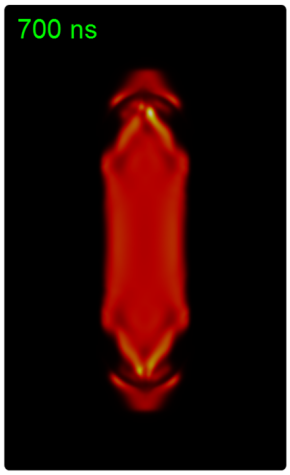

Figure 2.59: Plasma density at $t = 700ns$ for $E = 52\%E_b$. Maximum density value is $9 \times 10^{21}\ m^{-3}$.

case of 1 MV/m, corresponding to a RMS field of the stationary wave of 1,41 MV/m or 47% of the 3 MV/m breakdown field, the energy absorption remains almost constant during 1000 ns and the temperature after an initial increase to approx. 550 K, stabilizes at values of 450 K (figures 2.60 and 2.61, denoting that the density drop caused by the initial heating is not enough for sufficient ionization to occur in order to increase the energy absorption and to sustain the initial plasma.

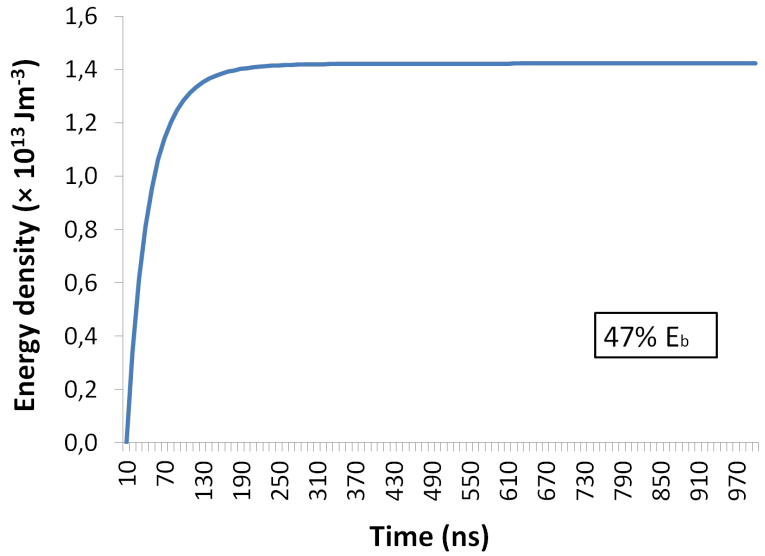

Figure 2.60: Absorbed energy density versus time for $E = 47\%E_b$.

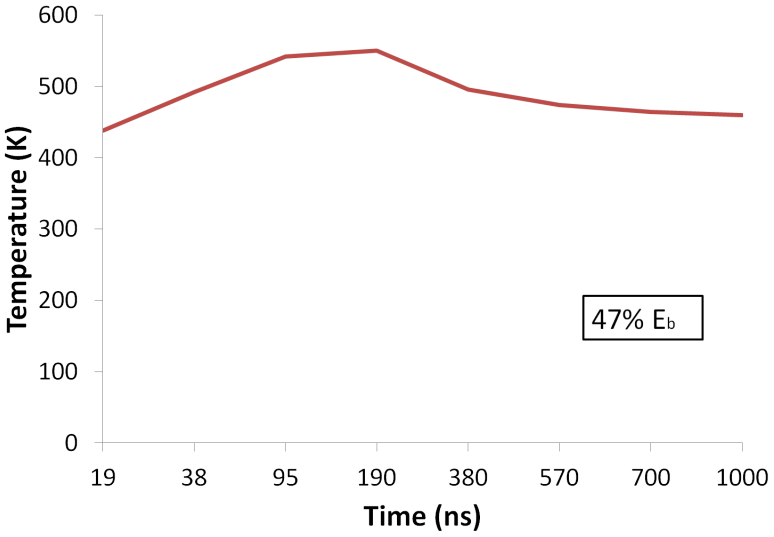

Figure 2.61: Gas temperature versus time for $E = 47\%E_b$.

At a time of 500 ns, the ionization becomes dominant at the plasma core, as the gas density reaches values lower than $0.6\times\rho_{amb}$, and the electrons density starts to increase until approx. 700 ns. As the temperature relaxes and diffusion takes place, and the energy absorption rate is not high enough, the gas density starts to increase again in the plasma core, leading to sub-critical values of the reduced electric field and thus negative

effective ionization frequency as shown in figure 2.62. The electrons density is continuously decreasing beyond the time instant of 700 ns, as attachment and recombination takes hold, and diffusion spreads the electron population favorably in the direction of the electric field (y-direction) (see figure 2.63.

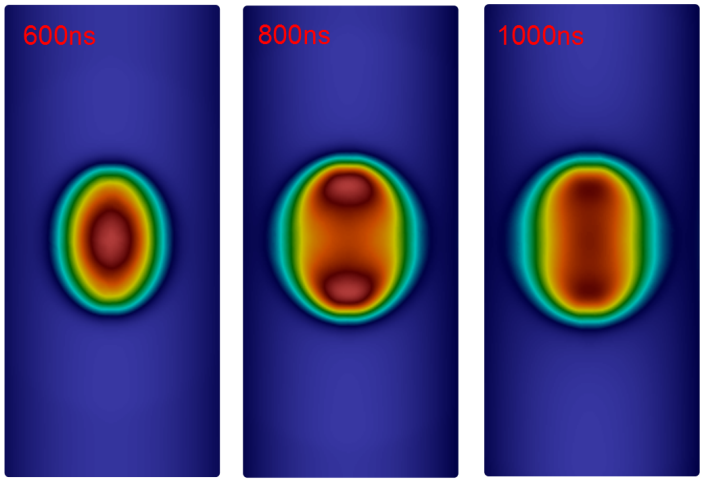

Figure 2.62: Effective ionization frequency versus time for $E = 47\%E_b$. Maximum values are 1.1×10^7,2.6×10^6, 0 s^{-1} respectively. Minimum values are -2.36×10^7, -2.35×10^7, 2.36×10^7 s^{-1} respectively.

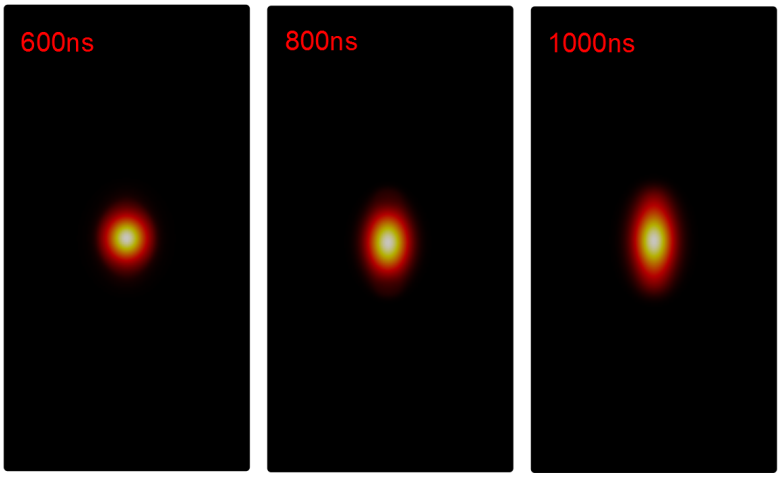

Figure 2.63: Plasma density versus time for $E = 47\%E_b$. Maximum densities are 1.37×10^{18}, 1.04×10^{18} and 1.58×10^{17} m^{-3} respectively.

These results confirm the experimental and numerical findings of [69]. The authors demonstrate that after an initial near - exponential decay of the electrons density, runaway ionization takes place and the streamer

starts to develop. For fields equal to 50% of the breakdown one, and an initial ionization density of $10^{22}m^{-3}$, the ionization becomes dominant at around 100 ns while we have calculated this behavior at a time of 700 ns. This is obviously linked with the exact value of the incident electric field, as the time delay between the energy absorption - gas heating and critical gas density drop will depend on the rate of the energy absorbed. Below a certain threshold of the EM field, the near-exponential decay continues as the density drop in the gas is not enough to cause runaway ionization. This has been numerically demonstrated in [69] for fields equal to 25% of the breakdown one. Exact comparison between the results obtained here and the ones presented in [69], is difficult to make as firstly their model is more simplified and secondly the operating microwave frequency is not the same. Nevertheless, we can conclude that indeed sub-critical fields can sustain and develop an initial seed electron density, if its value is high enough for fast gas heating to occur. The initial temperature rise is thus critical : For a temperature rise at a level of 500 K, the plasma can not be sustained - developed. Consistent with figure 2.64, a gas density drop to values of less than $0.6\times\rho_{amb}$ is required in order for the ionization to overcome attachment for the $E = 52\%E_b$ and less than $0.56\times\rho_{amb}$ for the $E = 47\%E_b$ case. Note that even though this difference between the two cases may seem small, the ionization frequency is a strongly non-linear function of the reduced electric field and thus even such small difference can have (as we have seen) strong impact on the plasma transport coefficients and therefore on its evolution.

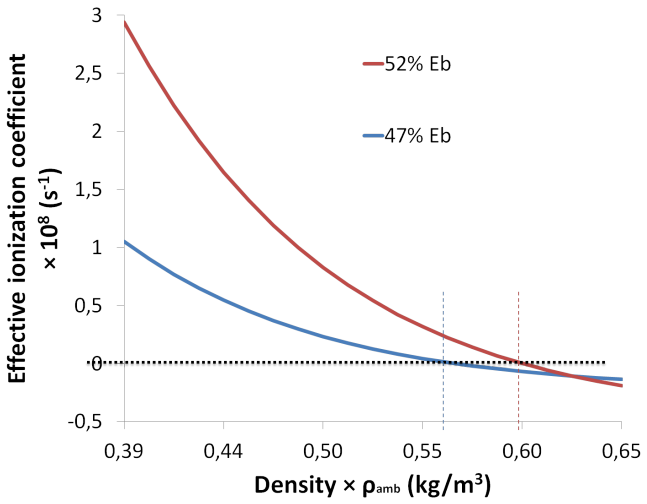

Figure 2.64: Effective ionization frequency versus gas density for $E = 52\%E_b$ and $E = 47\%E_b$.

2.4 Conclusion - Perspectives

A computational model has been developed to describe microwave discharges formation and evolution based on a simplified plasma-fluid model coupled with the Maxwell equations that describe the propagation and behavior of electromagnetic waves. This coupling has been achieved via the electron current term and a simplified momentum equation. In order to study microwave discharges and breakdown in air in a more accurate level, the numerical code has been expanded in three dimensions. A novel implicit coupling of the equations based on the Alternative Direction Implicit scheme for the Maxwell equations, has been developed, allowing for computational reduction that made three dimensional simulations possible. Numerical experiments on the computational solver's accuracy and CPU time reduction have been performed, demonstrating

the efficiency of the proposed method especially for highly refined meshes. These numerical experiments, have been based on microwave breakdown under atmospheric conditions in air and streamer development under a stationary electric field in order to compare with explicit solvers and results. Then, we have studied the microwave breakdown and pattern formation in freely localized discharges, in three dimensions, and compare them with two dimensional simulations and experimental results. These simulations, clearly demonstrate, the three dimensional effects of such plasma discharges, that can not be neglected if accurate calculations of the plasma occupied volume and heat absorption (linked to the electron density) are necessary - as is the case for energy deposition flow control applications. Moreover, the effects of gas heating have been investigated, coupling the numerical solver with a compressible Euler solver taking into account real-gas effects. The results of these simulations, again, demonstrate quite clearly that the evolution of microwave discharges include complex interaction between different physical phenomena : The intense gas heating due to the Joule heating source term, leads to a change of the initial gas density and thus a change in the plasma transport coefficients. Moreover, under a stationary EM wave, the streamer development stops at lengths close to its resonant length. This phenomenon, experimentally observed by various authors but not explained properly, is due to the blast wave formation due to the fast gas heating, and the consequent drop of the ionization frequency at the shock wave zone. Furthermore, we have studied the possibility of using sub-critical fields to sustain and develop a pre-ionised zone (by laser for example). Indeed, as has been observed in experiments, depending on the electric field's strength as a portion of the critical for breakdown field, a microwave plasma discharge can not only be sustained but also elongate in the electric field's direction forming a streamer. This effect, is due to the initial energy absorption by the dense plasma zone and the consequent gas heating - leading to a reduced effective field in the core of the initial plasma zone that is overcritical and thus ionization becomes dominant.

In figure 2.65, the key parameters for plasma breakdown and development are summarized. From the electromagnetic point of view, the EM waves frequency plays an essential role as firstly controls the maximum density that the plasma can reach before shielding occurs (approximately when the plasma frequency equals the EM waves one). Moreover, the plasma will develop differently in a high frequency field than in a lower frequency one because the wavelength of the latter is bigger and thus the interaction between plasma and EM wave length scales is weak. The microwave power is also crucial. Electric fields that are below the critical for breakdown one, can not cause breakdown, unless as we have seen, a pre-ionized region exists or the energy is concentrated in a region via initiators or reflectors. The polarization of the field leads also to different shapes of plasma. Regarding the plasma itself, the initial density of a plasma volume is of utmost importance under sub-critical fields, as it controls the energy absorption (along with the EM field intensity of course). The time-scales ratio between sufficient energy absorption and consequent gas density drop for an above critical reduced effective field and diffusion - attachment of the initial electron population is obviously critical. The diffusion, effective ionization and recombination coefficients have a strong influence on the plasma dynamics as they control the growth of the plasma density and the plasma expansion in space. From the gas point of view, again, the density drop along with the time scales associated to that, due to the gas heating will alter the plasma transport coefficients in a non-linear way that can also be crucial. Furthermore, as we have seen, the blast wave intensity, formation and propagation along with its speed (and relevant time scales) can have a big impact on the development of a plasma streamer. Finally, the initial gas pressure affects directly the reduced field that controls the plasma transport coefficients (the diffusion coefficient scales as 1/p while the ionization frequency scales as p).

The numerical solver presented in this chapter, is able as we've seen, to produce quite accurate representations of experimental configurations and provide more insights on the complex interaction between EM waves,

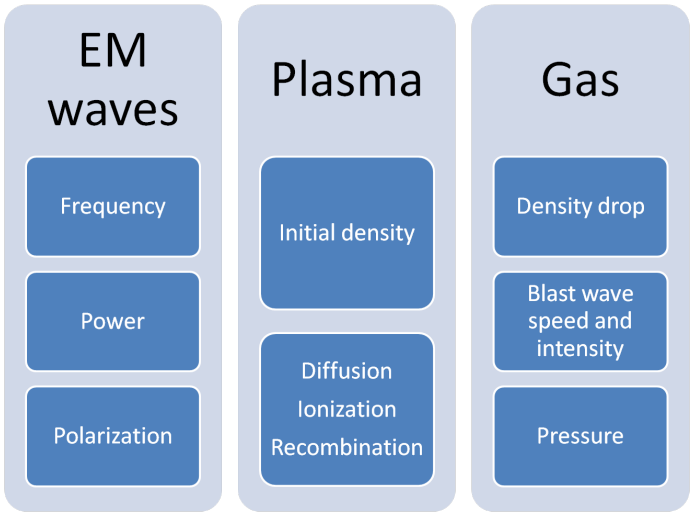

Figure 2.65: Key parameters of microwave breakdown and evolution.

gas and plasma. Nevertheless, even if the computational gain compared to fully explicit schemes is large, even more refined three-dimensional calculations are necessary in order to explore in depth the possibilities of the physical model and the accuracy of the numerical one. Moreover, in order to obtain accurate data for the energy absorption and volume occupation of such plasma discharges - essential for flow control applications - the gas heating effects have to be taken into account and thus three dimensional CFD solver has to be coupled to the system. All these combined, make the computational cost quite high and thus further improvements have to be considered. The GMRES numerical scheme can be a very interesting candidate for highly accurate simulations with large time steps (or CFL numbers) especially when it is preconditioned by the ADI scheme. Numerical experiments performed in MATLAB, have demonstrated that such a scheme can converge to the C-N solution, 4-5 times faster than the conventional preconditioned GMRES (with a LU preconditioner for example). Besides the numerical issues of course, the simplified physical model has also its limitations. More in-depth description of the plasma trasport properties as well as the addition of an energy equation for the electrons may be necessary especially for the cases in which the gas temperatures exceed a threshold of some thousands of degrees (more than 3000-4000 K). Concerning the physical model itself, it presents limits of validity, as the simplifying approximations are not be valid for the cases when the gas density drops greatly, and thus the mean free path increases (local field approximation). The use of an equation for the electrons temperature is then necessary. In cases of extreme gas temperatures (more than 4000 K), chemical reactions can also take place and the plasma transport coefficients are strongly modified. Such need of improvement for the physical model, has to be carefully studied and validated as it will render the numerical simulation way more demanding in computational resources.

The development of the solver presented in this chapter, along with possible improvements of the physical and numerical model, open the path to detailed simulations of microwave discharges that can be used to quantify the energy absorbed by the plasma and consequently transfered to gas as heat. The importance of the three dimensional effects as well as the strong coupling between the plasma and the gas, as demonstrated, is great and future simulations have to take such factors into account. Parametric studies on key parameters as

presented in figure 2.65, are now possible - studies that can provide more accurate data in order to clarify the energy balance between the microwave power, the plasma and the gas and also to justify the applicability of such discharges in flow control applications. As a near-future study (that has already started), the experiments presented in [72] (see section 1.3.1) can be investigated numerically with this model, simulating the concentration of microwave energy to local maximas due to the reflection by a mirror in low-pressure supersonic flows. Then, the creation of the plasmoids can be quantified in terms of occupying volume as well as energy absorption and complete CFD simulations can be performed investigating the effect of the energy deposition on the wave drag of a cylinder in a supersonic flow, corresponding to the experiments of [73, 72].

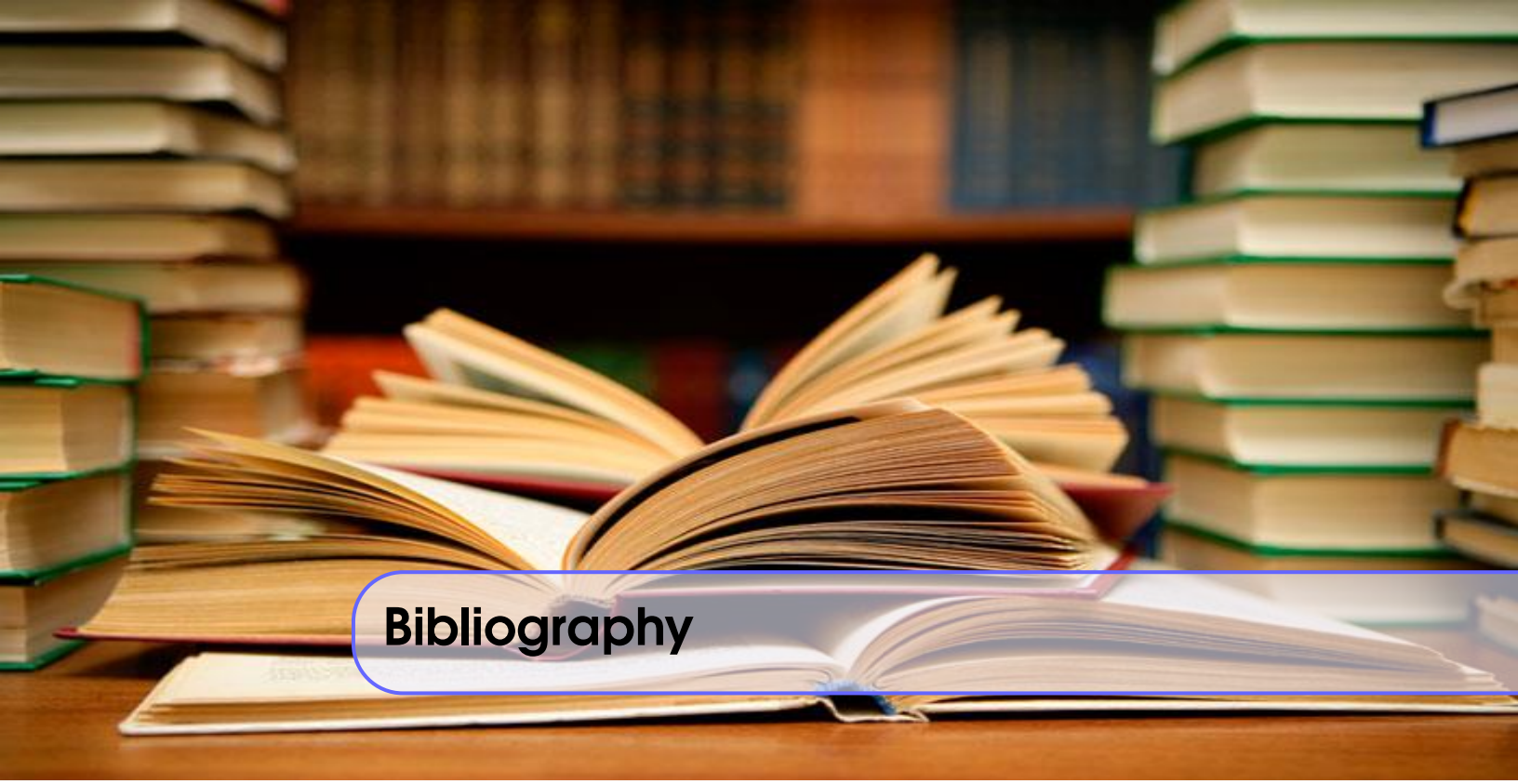

Bibliography

[1] Kirill V Khodataev. “Microwave Discharges and Possible Applications in Aerospace Technologies”. In: *Journal of Propulsion and Power* 24.5 (2008), pages 962–972.

[2] Doyle D Knight. “Survey of aerodynamic drag reduction at high speed by energy deposition”. In: *Journal of Propulsion and Power* 24.6 (2008), pages 1153–1167.

[3] Guillaume Dufour, Bruno Fornet, and François Rogier. “Numerical modelling of supersonic flow actuated by laser-induced plasma”. In: *International Journal of Aerodynamics* 3.1 (2013), pages 122–134.

[4] MI Ryvkin and AA Gorynya. “Gas dynamic effect of microwave discharge on supersonic cone-shaped bodies”. In: (2004).

[5] Yuri F Kolesnichenko et al. “MW energy deposition for aerodynamic application”. In: *AIAA paper* 361 (2003), page 2003.

[6] Doyle Knight et al. “Interaction of microwave-generated plasma with a blunt body at Mach 2.1”. In: *AIAA Paper* 846 (2009), page 2009.

[7] Nina Yurchenko et al. “Control of flow characteristics using localized plasma discharges”. In: *47th AIAA Aerospace Sciences Meeting and Exhibition*. 2009, pages 5–8.

[8] Bhaskar Chaudhury et al. “Physics and modelling of microwave streamers at atmospheric pressure”. In: *Journal of Applied Physics* 110.11 (2011), page 113306.

[9] Guo Qiang Zhu, Jean-Pierre Boeuf, and Bhaskar Chaudhury. “Ionization–diffusion plasma front propagation in a microwave field”. In: *Plasma Sources Science and Technology* 20.3 (2011), page 035007.

[10] AL Vikharev and BG Eremin. “Microwave discharge in a quasioptical resonator”. In: *Zhurnal Eksperimental’noi i Teoreticheskoi Fiziki* 68.2 (1975), pages 452–455.

[11] VS Barashenkov et al. “Breakdown in air in a rising microwave field”. In: *Technical Physics* 45.10 (2000), pages 1265–1270.

[12] Yoshiteru Hidaka et al. “Plasma structures observed in gas breakdown using a 1.5 MW, 110 GHz pulsed gyrotrona)”. In: *Physics of Plasmas (1994-present)* 16.5 (2009), page 055702.

[13] Bhaskar Chaudhury and J-P Boeuf. “Computational studies of filamentary pattern formation in a high power microwave breakdown generated air plasma”. In: *Plasma Science, IEEE Transactions on* 38.9 (2010), pages 2281–2288.

[14] Allen Taflove. “Application of the finite-difference time-domain method to sinusoidal steady-state electromagnetic-penetration problems”. In: *Electromagnetic Compatibility, IEEE Transactions on* 3 (1980), pages 191–202.

[15] Allen Taflove and Susan C Hagness. “Computationai Electrodynamics”. In: (2000).

[16] MA Jensen and Y Rahmat-Samii. “Finite difference and finite volume time domain techniques in electromagnetics: A comparative study”. In: *Radio Science* 31.6 (1996), pages 1823–1836.

[17] Adnane Hamiaz et al. “Finite Volume Time Domain modelling of microwave breakdown and plasma formation in a metallic aperture”. In: *Computer Physics Communications* 183.8 (2012), pages 1634–1640.

[18] JS Hesthaven and T Warburton. “Discontinuous Galerkin methods for the time-domain Maxwell’s equations”. In: *Applied Computational Electromagnetics Society Newsletter* 19.1 (2004), page 4.

[19] Laura Pebernet et al. “A Discontinuous Galerkin Formalism to Solve the Maxwell-Vlasov Equations. Application to High Power Microwave Sources”. In: *Scientific Computing in Electrical Engineering SCEE 2010*. Springer, 2012, pages 183–192.

[20] GB Jacobs and Jan S Hesthaven. “Implicit–explicit time integration of a high-order particle-in-cell method with hyperbolic divergence cleaning”. In: *Computer Physics Communications* 180.10 (2009), pages 1760–1767.

[21] GJM Hagelaar, K Hassouni, and A Gicquel. “Interaction between the electromagnetic fields and the plasma in a microwave plasma reactor”. In: *Journal of applied physics* 96.4 (2004), pages 1819–1828.

[22] Patrick J Ford et al. “A finite-difference time-domain simulation of high power microwave generated plasma at atmospheric pressures”. In: *Physics of Plasmas (1994-present)* 19.7 (2012), page 073503.

[23] Jean-Pierre Boeuf, Bhaskar Chaudhury, and Guo Qiang Zhu. “Theory and of self-organization and propagation of filamentary plasma arrays in microwave breakdown at atmospheric pressure”. In: *Physical review letters* 104.1 (2010), page 015002.

[24] Joseph T Mayhan and Ronald L Fante. “Microwave Breakdown Over a Semi-Infinite Interval”. In: *Journal of Applied Physics* 40.13 (1969), pages 5207–5211.

[25] Larry K Warne, Roy E Jorgenson, and Scott D Nicolaysen. “Ionization coefficient approach to breakdown in nonuniform geometries”. In: *Sandia Report SAND2003-4078* (2003).

[26] K. Yee. “Numerical solution of initial boundary value problems involving Maxwell’s equations in isotropic media”. In: *Antennas and Propagation, IEEE Transactions on* 14.3 (1966), pages 302–307.

[27] Calvin H Wilcox. “An expansion theorem for electromagnetic fields”. In: *Communications on Pure and Applied Mathematics* 9.2 (1956), pages 115–134.

[28] Alvin Bayliss and Eli Turkel. “Radiation boundary conditions for wave-like equations”. In: *Communications on Pure and Applied Mathematics* 33.6 (1980), pages 707–725.

[29] Björn Engquist and Andrew Majda. “Absorbing boundary conditions for numerical simulation of waves”. In: *Proceedings of the National Academy of Sciences* 74.5 (1977), pages 1765–1766.

[30] Gerrit Mur. "Absorbing boundary conditions for the finite-difference approximation of the time-domain electromagnetic-field equations". In: *Electromagnetic Compatibility, IEEE Transactions on* 4 (1981), pages 377–382.

[31] Jean-Pierre Berenger. "A perfectly matched layer for the absorption of electromagnetic waves". In: *Journal of computational physics* 114.2 (1994), pages 185–200.

[32] Zachary S Sacks et al. "A perfectly matched anisotropic absorber for use as an absorbing boundary condition". In: *Antennas and Propagation, IEEE Transactions on* 43.12 (1995), pages 1460–1463.

[33] Stephen D Gedney. "An anisotropic PML absorbing media for the FDTD simulation of fields in lossy and dispersive media". In: *Electromagnetics* 16.4 (1996), pages 399–415.

[34] Allen Taflove and Susan C Hagness. "Computationai Electrodynamics". In: (2000).

[35] Weng Cho Chew and William H Weedon. "A 3D perfectly matched medium from modified Maxwell's equations with stretched coordinates". In: *Microwave and optical technology letters* 7.13 (1994), pages 599–604.

[36] J-P Berenger. "Improved PML for the FDTD solution of wave-structure interaction problems". In: *Antennas and Propagation, IEEE Transactions on* 45.3 (1997), pages 466–473.

[37] John H Beggs et al. "Finite-difference time-domain implementation of surface impedance boundary conditions". In: *Antennas and Propagation, IEEE Transactions on* 40.1 (1992), pages 49–56.

[38] Jongwoo Lee and Bengt Fornberg. "Some unconditionally stable time stepping methods for the 3D Maxwell's equations". In: *Journal of Computational and Applied Mathematics* 166.2 (2004), pages 497–523.

[39] G Sun and CW Trueman. "Unconditionally stable Crank-Nicolson scheme for solving two-dimensional Maxwell's equations". In: *Electronics Letters* 39.7 (2003), pages 595–597.

[40] G Sun and CW Trueman. "Unconditionally-stable FDTD method based on Crank-Nicolson scheme for solving three-dimensional Maxwell equations". In: *Electronics Letters* 40.10 (2004), pages 589–590.

[41] Takefumi Namiki. "A new FDTD algorithm based on alternating-direction implicit method". In: *Microwave Theory and Techniques, IEEE Transactions on* 47.10 (1999), pages 2003–2007.

[42] Takefumi Namiki. "3-D ADI-FDTD method-unconditionally stable time-domain algorithm for solving full vector Maxwell's equations". In: *Microwave Theory and Techniques, IEEE Transactions on* 48.10 (2000), pages 1743–1748.

[43] SJ Cooke et al. "A leapfrog formulation of the 3-D ADI-FDTD algorithm". In: *International Journal of Numerical Modelling: Electronic Networks, Devices and Fields* 22.2 (2009), pages 187–200.

[44] Kane S Yee et al. "Numerical solution of initial boundary value problems involving Maxwell's equations in isotropic media". In: *IEEE Trans. Antennas Propag* 14.3 (1966), pages 302–307.

[45] Xiang-Hua Wang et al. "A convolutional perfect matched layer (CPML) for one-step leapfrog ADI-FDTD method and its applications to EMC problems". In: *Electromagnetic Compatibility, IEEE Transactions on* 54.5 (2012), pages 1066–1076.

[46] Theng Huat Gan and Eng Leong Tan. "Stability and dispersion analysis for three-dimensional (3-D) leapfrog ADI-FDTD method." In: (2012).

[47] Salvador G Garcia et al. "On the dispersion relation of ADI-FDTD". In: *Microwave and Wireless Components Letters, IEEE* 16.6 (2006), pages 354–356.

[48] Jian-Yun Gao and Hong-Xing Zheng. “One-step leapfrog ADI-FDTD method for lossy media and its stability analysis”. In: *Progress In Electromagnetics Research Letters* 40 (2013), pages 49–60.

[49] Serge Piperno, Malika Remaki, and Loula Fezoui. “A nondiffusive finite volume scheme for the three-dimensional Maxwell’s equations on unstructured meshes”. In: *SIAM Journal on Numerical Analysis* 39.6 (2002), pages 2089–2108.

[50] Bruno D Welfert. “Analysis of iterated ADI-FDTD schemes for Maxwell curl equations”. In: *Journal of Computational Physics* 222.1 (2007), pages 9–27.

[51] Philip L Roe. “Approximate Riemann solvers, parameter vectors, and difference schemes”. In: *Journal of computational physics* 43.2 (1981), pages 357–372.

[52] Randall J LeVeque and Randall J Le Veque. *Numerical methods for conservation laws*. Volume 132. Springer, 1992.

[53] Randall J LeVeque. *Finite volume methods for hyperbolic problems*. Volume 31. Cambridge university press, 2002.

[54] P Glaister. “An approximate linearised Riemann solver for the Euler equations for real gases”. In: *Journal of Computational Physics* 74.2 (1988), pages 382–408.

[55] Meng-Sing Liou, Bram Van Leer, and Jian-Shun Shuen. “Splitting of inviscid fluxes for real gases”. In: *Journal of Computational Physics* 87.1 (1990), pages 1–24.

[56] Pierre-Arnaud Raviart. *Numerical approximation of hyperbolic systems of conservation laws*. Volume 118. Springer, 1996.

[57] M Capitelli et al. “Transport properties of high temperature air in local thermodynamic equilibrium”. In: *The European Physical Journal D-Atomic, Molecular, Optical and Plasma Physics* 11.2 (2000), pages 279–289.

[58] Timothy D Drysdale and Tomasz P Stefanski. “Parallelisation of implicit time domain methods: progress with ADI-FDTD”. In: *Piers Online* 5.2 (2009), pages 117–120.

[59] T Unfer and JP Boeuf. “Modelling of a nanosecond surface discharge actuator”. In: *Journal of physics D: applied physics* 42.19 (2009), page 194017.

[60] NA Popov. “Investigation of the mechanism for rapid heating of nitrogen and air in gas discharges”. In: *Plasma physics reports* 27.10 (2001), pages 886–896.

[61] MS Benilov and GV Naidis. “Modelling of discharges in a flow of preheated air”. In: *Plasma Sources Science and Technology* 14.1 (2005), page 129.

[62] Sang Ki Nam and John P Verboncoeur. “Theory of filamentary plasma array formation in microwave breakdown at near-atmospheric pressure”. In: *Physical review letters* 103.5 (2009), page 055004.

[63] Alan M Cook et al. “Observation of plasma array dynamics in 110 GHz millimeter-wave air breakdown”. In: *Physics of Plasmas (1994-present)* 18.10 (2011), page 100704.

[64] LP Grachev, II Esakov, and SG Malyk. “A spherical plasmoid with a diffuse boundary in a linearly polarized quasistatic electromagnetic field”. In: *Technical Physics* 46.6 (2001), pages 668–672.

[65] Konstantinos Kourtzanidis, François Rogier, and J-P Boeuf. “ADI-FDTD modeling of microwave plasma discharges in air towards fully three-dimensional simulations”. In: *"ADI-FDTD modeling of microwave plasma discharges in air towards fully three-dimensional simulations", Submitted to Computer Physics Communications (2014)* (2014).

[66] Qianhong Zhou and Zhiwei Dong. “Modeling study on pressure dependence of plasma structure and formation in 110 GHz microwave air breakdown”. In: *Applied Physics Letters* 98.16 (2011), page 161504.

[67] AL Vikharev et al. “Formation of the small-scale structure in a microwave discharge in high-pressure gas”. In: *Soviet Journal of Plasma Physics* 18.8 (1992), pages 554–560.

[68] Mario Capitelli et al. *Plasma kinetics in atmospheric gases*. Springer, 2000.

[69] JB Michael et al. “Subcritical microwave coupling to femtosecond and picosecond laser ionization for localized, multipoint ignition of methane/air mixtures”. In: *Journal of Applied Physics* 108.9 (2010), page 093308.

[70] James B Michael, Matthew R Edwards, and Richard B Miles. “Time-resolved temperature measurements of laser-designated, microwave driven ignition”. In: *AIAA 2011 - 1020* (2011).

[71] K Mishima et al. “Effect of quantum interference on tunneling photoionization rates of N2 and O2 molecules.” In: *The Journal of chemical physics* 122.10 (2005), pages 104312–104312.

[72] Yu F Kolesnichenko et al. “Microwave energy release regimes for drag reduction in supersonic flows”. In: *AIAA Paper* 353 (2002), page 2002.

[73] VM Shibkov et al. “Freely localized microwave discharge in a supersonic gas flow”. In: *Plasma physics reports* 31.9 (2005), pages 795–801.

Simulations numériques de l'actionneur DBD

Presentation

Un Decharge à Barrière Diélectrique (DBD) ionise une partie du gaz et les particules créées transfèrent leur quantité de mouvement aux molécules de gaz, créant une force de corps qui agit dans l'écoulement. Une représentation schématique d'un actionneur DBD de surface et la formation de plasma peut être vu sur la figure B.1. La prédiction de la distribution de force de corps est de la plus haute importance. Dans le la dernière décennie, plusieurs approches ont été proposées pour estimer cette distribution de force.

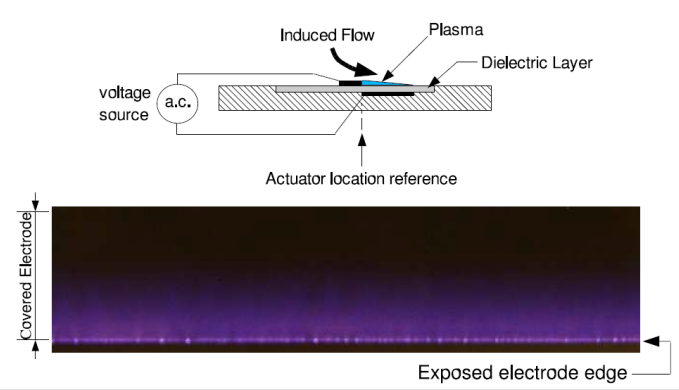

Figure B.1: Représentation schématique d'un SDBD et de la formation de plasma [1].

Les auteurs de [2, 3], ont développé un modèle fluide pour le plasma, basée sur des solutions des equations de transport d'électrons et d'ions - la continuité et le transfert de quantité de mouvement - couplée à l'équation de Poisson en deux dimensions. Le modèle physique est semblable à celle de [4]. Ils ont calculé la force du corps produit par l'actionneur par rapport à différents paramètres (tension, fréquence, propriétés diélectriques).

Leurs résultats sont en excellent accord avec les observations expérimentales. La force obtenue atteint des valeurs de plusieurs 10 mN / m, et elle augmente avec l'amplitude de la tension et est favorisée par les basses fréquences du signal de courant alternatif. Dans la figure B.2, l'évolution de la x-dirigé force totale intégré dans l'espace et moyenné dans le temps est tracée pour différentes fréquences.

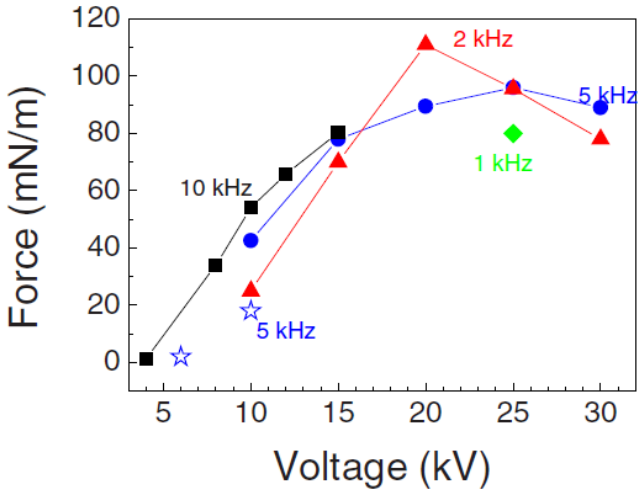

Figure B.2: La force X-dirigé en fonction de la tension appliquée pour différentes fréquences. Les symboles étoiles correspondent aux mesures de [5] à 5 kHz.

La simulation numérique de SDBDs est particulièrement difficile et un effort particulier a été consacré à la conception d'un solveur efficace. De schémas implicites [6] ont été testés ainsi que des stratégies asynchrones qui étaient très prometteur pour les problèmes multi-échelles [7]. Ces travaux ont démontré la capacité d'un tel modèle numérique à fournir de tendances physiquement pertinentes de ce type de décharge et également à prédire la vitesse du jet produit mais aucune comparaison quantitative n'a encore été effectué entre les mesures et les calculs.

L'objectif de ce chapitre est d'utiliser des solveurs déjà développés, l'un à l'ONERA et l'autre à LAPLACE, afin d'une part, de calculer la force du corps exercée par le fonctionnement de l'actionneur DBD et la coupler avec de solveurs CFD, en tenant compte les effets turbulents, afin d'étudier l'ecoulement induit et de le comparer avec les résultats expérimentaux. Deuxièmement, nous cherchons à réaliser des études paramétriques sur différentes conditions de fonctionnement des DBD pour enquêter sur leur gamme de fonctionnement optimisée. Enfin, des simulations simples d'applications de contrôle d'ecoulement sont envisagées, afin de démontrer les possibilités de ces actionneurs.

Modèle physique

Le modèle physique utilisé dans ce chapitre fournit une description fine du plasma tout en gardant un schéma cinétique simple. La chimie de l'air est en effet très complexe et implique de nombreuses espèces et réactions [8], de sorte que la complexité des calculs requis pour une description complète serait trop grand. Par conséquent, suivant ici l'approche de J.P Boeuf [2] un schéma simplifié est utilisé qui est tout de même as-

sez complexe à obtenir un comportement pertinent de la force de corps par rapport aux paramètres de décharge.

Le modèle consiste à résoudre les équations de continuité et de quantité de mouvement pour un ensemble d'espèces simplifiées composées d'ions positifs (+) a noté comme p, les ions négatifs (-) ont noté comme n et d'électrons, a noté comme e. Le transport est décrit dans l'approximation de dérive-diffusion en utilisant de coefficients tabulés en fonction de E / N (approximation du champ local). L'équation de continuité pour les particules chargées de type i, s'écrit ainsi:

$$\partial_t n_i + \nabla.(\mathbf{U_i} n_i) = S_i \tag{B.1}$$

Le terme source cinétique prend en compte l'ionisation directe par impact électronique, l'attachement et la recombinaison volumique électrons / ions et ion / ion et s'écrit:

$$S_e = (\alpha - \eta) U_e n_e - r_{ep} n_e n_p \tag{B.2}$$

$$S_p = \alpha U_e n_e - r_{ep} n_e n_p - r_{np} n_n n_p \tag{B.3}$$

$$S_n = \eta U_e n_e - r_{np} n_n n_p \tag{B.4}$$

où $\gamma_i = U_i n_i$ est le flux de particules chargées pour chaque espèce i.
Le logiciel Bolsig + est utilisé pour obtenir les coefficients d'ionisation (α) et d'attachement (η) et la mobilité des électrons (μ_e) pour un mélange de $77\%N2 - 23\%O2$. La mobilité ionique est fixe et égale pour les deux types d'ions.

Le flux de particules chargées γ_i a une forme de dérive-diffusion et la vitesse de dérive s'écrit:

$$\mathbf{U_i} = U_g + sgn(q_i)\mu_i \mathbf{E} + D_i \nabla n_i \quad sgn(q_i) = +,\ if\ i = p,\ else\ sgn(q_i) = - \tag{B.5}$$

et le coefficient de diffusion pour chaque espèce i, s'écrit:

$$D_i = \frac{-\mu_i k_B T_i}{e} \tag{B.6}$$

Les températures de particules chargées sont censés constante et égale à 1 eV pour les électrons et à la température ambiante pour les ions.

Le champ électrique suit la loi de Poisson et est ensuite lié à la charge totale déposée par les particules ionisées.

$$\nabla.(\varepsilon_r \mathbf{E}) = \frac{1}{\varepsilon_0} \sum_i q_i n_i + \sigma \delta_S, \quad \mathbf{E} = -\nabla \Phi \tag{B.7}$$

où ε_0 est la permittivité du vide, ε_r est la permittivité relative, Φ est le potentiel électrique et $\sigma\ delta_S$ représente la contribution des charges déposé par la décharge sur la surface diélectrique. Un circuit électrique est prise en compte pour calculer la variation de potentiel électrique en fonction du courant total qui circule

dans le circuit: V = $V_0 ri$, où R désigne la résistance du circuit externe ($\approx 0,1$ Ohm).

Les conditions aux limites prises en compte sont l'émission secondaire d'électrons à la surface diélectrique $\mathbf{J_e} = -\ gamma \mathbf{J_p}$ ou une valeur prescrite de la densité minimale ($10^{12} m^{-3}$). Ni photo-ionisation ni les processus de photo-émission sont pris en compte.

La force du corps exercée par la décharge sur l'écoulement est donnée par $\mathbf{f} = \sum_i Q_i n_i \mathbf{E}$ [2].

Simulations avec le solveur de l'ONERA

Le code numérique de la présente section, est le travail des chercheurs et ingénieurs du departement DTIM et la unité M2SN de l'ONERA, Toulouse. Ce solveur, COPAIER, est capable de calculer la force générée par un actionneur DBD et le vent ionique résultant via un couplage avec le code CFD - CEDRE de l'ONERA. Le système d'équations B.1, B.5 est résolu en utilisant un schéma de volumes finis, de deuxième ordre et explicite et B.7 est résolu en utilisant une méthode des éléments finis. En raison de la grande mobilité des électrons, un schéma semi-implicite a été écrites, afin de réduire le temps de calcul. Une méthode de sous-étape locale est utilisée, lié au transport des espèces les plus lourdes et le transport des électrons et la cinétique sont intégrés sur ce pas de temps. En outre, une stratégie de maillage couplé structurée / non structurée a été mis au point dans le but d'améliorer la qualité de la résolution près de la pointe de l'anode où l'intensité du champ électrique est plus haute et où la charge électrique est créé
.

Dans cette section, nous étudions la configuration d'intérêt [9] à une fréquence de $F = 14kHz$ et une tension de fonctionnement de $V_0 = 21kV$. La permittivité diélectrique relative est $\varepsilon_r = 3$, l'épaisseur du diélectrique est d'environ $r = 3$ mm. L'anode est de 70 μ m d'épaisseur et $w = 5cm$ longue et la cathode est de $20cm$.

Sur la figure B.3 (a), la force moyenne dans le temps est présentée définie par

$$\mathbf{F_T}(x) = \frac{1}{T}\int_0^T \mathbf{f}(s+\Delta t, x)ds \tag{B.8}$$

où Δt est un décalage de temps après laquelle toutes les quantités calculées peuvent être considérés comme périodique. La valeur maximale de la force parallèle se trouve près de la pointe de l'électrode supérieure, où l'intensité du champ électrostatique est la plus élevée. La valeur maximale est d'environ $12kN/m^3$, mais il est en baisse de façon exponentielle avec la distance à la pointe de l'anode et peut être considérée comme nulle en dehors d'une région de 1 mm de largeur et 1 mm de hauteur. La force a été intégrée sur l'ensemble de calcul domaine A, selon l'équation B.9, et sa variation dans le temps a été tracée sur une période (voir figure B.3) .

$$\mathbf{F_{vol}}(t) = \int_A \mathbf{f}(s+\Delta t, x)dx \tag{B.9}$$

La force totale exercée par l'actionneur est donnée par B.10:

$$\frac{1}{T}\int_0^T \int_A \mathbf{f}(s+\Delta t, x)dsdx \tag{B.10}$$

La valeur calculée pour ce set-up est d'environ 19 m N / m et la valeur expérimentale donnée par Durscher et Roy [9] est d'environ 20 m N / m.

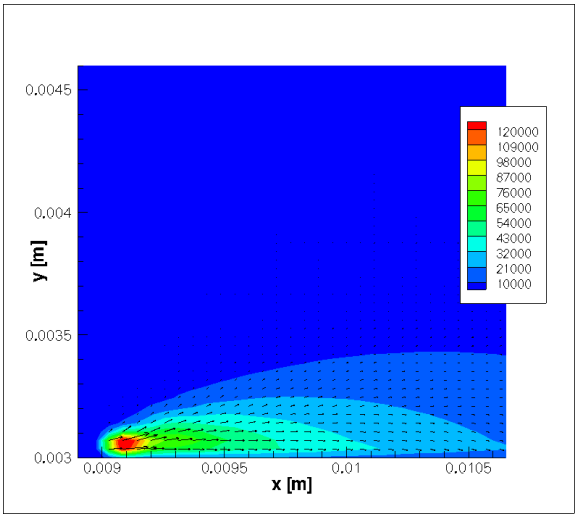

(a) Contours de $\mathbf{F_T}$ (en N/m^3)

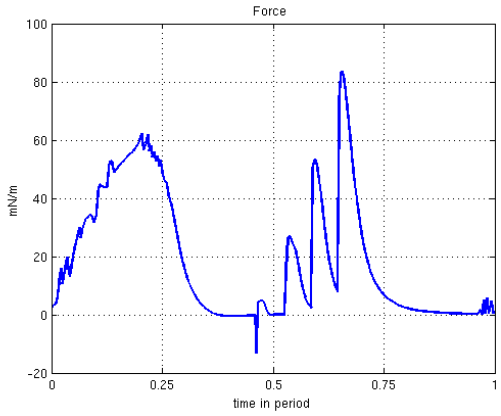

(b) Évolution de F_{vol} (en millinewtons sur mètres) vs. temps

Figure B.3: Force du corps

Une étude paramétrique de la variation de la force totale à l'égard de la tension de fonctionnement et la fréquence a été effectuée B.4.

Nous observons que plus la fréquence est élevée, plus la force produite est grande. La force totale obtenue pour une fréquence 7 de kHz et 21 de tension kV est 14.3mN $/m$ et le mesuré expérimentalement est environ $15mn/m$ [9]. Pour 16 kV et 14 kHz la force calculée est $10mn/m$ alors qu'elle est mesurée $7mn/m$ dans les expériences. Et pour 7 kHz les forces calculées et mesurées sont respectivement 5.2mN et 3mn/m. En conclusion, ces résultats de calcul sont en accord avec les résultats expérimentaux de Durscher et Roy.

La force calculée par la modélisation du plasma est introduit comme un terme source dans un solveur CFD. Les simulations ont été réalisées avec le code de l'ONERA, CEDRE. La force totale est en moyenne sur une

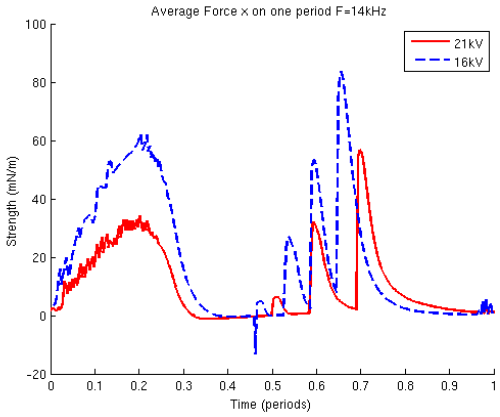

(a) 16kV et 21 kV

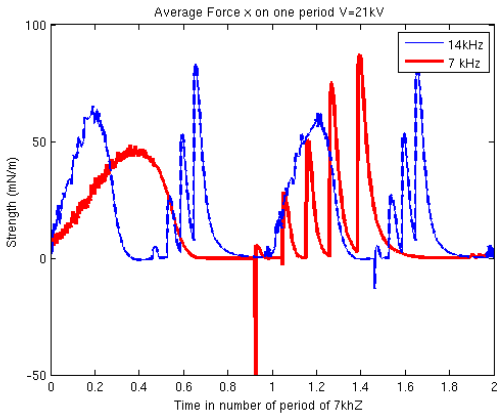

(b) 14kHz et 7 kHz

Figure B.4: Force d'espace totale moyenné

période et cette valeur moyenne est constamment appliqué comme un terme source au cours de la simulation. Nous avons effectué deux calculs, en supposant d'abord le flux laminaire et d'autre part en utilisant un modèle turbulent k ω, sur la base des expériences numériques de [10]. Nous présentons le composante parallèle, U_x, et perpendiculaire, U_y, de la vitesse induite sur la figure B.5. On constate que le maximum de la vitesse parallèle est très près de l'anode qui est situé à $x = 5mm$ lorsque la valeur maximale est plus que 8 m/ s.

La figure B.6 montre le profil de la vitesse parallèle à différents endroits. Ces valeurs de vitesse du jet sont différentes de celles mesurées par Roy et Durscher qui a montré que la vitesse maximale à 15mm de la pointe de l'anode, est d'environ 5 m/ s, ce qui est plus grande que celle calculée. La discrétisation temporelle de la force du corps a été également étudié et cette étude a montré que cela peut avoir un effet sur les profils de vitesse et peut produire la différence notée entre nos simulations et les résultats expérimentaux.

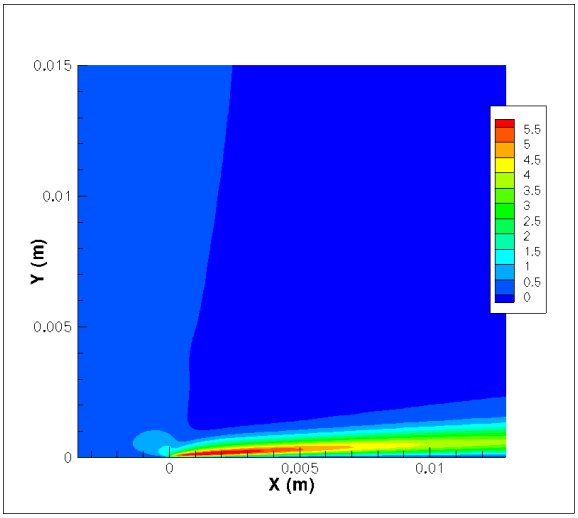

(a) contour de U_x

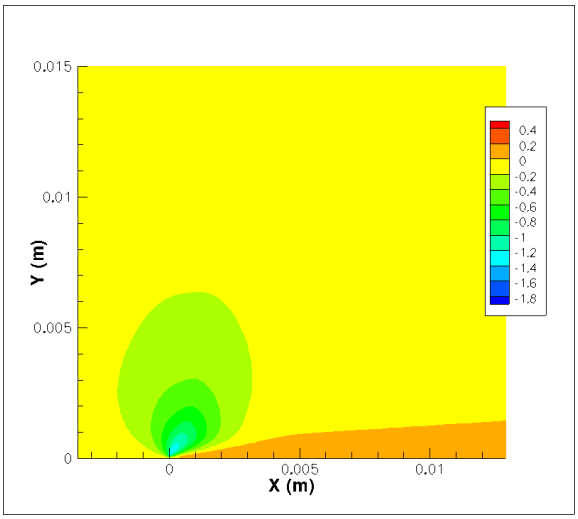

(b) contour de U_y

Figure B.5: Composantes de vitesse.

Simulations avec le solveur de LAPLACE

Dans cette section, nous avons utilisé le solveur numérique de la décharge à barrière diélectrique créée en LAPLACE, UPS, Toulouse [11]. Le modèle physique est semblable à celui décrit précédente en tenant compte des électrons, des ions positifs et négatifs [12]. La procédure numérique utilisée est basée sur l'intégration asynchrone en temps et une technique de raffinement adaptatif de maillage [7, 13]. La combinaison de ces deux techniques conduit à des calculs beaucoup plus rapides (un facteur de 100 ou plus) [13].

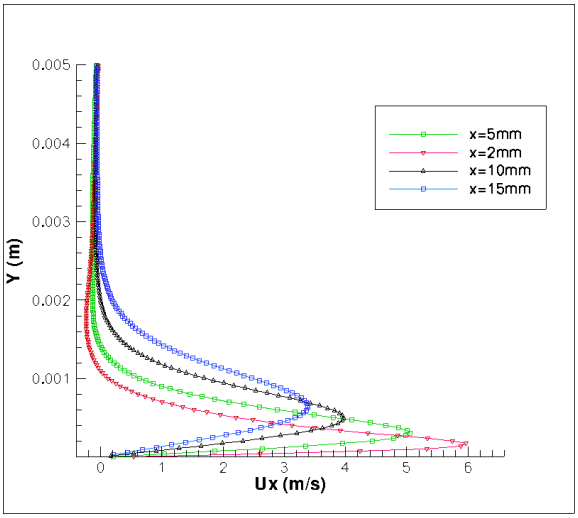

Figure B.6: U_x à différents endroits

Le domaine de calcul est de 3,2 x 1,6 cm, y compris le couche diélectrique avec une permittivité relative de 5. Il n'y a pas d'écart horizontal entre les électrodes et le maillage initial est raffiné autour de la pointe de l'électrode supérieure (figures B.7 et B.8).

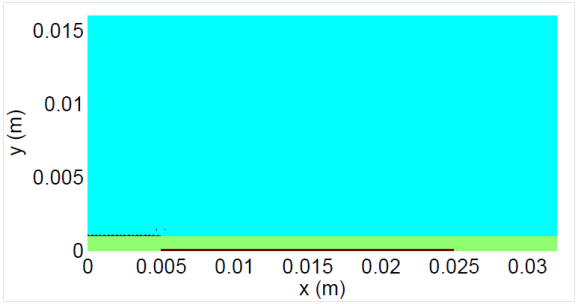

Figure B.7: Domaine de calcul pour la décharge

Couplage avec FLUENT®

A partir des simulations avec le modèle numérique décrit ci-dessus, la force distribuée dans l'espace ainsi que la force moyenne dans le temps ont été obtenus. La force répartie a été introduite comme un terme source de quantité de mouvement en utilisant une fonction définie par l'utilisateur dans FLUENT®. Les approches numériques utilisées dans les simulations avec FLUENT® ainsi que des résultats de validation et d'optimisation peuvent être résumées comme suit:

— 2D-stationnaire, double précision, solveur implicite couplé sur une plaque plane.
— Discrétisation de second ordre pour toutes les variables.
— Initialisation avec une valeur de la vitesse axiale de 1 m / s et 0 pour toutes les autres variables dans l'ensemble du domaine.

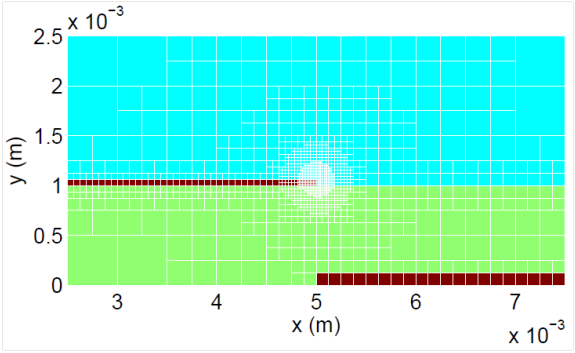

Figure B.8: Maillage autour de la pointe de l'électrode supérieure

— L'ajout de chaleur due à plasma a été négligé (sauf mention) car les simulations ont montré son petit effet sur les profils et les amplitudes de la vitesse.
— L'effet de la force Y dans le comportement de l'écoulement est vraiment petite et il peut probablement être négligé.

Étude sur la turbulence

Les auteurs de [14] ont fait des expériences sur un seul DBD sur une plaque plane, en obtenant les profils de vitesse pour une tension V = 11 kV et une fréquence f = 11.7kHz.

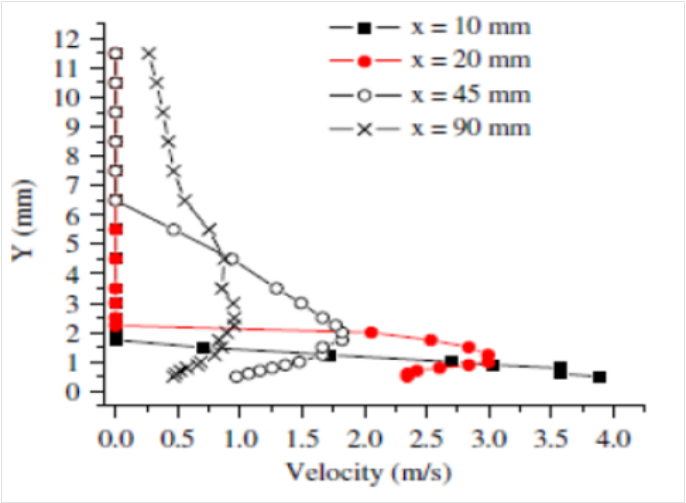

Figure B.9: Profils de vitesse pour V=11kV and f=11.7kHz sur une plaque plan [14]

Sur la base de ces résultats qui sont présentés dans la figure B.9, les études sur l'actionneur 11 kHz-12kV DBD étaient tenue en se concentrant sur les effets de turbulence, avec une épaisseur de diélectrique identique à celle étudiée dans le document mentionné et égale à 4 mm. La solution diffère des résultats expérimentaux. L'hypothèse laminaire de l'écoulement semble de surestimer les vitesses maximales et

sous-prédire la diffusion de l'écoulement, conduisant à une couche limite plus faible et par conséquent un jet de paroi plus mince qui diffuse plus lentement.

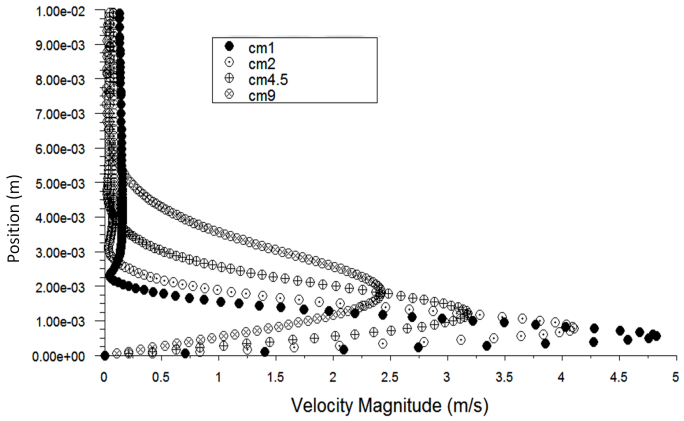

Figure B.10: Profils de vitesse à 1, 2, 4.5 et 9 cms de la région de plasma. Hypothèse laminaire.

Avec le modele kε "realizable" les amplitudes de la vitesse maximale approchent celles mesurées dans l'expérience mais l'épaisseur de la couche qui est formée est surestimée alors que avec le modèle k ω SST , les résultats obtenus correspondent aux expériences beaucoup mieux. Les profils de vitesse obtenus avec les deux modèles sont tracée dans les figures B.11 et B.12.

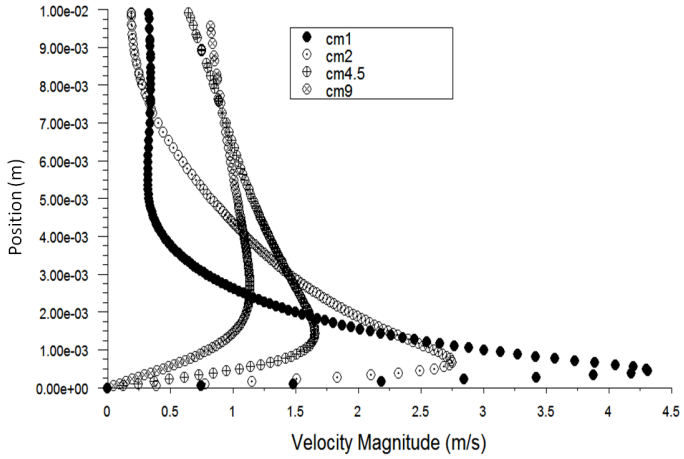

Figure B.11: $k\varepsilon$ realizable - Profils de vitesse

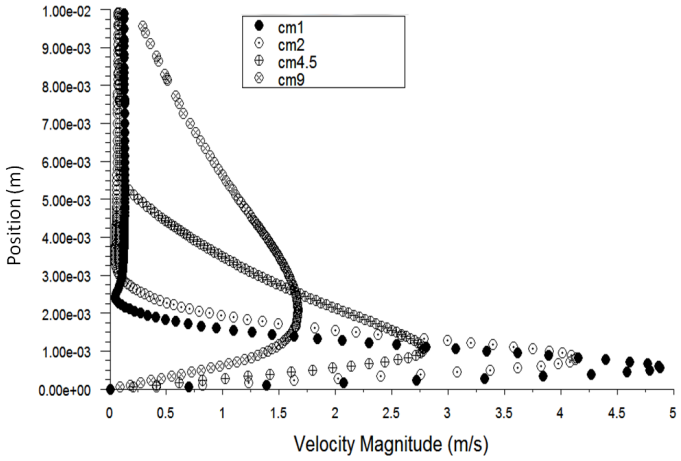

Figure B.12: $k\omega$ SST - Profils de vitesse

Application

Transition laminaire - turbulente

Le frottement de la peau est causée par la trainée visqueuse dans la couche limite autour de l'objet. Le coefficient de frottement de la peau, C_f, est défini comme:

$$C_f = \frac{1}{2}\tau_w U_o \rho \tag{B.11}$$

La transition laminaire-turbulente conduit à une augmentation de la contrainte de cisaillement de paroi local et du coefficient de friction de la peau. Un représentation schématique de cet effet est montré dans la figure B.13. En utilisant le modèle turbulent SST-transition qui fournit couramment, et un écoulement extérieur de 17,2 m / s, la simulation a montré que la transition se produirait à x = 0,28 m du bord d'attaque, lorsque la théorie donne une valeur de 0,29 M. Sur la base de ces résultats, le même calcul était effectuée avec l'actionneur à plasma de 11 kHz et 12 kV (même géométrie que précédente). Le graphique de la comparaison du coefficient de frottement de la peau est tracé dans la figure B.14. Le ligne verte correspond au cas sans actionnement et la ligne jaune au cas avec actionnement. On voit que l'actionnement de DBD retarde la transition d'environ 0,05 mètres.

Contrôle sur un profil d'aile

L'étude suivante a effectué sur la NACA 0021, un profil aérodynamique symétrique avec une corde de 1 mètre. Gambit ® a été utilisé pour le maillage du domaine autour la surface portante. La zone de plasma a été mis sur le bord d'attaque correspondant aux expériences et la simulation faite par Orlov et al [15, 16]. Le modèle de transition SST était utilisé à attraper la turbulence dans l'écoulement, ainsi que la transition et le point de séparation. Le problème stationnaire a été considéré. Des simulations ont été effectuées avec l'actionneur de plasma, mais son influence sur les coefficients aérodynamiques du profil d'aile était presque négligeable comme tracée dans B.15.

Néanmoins, Orlov conclut, que près de l'angle d'attaque critique les effets de plasma peut modifier l'écoulement positivement (voir figure B.15, ce qui augmente le coefficient de portance et donc retarder le décrochage, mais comme mentionné ci-dessus, il est difficile à capter ces effets près de cette zone avec un

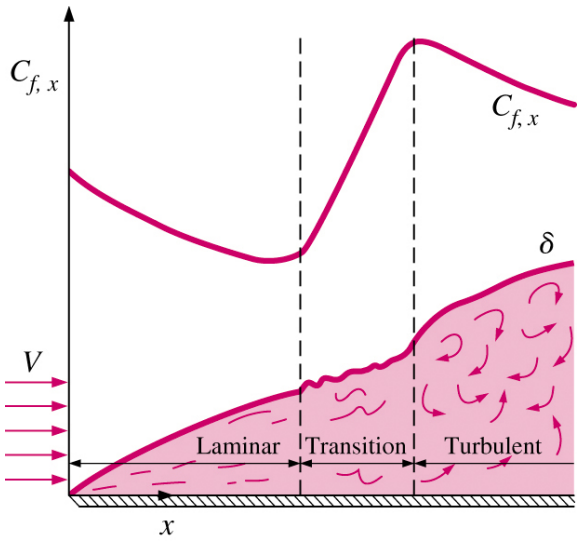

Figure B.13: Transition laminaire-turbulente et coefficient de friction de la peau.

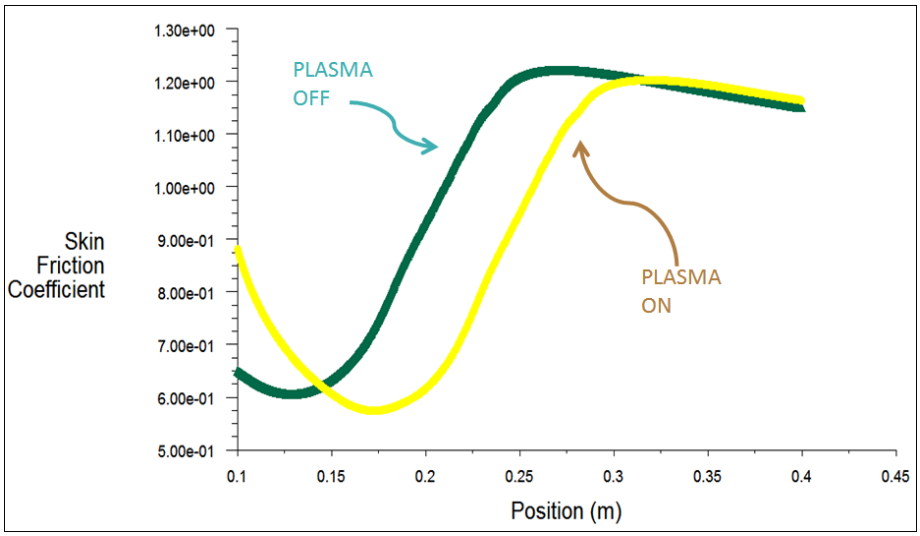

Figure B.14: Transition laminaire-turbulente due au DBD

solveur RANS stationnaire. Cet inconvénient nous a motivé à étudier l'influence de la actionneur sur le point de transition, afin de connecter ce travail à la section précédente.

Pour le même cas, le coefficient de friction de la peau avec et sans plasma est présenté côte-à-côte dans la figure B.16. Nous pouvons remarquer que lorsque l'actionnement est activé, la point de transition remonte sur une distance de près de 4 cm. Cette transition précoce peut être la cause pour retarder le décrochage à grandes angles d'attaque.

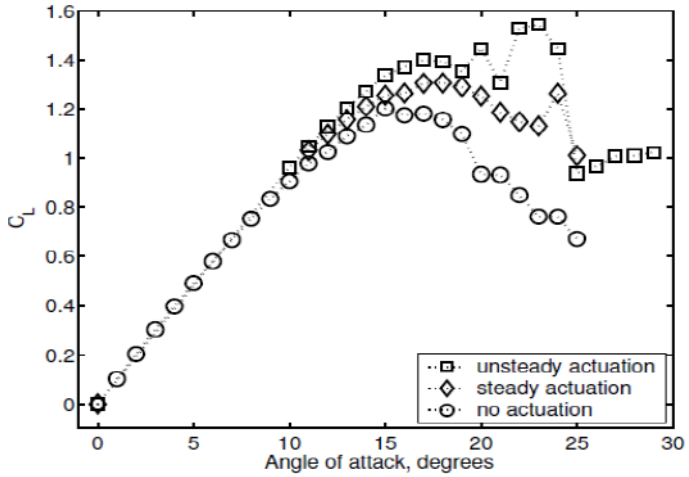

Figure B.15: Coefficient de portance vs angle d'attaque [15, 16]

Conclusion

L'actionneur DBD a été modélisée en utilisant deux solveurs différents basés sur des modèles physiques similaires - celui développé à l'ONERA et l'autre à LAPLACE. Nous avons effectué plusieurs études dans différents régimes de fonctionnement, ce qui démontre la capacité des modèles utilisés à reproduire l'effet du vent ionique de ces actionneurs. Des études paramétriques ont montré que les modèles donnent une estimation assez précise de la force produite par le DBD par rapport à des mesures expérimentales. La modélisation de la turbulence a été essentielle pour une représentation précise de l'écoulement du jet de paroi. Des applications aérodynamiques de contrôle d'écoulement ont démontré les effets possibles de ces actionneurs pour la transition laminaire - turbulente et l'amélioration de la portance.

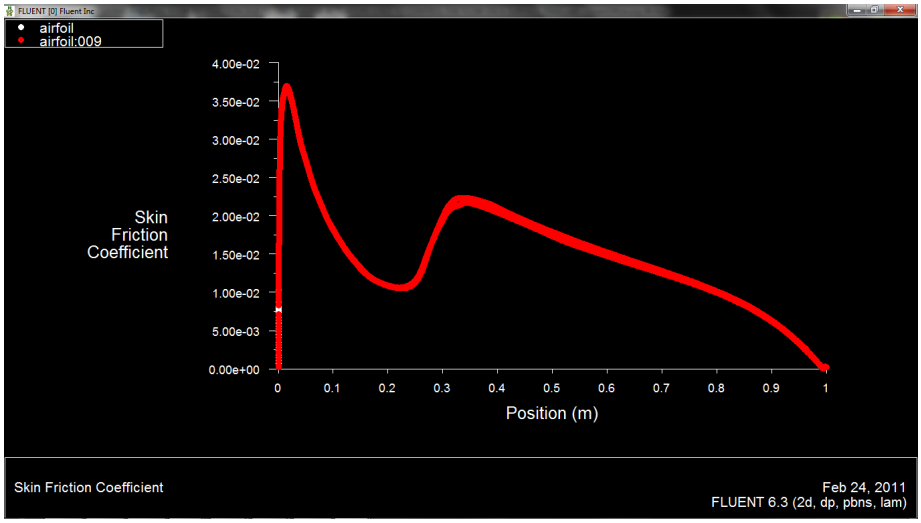

(a) plasma OFF

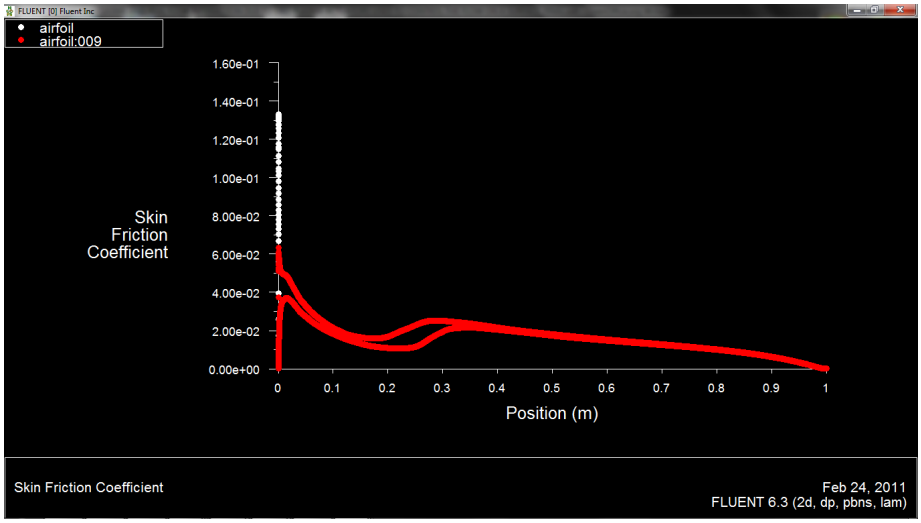

(b) plasma ON

Figure B.16: Coefficient de friction de la peau

Références Bibliographiques

[1] Thomas C Corke, Martiqua L Post, and Dmitriy M Orlov. "Single dielectric barrier discharge plasma enhanced aerodynamics: physics, modeling and applications". In: *Experiments in Fluids* 46.1 (2009), pages 1–26.

[2] JP Boeuf and LC Pitchford. "Electrohydrodynamic force and aerodynamic flow acceleration in surface dielectric barrier discharge". In: *Journal of Applied Physics* 97.10 (2005), page 103307.

[3] JP Boeuf, Y Lagmich, and LC Pitchford. "Contribution of positive and negative ions to the electrohydrodynamic force in a dielectric barrier discharge plasma actuator operating in air". In: *Journal of Applied Physics* 106.2 (2009), page 023115.

[4] Alexandre V Likhanskii et al. "Modeling of dielectric barrier discharge plasma actuators driven by repetitive nanosecond pulses". In: *Physics of Plasmas (1994-present)* 14.7 (2007), page 073501.

[5] Takashi Abe et al. "Experimental study for momentum transfer in a dielectric barrier discharge plasma actuator". In: *AIAA journal* 46.9 (2008), pages 2248–2256.

[6] Y Lagmich et al. "Model description of surface dielectric barrier discharges for flow control". In: *Journal of Physics D: Applied Physics* 41.9 (2008), page 095205. URL: `http://stacks.iop.org/0022-3727/41/i=9/a=095205`.

[7] Thomas Unfer et al. "An asynchronous scheme with local time stepping for multi-scale transport problems: Application to gas discharges". In: *Journal of Computational Physics* 227.2 (2007), pages 898–918.

[8] A A Matveyev I A Kossyi A Yu Kostinsky, T V P SilakovUnfer, and JP Boeuf. "Kinetic scheme of the non-equilibrium discharge in nitrogen-oxygen mixtures". In: *Plasma Sources Science and Technology* 1.207 (1992), pages 207–220.

[9] Ryan Durscher and Subrata Roy. "Evaluation of thrust measurement techniques for dielectric barrier discharge actuators". In: *Experiments in fluids* 53.4 (2012), pages 1165–1176.

[10] Konstantinos Kourtzanidis. “Numerical Simulation of Plasma Actuators for Flow Control”. In: *51ST AIAA AEROSPACE SCIENCES MEETING, Texas, USA 2013-0134* (2013).

[11] JP Boeuf et al. “Electrohydrodynamic force in dielectric barrier discharge plasma actuators”. In: *Journal of Physics D: Applied Physics* 40 (2007), page 652.

[12] JP Boeuf et al. “Electrohydrodynamic force in dielectric barrier discharge plasma actuators”. In: *Journal of Physics D: Applied Physics* 40.3 (2007), page 652.

[13] Thomas Unfer et al. “Multi-scale gas discharge simulations using asynchronous adaptive mesh refinement”. In: *Computer Physics Communications* 181.2 (2010), pages 247–258.

[14] E. Moreau, R. Sosa, and G. Artana. “Electric wind produced by surface plasma actuators: a new dielectric barrier discharge based on a three-electrode geometry”. In: *Journal of Physics D: Applied Physics* 41 (2008), page 115204.

[15] Dmitriy M. Orlov. “Modelling and simulation of single dielectric barrier discharge plasma actuators”. PhD thesis. University of Notre Dame, PhD thesis, 2006.

[16] D.M. Orlov et al. “Modeling and experiment of leading edge separation control using SDBD plasma actuators”. In: *AIAA paper* 877 (2007), page 2007.

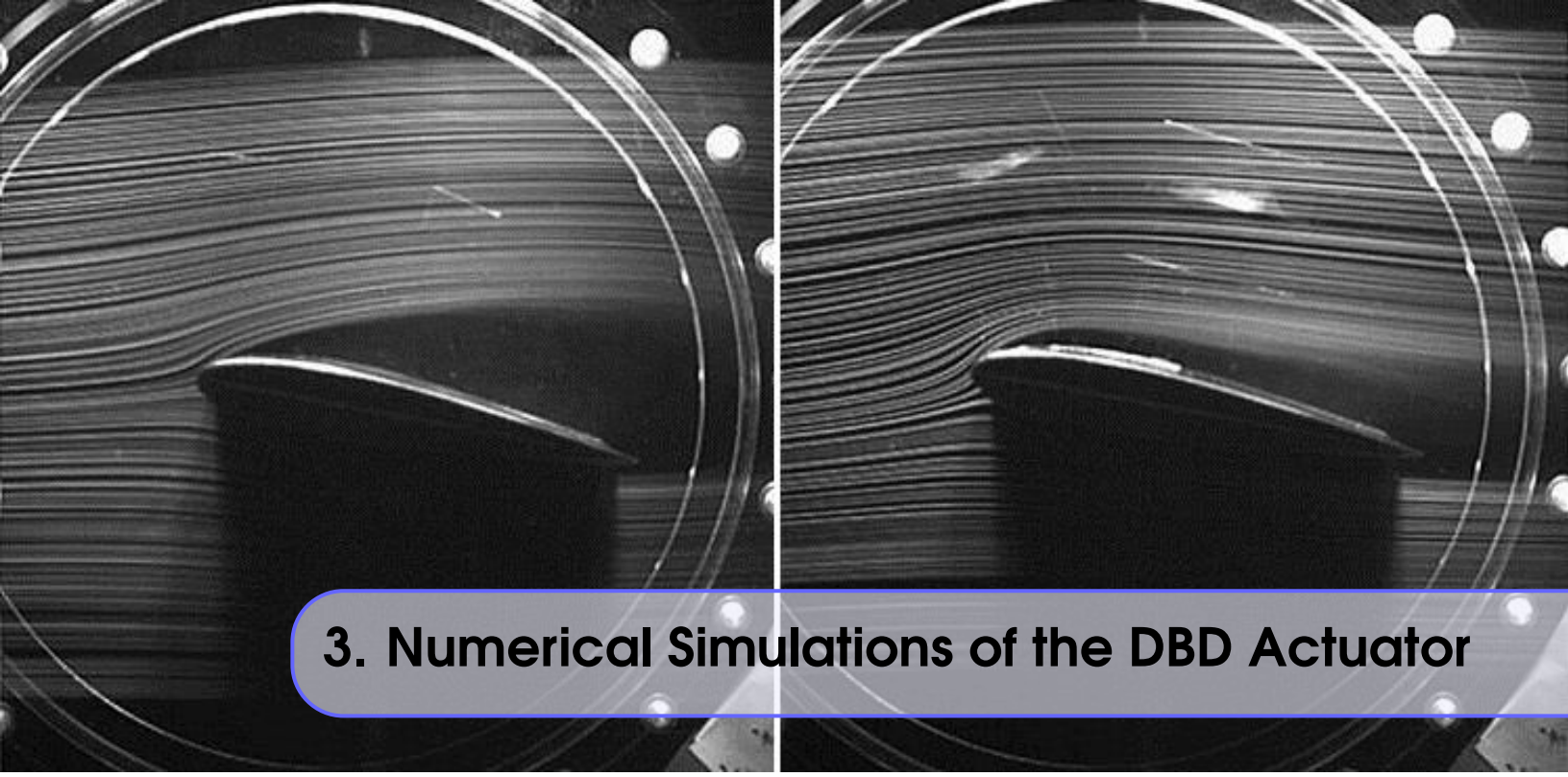

3. Numerical Simulations of the DBD Actuator

3.1 Presentation and literature review

A Dielectric Barrier Discharge ionizes a part of the gas and the created charged particles transfer their momentum to the gas molecules, creating a body force which acts on the flow. A schematic represantation of a surface DBD actuator and the plasma formation can be seen in figure 3.1. The prediction of the body force distribution is of utmost importance when one wants to perform flow control simulations using SDBD actuators. In the last decade, several approaches have been proposed to estimate this force distribution.

In a first attempt[2], a description of the DBD has been done with a plasma modeling proposed by Suzen but some parameters of the model have to be fixed and correction remains necessary to fit experimental results, limiting its ability to predict other SDBDs. Several studies focus on the measurement of induced gas velocity using Particle Image Velocimetry and the extraction of thrust produced [3, 4]. In these works, the authors use the velocity field measurements of a SDBD actuator in order to identify the corresponding body force distribution which would be needed to produce the same results with a Navier Stokes solver. Following the same idea, these approaches have shown that it is possible to identify phase- and space-wise the body force characteristics [5, 6]. These methods are proved to be accurate but cannot provide predictive informations on other devices because there are based on specific experiments.

One other attempt of describing the body force is based on a fine description where the barrier dielectric discharge is (almost) entirely modeled. In [7], the authors modeled the weakly ionized air plasma as a four-component mixture of neutral molecules, electrons, and positive and negative ions, that included ionization and recombination processes. Their simulations indicated the importance of the presence of negative ions in the air as stated in [1]. In this scope, significant works have been conducted by the group of J.P. Boeuf[8, 9]. Thanks to these simulations, a physical understanding of the SDBD was given, which showed trends with respect to discharge parameters consistent with the experiments. Their work was successfully extended to the

Photo by ISAS/JAXA

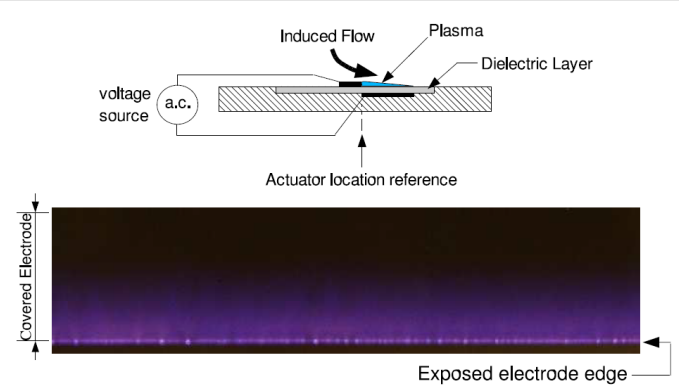

Figure 3.1: Schematic representation of a SDBD and plasma formation [1].

nanosecond-DBD modeling[10].

Focusing on the last group [8, 9], a fluid model for the plasma, based on solutions of electron and ion transport equations - continuity and momentum transfer - coupled with Poisson's equation in two dimensions has been used. The model accounts for the charging of the dielectric surface due to the incident charged particle fluxes. The physical model is similar to the one in [11]. They have calculated the body force produced by the actuator versus different parameters (voltage, frequency, dielectric properties). Their results are in excellent agreement with experimental observations. Their simulations reveal that at high frequencies and low voltage amplitude, the contributions of positive ions are dominant, while the contribution of negative ions to the total EHD force is dominant at low frequencies and high voltage amplitudes. This behavior has a straight impact to the production of the body force and the consequent induced flow. Thus, the choice of waveforms for the excitation ac source is strongly depending to the frequency of operation. The simulation results for the space distribution of the force reveals interesting facts too. For the positive phase, it is concentrated near the exposed electrode due to the positive ions that restart there after each streamer discharge. In the negative phase, the more spread, continuous, negative ion cloud leads to a more diffused force distribution between the two electrodes. Consistent with the experiments, the force obtained reaches values of several 10 mN/m, increases with voltage amplitude and is being favored by lower frequencies of the ac signal. In figure 3.2, the evolution of the total integrated in space and averaged in time x-directed force is plotted for different frequencies.

In [13], three-dimensional discharge plasma simulations of a single DBD plasma actuator have been performed. Their model consists of the same set of equations and assumptions as in [8], in three dimensions. They have successfully simulated the micro-discharges in a glow regime and the filamentary ones corresponding on positive and negative step signals of the applied voltage. Interestingly, they observed that the spanwise body force calculated was strongly non-uniform. Its average values and distribution though, both in time and space, is close to ones obtained by 2D simulations, validating the two-dimensionality hypothesis of most simulation attempts.

The numerical simulation of SDBDs is particularly challenging and a special effort has been spent to design an efficient solver. Implicit schemes[14] have been tested as well as asynchronous strategies which were very promising to compute large multiscale problems[15]. These works have proved the ability of such

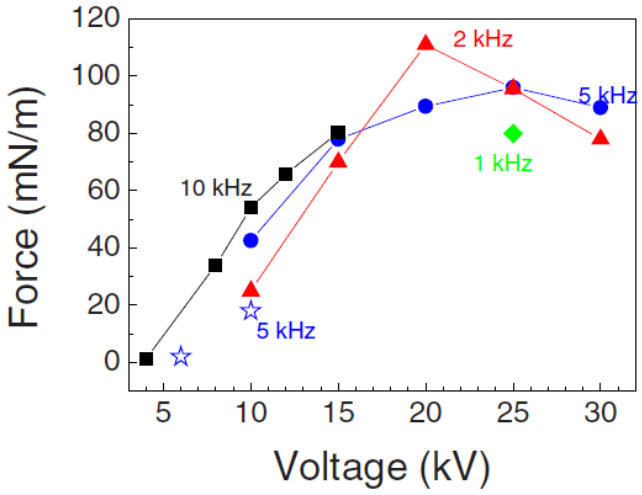

Figure 3.2: X-directed force vs applied voltage for different frequencies. The star symbols correspond to the measurements of [12] at 5 kHz.

a numerical model to provide physically relevant trends of this kind of discharge with various parameters and also to predict the produced jet velocity[16], but no quantitative comparison has yet been performed between measurements and computation.

The objective of this chapter is to use already developed solvers, one at ONERA and one at LAPLACE, in order firstly, to calculate the body force exerted by the operation of the DBD actuator and couple it with CFD solvers, taking into account turbulent effects, in order to study the induced flow and compare it with experimental results. Secondly, we aim to perform parametric studies on different operational conditions of the DBDs to investigate their optimized range of operation. Lastly, some simple simulations of flow control applications are envisioned, to demonstrate the possibilities of such actuators as flow control devices.

The organization of this chapter is the following : Firstly in section 3.2, the physical model used is presented. Next, results from two different numerical techniques for modeling the DBD actuator are presented: In section 3.3 the solver (COPAIER) developed in ONERA has been used, aiming at testing the plasma model and to compare the obtained numerical results with the experimental ones obtained by [17] for a $14kHz - 21kV$ actuator in a quiescent atmosphere. The total body force exerted by the discharge as computed numerically is shown and compared with force balance measurements. Parametric studies are also presented for various voltages, frequencies and DBD parameters and compared with experimental results. In a quiescent flow, PIV measurements of the induced actuator wind, and computational results obtained by CFD are also presented and analyzed. Finally, the effects of the numerical and physical parameters are studied in order to evaluate the robustness of the modeling. This work has been conducted in the frame of the AVT190 NATO group on a standardized configuration. In section 3.4 the code developed in LAPLACE has been used. Presentation of the coupling method of this model with a commercial CFD software is followed by studies on the resulting wall jet produced by the DBD actuator. Various parametrical studies are then conducted especially on different turbulent models targeting a better reproduction of experimental results.

Finally in the same section, aerodynamic applications such as laminar to turbulent transition control and airfoil lift enhancement are presented. In section 3.5, we conclude and give some perspectives.

3.2 Physical Model

The physical model used in this chapter provides a fine description of the plasma although keeping a simple kinetic scheme. Air chemistry is indeed highly complex and involves many species and reactions[18], so that the computational complexity required for a complete description would be too large and with too much uncertainty. Hence, following here the approach of J.P Boeuf[8] a simplified scheme is used that is nonetheless complex enough to get a relevant behavior of the body force with respect to the discharges parameters.

In more detail, the model consists of solving the continuity and momentum equations for a set of simplified species composed of positive ions (+) noted as p, negative ions (-) noted as n and electrons, noted as e. The transport is described in the drift-diffusion approximation using coefficients tabulated as a function of E/N (local field approximation). The continuity equation for the charged particles of type i, reads :

$$\partial_t n_i + \nabla.(\mathbf{U_i} n_i) = S_i \tag{3.1}$$

The kinetic source term takes into account direct ionization by electron impact, attachment and electron/ion and ion/ion volumic recombination and reads :

$$S_e = (\alpha - \eta) U_e n_e - r_{ep} n_e n_p \tag{3.2}$$

$$S_p = \alpha U_e n_e - r_{ep} n_e n_p - r_{np} n_n n_p \tag{3.3}$$

$$S_n = \eta U_e n_e - r_{np} n_n n_p \tag{3.4}$$

where $\Gamma_i = U_i n_i$ is the charged particle flux for each species i.
The Bolsig+ software is used to obtain the ionization (α) and attachment (η) coefficient and the electron mobility (μ_e) for a $77\%N2 - 23\%O2$ mixture. The ion mobility is fixed and equal for both ion types.

The charged particle flux Γ_i has a drift-diffusion form and the drift velocity reads :

$$\mathbf{U_i} = U_g + sgn(q_i)\mu_i \mathbf{E} + D_i \nabla n_i \quad sgn(q_i) = +,\ if\ i = p,\ else\ sgn(q_i) = - \tag{3.5}$$

and the diffusion coefficient for each species i, reads:

$$D_i = \frac{-\mu_i k_B T_i}{e} \tag{3.6}$$

The charged particle temperatures are supposed to be constant and equal to 1 eV for electrons and to ambient temperature for ions.

The electric field follows the Poisson law and is then related to the total charge deposited by the ionized particles.

$$\nabla.(\varepsilon_r \mathbf{E}) = \frac{1}{\varepsilon_0}\sum_i q_i n_i + \sigma\delta_S, \quad \mathbf{E} = -\nabla\Phi \tag{3.7}$$

where ε_0 is the vacuum permittivity, ε_r is the relative permittivity, Φ is the electric potential and $\sigma\delta_S$ represents the contribution of the charges deposited by the discharge on the dielectric surface. These charges are obtained by time integrating charged particle fluxes to the surface. An electric circuit is taken into account to calculate the electric potential change in function of the total current that circulates in the circuit : $V = V_0 - RI$, where R denotes the resistance of the external circuit (≈ 0.1 Ohm).

The boundary conditions taken into account are secondary emission of electrons at the dielectric surface $\mathbf{J_e} = -\gamma\mathbf{J_p}$ or a prescribed value of the minimal density ($10^{12}m^{-3}$). Neither photo-ionization nor photo-emission processes are considered.

The body force exerted by the discharge on the flow is given by $\mathbf{f} = \sum_i q_i n_i \mathbf{E}$. This is an approximative equation, neglecting the force due to the non-perfect neutrality associated with charged particle gradients as well as the charged - particle momentum divergence force which are both negligible with respect to the Coulomb force acting on the charged particles [8]. As mentioned above, the kinetic scheme involves different reactions like recombination, ionization and attachment. The main characteristic times of these processes are related to the electric field. For example, the ionization frequency increases strongly with the electric field (varying from 10^{-12} s to 10^{-9} s), and so does the electron transport time step (which can also plummet to 10^{-12} s). The diffusion phenomenon also typically depends on the electric field and the maxwell time relaxation depends on the charge density and can be predominant in some situations. Hence, the simulation has to deal with these small typical times and also with the SDBD period whose value is about 10^{-4} s. In terms of characteristic lengths, we may compare the geometry of the SDBD (from cm to $100\mu m$), and the Debye length - to capture the dielectric relaxation effect - which is micrometric. The integration of all these different scales require a small time step and and a small step size that lead to highly multiscale simulations.

3.3 Validation and numerical simulations with ONERA's DBD solver

The numerical code of this section, is the work of the researchers and engineers at the Department of Information Treatment and Numerical Modeling (DTIM) and the Mathematical Modeling and Numerical Simulation (M2SN) unit of ONERA, Toulouse. This solver, COPAIER (COde PlasmA Instationnaire pour l'aEROdynamique), is capable of calculating the force generated by a DBD actuator and the resulting ionic wind via a coupling with the CFD ONERA's code CEDRE. We will describe briefly the key numerical points, and move on to numerical results and comparison with experimental data.

3.3.1 Numerical methods

The system of equations 3.1, 3.5 is solved using a second order explicit finite volume scheme and 3.7 is solved using a finite element method. Due to the large mobility of the electrons, a semi-implicit scheme has been written in order to reduce the CPU time. The electron motion is treated separately from the heaviest species : In most applications, the time step is governed by the CFL condition for the electrons that are the most mobile species. Here a local sub-step is used, linked to the transport of the heaviest species and the

electrons transport and kinetic are integrated on this time-step. In addition, a coupled structured/unstructured mesh strategy has been developed in order to improve the quality of the resolution close to the tip of the anode where the electric field strength at its highest and where the electric charge is created.

The experiments of interest[17] for the comparison with the numerical results have been conducted with the set of parameters of the SDBD actuator represented in figure 3.3.

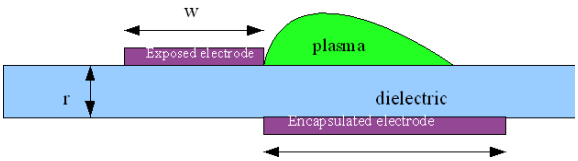

Figure 3.3: SDBD actuator

The relative dielectric permittivity is $\varepsilon_r = 3$, the thickness of the dielectric is about $r = 3mm$. The anode is $70\mu m$ thick and $w = 5cm$ long and the cathode is $20cm$ long.

3.3.2 Description of the test case and numerical parameters

In this section, we study the configuration at a frequency of $F = 14kHz$ and an operating voltage set to $V_0 = 21kV$. We have performed the simulation using a fine mesh (about 361000 cells) and a coarse mesh (about 26000 cells, see Figure 3.4). In both cases, the mesh is defined so that it can take into account the anode thickness (which is 70μ). As shown on both figures, the mesh is refined near the tip of the anode in order to have a good resolution of the body force. Typically, 50 to 80 % of the cells lay in the structured zone. The size of the computational domain is chosen large enough to avoid electrostatic perturbations due to the boundary of the computational domain. Typically the CPU time required to perform a simulation is about one day by actuator period on a single core of a 2.8 GHz Intel Xeon processor and on the coarse mesh.

3.3.3 Body force results

Simulating about four periods is enough to reach a periodical regime corresponding to the SDBD actuator period. The total charge deposited on the dielectric, plotted on figure 3.5, provides good information on the convergence toward the periodical regime.

One can note, that the figure shows the periodical behavior of the deposited charge after only two periods. On figure 3.6 (a), the time-averaged force is presented defined by

$$\mathbf{F_T}(x) = \frac{1}{T}\int_0^T \mathbf{f}(s+\Delta t, x)ds \tag{3.8}$$

where Δt is a time offset after which all the computed quantities can be considered as periodical. The maximum of the parallel force is located near the upper electrode tip where the strength of the electrostatic field is the highest. The value of the maximum is about $12kN/m^3$ but it is exponentially decreasing with the distance to the anode tip and can be considered as zero outside a region of $1mm$ width and $1mm$ height. This differs from other authors[6, 19] who find this non-zero force region to be twice as much long and high. Nevertheless, as it is expected, the main component of the force is parallel to the dielectric surface and as a consequence, the discharge pushes the gas molecules along the dielectric surface.
For evaluation purposes, the force has been integrated over the whole computational domain A, according to

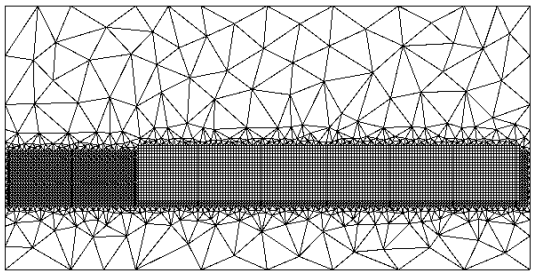

(a) Fine mesh

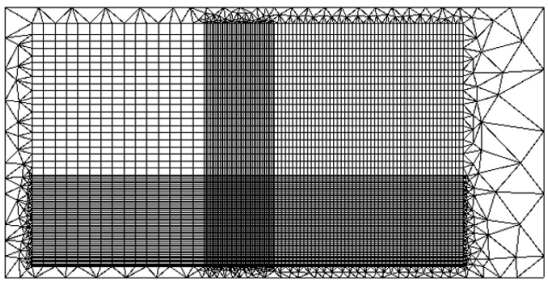

(b) Coarse mesh

Figure 3.4: typical meshes used in a SDBD simulation

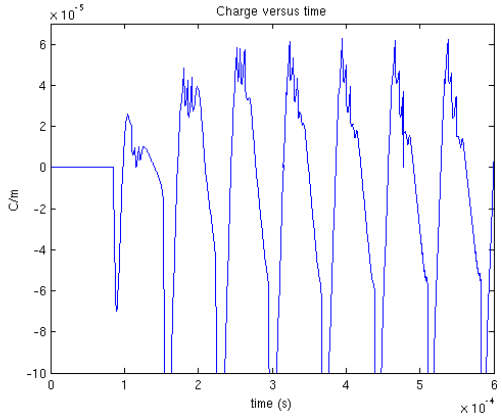

Figure 3.5: charge deposited on the dielectric surface)

equation 3.9, and its time variation has been plotted over one period (see figure 3.6) .

$$\mathbf{F_{vol}}(t) = \int_A \mathbf{f}(s+\Delta t, x)dx \tag{3.9}$$

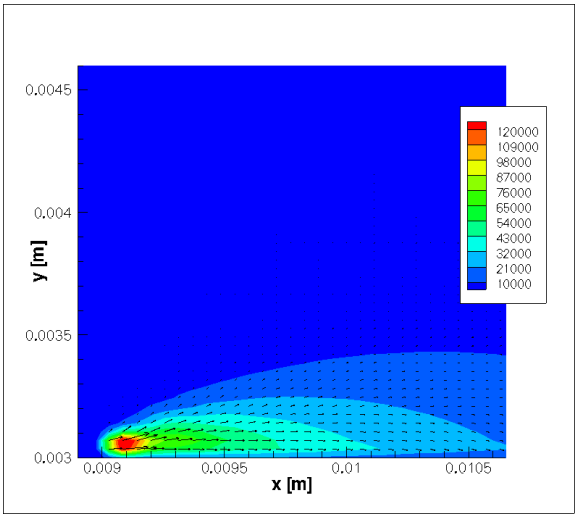

(a) Contours of $\mathbf{F_T}$ (expressed in N/m^3)

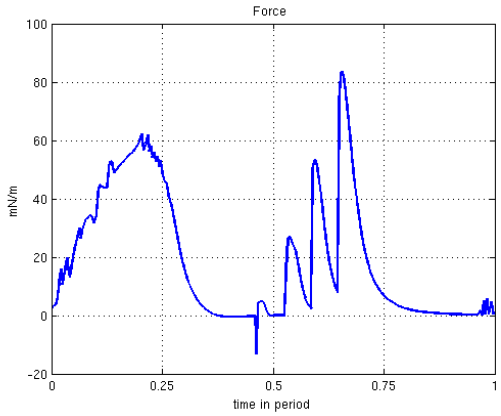

(b) Evolution of F_{vol} (in millinewtons over meters) vs. time

Figure 3.6: Body force

— From 0 to $\frac{T}{4}$ the positive ions are generated by ionization, so the space charge is positive and the force is directed along the Electric field near the tip of the anode. So, the main component of the force is parallel to the dielectric surface.
— From $\frac{T}{4}$ to $\frac{T}{2}$, the Electrostatic field is screened by a high density of ions that stops the ionization and the force decreases to zero.
— From $\frac{T}{2}$ to $\frac{3T}{4}$ when the applied potential goes to $-V_{max}$, positive charge deposited at the dielectric surface creates an intense electric field inducing a negative parallel force during a short time. The formation of a negative volume force precedes the streamer regime.
— From $\frac{3T}{4}$ to T, ionization of electrons and secondary electrons emission generates negative ions that goes to the anode in successive waves.

The negative force appears to be very important during a short time (some μs) but the effect seems to be underestimated here when one compares to the observation of experimenters[6]. Nevertheless, no measurement of the negative force was available until now on this configuration.

The total force exerted by the actuator is given by 3.10:

$$\frac{1}{T}\int_0^T \int_A \mathbf{f}(s+\Delta t,x)dsdx \tag{3.10}$$

The computed value for this set-up is about 19 mN/m and the experimental value given by Durscher and Roy[17] is approximately 20 mN/m. Hence, the discrepancy between measurement and modeling is here less than 1 mN/m which is a good estimation, being given the low level of complexity of the modeling. Simulations with fine and coarse meshes showed a small difference between the results of the total force (less than 5 %) while the computational time proved to be significantly lower. In consequence, all the simulations have been performed with the coarse mesh.

3.3.4 Parametric study

A parametric study of the total force variation with respect to the operating voltage V_0 has been performed. The frequency is set to $F = 14kHz$. On the figure 3.7 is shown the total body force for voltages ranging from 14kV to 28kV. We observe a small discrepancy of the total body force (less than 1 mN/m) for voltages around

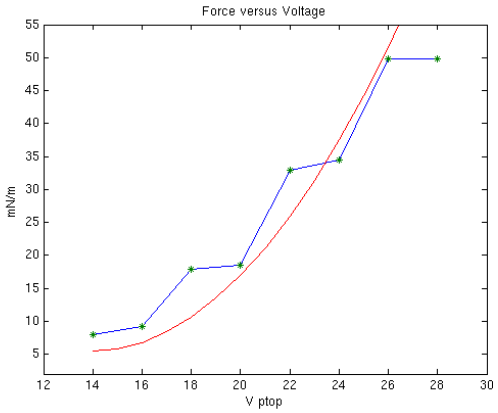

Figure 3.7: Total force (in millinewtons over meters) versus voltage (peak-to-peak)

$V_0 \approx 21kV$ and a larger one for low voltages. In the range of high voltages (larger than $26kV$), the body force reaches a threshold. This phenomenon has been noticed by many experimentalists in other configurations: for example the induced velocity does not increase with the voltage for high enough voltage[20]. This fact has also been noted by the group of J.P. Boeuf[9], which suggests that the induced velocity will eventually reach a limit.

A comparison of the values of $\mathbf{F_T}$ at $F = 7kHz$ and $V = 16kV$ is also shown on Figure 3.8 .

We observe that the total force is mostly created during the positive part of the cycle while the streamers triggered later in the negative part seem to hold only a minor contribution. As it has been noticed, the positive cycle describes a regime of glow discharge and the negative one is formed of successive streamers triggered at different times depending strongly on the slope of the applied potential. On figure 3.8 (b), we observe that the higher the frequency, the greater the force produced. The total force obtained for a 7kHz frequency and 21kV

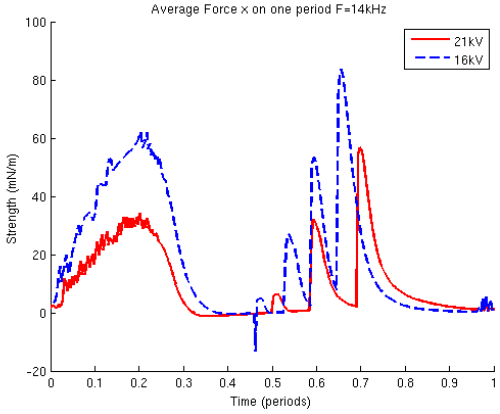

(a) 16kV and 21 kV

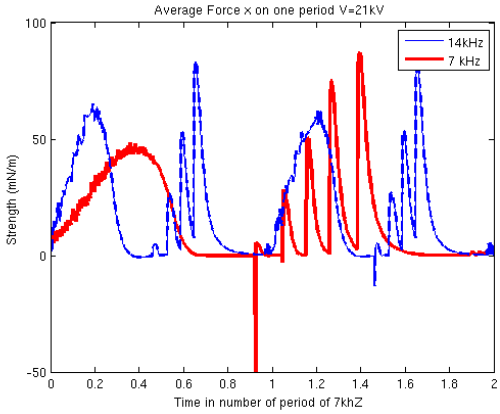

(b) 14kHz and 7 kHz

Figure 3.8: Total space averaged force

voltage is $14.3mN/m$ and the experimentally measured one is about $15mN/m$[17]. For $16kV$ and 14kHz the computed force is $10mN/m$ while it is measured $7mN/m$ in experiments. And for 7kHz the computed and measured forces are respectively $5.2mN$ and $3mN/m$. In conclusion, these computation results are consistent with the experimental results of Durscher and Roy but the discrepancy is larger at small operating voltages.

3.3.5 Flow computations

In this subsection, flow computations performed with the numerical body force provided by our numerical model are presented, corresponding to typical flat plate experimental cases. To that extent, the force computed by the plasma modeling is introduced as a source term in a CFD solver. The simulations have been performed with the in-house CFD code of ONERA, CEDRE.

The total force is averaged over one period and this mean value is constantly applied as a source term during the simulation. The convergence of the solution toward a steady state is reached after about 0.5s of

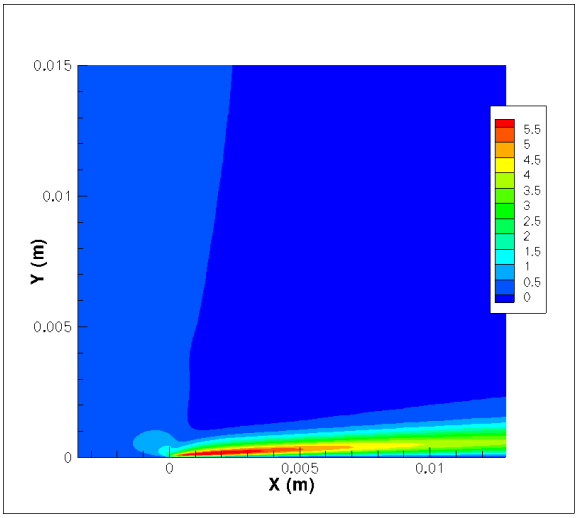

(a) contour of U_x

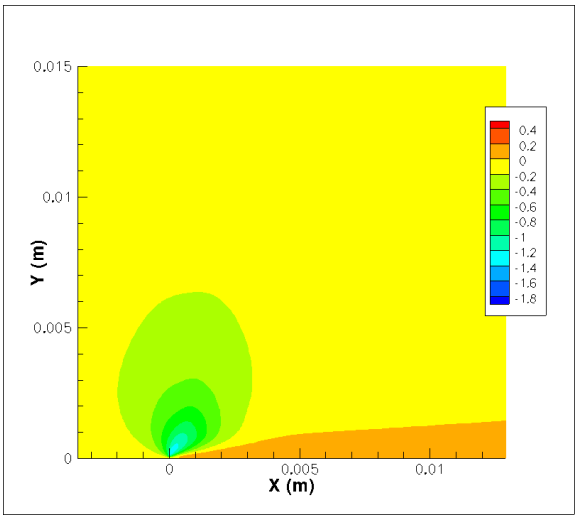

(b) contour of U_y

Figure 3.9: Velocity components

physical time. We have performed two computations, firstly assuming the flow as laminar and secondly using a turbulent $k-\omega$ model, which describes better the wall-jet nature of the flow, based on the numerical experiments of [16] (see also next section). We have observed here too, that the main effect of the turbulence is a change on the velocity profiles of the flow's boundary layer, especially downstream the actuator's position. The turbulent boundary layer is, as expected, thicker and corresponds better to experimental results while the maximum velocities tend to be slightly smaller. Near the actuator's anode, the turbulent effects are almost negligible, possibly due to the time scales concerning the evolution of the boundary layer and the wall jet formation itself. A more adapted turbulent model, i.e. a transitional one, as well as more refined in both time

and space simulations (towars maybe a LES simulation) could spread more light on these scales that are hard to be captured. We present the parallel, U_x, and perpendicular component, U_y, of the induced velocity on the figure 3.9. It can be observed that the maximum of the parallel velocity is very close to the anode which is located at $x = 5mm$ where the maximum value is more that $8m/s$. It corresponds to an acceleration of the flow due to the body force which is very large near the exposed electrode. The perpendicular velocity is negative and its maximum amplitude is $-1.8m/s$ which is reached a little over the exposed electrode. This corresponds to the region of suction.

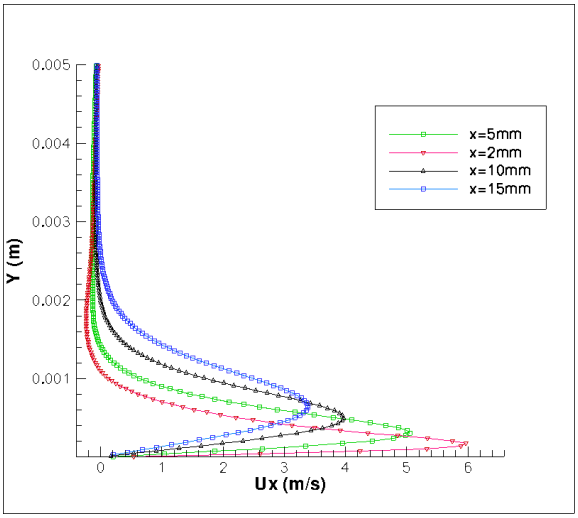

Figure 3.10: U_x at differents locations

Figure 3.10 shows the profile of the parallel velocity at different locations. These values of jet velocity are different from those measured by Roy and Durscher who showed that the maximum parallel velocity reached at $15mm$ from the anode tip, is approximately $5m/s$, which is larger than the computed one.

Effects of temporal discretization of the body force

In chapter 1, we have talked about the efforts made by the research community to accurate measure the body force produced by a SDBD actuator. Some authors support the idea of a PUSH-push mechanism due to different magnitude but always positive force during the positive and negative half-cycle of the AC operation [21], while others tend towards a push-pull mechanism as they have measured negative x-forces at the beginning of the positive half-cycle [22, 5]. In our simulations so far, the body force has been averages in a period. In order to study the effects of the temporal evolution of the body force on the induced flow, we have performed numerical simulations in FLUENT, using a discretized in time body force. We chose to divide the body force in four temporal steps and average the force in each of them. A compressible solver has been used, in unsteady mode with a time-step corresponding to the force's temporal discretization, $\Delta t = 1.78 \times 10^{-5}$ s. The $\kappa\omega$ SST turbulent model has been used and we have performed simulations for more than 30 periods. In figure 3.11, the maximum calculated x-velocity is plotted versus time. We note, that the maximum velocity presents an "oscillating" behaviour, denoting that the actuator works in a pseudo-pulsing regime with a frequency almost double the frequency of the AC circuit.

That means that the temporal evolution of the body force has an effect on the induced flow even though the force generated by the plasma itself rests always positive during the AC cycle (except an almost instantaneous

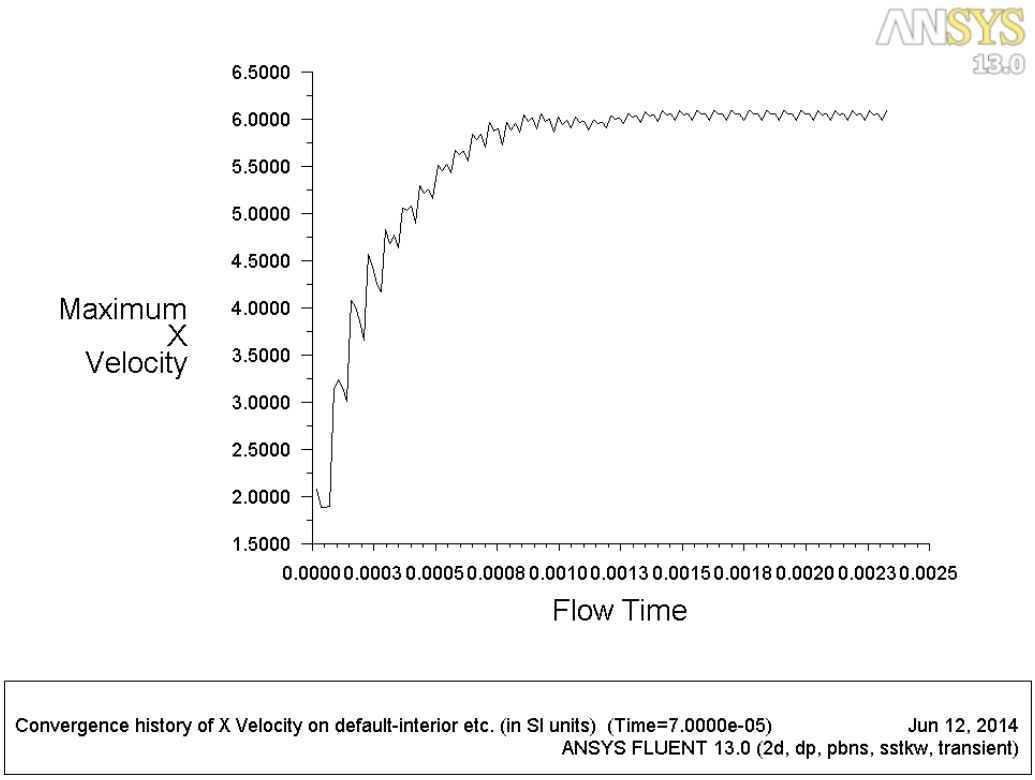

Figure 3.11: Maximum x-directed velocity versus time.

low negative force presented before the streamer regime). This phenomenon could have its roots on viscous effects and turbulent losses that could cause the deceleration of the flow as proposed by [6]. The vortical structure that is created by the induced flow in short distances from the electrodes can also be a reason for the deceleration, due to its spin and inertia. Therefore, our simulations tend to confirm a push-push mechanism rather than a push-pull one. Moreover the temporal discretization of the force seems to reinforce the velocity close to the electrodes when compared to the steady state solution (with an average body force in the AC period) as shown in figure 3.12. More precise calculations, with a LES model, should though be performed to confirm this claim. Furthermore, the influence of the temporal evolution of the body force in one AC cycle, at further distances has to be studied with longer simulations.

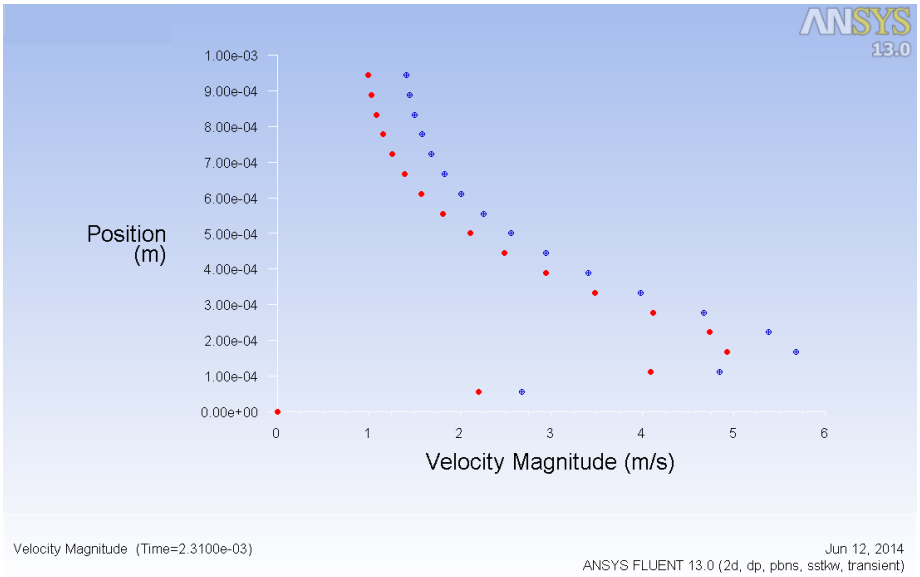

Figure 3.12: Velocity profiles at $x = 0.5$ mm from the anode. RED line : Averaged force/steady state. BLUE line : Unsteady force at $t = 2.31ms$

3.4 Numerical simulations and flow control applications with LAPLACE's DBD solver

In this section, we have used the numerical solver of the Dielectric Barrier Discharge created in LAPLACE, UPS, Toulouse [23]. The physical model is similar to the previous described one taking into account electrons, positive and negative ions [24]. The numerical procedure used is based on asynchronous time integration and an asynchronous adaptive mesh refinement technique [15, 25] to save substantial computation time thus making parametric study on the ElectroHydroDynamical (EHD) force feasible for Dielectric Barrier Discharges of realistic dimensions ie several centimeters. Generally in the modeling of gas discharges 2 main schemes are used. Fully explicit methods and semi explicit methods. In fully explicit schemes, the time step of the computation is limited by the CFL (Courant–Friedrichs–Lewy) condition so that all the information needed to form the correct solution can be accessed , and the dielectric relaxation time (the time scale associated with the coupling between the charged particle transport equations and Poisson equation). In semi explicit schemes, these problems are not presented but the schemes are quite diffusive and produce large errors.The technique that is proposed and used for the simulation of the plasma formation in [23] is an explicit time stepping locally adapted scheme in terms of the stability condition for each species. It is assumed that each flux or source term is updated independently according to a refresh time tag with respect to a global simulation clock. Thus, for the scheme to be stable each local time step is limited now by the local value of the CFL condition , that leads to reduced numerical diffusion but the local CFL time can be very different in different regions of the simulation domain. Transportiveness is guaranteed if no shock waves are present. This method, by performing time integration of the transport equations with different time steps at different locations of the grid, leads to a CPU time gain of about 10 times in comparison to previous used methods. The numerical scheme used for the integration of the charged particle transport equations is the MUSCL scheme which is based on a linear piecewise reconstruction of the interface states based on the cell-centered values

giving second order space accuracy. The multi-scale nature of the problem in space and the fact that only small regions need a very fine grid impose the use of an adaptive mesh refinement technique. This technique takes 2 criteria into account. First the pseudo-Debye length and secondly the velocity jumps for the N-S equations. If any component of the neutral gas velocity differs by more than 1 mm/s the cell is refined. A cell is merged if the velocity components differ less than 0.1 mms - 1. If any of the refinement criteria are met, the cell is refined and the cells are merged only when both fusion criteria are met. In order to keep the total cell number under control, different minimal cell size are used for each criterion. The combination of the asynchronous time integration and adaptive mesh refinement (AAMR) leads to much faster calculations (a factor of 100 or more) [25].

The computational domain is 3.2 x 1.6 cm including the dielectric layer with a relative permittivity of 5 (figure 3.13). The lower buried electrode is grounded and the high voltage is applied on the upper electrode. There is no horizontal gap between the electrodes, the initial mesh is concentrically refined around the upper electrode tip (figure 3.14).

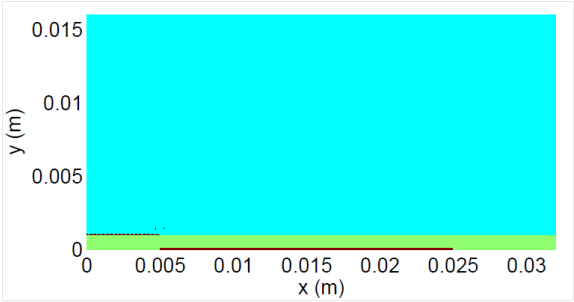

Figure 3.13: Computational Domain for the discharge

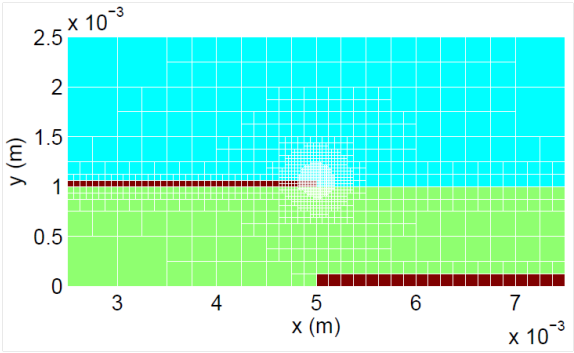

Figure 3.14: Mesh near the exposed electrode

3.4.1 Coupling with CFD solver

From the simulations with the numerical model described above, the space distributed plasma induced force as well as for the time-averaged force have been obtained. These data have values in N/m^3 . The problem that arises here was how could we import these data to FLUENT®(the well known commercial

CFD software) so that we can couple this force with the Navier-Stokes(N-S) solver. From a general point of view this seems easy. FLUENT® provides an option in which we can easily import a source term as momentum transfer and/or heat transfer to the N-S equations. This is quite easy if we suppose that we have a uniform distributed force so that we can just impose a constant force inside the plasma region. Here though we want to impose the spatial distributed force so that we can compare the assumption made by Mateo[26] and many other researchers for the constant force and also to understand further the exact contribution of the plasma induced force in the flow.

This had to be done using a User Defined Function in FLUENT®. A user-defined function, or UDF, is a function that can be dynamically loaded with the FLUENT® solver to enhance the standard features of the code. UDFs are written in the C programming language and they can be interpreted or compiled inside FLUENT® or by using an external compiler.

First the data from the plasma simulation have to be exported. In MATLAB®, the space distributed force and heat was re-meshed with a structured grid. This was essential so that an identical mesh could be created using GAMBIT (the commercial meshing tool used here) and the data of each cell could be copied and imported to the plasma zone in FLUENT® using a UDF. The x-oriented force as well as the y-oriented one were placed as inputs of momentum addition in each cell, using as said before a UDF. The same procedure has been used for the energy source addition in each cell of the plasma zone, though its effects were finally not considered in this study as they were negligible.

3.4.2 Meshing

The original plasma domain from the plasma-model simulations was reduced to a rectangle of dimensions 0.002x0.0008 m, were the plasma intensity and force is important. This was made to minimize the total number of cells of the full domain(which were linked to the plasma zone refined mesh) and consequently the CPU time of the simulation.

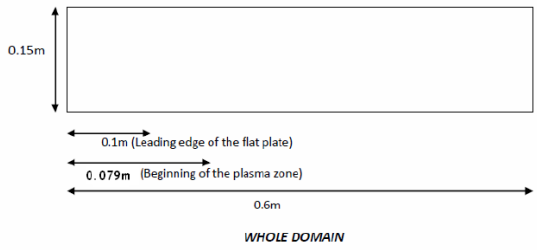

Figure 3.15: Simulation domain for the flat plate in FLUENT®.

The simulation domain was a flat plate with the plasma force was supposed to act 0.079 m after the leading edge of the plate as can be seen in figure 3.15. The whole domain was meshed with the GAMBIT® software.

In the plasma region (figure 3.16), a structured grid of 40x81 cells was used, so that the integrated force obtained by the simulations in FLUENT® would be an accurate represantation to its value from the plasma model simulation. This refinement has been selected through a mesh convergence study. Around the plasma zone 2 different zones were created. The first is a structured mesh zone, close to the flat plate, refined enough to capture the boundary layer effects as well as the plasma induced flow which acts really close to the flat plate. The rest of the domain was meshed with an unstructured grid to reduce the cells' numbers of the total mesh.

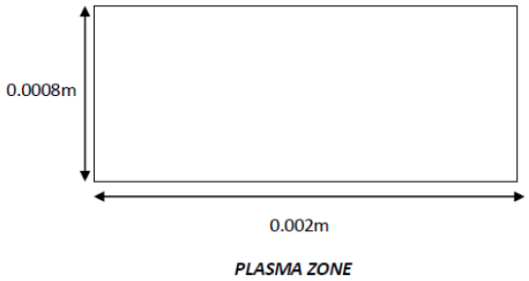

Figure 3.16: Plasma zone dimensions.

Eventually, the structured-unstructured mesh approach leads to converged simulations almost 10 times faster compared to a fully structured mesh.

3.4.3 Numerical aspects

The numerical approaches used in the simulations with FLUENT® can be summarized as follow:

— 2D-steady, double precision, coupled implicit solver.
— Symmetry Boundary condition.
— Second order discretization for all variables.
— Initialization with a value for the axial velocity of 1m/s and 0 for all the other variables in the whole domain.
— The heat addition due to plasma was neglected (except when mentioned) as simulations showed its small effect on the velocity profiles and magnitudes.

Turbulent models were used, expecting the flow to be partially or fully turbulent. For our cases especially when only the plasma induced flow is resolved we need to use a Low- Reynolds turbulent approach as well as a near wall model approach because the plasma flow occurs really close to the wall in a region where the viscous forces are dominant. To validate that the mesh was fine enough so that the near-wall approach could be valid, the y+ values were plotted along the flat plate and a maximum value of 2 was observed while for most of the cells the value is below 1. That agrees with the need of a turbulent model that is valid throughout the near wall region, as described above.

Two different models were chosen for this purpose. The $k\varepsilon$ realizable and the $k\omega$ SST model. The first is a 2-equation model that means, it includes two extra transport equations,turbulent kinetic energy and the turbulent dissipation , to represent the turbulent properties of the flow. This allows a two equation model to account for history effects like convection and diffusion of turbulent energy. For this study a new improved version of this model was used – the kε Realizable model. The $k\omega$ SST(Shear Stress Transport) model is a model that blends the $k\varepsilon$ and the $k\omega$ model in order to overcome the shortcomings of both. Moreover the SST version of this model accounts with problems in the prediction of pressure induced separation. A blending function that allows switching between the $k\omega$ model in the sub and log layer and the $k\varepsilon$ model in the outer region of the boundary layer and in free shear flows, provides superior overall performance.

3.4.4 Validation cases and general aspects

Various test cases were simulated with the method described above, to validate the coupled model and check the importance of some physical parameters of the flow. Firstly, a comparison with Jean-Charles Mateo-Velez work[26] who used the CEDRE® code -developed by ONERA- for a constant and uniform x-directed

force of 500 N/m^3 showed the ability of FLUENT® to model such kind of cases with its build-in momentum source term addition. A mesh convergence study has been also performed showing the importance of a well refined mesh to the accuracy of the results. Next, the plasma model data were imported in FLUENT® with the UDF function. The mesh described above and the solver's parameters have been compared with the Blasius solution for a flat plate without the plasma actuation in order to validate the numerical and mesh choices and showed excellent agreement. These test-cases simulations have been performed for a 2 kHz - 10 kV DBD actuator. The resulting time-averaged horizontal force as well as its space distribution is shown in figure 3.17.

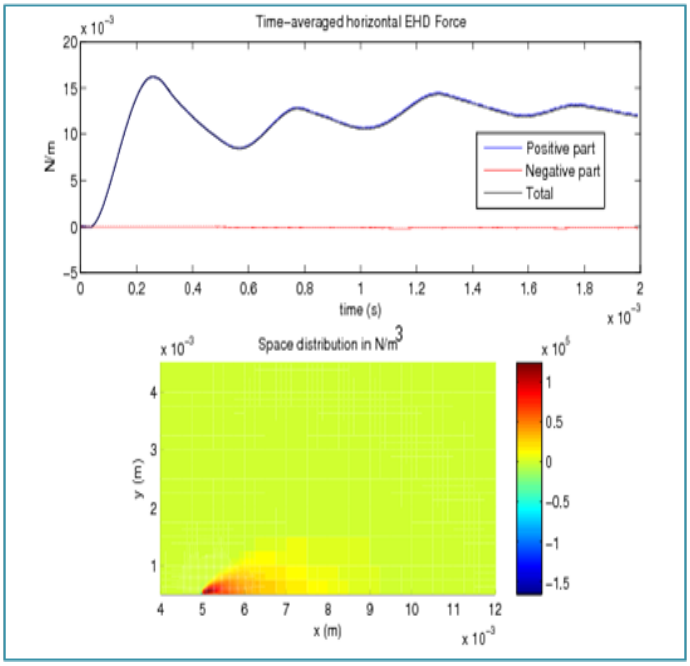

Figure 3.17: Time averaged (top) and space distributed (bottom) horizontal force for the V=10kV and f=2kHz DBD actuator.

We can summarize the most important results as follows:

— The mesh refinement is important when we want to model the real distributed force and can lead to errors of 8%. The CPU time needed for convergence was of about 1 day for this case.

— The Y force effect in the flow behavior is really small and it can probably be neglected.

— The boundary layer is significant modified by the plasma flow, being reduced all along the length of the plate, between 85% ,in the plasma actuator area, and 19% at 0.5 m after the leading edge of the flat plate. An also interesting results is that even before the actuator at a distance of 0.07 m , a 10% decrease of the B.L. thickness has been observed.

— The plasma force leads to an increase of the friction coefficient and also the total drag force on the plate. For the distributed force the increase in the drag force is almost 38% .

— The heat generated by the plasma does not have effects in steady calculations. A difference of 1% has been calculated in the maximum velocities obtained. Though unsteady cases with highly refined mesh and time steps that could represent its effects are necessary to check its real effects.

— The pulsation of the plasma force (as it is not constant over a period but it rather consists of two zones of high force corresponding to the positive and negative phase of the sinusoidal pulse) implies a compressibility effect in the evolution of its flow. Unsteady calculations using an unsteady force interpolated over a sinus signal, showed us that a phase shift exists between different distances from the plasma zone (see 3.18). Longer calculations should be made to justify this result.

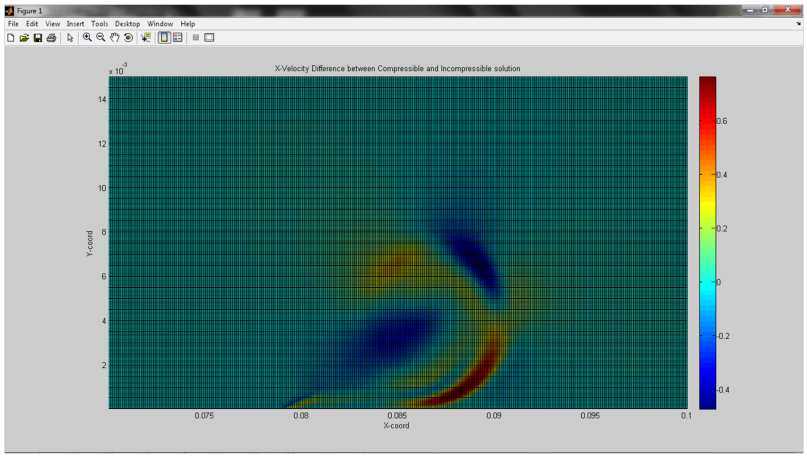

Figure 3.18: X-velocity difference between compressible and incompressible solution at $t = 10.875$ ms.

3.4.5 Study on turbulence

In the paper 'Electric wind produced by surface plasma actuators: a new dielectric barrier discharge based on a three-electrode geometry' of E.Moreau et al. [27] did experiments on a single DBD actuator on a flat plate, obtaining the velocity profiles for an input voltage V=11kV and a frequency f=11.7kHz.

As E.Moreau states "Concerning the DBD , the maximum velocity is reached at the plasma extension limit, i.e. x =10 mm, and is equal to about $4ms^{-1}$ at 0.5mm above the wall. When the value of x increases above this limit, the value of the maximum velocity decreases, and it is obtained further from the wall, because of the diffusion towards the ambient air." Based on these results that are presented in figure 3.19, studies on the 11 kHz-12kV DBD actuator were held focusing on the turbulent effects and models, with a dielectric thickness identical to the one studied in the mentioned paper and equal to 4mm.

The motivation for this study is the following : The plasma flow approaches the concept of a wall jet. In [28] , the authors investigated experimentally round impinging jets and calculated that the flow becomes fully developed at between 20 and 25 times the nozzle exit height. Thinking that the flow from the plasma could start as laminar and transit to turbulent especially consider the really small Reynolds number of the flow if we consider the plasma flow as a wall jet and taking into account the tiny height of this "wall jet" ($D = 0.0008m$) that corresponds to a $Re_D = 334$, a turbulent model could give us better results.

In figure 3.20 the velocity profiles for 4 different sections of the flat plate can be seen at 1, 2, 4.5 and 9 cms from the beginning of the plasma zone(end of the 1st electrode).No turbulent model was used for these cases supposing that the flow was laminar all over the domain. The solution differs from the experimental results . The laminar assumption of the flow seems to over-predict the maximum velocities and under-predict the diffusion of the flow, leading to a smaller boundary layer and consequently thinner wall jet that diffuses slower.

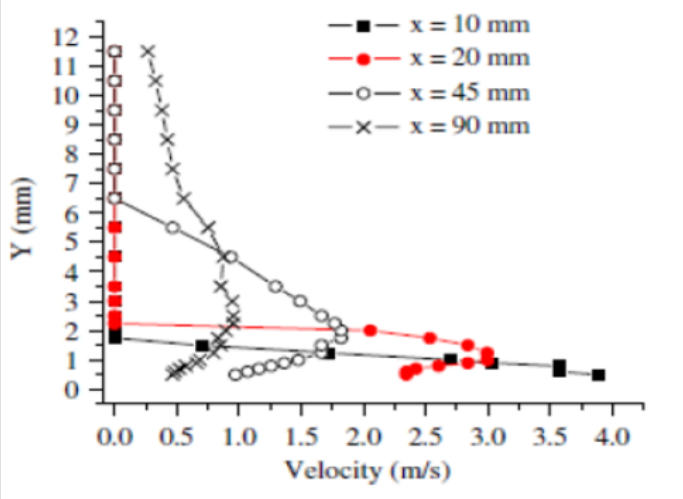

Figure 3.19: Velocity profiles for V=11kV and f=11.7kHz for different sections over a flat plate

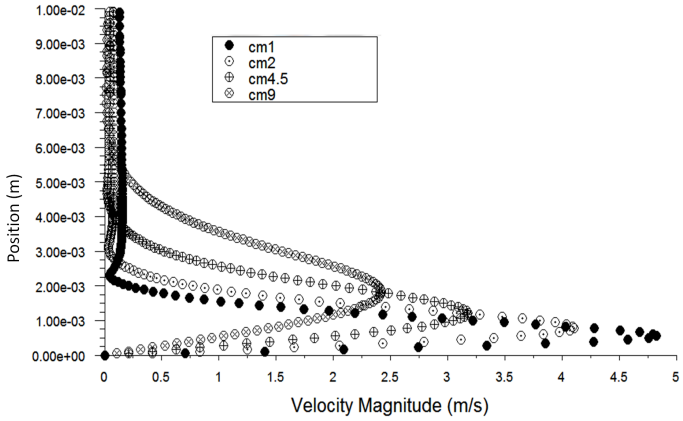

Figure 3.20: Velocity profiles at 1, 2, 4.5 and 9 cms from the plasma zone. Laminar assumption of the flow.

Using the two turbulent models that were mentioned in the previous subsections, we obtain results that approach the experimental data for the boundary layer thickness and the jet diffusion way better than the laminar case. With the $k\varepsilon$ realizable model the maximum velocity magnitude approach the ones measured in the experiment but the thickness of the layer that is formed is overestimated while with the $k\omega$ SST model, the results obtain seem to fit the experimental one a lot better. The velocity profiles obtained with both models are plotted in figures 3.21 and 3.22. Nevertheless, the pick velocity of the profiles with the $k\omega$ SST model reaches values almost $1ms^{-1}$ higher than the ones measured by Moreau. The author though, used a very thin pitot tube(close to 1mm of diameter) for the measurements. That means that really close to the flat plate and inside the height of the pitot tube diameter no actual values could be obtained but only a mean value. This fact, could be an explanation as in our simulation, the velocity is calculated at 25 points inside the first 1mm from the flat plate. The temporal evolution of the force could also have an effect that it is not taken into

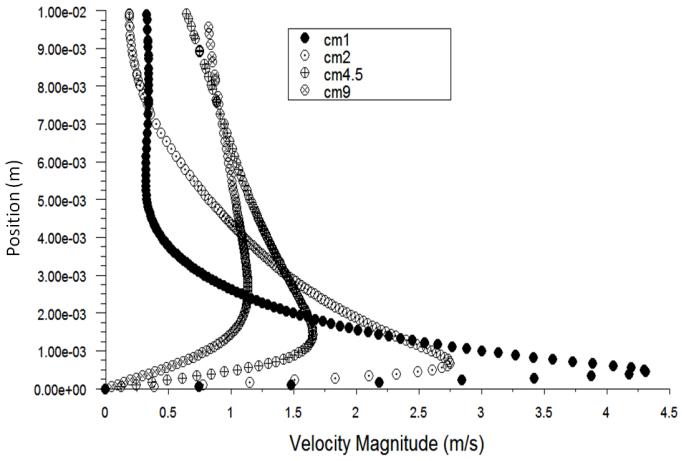

Figure 3.21: Turbulent $k\varepsilon$ realizable case - velocity profiles

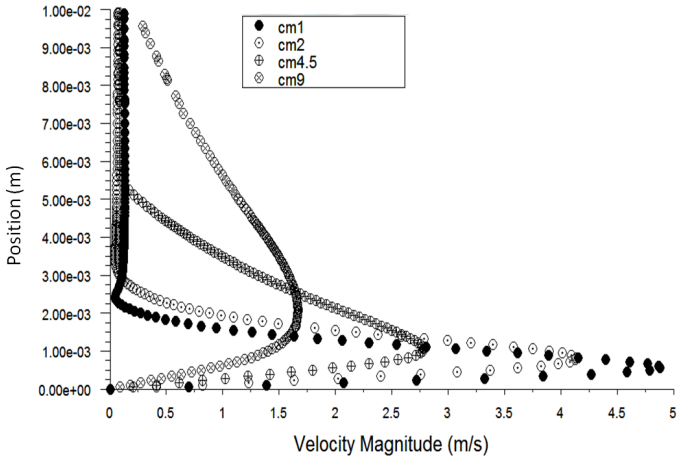

Figure 3.22: Turbulent $k\omega$ SST case - velocity profiles

account in this set of simulations. Nevertheless, our results demonstrate the importance of turbulence in order to capture accurately the flow characteristics of the induced wall jet.

3.4.6 Parametric study

As a continuation of the previous work, we present in this section a parametric study of a DBD actuator over a flat plate. The parameters for the simulations were identical were chosen as follows, based always on the turbulent studies:

— 2D-steady, double precision, incompressible, coupled implicit solver.
— Symmetric boundary condition.
— $k\omega$ SST turbulent model.
— Second order discretization for all variables.

The data for the plasma force were obtained for two different frequencies of 5 kHz and 10 kHz (the 2 kHz case is also plotted) of pulsation and for voltages between 4 to 30 kV for the 10 kHz DBD and between 8 and 30 kV for the 5kHz DBD. The dielectric thickness was chosen to match the experiments made by Roth et al in [29], i.e. 1mm.

The convergence of the mesh, were achieved with the same grid of 40x81 cells inside the plasma zone. In figures 3.23 and 3.24, the integrated axial force was calculated and compared with the data from the plasma simulation showing the well agreement of the two simulations.

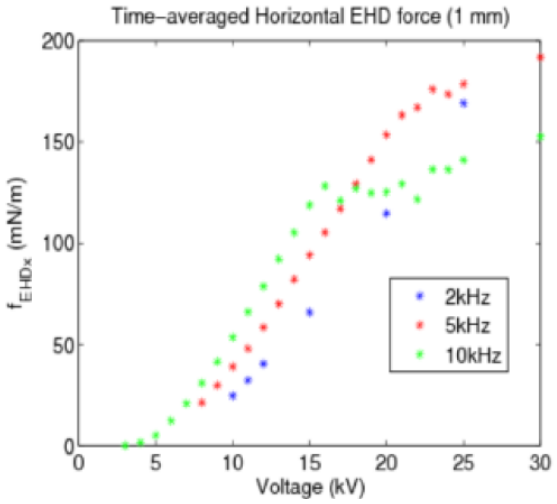

Figure 3.23: Integrated axial force - Plasma model

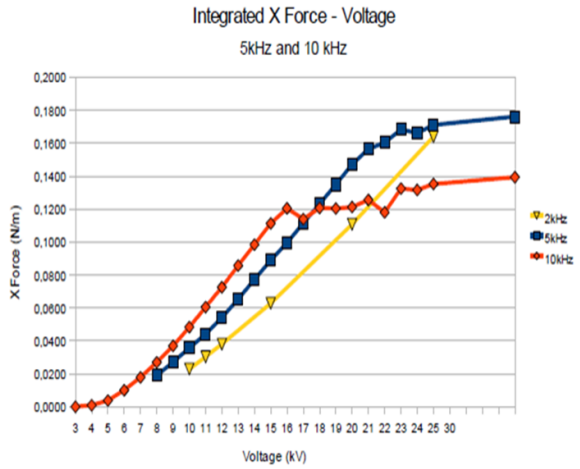

Figure 3.24: Integrated axial force - After interpolation in FLUENT

The maximum velocity obtained from the plasma actuation for each case are plotted in figure 3.25. Note that these velocities were calculated at a distance of 1cm from the start of the plasma zone. We observe the

good agreement of the results with the force evolution, while the magnitudes of the velocities seem to differ from the ones measured by Roth, which were lower than the simulated ones. We notice though, that for higher voltages Roth does not provide data as the dielectric layer can not support such values. As it has been observed in various experiments and cited in numerous publications, the DBD actuators face a limit on the maximum velocities and force that can produce. For the 5 kHz case this happens at a voltage of 23kV, when for the 10 kHz case at a voltage of approximately 16kV. The two curves cross each other, signifing that for higher voltages, lower frequencies produce higher forces and consequently higher velocities. The opposite occurs for low voltages.

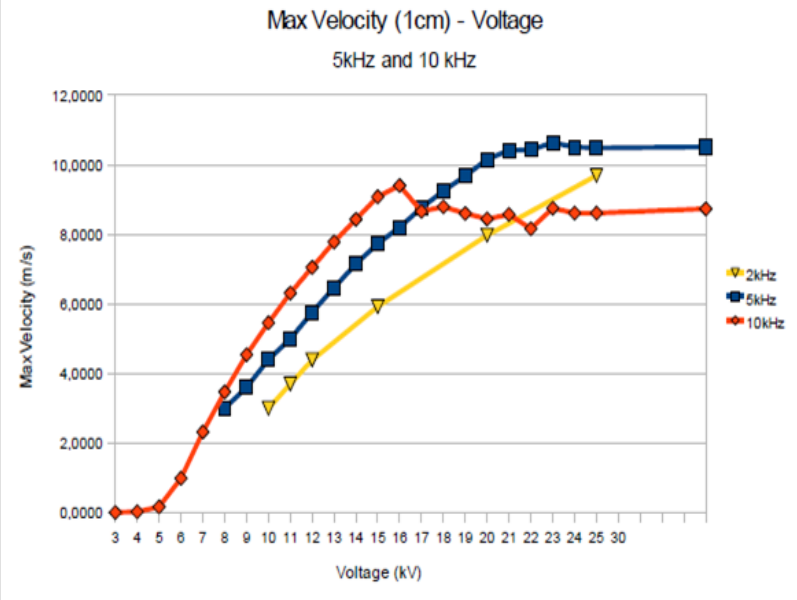

Figure 3.25: Maximum velocities 1cm from the plasma zone for different voltages - 5 and 10 kHz

3.4.7 Flow control applications

Laminar to turbulent transition modification

Turbulence, being extremely chaotic and unsteady, introduces drag in the form of viscous forces and friction that for aerospace applications is crucial. For many years, the instability of laminar boundary layer flows and the transition to turbulence have maintained a constant interest in fluid mechanics problems. This interest results from the fact that transition controls important aerodynamic quantities such as drag or heat transfer. Most of the efforts nowadays is to reduce the drag coefficient of an airfoil and so of a wing and an airplane even for 0.5% - that leads to a huge economic benefit for each flight. So in this point of view a delay of the transition point on an airfoil would reduce the total drag coefficient. They showed that the form of the velocity profile is crucial to maintain the laminar boundary layer. DBD plasma actuators are able to change the boundary layer characteristics and hence to exert an effect on the skin friction. Drag on flat plate is mostly due to friction created by laminar, transitional, and turbulent boundary layers. Skin friction arises from the friction of the fluid against the "skin" of the object that is moving through it. The skin friction coefficient, Cf,

is defined as:

$$C_f = \frac{1}{2}\tau_w U_o \rho \tag{3.11}$$

Skin friction is caused by viscous drag in the boundary layer around the object. The boundary layer at the front of the object is usually laminar and relatively thin, but becomes turbulent and thicker towards the rear. The position of the transition point depends on the shape of the object. In laminar boundary layer a lower skin friction is observed due to the characteristic velocity profile of laminar flow. However, the boundary layer inevitably thickens and becomes less stable as the flow develops along the body, and eventually becomes turbulent, the process known as we saw as boundary layer transition.

The transition leads to an increase of the local wall shear stress and of the skin friction coefficient. A schematic represantation of this effect is shown in figure 3.26 To study the effect of the plasma actuator on the transition point, a validation of the CFD solver for a case without actuation has been performed and the transition point found by the jump to the skin friction coefficient has been compared to the classical empirical equations that give the exact point on a flat plate where the transition occurs. Using the SST-transition turbulent model that fluent provides, and an external flow of 17.2 m/s, the simulation showed that transition would occur at x=0.28m from the leading edge, when the theory gives a value of 0.29m. Based on that results, the same calculation was performed with the plasma actuator of 11kHz and 12 kV(same geometry as previous).

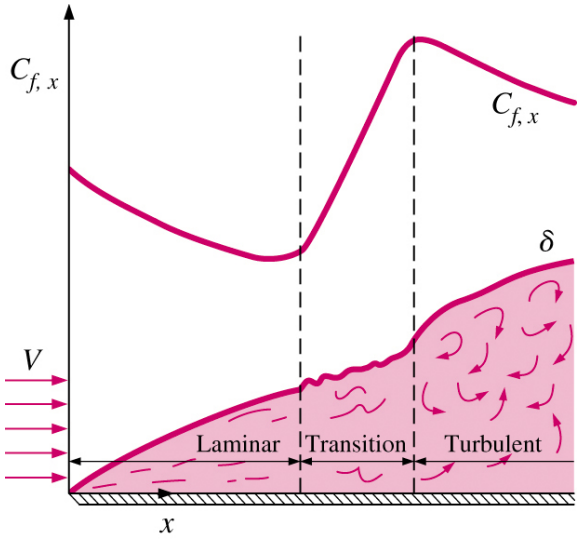

Figure 3.26: Skin friction coefficient during laminar to turbulent transition

The comparison graph of the skin friction coefficient is plotted in figure 3.27. The green line corresponds to the case without actuation and the yellow line to the case with actuation. It can be seen that the actuation of the DBD delays the transition for approximately 0,05 meters. The addition of momentum inside the boundary layer re-energizes the last,decreasing the momentum thickness of the boundary layer and not letting the viscous forces to become dominant and produce turbulence. The increased velocities near the plasma zone diffuse fast inside the main flow and so the flow inevitably transits to turbulent but delayed. This leads to a slightly decrease of the skin friction coefficient to 0.0036, a change of 3%, which though could be crucial for an aerospace application. Higher inlet velocities tend to decrease the plasma effect on the transition point.

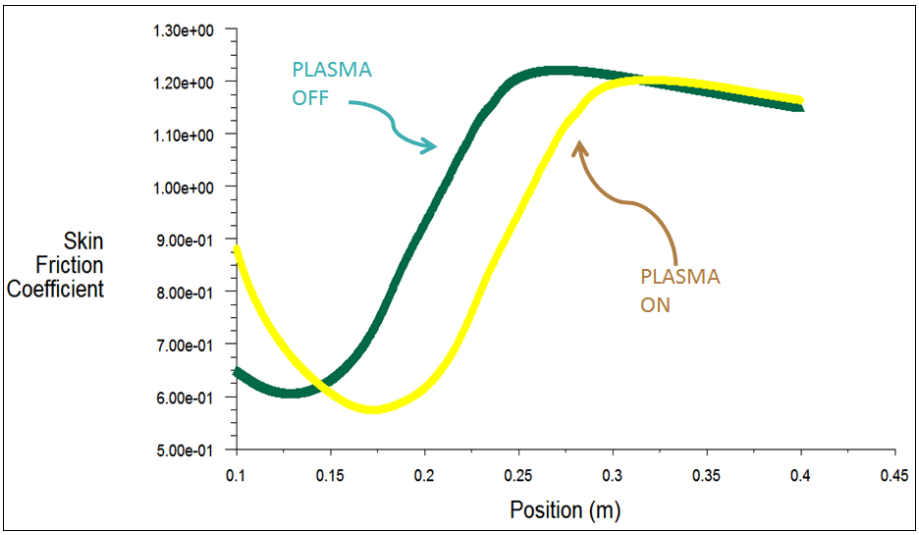

Figure 3.27: Laminar to turbulent transition modification due to plasma actuation

Plasma Flow Control on an Airfoil

The following study has performed on the NACA 0021, a symmetric airfoil with a cord of 1 meter. The GAMBIT® software was used again for the meshing of the domain around the airfoil. The plasma zone was put on the leading edge matching the experiments and the simulation made by Orlov et al [30, 31].

The plasma zone was modeled with 21x40 cells for time saving reasons(for the 11kHz and 12 kV actuator this refinement gives quite accurate results for the distributed force) while around and close to the airfoil a structured grid was created to model properly the turbulent effects that we are searching for as well as the behavior of the flow with the actuator on. The domain for the structured grid was separated into 9 subdomains to control the skewness of the cells and the quality of the mesh (figure 3.28). After that structured zone, an unstructured one was created for saving CPU time and 13 new sub domains were created for the same reasons as mentioned above and also to produce a fine structured mesh on the trailing edge zone, where the wake will occur and the unsteady effects imply a fine grid.

For the unstructured mesh a pave scheme with triangular elements were used. The structured grid was created using a map scheme with quadratic elements . The mesh was refined near the airfoil and coarsened away from it.

The total mesh size was 1.197.148 cells. Attention has to be paied when the plasma force is imported in FLUENT®. The x and y force that were imported with the UDF were acting along the x and y axis that unfortunately is standard and prescribed by GAMBIT®.This is the global coordinate system that is hooked on the leading edge of the airfoil. The system can be changed though the udf reads and implies the force on the global system and so it had to be modified so that the two forces acting on each cell would act on a coordinate system that eventually will give us the momentum with a direction that follows the suction side of the airfoil. The boundary conditions used were velocity inlets for the left, upper and lower surface and pressure outlet for the right surface. The simulations were made using the incompressible, pressured based, coupled solver due to problems in convergence and unphysical results obtained with the segregated one. Second order discretization was used for all the variables and the SST transition model to catch the turbulence in the flow as well as the transition and separation point. The steady problem was considered due

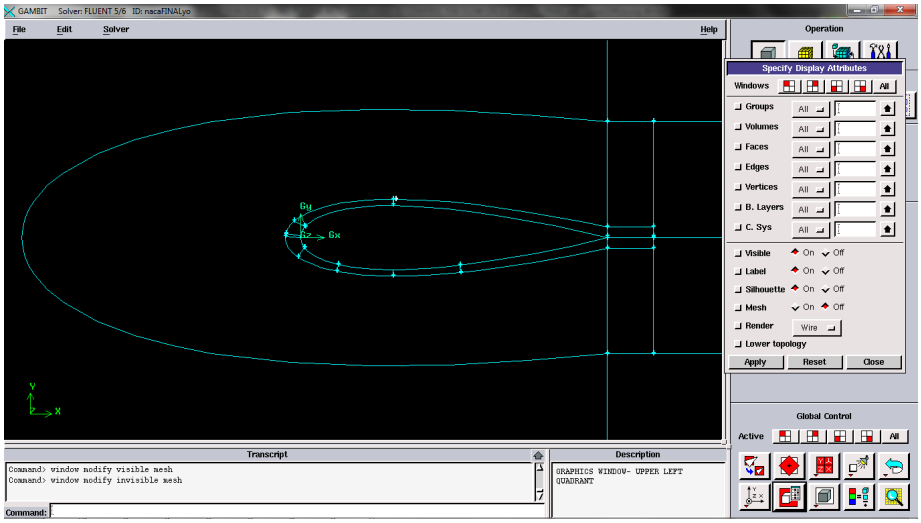

(a) Domain repartition

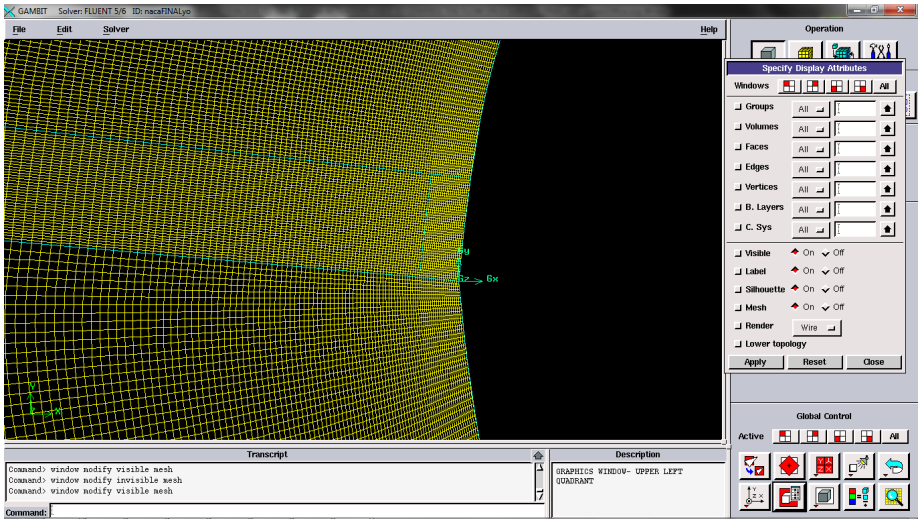

(b) The mesh around the plasma zone

Figure 3.28: Mesh around the airfoil

to time limitations. Validation of the good convergence and reliability of the results obtained without the plasma actuation was performed by comparing the lift and drag coefficient for different angles of attack to the results obtained by the XFOIL® software for a Re=710233 ($U_o 10.66 m/s$), where

$$Re = \frac{\rho U_o L}{\mu} \tag{3.12}$$

is the Reynolds number. The results deviate from the ones XFOIL® predicts only near the critical angle

of attack where unsteadiness plays a crucial role. The same simulations were performed with the plasma actuator on, but its influence on the airfoil's coefficients was almost negligible as plotted in 3.29.

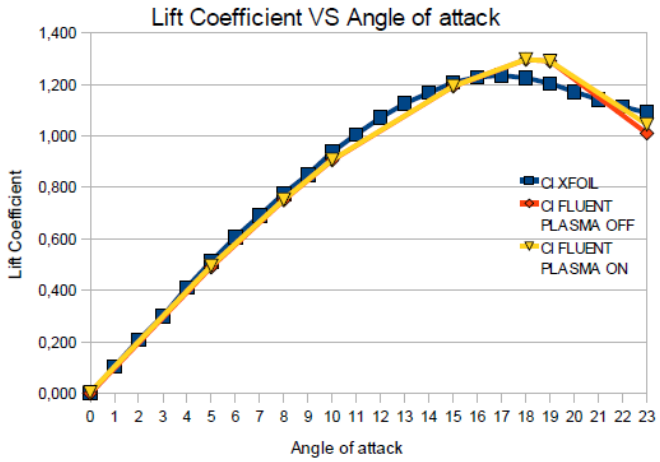

Figure 3.29: Lift coefficient vs angle of attack predicted by XFOIL and simulated with plasma actuation on and off

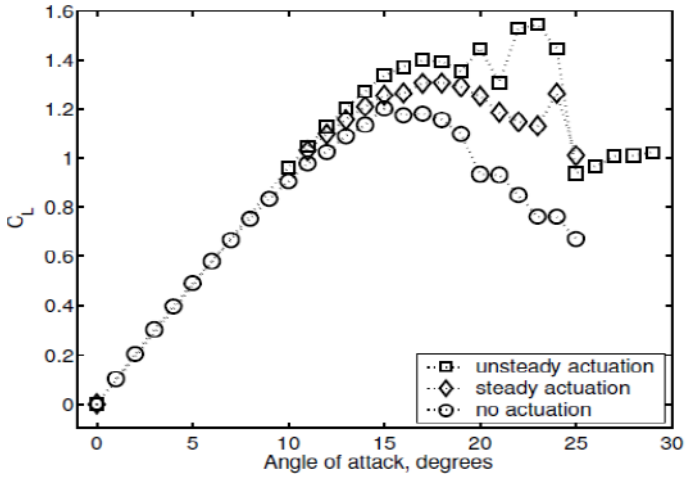

Figure 3.30: Lift coefficient vs angle of attack - Orlov's results

Though as Orlov concludes, near the critical angle of attack the plasma effects can modify the flow positively (see figure 3.30, increasing the lift coefficient and thus delaying the stall of the airfoil but as mentioned above it is not easy to capture these effects near this zone with a steady RANS solver. This inconvenience though motivated us to study the influence of the actuator on the transition point of the airfoil, connecting this work with the previous section. XFOIL® gives also a prediction of the point where the flow will transit from laminar to turbulent. For 0 degrees angle of attack it predicts that this will happen

at a distance x/c = 0,232 . That means that on both sides of the airfoil our simulation should show that at 0,232 meters from the leading edge the skin friction coefficient 'jumps' due to the turbulent flow that occurs there. Below we can see that indeed FLUENT® and the SST transitional model gives us values close to the expected ones, and validates our simulation. For the same case the plot with the plasma actuation off and on

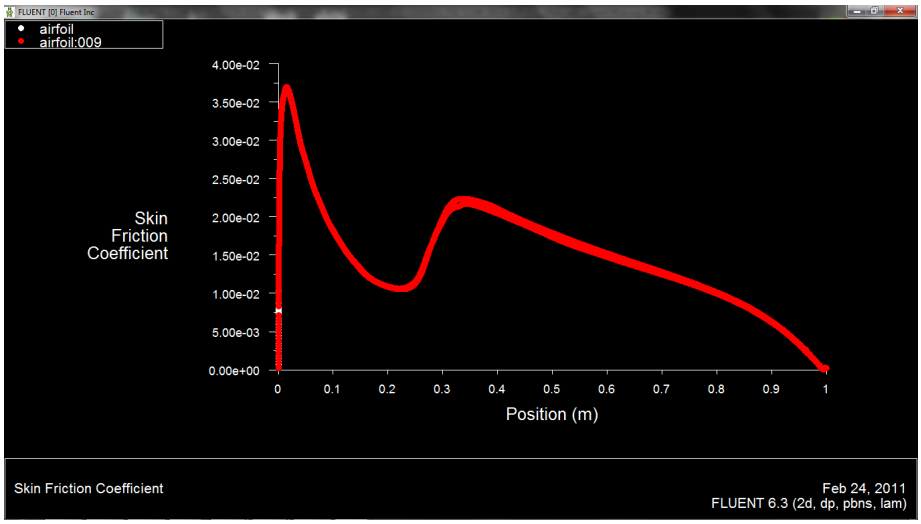

(a) plasma actuation OFF

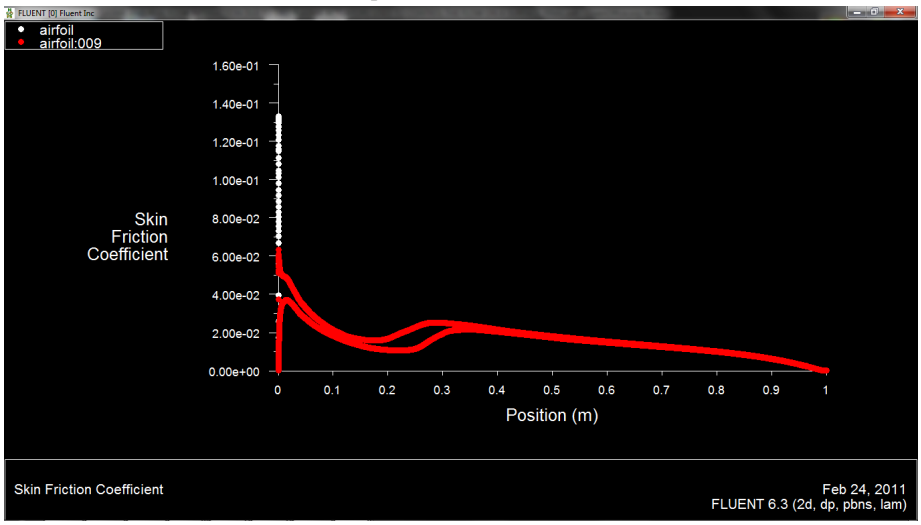

(b) plasma actuation ON

Figure 3.31: Skin friction on the airfoil

is presented side-by-side in figure 3.31. We can notice that when the actuation is on, the transition on the upper side of the airfoil is faster and the transition point goes back for a distance of almost 4cm. This result contradict with the flat plate results that we had where the transition was delayed by the act of the plasma

force. This effect can be explained if we think that the plasma force acts on the leading edge. At this point without the actuation the free flow is stagnated and the flow follows the airfoil curve accelerating on both sides until the maximum camber of the airfoil. After this point the flow starts to slow down and an adverse pressure gradient appears. This is the most common reason for transition over an airfoil. It is known that boundary layers at high Reynolds numbers can withstand very little adverse gradient and one may assume that once the gradient is adverse transition will occur.

When the actuation is on, the flow is accelerated much more as we saw before. This leads to an increase velocity and so the boundary layer is more sensible to increasing pressures that appear after the max camber point (at 0.21 meters). This is the reason why transition occurs faster on the suction side of the airfoil, where the plasma force is directed.

The lower side of the airfoil remains unaffected and the transition point remains the same as the non actuated case. Finally for visualization purposes, the action of the plasma force on the leading edge is presented in figure 3.32. The plasma flow is directed to the upper part of the airfoil producing an accelerating zone due to the camber of the airfoil. The stagnation area remains the same though the zero velocities that appear there, makes the plasma flow to have a significant velocity in the flow that modifies the boundary layer.

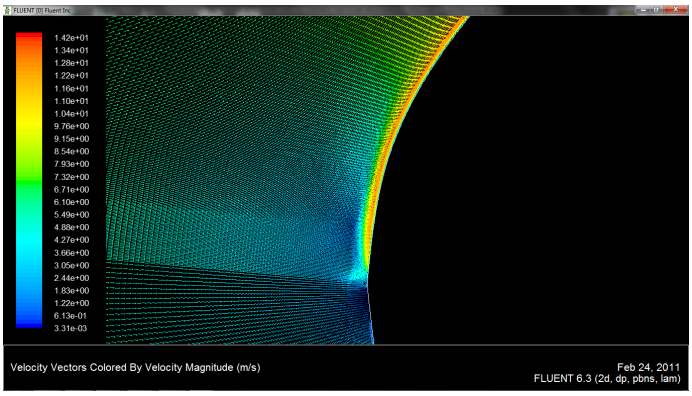

Figure 3.32: Velocity magnitude vectors near the plasma zone for $U_o = 10.66 m/s$

3.5 Conclusion - Perspectives

The DBD actuator has been modeled using two different solvers based on similar physical models - one developed at ONERA and one at LAPLACE. We have performed various studies under different operational regimes, demonstrating the ability of the used models to reproduce the ionic wind effect of such actuators. Parametric studies showed that the models give an quite accurate estimation of the force produced by the DBD's as compared to experimental measurements.

Concerning ONERA's solver, the numerical results have shown a good estimation of the total body force compared with measurements for a large range of operating voltages and for some values of the working frequency. The description of the body force variations in time and in space by numerical simulation show a good correlation with the observations noticed in many experimental works. Nevertheless, some differences such as the presence of a negative force for a 14kHz SDBD actuator, have been noted that lead to some discrepancy on the induced velocity results. Unsteady calculations taking into account the temporal evolution of the body force inside a period of actuation can reveal more information about its

effect on the induced flow. Our simulations demonstrated that the flow is being accelerated and decelerated at each period due to the unsteady force, results that tend to agree more with a push-push action of the actuator.

Concerning LAPLACE's solver, the calculated force has been introduced in a commercial CFD solver (FLUENT®) to investigate some of the induced flow characteristics. The plasma induced flow acts like a wall jet, modifying the boundary layer in a flow over a surface and reducing its thickness. Turbulence is a major factor of the plasma induced flow. The k- ω SST turbulent model led to results closer to experimental ones. The laminar to turbulent transition over a flat plate can be delayed with the plasma actuator. A leading-edge DBD plasma actuator of a 11 kHz frequency and 12 kV voltage does not seem to have a big influence on the stall of a symmetric airfoil. The lift coefficient does not depend on the actuator for angles of attack lower or close to the stall one although it modifies the transition point considerably, but for a completely stalled airfoil it increases the lift coefficient possible due to the earlier transition to turbulence. Thus the position of the plasma actuator is essential for the positive effects on the lift.

The plasma model used in this chapter, has been proved quite accurate in calculating the force produced by a DBD actuator as well as the evolution of the plasma. The model even though capable of capturing the ionic cloud formation and development poses questions on the phase of streamer development and propagation, where many physical phenomenas can be involved. A study on the reasons for electron concentration - responsible for the streamer's propagation - at the head of the streamer in a more theoretical-mathematical point of view could shed some light on this problem. Concerning, the ionic wind behavior simulations with an unsteady solver and a pulsed regime (with a possible parametric study on the duty cycle influence), as well as more refined (possible LES) calculations, can provide more accurate results on important aspects of flow control theory such as turbulence modification and vortex shedding. More generally, experimental and modeling studies have to be continued to sharpen the accuracy of the results and measurements so that the relevance of the numerical simulation as a prediction tool can be validated. As DBD actuators have been extensively researched in the last decade, their use and applicability seems to be constrained by their limited to some m/s induced flow and thus different applications should be considered. UAV's or even wind turbines work under flow conditions (low speeds) that can be effectively modified by the plasma induced flow from a DBD actuators. Thus, in parallel with the continuation of the models' validation procedure, future work can include numerical simulations of flow control applications under such flow regimes.

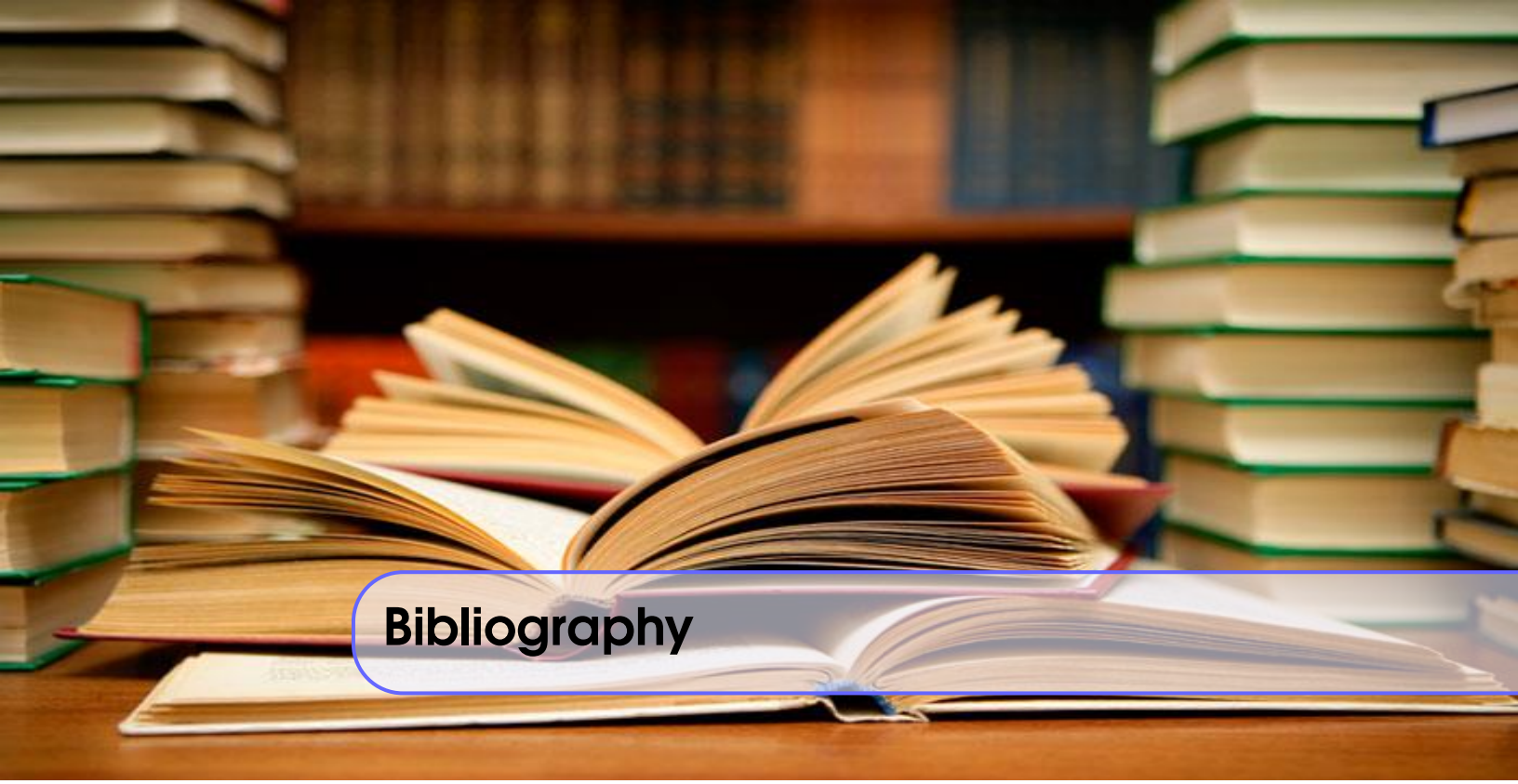

Bibliography

[1] Thomas C Corke, Martiqua L Post, and Dmitriy M Orlov. "Single dielectric barrier discharge plasma enhanced aerodynamics: physics, modeling and applications". In: *Experiments in Fluids* 46.1 (2009), pages 1–26.

[2] YB Suzen et al. "Numerical simulations of plasma based flow control applications". In: *AIAA paper* 4633 (2005), page 2005.

[3] Thomas Albrecht et al. "A method to estimate the planar, instantaneous body force distribution from velocity field measurements". In: *Physics of Fluids (1994-present)* 23.2 (2011), page 021702.

[4] M Kotsonis and S Ghaemi. "Performance improvement of plasma actuators using asymmetric high voltage waveforms". In: *Journal of Physics D: Applied Physics* 45.4 (2012), page 045204. URL: `http://stacks.iop.org/0022-3727/45/i=4/a=045204`.

[5] Mathias Neumann et al. "Determination of the phase-resolved body force produced by a dielectric barrier discharge plasma actuator". In: *Journal of Physics D: Applied Physics* 46.4 (2013), page 042001.

[6] N Benard, A Debien, and E Moreau. "Time-dependent volume force produced by a non-thermal plasma actuator from experimental velocity field". In: *Journal of Physics D: Applied Physics* 46.24 (2013), page 245201.

[7] AV Likhanskii et al. "Modeling of interaction between weakly ionized near-surface plasmas and gas flow". In: *AIAA Paper* 1204 (2006), page 2006.

[8] JP Boeuf and LC Pitchford. "Electrohydrodynamic force and aerodynamic flow acceleration in surface dielectric barrier discharge". In: *Journal of Applied Physics* 97.10 (2005), page 103307.

[9] JP Boeuf, Y Lagmich, and LC Pitchford. "Contribution of positive and negative ions to the electrohydrodynamic force in a dielectric barrier discharge plasma actuator operating in air". In: *Journal of Applied Physics* 106.2 (2009), page 023115.

[10] T Unfer and JP Boeuf. "Modelling of a nanosecond surface discharge actuator". In: *Journal of physics D: applied physics* 42.19 (2009), page 194017.

[11] Alexandre V Likhanskii et al. "Modeling of dielectric barrier discharge plasma actuators driven by repetitive nanosecond pulses". In: *Physics of Plasmas (1994-present)* 14.7 (2007), page 073501.

[12] Takashi Abe et al. "Experimental study for momentum transfer in a dielectric barrier discharge plasma actuator". In: *AIAA journal* 46.9 (2008), pages 2248–2256.

[13] Hiroyuki Nishida, Taku Nonomura, and Takashi Abe. "Three-dimensional simulations of discharge plasma evolution on a dielectric barrier discharge plasma actuator". In: *Journal of Applied Physics* 115.13 (2014), page 133301.

[14] Y Lagmich et al. "Model description of surface dielectric barrier discharges for flow control". In: *Journal of Physics D: Applied Physics* 41.9 (2008), page 095205. URL: `http://stacks.iop.org/0022-3727/41/i=9/a=095205`.

[15] Thomas Unfer et al. "An asynchronous scheme with local time stepping for multi-scale transport problems: Application to gas discharges". In: *Journal of Computational Physics* 227.2 (2007), pages 898–918.

[16] Konstantinos Kourtzanidis. "Numerical Simulation of Plasma Actuators for Flow Control". In: *51ST AIAA AEROSPACE SCIENCES MEETING, Texas, USA 2013-0134* (2013).

[17] Ryan Durscher and Subrata Roy. "Evaluation of thrust measurement techniques for dielectric barrier discharge actuators". In: *Experiments in fluids* 53.4 (2012), pages 1165–1176.

[18] A A Matveyev I A Kossyi A Yu Kostinsky, T V P SilakovUnfer, and JP Boeuf. "Kinetic scheme of the non-equilibrium discharge in nitrogen-oxygen mixtures". In: *Plasma Sources Science and Technology* 1.207 (1992), pages 207–220.

[19] J Kriegseis et al. "Velocity-information-based force-term estimation of dielectric-barrier discharge plasma actuators". In: *Journal of Physics D: Applied Physics* 46.5 (2013), page 055202.

[20] Maxime Forte et al. "Optimization of a dielectric barrier discharge actuator by stationary and non-stationary measurements of the induced flow velocity: application to airflow control". In: *Experiments in Fluids* 43.6 (2007), pages 917–928.

[21] CL Enloe et al. "Plasma-induced force and self-induced drag in the dielectric barrier discharge aerodynamic plasma actuator". In: *AIAA Paper* 1622 (2009), page 2009.

[22] A Debien et al. "Unsteady aspect of the electrohydrodynamic force produced by surface dielectric barrier discharge actuators". In: *Applied Physics Letters* 100.1 (2012), page 013901.

[23] JP Boeuf et al. "Electrohydrodynamic force in dielectric barrier discharge plasma actuators". In: *Journal of Physics D: Applied Physics* 40 (2007), page 652.

[24] JP Boeuf et al. "Electrohydrodynamic force in dielectric barrier discharge plasma actuators". In: *Journal of Physics D: Applied Physics* 40.3 (2007), page 652.

[25] Thomas Unfer et al. "Multi-scale gas discharge simulations using asynchronous adaptive mesh refinement". In: *Computer Physics Communications* 181.2 (2010), pages 247–258.

[26] Jean-Charles Mateo-Velez. "Modélisation et simulation numérique de la génération de plasma dans les décharges couronnes et de son interaction avec l'aérodynamique". PhD thesis. Thèse de l'Ecole Nationale Supérieure de l'Aéronautique et de l'Espace, 2006.

[27] E. Moreau, R. Sosa, and G. Artana. “Electric wind produced by surface plasma actuators: a new dielectric barrier discharge based on a three-electrode geometry”. In: *Journal of Physics D: Applied Physics* 41 (2008), page 115204.

[28] JW Hall and D Ewing. “On the dynamics of the large-scale structures in round impinging jets”. In: *Journal of Fluid Mechanics* 555 (2006), pages 439–458.

[29] J.R. Roth and X. Dai. “Optimization of the aerodynamic plasma actuator as an electrohydrodynamic (EHD) electrical device”. In: *AIAA paper* 1203 (2006).

[30] Dmitriy M. Orlov. “Modelling and simulation of single dielectric barrier discharge plasma actuators”. PhD thesis. University of Notre Dame, PhD thesis, 2006.

[31] D.M. Orlov et al. “Modeling and experiment of leading edge separation control using SDBD plasma actuators”. In: *AIAA paper* 877 (2007), page 2007.

Simulations numériques de l'actionneurJSP

Présentation

Dans ce chapitre, nous nous concentrons sur un nouveau concept qui a été récemment proposé par John Hopkins Applied Physics Lab ([1], [2]) et amélioré par d'autres groupes ([3], [4]): la sparkjet ou jet synthétique plasma (JSP ou sparkjet à partir de maintenant). En raison de ses dimensions minuscules (moins de 1 cm dans toutes les directions) noir, la synthèse d'actionnement du JSP peut être utilisé tres efficace pour les applications de contrôle d'écoulement. Les caractéristiques importantes de l'actionneur telles que la distribution de sa température interne ou la masse éjectée par impulsion sont expérimentalement difficile à mesurer. Récemment, un modèle complet de l'actionneur de JSP a été proposé par le groupe de l'ONERA cite 7. Il contient un aperçu plus physique que les modèles précédents.

L'objectif de ce chapitre, est d'introduire certains aspects physiques dans le modèle numérique de [5], et de réaliser des études sur le fonctionnement du JSP sous différentes conditions opérationnelles et géométriques, pour son optimisation. Le travail dans ce chapitre, a été entrepris au cours des 5 dernières années par de divers chercheurs et doctorants. Les premiers développements ont été faites par G. Quint, F. Rogier et G. Dufour de DTIM, ONERA. Suivi, la plupart des études paramétriques ont été menées par G. Sary, stagiaire au DTIM, ONERA au cours de son stage en ISAE, sous la direction de F. Rogier. Au cours de son stage, la collaboration à l'ONERA, a conduit à des résultats qui seront présentés ici, le couplage avec le code CFD CEDRE de l'ONERA, et a servi comme la base pour les simulations plus complexes réalisées et toujours etudiées à la DMAE, ONERA. La recherche a bénéficié d'un financement de la Communauté européenne dans le cadre du programme FP7 / 2007-2013 au titre de l'accord no.234201 et le projet PLASMAERO.

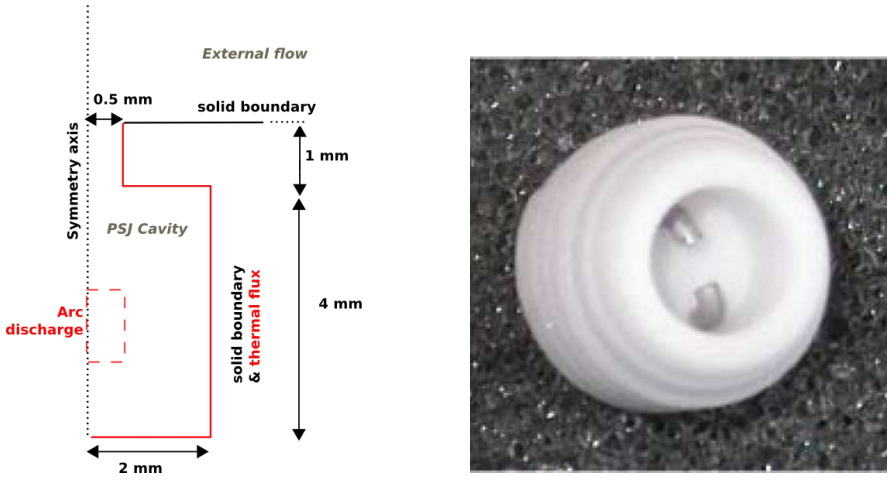

Figure C.1: Schéma d'une cavité JSP simple et réalisation expérimentale

Modèles physiques et numériques

L'actionneur jet synthétique plasma (JSP) est une cavité avec une géométrie à peu près cylindrique (4 mm de largeur sur 4 mm de hauteur) contenant une paire d'électrodes (voir figure C.1). L'énergie électrique est fournie aux électrodes de façon à créer un arc à l'intérieur de la cavité et un jet de grande vitesse. Par conséquence, une phase d'aspiration suit, qui remplisse la cavité avec de l'air ambiant et la préparer pour les impulsions suivantes. Cette configuration a déjà été décrite de manière approfondie et analysé dans [5] et donc nous nous appuierons ici sur le même modélisation 2D-axisymétrique.

Le modèle a été divisé en deux sous-modèles couplés (voir figure C.2). La première concerne le dépôt d'énergie à travers un arc électrique au voisinage des électrodes, en l'absence de la cavité. Il décrit la formation de plasma entre deux électrodes dans une configuration axisymétrique. Ce modèle est couplé à un circuit RLC décrivant l'alimentation électrique par un générateur externe. Le deuxième sous-modèle, concerne le chauffage de l'air dans la cavité et le fonctionnement réel de l'actionneur. Il utilise la distribution de l'énergie calculée par le premier sous-modèle en tant que terme source et calcule les effets sur l'actionneur qui en résulte. Il fournit le taux de débit massique, la quantité de mouvement et l'énergie à l'échappement du JSP en fonction du temps.

Principales hypothèses des modèles

1. Le plasma est supposé être à l'équilibre thermodynamique local.
2. Les effets de viscosité sont négligés.
3. Le dépôt d'énergie est axisymmetrique. L'évolution de l'écoulement est régi par les équations d'Euler en 2D axisymétrique:

$$\frac{\partial}{\partial t}(r\mathbf{U}) + \frac{\partial}{\partial r}[r\mathbf{F}(\mathbf{U})] + \frac{\partial}{\partial z}[r\mathbf{G}(\mathbf{U})] \quad = \quad \mathbf{S},$$

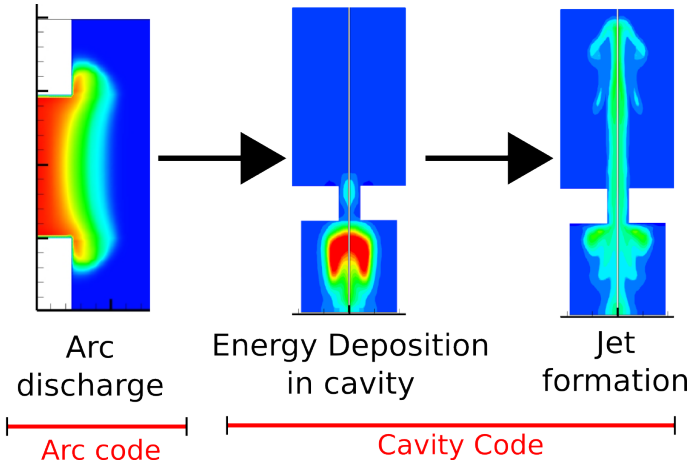

Figure C.2: Schéma d'une simulation sur une période. Code arc et le code fluide.

avec

$$\begin{aligned}
\mathbf{U} &= (\rho, \rho v_r, \rho v_z, \rho E)^t \\
\mathbf{F}(\mathbf{U}) &= \left[\rho v_r,\ \rho v_r^2 + p,\ \rho v_r v_z,\ v_r(\rho E + p)\right]^t \\
\mathbf{G}[\mathbf{U}) &= \left[\rho v_z,\ \rho v_r v_z,\ \rho v_z^2 + p,\ v_z(\rho E + p)\right]^t \\
\mathbf{S} &= \left[0,\ p,\ 0,\ r\sigma E_e^2 - rU_{rad} + rS_{diff}\right]^t
\end{aligned}$$

où $r\sigma E_e^2$, représente les termes sources de chauffage par effet Joule. U_{rad}, représente les pertes d'énergie radiative et est proportionnelle au coefficient d'émission net (NEC) dont la valeur est donnée par des tables en fonction de T et P fournis par Cressault et al. [6]. Un schéma explicite de Roe a été utilisée pour résoudre le système d'équations fluide. Un flux d'énergie thermique a été ajoutée à des parois de la cavité.

4. La résistance de l'arc R_{arc} permet de calculer la chute de tension dans le circuit externe. Elle est donnée par l'expression suivante:

$$R_{arc} = \frac{L_{arc}^2}{\int_{plasma} \sigma(x)dx} \tag{C.1}$$

où σ est la conductivité du plasma qui dépend des valeurs de température et de pression locale. Une grande partie de l'énergie électrique fournie est consommée dans la gaine à proximité de l'électrode. Une résistance de la gaine a été également mis en place pour prendre en compte les pertes d'énergie observées dans le bilan énergétique.

Le courant I entre les électrodes est spatialement constante dans l'espace inter-électrodes. Ainsi, le champ électrique est obtenu à partir de le courant de décharge I par la loi d'Ohm: $E_e = L_{arc}R_{arc}\mathbf{I}$.

Les interactions entre chaque solveur sont représentés dans la figure C.3. Les temps caractéristiques dépend de la fréquence d'actionnement ainsi que les paramètres du circuit externe. Une description plus détaillée des solveurs numériques peut être trouvé dans [5].

Le circuit capacitif électrique d'alimentation (circuit RLC [5]), utilise un condensateur de15 nF pour

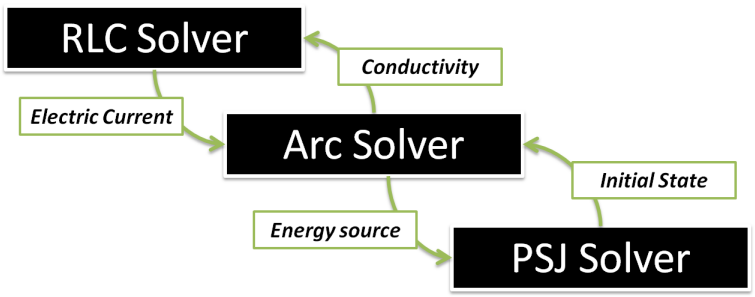

Figure C.3: Schème de couplage entre les sous-solveurs

induire périodiquement un arc électrique à l'intérieur de la cavité à une fréquence de 1 kHz. Le condensateur est chargé jusqu'à la tension de claquage de l'air, dont la valeur dépend de la densite et de la pression locale (dans des conditions atmosphériques, il est ≈2.7kV). La colonne électrique initial de l'arc est initialisé en utilisant la même approche simple comme dans [5]. Ainsi, nous élevons localement la température du fluide à 7500 K à travers la colonne d'arc tout en maintenant soit la pression ou la masse volumique à sa valeur ambiante.

Résultats numériques

Dans cette section, le comportement d'une seul écoulement de type jet induite par la décharge est présenté. Le dépôt d'énergie génère une surpression à l'intérieur de la cavité (en ordre de 0,4 bar) qui force l'ecoulement à l'extérieur de la cavité à grande vitesse . La vitesse à l'intérieur du noyau du jet élève à 700 ms^{-1} (figure C.4 (b)) bien que le front du jet se déplace beaucoup plus lentement (environ 160 ms^{-1} entre 0,5 et 1 cm à l'extérieur du col de la cavité - cette valeur correspond aux mesures dans [7] pour un actionneur de basse fréquence).

Un comportement quasi-stationnaire est obtenu après environ 10 ms (ou 10 impulsions). A partir de ce moment, le jet est vraiment synthétique, comme vu dans la figure C.5 (a) (ie son débit massique net est nulle sur une période). Ensuite, le jet expulse environ 5,2 μg (8,5 % de la masse initiale du JSP) pendant chaque impulsion, à un taux de débit massique d'environ 49 $mg.s^{-1}$. Le fluide à l'intérieur de la cavité est relativement chaud avec une température qui tombe en dessous de 900 K.

Des études paramétriques sur la fréquence de fonctionnement, la capacité et l'influence de la géométrie de l'actionneur ont été réalisées. Nous pouvons résumer les résultats comme suit:

— Les fréquences plus élevées conduisent à une cavité plus chaude et une masse expulsé moins grande (en raison de la recharge moins efficace).
— La masse expulsé est remarquablement linéaire avec la capacité. En ce qui concerne la température et la vitesse, ils augmentent avec l'énergie de la décharge.
— La masse expulsé augmente et la température diminue avec des ouvertures du col plus larges.
— La recharge est beaucoup plus efficace dans le cas d'une cavité convergente.

Étude aérodynamique

Ayant vérifié le modèle numérique et sa capacité à décrire la décharge d'arc et le jet synthétique conséquente, les données peuvent être importés dans un solveur CFD pour de simulations couplés. Ce couplage a

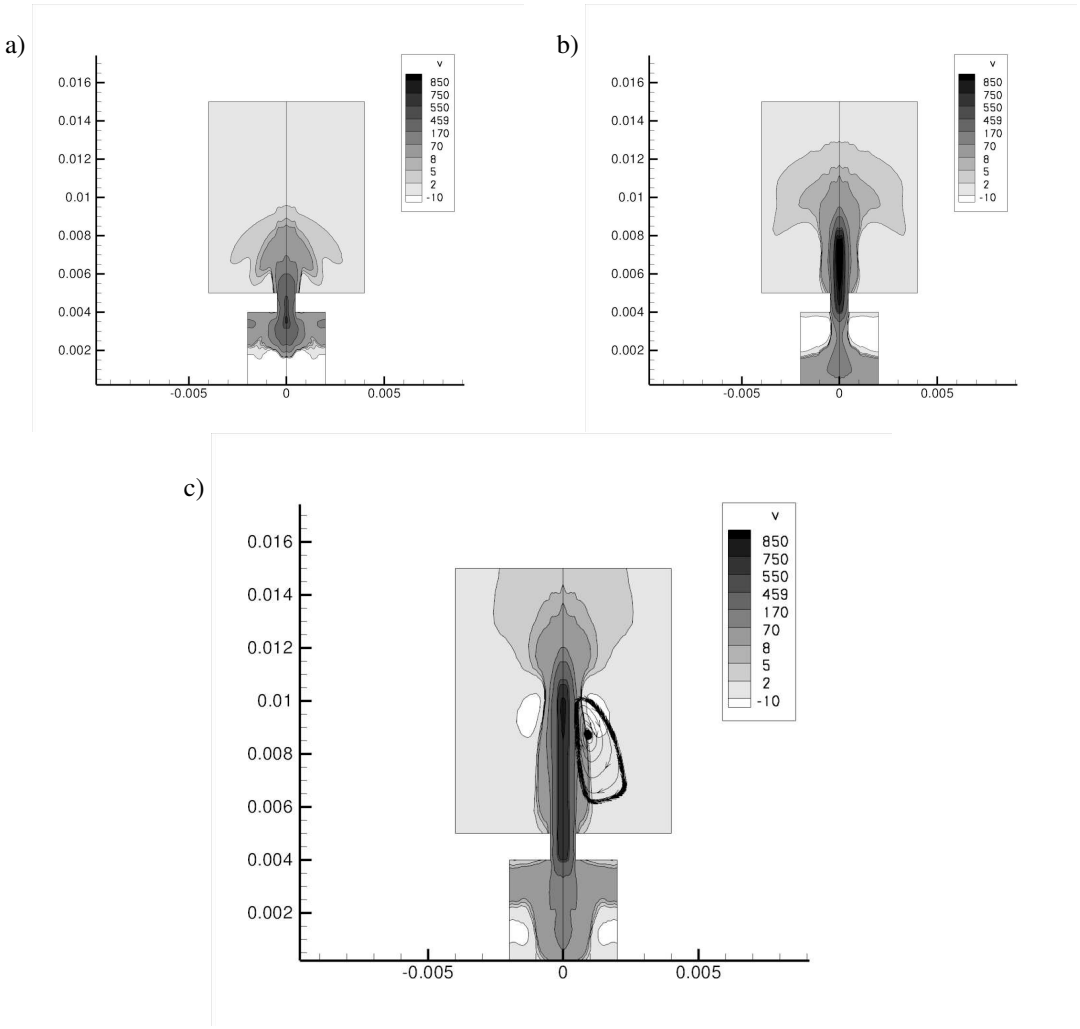

Figure C.4: La distribution de la vitesse dans le jet à 12 (a), 25 (b) et 37 (c) μs après le claquage.

été effectué en CEDRE ® (solveur CFD de l'Onera) via des termes sources dans les équations compressibles N-S. La quantité de mouvement et l'énergie ont été moyennés dans 100 μ s(avec les conditions de fonctionnement de $f = 1kHz, C = 15nF$ et un diamètre 1 mm de l'orifice), et interpolée dans un maillage 3D sur une plaque plane, créée en ICEM®. Dans les figures C.6 et C.7, le domaine de simulation ainsi que le maillage généré, (bien raffiné près de la couche limite afin de capturer les paramètres de turbulence ainsi que près de la zone d'actionnement du JSP) sont présentés. Le choix d'une plaque plane a été fait afin de valider notre résultats avec les résultats expérimentaux dans des configurations similaires - principalement fournis par le projet PLASMAERO.

Une simulation complète du JSP qui interagit avec une écoulement externe de 40m / s, ce qui correspond à un nombre de Reynolds de $2,67 \times 10^6$, a été envisagée. Le modèle turbulent utilisé est le k - ω.

Ce cas a été choisi afin que nous puissions comparer et valider qualitativement les résultats avec des

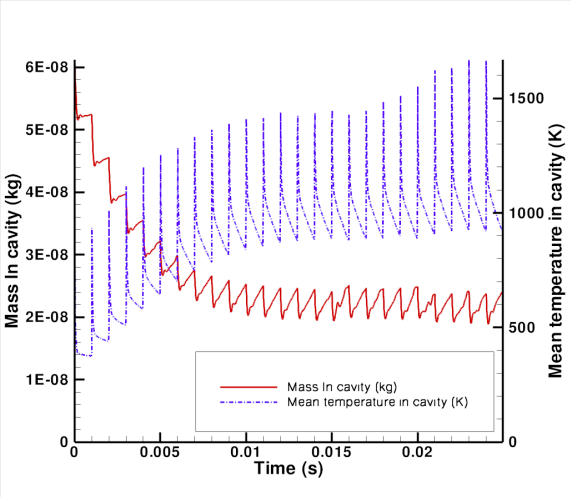

Figure C.5: Masse et température en fonction du temps.

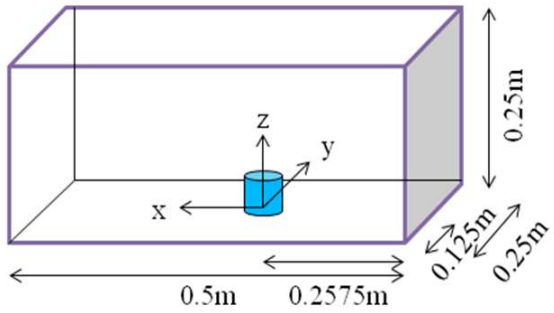

Figure C.6: Domaine de la simulation pour la plaque plane

expériences similaires réalisées dans [8] où un modèle de plaque plane avec une JSP intégré et sous la même conditions externes comme la simulation, a été étudiée. Le formation d'un tourbillon autour de l'axe de l'écoulement principal etait observé, qui s'élève et se propage dans le champ d'écoulement.

Lorsque l'actionneur de JSP est "branché" dans la simulation, deux tourbillons, de haut intensité, parallèles et tournant en sens inverse autour de l'axe z sont clairement capturé, créé par le jet et son interaction avec l'écoulement principal - tourbillons qui se déplacent dans la direction x (voir C.8 et C.9). Outre ces deux tourbillons cependant, l'apparition de une autre série de tourbillons peut être remarqué, surélevée à partir de la plaque plane et tournant autour de l'axe Y pendant qu'ils se propagent également dans la direction x. Ces paires de tourbillons sont en bon accord avec les écoulements de type "cross-flow".

Conclusion

Le Jet Synthétique Plasma a été numériquement étudiée par deux modèles couplés. Les résultats obtenus dans ce chapitre sont prometteurs pour l'optimisation du JSP et la meilleure compréhension des mécanismes

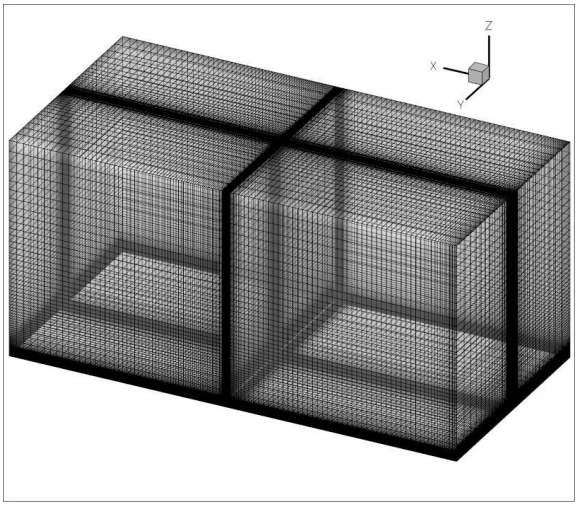

Figure C.7: Le maillage 3D

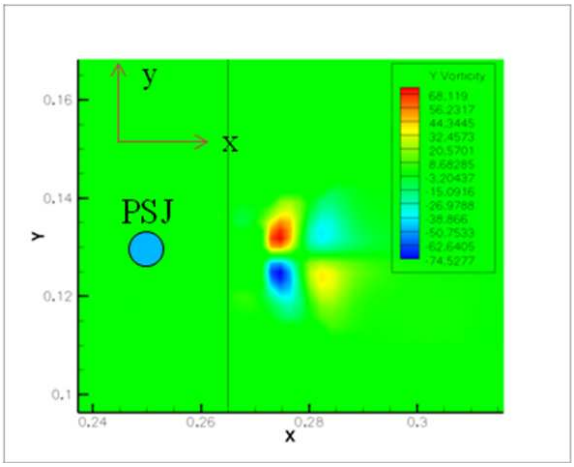

Figure C.8: Contours de y-vorticité - t=To + 70 μs

qui limitent ses performances. Nous avons vu que la vitesse du jet est réduite par l'augmentation de la fréquence de fonctionnement tandis que l'augmentation de la capacité entraîne une augmentation de la vitesse du jet expulsé. La forme de la cavité a également une grande influence sur la vitesse et la masse expulsé: plus grand rayons du col entraînent une augmentation de masse expulsé et une diminution de la vitesse de réaction. La forme de la section convergente du col a un effet important sur la répartition de la température à l'intérieur de la cavité, étant distribué de manière plus uniforme pour une forme coudée, et donc le remplissage de la cavité est plus efficace. Un exemple d'un modèle 3D d'une plaque plate avec une vitesse d'écoulement de 40 ms^{-1}, démontre l'effet du JSP : les tourbillons forment et se propagent dans la direction de l'écoulement, en accord avec les écoulements classiques de type "cross-flow".

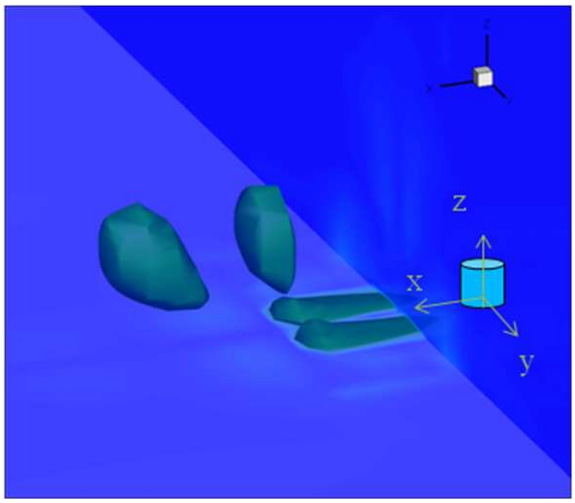

Figure C.9: Iso-surfaces de vorticité - t=To + 70 μs

Le solveur JSP peut être améliorée surtout en termes de la description de l'arc, bien que l'approche simplifiée qui a été utilisé fournit des résultats très précis sans avoir besoin d'une description détaillée de la physique des plasmas de l'arc et donc avec un coût de calcul réduit. Cela a été démontré par les travaux des chercheurs de DMAE, ONERA, Toulouse qui ont effectué de simulations tridimensionnelles LES de l'opération du JSP intégré dans une plaque plane [9], en utilisant le terme source fourni par le solveur de JSP presenté dans ce chapitre (transformée en trois dimensions).

Références Bibliographiques

[1] KR Grossman, BZ Cybyk, and DM VanWie. “Sparkjet actuators for flow control”. In: *AIAA Paper* 57 (2003), page 2003.

[2] Bohdan Z Cybyk et al. “Computational assessment of the sparkjet flow control actuator”. In: *AIAA Paper* 2003-3711 (2003).

[3] Daniel Caruana et al. “The “plasma synthetic jet” actuator. aero-thermodynamic characterization and first flow control applications”. In: *AIAA* 1307 (2009), page 2009.

[4] Venkat Narayanaswamy et al. “Investigation of plasma-generated jets for supersonic flow control”. In: *46th AIAA Aerospace Sciences Meeting and Exhibit*. 2008, pages 2008–285.

[5] Guillaume Dufour et al. “Physics and models for plasma synthetic jets”. In: *International Journal of Aerodynamics* 3.1 (2013), pages 47–70.

[6] Y Cressault et al. “Influence of metallic vapours on the properties of air thermal plasmas”. In: *Plasma Sources Science and Technology* 17.3 (2008), page 035016.

[7] Pierrick Hardy. “Etude et qualification aérothermodynamique et électrique d’un actionneur plasma de type jet”. PhD thesis. Toulouse, ISAE, 2012.

[8] Daniel Caruana. “The Plasma Synthetic Jet Actuator for Separation Control”. In: *ERCOFTAC Bulletin* 94 (2013).

[9] F. Chedevergne. “Simulations LES d’un jet synthetique plasma”. In: *Technical report* 1/21098 (2013).

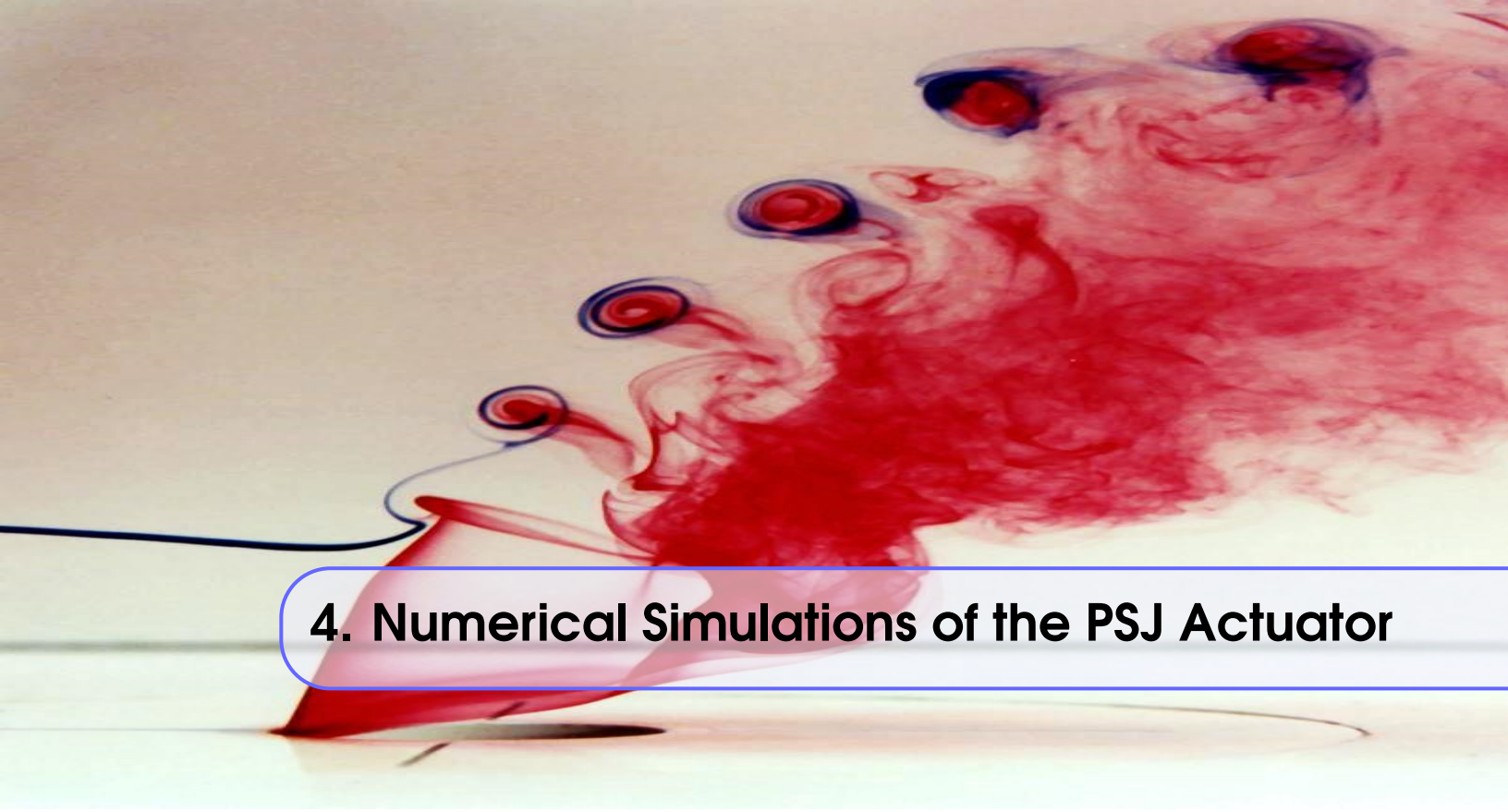

4. Numerical Simulations of the PSJ Actuator

4.1 Presentation

In this chapter, we are focusing on a new concept that has been recently proposed by John's Hopkins Applied Physics Lab ([1],[2]) and improved by others groups ([3], [4]) : the sparkjet plasma synthetic jet actuator (referred to PSJ or sparkjet from now on). Because of its tiny dimensions (smaller than 1 cm in every direction), the Plasma Synthetic Jet actuator (or PSJ) may be used in multiple actuators groups and placed wherever needed on an aircraft body. However, commonly used experimental characterization techniques of the jet velocity distribution such as Particle Image Velocimetry, pose problems in matter of cost and complexity. This is even more true for internal flows inside the actuator's cavity, flows which can barely be observed in realistic experimental setups without largely impacting the flow going through the actuator's neck and inside the entire cavity. Thus, important characteristics of the actuator like its internal temperature distribution (to ensure the cavity's integrity over the long term) or mass ejected per pulse (related to the momentum brought to the fluid) are experimentally hard to measure in conditions similar to the ones of an in-service actuator in periodic regime. Therefore, in order to get a better understanding of the flow inside the cavity as well as the resulting jet's velocity distribution, we propose to describe the actuator by numerical simulation of both the plasma generated between the electrodes and the resulting cavity flow. Such simulations can also provide information for a possible improvement of the actuator in terms of jet velocity and mass flow rate(for example). Physical constraints, especially on the temperature inside the cavity, could be set to ensure the sustainability of an operating configuration.

In the last years, several numerical simulations have been conducted, in order to better understand the energy transfer mechanism from the capacitors to the gas and then the jet's formation. The John Hopkins group has developed a sparkjet model using analytical solutions as well as a CFD solver. They described the

Photo by National University of Singapore

different stages of the actuator's operation ([5] and [6]) and evaluated an efficiency coefficient describing the part of the energy stored in the capacitors, actually used to heat the cavity's air. Their model does not describe the refresh stage and is limited to a single discharge pulse. A study has also been carried out by Rutgers University ([7]) to characterize a single pulse of a Plasma jet. The authors model the energy deposition by a uniform temperature initial condition in the whole cavity. They performed a parametric study of the geometry's cavity in a quiescent air and then computed by 3D CFD simulations the plasma jet's evolution in a turbulent supersonic cross flow.

Recently, a full model of the PSJ actuator has been proposed by ONERA's group [8]. It contains more physical insights (real gas effect, discharge modeling...) than the previous models and therefore provides information on the gas into the cavity as well as in the plume.

In this chapter, the objective is to introduce some more physical aspects in the numerical model of [8], and to perform studies on the operation of the PSJ under different working and geometrical conditions, towards its optimization. The work in this chapter, has been undertaken during the past 5 years by various researchers and PhD candidates. The first developments have been made by G. Quint, F. Rogier and G. Dufour from DTIM, ONERA. Following up, most of the parametric studies and enhancement have been conducted by G. Sary, an intern at DTIM, ONERA during his master thesis in ISAE, under the supervision of F. Rogier. During his internship, the collaboration in ONERA, led to the results that will be presented here, the coupling with ONERA's CFD code CEDRE, and provided the basis for the more complex simulations performed and still under numerous studies at the DMAE, ONERA that are briefly presented in the last section. The research leading to these results has received funding from the European Community's Sev- enth Framework Program FP7/2007-2013 under agreement no.234201 and project PLASMAERO.

The organization of this chapter is the following: The introduced novelties in the numerical model of are [8] detailed and discussed in section 4.2. Section 4.3 is dedicated to a physical description of a single arc discharge. The computation of the periodic regime of the actuator, where simulations over many arc discharges and refill cycles have been performed are also presented. The computation of this regime, and most importantly the associated jet's energy and velocity distribution open path to further studies where the true influence of such a jet might be evaluated in meaningful conditions. Parametric studies of the actuator has also been undertaken. This studies provide some useful insights about the jet's main characteristics versus some of the actuator design parameters related to either the power supply unit or the actuator geometry. Finally some early simulation results on the interplay between a Plasma Synthetic Jet and a representative aeronautical flow are presented. These simulations over a flat plate flow illustrate the main expected effect of the actuator for aerodynamic flow control : The vortices generation. In section 4.4, we conclude and present some results of the on-going further research held by DMAE, ONERA.

4.2 Physical and Numerical Modeling

4.2.1 Actuator modeling

In actual realizations, the Plasma Synthetic Jet (PSJ) actuator is a cavity with a roughly cylindrical geometry (4 mm wide by 4 mm tall) containing a pair of electrodes (see figure 4.1). Electric power is supplied to the electrodes so as to create an arc discharge inside the cavity and in the end a high velocity flow through a hole bored in one of the lids. Consequently, a suction phase follows, refilling the cavity with ambient air and preparing the cavity for further pulses. This setup has already been thoroughly described and analyzed

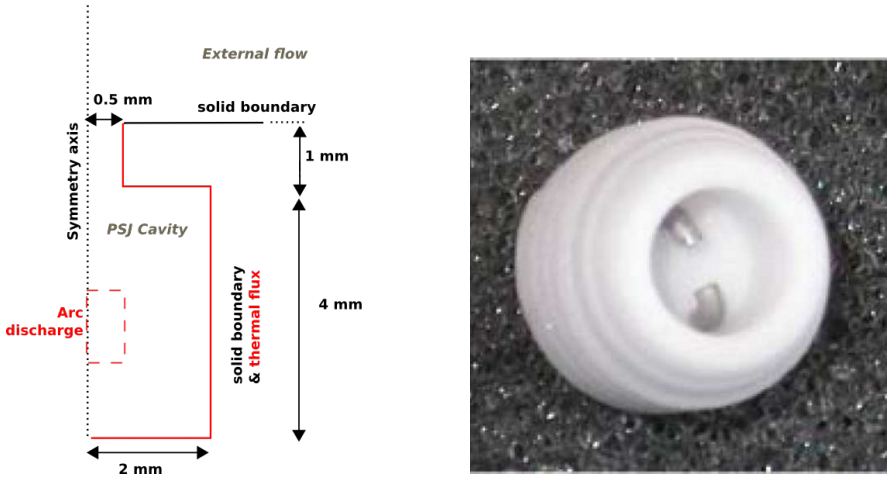

Figure 4.1: Schematic of a simple PSJ cavity and experimental realization

in [8] and thus we will rely here on the same 2D-axisymmetric modeling. Key differences arising from the different goal of this study will however be underlined. Namely, while these earlier works studied a single energy deposition inside a cavity initially at standard conditions (300 K, 1 atm), here energy deposition will be performed at a fixed frequency and computed over several cycles. The periodic behavior of the cavity and most importantly the characteristics of the resulting jet can then be studied.

4.2.2 Arc discharge and cavity modeling

The model has been split into two coupled sub-models (see figure 4.2). The first one deals with the energy deposition through electric arcing in the vicinity of the electrodes in absence of the cavity. It describes the plasma formation between both electrodes in an axisymmetrical configuration. This model is coupled to the series RLC circuit equations describing the electrical supply by an external generator. The second sub-model, focuses on the air's heating in the cavity and the actual operation of the actuator. It uses the energy distribution computed by the first sub-model as source term and calculates the resulting effects on the actuator. It provides the flow mass rate, momentum and energy at the PSJ's exhaust versus time.

4.2.3 Main assumptions of the models

1. The plasma is assumed to be at local thermodynamic equilibrium. This assumption is verified under the conditions of temperature and pressure reached in this discharge. In such type of arc discharges, collisional processes govern now the transitions and chemical reactions in the plasma instead of the radiative phenomena. The higher the pressure and the temperature, the more intense the elastic collisions that occur between the ions and the electrons. So the electrons under such conditions lose some of their higher energy to neutral particles and ions(which are heavier and therefore their mobility and temperature is lower than the electrons) and the local thermodynamic equilibrium hypothesis is realistic. In figure 4.3, the evolution of the electronic and the heavier particle's (hydrogen in this case) temperature with the pressure in an arc discharge, has been plotted, based on an energy balance equation where the elastic collisions dominate [9]. It can be observed that the 2 temperatures deviate only for low pressures, while they coincide for higher values. Thus, the plasma and the air, considered as fluids with same temperature, have been modeled with the properties of a real gas, due to the high

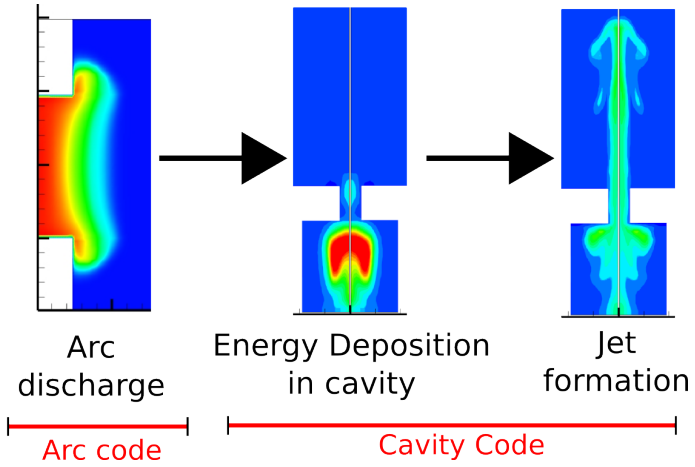

Figure 4.2: Schematic of a simulation run over one period. Arc code and cavity-fluid flow code.

temperatures reached, that follows tabulated real gas laws given by Capitelli *et al.* in [10].

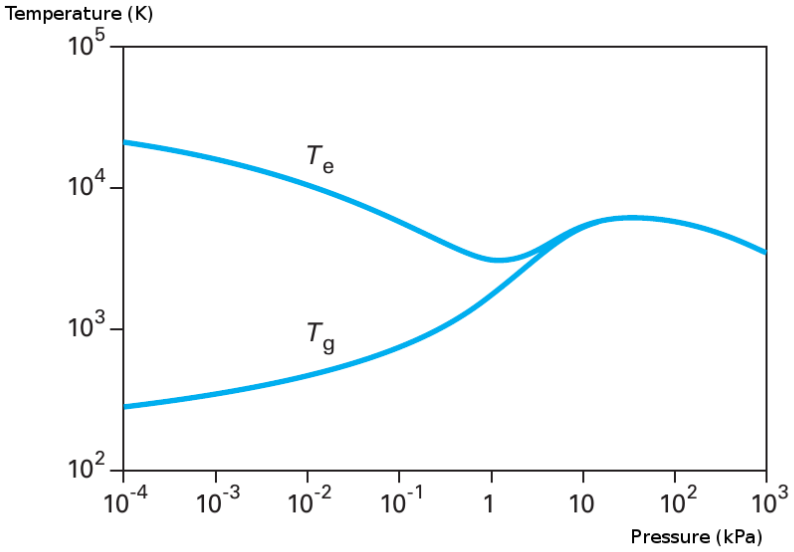

Figure 4.3: Electrons and heavy particles' temperature vs pressure over one period

2. The plasma is assumed optically thin and thus all energy radiated by the plasma is considered lost (radiative heating of the walls is assumed negligible in comparison to convective heating). The absorption coefficients of air at standard conditions of density and temperatures as high as 12000 K have been determined in [11]. For photons ranging from UV to far IR, it is shown that an effective length over which we can expect significant radiation absorption is often much larger than 1 cm and

thus is larger than the characteristic dimensions of the cavity. This specific value is reached for normal air density, temperature of 2000 K and 5.6 eV of photon energy. For higher temperatures and lower densities, it is seen that absorption occurs on even longer lengths (10 times longer at 12000 K and normal air density). Thus, because of the reduced size of the cavity, radiation absorption by the cold gas surrounding the discharge can be safely neglected. Local radiation re-absorption by the plasma inside the relatively hot arc discharge region, has been taken into account via proportionality with a net emission coefficient (see equations below).

3. The viscosity effects are neglected. Although this hypothesis is simplistic, it allows the exploration of basic trends of the actuator while keeping a reasonable computation cost. Future calculations will take these effects into account.
4. The energy deposition is axisymmetric. This assumption of azimuthal symmetry is one of the strongest assumptions of this model. The main reason behind this assumption is the reduction of the computation time of the simulation to a reasonable scale, while retaining the main flow characteristics and modeling microscopically the problem.
   Regarding the arc formation, this assumption is justified by the geometry of the electrodes and their placement inside the cavity. Indeed in the experimental setup the electrodes are made of two metallic straight and cylindrical wires, placed inside the cavity on the same axis.
   The jet formation and the operation of the zero-net-mass actuator is surely more complex. Most of the previous studies on synthetic jet actuators similar to plasma ones, prove that three-dimensional vortex interaction is an active mechanism in such actuators and thus the vortex spreading and intensity is inevitably underestimated in a two dimensional axisymmetric simulation. The effect of the three dimensional flow is mostly due to small scale disturbances, which modify mostly the far-field of the jet (away from its orifice) [12, 13, 14]. Comparing the numerical results with experiments of axisymmetric synthetic jets triggered by a piston inside a cavity as in [15], show that qualitatively a reasonable agreement is achieved concerning the near-flow field of the jet. Numerical simulations of similar synthetic jets of piezoelectric actuation[16], conclude to the same point - the validity of a 2D-axisymmetric modeling of such actuators compared to a 3D one, for, as stated, the results of the 3D model showed that the most relevant deformations occur in the z and radial directions. Concluding, even if the uniformity of a two dimensional axisymmetric simulation is not totally representative of the problem's real physics, the numerical model presented here is capable of capturing the main characteristics of the jet's formation as well as the formation of the vortices and can give insights of their applicability.
   A second point that needs to be clarified is the effect of the cavity mostly during the suction phase, where three dimensional instabilities may be produced in the flow. It is quite obvious that the three dimensional geometry of the cavity (which includes the electrodes), combined with the external flow will introduce disturbances that are no longer axisymmetric. The question that arises here is whether these disturbances will play a major role in the vortex formation and the jet's attributes.
   As stated in [17], depending on the stroke length (i.e. L=integral of velocity at orifice over a period) over the diameter of the orifice (D), some of the vorticity can be re-ingested into the cavity. This vortice re-ingestion, will modify the flow field inside the vacity in a three-dimensional way and consequently the whole periodic operation of the actuator. In the PSJ actuator and under the conditions of this work, L/D is greater than 10 and no re-ingestion is taking place (which is the case for values of L/D greater than 3 [17]). Thus the cavity flow is not modified by the external vortex rings. Furthermore, the small dimensions of the cavity and its orifice combined with the time characteristics of the synthetic jet operation (we remark that the suction phase takes place in a big time scale-for f=1kHz, the cavity being refilled in approximately 0.9 ms) and the external flow's ones, imply that the suction phase

will not modify strongly the flow field in the external flow especially in the far-field. Besides, inside the boundary layer and really close to the cavity's orifice the velocity of the external flow reduces significantly. Thus the refilling of the cavity will affect mostly a thin layer really close to the walls that can be approximated as quasi-quiescent (and with small scale turbulent eddies). The real effect of the external flow in the asymmetry that may occur inside the cavity and thus the impact of this asymmetry on the actuator's operation falls outside the preliminary study of this work but should be investigated in future studies.

Taking into account the above reasoning, the 2D-axisymmetrical simulation of the PSJ can be described as a fair compromise of computational cost and physical-realistic representation of the flow features, under the specific conditions presented in this chapter. A 3D-solver is although required for the description of the vortex creation, spreading and impact due to the actuation of a jet in a cross flow. An illustrative example of such an effect can be found in the last section of this chapter.

The flow evolution is governed by the 2D axisymmetrical inviscid Euler equations:

$$\frac{\partial}{\partial t}(r\mathbf{U}) + \frac{\partial}{\partial r}[r\mathbf{F}(\mathbf{U})] + \frac{\partial}{\partial z}[r\mathbf{G}(\mathbf{U})] = \mathbf{S},$$

with

$$\begin{aligned}
\mathbf{U} &= (\rho, \rho v_r, \rho v_z, \rho E)^t \\
\mathbf{F}(\mathbf{U}) &= \left[\rho v_r,\ \rho v_r^2 + p,\ \rho v_r v_z,\ v_r(\rho E + p)\right]^t \\
\mathbf{G}[\mathbf{U}] &= \left[\rho v_z,\ \rho v_r v_z,\ \rho v_z^2 + p,\ v_z(\rho E + p)\right]^t \\
\mathbf{S} &= \left[0,\ p,\ 0,\ r\sigma E_e^2 - rU_{rad} + rS_{diff}\right]^t
\end{aligned}$$

where $r\sigma E_e^2$, represents the Joule heating source terms. As for U_{rad}, it represents the radiative energy losses and is proportional to the net emission coefficient (NEC) whose value is given by tables depending on T and P provided by Cressault et al. [18].

5. The arc resistance R_{arc} allows to compute the voltage fall into the external circuit. It is given by the following expression :

$$R_{arc} = \frac{L_{arc}^2}{\int_{plasma} \sigma(x)dx} \tag{4.1}$$

where σ is the plasma's conductivity that depends on the local temperature and pressure values. A large part of the electrical energy supplied is consumed in the sheath near the electrode. A sheath resistance has been also introduced to take into account the energy losses observed in the energy balance.

The current I between electrodes is spatially constant in the inter-electrodes space. So, the electric field is obtained from the discharge current I by Ohm's law: $E_e = L_{arc}R_{arc}\mathbf{I}$.

6. The modeling does not describe the arc's formation during the first nanoseconds. This part should be modeled precisely by a specific plasma model. It is assumed, that the initial state of the arc is known after the first current pulse.
7. The breakdown voltage depends on the initial gas state as an analytical function.

The interactions between each solver is pictured in figure 4.4. The typical time stepping depends on the actuator frequency and also the parameters of the external circuit. A more detailed description of the numerical solvers can be found in [8].

In the arc model, it is assumed that the deposition duration is short enough so that the arc won't be influenced by the cavity walls. It may be seen on figure 4.6, that most of the energy deposition of the discharge

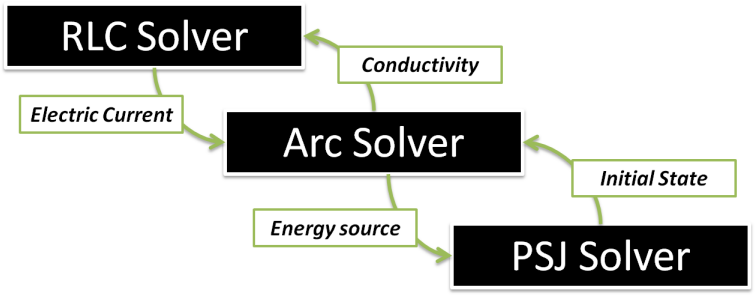

Figure 4.4: Scheme of the coupling between the sub-solvers

occurs during the first 5 μs. Given a cavity's radius of 2 mm, comparison with figure 4.7 shows that at $t = 5\,\mu s$, the blast wave radius, generated by the cylinder-like energy deposition, and described by the Taylor-Sedov solution barely had time to reach the opposite wall (at that moment, its distance from the axis is 1.75 mm). Therefore we can conclude that the hypothesis of neglecting arc-cavity walls interactions is consistent with the simulation.

4.2.4 Key differences with earlier modeling

An explicit Roe Scheme has been used for solving the fluid equation system. This fluid solver is the same as described in chapter 2 in axi-symmetric coordinates. This kind of shock-capturing scheme is particularly well adapted to the propagation of an high velocity jet into a low velocity medium. A mesh convergence study has been performed and has shown relative independence of the results over mesh size. For the simulations described here, 2500 cells have been sufficient for good numerical resolution .In the frame of this work, a thermal energetic flux has been added at the walls of the cavity. A justification of this addition can be given, as following: since the periodic flow inside the cavity has to be modeled, both the ejection of gas and refill of the cavity with ambient air need to be simulated. It is however clear that the mass flow rate of the suction phase is strongly coupled with the density of the fluid inside the cavity and hence to its temperature. Because of the cavity's geometry, its cooling is only possible through convective heat transfers at walls (heat transfer at electrodes is neglected). This thermal flux is given by :

$$\phi_{conv} = h_{conv}(T_{fluid} - T_{wall})$$

where h_{conv} is the convective heat transfer coefficient, T_{fluid} the local temperature of the fluid in vicinity of walls and T_{wall} the temperature of the cap of the cavity, whose temperature is fixed at 300 K. A convective coefficient h of 50 $W.m^{-2}.K^{-1}$, has been chosen, being in agreement to experimental values measured for the convective heat transfer with air outside the cavity (45 $W.m^{-2}.K^{-1}$, in [19]). Inside the cavity, the coefficient relative to heat transfers is most likely bigger because of forced convection and was estimated to a value of 150 $W.m^{-2}.K^{-1}$ empirically. Thus, our model underestimates cooling of the cavity. Nevertheless, physically, once periodic behavior is reached, the walls of the cavity will have heated up and heat transfers will be limited by convective transfers with external air. Consequently, simulated heat fluxes during quasi-periodic regime will admit a maximum value close to the one which was experimentally measured and has been cited just above [19].

4.2.5 Initial conditions and standard setup of the actuator

When not explicitly mentioned otherwise, simulations described in this work used the following initial conditions and design choices. The initial conditions and geometrical parameters of the simulations have been chosen as : :
The electric capacitive power supply circuit (series RLC circuit, see figure 4.5 or [8]), uses a 15 nF capacitor to induce periodically electric arcing inside the cavity at a 1 kHz frequency (common experimental values are in the order of 600 Hz). The capacitor is charged up to the breakdown voltage of the air gap, whose value depends on the local density and pressure(at atmospheric conditions it is abour 2.7kV). The initial electric arc column is initialized using the same simplifying approach as in [8]. Thus, we raise locally the fluid's temperature to 7500 K across the arc column while keeping either the pressure or the density at its ambient value. A detailed analysis of two reasonable initial conditions in the arc is also given in section 4.3.1.
The shape of the cavity itself is kept unchanged and is described in figure 4.1. Only its neck will be subject to change in the geometric study.
Finally, the fluid in the computational domain is initially at rest and at atmospheric conditions (300 K, 1 atm).

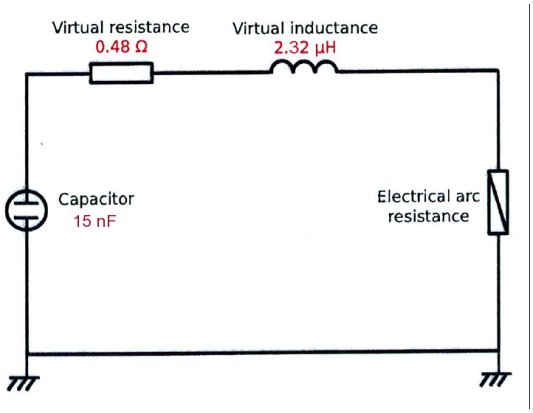

Figure 4.5: Series RLC electric circuit used to model the power supply and the arc discharge

4.3 Numerical Results

4.3.1 Single pulse results description and discussion

Spark description

For these arc simulations, we used a breakdown voltage of 3.5 kV and a 15 nF capacitor. Fluid between the electrodes is initialized with an ambient pressure and a temperature of 7500 K similarly to the discharge model described in [8]. Arguably, the later plasma development might depend on this initial condition (at high temperature and ambient pressure in this case). Hence, we will give here a brief description of a spark discharge initially at ambient pressure and point out some differences with an initial condition at ambient density and high temperature (and thus high pressure). Both initial conditions are detailed in table 4.1.

Differences between the two initial conditions

Qualitatively, the behaviours observed for the two types of initial conditions were very similar. However, while the stored power in the capacitor was identical, the total deposited energy is larger using the ambient density initial condition (see figure 4.6a). This may be attributed to a larger equivalent plasma resistor

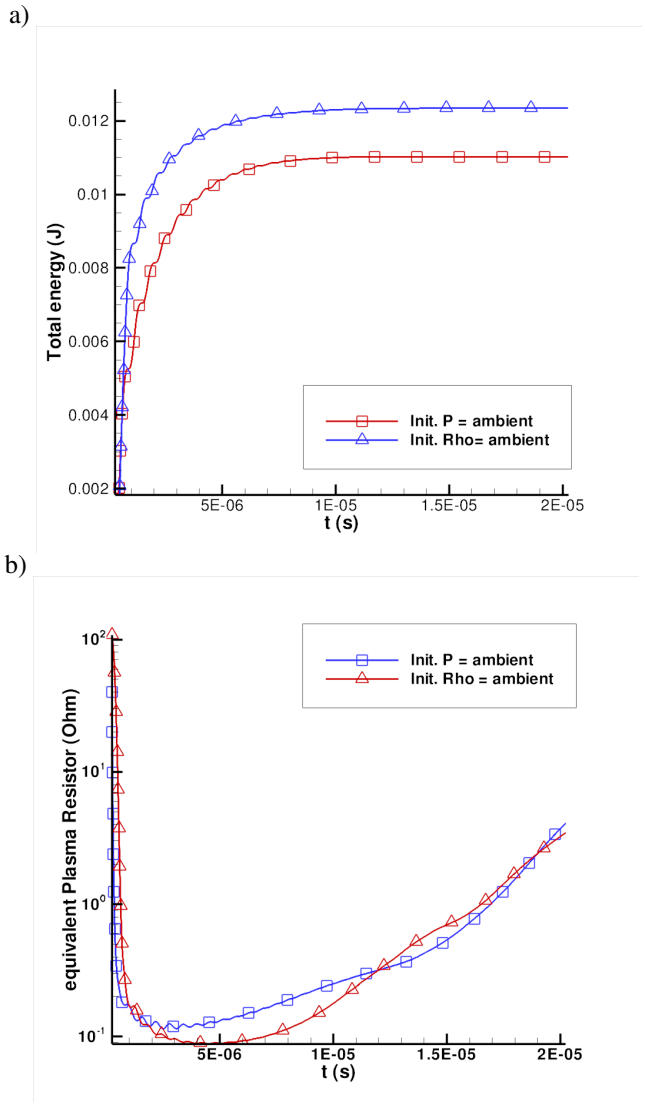

Figure 4.6: Cumulative energy deposition(a) and plasma resistance(b) during the spark for two initial conditions

(because of the lower plasma conductivity at higher pressures) during the early discharge, as observed in figure 4.6b. Indeed a large proportion of the total energy gets deposited during the first 2 microseconds and it is also on this time frame that the profiles corresponding to the two initial conditions differ the most (after that, electric power input is almost null due to the low resistance in both cases). Thus, the key difference could be the pressure during the first instants of the discharge.
Plasma region evolution is also slightly different between the two initial conditions. Radii of the blast wave and the plasma region have been represented for the two initial conditions, as well as the self similar solution

Pressure	Density	Temperature
P=ambient 1 atm	$0.004 kg.m^{-3}$	7500 K
ρ= ambient 31 atm	$1.225 kg.m^{-3}$	7500 K

Table 4.1: Two studied initial conditions for the arc discharge

representing the early propagation of the blast wave (figure 4.7). While the blast waves stay close together for both initial conditions, the plasma region grows faster when the ambient density initial condition is used. It may then be hypothesized that cavity heating with an ambient initial density condition could be slightly more uniform although not qualitatively different.

As a conclusion, since the two initial conditions appear to behave very similarly and produce the same order of magnitude of energy deposition, it is safe not to distinguish between the two initial states for the rest of this qualitative study. Although, differences exist, imprecision notably on energy loss terms render them negligible.

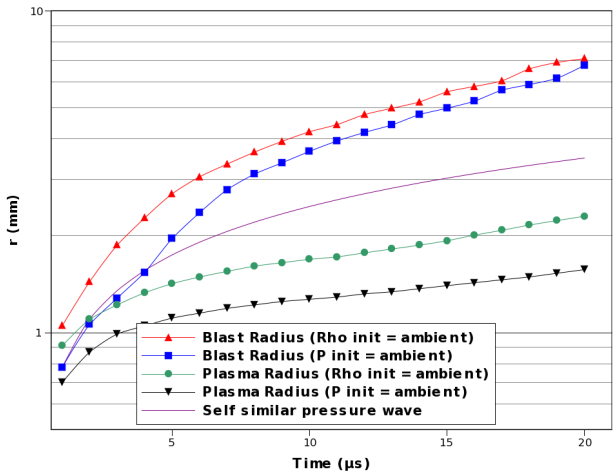

Figure 4.7: Time evolution of plasma and blast wave radii

Cavity and PSJ flow description

In this section, the behaviour of a single discharge induced flow and energy distribution inside as well as outside the cavity, will be presented.

Energy deposition inside the cavity is easily seen in figure 4.8 (a). At that point, the arc discharge is not delivering power anymore and the fluid behavior is only governed by pressure and thermal gradients. This energy deposition generates an over pressure inside the cavity (in order of 0.4 bar) which forces the flow at high velocity outside the cavity. This creates velocities inside the core of the jet as high as 700 $m.s^{-1}$ (figure 4.9(b)) although the tip of the jet moves much slower (around 160 $m.s^{-1}$ between 0.5 and 1 cm outside the neck of the cavity, this value corresponds to the measurements in [20] for a low frequency actuator). The high velocity jet assumes an arrow-shape which is visible on the velocity distribution (figures 4.9(a) and (b)) and more clearly on the temperature distribution (figure 4.8(b)). A toroidal eddy also forms close to the jet tip

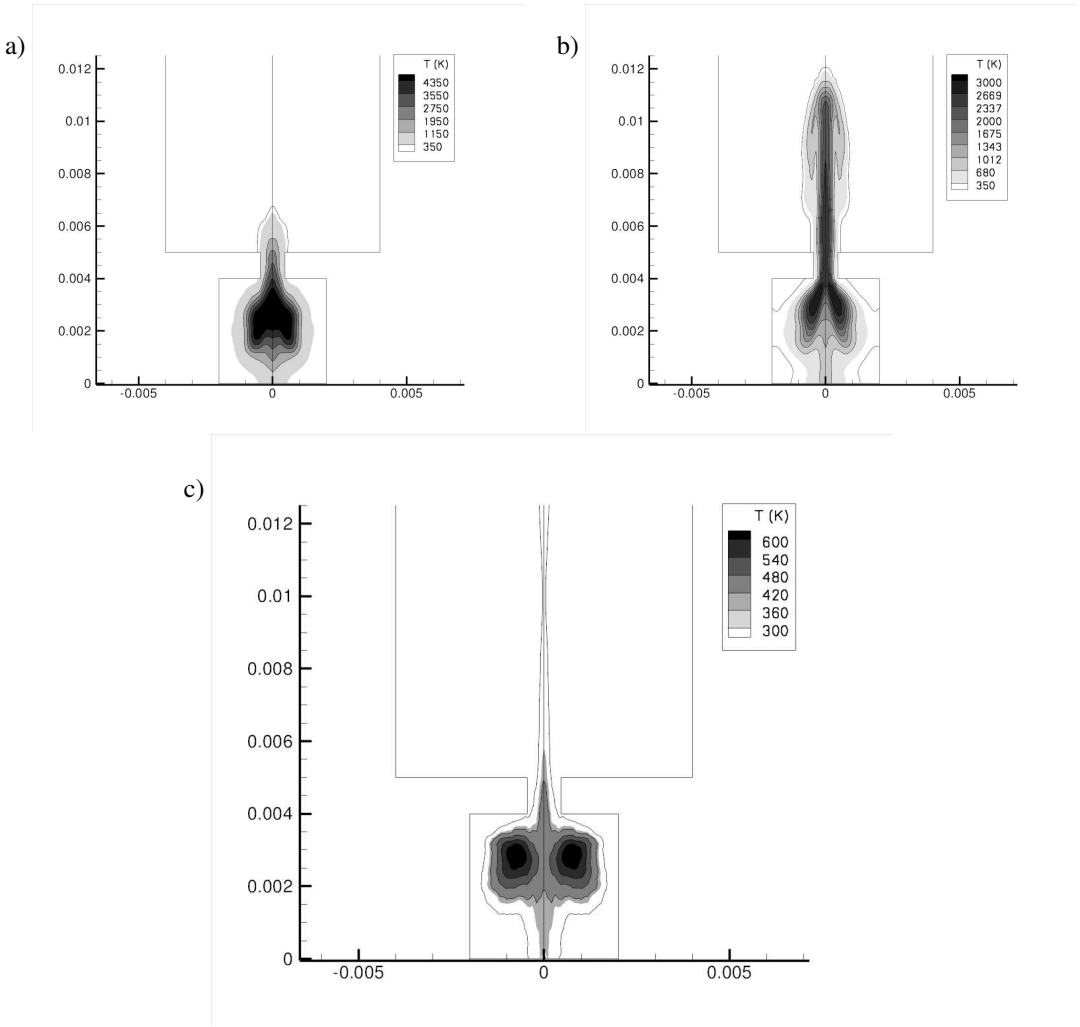

Figure 4.8: Temperature distribution in the jet at 12 (a), 38 (b) and 600 (c) μs after breakdown

and is carried along the jet. This eddy, which might form because of the brutal opening of the neck, is visible on streamlines in figure 4.9(c). This particular flow has been observed on strioscopy visualizations and is mentioned in [20].
Over the jet duration, temperatures reach over 2000 K at its core while the density is about 0.2 $kg.m^{-3}$. One may notice the residual heat inside the cavity which takes an annular shape around the neck constriction. It seems straightforward to assume that this is caused by the "corner" inside the cavity and that this "hot" zone might hinder the refill of the cavity. This motivates the geometric study of the cavity in section 4.3.5.

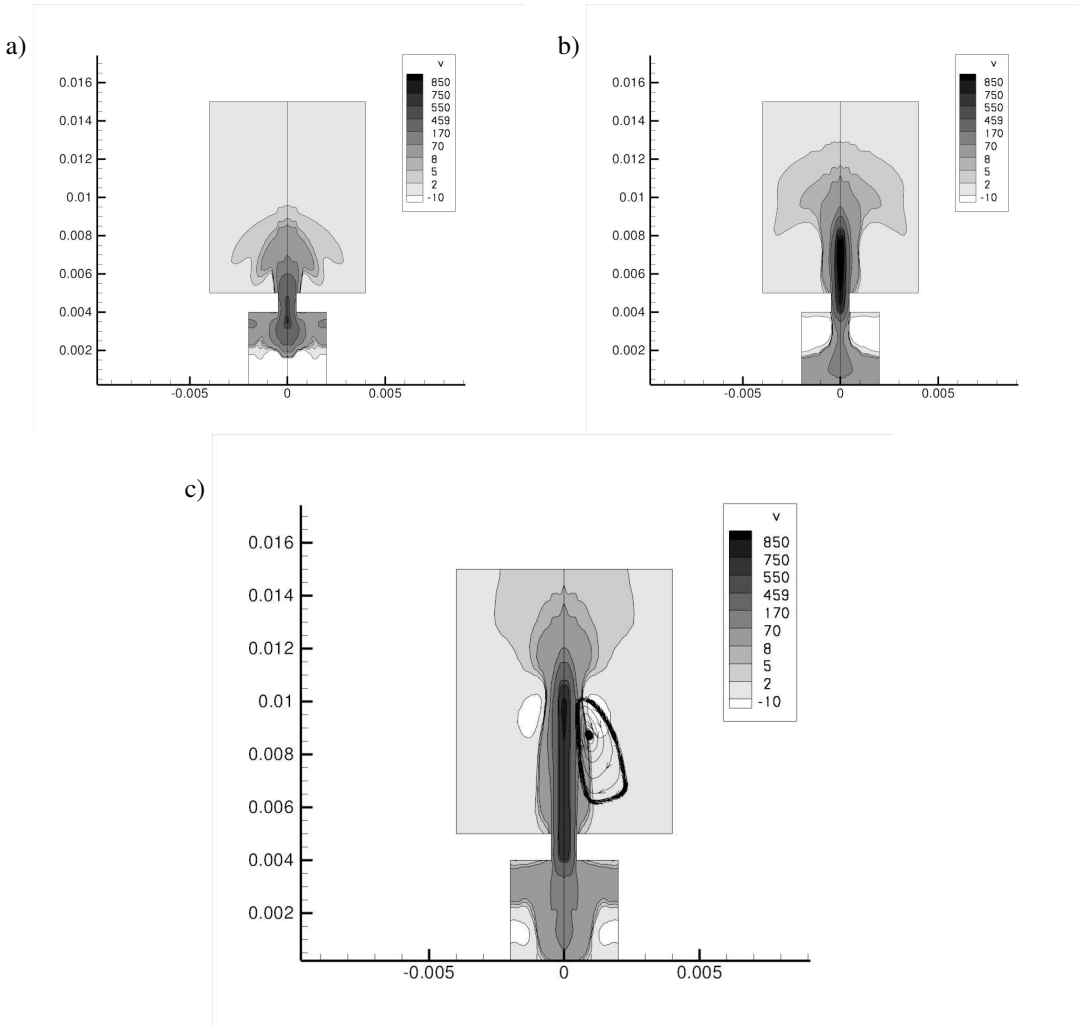

Figure 4.9: Velocity distribution in the jet at 12 (a), 25 (b) and 37 (c) μs after breakdown

4.3.2 Periodic behavior

Simulations of more than one discharge pulse led to the quasi-static periodic behavior of the actuator after approximately 25 pulses. Below the results of these simulations, will be presented.

Synthetic graphs

The quasi-static behaviour of the actuator is readily visible on 2D visualizations of the flow. However, some synthetic graphs such as the total mass contained and the mean fluid temperature inside the cavity show this periodicity even more clearly. This simulation has been carried out for an actuator operating at 1 kHz frequency, using a 15 nF capacitor and a constant breakdown voltage of 2.7 kV. Once the quasi-static behavior is obtained, 7 mJ of electric energy are deposited in the fluid during each pulse. The most simple shape of cavity has been used here : cylindrical with a cylindrical nozzle. For these graphs, fluid in the nozzle has been

taken into account as well.

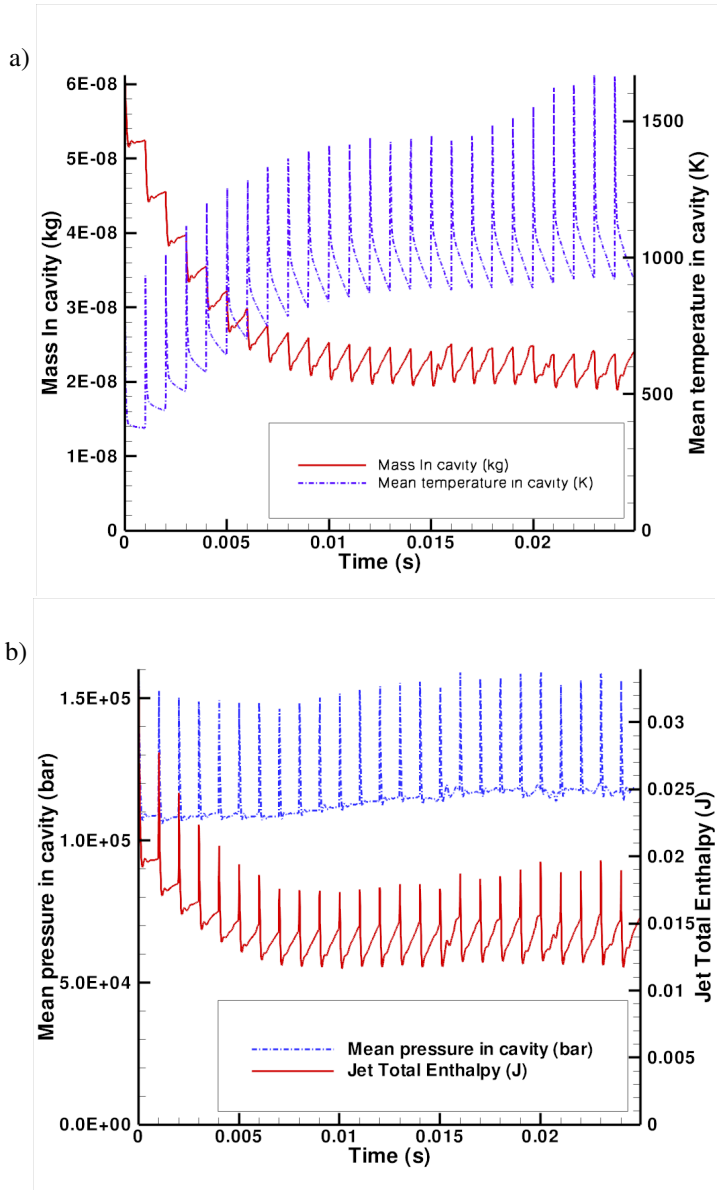

Figure 4.10: Periodicity of macroscopic - a) Mass and mean Temperature versus time and b) Mean pressure and total jet enthalpy versus time values.

Quasi-static behavior is obtained after roughly 10 ms (or 10 pulses) for all represented graphs. Starting from this moment, the jet is truly synthetic, as seen in figure 4.10(a) (i.e. its net mass flow is null over one period). Afterwards, the jet expels about 5.2 μg (8.5% of the PSJ's initial mass) during each pulse, at a

mass flow rate of approximately 49 $mg.s^{-1}$. The fluid inside the cavity gets relatively hot with a temperature never falling below 900 K. In figure 4.10(b), the mean pressure in the cavity as well as the total enthalpy are plotted (with heat transfers through walls removed over each period). Thus the total enthalpy of the jet and enthalpy gained during each refill (through mass effects)can be determined. The over-pressure during each pulse reaches 0.4 bar and about 6.3 mJ of total enthalpy are carried away with each pulse (amplitude of the peak). This figure also demonstrates that the periodic regime has been obtained : electric energy to enthalpy conversion, jet total enthalpy and enthalpy gained through refill keep constant magnitudes over the last 5 periods. Figure 4.10(a), clearly shows that cavity refill and fluid cooling are strongly correlated. What rests to determine in the next sections, is whether the cooling of the cavity drives its refilling or the opposite.

Temperatures inside the cavity during the periodic regime might be excessive. In fact, operating frequency in this simulation is higher than experimentally used ones (around 600 Hz), and at this rate, the actuator's integrity might degrade quickly. It is however likely that using a constant breakdown voltage is in this case unrealistic. Indeed, total mass inside the cavity and mean density are diminishing and so should breakdown voltage. Therefore, total deposited energy during next pulses would probably be smaller, hence reducing the minimum temperature over one period. This effect will be studied more specifically in section 4.3.3.

Heat distribution in cavity

Operating conditions here are the same as in section 4.3.2. As mentioned earlier, during each pulse, a part of the hot jet gets trapped in the corner of the cavity, thus heating it and most likely reducing the actuator's mass outflow rate for further pulses (because of the less efficient refill phase, linked to the lower density of the fluid inside the cavity). Figure 4.11 clearly shows a highly-localized annular hot zone around the neck of the cavity. The cooler zone on the axis corresponds to the refill of the cavity by exterior fluid. A thermal boundary layer effect around this hot zone is also visible, effectively limiting thermal transfers through the cavity walls. Thus, a more efficient cavity geometry, such as a one with a conical neck, would normally reduce the size of this zone, and in the end enable a quicker refill of the cavity, and thus a larger expelled mass. This effect will be confirmed in section 4.3.5.

4.3.3 Power supply circuit coupling

So far, the electrode's gap breakdown voltage was kept constant at 2.7 kV. Thus, the capacitor always contained initially the same amount of electric energy, though physically this should depend on the fluid's state. It is therefore possible to complete the coupling between the arc discharge and the fluid by charging the capacitor up to the "real" breakdown voltage computed from the fluid in the inter-electrodes space. In addition to rendering the discharge model more realistic, this will enable the comparison of the simulated breakdown voltage in periodic regime with experimentally obtained data.

An experimental law of breakdown voltage through the air gap between the electrodes versus air density has been determined in [20]. Breakdown voltage is then given by :

$V_{breakdown} = A\rho l + B\sqrt{\rho l}$,

ρ being the gas density between electrodes, l the length of the air gap (2 mm in our case), A and B two constants equal respectively to 1.4785×10^5 and 1.2882×10^5.

This simulation has been carried out using a converging geometry (conical with a 45° half angle, see figure 4.15a, while limiting the maximum breakdown voltage to 3.5 kV. The reason for this is the seemingly non-physical overheating of the gap for higher voltages, with temperatures locally exceeding 60000 K. This is probably linked to the simplified energy deposition used in the model. Hence, in order to ensure a realistic arc discharge is obtained, voltage is expected to drop below this threshold once periodic regime is reached.

Simulations of the quasi-static behavior show an almost constant breakdown voltage of 3250 V, which corresponds to 9.2 mJ of electric energy deposited in the cavity and $7.74\,\mu g$ of fluid expelled per pulse. These

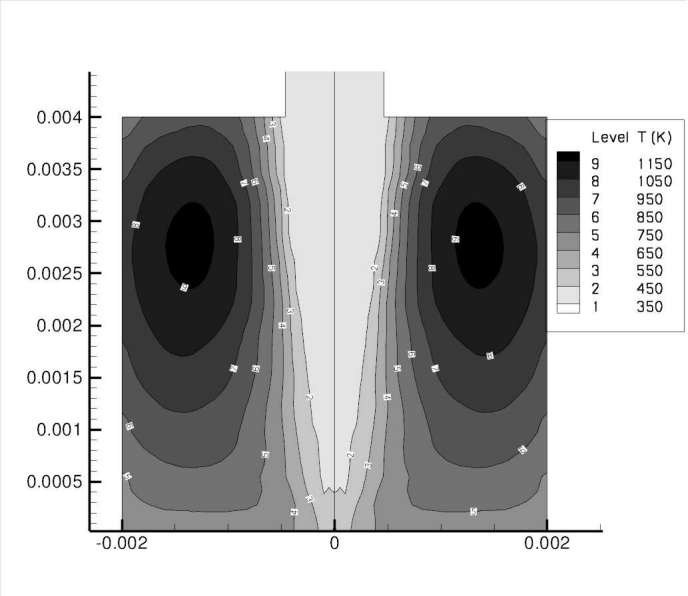

Figure 4.11: Quasi-static temperature distribution right before the next pulse (non-converging neck)

values cannot be directly compared to those given in section 4.3.2 though, since geometries are different. This explains the more favorable mass balance in this case, see section 4.3.5.
Interestingly, initial voltage in the capacitor can be easily and accurately measured experimentally. Therefore, this allows us to obtain an estimation of the density in the cavity and to compare experimental breakdown voltages with our model. In [20], the author shows that at an operating frequency of 1 kHz and using a 15 nF capacitor, breakdown voltage in periodic regime is established at 3.1 kV. This value is really close to the one we obtained, and might allow us to fine tune the energy deposition phase.

4.3.4 Validation - Experimental Comparison

The results of the numerical modeling of the actuator have been validated against experimental studies from the ONERA's work on the Plasma synthetic jet actuator as well as John Hopkins University's one[21, 22, 20]. Temperature magnitudes of the jet are in close agreement with the experimental results, for similar operation regimes. The experiments demonstrate maximum velocities smaller to the ones computed by the numerical model. This difference can be explained by the neglected turbulent features of the jet flow, that lead to increased velocities and also to the sensitivity of the experimental methods. Nevertheless, the higher values observed in the simulations, occur inside the core of the jet while the tip velocity of the jet agrees with the experimental values of [20]. The flow field inside the cavity remains a big problem for experimental investigation due to the high temperatures occurring there. The toroidal vortices and the arrow shape of the jet, have been experimentally observed in various studies of synthetic jet actuators [20, 17]. Moreover, in [22], the generation of a vortex structure due to the actuation of the plasma synthetic jet and its interaction with an external subsonic flow has been demonstrated experimentally. This experiment will be used as baseline for the CFD calculations in the last chapter.

4.3.5 Parametric study

In this section, a qualitative study of the influence of several parameters on both energy deposition and cavity geometry will be presented. Each point of these graphs correspond to different sets of parameters and different simulations. These parameters were chosen around a reference actuator, composed of a 15 nF capacitor operating at 1 kHz, with a cavity ended by a cylindrical neck 1 mm wide. It should be kept in mind that because of the inaccuracy of the energy deposition phase (energy loss in sheaths and constant breakdown voltage), only qualitative differences between the different configurations are intended to be presented.

Influence of electric supply circuit characteristics

In this section, fluid variables were averaged over the cavity, nozzle excluded. Mean velocities given here have also been computed on a longer propagation length (2 cm ahead of the actuator, instead of 0.5 cm earlier), hence the slower velocities. Therefore, some discrepancies with earlier results, however slight, may be observed. Qualitative trends shown on each graph are self-consistent though.

Operating frequency

The behavior of the actuator for several operating frequencies seems physically correct (figure 4.12) : qualitatively we observe that, the higher the frequency, the hotter the cavity and the less mass is expelled (because of the less efficient refill). This remark has to be moderated though : as mentioned earlier, breakdown voltage is fixed in these simulations, and thus the capacitor always stores the same amount of energy. Experimentally, the actuator should deposit less and less energy as the cavity gets hotter, and so would not reach the extreme temperature of the figure 4.12 at 4 kHz. As for the jet velocity, it stays in the order of 90 $m.s^{-1}$ for frequencies up to 1 kHz, and then sharply decreases at 4 kHz (a tendency which has been observed experimentally for the actuator, [20]). This might be explained by a "saturation" of the actuator, which does not get refilled long enough to sustain a jet at this frequency. For that matter, the actuator is known not to be able to function properly at such a high frequencies, mainly because of overheating of the cavity.

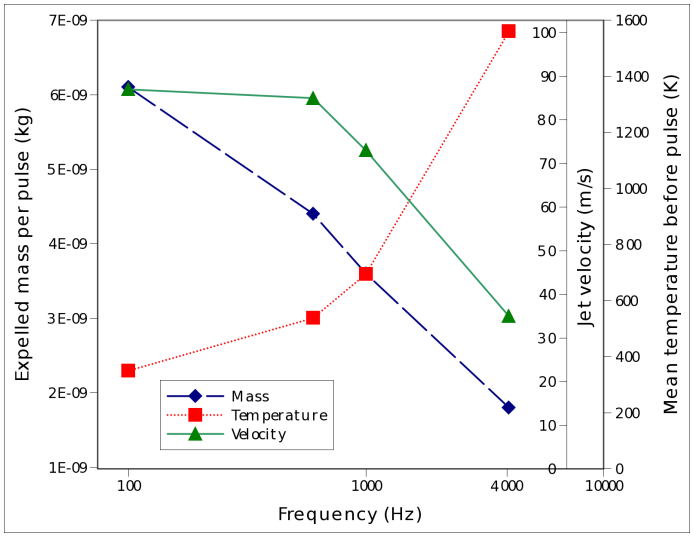

Figure 4.12: Influence of operating frequency on expelled mass, fluid temperature and jet velocity

Capacity

The same study was carried for various capacitors used in the power supply (directly proportional to the stored energy). Results are plotted on figure 4.13. Expelled mass is remarkably linear with the capacitance, more mass being carried with the jet for more energetic sparks. As for temperature and velocity, these logically increase with the energy of the discharge. It would however be tendentious to extract more information (for instance about the velocity gain between two cases) than this global behavior since data have been heavily averaged and energy deposition modeling still needs improvement.

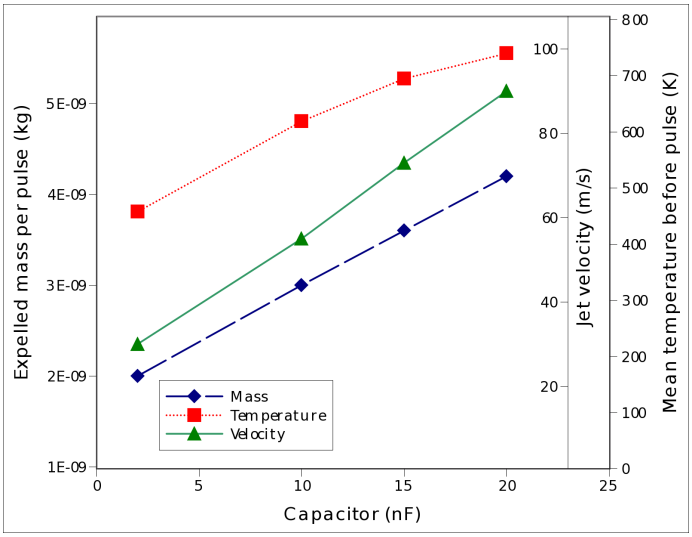

Figure 4.13: Influence of the capacitor on expelled mass, fluid temperature and jet velocity

Influence of actuator geometry

Simulations in this section are done for several geometries of the cavity's neck. It has to be reminded that since our fluid is ideal, results have to be analyzed cautiously, especially because of missing boundary layer effects which would be significant for tighter geometries. Therefore, the neck will always be kept wider than 1 mm (a common experimental size).

Neck radius

Figure 4.14 shows an interesting behavior : as might be expected, expelled mass increases and temperature decreases with wider openings. This is easily explained by a more efficient refill of the cavity and quicker exchanges of thermal energy with the external flow. However, jet velocity decreases when a wider neck is used. It is probably the result of the less intense pressure gradient at the neck, expelling mass in way that is rather blob-like than jet-like. This would need to be compared against experimental data though.

Neck shape

In this section, the importance of the geometrical shape of the neck will be demonstrated. As shown in figure 4.15a, both the cavity and top section of the neck are kept identical, while a tapered cone is introduced in-between. Three different half cone angle were used for this converging section : 90° (no cone), 45° and 27° (designated respectively by Cyl, Col45 and Col27 on figure 4.15b). Arguably, this introduces a variation in the volume of the cavity. However, with this geometry corners are completely avoided and a different

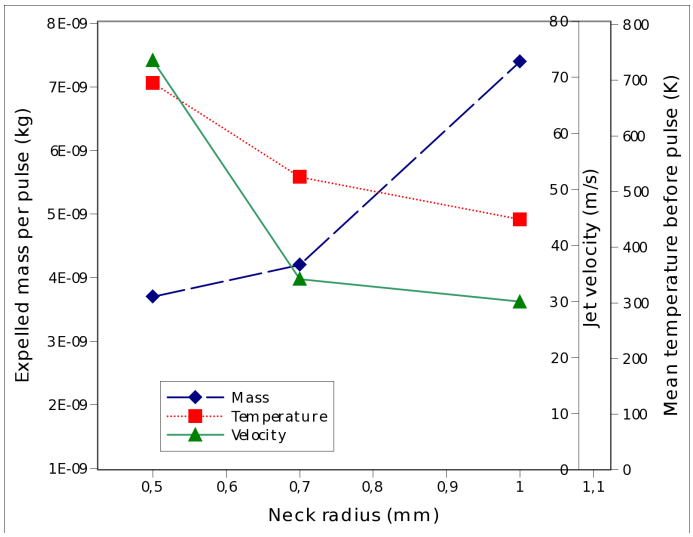

Figure 4.14: Influence of neck radius on expelled mass, fluid temperature and jet velocity

thermal distribution is established (compared to the one in section 4.3.2). Furthermore a more efficient refill mechanism can be observed, even if the top section of the cavity stays the unchanged.

On the contrary to preceding plots, synthetic data here were integrated over the whole cavity, neck included. Thus, total ejected mass will be larger in this case.

Even if the cavity volume changes slightly, figure 4.15 shows that, with the same entry section, the refill is much more efficient in the case of converging cavity shape. However, surprisingly, the mean temperature in the cavity is hotter with the two converging shapes : it reaches a value of 1200 K for the most acute cone, 1050 K for the other converging shape and 930 K in the non-converging case (figures not presented). Quasi-static heat distribution in the cavity is also radically different (figure 4.16a, compared to 4.11b). It is seen on simulations that while heating of the gas assumes roughly the same shape as before during the first pulses (annular shape close to the cylindrical neck), the narrowing of the neck causes the two sides of this zone to “connect” on the axis (figure 4.16a). Heat builds-up uniformly under this radial plane and ends up forming a piston-like mechanism visible both on temperature and density distribution : filling of the cavity with cold gas does not happen anymore along the axis (figure 4.16b) but all over the section of the cavity. Because of this “piston” effect, cooling of the cavity with exterior fluid seems not to affect the hot gas on the axis directly anymore, which then stays as far as possible from cavity walls, where convective heat transfers still occur.

The mechanism seen here is an interesting behavior which could not be seen if the arc energy were introduced uniformly. Thus, it is a unique feature of our model. Still, this mechanism would need support from experimental evidence, with for instance several mean temperature profiles for different cavity shapes, which could confirm an higher global temperature in the case of a converging shape.

4.3.6 Aerodynamic study

The modeling of the PSJ actuator and its effects on flow control applications include time and space scales so different that a unified coupled approach proves to be almost impossible in terms of CPU time. Thus, having verified the numerical model and its capacitance to describe the arc discharge and the consequent synthetic jet

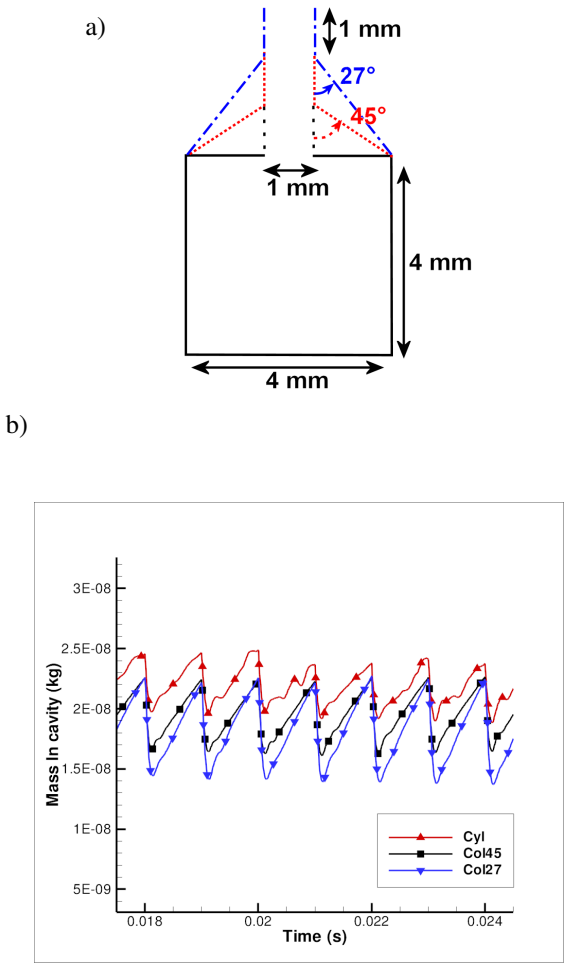

Figure 4.15: a) Studied geometries of the cavity and b) Ejected mass in periodic regime for three neck shapes.

formation, data can be extracted and imported into a CFD solver for further simulations. This coupling has been performed in CEDRE® (ONERA's house-built CFD solver) via source terms in the compressible N-S equations. The momentum and energy source terms have been averaged in 100 μs, extracted from the PSJ simulation of the reference actuator (with operation conditions of $f = 1kHz, C = 15nF$ and a $1mm$ diameter of the orifice), and interpolated into a 3D mesh over a flat plate, created in ICEM®. In figures 4.17 and 4.18, the simulation domain as well as a the generated mesh, (properly refined near the boundary layer to capture the turbulent parameters as well as near the PSJ actuation zone) are presented. The choice of a flat plate has been made in order to validate our results with experimental ones in similar configurations mainly provided by EU's PLASMAERO project.

Before the presentation of some preliminary results of the CFD coupling, it is essential to understand how a jet flow crossing an external one, can have positive aerodynamic effects on an aircraft's performance.

a)

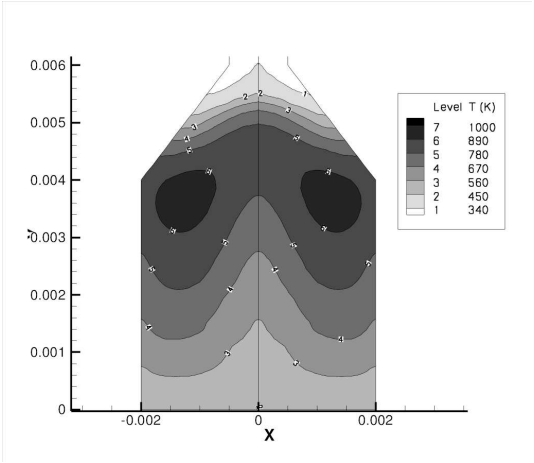

b)

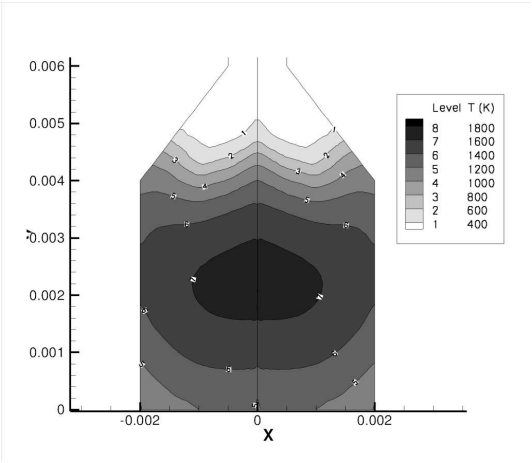

Figure 4.16: Quasi-static temperature distribution(converging neck): a) 6th pulse(transition between the two temperature distributions) and b) 25th pulse

The jet cross flow is a well known flow, both experimentally and numerically, that we meet in numerous applications today[23, 24]. In aerospace applications though the most important aspect of such flows is the instabilities that the jet flow(of velocity comparable to the free-stream one or even higher) introduces into the main fluid flow. These instabilities are related to the vortex-sheet structures that occur due to the interaction of the two flows. These vortices can either provoke the laminar to turbulent transition of the flow's boundary layer or create, due to the unsteady actuation mode[25], flow patterns that can enhance the mixing of the fluid(combustion applications) or cancel already existing vortices (i.e.the wing tip ones for external

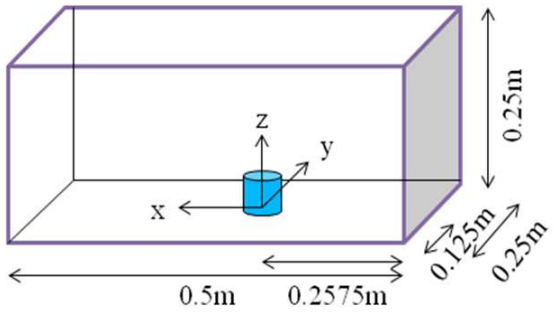

Figure 4.17: Simulation domain for the flat plate

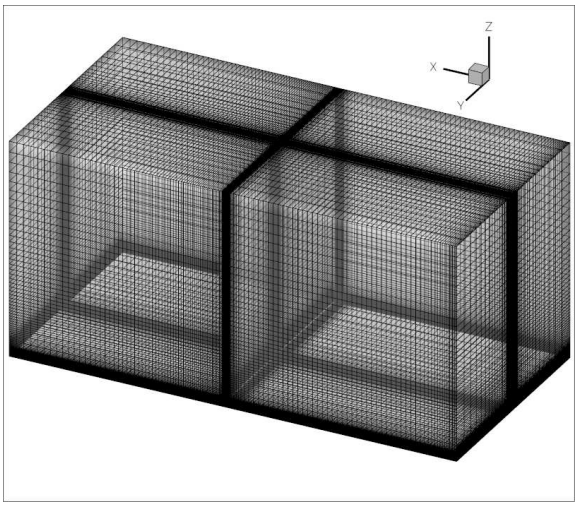

Figure 4.18: The 3D mesh

aerodynamics of aircrafts). A typical flow pattern in the wake of the jet-main flow interaction can be seen in figure 4.19, as reported in various publications[26, 27, 28].

Simulations without an external flow, verified the good integration of the source terms inside the numerical domain. Calculations with more refined meshes, high-marked the importance of a well refined zone around the jet - meshes that will be used for further and more precise simulations. Moving forward with a more realistic case, the full simulation of the PSJ interacting with an external flow of 40m/s, resulting in a Reynolds number of 2.67×10^6, has been considered.

This baseline simulation case has been chosen so that we can compare and validate qualitatively the results with similar experiments performed in [22]. There, a flat plate model with an embedded plasma synthetic jet and under the same external conditions as the simulation, has been studied. The 3- component PIV technique has been implemented to characterize the vortex by using phase-shifting time-average measurements. In figures 4.21 and 4.22 , the results at a distance of 40 mm after the actuator and in the direction of the flow, are presented. These results correspond to a capacitor value of 20 nF mounted into a RC circuit, a frequency of 10 Hz and a fully turbulent boundary layer(tripped). The values of the pitch α and skew β angles for the jet

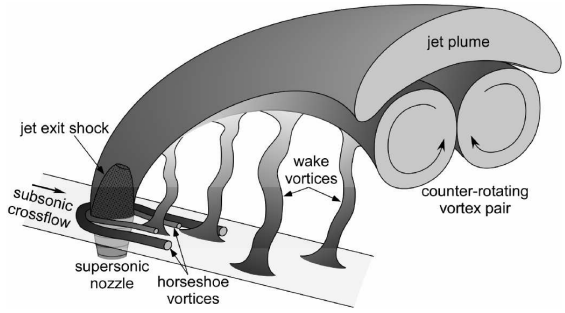

Figure 4.19: Flow structure of a symmetric jet cross flow

exhaust were fixed at 30 and 60 degrees respectively (see figure 4.20). The formation of a vortex around the axis of the main flow is clearly visible in the PIV results that elevates and propagates into the flow field.

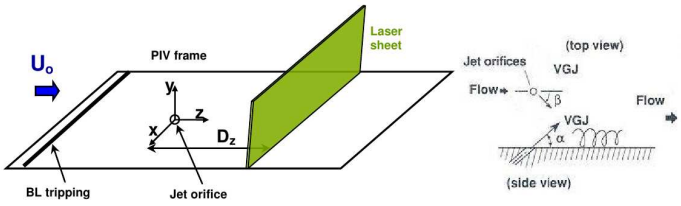

Figure 4.20: The experimental configuration for the PIV measurements [22].

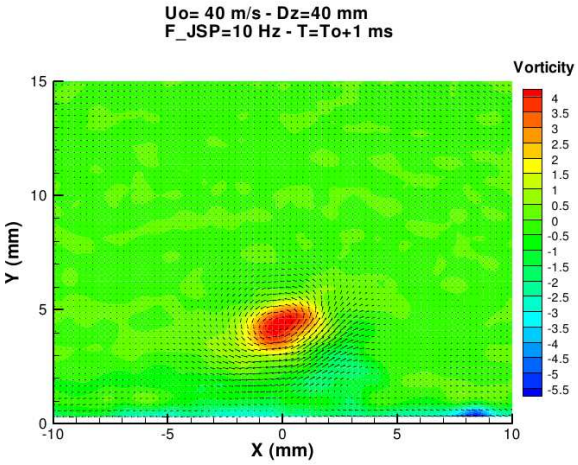

Figure 4.21: Vorticity vectors and contours, 1 ms after the actuation of the sparkjet - PIV measurements [22].

The numerical simulation of a similar case could give some basic details on the validity of our model, at least concerning the aspect of vortex creation due to the interaction of the jet with the external flow.

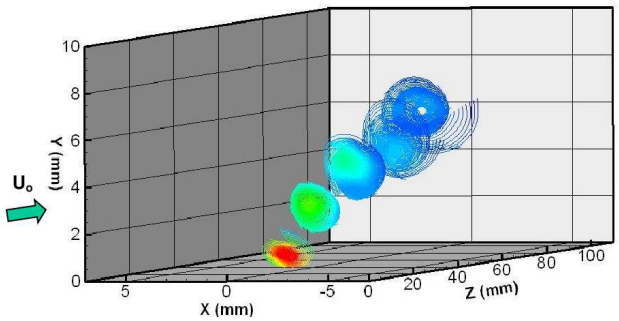

Figure 4.22: Vortex locations - PIV measurements [22].

Quantitative comparison between the simulation and the experiments is not yet possible due to the different operational regimes.

Firstly, a converged solution of the flow over the flat plate has been achieved, verified by the agreement of the boundary layer thickness given by Blasius for a fully turbulent boundary layer under the same inlet conditions and the simulation's one (value of around 1.1 mm, at a distance of 0.5 m after the leading edge of the plate). The turbulent model used was the k-ω one, with a turbulent wall-model addition.

The turbulent kinetic energy as well as the specific dissipation rate have been initialized considering fully turbulent flow in the whole domain.

When the PSJ actuator is "plugged in" the simulation, two parallel and counter rotating around the z-axis vortices of high intensity are clearly captured, created by the jet formation and its interaction with the main flow - vortices that travel in the x-direction with the flow (see 4.23 and 4.24). Besides these two vortices though, the appearance of another set of vortices can be noticed, elevated from the flat plate, not that intense and rotating around the y axis while they also propagate in the x-direction. These pairs of vortices agree well with well-studied flow fields around a cylinder normal to the main flow, where the flow swirls around the cylindrical object and similar pairs of vortices occur (as mentioned above).

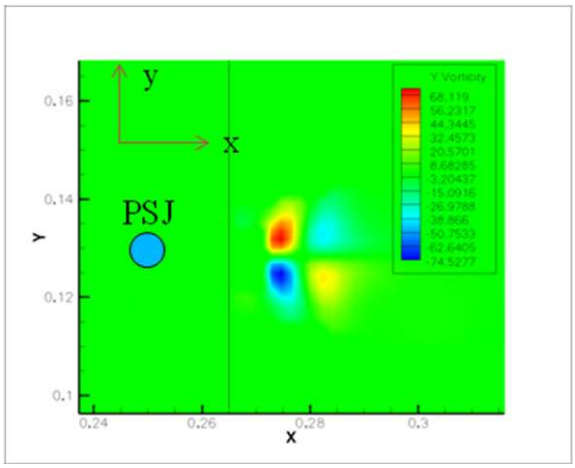

Figure 4.23: Contours of y-vorticity - t=To + 70 μs

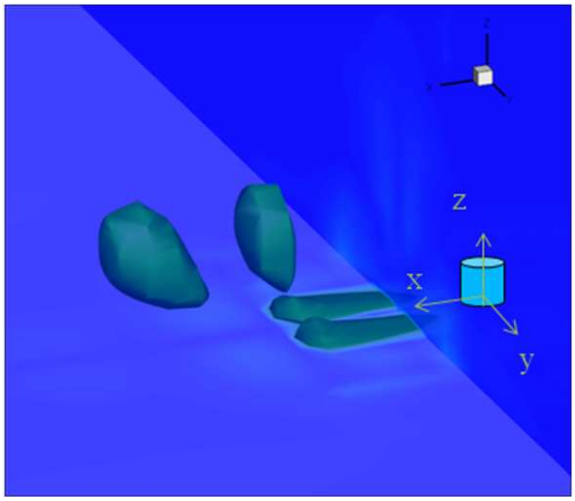

Figure 4.24: Iso-surfaces of vorticity magnitude - t=To + 70 μs

The results obtained from the PSJ-CFD coupling, indicate that further simulations should be performed and compared with experimental results. Even if these results do not describe in full extend the real problem, they are nevertheless a qualitative proof for the validity of the coupled approach.

More detailed and accurate simulations will include a full flat plate study with an inclined actuator(on z and y axis), and the effects of the vortices and subsequent turbulence on the laminar to turbulent transition and reattachment of a detached flow.

4.4 Conclusion - Perspectives

The Plasma Synthetic Jet actuator has been numerically investigated by 2 models: One describing the hydrodynamics of the short-living relatively hot gas bubble resulting from the arc discharge, and one coupling it via a Joule heating source term with the Euler equations, under some simplifying hypotheses. Parametric studies on the geometrical aspects of the actuator as well as its electrical inputs have been performed, improving its operation and efficiency, and resulting in a quasi-periodic pulsed regime. Furthermore, from this converged regime, momentum and energy source terms have been extracted and coupled into CEDRE (ONERA's CFD code).

The results obtained in this chapter are promising for the optimization of the PSJ and the better understanding of the mechanisms that limit its performance. We have seen that the jet's velocity is decreased with increasing frequency of operation while the increase of the capacitance leads to an increase of the expelled jet's velocity. The cavity's shape has also a big influence on the jet's velocity and expelled mass : Larger neck radius lead to increased expelled mass and decreased jet's velocity. The converging section shape of the neck has an important effect on the temperature distribution inside the cavity, being more uniformly distributed for a cone angled shape, and thus the refilling of the cavity is more efficient. An illustrative example of a 3D model of a flat plate with a free-stream velocity of 40 $m.s^{-1}$, demonstrate the effect of the PSJ, as vortices form and propagate in the direction of the flow, consistently with classic cross-jet flows.

The PSJ solver can be improved mostly in terms of the arc description, although the simplified approach that has been used provides quite accurate results without the need of an extensive description of the arc plasma physics and thus with a reduced computational cost. This has been demonstrated by the work of the researchers at DMAE, ONERA, Toulouse who have performed three dimensional LES simulations of the PSJ operation embedded in a flat plate [29], using the source term provided by the PSJ solver of DTIM (transformed in three dimension). They have integrated a real-gas solver in CEDRE, and used an explicit Runge-Kunta 2 scheme of temporal integration and a Roe scheme for the fluxes. The subgrid-scale model for the LES was the one of Smagorinsky. In figure 4.25, the computational mesh in different views is shown.

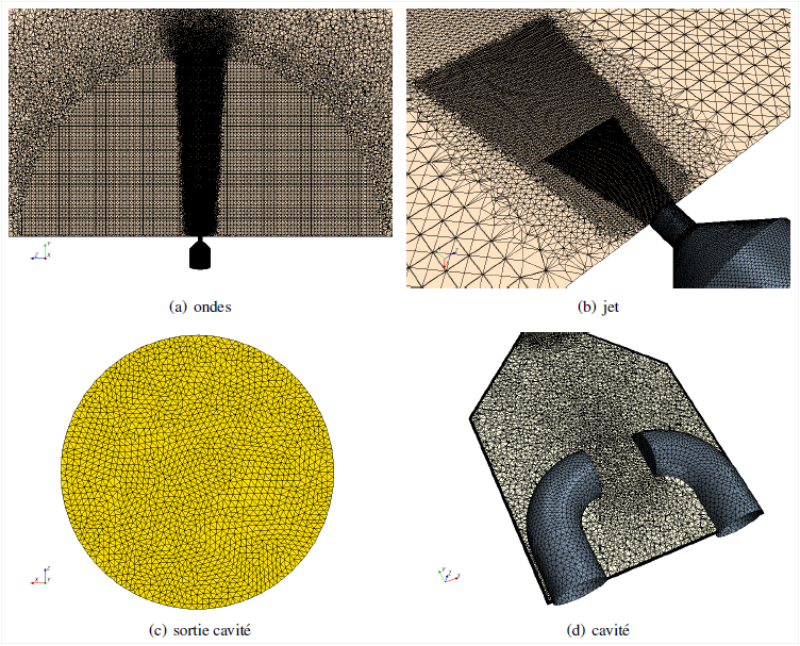

Figure 4.25: Computational mesh for the PSJ operation [29]. a) Whole domain b) Jet c) Cavity's exit d) Cavity.

These refined calculations demonstrate the complex nature of the PSJ operation, from the development inside the cavity due to the arc discharge till its expulsion and turbulent interaction with the nozzle's lips and external development. In figure 4.26, temperature and pressure contours inside the cavity are shown at initial times. In figure 4.27, energy iso-surfaces colored by axial velocity and mass gradient iso-contours outside the cavity are shown at further times.

The results on the jet's velocity, compared with a square function source term in time and experimental measurements, is shown in figure 4.28. The instationary effects which are taken into account with the PSJ solver, provide results that are in very good agreement with the experimental ones. This, validates the model and the coupled approach in a certain extend.

Taking into account radiation and conduction effects as thermal effects can lead to a more precise description of the jet. Moreover, future developments shall include validation of the CFD - LES model, longer simulations over more than one pulsations, and flow control simulation taking into account external flows.

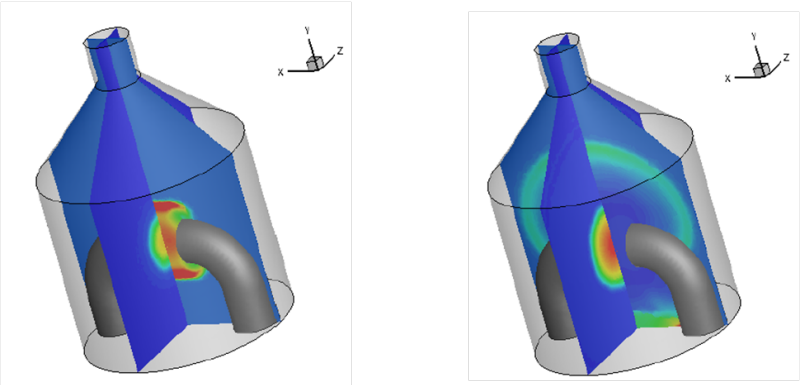

Figure 4.26: Temperature (zy plane) and pressure (xy plane) contours inside the cavity at times of 1 and 4 μ s. [29].

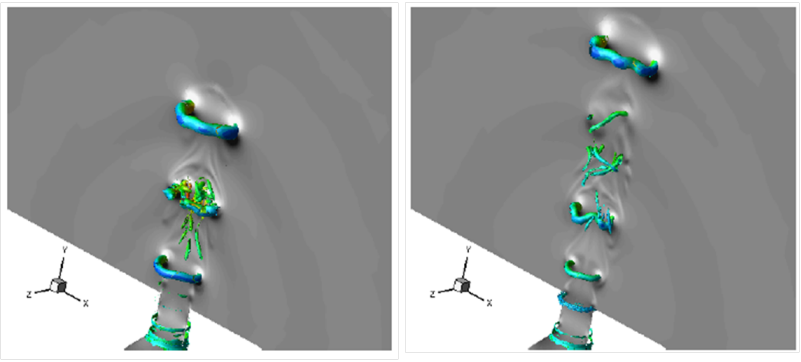

Figure 4.27: Energy iso-surfaces colored by axial velocity and mass gradient iso-contours at times of 70 (left) and 130 (right) ns [29].

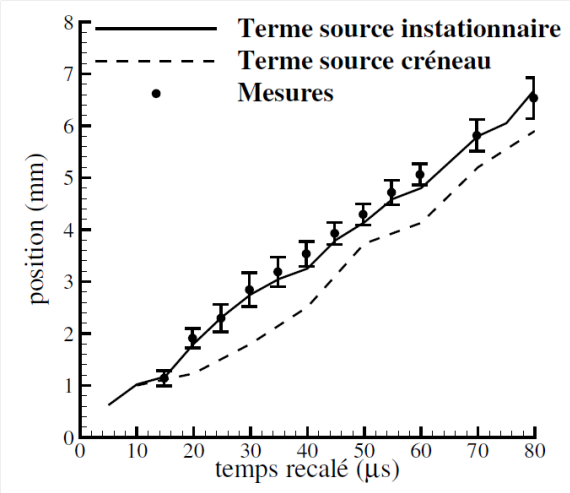

Figure 4.28: Jet's front position versus time [29]. Full line : Instationary source term. Dotted line : Square function source term. Dots : Experimental measurements

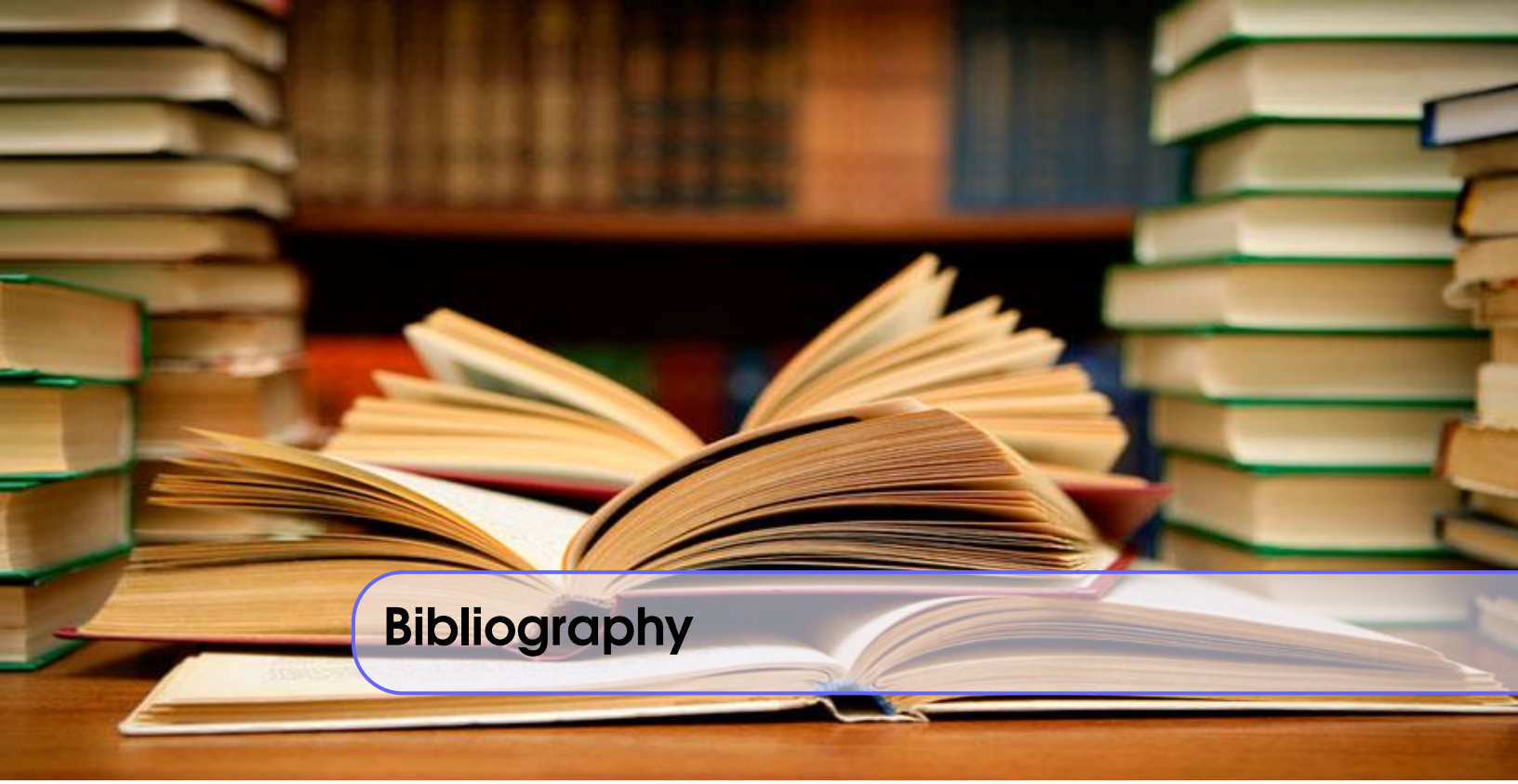

Bibliography

[1] KR Grossman, BZ Cybyk, and DM VanWie. “Sparkjet actuators for flow control”. In: *AIAA Paper* 57 (2003), page 2003.

[2] Bohdan Z Cybyk et al. “Computational assessment of the sparkjet flow control actuator”. In: *AIAA Paper* 2003-3711 (2003).

[3] Daniel Caruana et al. “The “plasma synthetic jet” actuator. aero-thermodynamic characterization and first flow control applications”. In: *AIAA* 1307 (2009), page 2009.

[4] Venkat Narayanaswamy et al. “Investigation of plasma-generated jets for supersonic flow control”. In: *46th AIAA Aerospace Sciences Meeting and Exhibit*. 2008, pages 2008–285.

[5] Sarah J Haack et al. “Development of an analytical sparkjet model”. In: *5th Flow Control Conference*. 2010, pages 28–1.

[6] KR Grossman et al. “Characterization of sparkjet actuators for flow control”. In: *AIAA Paper* 89 (2004), page 2004.

[7] Kellie Anderson and Doyle D Knight. “Characterization of Single Pulse of Plasma Jet”. In: *AIAA, 2012 - 0188* (2012).

[8] Guillaume Dufour et al. “Physics and models for plasma synthetic jets”. In: *International Journal of Aerodynamics* 3.1 (2013), pages 47–70.

[9] Pierre Fauchais. “Plasmas thermiques: aspects fondamentaux”. In: *Techniques de l’ingénieur. Génie électrique* 3.D2810 (2005).

[10] M Capitelli et al. “Transport properties of high temperature air in local thermodynamic equilibrium”. In: *The European Physical Journal D-Atomic, Molecular, Optical and Plasma Physics* 11.2 (2000), pages 279–289.

[11] Roland Edward Meyerott, J Sokoloff, and RW Nicholls. *Absorption coefficients of air*. Technical report. DTIC Document, 1960.

[12] Christopher L Rumsey. “Proceedings of the 2004 Workshop on CFD Validation of Synthetic Jets and Turbulent Separation Control”. In: (2007).

[13] Declan Hayes-McCoy and Xi Jiang. “Direct computation of zero-net-mass-flux synthetic jets”. In: (2007).

[14] Declan Hayes-McCoy. “Direct computations of a synthetic jet actuator”. In: (2012).

[15] Gaetano Maria Di Cicca et al. “Near Field Study of a Synthetic Jet”. In: *laser* 2000 (2004), page 2.

[16] David Durán and Omar D López. “Computational Modeling of Synthetic Jets”. In: *Mechanical Engineering Thesis* (2010).

[17] Michael et al. Mueller. “Flow structure and performance of axisymmetric synthetic jets”. In: *AIAA 2001-1008* (2001).

[18] Y Cressault et al. “Influence of metallic vapours on the properties of air thermal plasmas”. In: *Plasma Sources Science and Technology* 17.3 (2008), page 035016.

[19] A. Belinger. “Alimentations électriques et étude énergétique d’un gènèrateur de jets synthètiques á plasma”. PhD thesis. Université de Toulouse, 2011.

[20] Pierrick Hardy. “Etude et qualification aérothermodynamique et électrique d’un actionneur plasma de type jet”. PhD thesis. Toulouse, ISAE, 2012.

[21] Sarah H Popkin, Trent M Taylor, and Bohdan Z Cybyk. “Development and Application of the SparkJet Actuator for High-Speed Flow Control”. In: *Johns Hopkins APL technical digest* 32.1 (2013), pages 404–418.

[22] Daniel Caruana. “The Plasma Synthetic Jet Actuator for Separation Control”. In: *ERCOFTAC Bulletin* 94 (2013).

[23] Sergio LV Coelho and JCR Hunt. “The dynamics of the near field of strong jets in crossflows”. In: *Journal of Fluid Mechanics* 200 (1989), pages 95–120.

[24] Suman Muppidi and Krishnan Mahesh. “Direct numerical simulation of round turbulent jets in crossflow”. In: *Journal of Fluid Mechanics* 574 (2007), pages 59–84.

[25] David Greenblatt and Israel J Wygnanski. “The control of flow separation by periodic excitation”. In: *Progress in Aerospace Sciences* 36.7 (2000), pages 487–545.

[26] Steven J Beresh et al. “Vortex structure produced by a laterally inclined supersonic jet in transonic crossflow”. In: *Journal of propulsion and power* 23.2 (2007), pages 353–363.

[27] Richard J Margason. “Fifty years of jet in cross flow research”. In: *In AGARD, Computational and Experimental Assessment of Jets in Cross Flow 41 p (SEE N94-28003 07-34)*. Volume 1. 1993.

[28] TF Fric and A Roshko. “Vortical structure in the wake of a transverse jet”. In: *Journal of Fluid Mechanics* 279 (1994), pages 1–47.

[29] F. Chedevergne. “Simulations LES d’un jet synthetique plasma”. In: *Technical report* 1/21098 (2013).

Conclusions Générales

La simulation numérique des actionneurs plasma est un domaine d'étude très riche, qui intègre des physiques différents et des interactions complexes. La nature multi-physique, multi-échelle des actionneurs plasma pose des problèmes numériques difficiles. Des modèles physiques simplifiés sont donc nécessaires ainsi que des méthodes numériques performantes. En outre, les modèles physiques eux-mêmes doivent être adaptés pour chaque type de plasma étudié. Ces modèles, bien que simplifiés, peuvent fournir des informations importantes sur la physique impliquée.

Pour les décharges micro-ondes, nous avons vu que des simulations en trois dimensions sont essentielles pour une description précise de la dynamique du plasma. Ces simulations sont coûteuses par rapport au temps de calcul, et les modèles couplés de manière implicite offrent une solution vers une représentation plus précise et raffiné de l'évolution du plasma. Les effets de chauffage du gaz ne peuvent pas être négligés (sauf pour les premiers temps) en raison de la forte dépendance de l'évolution du plasma sur la densité du gaz . Le solveur numérique développé, peut être utilisé pour calculer des aspects importants de ces décharges, tels que le taux d'absorption de l'énergie et le volume du plasma, qui sont essentiels pour calibrer et étudier le dépôt d'énergie d'un actionneur microondes.

L'actionneur DBD a été étudiée en utilisant deux schémas numériques afin de valider la capacité du modèle de reproduire le vent ionique et de le comparer avec les résultats expérimentaux. Diverses études paramétriques ont été effectuées, montrant une bonne concordance entre les résultats obtenus et les observations et mesures expérimentales. Des simulations CFD, en utilisant la force du corps calculé à partir des solveurs DBD, ont également été réalisées, démontrant l'importance de la turbulence pour reproduire correctement les mesures expérimentales. Des applications de base de contrôle d'écoulement ont été étudiés, démontrant les effets possibles de l'actionneur su la transition laminaire - turbulent et l'amélioration de la portance.

Pour l'actionneur jet synthétique plasma (JSP), notre travail a montré que le modèle basé sur les équations

(EMHD) électro-magnéto-hydrodynamique et l'hypothèse LTE (équilibre thermodynamique local) en tenant compte des effets de gaz réel et un circuit électrique équivalent, décrit assez bien le transfer de l'énergie de l'arc au gaz. Des études paramétriques ont montré l'influence des paramètres opérationnels et géométriques sur le fonctionnement et l'optimisation de l'actionneur. Les simulations effectuées ont montré la capacité de l'approche couplée à reproduire les résultats expérimentaux. Ces deux dernières solveurs, pour le DBD et le PSJ, peuvent être utilisés pour de calculs CFD plus complexes (après la validation nécessaire bien sûr) ou pour leur optimisation.

La procédure numérique cependant, doit être validé par des expériences. Comme les ressources de calcul restreint les calculs, les modèles physiques sont simplifiées et les schémas numériques introduisent des erreurs numériques dans les solutions. La puissance et la vitesse du calcul de futurs ordinateurs, va sûrement rendre de simulations plus complexes possibles - de simulations qui peuvent fournir des informations de base ainsi que les résultats appliqués sur la capacité d'actionneurs plasma à modifier positivement l'aérodynamique d'un avion.

D'un point de vue plus général, ce travail s'est réalisé dans un environnement multidisciplinaire qui comprend la physique des plasmas, la dynamique des fluides, l'électromagnétisme et les mathématiques appliquées. La nécessité de comprendre le comportement et le fonctionnement des actionneurs de plasma, oblige les communautés de recherche de ces domaines à se réunir, complétant le cercle des connaissances nécessaires, sur le chemin de l'objectif principal: l'amélioration de l'avionique commerciale, en termes d'efficacité, de coût et d'impact environnemental dans un monde où le transport rapide et sûr est un moyen d'échange d'informations, de connaissances et de cultures, plutôt qu'un privilège.

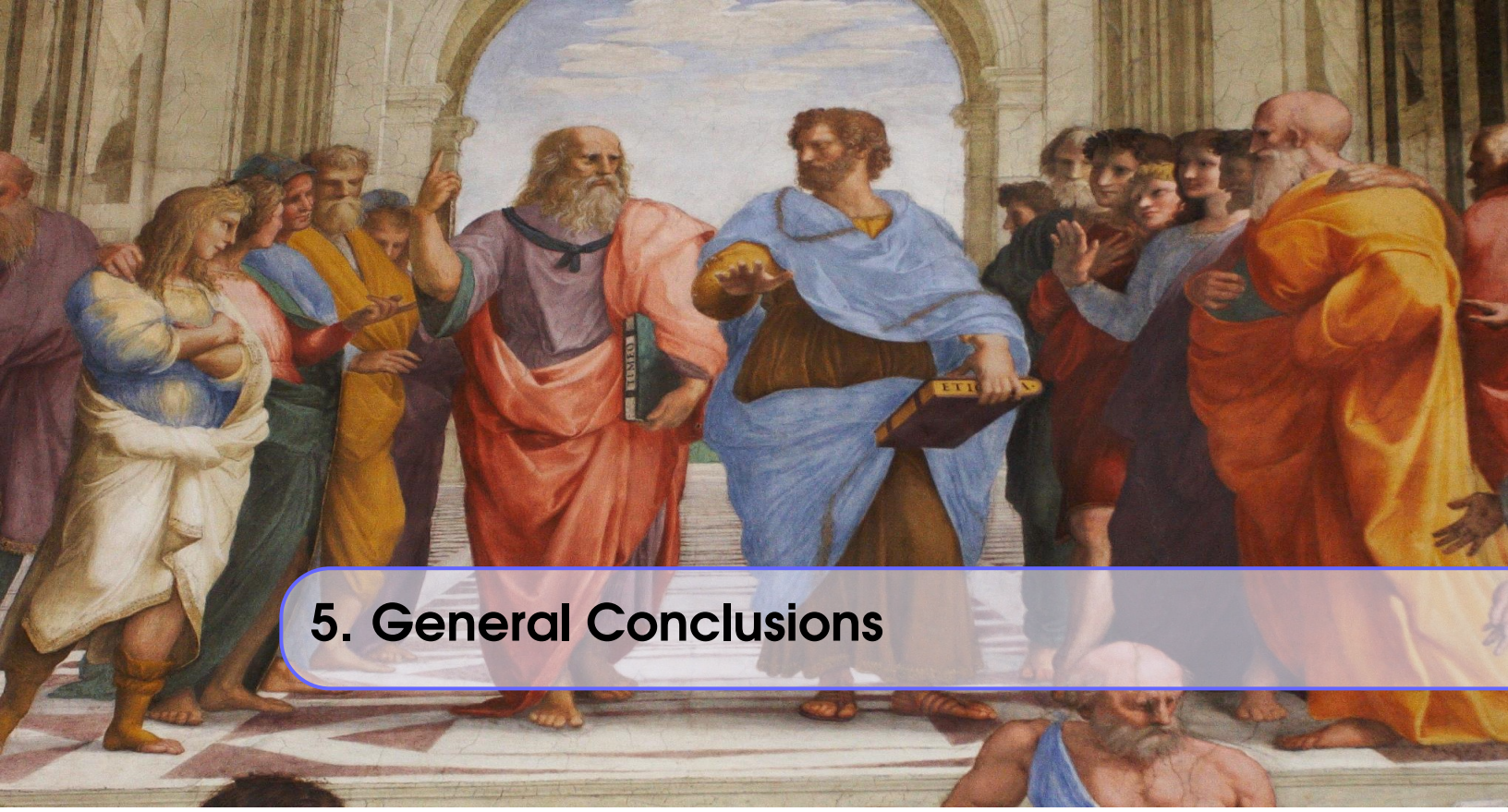

5. General Conclusions

The aerospace world is a continuously evolving world, where the search for innovations and research breakthroughs is constant. In the domain of aerodynamics, flow control has been proven to be a major factor for advancing towards more efficient engineering projects as well as for surpassing barriers that limit our ability for faster, cleaner and safer flights. In this thesis, we have dealt with a novel approach for aerodynamic flow control applications that refer to plasma actuators and the numerical simulation of such. Plasma actuators provide advantages compared to classic flow control mechanisms. They can provide real-time control due to their high frequency of operation. They lack mechanical parts and their fabrication is relatively simple. Some of them can be highly energetic and others can be easily embedded on an aerodynamic body. Despite these advantages though, each different kind of plasma actuator has its own drawbacks or it is not yet well studied - understood. As experimental results are either difficult or expensive to perform, numerical simulations can provide important information on the plasma itself, the underlying physics as well as the ability of such actuators as flow control mechanisms.

As we have seen in this thesis, the numerical simulation of plasma actuators is a highly demanding field, that integrates different physics and complex interactions. The multi-physics, multi-scales nature of plasma actuators poses challenging numerical problems. Despite this fact, simplified physical models can be numerically resolved efficiently with the use of adapted numerical methods. In addition, the physical models themselves need to be adapted for each different kind of plasma studied. These models, although simplified, can provide important information about the physics involved. For microwave discharges, we have seen than three-dimensional simulations are essential for an accurate description of the plasma dynamics. Such simulations are costly with respect to computational time, so implicit coupled models such as the one developed and presented (an Alternative Direction Implicit (ADI) - FDTD scheme coupled with a simplified plasma-fluid model), provide a solution towards more precise and refined representation of the plasma evolution. Moreover, as demonstrated with a coupling approach between the EM-plasma solver and an Euler-real gas one, the effects of gas heating can not be neglected (except for early times) because of the strong dependence of the plasma development on the gas density. The numerical solver can be used in order

to calculate important aspects of such discharges, such as energy absorption rate and volume occupation, that are essential in order to calibrate and investigate aerodynamic flow control possibilities based on energy deposition. The DBD actuator has been studied using two numerical schemes based on the same physical model (which is based on a drift-diffusion and the Poisson equation and performs quite well regarding body force prediction) in order to validate the model's ability of reproducing the ionic wind and compare it with experimental results. Various parametric studies have been performed, showing good agreement of the obtained results to experimental observations and measurements. CFD simulations, using the calculated body force from the DBD solvers, have also been performed, demonstrating the importance of turbulence in order to properly reproduce experimental measurements of velocity profiles over a flat plate and basic flow control applications have been studied, demonstrating some possible effects of the actuator's induced flow on laminar to turbulent transition and lift enhancement. For the Plasma Synthetic Jet (PSJ) actuator, our work showed that a model based on the electro-magneto-hydrodynamic (EMHD) equations and the L.T.E. (local thermodynamic equilibrium) assumption taking into account real gas effects and an equivalent electric circuit providing the time dependent source terms for the EMHD system, describe quite well the energy transformation from the arc to the gas. Parametric studies has shown the influence of operational and geometrical parameters on the operation and optimization of the actuator, with regard to jet's formation its three-stage function. The simulations performed demonstrated the ability of the coupled approach to reproduce experimental results quite well. Both of these last solvers, for the DBD and the PSJ actuator, can be used for more complex CFD calculations (after the necessary validation of course) or optimization purposes.

The numerical procedure though, is still obliged to be validated by experiments. As the computational resources restricts the calculations, the physical models are simplified and the numerical schemes introduce numerical error in the solutions. Thus, as we move forward, step by step, in more complex models and schemes of higher accuracy, experiments need to be conducted in order to provide the necessary for validation data. The computational power and speed of future computers, will surely make more complex simulations possible - simulations that can provide basic insights as well as fast applied results of the ability of plasma actuators to positively modify the aerodynamics of an aircraft.

In a more generic point of view, the research linked to this thesis is incorporated into a multi-disciplinary environment that includes plasma physics, fluid dynamics, electromagnetics and applied mathematics - numerical analysis. The need of understanding the behavior and operation of plasma actuators, forces the research communities of such broadband domains to come together, completing the circle of necessary knowledge, on the way for the main objective : The improvement of commercial avionics, in terms of efficiency, cost and environmental impact for a world where fast and safe transportation is a means of information, knowledge and cultural exchange rather than a privilege.